International Journal of Antennas and Propagation

Advances in Antenna Array Processing for Radar

Guest Editors: Hang Hu, Ulrich Nickel, and Krzysztof Kulpa

Advances in Antenna Array Processing for Radar

International Journal of Antennas and Propagation

Advances in Antenna Array Processing for Radar

Guest Editors: Hang Hu, Ulrich Nickel, and Krzysztof Kulpa

Editorial Board

Contents

Hindawi Publishing Corporation
International Journal of Antennas and Propagation
Volume 2013, Article ID 416096, 2 pages
http://dx.doi.org/10.1155/2013/416096

Editorial

Advances in Antenna Array Processing for Radar

Hang Hu,[1] Ulrich Nickel,[2] and Krzysztof Kulpa[3]

[1] *Institute of Electronics and Information Engineering, Harbin Institute of Technology, Harbin 150001, China*
[2] *Fraunhofer Research Institute for Communication, Information Processing and Ergonomics (FKIE), 53343 Wachtberg, Germany*
[3] *Institute of Electronic Systems, Warsaw University of Technology, 00-665 Warsaw, Poland*

Correspondence should be addressed to Hang Hu; huhang@hit.edu.cn

Received 21 November 2013; Accepted 21 November 2013

Array processing is classically not considered as an antenna topic but more as a signal processing topic. So why did we publish a special issue on this topic for this journal? Today, with modern array antennas, the separation between the antenna and signal processing worlds becomes more and more obsolete. Printed antennas are often designed as arrays that are summed in an analog manner, which is already (analog) array processing. The flexibility that digital processing provides leads antenna engineers to design array antennas with digital summation of the element antennas. But with a digital array antenna all the possibilities of array signal processing are realizable which creates a broad scope for antenna design. This special issue is intended to provide the antenna community with a flavor of the multiple options that antenna array processing offers. This issue cannot cover the complete bandwidth of topics in radar antenna array processing as this would fill many textbooks and is a continuing process. But we hope that we can give some inspiration of what is possible.

Antenna arrays for radar systems, communication, and sonar installations are now an established technology. However, there are close links between the array and the different algorithms and techniques which are often not recognized. To fully exploit the advantages of array techniques it is necessary to account for these interrelations in the system design.

Ideally digital processing of array data should be done as close to the element as possible, if this is possible given the size, weight, and cost of the hardware. As a cost effective compromise hardwired analog summation of subarrays can be used to reduce cost and weight. This has created a realm of possibilities for building array hardware structures and for multichannel processing schemes. Examples are not only many algorithms of nonlinear wave parameter estimation and adaptive interference suppression but also array configurations with sparse arrays and various types of subarrays. These configurations constitute special solutions of a hardware compromise between analog and digital processing. Furthermore, we have sophisticated processing methods involving higher order statistics and methods of compressed sensing, which both lead to virtual arrays of larger size and potentially better resolution properties. And finally, one can combine spatial and temporal processing (in particular space-time adaptive processing, STAP).

The purpose of this special issue is to bring together these antenna and processing related aspects, linking the theoretical possibilities with the operational aspects and hardware constraints. From the manifold submissions we have selected 18 interesting papers. Starting with a tutorial on achievements and challenges of array processing (U. Nickel) the papers then cover topics of array optimization and adaptive processing for thinned arrays and subarrayed arrays (P. Lombardo et al.), array configuration and adaptive interference cancellation for passive radar (M. Villano et al.).

Array design and array processing for multichannel input/multichannel output radar (MIMO radar) systems are a fascinating extension of array technology exploiting spatial diversity. We have two papers that consider this technique, that is, detection in compound-Gaussian clutter with hybrid MIMO (J. C. Ding et al.) and direction finding for bistatic MIMO with circular array (Y. H. Cao et al.). Space-time array processing (STAP) is another powerful extension of classical spatial array processing. We have contributions on

deterministic aided STAP detection (J. F. Degurse et al.), clutter suppression using cross beam (Y. L. Wang et al.), superresolution using adaptive incremental multiparameter estimator (Z. B. Wang et al.), and applications of STAP in the exciting field of surface wave radar (X. Zhang et al. and Y. J. Li et al.). A special case of STAP with a topical application is synthetic aperture radar (SAR). There are three papers that consider exemplary problems of this kind, that is, phase pattern calibration (M. Bachmann et al.), SAR in the presence of dictionary mismatch (A. S. Khwaja et al.), and in-flight antenna pattern characterization (G. C. Alfonzo et al.). And finally we have a number of papers that present novel ideas and extensions like parallel factor analysis (PARAFAC) for passive localization (J. Chen et al.), spectrum sensing under cognitive radar (M. S. Shbat et al.), transmit virtual aperture array for through the wall imaging radar (B. Y. Lu et al.), tracking compensation for phased array radar (J. Mar et al.) and operating frequency selection for high-frequency (HF) radar (S. Y. Yang et al.) that are made possible with array antennas.

We would like to thank all authors for their highly professional contributions and the reviewers for their time and effort. We hope that this collection of papers will activate the curiosity of the readers about these exciting new ideas. At least we hope that you will enjoy the compilation of such a broad and rich variety of ideas.

Hang Hu
Ulrich Nickel
Krzysztof Kulpa

Hindawi Publishing Corporation
International Journal of Antennas and Propagation
Volume 2013, Article ID 206173, 13 pages
http://dx.doi.org/10.1155/2013/206173

Research Article

Planar Thinned Arrays: Optimization and Subarray Based Adaptive Processing

P. Lombardo,[1] R. Cardinali,[2] M. Bucciarelli,[1] D. Pastina,[1] and A. Farina[3]

[1] *Department DIET, University of Rome "La Sapienza", Via Eudossiana 18, 00184 Rome, Italy*
[2] *Consorzio SESM, Via Tiburtina 1238, 00131 Rome, Italy*
[3] *Selex ES, A Finmeccanica Company, Via Tiburtina Km 12.400, 00131 Rome, Italy*

Correspondence should be addressed to M. Bucciarelli; mbucciarelli@infocom.uniroma1.it

Received 5 April 2013; Accepted 13 October 2013

Academic Editor: Ulrich Nickel

A new approach is presented for the optimized design of a planar thinned array; the proposed strategy works with single antenna elements or with small sets of different subarray types, properly located on a planar surface. The optimization approach is based on the maximization of an objective function accounting for side lobe level and considering a fixed number of active elements/subarrays. The proposed technique is suitable for different shapes of the desired output array, allowing the achievement of the desired directivity properties on the corresponding antenna pattern. The use of subarrays with a limited number of different shapes is relevant for industrial production, which would benefit from reduced design and manufacturing costs. The resulting modularity allows scalable antenna designs for different applications. Moreover, subarrays can be arranged in a set of subapertures, each connected to an independent receiving channel. Therefore, adaptive processing techniques could be applied to cope with and mitigate clutter echoes and external electromagnetic interferences. The performance of adaptive techniques with subapertures taken from the optimized thinned array is evaluated against assigned clutter and jamming scenarios and compared to the performance achievable considering a subarray based filled array with the same number of active elements.

1. Introduction

As well known, the use of large array antennas allows obtaining patterns with good values of angular resolution. Amplitude tapering is typically used to lower the level of the side-lobes of the pattern. As a consequence usually a great number of Transmit/Receive (T/R) elements are needed, thus increasing the production cost.

Several techniques were studied in the past to reduce the number of active elements in the array with limited performance loss. Among them, thinning techniques allow to achieve low values of side-lobe level (SLL) without using amplitude tapering, thus with limited impact on the angular resolution. This is achieved when, among all the possible positions in the array, only a subset is actually occupied by T/R elements, inducing a density tapering.

Finding the best thinned array configuration is therefore the problem to be solved. The optimal result can be found only trying all the combinations of active elements among all the possible positions, but this brute approach is computationally consuming especially for large planar arrays. Therefore, several thinning techniques have been developed in the past, which can be divided in regular grid based and random location based techniques. In the first case, the possible positions form a regular grid; thinning can be performed (i) switching off several active elements depending on a statistic criterion or (ii) starting from an empty array and filling some positions according to a deterministic criterion. In the second case, T/R elements are displaced in random positions with proper statistical characteristics.

In [1] Sherman and Skolnik used an array with isotropic elements on concentric rings with different radial and angular spacing. This induces natural spatial tapering with effects on SLL depending on the uniformity of the radial spacing and on the number of allowed angular positions in each ring. In [2], Skolnik et al. proposed a technique where the spatial tapering is statistically determined, allowing a concentration of elements in the center of the array. Starting from [2], in [3]

Mailloux and Cohen studied a regular grid based thinning approach with the joint use of stepped amplitude tapering to further reduce the SLL. In [4, 5] Skolnik et al. proposed a trial-and-error technique called "Dynamic Programming," which has been devised to reduce the number of total trials with respect to the brute approach. As for the previous thinning approaches, "Dynamic Programming" is not supposed to reach the optimal array configuration. Moreover, its deterministic approach makes this technique suitable only for small arrays. More recently in [6], Keizer studied an iterative random technique, called Iterative Fourier Technique, to thin an array achieving a fixed number of active elements. The technique is based on the inverse discrete Fourier transform (IDFT) relation between the desired array pattern and the element excitations; moreover the iterative nature of this algorithm depends on the nonideal effects induced by the binary quantization of the actual element excitations.

The previous are regular grid based thinning approaches. Lo studied random location based thinning techniques in [7, 8], reaching some general and useful conclusions: for example, he stated that the number of active elements is linked with the desired SLL and that the angular resolution depends on the dimension of the resulting array and less on the elements distribution. Following the random location thinning approach, Steinberg succeeded in determining an estimate of the SLL knowing the number of elements, the dimension of the array, the wavelength, the steering direction of the pattern, and the frequency bandwidth of the signal, [9, 10]. Moreover, in [11] Steinberg and Attia used position and frequency diversity to reduce the SLL without impact on the main lobe of the pattern.

Also statistic global optimization algorithms have been applied to the problem of regular grid based thinning, where the objective function can be related to the SLL. Genetic algorithms [12–15] are well suited since the binary representation of the genes directly refers to the presence (1) or the absence (0) of an active element in the array. In [16], a genetic algorithm is used not to determine which element is active in the array but to determine the spacing of concentric rings according to Cantor sets where active elements should be placed, extending the original approach in [1]. In [17], a nested optimization algorithm integrating genetic algorithm and linear or quadratic programming is introduced to find the thinned array with the minimum number of active elements, whose excitations allow the achievement of a pattern with desired characteristics (such as minimum SLL or prescribed gain in a specific direction). Ant colony algorithm in [18] emulates the behavior of ants to determine the best thinned array configuration, based on the identification of the shortest path from nest to food. Here, the food is the desired SLL, the path is the set of active elements in the array, and the length is a figure of merit concerning the probability for an ant to pass from one node to another in the path that is the probability of an element in the array to be active. A Boolean version of the differential evolution algorithm is applied in [19], to cope with discrete-variable optimization problem. Also simulated annealing [20, 21] has been used to select simultaneously the active elements positions and weighting coefficient to reach the best SLL possible. Finally, particle swarm optimization has been proposed in [22] to cope with antenna design applications: in particular, the continuous and binary versions can be used to synthesize aperiodic or thinned arrays respectively, based on the minimum SLL criterion in the single-objective case or on a number of desired features of the antenna pattern in the multiobjective case.

In this paper, we consider two main issues: (i) the optimized design of planar thinned arrays at element or subarray level and (ii) the identification of suitable strategies to split the thinned array in multiple subapertures, adequate for the application of adaptive processing techniques for jammer cancellation.

The first issue addresses the practical problem of obtaining planar thinned arrays by disposing a certain number of active elements on a given planar surface. It is well known that good results can be obtained by randomly thinning the aperture and using irregular subarray configurations [23], but the absence of symmetry in the array structure strongly affect the design and production costs. Therefore, we aim at identifying thinned array structures with good performance in terms of SLL at the same time choosing the used subarrays from a limited number of different types. Subarray based thinning reduces the degrees of freedom in the array thus degrading the performance: therefore, suitable design approaches have to be identified to obtain good performance despite the constraints.

To this purpose we present two new statistical design techniques called sequential probabilistic element disposal (SPED) and sequential probabilistic subarray disposal (SPSD [24]), respectively. In our approach, the number of elements actually present in the array is fixed. Starting from the concepts in [1, 2], the proposed statistical approach does not decide whether or not to introduce a single element/subarray, but it selects the position inside the array that the new element/subarray should occupy. This is done according to a probability density function (PDF) derived from an amplitude tapering function favoring central positions with respect to the edges. This should correspond to a density tapering of the array and therefore results in an increased SLL. Moreover, starting from these two basic techniques, to improve efficiency and practical feasibility, several modified versions are also developed. The first modified version is based on the observation that there is a high probability of filling the central part of the array with active elements/subarrays. Therefore, a constrained version of SPED and SPSD is derived, where all the positions belonging to the center of the array (properly identified) are filled and the statistical procedure follows to reach the desired number of active elements. The second modified version is motivated by the observation that the use of larger subarrays is useful in terms of production costs but tends to degrade the thinned array performance unless high number of subarray types is considered. To avoid the use of SPSD with a large number of subarray types, we devise the wide subarray forcing (WFS) procedure; merging small adjacent subarrays allows obtaining an exponentially higher number of available types of larger subarrays, among which only a subset is considered valid. The performance analysis of the devised optimization

techniques shows that it is possible to design planar thinned arrays with assigned desired performance in terms of SLL. Moreover this analysis proves that the obtained thinned arrays are effective in lowering the SLL with limited impacts on the main lobe aperture of the corresponding pattern, in contrast with what would be obtained by considering filled arrays with the same number of active elements.

The second issue aims at verifying the feasibility of adaptive processing on a subarray based thinned aperture to mitigate either clutter or interferences. We identify suitable subaperture structures for the application of electronic counter-counter measures (ECCM) techniques. The performance analysis against simulated interference and clutter scenarios shows the quality of the obtained results.

The paper is organized as follows. Section 2 introduces the array structure model; Section 3 describes the optimization techniques to obtain element and subarray based thinned antennas with the desired characteristics. Section 4 shows some examples of thinned arrays obtained using the proposed design techniques, while Section 5 compares the performance of adaptive techniques applied to both thinned and filled arrays against jammer and clutter. Finally, we draw our conclusions in Section 6.

2. Array Structure Model

In order to develop the design techniques of a thinned planar array, we start from a filled array, containing $M \times N$ isotropic elements disposed on the intersections of a regular $M \times N$ grid.

Thinning consists in considering only a number N_A of active elements, over a total number of possible positions on the array $N_{\text{POS}} = MN$. Therefore, the thinning factor can be defined as

$$\eta = \frac{N_{\text{POS}}}{N_A}. \tag{1}$$

The procedure of thinning the array can be regarded as a transformation applied to the received signal vector at the element level, namely, to the $N_{\text{POS}} \times 1$ vector $\mathbf{x}_{\text{el}}$

$$\mathbf{x}_{\text{el}}(\theta, \varphi) = a \cdot \mathbf{s}_{\text{el}}(\theta, \varphi) + \mathbf{d}_{\text{el}}, \tag{2}$$

where $\mathbf{s}_{\text{el}}$ is target steering vector, a and (θ, φ) represent, respectively, the complex amplitude of the useful signal and its direction of arrival (DOA) angles in elevation and azimuth. We also define $\mathbf{d}_{\text{el}}$ as the disturbance signal (jammer plus noise) $N_{\text{POS}} \times 1$ vector and its $N_{\text{POS}} \times N_{\text{POS}}$ disturbance covariance matrix $\mathbf{M}_{\text{el}}$.

The steering and thinning procedure introduces a transformation applied on the received signal vector $\mathbf{x}_{\text{el}}(\theta, \varphi)$ that can be represented by the transformation matrix $\mathbf{T}_{\text{el}}$. Define the $N_{\text{POS}} \times N_{\text{POS}}$ matrix $\mathbf{S} = \text{diag}\{\mathbf{s}_{\text{el}}(\theta_0, \varphi_0)\}$ for steering purpose and the $N_{\text{POS}} \times N_A$ matrix $\mathbf{U}$, which selects the active elements in the array, for thinning. Thus, the global transformation is described by the $N_{\text{POS}} \times N_A$ matrix $\mathbf{T}_{\text{el}} = \mathbf{S} \cdot \mathbf{U}$. At element level, the $N_A \times 1$ received signal vector and the $N_A \times N_A$ disturbance covariance matrix will be given, respectively, by $\mathbf{x}(\theta, \varphi) = \mathbf{T}_{\text{el}}^H \mathbf{x}_{\text{el}}(\theta, \varphi)$ and $\mathbf{M} = \mathbf{T}_{\text{el}}^H \mathbf{M}_{\text{el}} \mathbf{T}_{\text{el}}$.

To generate subarray based thinned aperture, it is necessary to define also the shape, the size, and the orientation of the single subarray, as well as the grid of subarray centers. This grid has to be defined so that if we place a subarray on each element of the grid a full filling of the array area is obtained (i.e., absence of gaps).

In this case, the thinning procedure is described by a transformation of the received signal vector $\mathbf{x}_{\text{el}}(\theta, \varphi)$ in the $N_{\text{SUB}} \times 1$ thinned subarray vector $\mathbf{x}(\theta, \varphi)$. This is achieved considering the transformation matrix $\mathbf{T}_{\text{SUB}} = \mathbf{S} \cdot \mathbf{U} \cdot \mathbf{T}$, where $\mathbf{T}$ is a $N_A \times N_{\text{SUB}}$ transformation matrix which arranges N_A active elements in N_{SUB} subarrays. At subarray level, the $N_{\text{SUB}} \times 1$ received signal vector and the $N_{\text{SUB}} \times N_{\text{SUB}}$ disturbance covariance matrix will be given, respectively, by $\mathbf{x}(\theta, \varphi) = \mathbf{T}_{\text{SUB}}^H \mathbf{x}_{\text{el}}(\theta, \varphi)$ and $\mathbf{M} = \mathbf{T}_{\text{SUB}}^H \mathbf{M}_{\text{el}} \mathbf{T}_{\text{SUB}}$.

3. Thinned Array Design

The statistical technique for the thinned array generation described in [1, 2] starts from the conventional density tapering of the array elements. The single radiating element is introduced with a probability proportional to its weight depending on a given amplitude tapering function. This is effective in obtaining a set of thinned arrays with SLL close (in the average) to the level achievable by applying the selected amplitude tapering function to the corresponding filled array. Unfortunately this optimization algorithm does not allow setting a priori the number of active elements in the array and it does not cope with subarray based arrays.

To cope with these undesired features we introduce here two new techniques that we call Sequential Probabilistic Element Disposal (SPED) and sequential probabilistic subarray disposal (SPSD) for the design of a thinned antenna at element and subarray level, respectively. SPED and SPSD are still statistical approaches but properly modified to allow the design of the thinned array with a preassigned number of elements.

3.1. Sequential Probabilistic Element Disposal (SPED) Technique. The SPED technique is described in Figure 1. It uses the general scheme of Figure 1(a), with the single trial step described in Figure 1(b). Firstly, the set of possible positions is assigned and the counter and the minimum SLL are initialized (i.e., IND = 0 and $\text{SLL}_{\text{MIN}} = 0\,\text{dB}$). Then, the single trial of the technique follows. The first step of the single trial of the technique initializes the probability $p_1(j_k)$, $k = 1, 2, \ldots, N_{\text{POS}}$, to introduce an active element in the position j_k and the counter $m = 1$. Specifically, the probability $p_1(j_k)$ depends on a reference amplitude tapering $\mathbf{w} = [w_1, \ldots, w_{N_{\text{POS}}}]^T$ as follows:

$$p_1(j_k) = \frac{w_k}{\sum_{n=1}^{N_{\text{POS}}} w_n}, \quad k = 1, \ldots, N_{\text{POS}}. \tag{3}$$

In each iteration of the SPED, a realization i_m is extracted from the set of possible active element positions j_k, $k = 1, \ldots, N_{\text{POS}}$, with probabilities $p_m(j_k)$. A new element is inserted in position (i_m) and the active elements position vector $\mathbf{i} = [\mathbf{i}, i_m]$ is updated.

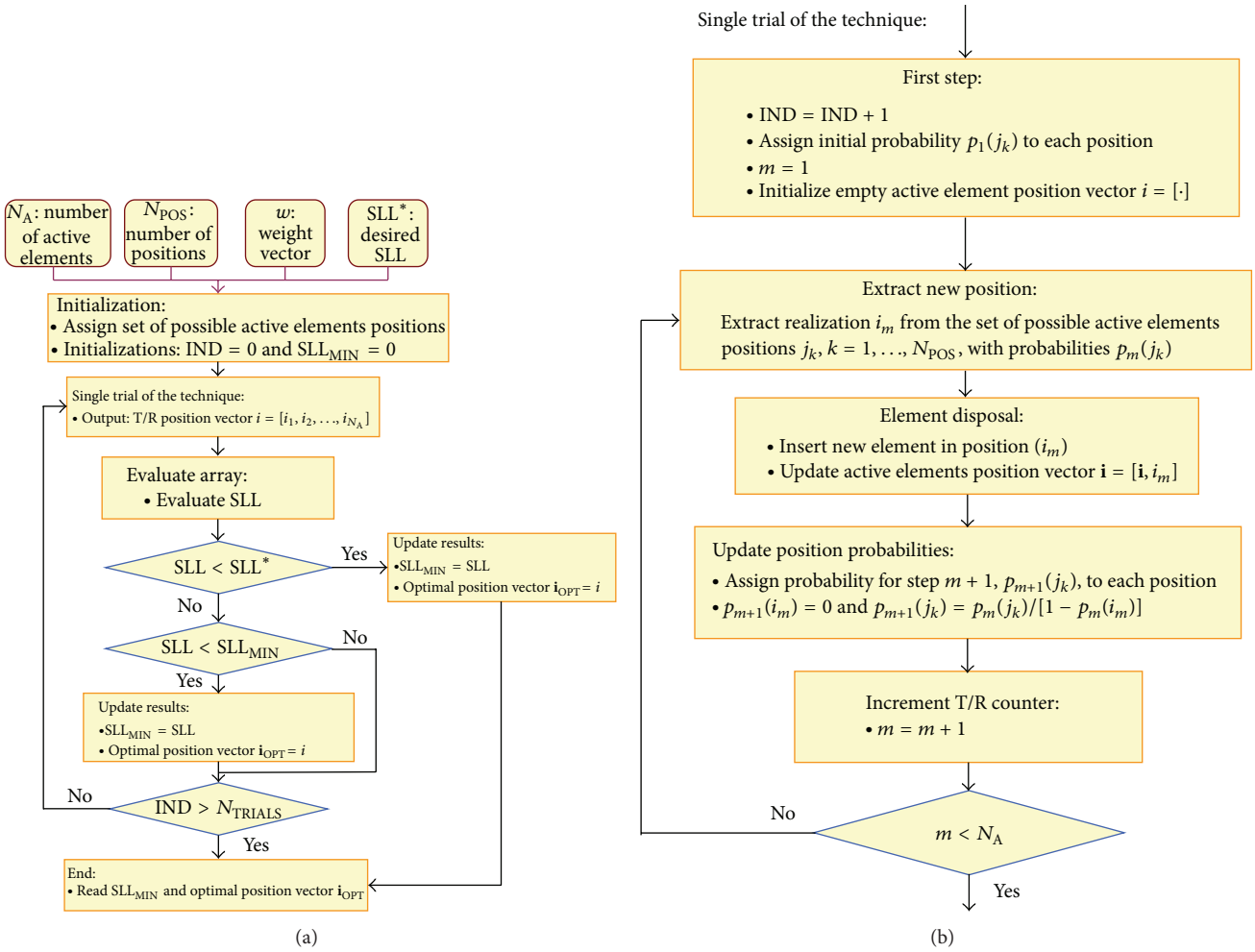

FIGURE 1: (a) SPED technique outer scheme (b) SPED single trial (inner block).

Then, the probabilities to assign each position are updated as follows:

$$p_{m+1}(i_m) = 0$$
$$p_{m+1}(j_k) = \frac{p_m(j_k)}{(1 - p_m(i_m))}. \quad (4)$$

When the desired number of active elements is introduced in the array (i.e., $m > N_A$), the single trial is complete.

The output of the single trial of the SPED is a thinned array; therefore, the SLL can be evaluated. If it is lower than the desired value SLL* the algorithm stops; otherwise, the SPED continues with the next trials. Anyway, a maximum number of allowed trials N_{TRIALS} is defined: in case the desired SLL* is not achieved, the algorithm stops when N_{TRIALS} have been executed. In such a case the output is given by the best achieved result represented by the vector of optimum positions $\mathbf{i}_{OPT}$ providing the lowest SLL_{MIN}.

The novelty introduced by the SPED is that the statistical approach is not used to decide whether or not to introduce a single element but to select the position inside the array that the new element should occupy. In this manner, the number of elements in the array is fixed and it is deterministically set by the thinning factor. This is different from thinning using dynamic programming [4, 5], where a deterministic approach is used to test all the possible insertions of an active element, including a pruning strategy to reduce the number of trials.

3.2. Sequential Probabilistic Subarray Disposal (SPSD) Technique. The "random" displacement of the active elements in the array, while guaranteeing an improvement of SLL, is a critical point in terms of ease and cost of design and manufacturing. A regular structure would be more convenient and would allow the scalability of the antenna design in relation to specific applications. As a trade-off between these two aspects, the thinned array can be designed based on subarrays; indeed keeping small the number of different subarray shapes and sizes is relevant for industrial production, to reduce design and manufacturing costs, as well as to allow scalable antenna designs.

A subarray is formed by several antenna elements and has to be considered as the basic tile of the array. When thinning is involved in the design step, the position of the entire subarray has to be set in lieu of the single active element. Moreover,

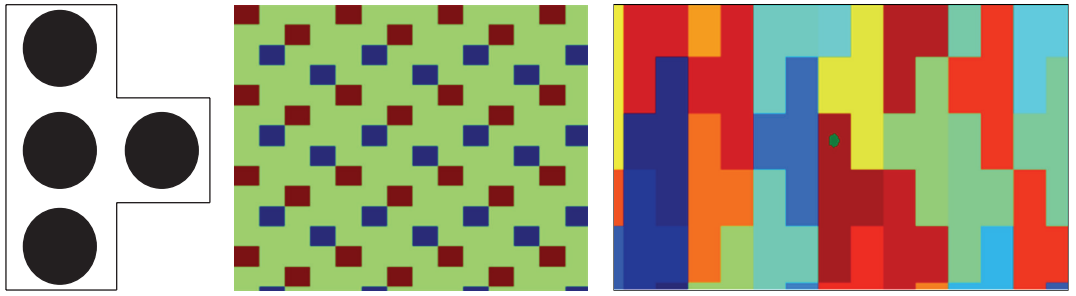

(a) (b) (c)

FIGURE 2: Example of (a) subarray, (b) grid of subarray centers, and (c) possible subarray displacement.

if subarrays with different shape and size are available, also the type of subarray to be filled in the array has to be decided.

To design a thinned array based on subarrays, a modified version of the SPED is here introduced called SPSD. The SPSD technique operates as follows. The first step involves the selection of the subarray shape and size D (as an example Figure 2(a) shows a triangular subarray with $D = 4$), as well as the subarray center and its original orientation. Moreover, it is necessary to define a grid containing all the possible positions $N_{\text{POS-SUB}}$ for the subarray centers (e.g., Figure 2(b)). Each subarray can be inserted with different orientations (Figure 2(b), red: original orientation and blue: rotation of 180°) starting from the center of the grid, to completely cover the array without overlapping (Figure 2(c)).

Thereafter, the N_{SUB} subarrays are sequentially introduced in a position that is randomly selected, in accordance with the weight corresponding to an assigned reference taper function. Specifically, we generalize the SPED procedure to cope with the subarray case. The technique is described in Figure 3(a), with the single trial described in Figure 3(b).

The first step of the single trial initializes the probability $p_1(j_k)$, $k = 1, 2, \ldots, N_{\text{POS-SUB}}$, to introduce a subarray in the position j_k and the counter $m = 1$.

Specifically, the probability $p_1(j_k)$ depends on reference amplitude tapering $\mathbf{w} = [w_1, \ldots, w_{N_{\text{POS-SUB}}}]^T$ as follows:

$$p_1(j_k) = \frac{w_k}{\sum_{n=1}^{N_{\text{POS-SUB}}} w_n} \quad k = 1, \ldots, N_{\text{POS-SUB}}. \tag{5}$$

At each iteration of the SPSD a realization i_m is extracted from the set of possible subarray positions j_k, $k = 1, \ldots, N_{\text{POS-SUB}}$, with probabilities $p_m(j_k)$. A new subarray is inserted in position (i_m) and the subarray position vector $\mathbf{i} = [\mathbf{i}, i_m]$ is updated.

Then, the probabilities to assign each position are updated as follows:

$$\begin{aligned} p_{m+1}(i_m) &= 0, \\ p_{m+1}(j_k) &= \frac{p_m(j_k)}{(1 - p_m(i_m))}. \end{aligned} \tag{6}$$

When the desired number of fully active subarrays N_{SUB} (and thus active elements N_A) is introduced in the array, the single trial is complete. Note that if both fully active and thinned subarrays are available, when a realization i_m is extracted the algorithm needs to decide what kind of subarray has to be inserted in the array. Again, this can be done using a statistical approach that promotes the selection of a fully active subarray near the center of the array or of a thinned subarray near the edge.

The same stop condition of the SPED technique applies also to SPSD.

3.3. Strategies for Elements/Subarrays Sorting. Equations (3) and (5) associate a certain amplitude weight and therefore a corresponding probability to a specific position in the array. The basic rules of this association, based on the sorting of all the possible positions in the array, are important in adapting the SPED and SPSD algorithms to different kinds of planar arrays and therefore to different directivity characteristics of the corresponding antenna pattern.

First of all consider a circular array; in this case, according to [1, 2], a sorting of all the possible positions based on the radial distance from the center of the array is adequate, due to the particular symmetry (Figure 4(a): dark red subarrays are the farthest from the center). In this way, positions near to the center should benefit of a higher probability than the side positions, according to the characteristics of the amplitude tapering functions. Tie situations can be solved using the angular displacement of each position with respect to a reference direction.

In a rectangular array, this ordering strategy greatly penalizes the farthest elements outside a circular region around the array center. To this purpose, instead of sorting the positions according to concentric circles, it is more appropriate to sort them in concentric frames, where each frame is characterized by the same ratio between the greatest and the smallest dimensions of the array (Figure 4(b): dark red subarrays belong to the outer frame). Positions are therefore ordered first of all according to the frame (from the inner to the outer). Positions belonging to the same frame are then sorted according to the distance from the center of the array: positions in the same frame and at the same distance are finally ordered using the angle between the position and a reference direction.

Obviously SPED and SPSD techniques can also be used jointly with other sorting strategies; moreover, array shapes

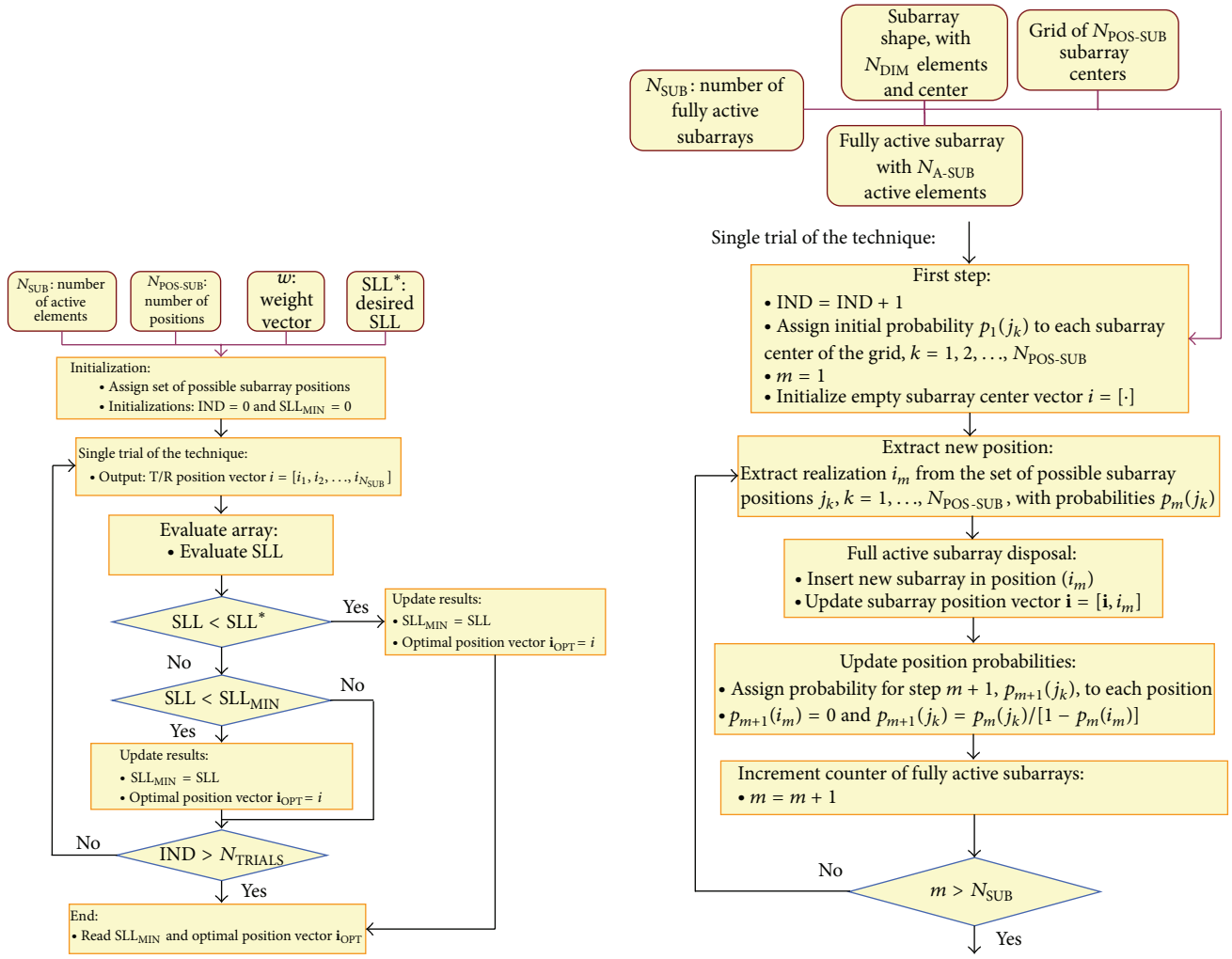

Figure 3: (a) General statistical technique outer scheme (b) SPSD single trial (inner block).

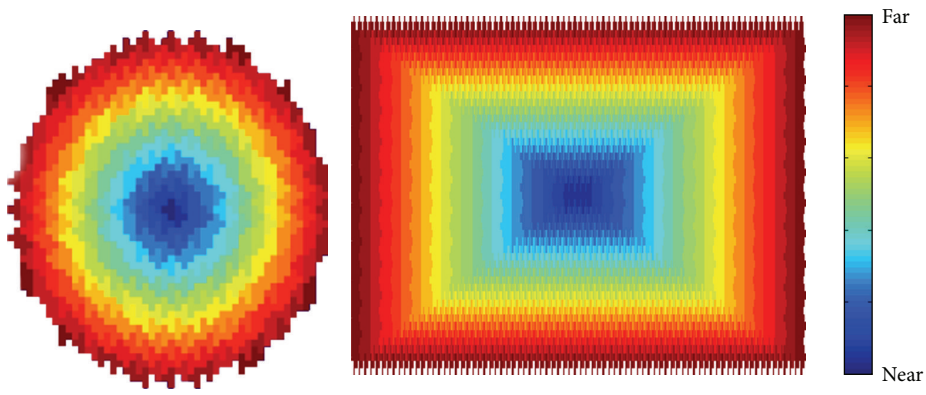

Figure 4: Subarray sorting approach for (a) circular and (b) rectangular arrays.

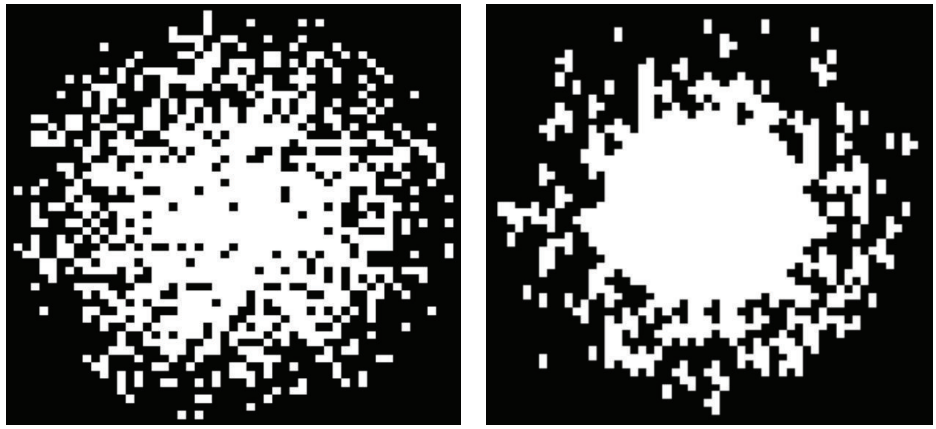

(a) (b)

Figure 5: Circular thinned array with (a) SPED and (b) Constrained SPSD.

different from circular and rectangular could also be considered. Such flexibility of the proposed techniques is well suited for the achievement of a thinned array able to fulfill the requirements not only relative to the SLL (that depends on the displacement of the active elements) but also on the directivity of the achievable pattern (which is more sensitive to the maximum distance between active elements in the array).

3.4. Improving SPED/SPSD Efficiency and Practical Feasibility. Since SPED and SPSD are statistical approaches that use a PDF achieved from an amplitude tapering function, it is straightforward to expect best results in terms of SLL when active elements fill the central area of the array. Following this observation, we propose a modified version of the SPED/SPSD techniques, named Constrained SPED/SPSD, which starts by filling the central part of the array (with proper dimension). In this way the statistical procedure is applied only to the remaining elements to reach the desired number of active elements. This approach guarantees that only configurations with "reasonably good" SLL are generated and makes the algorithm faster than the initial SPED/SPSD.

As it will be clear in the following section, good SLL results can be reasonably obtained by the SPSD and by the Constrained SPSD, when using subarrays with a small size. Large subarrays are preferable in terms of design and production costs but tend to degrade the thinned array performance, in terms of achievable SLL. This degradation can be partially mitigated by using multiple types of subarray, which also allows a reasonable convergence. However, a considerable increase of the number of subarray types is not a desirable condition. Therefore, a trade-off is needed between the achievement of the desired performance and the cost avoidance. To this aim, we propose a further approach that allows us to obtain a thinned array based on a set of wider subarrays, starting from the thinned array provided in output by SPSD based on smaller subarrays.

Wider subarrays can be obtained by merging adjacent smaller subarrays, thus considerably increasing the number of available larger subarrays types. The wide subarray forcing (WSF) technique allows reducing this number, by operating as follows:

(i) adjacent small subarrays in the original thinned array are merged;

(ii) among all the possible large subarrays, achievable when merging all used small subarrays, a valid sub-set is defined, that is, containing the more frequent large subarrays in the merged thinned array;

(iii) for each larger subarray in the merged thinned array, we measure the Hamming distance for all selected subarray types. (The Hamming distance between two subarrays is the number of positions where they differ in terms of active elements). Now, we have two possibilities: (a) to replace the merged subarray with the one with closer measure, or (b) to randomly replace it with one of the selected subarray types, with a probability inversely proportional to their distance measure. Next section provides an example of this procedure.

4. Performance Analysis

In this section, we discuss the design of thinned arrays with a SLL better than −23 dB. We consider both the cases of a circular array (with $N_A = 1024$) and a rectangular array (with $N_A = 2500$). Section 4.1 presents the results of the design techniques while Section 4.2 compares the performance of the achieved thinned arrays to those of the corresponding filled arrays.

4.1. Design Examples. For the circular case, the output thinned array resulting from SPED is shown in Figure 5(a); in particular, this result has been obtained staring from an array with $N_{\text{POS}} = 2121$ positions: the designed one has $N_A = 1024$ active elements and assures an SLL = −24.93 dB. As it is apparent in Figure 5(a), the central disk of the array is quite full, justifying the eventual use of the constrained version

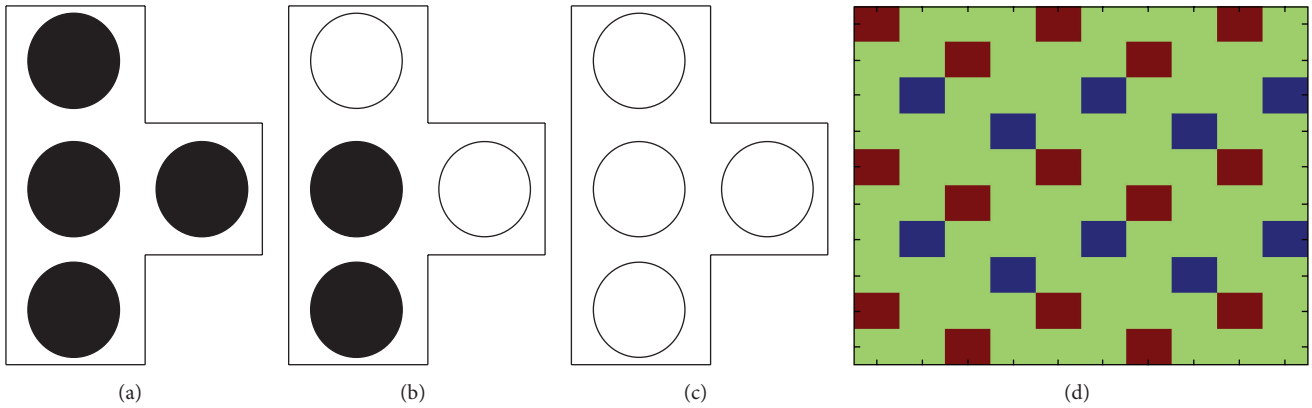

FIGURE 6: Subarray type of size 4 (a) fully active, (b) thinned for SPSD, and (c) grid of centers scheme.

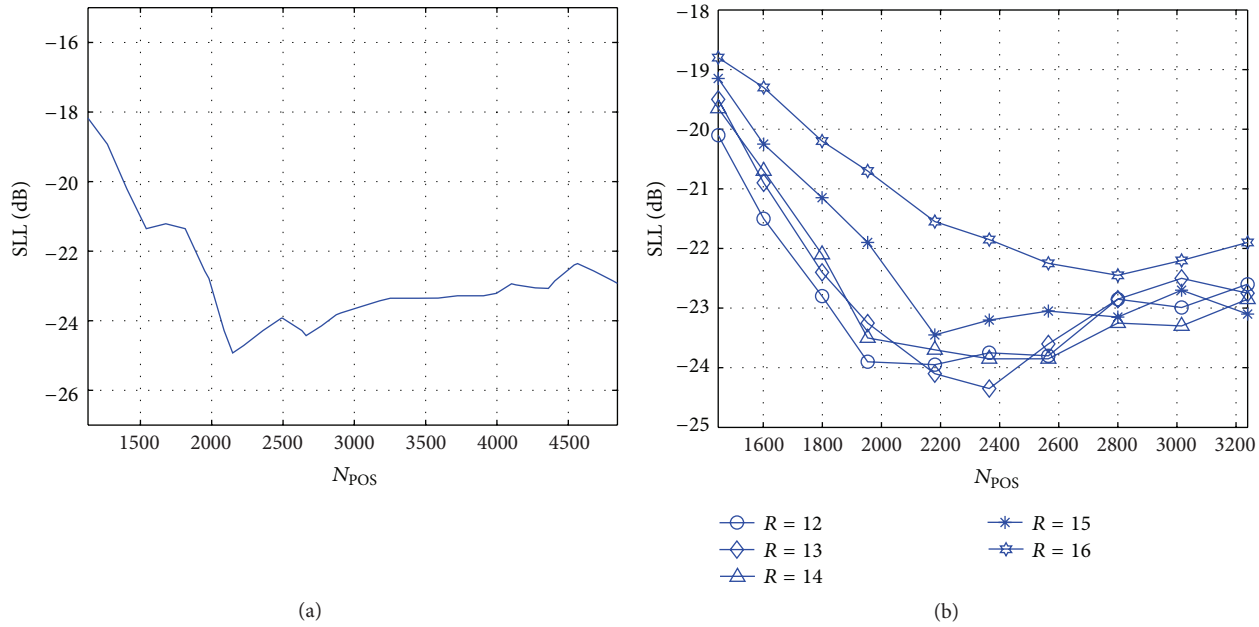

FIGURE 7: SLL for different N_{POS} for (a) SPED and (b) Constrained SPSD varying with radius R.

of the algorithm. Figure 7(a) shows the best SLL provided by SPED technique when varying the number of possible positions N_{POS} (namely varying the size of the array) and keeping fixed the number of active elements. This figure highlights the dependence of the achievable performance on the thinning factor: the minimum value is reached in correspondence of the thinned array shown in Figure 5(a), therefore with $\eta = 2021/1024 = 2.07$.

Figure 5(b) shows the output of the Constrained SPSD using three kinds of subarrays of size 4 (Figures 6(a), 6(b), and 6(c)): one fully active, the second one thinned with two active elements, and the third one empty, the latter being inserted when a position is not selected. Moreover, a suitable grid of centers is defined (a zoom of the central part in Figure 6(d)) and different values of the radius R (normalized to the inter-element distance) of the constrained inner circle are considered. The SLLs reported in Figure 7 are obtained again while varying N_{POS} and keeping fixed $N_A = 1024$. As it is apparent also in this case the best results are achieved with a thinning factor near 2. Figure 5(b) reports the achieved array configuration that yields a SLL of −24.35 dB, occurring for $R = 13$. It appears that the combined use of two different types of subarrays and the constrained full center allows almost the same SLL of the SPED.

To show the results achievable by the WSF technique, introduced in the previous section, we start from subarrays of small size. To optimize the result, we use appropriate suitable grid of centers (Figure 8) and set a filled inner circle radius R of 14 elements. Starting with the subarrays with size $D = 4$ shown in Figure 6, we first obtain the thinned array of Figure 9(a). All the possible subarrays of size 8 achievable by merging adjacent smaller subarrays are shown in Figure 10. By applying the WSF technique, only subarrays from 1 to 4 are considered acceptable and we obtain the thinned array

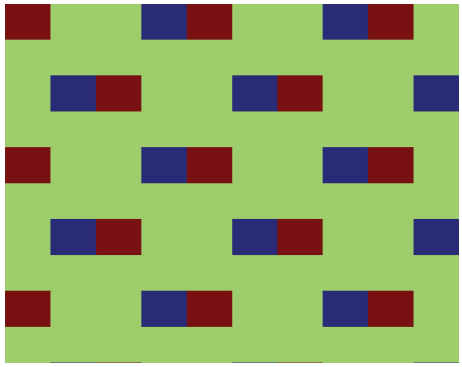

Figure 8: Used grid of centers.

Table 1: Comparison between thinned and filled arrays.

Scheme	Taper	
Circular thinned array ($N_A = 1024$)	No tapering	SLL = −24 dB
Circular filled array ($N_A = 1024$)	No tapering	SLL = −17 dB
Circular filled array ($N_A = 1024$)	Tapering	SLL = −24 dB
Rectangular thinned array ($N_A = 2500$)	No tapering	SLL = −23 dB
Rectangular filled array ($N_A = 2500$)	No tapering	SLL = −13 dB
Rectangular filled array ($N_A = 2500$)	Tapering	SLL = −23 dB

of Figure 9(b). Both the thinned arrays have a SLL of nearly −24.3 dB.

Similar results could be shown also for the rectangular case. As an example, the output of the constrained SPSD technique is shown in Figure 11. By using a thinning ratio $\eta = 2.7$ and constraining a full center of 343 fully active subarrays a SLL of −23.17 dB is achieved.

4.2. Comparison between Thinned and Filled Arrays. The cir- cular and rectangular thinned arrays in Figure 5(b) and Figure 11 are compared with the corresponding filled arrays, with the same number of active elements. In Table 1, we report the array characteristics.

Circular and rectangular filled arrays provide a pattern with a SLL of about −17 dB and −13 dB, respectively. To achieve the same SLL of the thinned array, a taper function must be applied so that the main lobe widens. The use of the thinned array is therefore effective in achieving the improved SLL with reduced effects on the main lobe width. This is apparent from Figures 12 and 13 where the main lobe width is reported for both thinned and filled arrays, for the circular and the rectangular arrays, respectively, being the u and v axes defined as follows:

$$u = \cos(\theta)\cos(\varphi) \qquad v = \cos(\theta)\sin(\varphi). \tag{7}$$

5. Adaptive Techniques for SPSD Based Thinned Arrays

If multiple receiving channels are available, connected to different antenna apertures, multi-channel adaptive techniques can be exploited to mitigate the effect of electromagnetic interferences and clutter returns for the thinned array. Consider the design of the subapertures to be connected to the independent receiving channels. With Constrained SPSD, we observe that the inner part of the array is always filled: this part presumably yields a nice main beam, with a slight increase of the beam width with respect to the one achieved if using the entire antenna. This central part can be connected to the main channel, while the external subarrays or groups of them can be eventually connected to a few auxiliary channels for a side-lobe canceller scheme, as shown in Figure 14.

Two different adaptive cancellation filters are applied. They are forced to achieve the quiescent design pattern in the absence of interference. The filters are mismatched optimum detector (MOD) filter [25, 26] and a generalized side-lobe canceller (GSLC) filter [27, 28].

The MOD filter is based on the definition of a mismatched target vector $\mathbf{s}_T$, selected as $\mathbf{s}_T = \mathbf{M}^{(0)}\mathbf{q}$, where $\mathbf{M}^{(0)}$ is the thermal noise covariance matrix and $\mathbf{q}$ is the desired subarray weight vector when only the thermal noise is present. The optimum filter to detect $\mathbf{s}_T$ is used:

$$\mathbf{w}_{\mathrm{MOD}} = \mathbf{M}^{-1}\mathbf{s}_T, \tag{8}$$

where $\mathbf{M}$ is the covariance matrix of disturbance. In absence of jammer $\mathbf{M} = \mathbf{M}^{(0)}$ and $\mathbf{w}_{\mathrm{MOD}} = \mathbf{q}$.

The GSLC filter is based on the generation of an orthogonal space formed by the matrix $\mathbf{B}$, which selects the subarrays of the auxiliary channels. Besides, we define the vector $\mathbf{t}$ which selects the main channel. The weight vector of the GSLC filter can be expressed as follows:

$$\mathbf{w}_A = -\left(\mathbf{t}^H\mathbf{MB}\right)\cdot\left(\mathbf{B}^H\mathbf{MB}\right)^{-1}. \tag{9}$$

The performance is evaluated by considering the signal to clutter ratio (SCR), defined as the ratio between the received useful signal power and the clutter power, and the signal to disturbance ratio (SDR), defined as the ratio between the received useful signal power and the disturbance power where disturbance is the sum of the thermal noise and the jammer.

To show the performance of the proposed algorithms the circular thinned array in Figure 9(b) is considered and it is compared to several circular filled arrays, with the same number of active elements. In Table 2, we show the tested array configurations. "A" schemes refer to the thinned array obtained with Constrained SPSD and WSF: therefore amplitude tapering is not used to achieve the desired level of SLL = −24 dB. The "C" schemes refer to the filled arrays: we considered also the possibility of applying amplitude tapering (a_i coefficients in Figure 14) both in transmission (TX) and in reception (RX). In Table 2, the SLLs of the TX and RX patterns are highlighted.

The performance of the adaptive schemes against electromagnetic interference is analyzed by simulating two different

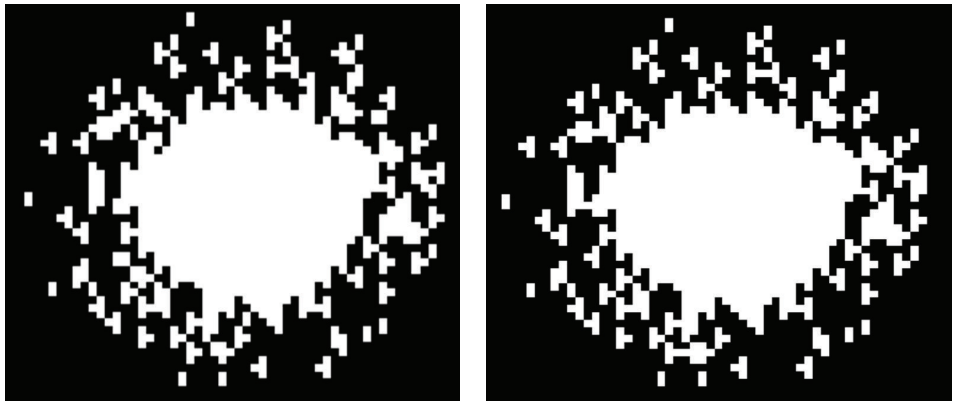

(a) (b)

Figure 9: Achieved array configuration (a) with subarray of dimension 4 and (b) with subarray of dimension 8 after WSF.

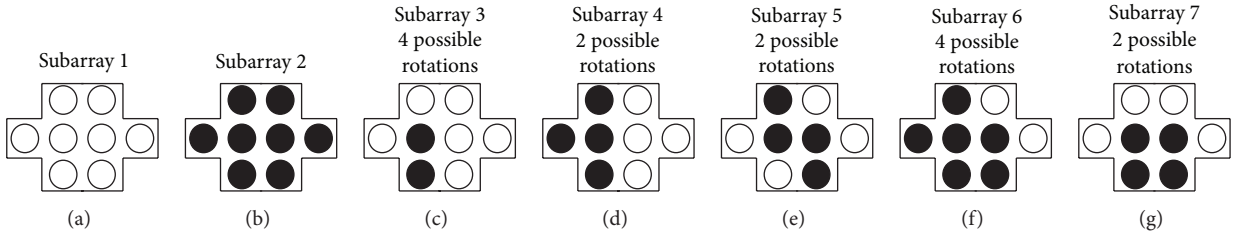

Figure 10: Possible Subarray type of size 8.

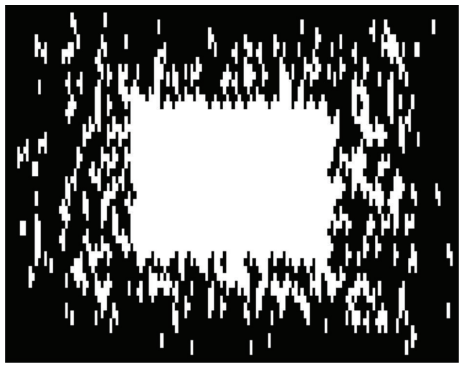

Figure 11: Rectangular thinned array using subarrays and grid of centers of Figure 6.

Table 2: TX/RX schemes.

Scheme	TX	RX
A1	No tapering (SLL = −24 dB)	No tapering (SLL = −24 dB)/MOD
A2	No tapering (SLL = −24 dB)	No tapering (SLL = −24 dB)/GSLC
C1	No tapering (SLL = −17 dB)	Tapering (SLL = −24 dB)/MOD
C2	Tapering (SLL = −24 dB)	Tapering (SLL = −24 dB)/MOD
C3	No tapering (SLL = −17 dB)	Tapering (SLL = −30 dB)/MOD

scenarios, with characteristics reported in Table 3. In the first a single jammer is considered with a variable DoA, while in the second scenario a second jammer impinges on the antenna from a fixed direction. For both jammers a Jammer to Noise Ratio (JNR) of 40 dB is considered.

Figure 15 shows the SDR as a function of the variable jammer azimuth angle obtained using the 16 outer subarrays as subapertures connected to auxiliary receiving channels and the remaining connected to the main receiving channel. The performance of the thinned arrays are comparable with the filled ones, except for the filled array with an amplitude tapering applied in transmission that lowers the transmitted power while reaching the thinned array SLL.

To evaluate the performance of the adaptive scheme against clutter returns, we simulated a scenario with the Constrained SPSD and WSF thinned antenna 20 m above earth surface, being the elevation steering angle 5°. In this case, clutter echoes are received by the first side-lobes of the antenna and the acquisition configuration could suffer from clutter since returns from the ground could share the same resolution cell of a potential target with comparable powers.

Figure 16 shows the SCR versus the target range. It is apparent that the thinned array yields better performance than the filled ones. The superiority of the thinned array against clutter is demonstrated when no attempt is made to

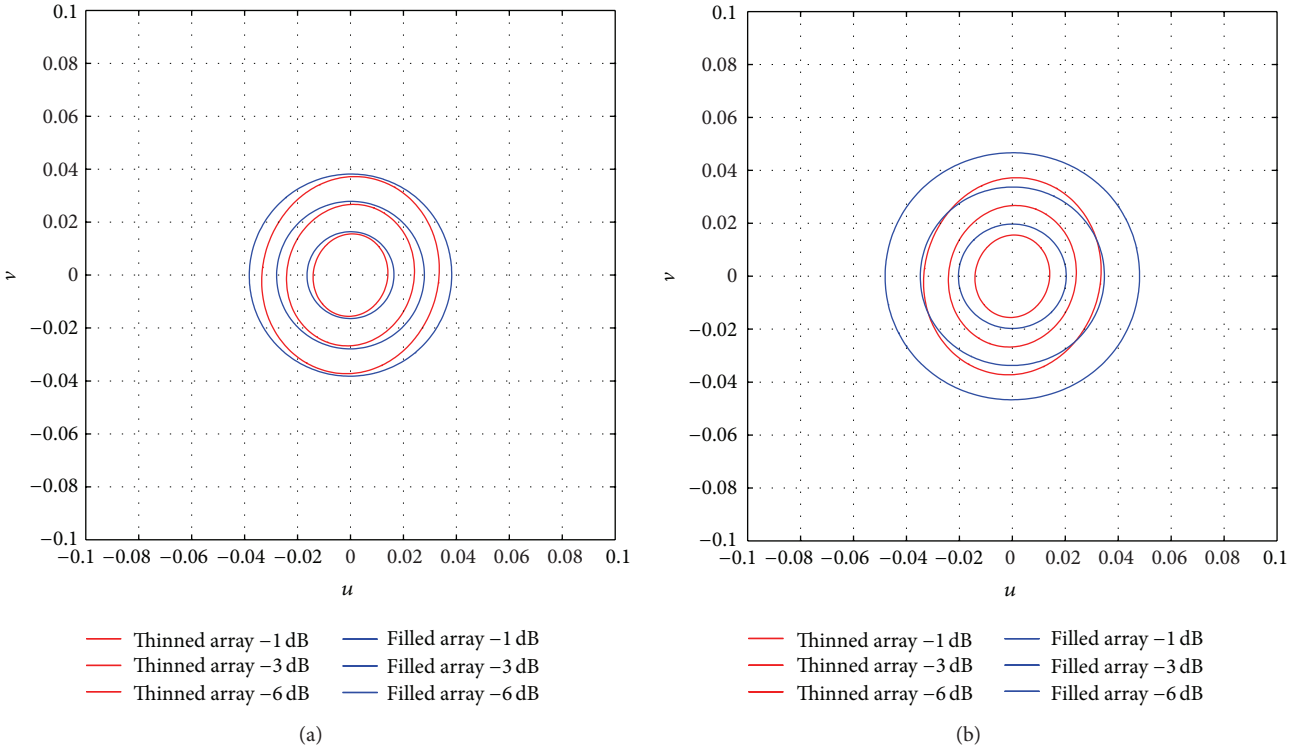

FIGURE 12: Comparison between the main lobe aperture of a thinned circular array and a filled array with the same number of active elements (a) without and (b) with amplitude tapering.

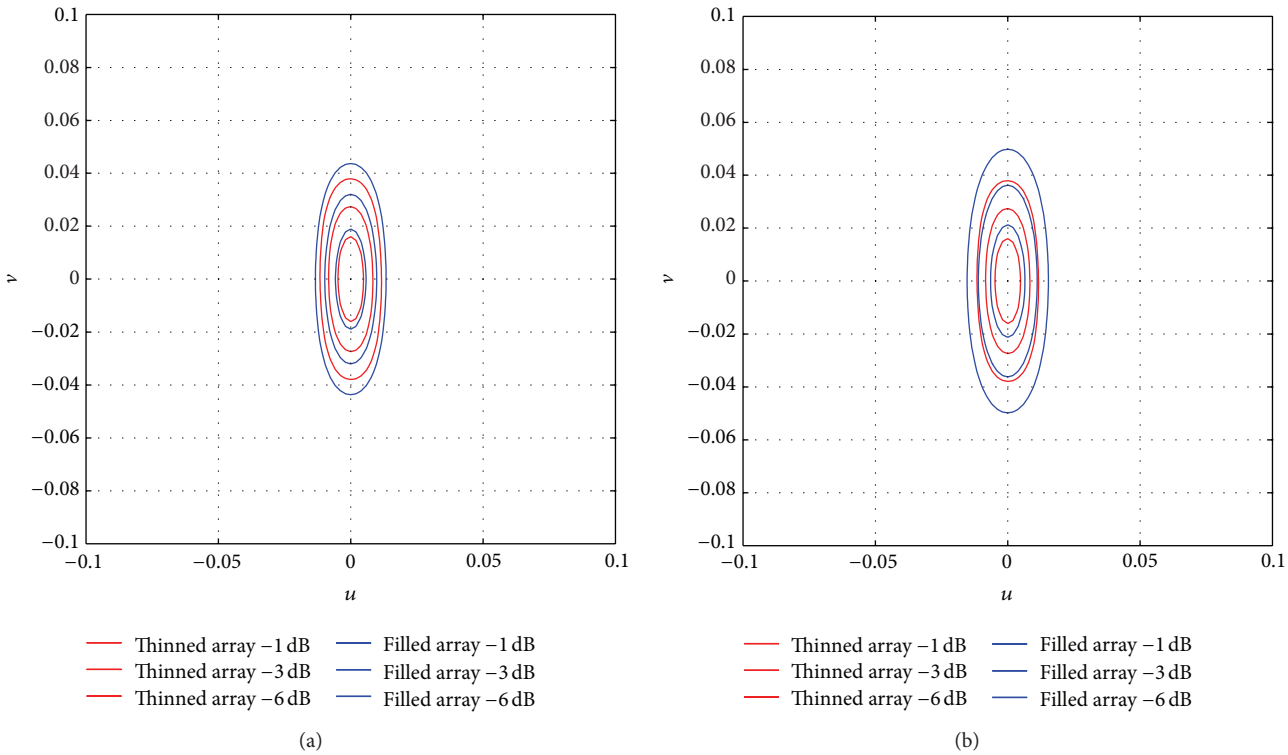

FIGURE 13: Comparison between the main lobe aperture of a thinned rectangular array and a filled array with the same number of active elements (a) without and (b) with amplitude tapering.

Table 3: Scenarios for the performance study.

Scenario	Target DOA (θ_T, φ_T)		jammer DOA (θ_j, φ_j)		JNR (dB)
1 jammer	$\theta_T = 5^\circ$	$\varphi_T = 0^\circ$	$\theta_j = 5^\circ$	$-60^\circ \le \varphi_j \ge 60^\circ$	40
2 jammers	$\theta_T = 5^\circ$	$\varphi_T = 0^\circ$	$\theta_j = 5^\circ$	$\varphi_j = 10^\circ$	40
			$\theta_j = 5^\circ$	$-60^\circ \le \varphi_j \ge 60^\circ$	40

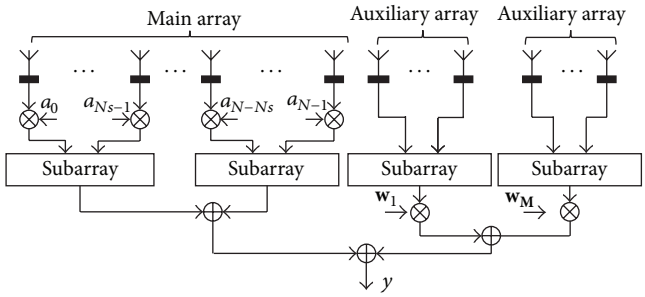

Ns: subarray size

N: centre elements

M: number of auxiliary channels

Figure 14: Adaptive cancellation scheme.

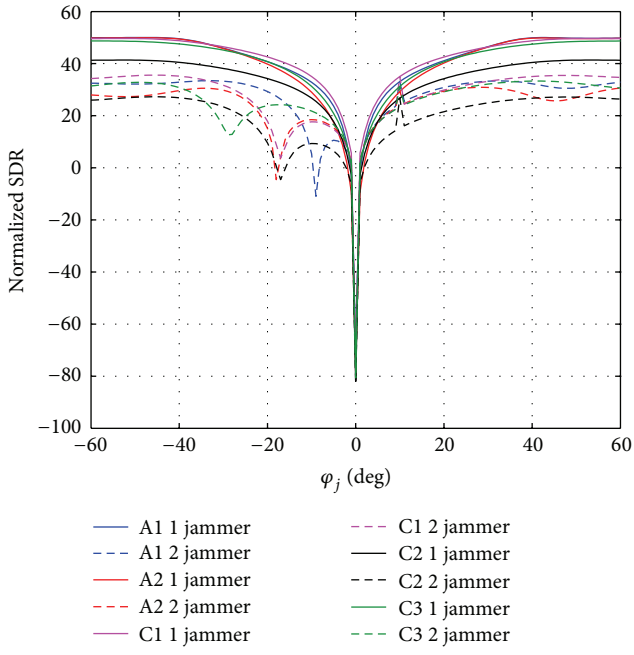

Figure 15: SDR versus jammer azimuth angle.

impose amplitude taper for further side-lobe suppression. This mainly depends on the fact that thinned arrays reach low SLL at clutter DoA without a significant increase of the main-lobe aperture, differently from the filled array cases where the reduction of the side-lobes using a tapering function is paid in terms of pattern main-lobe widening and gain reduction.

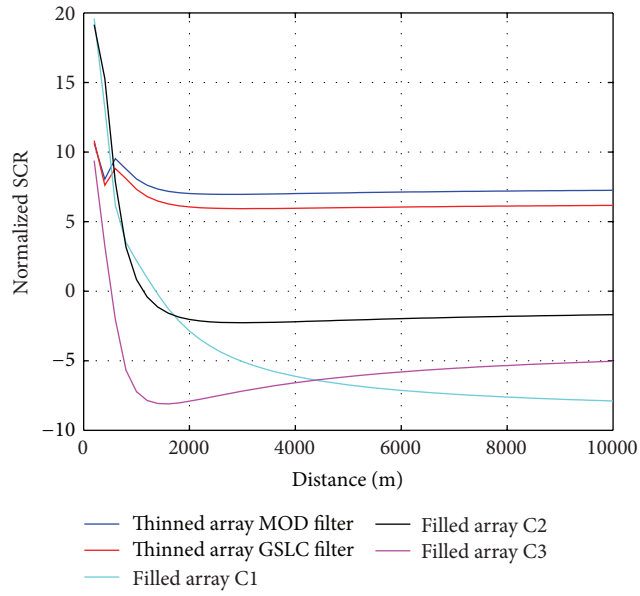

Figure 16: SCR versus target distance.

6. Conclusions

The SPED and SPSD optimization techniques and their Constrained versions have been proposed for the design of optimized element and subarray based planar thinned arrays using an assigned number of active elements and assuring a desired level of SLL. Since the SPSD technique operates effectively for a limited number of small-sized subarrays, a WSF approach has been introduced to increase the subarray size; this approach does not need a significant increase of the number of different subarray types and achieves comparable performance in terms of SLL. All the proposed techniques have been shown to be effective for practical planar thinned array design and adaptable to different planar array shapes. Moreover, possible adaptive solutions have been discussed suitable for SLC schemes based on the MOD and GSLC filters using the circular thinned arrays produced by the use of Constrained SPSD and WSF. An analysis has been conducted to compare the performance in terms of jammer and clutter cancellation of the thinned array with respect to several configurations of filled arrays with the same number of active elements using amplitude tapering to lower the SLL. The proposed comparative analysis showed that for the considered study cases the adaptive thinned array is able to yield better performance than the adaptive filled arrays when clutter cancelation is considered and has a comparable behavior in terms of jammer reduction.

References

[1] J. W. Sherman and M. I. Skolnik, "Thinning planar array antennas with ring arrays," *IRE International Convention Record*, vol. 11, part 1, 1963.

[2] M. I. Skolnik, J. W. Sherman, and F. C. Ogg, "Statistically designed density-tapered arrays," *IEEE Transactions on Antennas and Propagation*, vol. 12, pp. 408–417, 1964.

[3] R. J. Mailloux and E. Cohen, "Statistically thinned arrays with quantized element weights," *IEEE Transactions on Antennas and Propagation*, vol. 39, no. 4, pp. 436–447, 1991.

[4] M. I. Skolnik, G. Nemhauser, and J. W. Sherman, "Dynamic programming applied to unequally spaced arrays," *IEEE Transactions on Antennas and Propagation*, vol. 12, pp. 35–43, 1964.

[5] M. I. Skolnik, G. Nemhauser, L. C. Kefauver, and J. W. Sherman, "Thinned, unequally spaced arrays designed by dynamic programming," in *Proceedings of the Antennas and Propagation Society International Symposium*, vol. 1, pp. 224–227, Boulder, Colo, USA, July 1963.

[6] W. P. M. N. Keizer, "Large planar array thinning using iterative FFT techniques," *IEEE Transactions on Antennas and Propagation*, vol. 57, no. 10, pp. 3359–3362, 2009.

[7] Y. T. Lo, "A spacing weighted antenna array," *IRE International Convention Record*, vol. 10, pp. 191–195, 1962.

[8] Y. T. Lo, "A mathematical theory of antenna arrays with randomly spaced elements," *IEEE Transactions on Antennas and Propagation*, vol. 12, pp. 257–268, 1964.

[9] B. D. Steinberg, "The peak sidelobe of the phased array having randomly located elements," *IEEE Transactions on Antennas and Propagation*, vol. 20, pp. 129–136, 1972.

[10] B. D. Steinberg, "Comparison between the peak sidelobe of the random array and algorithmically designed aperiodic arrays," *IEEE Transactions on Antennas and Propagation*, vol. 21, pp. 366–370, 1973.

[11] B. D. Steinberg and E. H. Attia, "Sidelobe reduction of random arrays by element position and frequency diversity," *IEEE Transactions on Antennas and Propagation*, vol. 31, no. 6, pp. 922–930, 1983.

[12] R. L. Haupt, J. J. Menozzi, and C. J. McCormack, "Thinned arrays using genetic algorithms," in *Proceedings of the Antennas and Propagation Society International Symposium*, pp. 712–715, Ann Arbor, Mich, USA, July 1993.

[13] R. L. Haupt, "Thinned arrays using genetic algorithms," *IEEE Transactions on Antennas and Propagation*, vol. 42, no. 7, pp. 993–999, 1994.

[14] D. J. O'Neill, "Element placement in thinned arrays using genetic algorithms," in *Proceedings of the Oceans Engineering for Today's Technology and Tomorrow's Preservation (OCEANS '94)*, vol. 2, pp. 301–306, Brest, France, September 1994.

[15] K. K. Yan and Y. Lu, "Sidelobe reduction in array-pattern synthesis using genetic algorithm," *IEEE Transactions on Antennas and Propagation*, vol. 45, no. 7, pp. 1117–1122, 1997.

[16] S. Hebib, N. Raveu, and H. Aubert, "Cantor spiral array for the design of thinned arrays," *IEEE Antennas and Wireless Propagation Letters*, vol. 5, no. 1, pp. 104–106, 2006.

[17] J. Corcoles and M. A. Gonzalez, "Efficient combined array thinning and weighting for pattern synthesis with a nested optimization scheme," *IEEE Transactions on Antennas and Propagation*, vol. 60, pp. 5107–5117, 2012.

[18] O. Quevedo-Teruel and E. Rajo-Iglesias, "Ant colony optimization in thinned array synthesis with minimum sidelobe level," *IEEE Antennas and Wireless Propagation Letters*, vol. 5, no. 1, pp. 349–352, 2006.

[19] L. Zhang, Y.-C. Jiao, Z.-B. Weng, and F.-S. Zhang, "Design of planar thinned arrays using a boolean differential evolution algorithm," *IET Microwaves, Antennas and Propagation*, vol. 4, no. 12, pp. 2172–2178, 2010.

[20] V. Murino, A. Trucco, and C. S. Regazzoni, "Synthesis of unequally spaced arrays by simulated annealing," *IEEE Transactions on Signal Processing*, vol. 44, no. 1, pp. 119–123, 1996.

[21] P. Chen, Y. Zheng, and W. Zhu, "Optimized simulated annealing algorithm for thinning and weighting large planar arrays in both far-field and near-field," *IEEE Journal of Oceanic Engineering*, vol. 36, no. 4, pp. 658–664, 2011.

[22] N. Jin and Y. Rahmat-Samii, "Advances in particle swarm optimization for antenna designs: real-number, binary, single-objective and multiobjective implementations," *IEEE Transactions on Antennas and Propagation*, vol. 55, no. 3, pp. 556–567, 2007.

[23] U. Nickel, "Subarray configurations for digital beamforming with low sidelobes and adaptive interference suppression," in *Proceedings of the IEEE International Radar Conference*, pp. 714–719, Alexandria, VA, USA, May 1995.

[24] P. Lombardo, R. Cardinali, D. Pastina, M. Bucciarelli, and A. Farina, "Array optimization and adaptive processing for sub-array based thinned arrays," in *Proceedings of the International Conference on Radar*, pp. 197–202, Adelaide, Australia, September 2008.

[25] P. Lombardo and D. Pastina, "Pattern control for adaptive antenna processing with overlapped sub-arrays," in *Proceedings of the International Radar Conference*, Adelaide, Australia, September 2003.

[26] P. Lombardo and D. Pastina, "Quiescent pattern control in adaptive antenna processing at sub-array level," in *Proceedings of the IEEE International Symposium on Phased Array Systems and Technology (PAST '03)*, Boston, Mass, USA, October 2003.

[27] A. Farina, *Antenna-Based Signal Processing Techniques For Radar Systems*, Artech House, Norwood, Mass, USA, 1992.

[28] A. Farina, P. Lombardo, and L. Ortenzi, "A unified approach to adaptive radar processing with general antenna array configuration," *Signal Processing*, vol. 84, no. 9, pp. 1593–1623, 2004.

Hindawi Publishing Corporation
International Journal of Antennas and Propagation
Volume 2013, Article ID 142602, 16 pages
http://dx.doi.org/10.1155/2013/142602

Research Article

Analysis of Moving Object Imaging from Compressively Sensed SAR Data in the Presence of Dictionary Mismatch

Ahmed Shaharyar Khwaja,[1] Muhammad Naeem,[1,2] and Alagan Anpalagan[1]

[1] *Department of Electrical and Computer Engineering, Ryerson University, Toronto, ON, Canada M5B 2K3*
[2] *Department of Electrical Engineering, COMSATS Institute of IT, Wah Campus, Wah 47040, Pakistan*

Correspondence should be addressed to Ahmed Shaharyar Khwaja; akhwaja@ee.ryerson.ca

Received 4 April 2013; Revised 4 October 2013; Accepted 6 October 2013

Academic Editor: Krzysztof Kulpa

We present compressed sensing (CS) synthetic aperture radar (SAR) moving target imaging in the presence of dictionary mismatch. Unlike existing work on CS SAR moving target imaging, we analyze the sensitivity of the imaging process to the mismatch and present an iterative scheme to cope with dictionary mismatch. We analyze and investigate the effects of mismatch in range and azimuth positions, as well as range velocity. The analysis reveals that the reconstruction error increases with the mismatch and range velocity mismatch is the major cause of error. Instead of using traditional Laplacian prior (LP), we use Gaussian-Bernoulli prior (GBP) for CS SAR imaging mismatch. The results show that the performance of GBP is much better than LP. We also provide the Cramer-Rao Bounds (CRB) that demonstrate theoretically the lowering of mean square error between actual and reconstructed result by using the GBP. We show that a combination of an upsampled dictionary and the GBP for reconstruction can deal with position mismatch effectively. We further present an iterative scheme to deal with the range velocity mismatch. Numerical and simulation examples demonstrate the accuracy of the analysis as well as the effectiveness of the proposed upsampling and iterative scheme.

1. Introduction

According to compressed sensing (CS) [1–3] theory, randomly undersampled signals can be reconstructed using linear programming [1], orthogonal matching pursuit (OMP) [4], and Bayesian methods [5–7]. The advantages gained by using CS are hardware simplification [8], reduction in equipment cost, data size, and acquisition time [9, 10], and deblurring and enhancing resolution from incomplete measurements [11].

Compressed sensing for synthetic aperture radar (SAR) is an active area of research for remote sensing. The use of CS based reconstruction can have an impact on the design of high resolution SAR systems as these systems encounter hardware design problems and require significant processing [12]. CS has been applied for imaging of static objects in through-the-wall SAR imaging [13–15], tomographic SAR imaging [16–18], and SAR image formation with reduced data [19], where advantage is taken of the fact that the observed scenes are sparse. The static scenes may not always be sparse. The scenes containing a few strong intensity moving scatterers in a weak stationary background present an opportunity for CS application as they are inherently sparse. These moving targets suffer from position displacement and defocusing due to motion [20]. The use of CS can help in reducing acquired data size as well as simultaneous motion parameter estimation imaging with reduced data. Sparsity can be further enhanced using clutter cancelation where the static parts of an observed scene are suppressed [21].

Compressed sensing for SAR moving object imaging has become an active area of research. References [22, 23] apply CS for moving target parameter estimation by defining a dictionary based on the response of moving objects for different motion parameters. Both of these references use clutter cancelation to enhance sparsity. Reference [24] makes use of distributed CS applied to along-track interferometric SAR data for moving target imaging and shows that distributed CS can offer better performance with less samples compared

Table 1: Comparison of existing references.

References	SAR moving target	Prior	Dictionary mismatch	Remarks
[6]	No	GBP	Yes	Superior performance of GBP over LP is shown by simulations
[13, 14]	No	LP	No	Apply CS for through-the-wall imaging
[15]	No	LP	Yes	Apply CS for through-the-wall imaging. Performance degradation due to pixel mismatch and wave propagation velocity shown by simulations
[16–18]	No	LP	No	Apply CS for tomographic SAR imaging
[19]	No	LP	No	Apply CS for focusing of static scenes
[7]	No	GBP	Yes	Fast implementation of GBP reconstruction shows superior performance by simulations
[21]	No	LP	No	Suggest clutter cancelation to enhance sparsity of a scene containing moving targets
[22]	Yes	LP	No	Apply CS for motion estimation
[23]	Yes	LP	Yes	Apply CS for motion estimation, performance degradation due to range velocity mismatch shown by simulations
[24]	Yes	LP	No	Apply distributed CS for motion estimation
[25]	Yes	LP	Yes	Apply CS for motion estimation; simulations show no performance degradation due to velocity mismatch
[26, 27]	No	LP	Yes	Performance degradation due to dictionary mismatch shown by simulations and theory

to traditional CS. Reference [25] uses CS for moving target parameter estimation for mono- and multistatic SAR configurations and simulated data. These references show that CS can achieve imaging of moving objects as well as moving object parameter estimation when SAR data are sampled at a rate less than the traditional Nyquist sampling rate.

Compressed sensing reconstruction algorithms use a dictionary in which the reconstructed signal is assumed to be sparse. However, the dictionary in which the signal is actually sparse may be different and the resulting dictionary mismatch causes a performance degradation [26, 27]. In order to apply CS for practical applications, it is necessary to study the reconstruction performance degradation in the presence of dictionary mismatch. Reference [26] shows that dictionary mismatch can be seen equivalent to multiplicative noise. It also shows that reconstruction error increases linearly with mismatch. Reference [27] considers the effect of dictionary mismatch in CS reconstruction. It shows that, in case of using a Fourier dictionary, reconstruction performance degrades considerably when a mismatch exists. Due to this reason, it recommends examining the effects of mismatch on radar imaging. Reference [15] has shown performance degradation by means of imaging examples for static targets in the presence of mismatch in position and wave propagation velocity. The authors in [15] also state that they are extending the initial results presented in [28] for dealing with position mismatch in through-the-wall imaging.

According to the best of our knowledge, dictionary mismatch analysis has not been done theoretically for CS moving target SAR imaging in the presence of position and range velocity mismatch. A summary of the main features of the existing references is given in Table 1. It shows that, in the existing literature, the theoretical analysis of the effects of dictionary mismatch for moving target CS SAR imaging have not been carried out. Therefore, it remains an open problem. It further shows that a prior other than Laplacian prior (LP), for example, Gaussian-Bernoulli prior (GBP), for CS moving target imaging has not been used. Similarly, a theoretical analysis to show the advantage of the prior in dealing with dictionary mismatch is also missing. In [29], we have partially studied this problem and its effects for SAR and inverse SAR. We showed that dictionary generation using upsampled parameters is required to deal with errors arising due to mismatch in positions and range velocity.

The emphasis of this paper is to show the performance degradation in case of a target moving in the range direction. The dictionary mismatch arising due to discretization and dictionary size considerations causes performance degradation in terms of mean square error (MSE) between actual and reconstructed results, especially when there is a range velocity mismatch. We examine reasons for this degradation and also show theoretically and experimentally that using GBP for CS reconstruction compared to the traditionally used LP can compensate for some amount of mismatch. The motivation of using a different prior is to make use of extra information in improving reconstructed image quality as shown in [30]. We propose to deal with CS SAR moving target imaging in the presence of dictionary mismatch due to positions and range velocity. The main contributions of this paper are as follows.

(1) We analyze dictionary mismatch and its effects theoretically, show MSE calculated from simulated SAR

data for different types of mismatch in range and azimuth pixels as well as range velocity, and give parameter resolution limits for maintaining a reasonable level of reconstruction accuracy. We show that CS SAR moving target imaging is very sensitive to range velocity mismatch.

(2) We analyze the problem by means of Cramer-Rao Bounds (CRB) and show theoretically that reconstruction with Gaussian-Bernoulli prior (CSGBP) instead of traditional Laplacian prior (CSLP) can deal with some mismatch effectively.

(3) We present simulation results using CSGBP reconstruction and show that its use can lead to lower MSE, especially when the dictionary mismatch is small. This can be used to deal with position mismatch and reduce upsampling in positions that is required to counter mismatch effects.

(4) We also propose to reconstruct in the presence of range-velocity mismatch using an iterative scheme, where dictionaries with different range velocities are created efficiently. The contrast of the reconstructed result is maximized.

We would also like to point out that we deal specifically with the case of pulsed SAR. Any extension of dictionary mismatch effects and parameter resolution calculations to other types of SAR will need to take into account the difference in imaging mechanism; for example, in case of continuous wave SAR, it is known that range velocity creates a shift in the range direction, which is absent in pulsed SAR. Therefore, results for mismatch analysis and resolutions in range position and range velocity will need to take this additional shift into account.

This paper is organized as follows. Section 2 presents the data model and formulation of moving target velocity estimation problem in case of CS SAR. Section 3 analyzes the effects of different kinds of dictionary mismatch, that is, range and azimuth positions and range velocity on CS SAR moving target imaging. Section 4 presents numerical and imaging examples to present the effects of dictionary mismatch in terms of MSE as well as the accuracy of the analysis and the effectiveness of the proposed method. Conclusions are given in Section 5.

2. System Model and Problem Formulation

In this paper, x denotes a scalar, $\mathbf{x}$ denotes a vector, and $\mathbf{X}$ denotes a matrix. We use $\mathbf{X}^H$ and $\mathbf{X}^T$ to denote conjugate transpose and transpose of $\mathbf{X}$, respectively. The same notation is used for Greek characters; that is, σ denotes a scalar, $\boldsymbol{\sigma}$ denotes a vector, and $\boldsymbol{\Sigma}$ denotes a matrix. We use $\boldsymbol{\Sigma}^H$ and $\boldsymbol{\Sigma}^T$ to denote conjugate transpose and transpose of $\boldsymbol{\Sigma}$, respectively. The function diag($\mathbf{x}$) represents a function that converts a vector $\mathbf{x}$ of size $N_t \times 1$ into a diagonal matrix of size $N_t \times N_t$ and det($\mathbf{X}$) represents the determinant of the matrix $\mathbf{X}$.

Synthetic aperture radar consists of an antenna mounted on a moving platform [31]. A pulsed SAR sends electromagnetic pulse $p(t)$ at a carrier frequency f_c and a chirp rate K. The pulse length is denoted by T_p. This pulse is given as

$$p(t) = \text{rect}\left(\frac{t}{T_p}\right)\exp\left(j2\pi f_c t - j\pi K t^2\right), \tag{1}$$

where

$$\text{rect}\left(\frac{t}{T_p}\right) = 1, \quad \text{if } 0 \le t \le T_p \\ = 0, \quad \text{otherwise}, \tag{2}$$

and $t = t_1, t_2, t_3, \ldots, t_{N_r}$. The signals are reflected from each scatterer in the observed scene. Let $\boldsymbol{\sigma_0}$ be a sparse vector of size $N_t \times 1$ that contains reflectivities for each point in the scene having different motion parameters. $\boldsymbol{\Psi_0}$ is an $N_s \times N_t$ matrix in which the signal is actually sparse and contains response of moving targets for every point in the scene with each considered motion parameter. Let $\boldsymbol{\Phi}$ be a sampling matrix of size $M \times N_s$, where $M < N_s$. This represents the case where the number of measurements is less than the required sampling rate due to data loss or intentionally reduced data acquisition to simplify the acquisition hardware [10], such as analog-to-digital converter. With different sampling configurations, one can get reasonable image reconstruction [13]. In this paper, we use undersampling in range direction as measurement operator. The raw data signal model can be written in one-dimensional form as [29]

$$\mathbf{s_0} = \boldsymbol{\Phi}\boldsymbol{\Psi_0}\boldsymbol{\sigma_0} + \boldsymbol{\varepsilon}, \tag{3}$$

where $\boldsymbol{\varepsilon}$ denotes measurement noise. $\boldsymbol{\Psi_0}$ contains the response of each moving point in 1D form. This response for nth moving point having kth range velocity is given as [29]

$$\mathbf{s}_n^k = \left[\tilde{s}_n^k(t_1,\tau_1), \tilde{s}_n^k(t_2,\tau_1), \ldots, \tilde{s}_n^k\left(t_{N_r},\tau_1\right), \right. \\ \tilde{s}_n^k(t_1,\tau_2), \tilde{s}_n^k(t_2,\tau_2), \ldots, \tilde{s}_n^k\left(t_{N_r},\tau_2\right), \ldots, \\ \left.\tilde{s}_n^k\left(t_1,\tau_{N_y}\right), \tilde{s}_n^k\left(t_2,\tau_{N_y}\right), \ldots, \tilde{s}_n^k\left(t_{N_r},\tau_{N_y}\right)\right]^T, \tag{4}$$

where

$$\tilde{s}_n^k(t_l,\tau_m) = p\left(t_l - \frac{2d_n^k(\tau_m)}{c}\right) \\ = \text{rect}\left(\frac{t_l - 2d_n^k(\tau_m)/c}{T_p}\right)\exp\left\{-jk_c d_n^k(\tau_m)\right\} \\ \times \exp\left\{-j\pi K\left(t_l - \frac{2d_n^k(\tau_m)}{c}\right)^2\right\}, \tag{5}$$

$$d_n^k(\tau_m) = \sqrt{(x_n - v_x^k\tau_m)^2 + h^2 + (y_n - V\tau_m)^2}. \tag{6}$$

The size of $\mathbf{s}_n^k$ is $N_s \times 1$. $\boldsymbol{\Psi}_\mathbf{0}$ is generated for initial velocity v_{xi} and final velocity v_{xf} for a total number of Nv_x range velocities. The dictionary element corresponding to a velocity v_x^1 is as follows:

$$\boldsymbol{\Psi}_\mathbf{0}{}^1 = \left[\mathbf{s}_1^1 \cdots \mathbf{s}_{N_s}^1\right]. \tag{7}$$

The final dictionary $\boldsymbol{\Psi}_\mathbf{0}$ is stored in an $N_s \times N_t$ matrix given as

$$\boldsymbol{\Psi}_\mathbf{0} = \left[\boldsymbol{\Psi}_\mathbf{0}{}^1 \mid \cdots \mid \boldsymbol{\Psi}_\mathbf{0}{}^{Nv_x}\right]. \tag{8}$$

Due to undersampling, the problem of recovering $\boldsymbol{\sigma}_\mathbf{0}$ from $\mathbf{s}_\mathbf{0}$ becomes an underdetermined problem. We can solve this problem by including a-priori information for getting the solution; for example, select a solution such that the number of nonzero coefficients is the smallest. This can be expressed as follows:

$$\min \left\|\boldsymbol{\sigma}_\mathbf{0}\right\|_0 \quad \text{subject to } \mathbf{s}_\mathbf{0} = \boldsymbol{\Phi}\boldsymbol{\Psi}_\mathbf{0}\boldsymbol{\sigma}_\mathbf{0}. \tag{9}$$

The number of nonzero coefficients is denoted by $\|\boldsymbol{\sigma}_\mathbf{0}\|_0$, known as l_0 norm. However, this minimization problem is nonconvex, which means that finding a global solution is difficult or not guaranteed. In addition, it is computationally difficult to solve as it requires search over all possible combinations of the columns of $\boldsymbol{\Phi}\boldsymbol{\Psi}_\mathbf{0}$. To deal with these issues, we use l_1 norm minimization. This minimization is a convex approximation of the l_0 norm minimization if a property known as restricted isometric property (RIP) is satisfied. This property essentially means that the columns formed by the matrix $\boldsymbol{\Phi}\boldsymbol{\Psi}_\mathbf{0}$ are sufficiently decorrelated with one another. The problem can be expressed as

$$\min \left\|\boldsymbol{\sigma}_\mathbf{0}\right\|_1 \quad \text{subject to } \mathbf{s}_\mathbf{0} = \boldsymbol{\Phi}\boldsymbol{\Psi}_\mathbf{0}\boldsymbol{\sigma}_\mathbf{0}. \tag{10}$$

In order to obtain a solution based on l_1 norm minimization, we use Laplacian prior (LP) [32] as follows:

$$\boldsymbol{\sigma}_\mathbf{0} \sim \exp\left(-\left\|\boldsymbol{\sigma}_\mathbf{0}\right\|_1\right). \tag{11}$$

If noise is Gaussian with variance s_ε^2, the solution is obtained by

$$\begin{aligned}\widehat{\boldsymbol{\sigma}}_\mathbf{0} &= \underset{\boldsymbol{\sigma}_\mathbf{0}}{\operatorname{argmax}} p\left(\boldsymbol{\sigma}_\mathbf{0} \mid \mathbf{s}_\mathbf{0}\right) \\ &= \underset{\boldsymbol{\sigma}_\mathbf{0}}{\operatorname{argmax}} p\left(\mathbf{s}_\mathbf{0} \mid \boldsymbol{\sigma}_\mathbf{0}\right) p\left(\boldsymbol{\sigma}_\mathbf{0}\right),\end{aligned} \tag{12}$$

where

$$p\left(\mathbf{s}_\mathbf{0} \mid \boldsymbol{\sigma}_\mathbf{0}\right) = \frac{1}{2s_{\varepsilon^2}} \exp\left\{-\left\|\mathbf{s}_\mathbf{0} - \boldsymbol{\Phi}\boldsymbol{\Psi}_\mathbf{0}\boldsymbol{\sigma}_\mathbf{0}\right\|_2^2\right\}. \tag{13}$$

The solution can be written as

$$\widehat{\boldsymbol{\sigma}}_\mathbf{0} = \underset{\boldsymbol{\sigma}_\mathbf{0}}{\operatorname{argmin}} \left\{-\log p\left(\mathbf{s}_\mathbf{0} \mid \boldsymbol{\sigma}_\mathbf{0}\right) - \log p\left(\boldsymbol{\sigma}_\mathbf{0}\right)\right\} \tag{14}$$

that leads to

$$\widehat{\boldsymbol{\sigma}}_\mathbf{0} = \underset{\boldsymbol{\sigma}_\mathbf{0}}{\operatorname{argmin}} \left\|\mathbf{s}_\mathbf{0} - \boldsymbol{\Phi}\boldsymbol{\Psi}_\mathbf{0}\boldsymbol{\sigma}_\mathbf{0}\right\|_2^2 + \lambda\left\|\boldsymbol{\sigma}_\mathbf{0}\right\|_1. \tag{15}$$

Thus, by using LP, we include the l_1 norm minimization in the solution. The parameter λ gives weight to a priori sparse information. Equation (15) can be solved using different recovery methods, for example, linear programming and OMP. The reconstructed result $\widehat{\boldsymbol{\sigma}}_\mathbf{0}$ is of size $N_t \times 1$ and can be written as

$$\widehat{\boldsymbol{\sigma}}_\mathbf{0} = \left[\widehat{\sigma}_{0,1}^1 \cdots \widehat{\sigma}_{0,N}^1 \cdots \widehat{\sigma}_{0,1}^{Nv_x} \cdots \widehat{\sigma}_{0,N}^{Nv_x}\right]^T, \tag{16}$$

where each entry of $\widehat{\boldsymbol{\sigma}}_\mathbf{0}$ shows the reconstructed reflectivity for each point in the scene for one velocity value; for example, $\widehat{\sigma}_{0,1}^1$ represents the reflectivity for a point at position (r_1, y_1) and having a velocity v_x^1. The result can be rearranged into Nv_x 2D matrices, each having a size $n_r \times n_y$, to show the estimated reflectivities at different velocities for SAR. The matrices of size $n_r \times n_y$ may also be summed to give a final focussed reconstructed result $\widehat{\boldsymbol{\Sigma}}_\mathbf{0}$, shown as follows:

$$\begin{aligned}\widehat{\boldsymbol{\Sigma}}_\mathbf{0} = \sum_{i=0}^{Nv_x - N} f\Big(&\widehat{\boldsymbol{\sigma}}_\mathbf{0}\left(i \times N + 1\right), \widehat{\boldsymbol{\sigma}}_\mathbf{0}\left(i \times N + 2\right), \ldots, \\ &\widehat{\boldsymbol{\sigma}}_\mathbf{0}\left((i+1) \times N\right), n_r, n_y\Big).\end{aligned} \tag{17}$$

$f(\widehat{\boldsymbol{\sigma}}_\mathbf{0}, n_1, n_2)$ is a function that rearranges an input $\widehat{\boldsymbol{\sigma}}_\mathbf{0}$ into a matrix of size $n_1 \times n_2$.

Dictionary mismatch can occur in the reconstruction process due to discretization of positions as well as range velocity; for example, instead of actual position of the scatterer (r_n, y_n) and velocity v_x^k, the basis has elements corresponding to $(r_n + \Delta r_n, y_n + \Delta y_n)$ and $v_x^k + \Delta v_x^k$. Considering $\boldsymbol{\Psi}$ as the mismatched dictionary, (3) can be rewritten as

$$\mathbf{s} = \boldsymbol{\Phi}\boldsymbol{\Psi}\boldsymbol{\sigma} + \boldsymbol{\varepsilon}, \tag{18}$$

and reconstruction using the mismatched dictionary $\boldsymbol{\Psi}$ causes the results to be decorrelated from $\widehat{\boldsymbol{\sigma}}_\mathbf{0}$ shown as follows:

$$\widehat{\boldsymbol{\sigma}} = \boldsymbol{\Psi}^H\boldsymbol{\Psi}_\mathbf{0}\widehat{\boldsymbol{\sigma}}_\mathbf{0}. \tag{19}$$

Therefore, the effects of dictionary mismatch are related to the correlation between the mismatched and the original dictionary. In the next section, we examine the effects of this correlation on the reconstruction. Furthermore, we present solutions for the recovery of $\boldsymbol{\sigma}_\mathbf{0}$ that can be written as

$$\widehat{\boldsymbol{\sigma}}_\mathbf{0} = \underset{\boldsymbol{\sigma}_\mathbf{0}, \boldsymbol{\Psi}_\mathbf{0}}{\operatorname{argmin}} \left\|\mathbf{s} - \boldsymbol{\Phi}\boldsymbol{\Psi}_\mathbf{0}\boldsymbol{\sigma}_\mathbf{0}\right\|_2^2 + \lambda\left\|\boldsymbol{\sigma}_\mathbf{0}\right\|_1, \tag{20}$$

where $\boldsymbol{\Psi}_\mathbf{0}$ is the actual dictionary. We present solutions for calculation of $\widehat{\boldsymbol{\sigma}}_\mathbf{0}$ using GBP that can reduce position mismatch effects, and propose an iterative scheme to recover $\widehat{\boldsymbol{\sigma}}_\mathbf{0}$ in the presence of range velocity mismatch.

3. Analysis of CS Moving Target Imaging in the Presence of Dictionary Mismatch

3.1. Effects of Position Mismatch. We consider a chirp signal that is commonly used in imaging radars and show the effects

of position mismatch on reconstruction. The reconstruction in the presence of mismatch depends upon the correlation between the original and the mismatched dictionaries, as given by (19). Therefore, any form of mismatch will cause erroneous results due to a correlation loss. This can be seen by taking the inner product of two chirp signals $s_1(t) = \exp(-j\pi K(t-t_1)^2)$ and $s_2(t) = \exp(-j\pi K(t-t_1)^2)$ having frequencies ranging from $-B/2$ to $B/2$. The signals are displaced with respect to each other by a duration $\Delta t_d = t_1 - t_2$. They consist of N samples with sampling time Δt_s. The correlation $|\langle s_2^H(t), s_1(t)\rangle|$ is

$$\begin{aligned}&\left|\left\langle \exp\left(j\pi K(t-t_2)^2\right), \exp\left(-j\pi K(t-t_1)^2\right)\right\rangle\right| \\ &\quad = \left|\sum_{n=0}^{\widetilde{N}-1} \exp\left(-j2\pi K\Delta t_d n\Delta t_s\right)\right|,\end{aligned} \tag{21}$$

where $t \in \{0, \Delta t_s, 2\Delta t_s, \ldots, (\widetilde{N}-1)\Delta t_s\}$. Δt_s should be less than $1/B$. Observing that $|\sum_{n=0}^{\widetilde{N}-1} \exp(-jxn)| = |\widetilde{N}\mathrm{sinc}((1/2)\widetilde{N}x)|$, we can write (21) as

$$\begin{aligned}&\left|\left\langle \exp\left(-j\pi K(t-t_1)^2\right), \exp\left(j\pi K(t-t_2)^2\right)\right\rangle\right| \\ &\quad = \widetilde{N}\left|\mathrm{sinc}\left(\pi B\Delta t_d\right)\right|,\end{aligned} \tag{22}$$

where $B = K\widetilde{N}\Delta t_s$. As the position mismatch increases, Δt_d increases and, with the increase of Δt_d, correlation decreases. Consequently, the amplitude of the reconstructed result will be reduced by a factor of $|\mathrm{sinc}(\pi B\Delta t_d)|$. The result of the correlation would be 0 when

$$\widetilde{\Delta t}_d = \Delta t_s \tag{23}$$

or

$$\widetilde{\Delta t}_d = \frac{1}{B}. \tag{24}$$

Consequently, if the two chirp signals are displaced by $\widetilde{\Delta t}_d$ with respect to each other, CS imaging will fail to reconstruct the correct position. An arbitrary element will be selected and cause a failure of the CS reconstruction model. Therefore, the smaller the distance between the dictionary elements, the smaller the mismatch and the better the reconstruction at the expense of larger dictionary size and higher number of computations. In effect, by making an oversampled dictionary, we can improve the reconstruction and this oversampling should be more than twice the sampling frequencies to reduce mismatch errors; that is,

$$\Delta t_d^{\max} < \frac{\widetilde{\Delta t}_d}{2}. \tag{25}$$

The implication of the above result will be studied in the next section. A moving target and the effects of mismatch in range and azimuth positions as well as range velocity on the moving target reconstruction are considered.

Table 2: Effect of mismatch on range and azimuth positions.

Mismatch type	Effect in range	Effect in azimuth
Range	Δr_n	$-\Delta r_n(\Delta v_x^k/V)\sin\theta_n$
Azimuth	$\Delta y_n(\Delta v_x^k/V)\sin\theta_n$	$-\Delta y_n$
Velocity	$y_n(\Delta v_x^k/V)\sin\theta_n$	$-r_n(\Delta v_x^k/V)\sin\theta_n$

3.2. Effects of Range Position, Azimuth Position, and Range Velocity Mismatch on Reconstruction of a Moving Target. First, we consider the equivalent static position of a moving point. A moving point at an initial position of r_n, y_n and having a velocity of v_x^k can be equivalently seen as a static point with coordinates r_m and y_m and rotated with an angle Θ_n^k [33]; that is:

$$\begin{aligned}r_m &= r_n + y_n\Theta, \\ y_m &= -r_n\Theta + y_n,\end{aligned} \tag{26}$$

where

$$\begin{aligned}\Theta_n^k &= \tan^{-1}\frac{v_x^k\sin\theta_n}{V} \\ &\approx \frac{v_x^k\sin\theta_n}{V}.\end{aligned} \tag{27}$$

Assuming that our dictionary is created with resolutions of s_r, s_y, and 1 m/s in range position, azimuth position, and range velocity, respectively, the mismatch effects on a moving target can be divided into 3 categories as follows.

(i) A subpixel mismatch in range position represented as Δr_n. This mismatch will lead to an equivalent shift of Δr_n in the range position and an equivalent shift of $-\Delta r_n(v_x^k\sin\theta_n/V)$ in the azimuth position.

(ii) A subpixel mismatch in azimuth position represented as Δy_n. This mismatch will lead to an equivalent shift of $\Delta y_n(v_{xn}\sin\theta_n/V)$ in the range position and an equivalent shift of $-\Delta y_n$ in the azimuth position.

(iii) A fraction of m/s mismatch in range velocity represented as Δv_x^k. This mismatch will lead to an equivalent shift of $y_n(\Delta v_x^k/V)\sin\theta_n$ in the range position and an equivalent shift of $-r_n(\Delta v_x^k/V)\sin\theta_n$ in the azimuth position. As an example, if a point in acquired raw data is at position (r_n, y_n) moving with a velocity $v_x^k + \Delta v_x^k$, and the dictionary contains elements with velocity v_x^k, the reconstructed estimate will be a point at position $(r_n + y_n(\Delta v_x^k/V)\sin\theta_n, y_n - r_n(\Delta v_x^k/V)\sin\theta_n)$ instead of the true position of (r_n, y_n). As r_n is large, the effect on azimuth position will be more evident even when range velocity mismatch is small. The mismatch effects due to Δr_n, Δy_n, and Δv_{xn}^k are summarized in Table 2.

3.3. Effects on Reconstruction for a Single Point in the Presence of Range Position, Azimuth Position, and Range Velocity Mismatch. Based on the above discussion, the effects of

mismatch on reflectivity reconstruction for a single element $\boldsymbol{\sigma_0} = \sigma_1^1\delta(r-r_1, y-y_1)$, where r_1 and y_1 are the pixel positions, can be summarized as follows.

(i) A mismatch of Δr_1 will cause a shift of Δr_1 in range position in the reconstructed result. The shift in azimuth position $-\Delta r_1(\Delta v_x^1/V)\sin\theta_1$ can be neglected as it is small due to the presence of V in the denominator. The result will be

$$\widehat{\boldsymbol{\sigma}}_{\mathbf{0}} = \sigma_1^1 \operatorname{sinc}\left(\pi\frac{\Delta r_1}{s_r}\right)\delta\left(r-r_1, y-y_1\right) \tag{28}$$

leading to a loss of amplitude.

(ii) A mismatch of Δy_1 will cause a shift of Δy_1 in azimuth position in the reconstructed result. The shift in azimuth position $\Delta y_1(\Delta v_x^1/V)\sin\theta_1$ can be neglected due to the presence of V in the denominator. The result will be

$$\widehat{\boldsymbol{\sigma}}_{\mathbf{0}} = \sigma_1^1 \operatorname{sinc}\left(\pi\frac{\Delta y_1}{s_y}\right)\delta\left(r-r_1, y-y_1\right) \tag{29}$$

leading to a loss of amplitude.

(iii) A range velocity mismatch Δv_x^1 causes a large shift in azimuth from the true position, given as $\Delta y_1^1 = -r_1\Delta v_x^1\sin\theta_1/V$. The shift in the range position $y_1(\Delta v_x^1/V)\sin\theta_1$ can be neglected. However, the shift in azimuth position cannot be neglected due to the presence of r_1 in the numerator that is of the order of 10^3 or higher. It can be further divided into 2 parts as follows.

(1) An interpixel displacement: $\lfloor \Delta y_1^1, s_y \rfloor$, where $\lfloor\cdot\rfloor$ is the floor operation.

(2) An intrapixel displacement: $\Delta y_1^1 \bmod s_y$, where mod is the modulo operation.

The reconstructed result will be

$$\begin{aligned}\widehat{\sigma}_0 = {} & \sigma_1^1 \operatorname{sinc}\left(\pi\frac{\Delta y_n^1 \bmod s_y}{s_y}\right) \\ & \times \delta\left(r-r_1, y-y_1+\left\lfloor \Delta y_1^1, s_y \right\rfloor\right)\end{aligned} \tag{30}$$

leading to a loss of amplitude and azimuth position shift.

(iv) In order to avoid the loss in amplitude as well as azimuth mispositioning of the reconstructed result, the dictionary can be created with higher parameter resolution. The dictionary resolutions in range and azimuth positions and range velocity are such that any mismatch does not lead to a misselection of elements. This can be achieved if the dictionary resolutions are less than half the pixel sizes. This ensures that a correct pixel positions is selected. These criteria can be expressed as follows for range and azimuth positions:

$$\widetilde{\Delta r} < \frac{s_r}{2}, \tag{31}$$

$$\widetilde{\Delta y} < \frac{s_y}{2}. \tag{32}$$

In case of velocity, the shift in azimuth position caused by range velocity mismatch should be less than half the pixel size; that is,

$$\Delta y_n^k < \frac{s_y}{2} \tag{33}$$

or

$$-r_n\frac{\Delta v_x^k}{V}\sin\left(\theta_n\right) < \frac{s_y}{2}. \tag{34}$$

As this shift is large for a larger value of r_n, we choose the farthest slant-range distance $r_{\max}$ to get a conservative estimate as follows:

$$\frac{r_{\max}\widetilde{\Delta v}_x\sin\left(\theta_{\max}\right)}{V} < \frac{s_y}{2}, \tag{35}$$

where the angle corresponding to $r_{\max}$ is $\theta_{\max}$. This leads to

$$\widetilde{\Delta v}_x < \frac{s_y V}{r_{\max}\sin\left(\theta_{\max}\right)}. \tag{36}$$

The limit given by (32) is also applicable for compensating intrapixel displacements due to velocity mismatch. Please note that due to the presence of $r_{\max}$ in the denominator, $\widetilde{\Delta v}_x$ is very small, which means that the dictionary needs to be created with very closely spaced velocity values.

When there is a moving scene consisting of a number of points given as

$$\boldsymbol{\sigma_0} = \sum_k\sum_n \sigma_n^k\delta\left(r-r_n, y-y_n\right), \tag{37}$$

the reconstructed result in the presence of mismatch is as follows:

$$\begin{aligned}\widehat{\boldsymbol{\sigma}}_{\mathbf{0}} = {} & \sum_k\sum_n \sigma_n^k \operatorname{sinc}\left(\pi\frac{\Delta r_n}{s_r}\right)\operatorname{sinc}\left(\pi\frac{\Delta y_n}{s_y}\right) \\ & \times \operatorname{sinc}\left(\pi\frac{\Delta y_n^k \bmod s_y}{s_y}\right)\delta\left(r-r_n, y-y_n+\left\lfloor \Delta y_n^k, s_y \right\rfloor\right).\end{aligned} \tag{38}$$

The three sinc functions represent a loss in estimated amplitude due to the mismatch, whereas the second term in the delta function represents a pixel-level shift.

3.4. Using CSGBP to Improve Performance in the Presence of Mismatch. In order to avoid errors due to dictionary mismatch, the dictionary needs to be created with upsampled positions and range velocity parameters. This high upsampling may not be feasible due to limited storage and computational complexity. We propose to reduce this high upsampling requirement by using a different prior as well as an iterative scheme. The chosen prior is GBP given as [6]

$$\sigma_{0,i}^{k} \sim (1-p)\,\delta\left(\sigma_{0,i}^{k}\right) + p\mathcal{N}\left(\mu_{\sigma}, s_{\sigma}^{2}\right), \tag{39}$$

where $\sigma_{0,i}^{k}$ is the ith element of $\boldsymbol{\sigma_0}$ moving with kth velocity. The main motivation of using this prior is to utilize a priori information about sparsity and signal strength for image reconstruction. $\boldsymbol{\sigma_0}$ can be assumed as q-sparse that is represented by the probability of active elements $p = q/N_t$ in $\boldsymbol{\sigma_0}$. The prior assumes that the probability of active elements, that is, an entry of $\boldsymbol{\sigma_0}$ being nonzero, is given by p and these active elements are represented by a Gaussian distribution with mean μ_σ and variance s_σ^2. The probability of an inactive element is given by $1-p$. The solution to recover $\boldsymbol{\sigma_0}$ from $\mathbf{s_0}$ for the prior can be obtained by rewriting (3) as follows:

$$\mathbf{s_0} = \boldsymbol{\Phi}\boldsymbol{\Psi_0}\,\mathrm{diag}\left(\mathbf{z_0}\right)\boldsymbol{\sigma_0} + \boldsymbol{\varepsilon}, \tag{40}$$

where $\mathbf{z_0} = [z_{0,1}^{1} \cdots z_{0,N}^{1} \cdots z_{0,1}^{N_{v_x}} \cdots z_{0,1}^{N_{v_x}}]^T$. The nth entry of $\mathbf{z_0}$ is 1 if the corresponding entry in $\boldsymbol{\sigma_0}$ is 1. In this case, $\boldsymbol{\sigma_0}$ can be recovered from $\mathbf{s_0}$ in two steps as follows.

(1) The 1st step is the solution to the following problem:

$$\begin{aligned}\widehat{\mathbf{z}}_{\mathbf{0}} &= \underset{\mathbf{z_0}}{\mathrm{argmax}}\, p\left(\mathbf{z_0} \mid \mathbf{s_0}\right) \\ &= \underset{\mathbf{z_0}}{\mathrm{argmax}}\, p\left(\mathbf{s_0} \mid \mathbf{z_0}\right) p\left(\mathbf{z_0}\right),\end{aligned} \tag{41}$$

where

$$p\left(\mathbf{z_0}\right) = p^{q}(1-p)^{N_t - q} \tag{42}$$

and $p(\mathbf{s_0} \mid \mathbf{z_0})$ is given on the next page. For the sake of convenience, we define $\mathbf{D} = \boldsymbol{\Phi}\boldsymbol{\Psi_0}$ and the covariance matrix is given as $\mathbf{R} = s_\sigma^2\mathbf{D}\,\mathrm{diag}(\mathbf{z_0})\mathbf{D}^H + s_\varepsilon^2\mathbf{I}$. The solution can be further written as

$$\widehat{\mathbf{z}}_{\mathbf{0}} = \underset{\mathbf{z_0}}{\mathrm{argmin}}\left\{-\log p\left(\mathbf{s_0} \mid \mathbf{z_0}\right) - p\left(\mathbf{z_0}\right)\right\}. \tag{43}$$

(2) The solution $\widehat{\mathbf{z}}_{\mathbf{0}}$ obtained from the 1st step is used to recover estimate of $\boldsymbol{\sigma_0}$ by using least squares solution given as

$$\widehat{\boldsymbol{\sigma}}_{\mathbf{0}} = \underset{\boldsymbol{\sigma_0}}{\mathrm{argmin}}\left\|\mathbf{s_0} - \boldsymbol{\Phi}\boldsymbol{\Psi_0}\,\mathrm{diag}(\widehat{\mathbf{z}}_{\mathbf{0}})\boldsymbol{\sigma_0}\right\|_2^2, \tag{44}$$

$$\begin{aligned}&p\left(\mathbf{s_0} \mid \mathbf{z_0}\right) \\ &\quad= \frac{1}{\det\left(\mathbf{R}\right)\pi^{M}} \\ &\qquad\times \exp\left\{-\left(\mathbf{s_0} - \mu_\sigma\mathbf{D}\mathbf{z_0}\right)^{H}\mathbf{R}^{-1}\left(\mathbf{s_0} - \mu_\sigma\mathbf{D}\mathbf{z_0}\right)\right\}.\end{aligned} \tag{45}$$

Furthermore, this model is suitable for man-made moving scatterers as they may be represented as consisting of a coherent mean part and variation of reflectivities can be represented by an incoherent part represented as variance; that is, $\boldsymbol{\sigma_0} \sim \mathcal{N}(\mu_\sigma, s_\sigma^2)$. In addition, noise $\boldsymbol{\varepsilon}$ can be assumed to be zero-mean Gaussian with variance s_ε^2; that is, $\boldsymbol{\varepsilon} \sim \mathcal{N}(0, s_\varepsilon^2)$. This CSGBP model can be solved using the algorithms in [6] or [7]. In [6], the raw data is correlated with each column of the matrix $\mathbf{D}$, and the presence or the absence of an element is decided by hypothesis testing. This testing is based on the assumption that the signal is distributed according to the GBP and the noise has Gaussian distribution. In [7], an efficient method is proposed for finding a combination of active and inactive elements.

3.5. Analysis of CSGBP and CSLP Performance in the Presence of Dictionary Mismatch Using Cramer-Rao Bounds. To show theoretically the advantage gained by using CSGBP reconstruction model given in (17) over CSLP model in (7), CRB of the vector $\widehat{\boldsymbol{\sigma}}_{\mathbf{0}}$ estimated from data vector $\mathbf{s_0}$ is calculated as the inverse of Fisher information matrix (FIM) $\mathbf{J}$. We consider $\boldsymbol{\Phi}$ to be identity matrix in (3) for the sake of convenience. The FIM bounds the estimation error in the following form:

$$E\left[\left(\boldsymbol{\sigma_0} - \widehat{\boldsymbol{\sigma}}_{\mathbf{0}}\right)\left(\boldsymbol{\sigma_0} - \widehat{\boldsymbol{\sigma}}_{\mathbf{0}}\right)^{T}\right] \geq \mathbf{J}^{-1}. \tag{46}$$

$\boldsymbol{\Phi}$ is assumed to be an identity matrix for the sake of convenience. $\mathbf{J}$ is decomposed into two parts [34];

$$\mathbf{J_D} = E_{\mathbf{s_0},\boldsymbol{\sigma_0}}\left[-\frac{\partial^2\left\{\log p\left(\mathbf{s_0} \mid \boldsymbol{\sigma_0}\right)\right\}}{\partial\boldsymbol{\sigma_0}^2}\right] \tag{47}$$

and $\mathbf{J_P}$ represents prior information matrix whose individual elements are given as

$$\mathbf{J_P} = E_{\mathbf{s_0},\boldsymbol{\sigma_0}}\left[-\frac{\partial^2\left\{\log p\left(\boldsymbol{\sigma_0}\right)\right\}}{\partial\boldsymbol{\sigma_0}^2}\right]. \tag{48}$$

Making use of the explanation given in [35] and smooth approximation; that is, $\|\boldsymbol{\sigma_0}\|_1 \approx \sum_{i=1}^{N}\left(|\sigma_{0,i}|^2 + \varepsilon\right)^{1/2}$, the FIM is given as

$$\mathbf{J_{LP}} = \left(\frac{\boldsymbol{\Psi_0}^{H}\boldsymbol{\Psi_0}}{s_\varepsilon^2}\right) \tag{49}$$

for the case where CSLP is used. When CSGBP is used, the FIM is

$$\mathbf{J_{GBP}} = \left(\frac{\boldsymbol{\Psi_0}^{H}\boldsymbol{\Psi_0}}{s_\varepsilon^2} + \frac{1-p}{s_\sigma^2}\right). \tag{50}$$

As (50) contains more information compared to (49), $\mathbf{J_{CSGBP}}$ in (50) will be larger and hence the estimation error will be lower that shows the improvement in performance. In case of a dictionary mismatch, using (18) and (19), (47) and (48) become

$$\widetilde{\mathbf{J}}_{\mathbf{D}} = \boldsymbol{\Psi}^{H}\boldsymbol{\Psi_0}E_{\mathbf{s_0},\boldsymbol{\sigma_0}}\left[-\frac{\partial^2\left\{\log p\left(\mathbf{s_0} \mid \boldsymbol{\sigma_0}\right)\right\}}{\partial\boldsymbol{\sigma_0}^2}\right] \tag{51}$$

and $\mathbf{J_P}$ represents prior information matrix whose individual elements are given as

$$\tilde{\mathbf{J}}_{\mathbf{P}} = \boldsymbol{\Psi}^H \boldsymbol{\Psi}_{\mathbf{0}} E_{\mathbf{s}_0,\boldsymbol{\sigma}_0} \left[-\frac{\partial^2 \{\log p(\boldsymbol{\sigma}_0)\}}{\partial \boldsymbol{\sigma}_0{}^2} \right]. \tag{52}$$

Equation (49) becomes

$$\tilde{\mathbf{J}}_{\mathrm{LP}} = \left(\frac{\left(\boldsymbol{\Psi}^H \boldsymbol{\Psi}_{\mathbf{0}}\right)\left(\boldsymbol{\Psi}_{\mathbf{0}}{}^H \boldsymbol{\Psi}_{\mathbf{0}}\right)}{s_\varepsilon^2} \right) \tag{53}$$

and (50) is rewritten as

$$\tilde{\mathbf{J}}_{\mathrm{GBP}} = \left(\frac{\left(\boldsymbol{\Psi}^H \boldsymbol{\Psi}_{\mathbf{0}}\right)^H \left(\boldsymbol{\Psi}_{\mathbf{0}}{}^H \boldsymbol{\Psi}_{\mathbf{0}}\right)}{s_\varepsilon^2} + \frac{(1-p)\left(\boldsymbol{\Psi}^H \boldsymbol{\Psi}_{\mathbf{0}}\right)}{s_\sigma^2} \right). \tag{54}$$

When no dictionary mismatch is present, $\boldsymbol{\Psi}^H \boldsymbol{\Psi}_{\mathbf{0}}$ has a maximum value along the diagonal elements. In case of mismatch, the diagonal elements of $\boldsymbol{\Psi}^H \boldsymbol{\Psi}_{\mathbf{0}}$ decrease. Subsequently, $\mathbf{J}$ decreases leading to an increase in estimated error. It can be inferred that, due to the prior information in (54), the increase of estimated error in the presence of dictionary mismatch is less when CSGBP is used. This can be seen in Figure 1, where an identity matrix of size 512 × 512 pixels is used as $\boldsymbol{\Psi}_{\mathbf{0}}$. $\boldsymbol{\Psi}$ is a mismatched basis that is decorrelated with $\boldsymbol{\Psi}_{\mathbf{0}}$ in varying proportions as follows:

$$\boldsymbol{\Psi} = \rho \boldsymbol{\Psi}_{\mathbf{0}} + \sqrt{1-\rho^2}\mathcal{N}(0,1), \tag{55}$$

where ρ is the degree of correlation and the measure $1-\rho$ can be seen equivalent to dictionary mismatch proportion. MSE is calculated using the expression

$$\mathrm{MSE}_{\mathrm{LP/GBP}} = \frac{1}{512} \mathrm{trace}\left(\mathbf{J}_{\mathrm{LP/GBP}}{}^{-1}\right). \tag{56}$$

It can be seen that using the model given in (39) lowers MSE that can help in countering effects of decorrelation arising due to dictionary mismatch.

3.6. Dealing with Range Velocity Mismatch Using Iterative CSGBP. As outlined in the previous section, CSGBP can compensate for some mismatch, which can help in reducing upsampling requirements. However, it is still not possible to deal with range velocity mismatch using only CSGBP. In general, CS SAR moving target imaging is very sensitive to range velocity mismatch. To avoid any error due to range velocity mismatch, the dictionary should be created with a very high resolution in range velocity; for example, for typical SAR configurations, this resolution can be of the order of 0.01 m/s. Such a high upsampling requirement is not feasible due to limited memory requirements and very high computations.

In this section, we propose to compensate for velocity mismatch by creating a dictionary iteratively, with range velocities varying at each iteration. In order to reduce the computational time, we make use of the following approximation to (6):

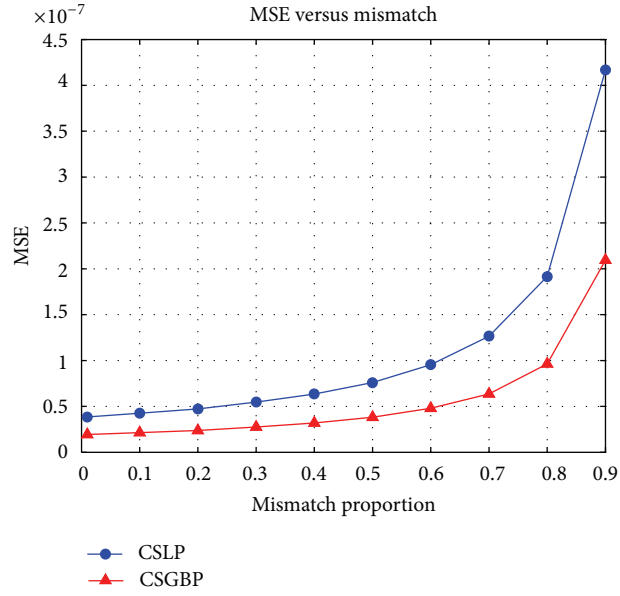

Figure 1: MSE using CSLP and CSGBP.

$$d_n^k(\tau_m) \approx r_n - v_{r,n}^k \left(\tau_m - \frac{y_n}{V}\right) + \frac{(\tau_m - y_n/V)^2}{2r_n}. \tag{57}$$

We can make use of this approximation to create $\tilde{s}_n^{k+1}(t_l, \tau_m)$ from $\tilde{s}_n^k(t_l, \tau_m)$ as follows:

$$\tilde{s}_n^{k+1}(t_l, \tau_m) \approx \tilde{s}_n^k(t_l, \tau_m) \exp\left(jk_c \Delta v_{r,n}^k (\tau_m - y_n/V)\right), \tag{58}$$

where $\Delta v_{r,n}^k = v_{r,n}^k - v_{r,n}^{k+1}$. This allows us to create a dictionary with varying mismatch iteratively using already computed dictionaries. Using the approximation, we propose the following scheme to reconstruct SAR image in the presence of dictionary mismatch.

(1) Create a dictionary with range and azimuth positions at a subpixel resolution. This resolution is chosen so as to meet the upsampling requirements given by (31) and (32). We chose an upsampling factor of 4 in position, which means that the maximum mismatch that can occur is 1/8 of the pixel size. This process is carried out only once.

(2) Carry out CSGBP reconstruction using the dictionary created in Step 1. Due to the upsampling chosen in the range and azimuth directions, and, due to the fact that the range velocity mismatch does not affect the range position, the result contains correct range position as well as range velocity. There will be azimuth position displacements due to range velocity that will be compensated in the next steps.

(3) For each set of reconstructed n_k points belonging to the same range velocity v_x^k, regenerate new dictionary

Table 3: Simulation parameters.

Carrier frequency	1.3 GHz	Incidence at center	40°
Chirp rate	1 GHz/s	Sensor velocity	100 m/s
Pulse duration	5 μs	Sensor height	2000 m
Pulse repetition frequency	140 Hz	Azimuth aperture	7°
Azimuth pixel size	0.7 m	Range pixel size	2.7 m

elements at the selected range positions using (58) and a velocity increment of $\lfloor \Delta y_n^k, s_y \rfloor$.

(4) Step 3 is repeated by incrementing the velocity in steps of $\lfloor \Delta y_n^k, s_y \rfloor$, until the reconstructed image is judged to be of the best quality for the n_k points. As a quality measure, contrast of the reconstructed vector is calculated as follows:

$$C_{\widehat{\boldsymbol{\sigma}}_0} = \frac{\left\langle \widehat{\boldsymbol{\sigma}}_0^2 \right\rangle}{\left\langle \widehat{\boldsymbol{\sigma}}_0 \right\rangle^2}, \tag{59}$$

where $\langle \cdot \rangle$ is the averaging operator.

(5) Steps 3 and 4 are repeated for each velocity in the dictionary where moving points were detected in Step 2.

4. Numerical and Imaging Results

This section presents numerical and imaging results. We give examples with MSE calculated for different amounts of mismatch in range, azimuth, and range velocity for SAR data, followed by imaging examples.

4.1. Numerical Results. The simulation parameters for SAR data are given in Table 3. A scene of size 50 m × 50 m or 12 × 70 pixels in range and azimuth directions is considered. Raw data corresponding to multiple points are simulated and 5% of range data are retained. Positions and amplitudes of these points are chosen randomly, whereas ground-range velocities are chosen randomly from a set of 7 velocities: {0, 3, 4, 5, −3, −4, −5} m/s. Performance in terms of dictionary mismatch is compared. For this purpose, data are generated using a dictionary $\boldsymbol{\Psi}_0$ and CS reconstruction is carried out using a mismatched dictionary $\boldsymbol{\Psi}$. The mismatch has a value of 0.01, followed by values from 0.1 to 0.7 with a step-size of 0.1. For range and azimuth pixels, the mismatch unit is pixel size, whereas, for range velocity, it is m/s. A series of simulation is carried out at a signal-to-clutter ratio (SCR) of 20 dB with randomly chosen positions and velocities of the moving targets. Reconstruction is carried out using CSLP and CSGBP and the resulting MSE between the original points and the reconstructed points are shown in Figure 2. MSE is calculated as follows:

$$\text{MSE} = \frac{1}{N_t} \sum_{n=1}^{N_t} \left| \sigma_0(n) - \widehat{\sigma}_0(n) \right|^2. \tag{60}$$

Four main parameters are used in CSGBP reconstruction: q, μ_σ, s_σ, and s_ε, which are initially estimated by using a-priori information. The value of q is decided according to the ratio of supposed active scatterers to total number of scatterers present in the data, whereas the values of μ_σ, s_σ, and s_ε are chosen based on SCR. They are then refined by trial and error to get the best results. In general, higher than required values of q, μ_σ, and s_σ help in producing weak scatterers but lead to more side lobes, whereas a higher value of s_ε suppresses weak scatterers. From Figure 2, the following observations can be made.

(i) In general, reasonable reconstruction is obtained when the effect of basis mismatch is less than 1/3 of a pixel size.

(ii) MSE is less in case of no range and azimuth pixel mismatch using CSGBP. Similarly, for a small mismatch in range and azimuth directions, the MSE level in case of CSGBP based reconstruction is less. Specifically, it can be remarked that although for the velocity mismatch, MSE increases when velocity mismatch reaches 0.1 m/s; however, in case of range and azimuth pixels mismatch, MSE is very small as long as pixel mismatch stays less than 0.3 of the pixel size. Thus, CSGBP can be used for better reconstruction and reduction of the dictionary size in practical scenarios, compared to CSLP based reconstruction, where the MSE is higher even in case of no dictionary mismatch.

(iii) MSE for range velocity is high using both methods. After the mismatch of 0.1 m/s, CSLP seems to give slightly lower MSE. The reason may be that CSGBP gives higher number of side lobes. Further simulations for the values of mismatch ranging from 0.01 to 0.1 in a step size of 0.01 m/s are shown in Figure 3. It can be seen that MSE using CSGBP is still smaller than that using CSLP. The reason for not reporting any ill effects of mismatch in velocity in [25] may be that the amount of mismatch considered is small for the configuration that was studied. There are two types of moving targets that are considered in [25], a slow one and a fast one. The former target has a range velocity of 2.35 m/s, whereas the latter target has a range velocity of 28.15 m/s. The range velocity mismatch for the slow target is 0.85 m/s, whereas, for the fast target, it is 0.45 m/s. The amount of mismatch is small to have any effect on the reconstruction for the particular case. This can be seen from reconstruction results in Figure 5 of [25] that shows focussing assuming no motion. The slow object, despite having a mismatch of 2.35 m/s in the range direction, is still focussed at the same position. Our results show theoretically as well as experimentally that a mismatch in velocity can have a serious impact on reconstruction.

(iv) The error increases gradually for position mismatch but increases very rapidly for range velocity mismatch. The reason is that, in case of range velocity mismatch, a large shift arises in azimuth direction. This is due to the reason that r_n is of the order of 10^3 m;

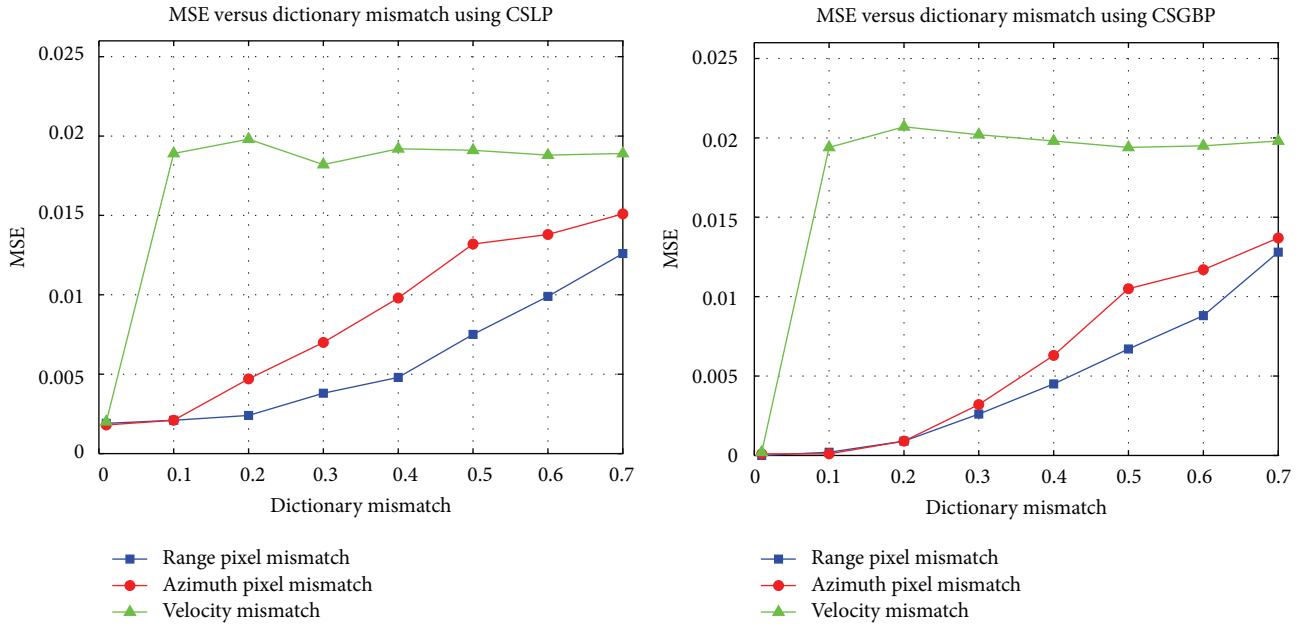

(a) MSE versus dictionary mismatch using CSLP

(b) MSE versus dictionary mismatch using CSGBP

Figure 2: MSE versus dictionary mismatch using CSLP and CSGBP.

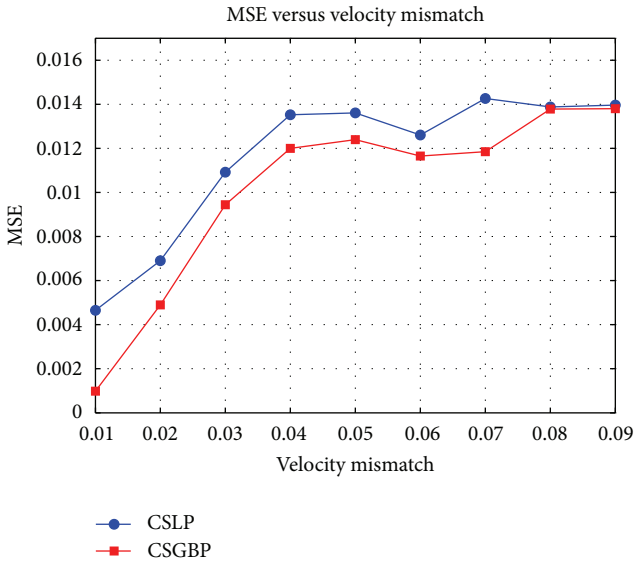

Figure 3: MSE for range velocity mismatch using CSLP and CSGBP.

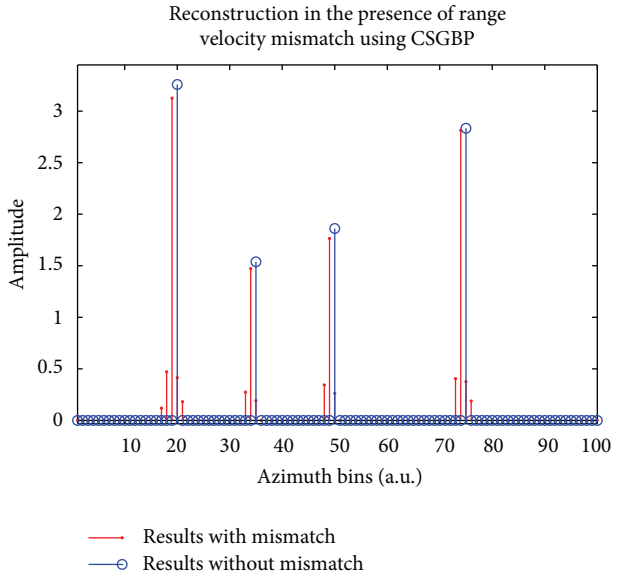

Figure 4: Effects of range velocity mismatch using CSGBP. A single-pixel shift and some side lobes can be seen.

for example, for a velocity mismatch of 0.05 m/s, $r_n = 2595$ m, and $\theta_n = 40^\circ$, there is a single-pixel shift between the original and reconstructed position. Thus, the reconstruction result will contain azimuth pixels shifted according to the mismatch, which leads to a sudden increase in MSE. As there is a total misalignment between actual and estimation positions, MSE rises and stays at a roughly constant maximum level. This is further demonstrated in Figure 4, where a reconstructed scene contains a single pixel shift with respect to the actual position. The reason is that there is a mismatch in range velocity of 0.05 m/s. A loss of amplitude and side lobes can be seen.

(v) The error in azimuth is more than that in range position in general, especially using CSLP. The reason is that there are more than one combination of r_n, y_n, and θ_n that lead to closely resembling values of r_m and y_m in (26); for example, for the parameters given in Table 3, we can see that r_n and y_n of 2594.5 m and

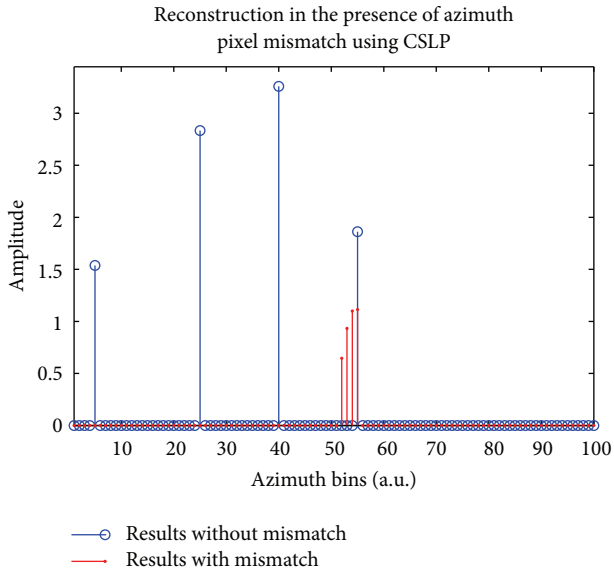

(a) Effects of azimuth pixel mismatch using CSLP. Only one position is identified correctly with a velocity of 3 m/s

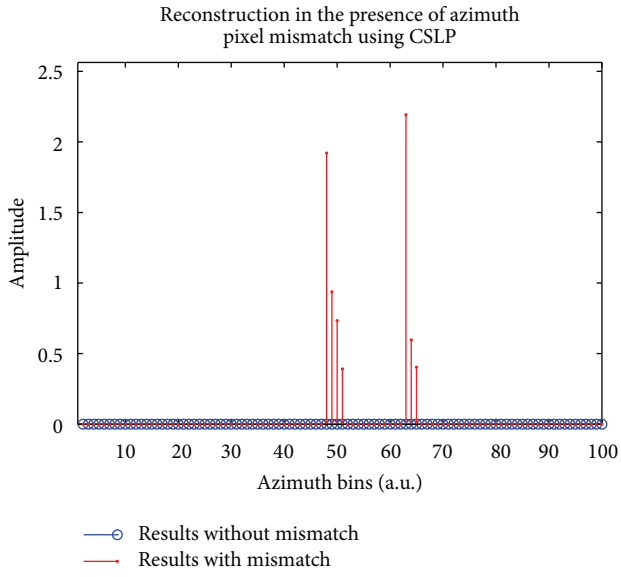

(b) Effects of azimuth pixel mismatch using CSLP. The scatterers are identified at a velocity of 4 m/s, instead of a velocity of 3 m/s. Scatterers are also shifted from their true positions

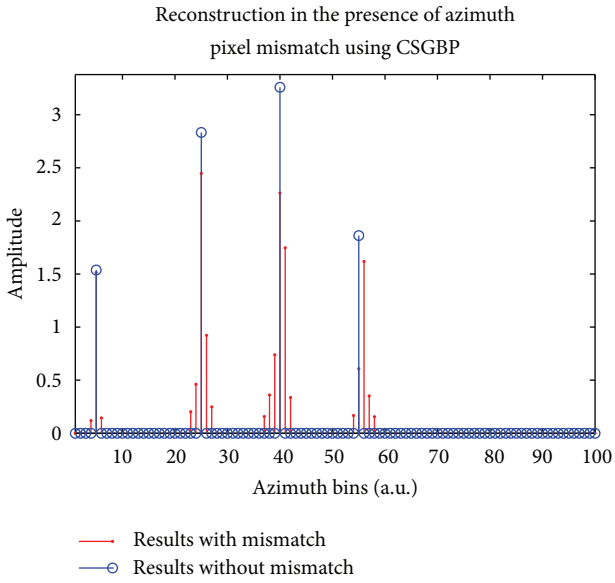

(c) Effects of azimuth pixel mismatch using CSGBP. The positions are identified correctly with the presence of higher side lobes

FIGURE 5: Effects of azimuth pixel mismatch using CSLP and CSGBP.

−25.7143 m with $v_x = 3$ m/s lead to r_m and y_m of 2594 m and −75.2693 m. The same values of r_m and y_m are obtained with similar value of r_n and $y_n = -9.1154$ m with $v_x = 4$ m/s as well as $y_n = 7.2128$ m and $v_x = 5$ m/s. Thus, it is possible that a dictionary mismatch will lead to selection of dictionary elements and subsequently, side lobes that are not in the immediate neighborhood. This is demonstrated in Figure 5, where there are 4 points at different azimuth positions having a velocity of 3 m/s. The mismatch is 0.1, 0.3, 0.5, and 0.7 of a pixel size. When CSLP is used to carry out reconstruction, only a single point is identified with a velocity of 3 m/s. This is shown in Figure 5(a). Two of the points are detected at shifted azimuth positions with a velocity of 4 m/s, as shown in Figure 5(b). The fourth point is not identified at all. In case of reconstruction using CSGBP, all of the four points are identified correctly as shown in Figure 5(c), albeit with higher side lobes. This also demonstrates the advantage offered by CSGBP by identifying correct positions and velocity even in the presence of pixel mismatch.

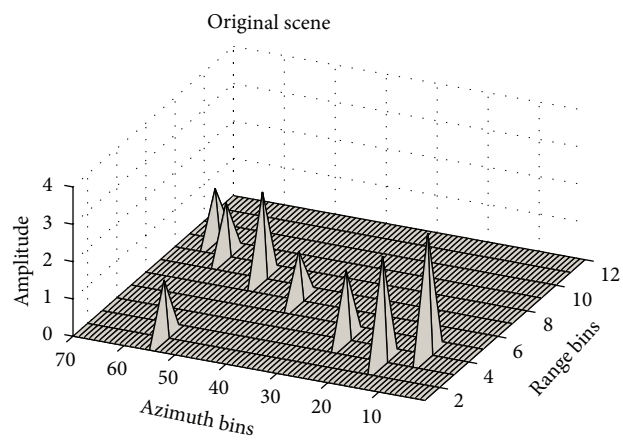

(a) Original scene used for showing effects of range and azimuth pixels mismatch

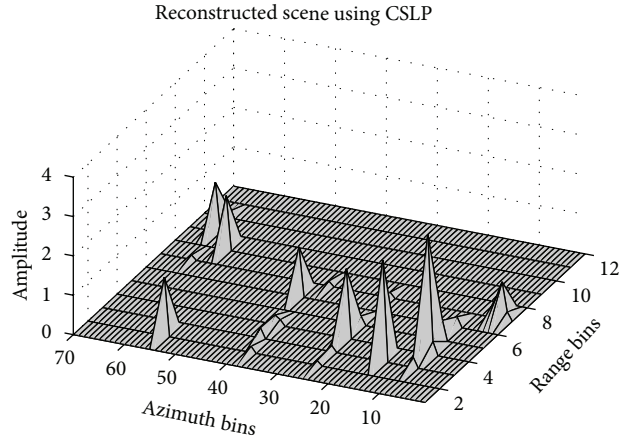

(b) Reconstruction using CSLP. One of the scatterers is not identified correctly

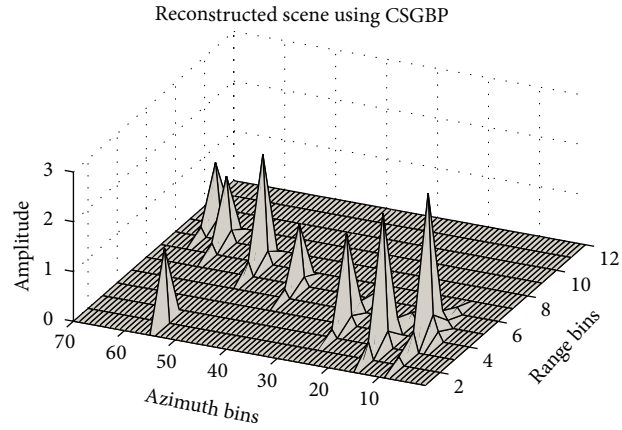

(c) Reconstruction using CSGBP. All positions are identified correctly

Figure 6: Reconstruction in the presence of range and azimuth pixels mismatch using CSLP and CSGBP.

4.2. Imaging Results. In this section, we compare the reconstruction performance of CSLP and CSGBP through imaging results and demonstrate the effectiveness of the proposed iterative CSGBP. Eight points are simulated at positions (2, 55), (3, 15), (4, 9), (4, 25), (6, 40), (7, 50), (8, 60), and (9, 65). The scene is shown in Figure 6(a). The velocities of the points are 3, 4, −5, 5, 4, −3, −4, and −5 m/s, respectively. Reconstruction is carried out in the presence of a mismatch of 1/8 of a pixel size in range and azimuth. Results using CSLP are shown in Figure 6(b), which shows that the point at (7, 50) is not reconstructed correctly. CSGBP results shown in Figure 6(c) indicate that all the points are correctly reconstructed. This demonstrates the superior performance of CSGBP. Furthermore, results using CSGBP show side lobes in the vicinity of actual positions, whereas, in case of CSGBP, the side lobes appear at positions that are not in the vicinity of actual positions. A further example is shown with a mismatch of 0.4 m/s in range velocity. The original scene is shown in Figure 7(a), where there are closely spaced scatterers roughly in the middle of the scene. They have a velocity of 4.4 m/s, whereas the closest velocity in the dictionary is 4 m/s. Reconstruction using both CSLP and CSGBP shows shifted results due to the mismatch. Furthermore, results obtained using CSLP were obtained at a velocity of 5 m/s. Result obtained using iterative CSGBP is shown in Figure 7(d), where the points are located at their correct positions. The velocity in the dictionary is increased iteratively with a step size of 0.05 m/s, until the highest contrast is achieved. A plot of contrast with velocity is shown in Figure 8, where it can be seen that the contrast is the highest when the velocity in the dictionary matches the actual velocity. This shows that creating dictionary elements iteratively and using contrast to measure quality are effective methods for dealing with CS moving target imaging in the presence of range velocity mismatch. Another example is shown with a scene in Figure 9(a). The points are at positions of (2, 5), (5, 45), (6, 34), (2, 70), (10, 15), and (7, 65). The point at (2, 5) has a velocity of −4.9 m/s, the point at (5, 45) has a velocity of −4 m/s, and the point at (6, 34) has a velocity of −3 m/s. The remaining points have a velocity of 3.3 m/s. Thus, there is a mismatch of 0.1 m/s and 0.3 m/s. The pixel at position (2, 5) has a 1/2 pixel mismatch in azimuth and 1/4 pixel mismatch in azimuth. The pixel at positions (6, 34) has a 1/4 pixel mismatch in azimuth and 1/2 pixel mismatch in range.

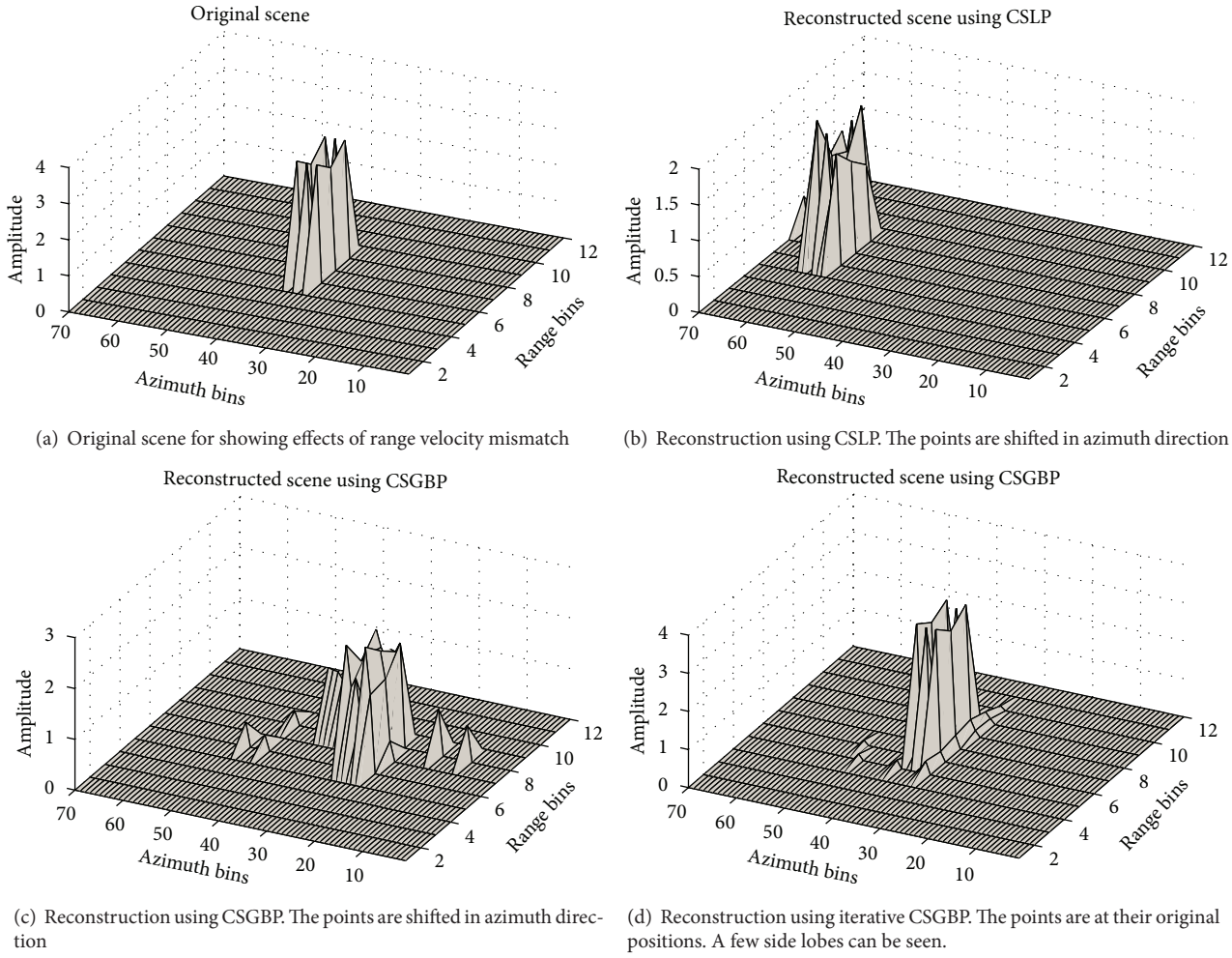

(a) Original scene for showing effects of range velocity mismatch

(b) Reconstruction using CSLP. The points are shifted in azimuth direction

(c) Reconstruction using CSGBP. The points are shifted in azimuth direction

(d) Reconstruction using iterative CSGBP. The points are at their original positions. A few side lobes can be seen.

Figure 7: Reconstruction using CSLP, CSGBP, and iterative CSGBP in the presence of range velocity mismatch.

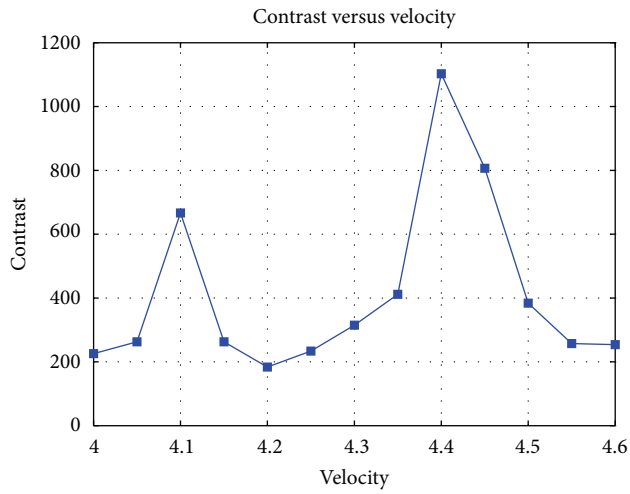

Figure 8: Contrast versus velocity. The velocity of the point is 4.4 m/s.

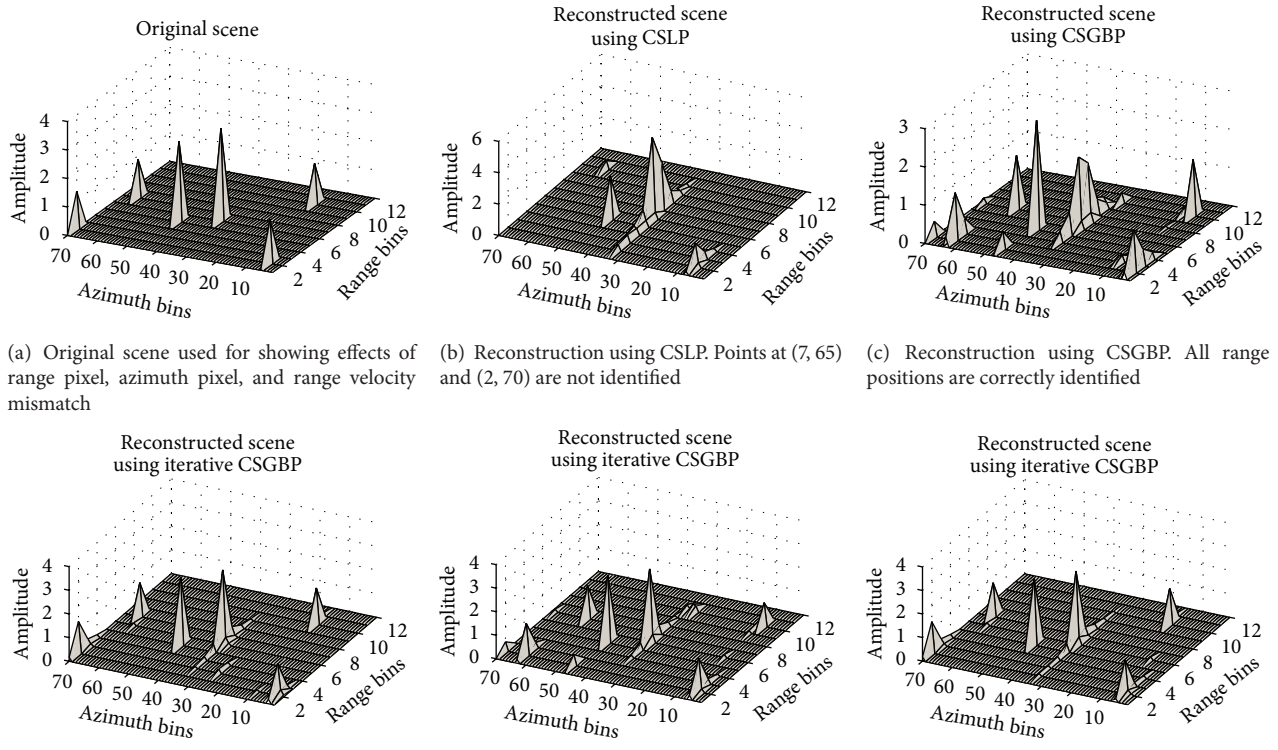

(a) Original scene used for showing effects of range pixel, azimuth pixel, and range velocity mismatch

(b) Reconstruction using CSLP. Points at (7, 65) and (2, 70) are not identified

(c) Reconstruction using CSGBP. All range positions are correctly identified

(d) Reconstruction using iterative CSGBP. Points moving at 3.3 m/s are focussed

(e) Reconstruction using iterative CSGBP. Point moving at −4.9 m/s is focussed

(f) Reconstruction using iterative CSGBP. All points are focussed

Figure 9: Reconstruction using CSLP, CSGBP, and iterative CSGBP.

CSLP reconstruction results with the dictionary containing elements at 1/4 pixel spacing are shown in Figure 9(b). CSLP is unable to detect two of the scatterers at positions (7, 65) and (2, 70); other scatterers having velocity mismatch are shifted in azimuth. CSGBP reconstruction results are shown in Figure 9(c). All the range positions are correctly identified, but the result is shifted in azimuth. Result using iterative CSGBP with velocity varying in a step size of 0.05 m/s for each velocity in the dictionary is shown in Figures 9(d)–9(f). The result obtained by maximizing the contrast for the point at (6, 34) is shown in Figure 9(d), where the points moving at 3.3 m/s are focussed at their true position. Some side lobes can be seen. Similarly, the point moving at −4.9 m/s is shown correctly focussed in Figure 9(e). Final result obtained using the calculated velocities is shown in Figure 9(f), where all the points are focussed at their true positions. Some side lobes can be observed.

5. Conclusion

In this paper, we studied compressed sensing (CS) synthetic aperture radar (SAR) moving target imaging in the presence of dictionary mismatch. We analyzed the sensitivity of the imaging process to range pixel, azimuth pixel, and range velocity mismatches. The mismatch analysis shows that the reconstruction error increases with mismatch and especially increases very rapidly in the presence of range velocity mismatch. Unlike existing references, we show that using a Gaussian-Bernoulli prior compared to the traditionally used Laplacian prior offers advantage in CS SAR imaging for dealing with small mismatch. This advantage is apparent in dealing with positions mismatch. We calculated Cramer-Rao bounds that demonstrate theoretically the lowering of mean square error between actual and reconstructed result by using the GBP. We show that creating an upsampled dictionary and using the GBP for reconstruction can deal with position mismatch. We also presented an iterative scheme to deal with the range velocity mismatch where dictionary elements are created efficiently. CS reconstruction is carried out at each iteration until the image contrast is maximized for each velocity. Numerical and imaging examples confirm the analysis and the effectiveness of the proposed upsampling and iterative scheme.

Notations and Symbols

t: Range time
f_c: Central frequency
r: Slant-range positions
y: Azimuth positions
k_c: $4\pi f_c/c$
K: Chirp rate
V: Sensor velocity
h: Antenna height
T_p: Pulse length
x: Ground-range positions

c: Speed of light
τ: Azimuth time
θ_n: Incidence angle at range r_n, equal to $\cos^{-1}(h/r_n)$
v_x^k: kth ground range velocity
$v_{r,n}^k$: Translational velocity, equal to $v_{r,n}^k = v_x^k \sin\theta_n$
s_r: Pixel size in range
s_y: Pixel size in azimuth
n_r: Number of range pixels in the scene
n_y: Number of azimuth pixels in the scene
N_r: Number of range pixels in raw data
N_y: Number of azimuth pixels in raw data
N_{vx}: Number of range velocities
N_t: $N \times N_{vx}$
N: $n_r \times n_y$
N_s: $N_r \times N_y$
$\mathbf{s_0}$: Raw data from all the points in the scene arranged in 1D form
$\mathbf{s}_n^k$: Raw data for nth point moving with kth velocity, arranged in 1D form
$\tilde{s}_n^k(t_m, \tau_n)$: Raw data element for range time t_m and azimuth time τ_n
$d_n^k(\tau_n)$: Radar-target distance for nth point moving with kth velocity
$\mathbf{\Psi_0}$: Original dictionary
$\mathbf{\Psi}$: Mismatched dictionary
$\boldsymbol{\sigma_0}$: Original reflectivity vector
$\boldsymbol{\sigma}$: Mismatched reflectivity vector
$\widehat{\boldsymbol{\sigma}}_\mathbf{0}$: Reconstructed reflectivity vector
$\widehat{\boldsymbol{\sigma}}$: Reconstructed reflectivity vector in the presence of mismatch
$\widehat{\mathbf{\Sigma}}_\mathbf{0}$: Reconstructed reflectivity in 2D
$\mathbf{\Phi}$: Sampling matrix
M: Number of columns of $\mathbf{\Phi}$
ε: Noise vector
$|\langle\ ,\ \rangle|$: Inner product
$\langle\cdot\rangle$: Averaging operation
Θ_n^k: Rotation angle with which a moving scatterer can be seen equivalent to a static scatterer
Δr_n: Subpixel mismatch in range position
Δy_n: Subpixel mismatch in azimuth position
Δv_x^k: Fraction of m/s mismatch in range velocity
Δy_n^k: Shift in range position due to range velocity mismatch
$\sigma_{0,n}^k$: Element of reflectivity vector at nth position and moving with kth velocity
$\widehat{\sigma}_{0,n}^k$: Reconstructed element of reflectivity vector at nth position and moving with kth vecloity
$\widetilde{\Delta r}$: Dictionary resolution for range
$\widetilde{\Delta y}$: Dictionary resolution for azimuth
$\widetilde{\Delta v}_x$: Dictionary resolution for range velocity
r_m: Range position for equivalent static point
y_m: Azimuth position for equivalent static point
p: Probability of active coefficients in $\widehat{\boldsymbol{\sigma}}_\mathbf{0}$
q: Sparsity of $\widehat{\boldsymbol{\sigma}}_\mathbf{0}$
ρ: Correlation
s_ξ^2: Variance for noise
s_σ^2: Variance of reflectivity vector
$\mathbf{I}$: Identity matrix
$C_{\widehat{\boldsymbol{\sigma}}_\mathbf{0}}$: Contrast of $\widehat{\boldsymbol{\sigma}}_\mathbf{0}$
FIM: Fisher information matrix
CSLP: CS reconstruction with Laplacian prior
CSGBP: CS reconstruction with Gaussian-Bernoulli prior
$\mathbf{J}_{\mathrm{LP}}$: FIM for CSLP without mismatch
$\mathbf{J}_{\mathrm{GBP}}$: FIM for CSGBP without mismatch
$\widetilde{\mathbf{J}}_{\mathrm{LP}}$: FIM for CSLP with mismatch
$\widetilde{\mathbf{J}}_{\mathrm{GBP}}$: FIM for CSGBP with mismatch.

References

[1] E. J. Candès and T. Tao, "Decoding by linear programming," *IEEE Transactions on Information Theory*, vol. 51, no. 12, pp. 4203–4215, 2005.

[2] E. J. Candès, J. Romberg, and T. Tao, "Robust uncertainty principles: exact signal reconstruction from highly incomplete frequency information," *IEEE Transactions on Information Theory*, vol. 52, no. 2, pp. 489–509, 2006.

[3] D. L. Donoho, "Compressed sensing," *IEEE Transactions on Information Theory*, vol. 52, no. 4, pp. 1289–1306, 2006.

[4] J. A. Tropp and A. C. Gilbert, "Signal recovery from random measurements via orthogonal matching pursuit," *IEEE Transactions on Information Theory*, vol. 53, no. 12, pp. 4655–4666, 2007.

[5] S. Ji, Y. Xue, and L. Carin, "Bayesian compressive sensing," *IEEE Transactions on Signal Processing*, vol. 56, no. 6, pp. 2346–2356, 2008.

[6] H. Zayyani, M. Babaie-Zadeh, and C. Jutten, "Bayesian pursuit algorithm for sparse representation," in *Proceedings of the IEEE International Conference on Acoustics, Speech, and Signal Processing (ICASSP '09)*, pp. 1549–1552, April 2009.

[7] P. Schniter, L. C. Potter, and J. Ziniel, "Fast bayesian matching pursuit," in *Proceedings of the 2008 Information Theory and Applications Workshop (ITA '08)*, pp. 326–332, San Diego, Calif, USA, February 2008.

[8] J. Ma, "Single-Pixel remote sensing," *IEEE Geoscience and Remote Sensing Letters*, vol. 6, no. 2, pp. 199–203, 2009.

[9] M. Lustig, D. Donoho, and J. M. Pauly, "Sparse MRI: the application of compressed sensing for rapid MR imaging," *Magnetic Resonance in Medicine*, vol. 58, no. 6, pp. 1182–1195, 2007.

[10] G. Shi, J. Lin, X. Chen, F. Qi, D. Liu, and L. Zhang, "UWB echo signal detection with ultra-low rate sampling based on compressed sensing," *IEEE Transactions on Circuits and Systems II*, vol. 55, no. 4, pp. 379–383, 2008.

[11] J. Ma and F.-X. Le Dimet, "Deblurring from highly incomplete measurements for remote sensing," *IEEE Transactions on Geoscience and Remote Sensing*, vol. 47, no. 3, pp. 792–802, 2009.

[12] X. Nie, D.-Y. Zhu, and Z.-D. Zhu, "Application of synthetic bandwidth approach in SAR polar format algorithm using the deramp technique," *Progress in Electromagnetics Research*, vol. 80, pp. 447–460, 2008.

[13] Q. Huang, L. Qu, B. Wu et al., "UWB through-wall imaging based on compressive sensing," *IEEE Transactions on Geoscience and Remote Sensing*, vol. 48, no. 3, pp. 1408–1415, 2010.

[14] W. Zhang, M. Amin, F. Ahmad et al., "Ultrawideband impulse radar through-the-wall imaging with compressive sensing," *International Journal of Antennas and Propagation*, vol. 2012, Article ID 251497, 11 pages, 2012.

[15] M. Duman and A. Gurbuz, "Performance analysis of compressive-sensing-based through-the-wall imaging with effect of unknown parameters," *International Journal of Antennas and Propagation*, vol. 2012, Article ID 405145, 11 pages, 2012.

[16] X. X. Zhu and R. Bamler, "Tomographic SAR inversion by L_1-norm regularization—the compressive sensing approach," *IEEE Transactions on Geoscience and Remote Sensing*, vol. 48, no. 10, pp. 3839–3846, 2010.

[17] X. X. Zhu and R. Bamler, "Super-resolution power and robustness of compressive sensing for spectral estimation with application to spaceborne tomographic SAR," *IEEE Transactions on Geoscience and Remote Sensing*, vol. 50, no. 1, pp. 247–258, 2012.

[18] A. Budillon, A. Evangelista, and G. Schirinzi, "Three-dimensional SAR focusing from multipass signals using compressive sampling," *IEEE Transactions on Geoscience and Remote Sensing*, vol. 49, no. 1, pp. 488–499, 2011.

[19] M. T. Alonso, P. López-Dekker, and J. J. Mallorquí, "A novel strategy for radar imaging based on compressive sensing," *IEEE Transactions on Geoscience and Remote Sensing*, vol. 48, no. 12, pp. 4285–4295, 2010.

[20] R. K. Raney, "Synthetic aperture imaging radar and moving targets," *IEEE Transactions on Aerospace and Electronic Systems*, vol. 7, no. 3, pp. 499–505, 1971.

[21] J. H. G. Ender, "On compressive sensing applied to radar," *Signal Processing*, vol. 90, no. 5, pp. 1402–1414, 2010.

[22] Q. Wu, M. Xing, C. Qiu, B. Liu, Z. Bao, and T.-S. Yeo, "Motion parameter estimation in the SAR system with low PRF sampling," *IEEE Geoscience and Remote Sensing Letters*, vol. 7, no. 3, pp. 450–454, 2010.

[23] A. S. Khwaja and J. Ma, "Applications of compressed sensing for sar moving-target velocity estimation and image compression," *IEEE Transactions on Instrumentation and Measurement*, vol. 60, no. 8, pp. 2848–2860, 2011.

[24] Y. G. Lin, B. C. Zhang, W. Hong, and Y. R. Wu, "Along-track interferometric SAR imaging based on distributed compressed sensing," *Electronics Letters*, vol. 46, no. 12, pp. 858–860, 2010.

[25] I. Stojanovic and W. C. Karl, "Imaging of moving targets with multi-static SAR using an overcomplete dictionary," *IEEE Journal on Selected Topics in Signal Processing*, vol. 4, no. 1, pp. 164–176, 2010.

[26] M. A. Herman and T. Strohmer, "General deviants: an analysis of perturbations in compressed sensing," *IEEE Journal on Selected Topics in Signal Processing*, vol. 4, no. 2, pp. 342–349, 2010.

[27] Y. Chi, L. L. Scharf, A. Pezeshki, and A. R. Calderbank, "Sensitivity to basis mismatch in compressed sensing," *IEEE Transactions on Signal Processing*, vol. 59, no. 5, pp. 2182–2195, 2011.

[28] O. Teke, A. C. Gurbuz, and O. Arikan, "A new OMP techniques for sparse recovery," in *Proceedings of the 20th Signal Processing and Communications Applications Conference (SIU '12)*, Fethiye, Turkey, April 2012.

[29] A. S. Khwaja and X.-P. Zhang, "Compressed sensing based image formation of SAR/ISAR data in presence of basis mismatch," in *Proceedings of the 2012 IEEE International Conference on Image Processing (ICIP '12)*, Orlando, Fla, USA, 2012.

[30] S. Yu, A. Shaharyar Khwaja, and J. Ma, "Compressed sensing of complex-valued data," *Signal Processing*, vol. 92, no. 2, pp. 357–362, 2012.

[31] G. Franceschetti and R. Lanari, *Synthetic Aperture Radar Processing*, CRC Press, Oxford, UK, 1999.

[32] E. G. Larsson and Y. Selén, "Linear regression with a sparse parameter vector," *IEEE Transactions on Signal Processing*, vol. 55, no. 2, pp. 451–460, 2007.

[33] M. Soumekh, *Synthetic Aperture Radar Signal Processing*, John Wiley and Sons, 1999.

[34] P. Tichavsky, C. H. Muravchik, and A. Nehorai, "Posterior Cramér-Rao bounds for discrete-time nonlinear filtering," *IEEE Transactions on Signal Processing*, vol. 46, no. 5, pp. 1386–1396, 1998.

[35] H. Zayyani, M. Babaie-Zadeh, and C. Jutten, "Bayesian cramer-rao bound for noisynon-blind and blind compressed sensing," http://arxiv.org/abs/1005.4316.

Hindawi Publishing Corporation
International Journal of Antennas and Propagation
Volume 2013, Article ID 826935, 10 pages
http://dx.doi.org/10.1155/2013/826935

Research Article

Deterministic Aided STAP for Target Detection in Heterogeneous Situations

J.-F. Degurse,[1] L. Savy,[1] S. Marcos,[2] and J.-Ph. Molinié[1]

[1] *Department of Electromagnetism and Radar, ONERA, 91120 Palaiseau, France*
[2] *Laboratoire des Signaux et des Systémes, Supélec-CNRS, University of Paris-Sud, 91192 Gif-sur-Yvette, France*

Correspondence should be addressed to J.-F. Degurse; jean-francois.degurse@lss.supelec.fr

Received 30 April 2013; Accepted 23 September 2013

Academic Editor: Ulrich Nickel

Classical space-time adaptive processing (STAP) detectors are strongly limited when facing highly heterogeneous environments. Indeed, in this case, representative target free data are no longer available. Single dataset algorithms, such as the MLED algorithm, have proved their efficiency in overcoming this problem by only working on primary data. These methods are based on the APES algorithm which removes the useful signal from the covariance matrix. However, a small part of the clutter signal is also removed from the covariance matrix in this operation. Consequently, a degradation of clutter rejection performance is observed. We propose two algorithms that use deterministic aided STAP to overcome this issue of the single dataset APES method. The results on realistic simulated data and real data show that these methods outperform traditional single dataset methods in detection and in clutter rejection.

1. Introduction

In the context of radar signal processing, the purpose of space-time adaptive processing (STAP) is to remove ground clutter returns, in order to enhance slow moving target detection. STAP performs two-dimensional space and time adaptive filtering where different space channels are combined at different times [1]. Filter's weights are adaptively computed from training data in the neighborhood of the range cell of interest, called cell under test (CUT). The estimation of these weights is always deducted, more or less directly, from an estimation of the covariance matrix of the received signal, which is the key quantity in the process of adaptation [2]. Any implementation of STAP processing must remain absolutely consistent with the strategy of radar processing whose purpose is to obtain a high probability of detection while keeping a very low probability of false alarm.

Classical space-time adaptive processing (STAP) detectors are strongly limited when facing a severe nonstationary environment such as heterogeneous clutter. Indeed, in these cases, representative training data are no longer available. The Maximum Likelihood Estimation Detector (MLED) [3] is a single dataset detector among others [4]. It only operates with the data from the cell under test, hence its performance is not impacted by nonstationarity. Of course, no environment is purely heterogeneous or homogeneous and the problem can be addressed by combining primary and secondary data [5]. We will here consider the environment to be heterogeneous enough to only use primary data. To make the primary data target-free, the MLED detector removes a thin part of the signal of the Doppler cell under test from the covariance matrix. A slight part of the clutter is removed along the target signal which implies a degradation of clutter rejection, especially if the number of Doppler cells is low. The less Doppler cells, the more the clutter removed from the covariance matrix and the worse the estimation of the covariance matrix. The bad estimation of the matrix can be addressed by using subspace methods [6] but the removal of some clutter is inherent to the APES method.

In this paper, we will show how we can overcome this problem by the use of deterministic aided STAP. Moreover, we will extend this method to the Stop-Band APES which greatly reduces the computational workload of the MLED detector.

Section 2 is devoted to the data model, and Section 3 summarizes the principle of the MLED APES-based detector and the Stop-Band APES algorithm. A deterministic based non-adaptive approach of space-time processing is presented in

Section 4. In Section 5, we describe two different approaches for deterministic aided STAP and finally, in Section 6, simulations are given to show that the proposed methods outperform the MLED and Stop-Band algorithms.

2. Data Model

Consider a radar antenna made of N sensors that acquires M_p pulse snapshots for each range gate l. We will only use the primary data so we will forget the range gate dimension, also called fast-time dimension. Then, the processing algorithm works independently in each range cell. We adopt the following two hypothesis models where H_0 and H_1 mean that no target or a target is present, respectively:

$$\begin{aligned} H_0 &: \ \mathbf{X} = \mathbf{N}, \\ H_1 &: \ \mathbf{X} = \alpha \mathbf{s}_s \mathbf{s}_t^T + \mathbf{N}, \end{aligned} \tag{1}$$

where the received data have been arranged into an $MN \times K_t$ matrix $\mathbf{X}$ with K_t being the number of training data pulse snapshots, M being the number of pulses of the spatio-temporal vector, and α being the complex amplitude of the target. $\mathbf{s}_s$ is the spatiotemporal steering vector (length NM), $\mathbf{s}_t$ is the temporal steering vector (length $K_t = M_p - M + 1$), and $\mathbf{N}$ is the interference (clutter plus noise) matrix.

We make use of a temporal sliding window to work on the temporal dimension; consequently, the estimated covariance matrix $\mathbf{R}$ is obtained from $\mathbf{X}$ as follows:

$$\mathbf{R} = \frac{1}{K_t} \mathbf{X}\mathbf{X}^H. \tag{2}$$

One classical STAP detector taken as reference uses the Adaptive Matched Filter (AMF) [1, 2]. The filter $\mathbf{w}$ is

$$\mathbf{w} = \frac{\mathbf{R}^{-1}\mathbf{s}}{\mathbf{s}_s^H \mathbf{R}^{-1} \mathbf{s}_s}. \tag{3}$$

Detection is achieved by comparing the output SNIR power of the matched filter to a threshold as follows:

$$\mathbf{P}_{\text{AMF}} = \frac{\left|\mathbf{s}_s^H \mathbf{R}^{-1} \mathbf{X}\right|^2}{\mathbf{s}_s^H \mathbf{R}^{-1} \mathbf{s}_s} \underset{H_1}{\overset{H_0}{\lessgtr}} \eta. \tag{4}$$

In case where a strong target is present at this range gate, $\mathbf{R}$ contains the target covariance matrix. Consequently, the target is removed with the clutter and it can no longer be detected by (4). This happens when many targets are moving at the same speed but are at different distances (roads, highways, convoys, etc.). Another problem with this detector is that the ground clutter has to be homogeneous on the range domain. Otherwise, the clutter used to estimate the covariance matrix will not be representative of the clutter that has to be canceled, leading to a bad clutter rejection.

3. APES-Based STAP Detectors

3.1. The Maximum Likelihood Estimation Detector. To overcome the previous issues of signal suppression or the none representativeness of secondary data, the MLED detector [7] based on the APES [8] algorithm removes the signal of interest from the covariance matrix. The problem is stated as follows:

$$\min_{\mathbf{w},\alpha} \left(\mathbf{w}^H \mathbf{X} - \alpha \mathbf{s}_t^T\right)\left(\mathbf{w}^H \mathbf{X} - \alpha \mathbf{s}_t^T\right)^H, \quad \text{s.t } \mathbf{w}^H \mathbf{s}_s = 1. \tag{5}$$

The obtained solution is

$$\mathbf{w} = \frac{\mathbf{Q}^{-1}\mathbf{s}_s}{\mathbf{s}_s^H \mathbf{Q}^{-1} \mathbf{s}_s}, \qquad \alpha = \frac{\mathbf{w}^H \mathbf{X} \mathbf{s}_t^*}{K_t}, \tag{6}$$

where

$$\mathbf{Q} = \mathbf{R} - \mathbf{g}\mathbf{g}^{\mathbf{H}}, \quad \mathbf{g} = \frac{\mathbf{X}\mathbf{s}_{\mathbf{t}}^*}{K_t}. \tag{7}$$

Detection is achieved using the output power normalized by the Adaptive Power Residue (APR = $\mathbf{w}^H Q w = \mathbf{s}_s^H \mathbf{Q}^{-1} \mathbf{s}_s$) as follows:

$$\mathbf{P}_{\text{MLED}} = \frac{\left|\mathbf{s}_{\mathbf{s}}^{\mathbf{H}} \mathbf{Q}^{-1} \mathbf{g}\right|^2}{\mathbf{s}_s^H \mathbf{Q}^{-1} \mathbf{s}_s} \underset{H_1}{\overset{H_0}{\lessgtr}} \eta. \tag{8}$$

To avoid strong signal loss due to covariance matrix estimation errors [9], one may use in addition diagonal loading [10] or subspace methods [11].

3.2. Extension to Stop-Band APES. Because the MLED algorithm is a high-resolution method, it requires an oversampling in Doppler frequency, typically by a factor four, to correctly work. Indeed, combining (5) and (6), it follows

$$\begin{aligned} &\mathbf{w}^H \left(\mathbf{X} - \mathbf{X}\frac{\mathbf{s}_{\mathbf{t}}^* \mathbf{s}_{\mathbf{t}}^{\mathbf{T}}}{\mathbf{s}_t^T \mathbf{s}_t^*}\right)\left(\mathbf{X} - \mathbf{X}\frac{\mathbf{s}_{\mathbf{t}}^* \mathbf{s}_{\mathbf{t}}^{\mathbf{T}}}{\mathbf{s}_t^T \mathbf{s}_t^*}\right)^H \mathbf{w} \\ &\quad = \mathbf{w}^H \mathbf{X} \left(\mathbf{I} - \mathbf{P}_{//}\right) \left(\mathbf{I} - \mathbf{P}_{//}\right)^H \mathbf{X}\mathbf{w}, \end{aligned} \tag{9}$$

where $\mathbf{P}_{//}$ is the projector into the target signal subspace:

$$\mathbf{P}_{//} = \frac{\mathbf{s}_{\mathbf{t}}^* \mathbf{s}_{\mathbf{t}}^{\mathbf{T}}}{\mathbf{s}_t^T \mathbf{s}_t^*} = \frac{\mathbf{s}_{\mathbf{t}}^* \mathbf{s}_{\mathbf{t}}^{\mathbf{T}}}{K_t}. \tag{10}$$

The problem (5) can then be recognized as a minimization of the interference-plus-noise energy outside the subspace spanned by the target as follows:

$$\min_{\mathbf{w}} \left\{\mathbf{w}^{\mathbf{H}} \mathbf{X} \left(\mathbf{I} - \mathbf{P}_{//}\right) \left(\mathbf{I} - \mathbf{P}_{//}\right)^H \mathbf{X}\mathbf{w}\right\}, \quad \text{s.t } \mathbf{w}^H \mathbf{s}_s = 1. \tag{11}$$

The solution is still $\mathbf{w} = (\mathbf{Q}^{(-1)}\mathbf{s}_s)/(\mathbf{s}_s^H \mathbf{Q}^{(-1)} \mathbf{s}_s)$ but with the more general form for $\mathbf{Q}$:

$$\mathbf{Q} = \frac{\mathbf{X}\mathbf{X}^H}{\mathbf{s}_t^T \mathbf{s}_t^*} - \frac{1}{K_t} \mathbf{X}\mathbf{P}_{//}\mathbf{X}^H. \tag{12}$$

This latest formulation not only shows the hyperresolution property along the frequency domain but also allows overcoming one major drawback of the MLED method for our application. The MLED has indeed a high-frequency resolution due to the sharpness of the projection $\mathbf{I} - \mathbf{P}_{//}$ with

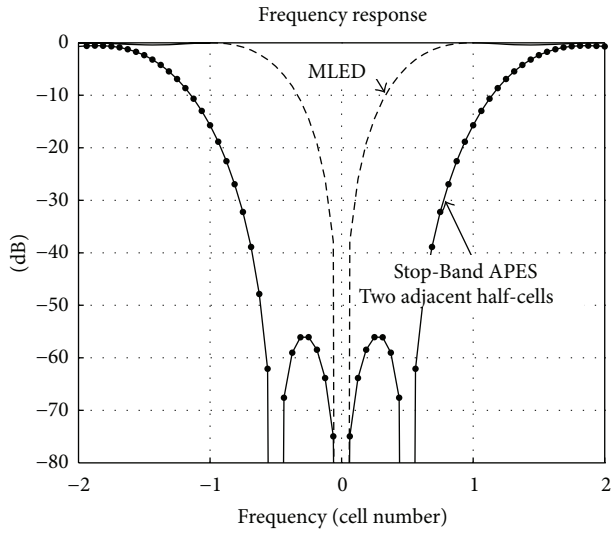

Figure 1: Spectral response of regular MLED $\mathbf{S} = \mathbf{s}_t$ (dash curve) and Stop-Band APES with two adjacent half-cells (solid curve).

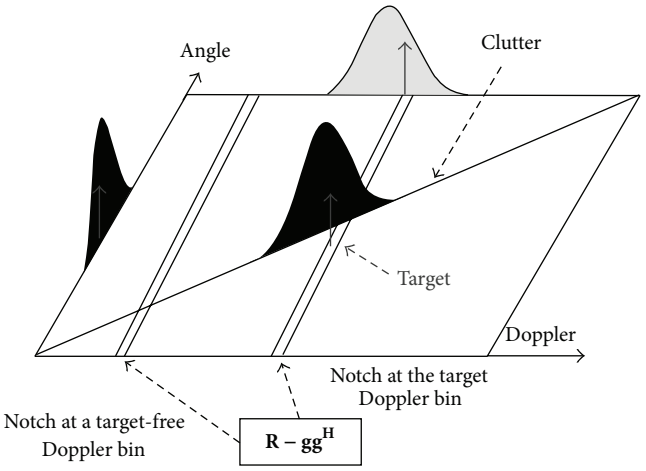

Figure 2: Angle-Doppler map showing the effect of MLED projector for two different Doppler bins.

$\mathbf{P}_{//} = (\mathbf{s_t^*}\,\mathbf{s_t^T})/(\mathbf{s}_t^T\,\mathbf{s}_t^*)$ (dash curve, Figure 1). This is a problem because it requires a strong oversampling to be sure to remove the signal of interest from the covariance matrix and so it leads to an important increase of the computing load. In order to avoid this problem, we propose a new detector called Stop-Band APES. The minimization is using a projector $\mathbf{P}_{//}$ on an extended subspace around the Doppler frequency f_0 under test. For instance, two adjacent half-cells can be added into the space spanned by $\mathbf{P}_{//} = \mathbf{S}_t^*(\mathbf{S}_t^T\mathbf{S}_t^*)^{-1}\mathbf{S}_t^T$ with

$$\mathbf{S}_t = \left[\mathbf{s_t}\left(f_0 - \frac{1}{2K_t}\right), \mathbf{s_t}\left(f_0\right), \mathbf{s_t}\left(f_0 + \frac{1}{2K_t}\right)\right]. \tag{13}$$

The sharpness and effectiveness of the cancellation around the target signal are characterized by the frequency response of the projector, which is, for a signal $\mathbf{X}$ at frequency f ($\mathbf{X} = \mathbf{s_t^T}(f)$), as follows:

$$\begin{aligned}\widetilde{P}_{\perp}(f) &= \left[\mathbf{s_t^T}(f)\left(\mathbf{Id} - \mathbf{P}_{//}\right)\right]\frac{\mathbf{s_t^*}(f)}{\mathbf{s_t^T}(f)\,\mathbf{s_t^*}(f)} \\ &= 1 - \mathbf{s_t^T}(f_1)\frac{\mathbf{P}_{//}}{K_T}\mathbf{s_t^*}(f).\end{aligned} \tag{14}$$

Figure 1 shows that building a projector with two adjacent half-cells is enough to correctly remove the signal in the cell under test. Nevertheless, compared to the MLED, the Stop-Band APES does not require oversampling of the Doppler resolution for the calculation and the application of the STAP filter. A zero-padding by a factor of 2 will still be required to access the signal that has to be evaluated every half-resolution cells for the creation of the projector [12, 13].

3.3. Limitations of the MLED and Stop-Band APES. In order to explore the use of subspace-based methods, we have to go deeper in the formulation of the MLED detector. Indeed, these methods will only work if the clutter subspace of the covariance matrix $\mathbf{R}$ remains very close to the clutter subspace of the target-free covariance matrix $\mathbf{Q}$. For a given distance cell, if there is no target at this range, the covariance matrix $\mathbf{R}$ only contains interference, that is, clutter and possibly jamming signal and noise, according to (2) as follows:

$$\mathbf{R} = \frac{\mathbf{X}\mathbf{X}^H}{K_t} = \frac{\mathbf{N}\mathbf{N}^H}{K_t}. \tag{15}$$

We can demonstrate [11] that the matrix $\mathbf{Q}$ is, without approximation:

$$\mathbf{Q} = \frac{\mathbf{N}\mathbf{N^H}}{K_t} - \frac{\mathbf{N}\mathbf{s}_t^*\,\mathbf{s}_t^T\mathbf{N}^H}{K_t^2}. \tag{16}$$

The matrix $(\mathbf{N}\mathbf{N^H})/K_t$ is the interference-plus-noise estimated covariance matrix, whereas $(\mathbf{N}\mathbf{s}_t^*\,\mathbf{s}_t^T\mathbf{N}^H)/(K_t^2)$ is the scalar product of interference-plus-noise vectors with their projection on $\mathbf{s}_t^*$. It follows from (16) that the modified covariance matrix $\mathbf{Q}$ used for MLED in (8) does no longer contain the target contribution and that the target will not be removed contrarily to the clutter by the MLED STAP filter (6).

The residual clutter-plus-noise covariance matrix is slightly different from the actual covariance matrix $(\mathbf{N}N^H)/K_t$ (Figure 2). The term $(\mathbf{N}\mathbf{s}_t^*\,\mathbf{s_t^T}\mathbf{N^H})/(K_t^2)$ represents the part of the clutter that is removed from the covariance matrix. The number of Doppler cells being usually high, the projector is consequently very sharp; that, the term $(\mathbf{N}\mathbf{s}_t^*\,\mathbf{s_t^T}\mathbf{N^H})/(K_t^2)$ is small and both MLED and Stop-Band APES, which removes a wider part of the clutter from the covariance matrix $(\mathbf{N}\mathbf{s}_t^*\,\mathbf{s_t^T}\mathbf{N^H})/(K_t^2)$, are all working. This effect can be seen on Figure 2 in a situation with and without target in the Doppler cell tested.

However, in a situation where the number of Doppler cells is low, we will observe a degradation of the clutter rejection performance of the MLED detector, and this degradation will

be even worse for the Stop-Band APES algorithm. This effect is due to the partitioning which is done only in time domain. If spatio-temporal partitioning is employed, only a single bin of the angle-Doppler plane is removed but the computational cost would hugely increase because of the angle-Doppler scanning. We will present in the next section a deterministic processing and, in Section 5, a new method that makes use of deterministic processing to solve this problem.

4. Deterministic Space-Time Processing

We will here briefly describe a nonadaptive space-time processing which is the basis of the deterministic aided STAP processing we will introduce in the following section. For a side-mounted antenna, the clutter occupies a one-dimension position in the two-dimensional Doppler-angle domain. The clutter Doppler frequency is a function of the receiving angle as follows:

$$f = \frac{2V}{\lambda}\sin\theta \Longrightarrow \theta = \sin^{-1}\left(\frac{\lambda f}{2V}\right) \tag{17}$$

with f being the Doppler frequency of the clutter, θ being the receiving angle, V being the platform speed, and λ being the wavelength of the radar frequency. Knowing this relation, we can build a filter that will remove all the signal that is in the 1D-domain driven by (17). The general form of the filter, which will be referred in the following to non-adaptive or deterministic processing, has the same form as AMF in (3) as follows:

$$\mathbf{w}^H = \frac{\mathbf{s_s^H}\mathbf{K}^{-1}}{\mathbf{s}_s^H\mathbf{K}^{-1}\mathbf{s}_s} \tag{18}$$

but with

$$\mathbf{K} = \frac{1}{k}\sum_{i=1}^{k}\mathbf{s_c}\left(\theta_i\left(f_i\right), f_i\right)\mathbf{s}_c^H\left(\theta_i\left(f_i\right), f_i\right) + \mathbf{\Gamma_N}, \tag{19}$$

where $\mathbf{\Gamma_N}$ is the true noise covariance matrix (identity matrix in our case), k is the number of mainlobe clutter patches, and $\mathbf{s}_c(\theta_i(f_i), f_i)$ is the space-time steering vector of angle θ_i and frequency f_i obtained with (17). In the same formulation of the filter as MLED and Stop-Band APES in (6), the matrix for each Doppler cell can be written as follows:

$$\mathbf{K}' = \frac{1}{k'}\sum_{i=1}^{k'}\mathbf{s_c}\left(\theta_i\left(f_i\right), f_i\right)\mathbf{s}_c^H\left(\theta_i\left(f_i\right), f_i\right) + \mathbf{\Gamma_N}, \tag{20}$$

where the vector $\mathbf{s}_c(\theta_i(f_i), f_i)$ is the predicted steering vector of the clutter. In this case, to process one Doppler cell, the steering vector $\mathbf{s_c}(\theta_0(f_0), f_0)$ of the Doppler cell under test and the two steering vectors $\mathbf{s_c}(\theta_{\pm1}(f_{\pm1}), f_{\pm1})$ from the adjacent Doppler cells are sufficient to correctly remove the clutter. However, the performance of this nonadaptive approach is very limited in practical situations because of the heterogeneity of the clutter (e.g urban or mountainous areas) and because of antenna/receivers calibration errors which make the real steering vector of the antenna slightly different from the actual steering vector used to build the covariance matrix.

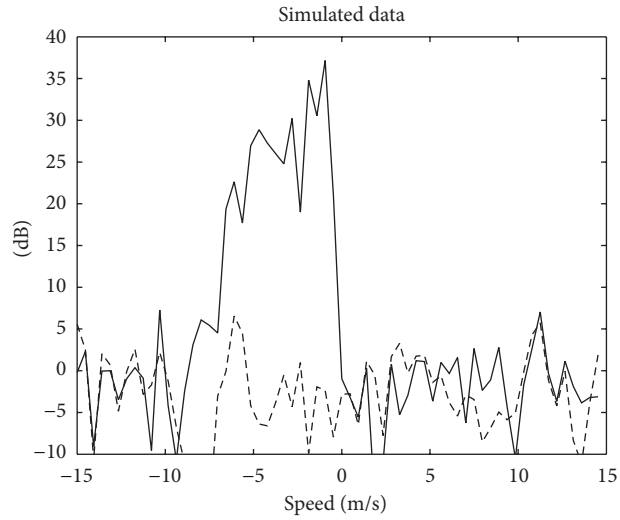

Figure 3: Comparison between sum channel (bold curve, negative speeds), deterministic (bold curve, positive speeds), and adaptive space-time processing (dash curve) on error-free simulated data.

To illustrate this effect, we compare the non-adaptive processing (18) to the classic adaptive processing on two sets of data. The first data are the simulated data that we build using the true spatial steering vector and the second set of data is made of realistic data simulated by a STAP simulator that emulates phases errors on the receiving channels and randomly adds impulsive echoes in the clutter. In both cases, clutter is Gaussian, homogeneous, and set to 40 dB. No target is present in these data. A side-looking antenna with four uniformly spaced subarrays is used. Aircraft speed is set to 100 ms^{-1}, radar frequency is 10 GHz, and the pulse frequency (PRF) is 2 kHz. The non-adaptive processing is only applied in the positive speed domain, that is to say that the negative speeds show the sum channel. The adaptive processing is applied on all the Doppler (speed) domains.

As we can see from Figures 3 and 4, non-adaptive processing works well on the error-free simulated data. The clutter-to-noise ratio (CNR) is close to 0 dB, like in the adaptive processing as shown on Figure 5, which implies an attenuation of 40 dB. On the realistic simulated data, the non-adaptive processing is not performing well, as it fails to suppress the clutter. Indeed, as we can see on Figure 6, the residual CNR is near 15 dB in the main lobe; the clutter attenuation is limited to 25 dB, implying many false alarms. The full range-Doppler maps also point out this effect in Figures 7 and 8. From these results, we deduce that we cannot use a non-adaptive space-time processing in real situations but we may use the deterministic of the clutter Doppler-angle relation together with adaptive processing to achieve better performance.

5. Deterministic Aided STAP

5.1. Deterministic Aided GMTI STAP. In GMTI operation, there are two main concerns about heterogeneous environments: clutter heterogeneity (land relief, urban environments) and high-density target area (roads, highways...).

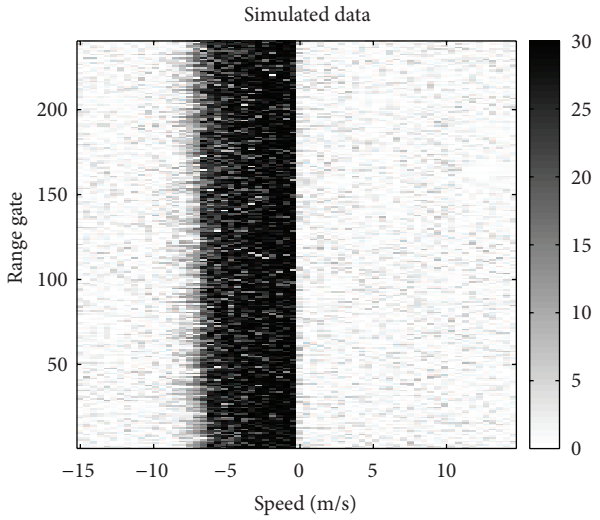

Figure 4: Range-Doppler map of the nonadaptive processing (positive speeds) and the sum channel (negative speeds) on error-free data simulated data.

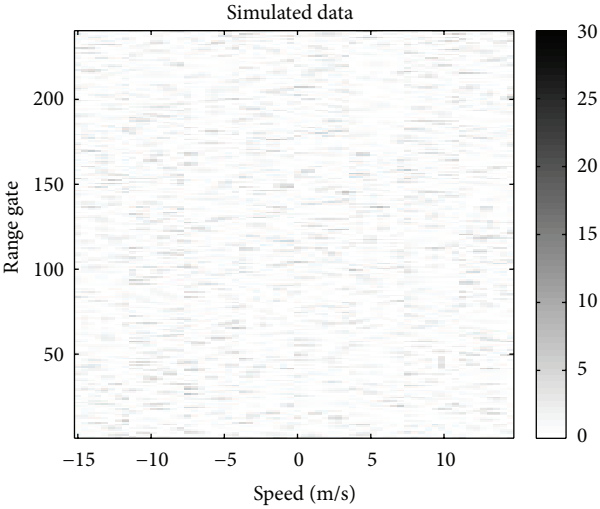

Figure 5: Range-Doppler map showing the performance of the adaptive processing on error-free data simulated data.

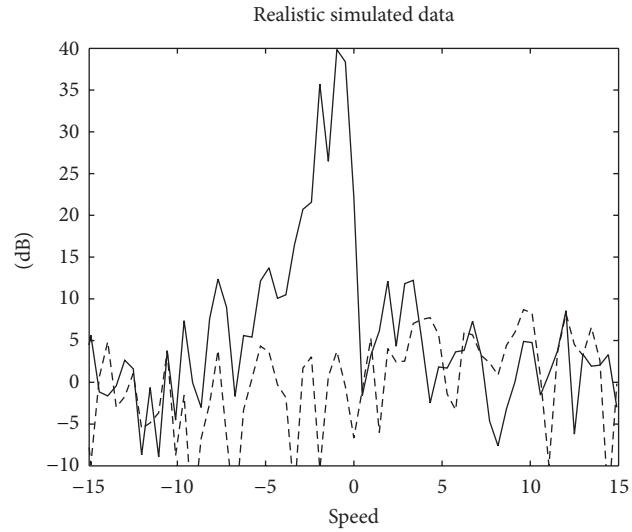

Figure 6: Comparison between sum channel (bold curve, negative speeds), deterministic (bold, positive speeds), and STAP (dash) on realistic data.

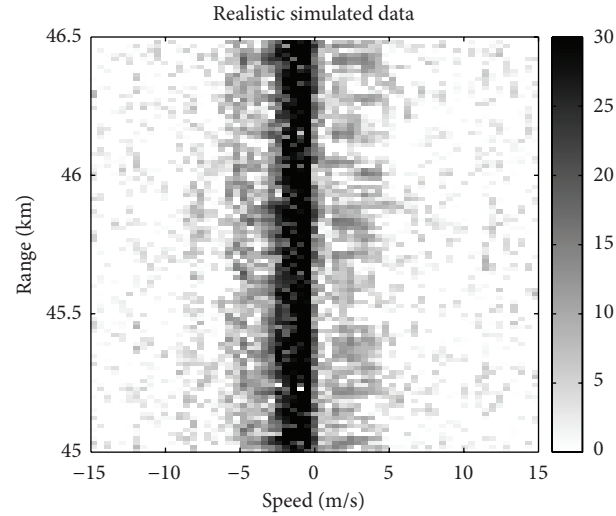

Figure 7: Range-Doppler map of the nonadaptive processing (positive speeds) and the sum channel (negative speeds) on realistic data.

In many cases, few training data are available and the use of single data set methods is a very helpful alternative (see Section 3.1 and Section 3.2). To overcome the problem of these methods pointed out in Section 3.3, we propose a new method that includes some aspects of the non-adaptive processing. We saw in (16) that the term $\mathbf{g}\mathbf{g}^{\mathbf{H}}$ in (7) removes the interest signal (if any) and also a small part of the clutter. The idea here is to try to readd this clutter into the covariance matrix. The covariance matrix is then as follows:

$$\mathbf{T} = \mathbf{R} - \mathbf{g}\mathbf{g}^{\mathbf{H}} + \mathbf{g}_{\mathbf{c}}\mathbf{g}_{\mathbf{c}}^{\mathbf{H}}, \tag{21}$$

where $\mathbf{g}_{\mathbf{c}}$ is the projection of $\mathbf{g}$ on the clutter steering vector $\mathbf{s}_{\mathbf{c}}(\theta(f), f)$ as follows:

$$\mathbf{g}_{\mathbf{c}} = \mathbf{P}_{\mathbf{c}}\mathbf{g} \tag{22}$$

with

$$\mathbf{P}_c = \frac{\mathbf{s}_{\mathbf{c}}(\theta(f), f)\,\mathbf{s}_{\mathbf{c}}^{H}(\theta(f), f)}{\mathbf{s}_{\mathbf{c}}^{H}(\theta(f), f)\,\mathbf{s}_{\mathbf{c}}(\theta(f), f)}. \tag{23}$$

We can demonstrate that the covariance matrix $\mathbf{Q}$ of (16) can now be written as follows:

$$\mathbf{T} = \frac{\mathbf{N}\mathbf{N}^{\mathbf{H}}}{K_t} - \frac{\mathbf{N}\mathbf{s}_t^{*}\mathbf{s}_t^{T}\mathbf{N}^{H}}{K_t^2} + \frac{\mathbf{P}_{\mathbf{c}}\mathbf{X}\mathbf{s}_t^{*}\mathbf{s}_t^{T}\mathbf{X}^{H}\mathbf{P}_{\mathbf{c}}^{\mathbf{H}}}{K_t^2}. \tag{24}$$

If the clutter follows the theoretical Doppler-angle relation of (17), then the projection of the signal on the angle-Doppler steering vector will be close to the clutter signal that has been

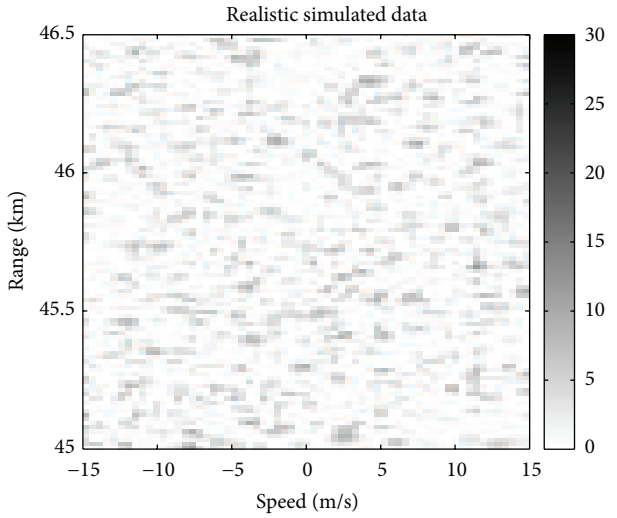

Figure 8: Range-Doppler map of the adaptive processing on realistic data.

removed from the matrix ($\mathbf{P_c X} \approx N$), and the covariance matrix $\mathbf{T}$ will be close to

$$\mathbf{T} \approx \frac{\mathbf{N}\mathbf{N}^{\mathbf{H}}}{K_t}. \tag{25}$$

Note that we do not need to set an arbitrary clutter power value because the energy of the clutter is included in $\mathbf{g_c}$ (cf. (22)).

In the case of Stop-Band APES, where the signal notch is wider, we use an extended projector $\mathbf{P_c}$ as follows:

$$\mathbf{P}_c = \frac{\mathbf{S_c}\mathbf{S_c^H}}{\mathbf{S_c^H}\mathbf{S_c}} \tag{26}$$

with

$$\mathbf{S}_c = \left[\mathbf{s_c}\left(\theta, f - \frac{\Delta f}{2}\right)\mathbf{s_c}(\theta, f)\,\mathbf{s_c}\left(\theta, f + \frac{\Delta f}{2}\right)\right]. \tag{27}$$

5.2. Deterministic Aided STAP Processing for Air-to-Air Mode. In air-to-air situations, the problem is different. The spectral occupation of the mainlobe clutter is much smaller than that of GMTI, whereas clutter sidelobes are much more powerful and have to be cancelled. Moreover, target density is very low, compared to GMTI. As we do not have access to a Doppler-angle relation of the mainlobe clutter, we propose another approach to readd this clutter which is partially removed in the APES-based methods. In air-to-air mode, the mainlobe clutter is pretty homogeneous in the range domain.

We will exploit this property to estimate the matrix $\mathbf{g_c}\mathbf{g_c^H}$ on the range gates domain. For each Doppler cell, the covariance matrix $\mathbf{T}$ is defined by

$$\mathbf{T} = \mathbf{R} - \mathbf{g}\mathbf{g}^{\mathbf{H}} + \mathbf{C}. \tag{28}$$

Table 1: Target position (GMTI data).

	Target 1	Target 2	Target 3
Speed (m/s)	3.0	5.30	5.85
Range (number)	214	138	149

However, the matrix $\mathbf{C}$ which was equal to $\mathbf{g_c}\mathbf{g_c^H}$ in (21) is now estimated as follows for each Doppler cells:

$$\mathbf{C} = \sum_{i=1}^{N} \frac{1}{N}\mathbf{g}_i\mathbf{g}_i^{\mathbf{H}}, \tag{29}$$

with $\mathbf{g}_i$ being the vector $\mathbf{g} = \mathbf{X}\mathbf{s}_t^*/K_t$ of the range cell i and N being the total number of range cells. If the clutter is homogeneous, then we can make the following approximation:

$$\mathbf{C} = \frac{1}{N}\sum_{i=1}^{N}\mathbf{g}_i\mathbf{g}_i^{\mathbf{H}} \approx \mathbf{g_c}\mathbf{g_c^H}. \tag{30}$$

This assumption implies that only the homogeneous component of the clutter will be readded in the covariance matrix. The density of the target has to remain low, otherwise useful signal will be nonnegligible in the matrix and SNR of targets will be attenuated. In the case of Stop-Band APES, (12) becomes

$$\mathbf{T} = \frac{\mathbf{X}\mathbf{X}^H}{\mathbf{s}_t^T\mathbf{s}_t^*} - \frac{1}{K_t}\mathbf{X}\mathbf{P}_{//}\mathbf{X}^H + \frac{1}{N}\sum_{i=1}^{N}\mathbf{X}_i\mathbf{P}_{//}\mathbf{X}_i^H, \tag{31}$$

with $\mathbf{X}$ the data of the range cell under test, $\mathbf{X}_i$ the data of the range cell i, and N the total number of range cells.

6. Results

6.1. GMTI Simulations. We test the GMTI deterministic aided STAP described in Section 5.1 on real airborne data. These data were obtained using the ONERA RAMSES radar system [14], which is a 4-channel ULA antenna. The aircraft speed is $V_a = 85\,\mathrm{m}\cdot\mathrm{s}^{-1}$, pulse repetition frequency is PRF = 1.5625 kHz, the number of range gates is 300, the number of time taps used to form the space-time data is $M = 6$, and the total number of time snapshots (radar pulses) is 64. Three targets are present in the scene (see Table 1).

The Doppler-range of the sum channel (Figure 9) clearly emphasizes the heterogeneous clutter. The next figures present the results for the classical STAP (estimation on 10 range gates with 2 guard cells), MLED STAP, Stop-Band STAP, and deterministic aided Stop-Band STAP (estimation on 3 range gates with no guard cells for all processing). No oversampling is used for the STAP processors (although a 2x zero-padding is needed to access the data of the half-resolution Doppler cells in the case of Stop-Band) except for the MLED detector, which uses a 4x-oversampling.

The classical STAP processing fails to correctly remove the heterogeneous clutter (Figure 10). The MLED STAP whose signal notch is very sharp also fails to completely remove the clutter. Due to its property of high resolution, the target Doppler extent is very thin and it is difficult to

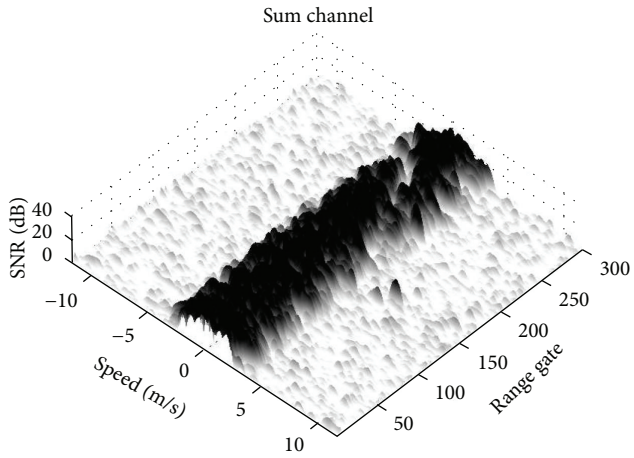

Figure 9: Range-Doppler map showing the sum channel of the RAMSES data.

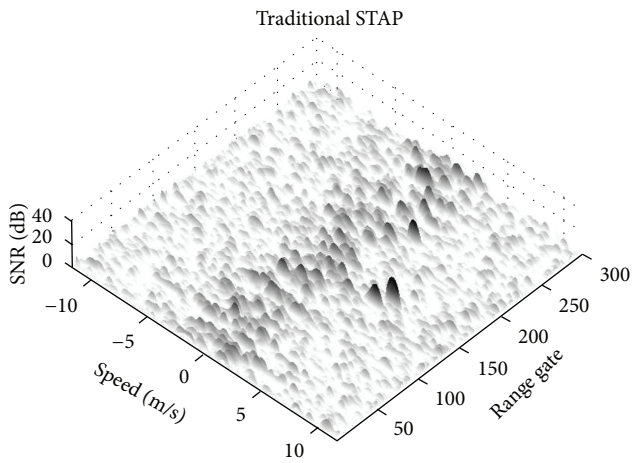

Figure 10: Range-Doppler map on RAMSES data showing the performance of classical STAP processing.

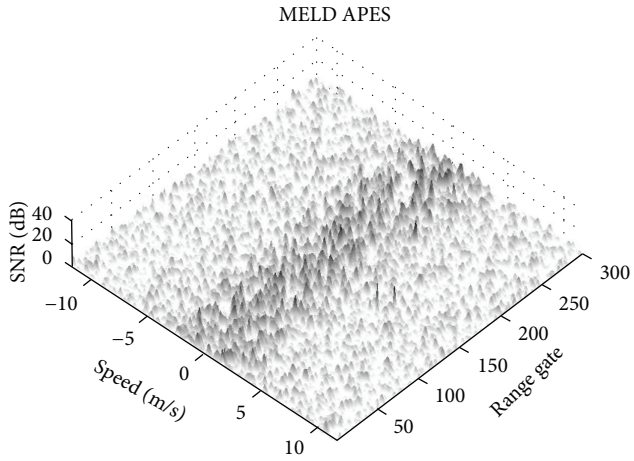

Figure 11: Range-Doppler map on RAMSES data showing the performance of the MLED detector.

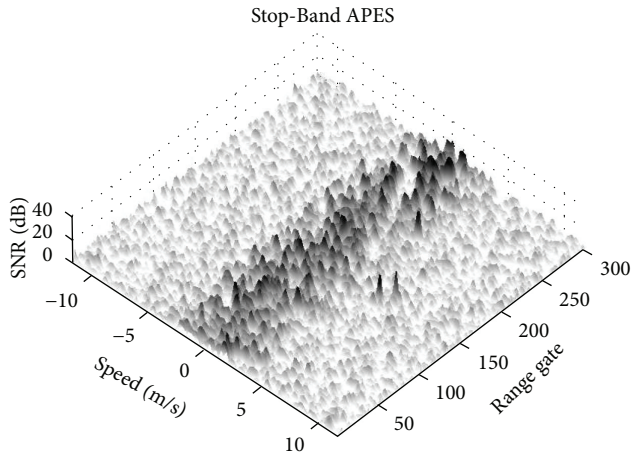

Figure 12: Range-Doppler map on RAMSES data showing the performance of the Stop-Band detector.

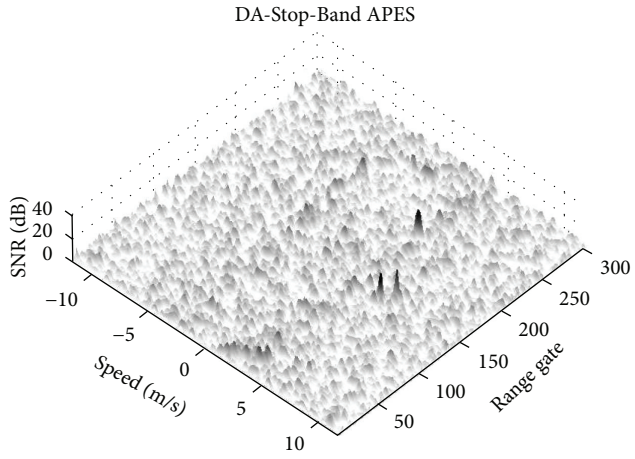

Figure 13: Range-Doppler map on RAMSES data showing the performance of the deterministic aidedc Stop Band detector.

distinguish the targets on the range-Doppler map (Figure 11). As predicted, the Stop-Bland STAP processing allows even more clutter to be present as shown in Figure 12, whereas the deterministic aided Stop-Band (DA-Stop-Band) effectively cancels the clutter (Figure 13). This is done without any attenuation on target 1 which lies in the clutter. Figure 14 points out the increased clutter attenuation of DA-Stop-Band over classical Stop-Band for range gate number 149, where target 3 is present. Figure 15 shows the superiority of DA-Stop-Band over classical STAP in clutter rejection for range gate 279, an area where the clutter is particularly powerful.

6.2. Air-to-Air Simulations. The air-to-air deterministic aided STAP (see Section 5.2) is tested on realistic synthetic data simulating an air-to-air MTI scenario. A front-looking AMSAR-like antenna [15] is used for the simulations. The aircraft speed is $V_a = 300\,\mathrm{m} \cdot \mathrm{s}^{-1}$, pulse repetition frequency is PRF = 20 kHz, and the number of range gates is 100, corresponding to a physical range of 52.5 km to 59.5 km. The number of time

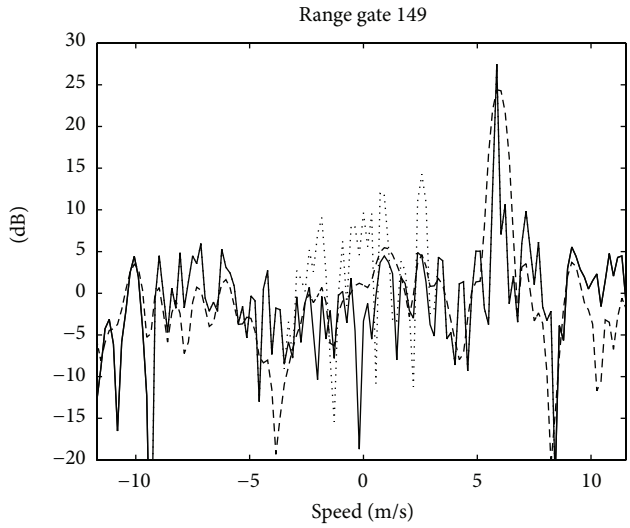

Figure 14: Comparison of classical STAP (dash curve) Stop-Band STAP (dot curve) and deterministic aided Stop-Band (solid curve) on RAMSES data for range gate number 149.

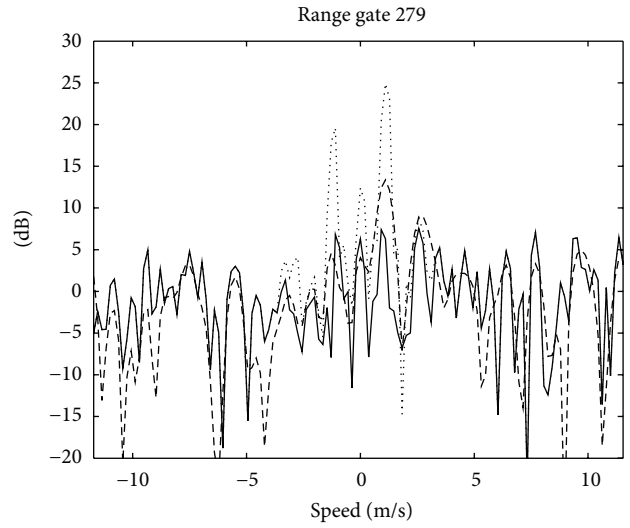

Figure 15: Comparison of classical STAP (dash curve) Stop-Band STAP (dot curve) and deterministic aided Stop-Band (solid curve) on RAMSES data for range gate number 279.

taps used to form of space-time data is $K^{\text{taps}} = 8$ and the total number of time snapshot (radar pulses) is 128. Five targets are present in the scene (see Table 2).

The sum channel (Figure 16) clearly shows that the mainlobe clutter (speeds from 230 to 280 m/s) and the sidelobes clutter occupy a wide part of the range-Doppler map. Only two targets on the left-upper part of the map are detectable without STAP processing. On Figure 17, we can see that the classical STAP processing successfully removes the homogeneous main lobe clutter and does not removes the heterogeneous sidelobes clutter. Classical Stop-Band processing cancels almost all the sidelobes clutter but does not suppress all the mainlobe clutter (see Figure 18), whereas DA-Stop-Band (Figure 19) totally removes it.

On Figure 20, the effect on clutter attenuation of the DA-Stop-Band is visible through a comparison with classical Stop-Band. We can also observe that both types of Stop-Band processings do not completely remove the sidelobes clutter; this issue can be overcome by using subspace-based algorithms instead of matrix inversion [11].

Table 2: Target position (air-to-air).

Targets	Speed (m/s)	Range (km)
1	50.03	58.425
2	100.22	55.425
3	115.026	57.00
4	185.0265	57.30
5	216.0296	59.475

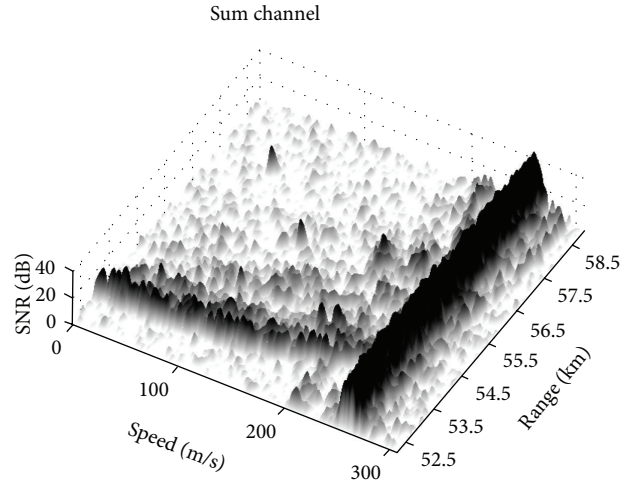

Figure 16: Range-Doppler map of the air-air realistic data showing the sum channel.

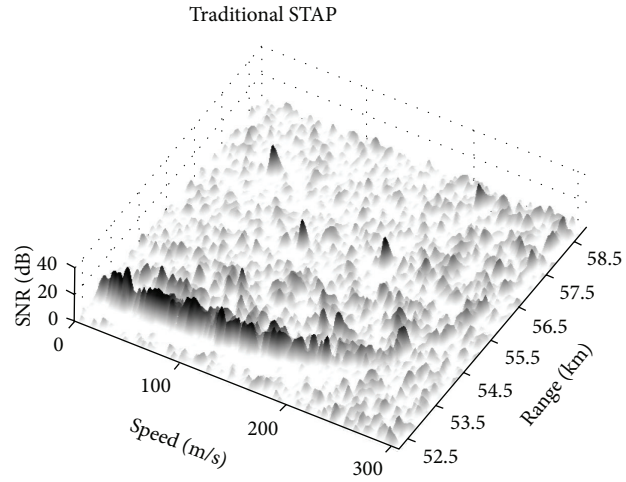

Figure 17: Range-Doppler map of the air-air realistic data showing the performance of MLED processing.

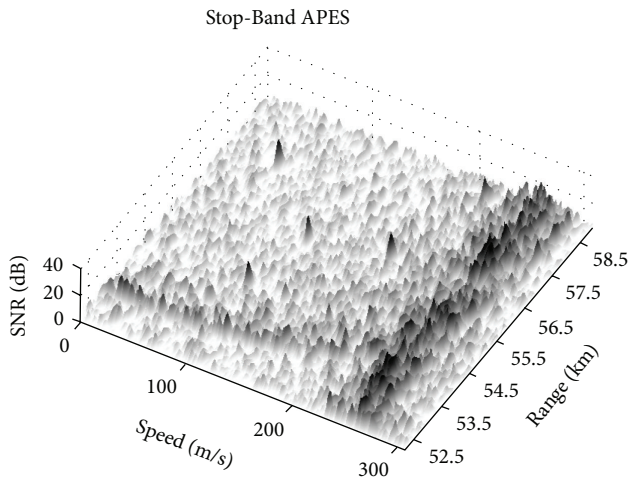

Figure 18: Range-Doppler map of the air-air simulated data showing the performance of Stop-Band STAP processing.

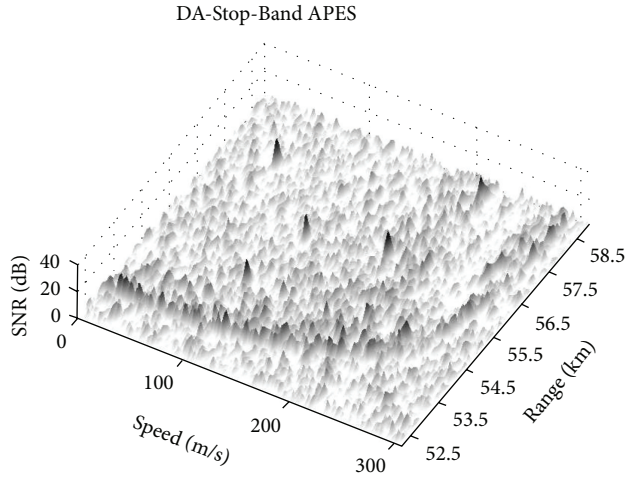

Figure 19: Range-Doppler map of the air-air simulated data showing the performance of deterministic aided Stop-Band STAP processing.

7. Conclusion

In this paper, we propose two deterministic aided algorithms both based on the APES method. The first algorithm which relies on the deterministic Doppler-angle relation of the clutter is particularly adapted for GMTI detectors. The results on real data show that it outperforms both classical STAP and APES-based algorithms. The second algorithm, which aims to remove the continuous component of the interference, is on the other hand well adapted to air-to-air modes. In this case, the continuous interference is the main lobe clutter. On realistic simulated data, it totally cancels the mainlobe clutter, whereas classical STAP and traditional APES-based algorithms fail, causing many false alarms.

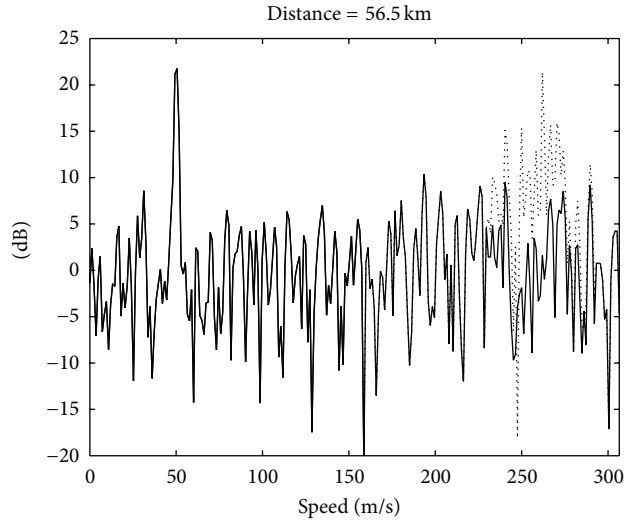

Figure 20: Comparison of Stop-Band STAP (dot curve) and Deterministic-Aided Stop-Band (solid curve) on air-air data at a distance of 58.5 km.

Acknowledgment

The authors would like to thank the DGA from the French Ministry of Defense for their support and funding.

References

[1] W. L. Melvin, "A STAP overview," *IEEE Aerospace and Electronic Systems Magazine*, vol. 19, no. 1, pp. 19–35, 2004.

[2] R. Klemm, *Principles of Space-Time Adaptive Processing*, The Institution of Electrical Engineers (IEE), 2002.

[3] E. Aboutanios and B. Mulgrew, "Evaluation of the single and two data set STAP detection algorithms using measured data," in *Proceedings of the IEEE International Geoscience and Remote Sensing Symposium (IGARSS '07)*, pp. 494–498, June 2007.

[4] P. Wang, H. Li, and B. Himed, "A new parametric GLRT for multichannel adaptive signal detection," *IEEE Transactions on Signal Processing*, vol. 58, no. 1, pp. 317–325, 2010.

[5] E. Aboutanios and B. Mulgrew, "Hybrid detection approach for STAP in heterogeneous clutter," *IEEE Transactions on Aerospace and Electronic Systems*, vol. 46, no. 3, pp. 1021–1033, 2010.

[6] M. Zatman, "Properties of Hung-Turner projections and their relationship to the eigencanceller," in *Proceedings of the 30th Asilomar Conference on Signals, Systems & Computers*, pp. 1176–1180, November 1996.

[7] E. Aboutanios and B. Mulgrew, "A stap algorithm for radar target detection in heterogeneous environments," in *Proceedings of the IEEE/SP 13th Workshop on Statistical Signal Processing*, pp. 966–971, July 2005.

[8] P. Stoica, H. Li, and J. Li, "New derivation of the APES filter," *IEEE Signal Processing Letters*, vol. 6, no. 8, pp. 205–206, 1999.

[9] L. E. Brennan and L. S. Reed, "Theory of adaptive radar," *IEEE Transactions on Aerospace and Electronic Systems*, vol. 9, no. 2, pp. 237–252, 1973.

[10] Y. L. Kim, S. U. Pillai, and J. R. Guerci, "Optimal loading factor for minimal sample support space-time adaptive radar," in *Proceedings of the IEEE International Conference on Acoustics,*

Speech and Signal Processing (ICASSP '98), vol. 4, pp. 2505–2508, May 1998.

[11] J. F. Degurse, S. Marcos, and L. Savy, "Subspace-based and single dataset methods for STAP in heterogeneous environments," in *Proceedings of the IET International Conference on Radar Systems (RADAR '12)*, pp. 1–6, Glasgow, UK, October 2012.

[12] J.-F. Degurse, L. Savy, R. Perenon, and S. Marcos, "An extended formulation of the maximum likelihood estimation algorithm. Application to space-time adaptive processing," in *Proceedings of the International Radar Symposium (IRS '11)*, pp. 763–768, September 2011.

[13] L. Savy and J. F. Degurse, "Stop-band apes: traitements adaptatifs en environnements heterogenes," *Revue Traitement du Signal*, vol. 28, pp. 231–256, 2011.

[14] P. Dubois-Fernandez, O. Ruault du Plessis, D. le Coz et al., "The ONERA RAMSES SAR system," in *Proceedings of the IEEE International Geoscience and Remote Sensing Symposium (IGARSS '02)*, vol. 3, pp. 1723–1725, June 2002.

[15] J.-L. Milin, S. Moore, W. Bürger, P.-Y. Triboulloy, M. Royden, and J. Gerster, "AMSAR—a european success story in AESA radar," *IEEE Aerospace and Electronic Systems Magazine*, vol. 25, no. 2, pp. 21–28, 2010.

Hindawi Publishing Corporation
International Journal of Antennas and Propagation
Volume 2013, Article ID 374342, 8 pages
http://dx.doi.org/10.1155/2013/374342

Research Article

Low-Grazing Angle Detection in Compound-Gaussian Clutter with Hybrid MIMO Radar

Jincan Ding, Haowen Chen, Hongqiang Wang, Xiang Li, and Zhaowen Zhuang

College Electronic Science and Engineering, National University of Defense Technology, Changsha 410073, China

Correspondence should be addressed to Jincan Ding; jincanding@163.com

Received 15 April 2013; Revised 12 September 2013; Accepted 17 September 2013

Academic Editor: Hang Hu

This paper focuses on the target detection in low-grazing angle using a hybrid multiple-input multiple-output (MIMO) radar systems in compound-Gaussian clutter, where the multipath effects are very abundant. The performance of detection can be improved via utilizing the multipath echoes. First, the reflection coefficient considering the curved earth effect is derived. Then, the general signal model for MIMO radar is introduced in low-grazing angle; also, the generalized likelihood test (GLRT) and generalized likelihood ratio test-linear quadratic (GLRT-LQ) are derived with known covariance matrix. Via the numerical examples, it is shown that the derived GLRT-LQ detector outperforms the GLRT detector in low-grazing angle, and both performances can be enhanced markedly when the multipath effects are considered.

1. Introduction

MIMO radar has gotten considerable attention in a novel class of radar system, where the term MIMO refers to the use of multiple-transmit as well as multiple-receive antennas. MIMO radar is categorized into two classes: the statistical MIMO radar and the colocated MIMO radar, depending on their antenna placement [1, 2]. The advantages of MIMO radar with colocated antennas have been studied extensively, which include improved detection performance, higher resolution [3], higher sensitivity to or detection of moving targets [4], and increased degrees of freedom for transmission beamforming [5]. MIMO radar with widely separated antennas can capture the spatial diversity of the target's radar cross section (RCS) [6]. This spatial diversity provides the radar systems with the ability to support the improvement of the target parameter estimation [7, 8], high resolution target localization [9], and tracking performance [10]. The hybrid MIMO radars can obtain superiority both from colocated and separated MIMO radar. Thus, we focus on the hybrid MIMO radar system in this paper.

Much published literature has concerned the issue of MIMO radar detection. Guan and Huang [11] investigated the detection problem of the MIMO radar system with distributed apertures in Gaussian colored noise and partially correlated observation channels. Tang et al. [12] introduced relative entropy as a measure to radar detection theory and analyzed the detection performance of MIMO radar and phased array radar. The authors in [13] investigated detection performance of MIMO radar for Rician target. In [14], the optimal detector in the Neyman-Pearson sense was derived for the statistical MIMO radar using orthogonal waveforms. The authors in [15] applied the Swerling models to target detection and derived the optimal test statistics for a statistical MIMO radar using nonorthogonal signal. For low-grazing angle detection of MIMO radar, the authors in [16] utilized the time reversal technique in a multipath environment to achieve high target detectability.

Low-grazing angle targets are difficult to detect, which is one of the great threats propelling radar development. Otherwise, detection of low-altitude targets is of great significance to counter low-altitude air defense penetration. However, up to now, this problem has not been effectively resolved. Multipath effect plays an important role in the low-altitude target detection, by which the target echo signal is seriously polluted, even counteracted [17]. Two aspects can be considered for multipath: suppressing multipath and utilizing it. However, in a statistical sense, detection may be enhanced by the presence of multipath [18].

In this paper, we consider low-grazing angle target detection in compound-Gaussian clutter for MIMO radar. The compound-Gaussian clutter represents the heavy-tailed clutter statistics that are distinctive of several scenarios, for example, high-resolution or low-grazing angle radars in the presence of sea or foliage clutter [19, 20]. To the end, the generalized likelihood ratio test (GLRT) and generalized likelihood ratio test-linear quadratic (GLRT-LQ) are derived.

2. Multipath Geometry Model

A point source at a distance of R_d from the receiver is considered. If the source is assumed to be a narrowband signal, it can be represented by

$$x(t) = ae^{j(\omega t+\varphi)}, \tag{1}$$

where a is the amplitude, ω is the angular frequency, and φ is the initial phase. In the presence of multipath, the received by the receiver consists of two components, namely, the direct and indirect signal. For a simple multipath model of a flat earth, the direct signal is given by

$$x_d(t) = x(t)\, e^{-j\kappa R_d}, \tag{2}$$

while indirect signal is

$$x_i(t) = x(t)\, \rho e^{j\phi} e^{-j\kappa R_i}, \tag{3}$$

where $\rho e^{j\phi}$ is the complex reflection coefficient, $\kappa = 2\pi/\lambda$ is the wave number, λ is wavelength, target range R_d can be obtained from the time delay, and R_i is the total length of the indirect path. Thus, the total received signal is given by

$$x_r(t) = x_d(t) + x_i(t). \tag{4}$$

To model the received signals more accurately, the curvature of the signal path due to refraction in the troposphere, in addition to the curvature of the earth itself, must be taken into account. The multipath geometry for a curved earth is given in Figure 1.

In (3), the term $\rho e^{j\phi}$ is the complex reflection coefficient. It generally consists of the Fresnel reflection coefficient divided into the vertical polarization Γ_v and horizontal polarization Γ_h, the divergence factor D due to a curved surface, and the surface roughness factor; that is, $\rho e^{j\phi} = \Gamma_{(v,h)} D \rho_s$. The vertical polarization and horizontal polarization Fresnel reflection coefficients are, respectively, as presented in [17]. Consider the following:

$$\Gamma_v \simeq \frac{\psi\sqrt{\varepsilon_c} - 1}{\psi\sqrt{\varepsilon_c} + 1}, \tag{5}$$

$$\Gamma_h \simeq \frac{\psi - \sqrt{\varepsilon_c}}{\psi + \sqrt{\varepsilon_c}}. \tag{6}$$

For horizontal polarization, ψ is the grazing angle and ε_c is the complex dielectric constant which is given by

$$\varepsilon_c = \frac{\varepsilon}{\varepsilon_0} - j60\lambda\sigma, \tag{7}$$

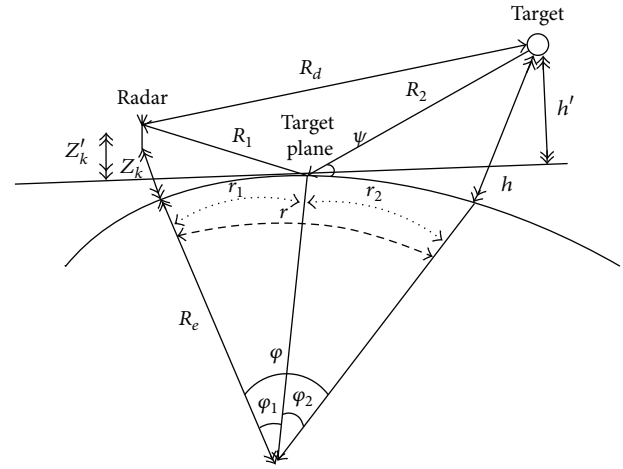

Figure 1: Multipath geometry for a curved earth.

where $\varepsilon/\varepsilon_0$ is the relative dielectric constant of the reflecting medium and σ is its conductivity. Thus, the Fresnel reflection coefficient is determined by the grazing angle under a deterministic condition.

When an electromagnetic wave is incident on a round earth surface, the reflected wave diverges because of the earth's curvature. Due to divergence, the reflected energy is defocused and radar power density is reduced. The divergence factor can be derived solely from geometrical considerations. A widely accepted approximation for the divergence factor D is given by

$$D \simeq \left(1 + \frac{2r_1 r_2}{R_e r \psi}\right)^{-1/2}. \tag{8}$$

The surface roughness factor ρ_s is given by

$$\rho_s = e^{-\mu},$$
$$\mu = \begin{cases} 2[2\pi\eta]^2, & \eta \le 0.1 \text{ rad}, \\ 0.16\eta^2 + 7.42\eta + 0.0468, & \text{otherwise}, \end{cases} \tag{9}$$

and η is the surface roughness factor given by

$$\eta = \frac{\sigma_H \psi}{\lambda} \tag{10}$$

and σ_H is the root-mean-square (RMS) surface height irregularity. For simplicity, the diffuse component is treated as the incoherent white Gaussian noise.

3. MIMO Radar Multipath Signal

Consider a narrowband MIMO radar system with $\widetilde{M}$ and $\widetilde{N}$ subarrays for transmitting and receiving, respectively. The mth transmit and nth receive subarrays have, respectively, M_m and N_n closely spaced antennas. $m = 1, \ldots, \widetilde{M}$, and $n = 1, \ldots, \widetilde{N}$, $M = M_1 + M_2 + \cdots + M_{\widetilde{M}}$ and $N = N_1 + N_2 + \cdots + N_{\widetilde{N}}$ are the total numbers of transmit and receive antennas, respectively. We assume that the subarrays are

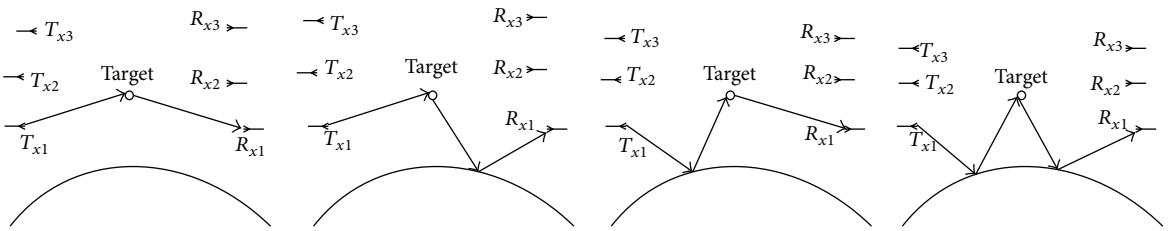

(a) Directly-directly path (b) Directly-reflected path (c) Reflected-directly path (d) Reflected-reflected path

Figure 2: Multipath MIMO radar.

sufficiently separated, and, hence, for each target, its RCSs for different transmit and receive subarray pairs are statistically independent of each other. The receive signal of MIMO radar can be expressed as [21]

$$\mathbf{Y} = \mathbf{A}(\phi)\,\mathbf{B}_{\phi}\mathbf{S}(\phi) + \mathbf{Z}, \tag{11}$$

where $\mathbf{A}(\phi) = \mathrm{diag}\{\mathbf{a}_1(\phi), \mathbf{a}_2(\phi), \ldots, \mathbf{a}_{\widetilde{N}}(\phi)\}$ is the steering matrix of receive subarrays and component $\{\mathbf{a}_n(\phi)\}_{n=1}^{\widetilde{N}}$ is the steering vector of nth receive subarray at direction ϕ. $\mathbf{B}_{\phi}$ denotes the RCSs for different transmit and receive subarray pairs with component $\{\beta_{mn,\phi}\}_{m,n=1,1}^{\widetilde{M},\widetilde{N}}$. $\mathbf{S}(\phi) = \mathbf{V}^T(\phi)\boldsymbol{\Phi}$ denotes the transmit signal matrix, where $\boldsymbol{\Phi} = [\boldsymbol{\Phi}_1^T, \boldsymbol{\Phi}_2^T, \ldots, \boldsymbol{\Phi}_{\widetilde{M}}^T]^T$ is the transmit waveform matrix, for each transmit subarray, the component $\boldsymbol{\Phi}_m^{\widetilde{M}\times L} = [\{s_{m1}(t)\}^T, \{s_{m2}(t)\}^T, \ldots, \{s_{mM_m}(t)\}^T]^T$, and $\{s_{ml}(t)\}_{\ell=1}^{M_m}$, $t = 1, 2, \ldots, L$ is the probing waveform of m subarray; $\mathbf{V}(\phi) = \mathrm{diag}\{\mathbf{v}_1(\phi), \mathbf{v}_2(\phi), \ldots, \mathbf{v}_{\widetilde{M}}(\phi)\}$ is the steering matrix of transmit subarray and the component $\{\mathbf{v}_m(\phi)\}_{m=1}^{\widetilde{M}}$ is the steering vector of mth transmit subarray at direction ϕ. $\mathbf{Y} = [Y_1^T, Y_2^T, \ldots, Y_{\widetilde{N}}^T]$ is the received data matrix and $\{Y_n\}_{n=1}^{\widetilde{N}}$ denotes received signal of the nth subarray. $\mathbf{Z} = [\mathbf{z}_1, \mathbf{z}_2, \ldots, \mathbf{z}_L]$ is the clutter matrix, each column $\{\mathbf{z}_\ell\}_{\ell=1}^{L}$ of which is modeled as spherically invariant random vectors (SIRV), and L is the number of data samples of the transmitted waveforms. We assume clutter distributing as the compound-Gaussian model, which represents the heavy-tailed clutter statistics that are distinctive of several scenarios, for example, high-resolution or low-grazing angle radars in the presence of sea or foliage clutter [19, 20]. The compound-Gaussian clutter $z = \sqrt{u}\chi$, where u and χ are the texture and speckle components of the compound model, respectively. The fast-changing χ is a realization of a stationary zero mean complex Gaussian process, and the slow-changing u is modeled as a nonnegative real random process [22].

We rewrite the received signal (11) in vector form, given by

$$\mathbf{y}_{\mathrm{dd}} = \mathbf{T}\boldsymbol{\beta} + \mathbf{n}, \tag{12}$$

where $\mathbf{y}^{NL\times 1} = \mathrm{Vec}(\mathbf{Y})$, $\mathbf{T}^{NL\times\widetilde{M}\widetilde{N}} = (\mathbf{S}^T \otimes \mathbf{A})$, $\boldsymbol{\beta}^{\widetilde{M}\widetilde{N}\times 1} = \mathrm{Vec}(\mathbf{B}_{\phi})$, $\mathbf{n}^{NL\times 1} = \mathrm{Vec}(\mathbf{Z})$, $\mathrm{Vec}(\bullet)$ is the vector operator, symbol $\otimes$ denotes the Kronecker product. Then and $\mathbf{n}$ is the compound Gaussian random vector with covariance matrix

$$\begin{aligned}\mathbf{C}_{\mathbf{n}}^{NL\times NL} &= E\left[\mathbf{n}\mathbf{n}^{\dagger}\right] = \mathbf{P}\otimes\mathbf{C},\\ \mathbf{P} &= \mathrm{diag}\left\{s_1^2, s_2^2, \ldots, s_L^2\right\} = \mathrm{diag}\left\{\lambda_1, \lambda_2, \ldots, \lambda_L\right\},\end{aligned} \tag{13}$$

where $\mathbf{P}$ is considered deterministic matrix with unknown parameters $\{\lambda_\ell\}_{\ell=1}^{L}$ and $\dagger$ denotes conjugate transpose.

4. Multipath Signal Model of MIMO Radar

In the presence of multipath, consider atmosphere refraction and the curved earth effect; the reflected signals from a point target of MIMO radar include four parts: directly-directly path, directly-reflected path, and reflected-directly path, reflected-reflected path. Assume the point target is located at $X_0 = (x_0, y_0)$ and reflected point in ground is located at $X_i = (x_i, y_i)$, $i = 1, 2$. Figure 2 illustrates a four-way MIMO radar propagation model with multipath.

The directly-directly path echo signal is given by (12). The directly-reflected path echo signal is

$$\mathbf{y}_{\mathrm{dr}} = \mathbf{T}\left(\mathbf{k}^{\mathrm{dr}} \odot \boldsymbol{\beta}\right) + \mathbf{n}, \tag{14}$$

where $\mathbf{K}^{\mathrm{dr}}$ is $\widetilde{M}\widetilde{N} \times 1$ amplitude of reflect coefficient and symbol $\odot$ represents the Hadamard product.

The reflected-directly path echo signal is

$$\mathbf{y}_{\mathrm{rd}} = \mathbf{T}\left(\mathbf{k}^{\mathrm{rd}} \odot \boldsymbol{\beta}\right) + \mathbf{n}. \tag{15}$$

The reflected-reflected path echo signal is

$$\mathbf{y}_{\mathrm{rr}} = \mathbf{T}\left(\mathbf{k}^{\mathrm{rr}} \odot \boldsymbol{\beta}\right) + \mathbf{n}. \tag{16}$$

Thus, the received signal of MIMO radar with multipath is

$$\begin{aligned}\mathbf{y}_{\mathrm{mp}} &= \mathbf{y}_{\mathrm{dd}} + \mathbf{y}_{\mathrm{dr}} + \mathbf{y}_{\mathrm{rd}} + \mathbf{y}_{\mathrm{rr}}\\ &= \mathbf{T}\left(\left(\mathbf{1} + \mathbf{k}^{\mathrm{dr}} + \mathbf{k}^{\mathrm{rd}} + \mathbf{k}^{\mathrm{rr}}\right) \odot \boldsymbol{\beta}\right) + \mathbf{n}\\ &= \mathbf{T}\left(\mathbf{k} \odot \boldsymbol{\beta}\right) + \mathbf{n},\end{aligned} \tag{17}$$

where $\mathbf{k} = \mathbf{1} + \mathbf{k}^{\mathrm{dr}} + \mathbf{k}^{\mathrm{rd}} + \mathbf{k}^{\mathrm{rr}}$ and $\mathbf{1}^{\widetilde{M}\widetilde{N}}$ is an $\widetilde{M}\widetilde{N}\times 1$ one vector.

5. MIMO Radar Detector in Compound-Gaussian Clutter

5.1. GLRT Detector Design. The problem of detecting with MIMO radar can be formulated in terms of the following binary hypotheses test:

$$\begin{aligned} H_0 &: \quad \mathbf{y}_{\mathrm{mp}} = \mathbf{n}, \\ H_1 &: \quad \mathbf{y}_{\mathrm{mp}} = \mathbf{T}\left(\mathbf{k} \odot \boldsymbol{\beta}\right) + \mathbf{n}. \end{aligned} \tag{18}$$

Standard GLRT is the following decision rule:

$$\frac{\max_{\boldsymbol{\beta},\lambda_1,\ldots,\lambda_L} f\left(\mathbf{Y} \mid H_1, \lambda_1, \ldots, \lambda_L, \boldsymbol{\beta}\right)}{\max_{\lambda_1,\ldots,\lambda_L} f\left(\mathbf{Y} \mid H_0, \lambda_1, \ldots, \lambda_L\right)} \underset{H_0}{\overset{H_1}{\gtrless}} \gamma_G, \tag{19}$$

where $f(\mathbf{Y} \mid H_1, \lambda_1, \ldots, \lambda_L, \boldsymbol{\beta})$ and $f(\mathbf{Y} \mid H_1, \lambda_1, \ldots, \lambda_L)$ denote the probability density functions (pdfs) of the data under H_1 and H_0, respectively. And the pdfs can be written, respectively, as

$$f\left(\mathbf{Y} \mid H_1, \lambda_1, \ldots, \lambda_L, \boldsymbol{\beta}\right) = \frac{1}{\pi^{NL} \det\left(\mathbf{C_n}\right)} \exp\left\{-\operatorname{tr}\left(\mathfrak{F}\right)\right\}, \tag{20}$$

where $\mathfrak{F} = \mathbf{C_n}^{-1}(\mathbf{y} - \mathbf{T}(\mathbf{k} \odot \boldsymbol{\beta})) \times (\mathbf{y} - \mathbf{T}(\mathbf{K} \odot \boldsymbol{\beta}))^{\dagger}$, and

$$f\left(\mathbf{Y} \mid H_0, \lambda_1, \ldots, \lambda_L\right) = \frac{1}{\pi^{NL} \det\left(\mathbf{C_n}\right)} \exp\left\{-\operatorname{tr}\left(\mathbf{C_n}^{-1}\mathbf{y}\mathbf{y}^{\dagger}\right)\right\}, \tag{21}$$

where det(•) and tr denote the determinant and the trace of a matrix, respectively.

The log-likelihood function of (21) is

$$\begin{aligned} \ln f\left(\mathbf{Y} \mid H_0, \lambda_1, \ldots, \lambda_L\right) = & -NL \ln \pi - L \ln \det\left(\mathbf{C}\right) \\ & - N \sum_{\ell=1}^{L} \ln \lambda_\ell \\ & - \sum_{\ell=1}^{L} \frac{\mathbf{y}^{\dagger}\left(E_{\ell\ell} \otimes \mathbf{C}^{-1}\right)\mathbf{y}}{\lambda_\ell}, \end{aligned} \tag{22}$$

where $E_{\ell\ell}$ denotes the elementary matrix with component $e(\ell, \ell) = 1$ and zero for others. Then, it is easy to obtain the Maximum Likelihood (ML) estimator of λ under H_0; that is

$$\widehat{\lambda}_\ell = \frac{\mathbf{y}^{\dagger}\left(E_{\ell\ell} \otimes \mathbf{C}^{-1}\right)\mathbf{y}}{N}. \tag{23}$$

According to [21], we rewrite the log-likelihood function of (20) as

$$\begin{aligned} & \ln f\left(\mathbf{Y} \mid H_1, \lambda_1, \ldots, \lambda_L, \boldsymbol{\beta}\right) \\ & = -NL \ln \pi - L \ln \det\left(\mathbf{C}\right) - N \sum_{\ell=1}^{L} \ln \lambda_\ell \\ & \quad - \sum_{\ell=1}^{L} \frac{\left(\mathbf{y}-\mathbf{T}\left(\mathbf{k} \odot \boldsymbol{\beta}\right)\right)^{\dagger}\left(E_{\ell\ell} \otimes \mathbf{C}^{-1}\right)\left(y - \mathbf{T}\left(\mathbf{k} \odot \boldsymbol{\beta}\right)\right)}{\lambda_\ell}. \end{aligned} \tag{24}$$

Thus, the ML estimator of $\{\lambda_\ell\}_{\ell=1}^{L}$ is

$$\widehat{\lambda}_\ell = \frac{\left(\mathbf{y}-\mathbf{T}\left(\mathbf{k} \odot \boldsymbol{\beta}\right)\right)^{\dagger}\left(E_{\ell\ell} \otimes \mathbf{C}^{-1}\right)\left(\mathbf{y}-\mathbf{T}\left(\mathbf{k} \odot \boldsymbol{\beta}\right)\right)}{N}. \tag{25}$$

The estimator $\boldsymbol{\beta}$ is [23]

$$\widehat{\boldsymbol{\beta}} = \left((\mathbf{Tk})^{\dagger}\mathbf{C_n^{-1}}\left(\mathbf{Tk}\right)\right)(\mathbf{Tk})^{\dagger}\mathbf{C_n^{-1}}\mathbf{y}. \tag{26}$$

Substituting the estimator $\{\widehat{\lambda}_\ell\}_{\ell=1}^{L}$, $\widehat{\boldsymbol{\beta}}$ under H_1 and H_0 into (19)–(21), the final GLRT becomes

$$\prod_{\ell=1}^{L} \frac{\mathbf{y}^{\dagger}\left(E_{\ell\ell} \otimes \mathbf{C}^{-1}\right)\mathbf{y}}{\left(\mathbf{y}-\mathbf{T}\left(\mathbf{k} \odot \widehat{\boldsymbol{\beta}}\right)\right)^{\dagger}\left(E_{\ell\ell} \otimes \mathbf{C}^{-1}\right)\left(\mathbf{y}-\mathbf{T}\left(\mathbf{k} \odot \widehat{\boldsymbol{\beta}}\right)\right)} \underset{H_0}{\overset{H_1}{\gtrless}} \gamma_G. \tag{27}$$

5.2. GLRT-LQ Detector Design. We rewrite the detection problem as

$$\begin{aligned} H_0 &: \quad y_{m,n} = z_{m,n}, \\ H_1 &: \quad y_{m,n} = \rho_{M_m N_n} \beta(m,n)\, T_{m,n} + z_{m,n}, \end{aligned} \tag{28}$$

where $\rho_{M_m N_n} = (1 + \rho_{M_m N_n}^{(\mathrm{dr})} + \rho_{M_m N_n}^{(\mathrm{rd})} + \rho_{M_m N_n}^{(\mathrm{rr})})$; $\rho_{M_m N_n}^{(\mathrm{dr})}$, $\rho_{M_m N_n}^{(\mathrm{rd})}$, $\rho_{M_m N_n}^{(\mathrm{rr})}$ are the amplitudes of reflect coefficient, because the grazing angles are different; the reflect coefficient $\rho_{M_m N_n}^{(\mathrm{dr})} \neq \rho_{M_m N_n}^{(\mathrm{rd})} \neq \rho_{M_m N_n}^{(\mathrm{rr})}$.

As the transmit-receive subarrays are widely separated, the clutter returns can be considered to be independent; hence, the low-grazing angle likelihood ratio test (LRT) detector for MIMO radar in the compound-Gaussian clutter is given by

$$\log \frac{p\left(y \mid H_0\right)}{p\left(y \mid H_1\right)} \underset{H_0}{\overset{H_1}{\lessgtr}} \gamma_{G\text{–}LQ}. \tag{29}$$

If we assume that covariance matrix $\mathbf{C}_c$ is known and according to [24], $p(y \mid H_0)$ and $p(y \mid H_1)$ are replaced by their Bayesian estimates, and, asymptotically, the generalized likelihood ratio test-linear quadratic (GLRT-LQ), extended to the MIMO case, is given by

$$\begin{aligned} & \Lambda(Y) \\ & = \frac{p\left(Y \mid H_1\right)}{p\left(Y \mid H_0\right)} = \frac{\prod_{m,n} p\left(y_{m,n} \mid H_1\right)}{\prod_{m,n} p\left(y_{m,n} \mid H_0\right)} \\ & = \prod_{m,n} \left[1 \times \left(1 - \frac{\left|T_{m,n}^{\dagger}\mathbf{C}_{m,n}^{-1}y_{m,n}\right|^2}{\left(T_{m,n}^{\dagger}\mathbf{C}_{m,n}^{-1}T_{m,n}\right)\left(y_{m,n}^{\dagger}M_{m,n}^{-1}y_{m,n}\right)}\right)^{-1}\right] \\ & \underset{H_0}{\overset{H_1}{\lessgtr}} \gamma_{G\text{–}LQ}, \end{aligned} \tag{30}$$

where $\mathbf{C}_{m,n}$ is the covariance matrix for the $m - n$ transmit-receive pair.

According to [24], the probability of false alarm P_{fa} is given by

$$P_{\text{fa}} = P\left(\prod_{i=1}^{I}\Lambda_i(y_i) > \gamma_{G-LQ} \mid H_0\right) = \gamma_{G-LQ}^{-L+1}\sum_{i=0}^{I-1}\frac{(W-I)^i}{i!}\left(\ln\gamma_{G-LQ}\right)^i, \tag{31}$$

where $I = \widetilde{M}\widetilde{N}$ and $W = M_m N_n$.

The probability of detection P_d is given by

$$P_d = P\left(\prod_{i=1}^{I}\Lambda_i(y_i) > \gamma_{G-LQ} \mid H_0\right). \tag{32}$$

For a given signal-to-clutter ratio (SCR), denoted by $\text{SCR}_{m,n}$, the amplitude of $\beta(m,n)$ is given by

$$\left|\beta(m,n)\right| = \sqrt{\text{SCR}_{m,n}\sigma^2}, \tag{33}$$

where σ^2 is the clutter power. In this paper, we consider that $|\beta(m,n)|$ is the same for all m and n.

6. Numerical Simulations

This section is devoted to the performance assessment of the GLRT and GLRT-LQ detectors in low-grazing angle for MIMO radar, when the texture component of clutter distributed as gamma distribution, leading to the wellknown K clutter model. Since the closed-form expressions of the GLRT detector for the probability of the detection and of alarm are not available, we resort to standard Monte Carlo.

In our first example, we, respectively, analyze the GlRT-LQ detectors considering multipath effect and without considering multipath effect. Assume MIMO radar is with three transmit antennas and two receive antennas, the heights of transmit arrays are fixed at 100 m, 200 m, and 300 m, the height of receive arrays are fixed at 100 m, and 200 m, and the target's height is fixed at 200 m. The (p,q), the element of the covariance matrix of the speckle component, is chosen as

$$\mathbf{C}_{p,q} = \sigma^2 \times 0.9^{|p-q|} \times \exp\left[j\left(\frac{\pi}{2}\right)(p-q)\right]. \tag{34}$$

Here, we select $\sigma^2 = 10.17$, $L = 16$. We define the signal-to-clutter pulse noise ratio (SCNR) by [25]

$$\text{SCNR} = \frac{1}{L}\frac{\sum_{\ell=1}^{L}\left[\mathbf{T}(\mathbf{k}\odot\boldsymbol{\beta})\right]^{\dagger}\left[\mathbf{T}(\mathbf{k}\odot\boldsymbol{\beta})\right]}{E\{u\}\,\text{tr}\{C_n\}}. \tag{35}$$

Figure 3 depicts the detection performance using GLRT-LQ detectors, as a function of the SCNR. The probability of false alarm is fixed at $P_{\text{fa}} = 10^{-4}$. For the given SCNR, the detection performance with multipath outperforms the one without considering multipath effect.

Figure 4 depicts the detection performance using GLRT detector, as a function of the SCNR. For the given SCNR, the detection performance with multipath outperforms the one without considering multipath effect.

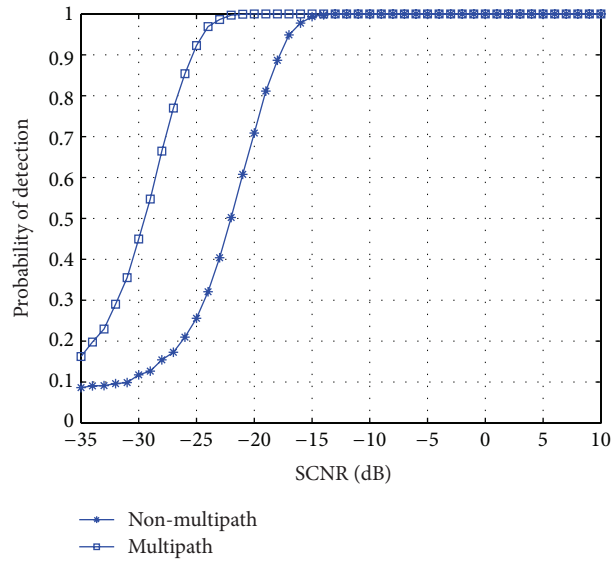

Figure 3: GLRT-LQ detector performance in low-grazing angle.

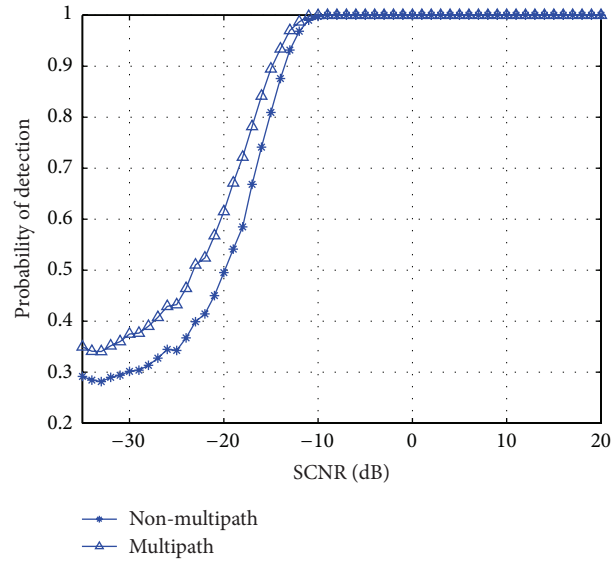

Figure 4: GLRT detector performance in low-grazing angle.

Figure 5 depicts the performance comparison between GLRT-LQ and GLRT detectors. From Figure 5, GLRT-LQ detector outperforms the GLRT detector in low-grazing angle for MIMO radar, respectively, with and without considering multipath effects.

Figures 6 and 7 depict the detection performance of GLRT-LQ and GLRT detector with different antenna numbers, respectively, as a function of SCNR. The probability of false alarm is set at $P_{\text{fa}} = 10^{-4}$; the transmit antenna and receive antenna are set at 2, 4, and 6, respectively. Figures 6 and 7 show that GLRT-LQ or GLRT detector can obtain

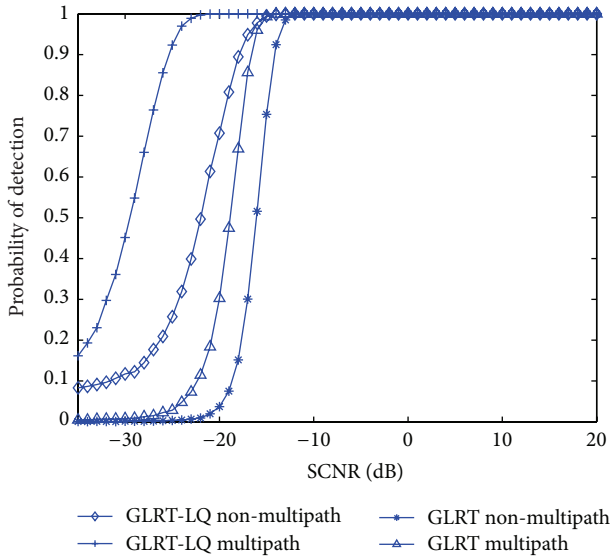

Figure 5: Comparison of GLRT-LQ detector and GLRT detector.

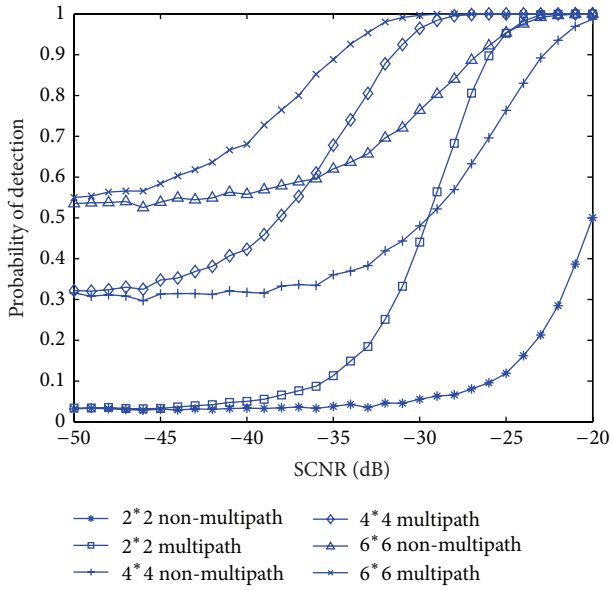

Figure 6: Detection performance of GLRT-LQ detector with different numbers.

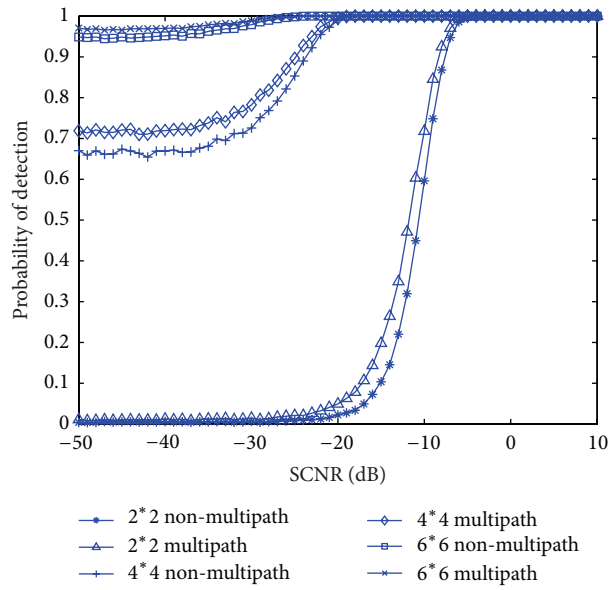

Figure 7: Detection performance of GLRT detector with different numbers.

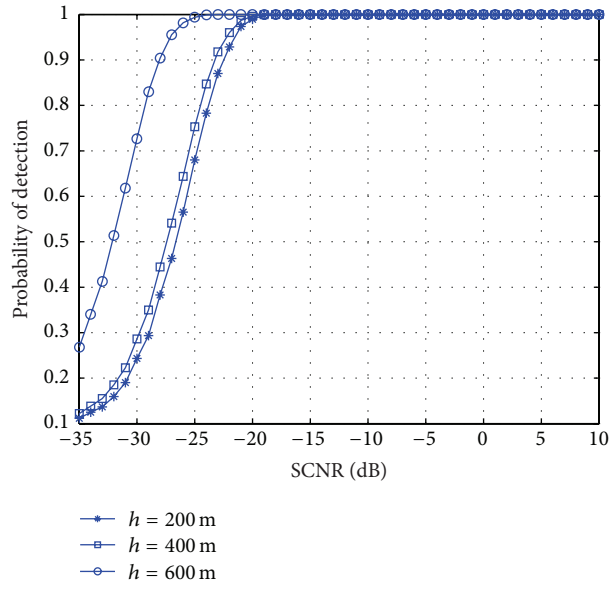

Figure 8: GLRT-LQ detector detection performance varies with the height of target.

better detection performance when there are more number of transmit antennas and receive antennas.

Figures 8 and 9 depict the detection performance of GLRT-LQ and GLRT detector with target height, respectively; the heights of target are fixed at 200 m, 400 m, and 600 m and the probabilities of false alarm are fixed at $P_{fa} = 10^{-4}$. Figures 8 and 9 show that the detection performance varies with the height of target. We can see that the performance increases with the height of target under the low-grazing scene. However, the performance does not always increase with the height of target, just as Figure 10. When the height of target is 1600 m, the condition of low-grazing angle is not satisfied. If we still take it for low-grazing angle, the detection performance will decrease.

7. Conclusion

In this paper, we have introduced the concept of reflection coefficient under considering curved earth effect and introduced general signal model for MIMO radar in low-grazing angle, firstly. Then, we have derived the GLRT-LQ and GLRT detectors, respectively. Furthermore, we have compared the performance of GLRT-LQ and GLRT detector for MIMO

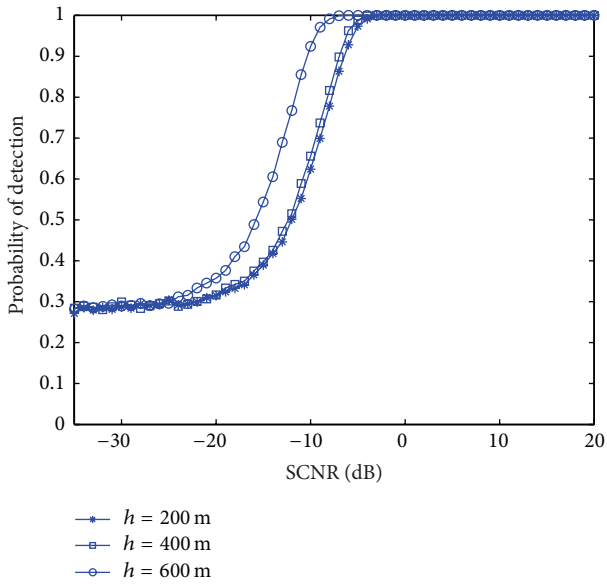

Figure 9: GLRT detector detection performance varies with the height of target.

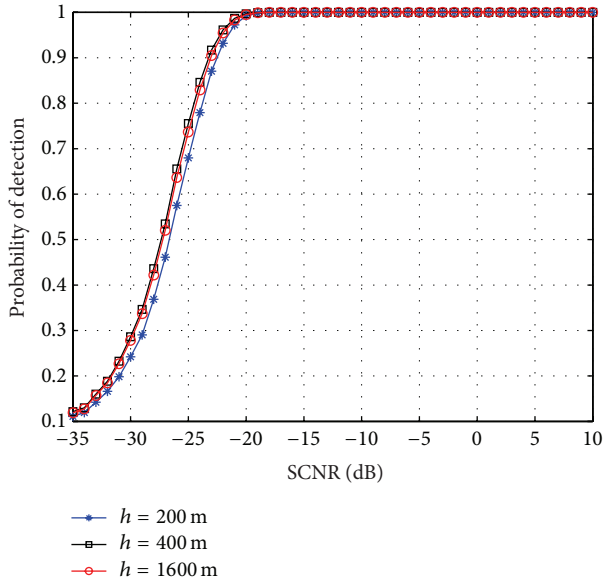

Figure 10: GLRT-LQ detector detection performance varies with the height of target.

radar between with multipath and without multipath effects. The simulation results have shown the importance of multipath effects for target detection in low-grazing angle and demonstrated that GLRT-LQ detector outperforms the GLRT detector in low-grazing angle.

Acknowledgments

The authors wish to thank the anonymous reviewers for their efforts in providing comments that have helped to significantly enhance the quality of this paper. This work was supported in part by the National Science Foundation of China under Grant no. 61302142.

References

[1] J. Li and P. Stoica, "MIMO radar with colocated antennas: review of some recent work," *IEEE Signal Processing Magazine*, vol. 24, no. 5, pp. 106–114, 2007.

[2] A. M. Haimovich, R. S. Blum, and L. J. Cimini, "MIMO radar with widely separated antennas," *IEEE Signal Processing Magazine*, vol. 25, no. 1, pp. 116–129, 2008.

[3] I. Bekkerman and J. Tabrikian, "Target detection and localization using MIMO radars and sonars," *IEEE Transactions on Signal Processing*, vol. 54, no. 10, pp. 3873–3883, 2006.

[4] K. W. Forsythe, D. W. Bliss, and G. S. Fawcett, "Multiple-input multiple-output (MIMO) radar: performance issues," in *Proceedings of the 38th Asilomar Conference on Signals, Systems and Computers*, pp. 310–315, Pacific Grove, Calif, USA, November 2004.

[5] P. Stoica, J. Li, and Y. Xie, "On probing signal design for MIMO radar," *IEEE Transactions on Signal Processing*, vol. 55, no. 8, pp. 4151–4161, 2007.

[6] J. Li and P. Stoica, *MIMO Radar Signal Processing*, Wiley-IEEE Press, New York, NY, USA, 2008.

[7] Q. He, R. S. Blum, H. Godrich, and A. M. Haimovich, "Target velocity estimation and antenna placement for MIMO radar with widely separated antennas," *IEEE Journal on Selected Topics in Signal Processing*, vol. 4, no. 1, pp. 79–100, 2010.

[8] H. W. Chen, Y. P. Chen, X. Li, and Z. W. Zhuang, "Extended ambiguity function for bistatic MIMO radar," *Journal of Systems Engineering and Electronics*, vol. 23, no. 2, pp. 109–114, 2012.

[9] N. H. Lehmann, A. M. Haimovich, R. S. Blum, and L. Cimini, "High resolution capabilities of MIMO radar," in *Proceedings of the 40th Asilomar Conference on Signals, Systems, and Computers (ACSSC '06)*, pp. 25–30, Pacific Groove, Calif, USA, November 2006.

[10] H. Godrich, V. M. Chiriac, A. M. Haimovich, and R. S. Blum, "Target tracking in MIMO radar systems: techniques and performance analysis," in *Proceedings of the IEEE International Radar Conference (RADAR '10)*, pp. 1111–1116, May 2010.

[11] J. Guan and Y. Huang, "Detection performance analysis for MIMO radar with distributed apertures in Gaussian colored noise," *Science in China F*, vol. 52, no. 9, pp. 1688–1696, 2009.

[12] J. Tang, Y. Wu, Y. N. Peng, and X. T. Wang, "On detection performance and system configuration of MIMO radar," *Science in China F*, vol. 52, no. 7, pp. 1250–1257, 2009.

[13] J. Tang, Y. Wu, Y. Peng, and X. Wang, "On detection performance of MIMO radar for Rician target," *Science in China F*, vol. 52, no. 8, pp. 1456–1465, 2009.

[14] E. Fishler, A. Haimovich, R. S. Blum, L. J. Cimini Jr., D. Chizhik, and R. A. Valenzuela, "Spatial diversity in radars: models and detection performance," *IEEE Transactions on Signal Processing*, vol. 54, no. 3, pp. 823–838, 2006.

[15] T. Aittomaki and V. Koivunen, "Performance of MIMO radar with angular diversity under swerling scattering models," *IEEE Journal on Selected Topics in Signal Processing*, vol. 4, no. 1, pp. 101–114, 2010.

[16] Y. Jin, J. M. F. Moura, and N. O'Donoughue, "Time reversal in multiple-input multiple-output radar," *IEEE Journal on Selected Topics in Signal Processing*, vol. 4, no. 1, pp. 210–225, 2010.

[17] D. K. Barton, "Low angle tracking," *Proceedings of the IEEE*, vol. 62, no. 6, pp. 687–704, 1974.

[18] S. L. Silon and B. D. Carlson, "Radar detection in multipath," *IEE Proceedings F*, vol. 146, no. 1, pp. 45–54, 1999.

[19] T. Lo and J. Litva, "Use of a highly deterministic multipath signal model in low-angle tracking," *IEE Proceedings F*, vol. 138, no. 2, pp. 163–171, 1991.

[20] M. I. Skolnik, *Radar Handbook*, McGraw-Hill, New York, NY, USA, 2nd edition, 1990.

[21] M. A. Richards, *Fundamentals of Radar Signal Processing*, McGraw-Hill, New York, NY, USA, 2005.

[22] K. D. Ward, C. J. Baker, and S. Watts, "Maritime surveillance radar. Part 1: radar scattering from the ocean surface," *IEE proceedings F*, vol. 137, no. 2, pp. 51–62, 1990.

[23] F. Gini, A. Farina, and G. Foglia, "Effects of foliage on the formation of K-distributed SAR imagery," *Signal Processing*, vol. 75, no. 2, pp. 161–171, 1999.

[24] G. Cui, L. Kong, and X. Yang, "Multiple-input multiple-output radar detectors design in non-Gaussian clutter," *IET Radar, Sonar and Navigation*, vol. 4, no. 5, pp. 724–732, 2010.

[25] M. Akcakaya and A. Nehorai, "Adaptive MIMO radar design and detection in compound-gaussian clutter," *IEEE Transactions on Aerospace and Electronic Systems*, vol. 47, no. 3, pp. 2200–2207, 2011.

Hindawi Publishing Corporation
International Journal of Antennas and Propagation
Volume 2013, Article ID 284698, 8 pages
http://dx.doi.org/10.1155/2013/284698

Application Article

Phase Pattern Calibration for Interferometric Applications in Spaceborne SAR Systems

Markus Bachmann, Marco Schwerdt, Gabriel Castellanos Alfonzo, and Dirk Schrank

German Aerospace Center (DLR), Oberpfaffenhofen, 82234 Weßling, Germany

Correspondence should be addressed to Markus Bachmann; markus.bachmann@dlr.de

Received 5 April 2013; Accepted 30 September 2013

Academic Editor: Ulrich Nickel

SAR is a widely used technique to acquire images for geoscience and earth observation applications. Active phased array antennas are commonly used in spaceborne SAR systems. For certain modes and applications, it is necessary to know the phase behavior of these phased array antennas. For applications utilizing the different polarization channels for interferometry, the phase difference between the polarizations needs to be calibrated very accurately as it is the main evaluation parameter. Also for single-pass interferometric missions, the difference between the two antennas in terms of phase gradients is of major importance. This paper demonstrates for the first time the usage of phase patterns in an operational interferometric SAR mission. It describes why these phase patterns are required and how they are used to fulfill the different goals of the missions. Then, the mathematical model to derive the phase of the antenna patterns is shown. Finally, the paper explains how the antenna patterns are calibrated in order to minimize their residual errors and describes in detail the measurements performed for this calibration and verification.

1. Introduction

Spaceborne Synthetic Aperture Radar (SAR) missions essentially contribute to geoscience for a better understanding of our global environment. With its all day, all night, and all weather imaging capabilities on the one hand and a high resolution on the other, SAR is an ideal tool to monitor these processes affecting our environment regularly and to help understanding the effects behind. In addition, SAR interferometry enables the generation of high resolution digital elevation models (DEMs) adding to the information content provided by nominal SAR images.

As SAR is an active system, it requires a transmit antenna to send radar pulses. The echoes are received with the same or a different antenna, stored and processed into SAR images. The antenna of such a system is commonly realized as an active phased array antenna. Like every antenna, it shows a certain radiation characteristic, the so-called antenna pattern, which is visible in the uncorrected SAR images. During processing, the influence of the antenna pattern is removed.

For nominal single polarized SAR images, only the influence of the amplitude of the pattern is relevant. This is described in detail in [1, 2]. Since the SAR imaging principle relies on coherently integrating the echoes from multiple transmit pulses spread over time and space, precise phase alignment between and within pulses is a critical component of the system performance.

Interferometric imaging exploits the phase difference between two slightly offset, highly colinear SAR images to infer terrain height. INSAR applications require very precise joint phase characterization of the transmit and reveice antenna patterns as a function of look angle.

This paper is divided thematically as follows: Section 2 describes the applications utilizing the phase information. Section 3 gives an overview about the challenges of phase pattern determination and calibration and Section 4 derives the mathematical background of the phase patterns. Section 5 provides the calibration approach and the results for the different phase pattern calibration aspects.

2. Phase Pattern Applications

Two main applications utilize the phase information of the SAR phased array antenna.

2.1. Polarimetric SAR Interferometry and the Dual Receive Antenna Mode. Polarimetric SAR Interferometry (PolInSAR) [3] is a widely used technique to determine soil and moisture of areas on the Earth's surface, tree heights, or vegetation growth. Multiple images acquired with two or even four polarizations during one acquisition are combined to extract the required information content. For PolInSAR the accurate and stable phase information between the polarization channels is essential since it must be corrected during processing to remove systematic perturbations that degrade system performance.

For PolInSAR, the accuracy of the phase knowledge needs to be better than 5 deg. This was the requirement for the TerraSAR-X mission, which performs SAR imaging for scientific and commercial customers and was launched in 2007. The same value was required for the L-band system ALOS/PALSAR [4]. The ALOS/PALSAR mission showed that it is possible to calibrate the phase balance down to an imbalance of 0.61 deg with a standard deviation of 2.66 deg [5].

One important parameter for PolInSAR is the cross-coupling between different polarizations. This isolation of the cross-talk for TerraSAR-X was already measured and is better than 34 dB [6, 7].

A topic closely related to PolInSAR is the usage of the Dual-Receive Antenna (DRA) capabilities of TerraSAR-X. For the DRA mode, the receive antenna is split in two halves in azimuth direction. The signal from both parts are received by two separate receiver chians and stored separately. Hence, two simultaneously acquired images with a small along-track baseline in azimuth direction are obtained. These images can be evaluated for applications like Along Track Interferometry (ATI) for Ground Moving Target Indication (GMTI) [8]. In the same way as for PolInSAR, well calibrated phase patterns are also important for the phase compensation in DRA acquisitions [9].

2.2. Bistatic Imaging. Multisatellite bistatic formations are currently becoming more and more popular in spaceborne SAR imaging. TanDEM-X, the first bistatic SAR formation, has been in orbit since 2010. For bistatic systems it is quite important to know the phase gradient for each beam in transmit and receive direction and especially individually for both satellites. Therewith, the monostatic and bistatic phase patterns of the satellites are derived in order to coherently combine the images for interferometric applications [10]. For bistatic missions using interferometry to determine heights on the Earth, the influence of the phase from the two receiving systems needs to be known and compensated for.

The main goal of the TanDEM-X mission is the derivation of a global Digital Elevation Model (DEM) [11]. The accuracy requirement of this mission in terms of phase accuracy can be derived from the overall mission requirement for the relative height error. The 90% relative height error of the DEM in a $1^\circ \times 1^\circ$ cell shall not exceed 2 m. The two satellites in space build a spaceborne interferometer with a height of ambiguity down to 30 m, where the height of ambiguity corresponds to one phase cycle of 2 pi or 360°. Hence, to achieve a relative height error of 2 m [11], the phase error of the overall system may not exceed 12 deg. Since receiver noise over areas with low backscatter return eats up the greatest part of this error budget, errors associated with the antenna pattern should be lower than 3 deg.

3. Challenges

The usefulness of an antenna model for nominal SAR imaging is given in detail in [1]. Here, only the main considerations important to the antenna phase patterns are described.

3.1. Great Number of Beams. Actual SAR missions host very flexible instruments. With different modes, hundreds of antenna beams can be used to acquire images for dedicated applications and purposes. Any of these beams can be used for polarimetry and interferometry. New imaging modes and antenna beams can even be added after the launch. These new beams were not measured on ground prior to launch. An accurate antenna model is essential to mathematically determine the antenna gain and phase patterns for each beam and thereby ensure in situ system performance.

3.2. Accuracy Requirement. The accuracy requirements of actual missions and their tight schedules make the measurement of all antenna patterns in orbit infeasible. Hence, the antenna model for TerraSAR-X was validated by on-ground measurements leaving only a few beams to be measured on orbit. A great advantage of the antenna model is that it can be adjusted over mission life time to reflect in-situ performance. Establishing different correction factors during commissioning phase and operational phase enables the adjustment and extension of the model to further improve system performance.

3.3. Need for Antenna Phase Patterns. A common way to account for the phase behaviour of an antenna is the definition and determination of a "phase center," that is, a geometrical point from which the antenna pattern appears to emanate. However, this phase center is only easily determined for a horn antenna. For a phased array antenna, individual phase and amplitude taper values can be applied to each subelement. For an untapered beam, the resulting phase variation is still very smooth over the main lobe of a beam shown by the red graph in Figure 1. It could still be possible, with a certain inaccuracy, to describe the phase of the entire array with a single phase center.

In the Shuttle Radar Topography Mission (SRTM) mission, for example, only beams steered in phase but not tapered in amplitude were used to realize the ScanSAR acquisitions [12] in C-band and the single swath acquisitions in X-band. The influence of the phase was analysed [13]. It was found that constant phase offsets were sufficient to describe the phase behaviour and no range angle dependent pattern was applied.

The antenna beams of TerraSAR-X are optimized to provide SAR images with high radiometric accuracy. For this purpose, the antenna pattern is steered and formed using individual phase and amplitude tapering coefficient. Figure 2 shows these excitation coefficients of an exemplary Stripmap beam. In the transmit direction no amplitude taper

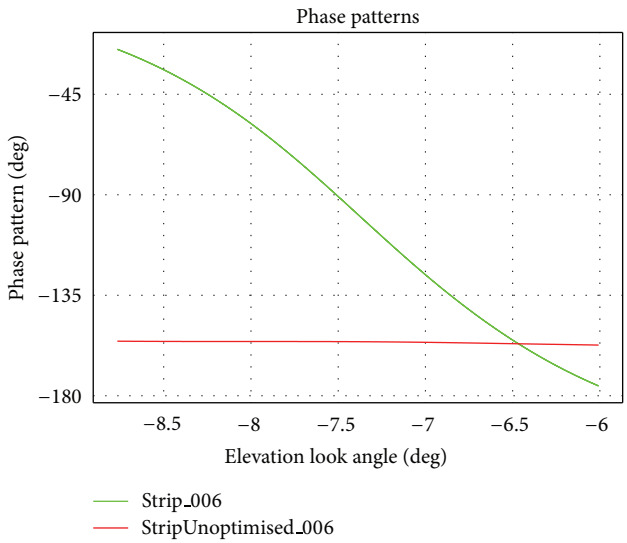

FIGURE 1: Phase patterns of a tapered (green) and an untapered (red) beam.

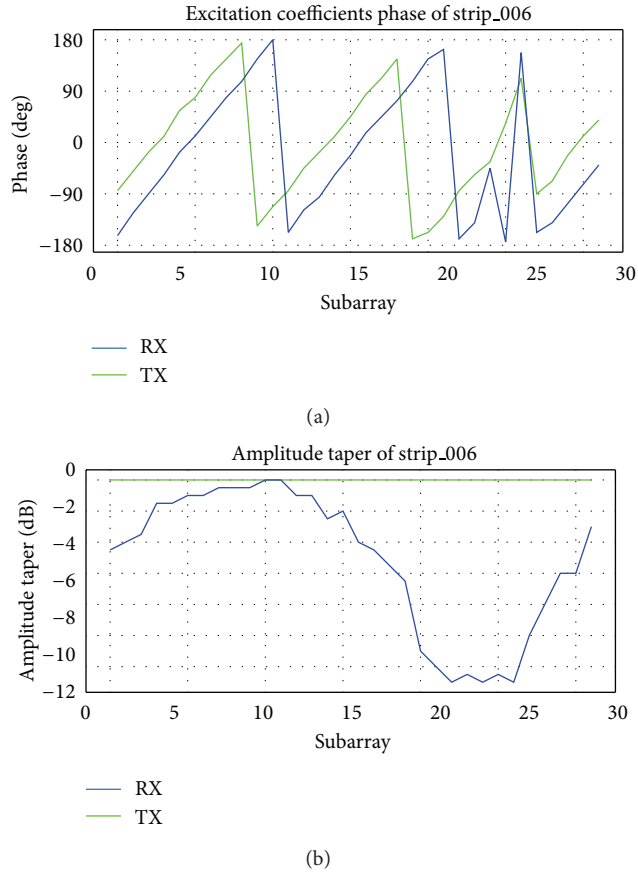

FIGURE 2: Excitation coefficients of a tapered stripMap-Beam.

is applied due to performance considerations. In receive up to −13 dB of the amplitude taper is used to attenuate the signal and thereby to optimize the performance; this is clearly visible in Figure 2. This amplitude taper for Stripmap beams results in a large phase variation over the beam width. This is again shown in Figure 1 where the phase gradient of the tapered beam is shown in green. Depending on the beam and the corresponding excitation coefficients, phase gradients of more than 180 deg can occur.

3.4. Relative and Absolute Phase Derivation. In practice, only a relative phase calibration $\Delta\varphi = \varphi_2 - \varphi_1$ is possible. For an absolute measurement of the phase, the orbit would have to be known within a fraction of the wave length. For an X-band system with a wave length of 3.1 cm, using GPS measurements, the orbital position of the satellite is determined on the order of 5 to 10 cm, which is at least an order of magnitude too coarse. Additionally, the influence of the atmosphere makes it very difficult to determine absolute phase.

For PolInSAR, however, the images for each polarization are taken quasi at the same time. The polarization is switched from pulse to pulse and the orbit trajectory is very stable over the SAR integration time. Hence, the influence of the orbit on the phase difference is very nearly zero and can be safely ignored.

For interferometric imaging on the other hand, the absolute baseline between the two antenna centers is critically important. Because of the orbital stability, this relative vector can be determined on the order of 1 mm (1 sigma) with space-based systems using double differential GPS measurements [14, 15]. Therefore, it is accurate enough for absolute height determination, provided that at least one ground control point is available, that is, a pixel or region in the image, with a precise knowledge of its absolute height and geolocation is available to calibrate the absolute height.

4. Antenna Pattern Modeling

4.1. Antenna Model Equation. The mathematics behind the antenna model was developed in the context of the TerraSAR-X mission in cooperation between EADS Astrium GmbH, Friedrichshafen, and the DLR. It was extended by DLR to apply the phase pattern concept for the TanDEM-X mission.

The antenna model itself mathematically calculates radiation patterns by the superposition of four inputs:

(i) radiation patterns of the single-antenna elements mounted in the final array configuration (to cover mutual coupling effects) measured on ground (pre-launch), the so-called embedded subarray patterns,

(ii) beam excitation coefficients (amplitude and phase) of each individual transmit/receive module (TRM),

(iii) exact geometrical dimensions of the array antenna including the vertical distances between the subarrays,

(iv) the current state of the SAR instrument including drifting and/or failed TRMs.

For active phased array antennas, the radiated pattern F_{beam} is calculated by [16, 17]

$$\overrightarrow{F}_{\text{beam}}(\varepsilon,\alpha) = \sum_{m=0}^{M-1}\sum_{n=0}^{N-1}\Big(\overrightarrow{C}_{\text{SA},mn}(\varepsilon,\alpha)\cdot a_{mn}\cdot E_{\text{SA},mn} \cdot e^{jk\sin\varepsilon\cos\alpha(-((N-1)/2)+n)\Delta y} \cdot e^{jk\cos\varepsilon\sin\alpha(-((M-1)/2)+m)\Delta x}\Big), \quad (1)$$

where ε and α are the desired elevation and azimuth angle, N and M are the amount of rows and panels of the subarrays, and Δx (panels) and Δy (rows) are the intersubarray distances. The wave number k includes the centre frequency 9.65 GHz of the system by the relation of $k = 2\pi/\lambda$. The embedded subarray patterns C_{SA}, the excitation coefficients a_{mn}, and the error matrix E_{SA} are described in the next section.

4.2. Antenna Model Inputs. The embedded subarray patterns C_{SA} comprise the physically measured complex radiation characteristics of the individual subarray elements. The embedded pattern of one subarray mounted within the array antenna describes the radiation characteristic of this subarray. In this way, mutual coupling effects and phase distortions are incorporated in the measurements. For the nominal acquisition, mismatch and gain are smooth over the bandwidth; therefore, only the embedded patterns at centre frequency need to be incorporated in the antenna model.

As input for the antenna model, all embedded subarrays of one panel, which is 32 subarrays in a column, were measured by Astrium. The patterns of the embedded patterns at different panels but situated at the same row are very similar to each other, independent from the position of the panel. The comparison of the measured patterns of whole panels showed that it is possible to use only the embedded patterns of one panel and substitute the others using their measured amplitude and phase offsets. These embedded patterns must be known with high accuracy, as they are one main input of the model. The measurements must be more accurate than the required setting accuracy of the TRMs, which is 0.5 dB in amplitude and 5 deg of phase; this corresponds to about 0.4 mm of baseline separation.

The commanded complex excitation coefficients are given by a_{mn}. These coefficients are provided in terms of amplitude and phase values row- and column-wise. For each beam commanded, one set of values is put in a common table. This table is available on board of the satellite to be applied to form the beam for each acquisition. It can be updated if necessary, for example, in case of contingencies.

Finally, the error matrix E_{SA} describes drifted or failed antenna elements. These are determined via a TRM characterization method [18]. With the method, the actual state of the TRMs is determined evaluating dedicated orthogonal code sequences routed through the TRMs sequentially.

To obtain the complete two-way antenna patterns, the equation is evaluated for transmit and receive separately. Both, the excitation laws and the error matrix are different for transmit and receive. In case of the excitation coefficients, the discrimination between transmit and receive allows greater flexibility for beam steering, as from signal-to-noise ratio point of view, the use of an amplitude taper is only reasonable in the receive path. Since the radar signals travel through the TRMs on different paths, for transmit via the high power amplifier and in receive through the low noise amplifier, the error matrix coefficients for the two paths will be different.

The accuracy of the antenna model depends strongly on the measurement accuracy of the embedded subarray patterns and on the stability of the instrument.

4.3. Phase Pattern Derivation, Calibration, and Compensation. To derive and generate the phase pattern φ_{beam} in elevation direction, (1) is evaluated:

$$\varphi_{\text{beam}}(\varepsilon) = \arctan\left(\overrightarrow{F}_{\text{beam}}(\varepsilon)\right). \quad (2)$$

For nominal acquisitions, the antenna is constantly steered to azimuth boresight. Hence, the phase variation in azimuth direction remains stationary. During phase calibration of the polarization, a slight polynomial dependency was recognized from the measurements. This dependency can be compensated by the relation

$$\varphi_{\text{polcor}}(\epsilon) = \left(\varphi_{c1}^2\varepsilon^2 + \varphi_{c3}\varepsilon + \varphi_{c3}\right) + \varphi_{\text{beam}}(\varepsilon) \quad (3)$$

with φ_{c1}, φ_{c2}, and φ_{c3} being determined by the polarimetric calibration described in Section 5.1.

Especially for bistatic acquisitions an adaption of the different phase origins of both satellites φ_{sat} has to be established by a phase correction:

$$\varphi_{\text{cor}}(\epsilon) = \varphi_{\text{sat}} + \varphi_{\text{polcor}}(\varepsilon) \quad (4)$$

which is determined by the interferometric calibration described in Section 5.3.

The resulting phase pattern is now unwrapped at phase wraps in the pattern. These phase wraps occur at nulls in the amplitude pattern, for example, between the main lobe and the first side lobe, where the phase jumps by 180 deg:

$$\varphi_{\text{unwrap}} = \text{unwrap}\left(\varphi_{\text{cor}}\right). \quad (5)$$

The corrected phase pattern is then stored and provided to the SAR processor, where the phase dependency of the image is compensated [19, 20]. The correction is applied on the single look slant range complex SAR (SSC) data. A reference DEM is used to determine the local incidence angles. These are then calculated back into antenna geometry, to correctly apply the phase pattern.

5. Calibration and Verification Results

5.1. Polarization Dependency

5.1.1. Purpose. For PolInSAR, the difference between the two polarizations is utilized. As the complete antenna pattern is formed by the superposition of embedded subarray patterns of the individual elements, these embedded patterns are the

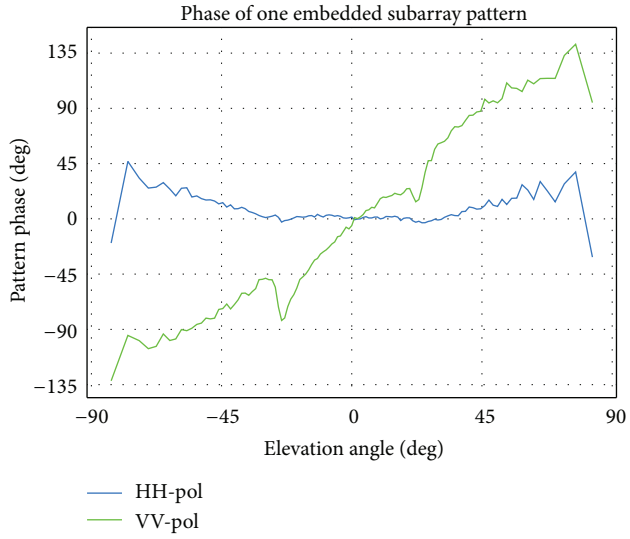

Figure 3: Phase deviation between HH and VV polarization for one subarray.

main influence for the polarization dependency. As depicted in Figure 3 the patterns show an elevation angle dependent phase gradient, which differs between HH and VV. This dependency makes it necessary to not only correct one offset between the polarizations but also provide a correction pattern covering each whole swath.

5.1.2. Approach. The impact of the phase deviations on the whole antenna was measured by an in-flight measurement campaign. Corner reflectors deployed in a calibration field around Oberpfaffenhofen were used as targets for several dual-pol acquisitions with different incidence angles from near to far range. In dual-pol acquisitions the polarization is switched from pulse to pulse either in transmit or receive direction or a combination of both. Hence, they provide the advantage that both polarizations are acquired from almost the same time and from the same orbital position and penetrating the same atmosphere under the same weather conditions. By comparing both resulting images, the phase difference can be determined very accurately.

5.1.3. Results. Initially, a variation of about 10 deg was observed over the elevation angle range. From these initial measurements, the polynomial correction described by (3) was derived. This correction is applied in the antenna model to adjust the embedded patterns.

The final results can be seen in Figure 4(a). The deviation between HH and VV polarization can be calculated by the antenna model very precisely. Figure 4(b) shows the deviation between HH and VV compared between the antenna model and the physical measurements. It reveals a standard deviation of only 1.69 deg (1 sigma).

By design, the polarization switch of the radar system is situated between the radiator and the TRM. Hence, all active components are the same for both polarizations. Only the passive radiators are different for both polarizations. However, they are recirocal. This reciprocity could be confirmed

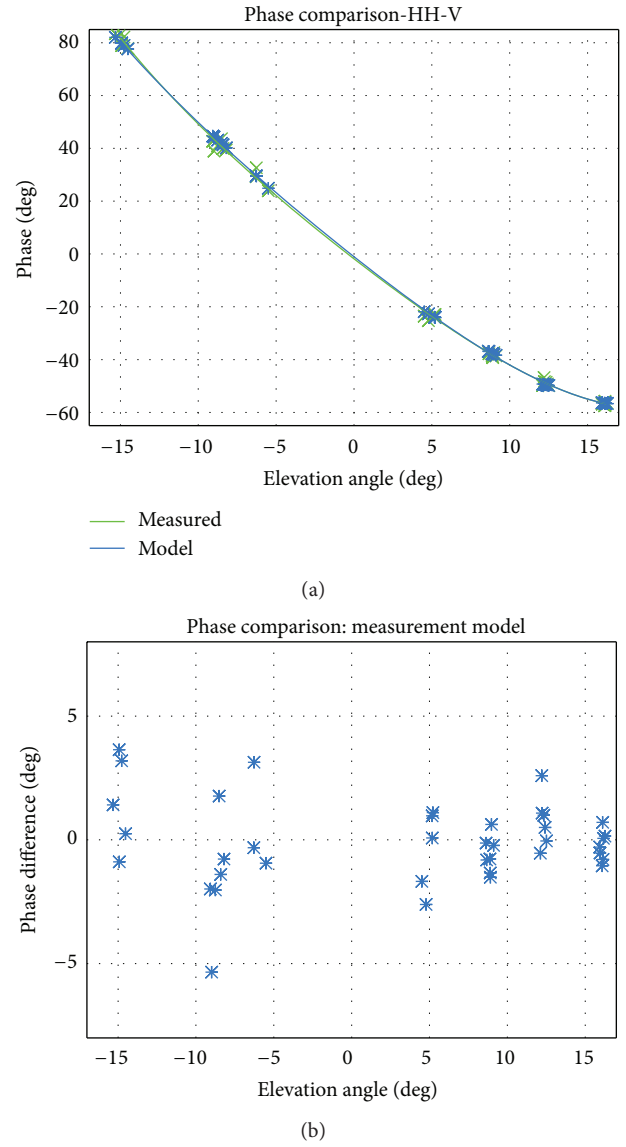

Figure 4: (a) Verification of the polarization dependent phase deviation: Measurements versus Antenna Model, (b) Deviation between HH-VV of the model and the measurements.

by evaluating dedicated Dual-Pol data takes with polarization combinations like HH/HV and VV/HV. Hence, the variation of all combinations including HV or VH polarized phase is equal or lower than the one for HH/VV.

5.2. Phase Pattern Shape

5.2.1. Purpose. The calibration and verification of the phase pattern shape is required to ensure that differently excited beams do not introduce an additional error into the system.

In TanDEM-X acquisitions, beams with and without amplitude taper are mixed for the acquisition of the DEM. In TanDEM-X, the Earth will be covered twice. The beams used for the second acquisition are shifted by half the beam width compared to the first acquisition. By this, areas with lower

antenna gain at the edges of the main lobe in one coverage are combined with a high antenna gain in the center of the main lobe from the other coverage. To keep the gain in the main lobe as high as possible, the beams are not amplitude tapered to flatten them. However, for difficult terrain like deserts, also optimized beams can be used to acquire additional data. These, in contrast, are the nominal Stripmap beams. Amplitude tapering is used to flatten and broaden the near beams to obtain sufficient performance over the whole swath. The beam to compare with is tapered in amplitude and shows a different taper in phase over the 32 subarrays in elevation on the TerraSAR-X satellite (Figure 1). Especially due to the taper in amplitude, the phase shows a steep gradient of about 50 deg per degree look angle, while the untapered beam is almost flat (compare Figure 1). An error in the modeling of this pattern would lead to phase trends in the interferograms and the DEMs.

By design, the antennas of both satellite systems are very similar. Hence, the phase behaviour is also very similar. However, if several modules of one antenna fail or drift, the phase behaviour would change severely. For this purpose, the quantification of the joint phase patterns incorporating both satellites is critically important for the system to meet its mapping specifications.

5.2.2. Approach. To evaluate the accuracy of the phase pattern shape, two DEMs acquired with different beams formed with two difference excitation coefficient sets can be compared. For this purpose, a beam covering the same coverage area but with different excitation coefficients and with no amplitude taper was designed and uploaded to the instrument

Two acquisitions are taken from the same orbital location, imaging the same test area on Earth, but with a lag of one repeat cycle (11 days). To study the accuracy of the antenna model, two beams illuminating the same swath but with different excitation coefficients are used. The different excitation coefficients lead to completely different shapes of the antenna pattern. The first beam is only steered by phase coefficients which lead to an antenna pattern with typical shape. The second beam is optimized to form a very flat pattern by using both phase and amplitude taper. By the use of the amplitude taper, also the embedded patterns of different rows are weighted differently. Hence, the comparison would reveal a mistaken usage of these inputs for phase pattern generation. The generated DEMs (see Figure 5 for an example of the test site near Quandong Airport, Australia) are annotated in lat/lon coordinates, which makes it easy to build the difference image of them. The difference image can then be integrated in flight direction to generate a DEM difference graph which is shown in Figure 6.

5.2.3. Results. To derive the corresponding phase error associated with the DEM difference in phase units, the height of ambiguity of the two acquisitions must be taken into account. For the first acquisitions this was $h_{\text{amb}} = 128$ m (untapered beam), and $h_{\text{amb}} = 131$ m (tapered beam) for the second acquisition. With a mean h_{amb} of 129.5 m the peak-to-peak height error Δh transforms by

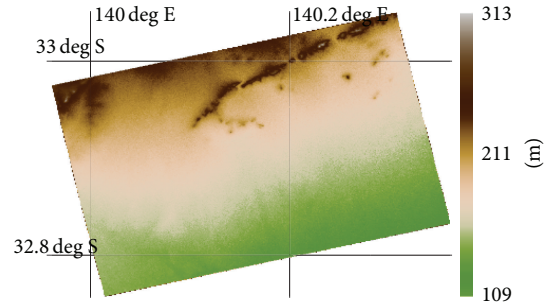

Figure 5: DEM of the Quandong test site.

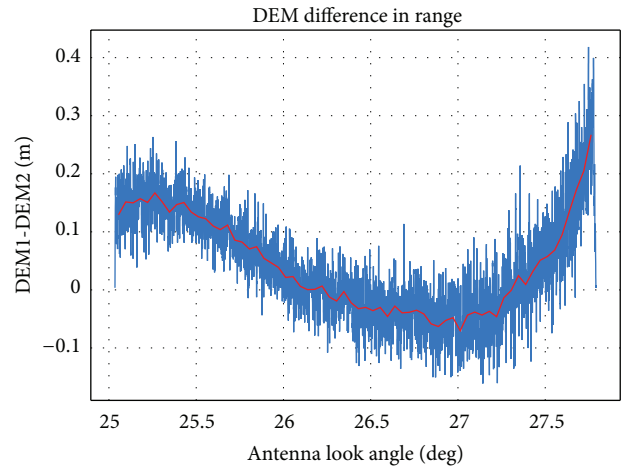

Figure 6: Resulting phase pattern deviation in flight direction of the difference between the two DEMs.

$$\varphi_{\text{err}} = \frac{\Delta h}{h_{\text{amb}}} 2\pi \tag{6}$$

into a peak-to-peak phase error of $\varphi_{\text{err}} = 0.85$ deg and a standard deviation of only 0.39 deg. Hence, the pattern shape has been accurately calculated by the antenna model.

5.3. Beam to Beam Dependency

5.3.1. Purpose. Proper phase compensation of the beam to beam dependency is important to remove systematic tilts in the DEM in range direction. As nine beams are required to cover the whole ground range of 240 km of one orbit at the equator, no shift between the beams or an overall trend should be present.

5.3.2. Approach. To verify the influence of the phase patterns from beam to beam, all individual DEMs acquired so far can be evaluated. For each DEM, the deviation from a reference DEM is calculated. In our case this reference DEM is an SRTM DEM globally improved using the height information of ICES at elevation datasets [21]. It is obvious that the accuracy of SRTM is lower than what would be expected for this verification. However, the SRTM swaths with 240 km ground range are much larger than TanDEM-X swaths with 30 km. The SRTM DEM is combined from ascending and

descending acquisitions. Due to the different inclinations of the Space Shuttle (SRTM) and TerraSAR-X/TanDEM-X, the swaths of both overlap randomly. In this way, a trend in the SRTM DEM is not systematically traced to the difference between SRTM and TanDEM-X average DEM heights. It has to be mentioned that the DEM scenes are not DEM-calibrated at this point, where DEM calibration means the compensation of range and azimuth trends for each individual scene separately with respect to the others.

5.3.3. Results. More than 50000 independently processed DEM scenes of the global DEM acquisition, each covering an area of 30 km × 50 km and about 10 million pixel, were evaluated using their mean height difference to the improved SRTM. Only the nine nominal TanDEM-X beams were evaluated covering an incidence angle range from 30 deg to 48.5 deg, which is the nominal incidence angle range for TanDEM-X DEM acquisitions.

To relate both satellites against each other, an interferometric calibration [22] was performed before determining the phase offsets between both satellites to be considered in (5). Here, one global phase offset per satellite that is valid for all acquisitions was derived and applied to calibrate the system which is explained in [20]. The intension of the present paper for this topic was to ensure that there is no residual trend over the beams caused by the antenna model.

Figure 6 shows the mean heights of all scenes plotted over the nine beams. The mean height of ambiguity for the scenes is about 60 m. With this, the phase accuracy calculated from the maximal deviation from Figure 7 of a height error of ±0.24 m using (6) is ±1.5 deg. No further systematic trend is evident in the residuals, and hence the interferometric calibration has reached its limits.

6. Conclusion

The knowledge of the phase gradient over the antenna look angle is of fundamental importance for certain applications in SAR image acquisition. For high performance SAR instruments with a multitude of beams and modes, modeling the antenna phase gradient offers significant performance advantages over purely instrumentally derived patterns.

The paper shows the generation and application of phase patterns for PolInSAR, for the Dual-Receive Antenna Mode and for a fully operational bistatic SAR system in space. The phase patterns are generated by an antenna model and calibrated in orbit with very high accuracy.

Considering the stringent requirement for phase pattern accuracy in high performance SAR systems, different applications have to be distinguished. Comparing the different polarizations over the whole look angle range, the phase difference between the phase patterns of each polarization channel is modeled with an accuracy better than 1.69 deg (1 sigma). An accuracy of 0.85 deg could be achieved comparing different amplitude taper and excitation coefficients of the antenna look angle used for the phase patterns. The average dependency from beam to beam is also better than ±1.5 deg comparing the nominal nine TanDEM-X beams.

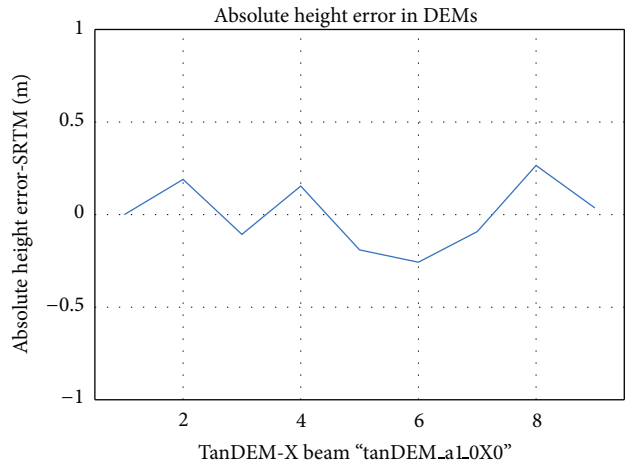

Figure 7: Beam to beam dependency of the phase pattern.

Acknowledgments

The work related to the TanDEM-X project mentioned in this paper is partly funded by the German Federal Ministry for Economics and Technology (Förderkennzeichen 50 EE 1035). The authors would like to thank the Calibration Team for deploying Corner Reflectors for the analysis and the SAR Processor/Interferometric Processor Team for processing the acquisitions and DEMs used for the analyses. Special thanks go also to the HR team for providing the infrastructure for the analyses. We also would like to thank the Astrium GmbH that built these very stable and reliable satellites.

References

[1] M. Bachmann, M. Schwerdt, and B. Bräutigam, "TerraSAR-X antenna calibration and monitoring based on a precise antenna model," *IEEE Transactions on Geoscience and Remote Sensing*, vol. 48, no. 2, pp. 690–701, 2010.

[2] M. Schwerdt, B. Bräutigam, M. Bachmann, B. Döring, D. Schrank, and J. Hueso Gonzalez, "Final TerraSAR-X calibration results based on novel efficient methods," *IEEE Transactions on Geoscience and Remote Sensing*, vol. 48, no. 2, pp. 677–689, 2010.

[3] K. P. Papathanassiou and S. R. Cloude, "Single-baseline polarimetric SAR interferometry," *IEEE Transactions on Geoscience and Remote Sensing*, vol. 39, no. 11, pp. 2352–2363, 2001.

[4] A. Rosenqvist, M. Shimada, N. Ito, and M. Watanabe, "ALOS PALSAR: a pathfinder mission for global-scale monitoring of the environment," *IEEE Transactions on Geoscience and Remote Sensing*, vol. 45, no. 11, pp. 3307–3316, 2007.

[5] M. Shimada, O. Isoguchi, T. Tadono, and K. Isono, "PALSAR radiometric and geometric calibration," *IEEE Transactions on Geoscience and Remote Sensing*, vol. 47, no. 12, pp. 3915–3932, 2009.

[6] I. Hajnsek, K. Papathanassiou, T. Busche et al., "Data quality and scientific analysis of fully polarimetric TerraSAR-X data," in *Proceedings of the POLInSAR*, 2011.

[7] M. Schwerdt, J. Hueso Gonzalez, M. Bachmann, D. Schrank, C. Schulz, and B. Döring, "Monostatic calibration of both

TanDEM-x satellites," in *Proceedings of the 30th IEEE International Geoscience and Remote Sensing Symposium (IGARSS '10)*, pp. 2636–2639, July 2010.

[8] M. Gabele, B. Brautigam, D. Schulze, U. Steinbrecher, N. Tous-Ramon, and M. Younis, "Fore and aft channel reconstruction in the TerraSAR-X dual receive antenna mode," *IEEE Transactions on Geoscience and Remote Sensing*, vol. 48, no. 2, pp. 795–806, 2010.

[9] M. Schwerdt, D. Schrank, M. Bachmann, C. Schulz, B. Döring, and J. Hueso Gonzalez, "TerraSAR-X Re-calibration and dual receive antenna campaigns performed in 2009," Proceedings of the 8th European Synthetic Aperture Radar Conference (EUSAR '10), 2010.

[10] P. A. Rosen, S. Hensley, R. Ian Joughin et al., "Synthetic aperture radar interferometry," in *Proceedings of the Geoscience and Remote Sensing Symposium (IGARSS '02)*, 2000.

[11] G. Krieger, A. Moreira, H. Fiedler et al., "TanDEM-X: a satellite formation for high-resolution SAR interferometry," *IEEE Transactions on Geoscience and Remote Sensing*, vol. 45, no. 11, pp. 3317–3340, 2007.

[12] S. Hensley, P. Rosen, and E. Gurrola, "The SRTM topographic mapping processor," in *Proceedings of the Intenational Geoscience and Remote Sensing Symposium (IGARSS '00)*, pp. 1168–1170, July 2000.

[13] M. Zink and D. Geudtner, "Calibration of the interferometric X-SAR system on SRTM," in *Proceedings of the IEEE International Geoscience and Remote Sensing Symposium (IGARSS '99)*, pp. 227–229, July 1999.

[14] J. Hueso Gonzalez, J. Walter Antony, M. Bachmann, G. Krieger, M. Schwerdt, and M. Zink, "Tests of the TanDEM-X DEM calibration performance," in *Proceedings of the International Geoscience and Remote Sensing Symposium (IGARSS '12)*, 2012.

[15] O. Montenbruck, M. Wermuth, and R. Kahle, "GPS based relative navigation for the TanDEM-X mission—first flight results," in *Proceedings of the 23rd International Technical Meeting of the Satellite Division of the Institute of Navigation*, pp. 2797–2807, September 2010.

[16] M. Bachmann, M. Schwerdt, B. Bräutigam, B. Grafmüller, A. Herschlein, and J. L. Álvarez-Pérez, "The TerraSAR-X antenna model approach," in *Proceedings of the 2nd International ITG Conference on Antennas (INICA '07)*, Munich, Germany, March 2007.

[17] C. A. Balanis, *Antenna Theory: Analysis and Design*, John Wiley & Sons, 2nd edition, 1997.

[18] B. Brautigam, M. Schwerdt, and M. Bachmann, "An efficient method for performance monitoring of active phased array antennas," *IEEE Transactions on Geoscience and Remote Sensing*, vol. 47, no. 4, pp. 1236–1243, 2009.

[19] T. Fritz and M. Bachmann, "L1b product phase pattern correction," Tech. Rep. TX-GS-TN-3031, TerraSAR-X Ground Segment, 2010.

[20] T. Fritz, C. Rossi, N. Yague-Martinez, F. Rodriguez-Gonzalez, M. Lachaise, and H. Breit, "Interferometric processing of TanDEM-X data," in *Proceedings of the IEEE International Geoscience and Remote Sensing Symposium (IGARSS '11)*, pp. 2428–2431, Vancouver, Canada, July 2011.

[21] M. Huber, B. Wessel, D. Kosmann et al., "Ensuring globally the TanDEM-X height accuracy: analysis of the reference data sets ICESat, SRTM and KGPS-tracks," in *Proceedings of the IEEE International Geoscience and Remote Sensing Symposium (IGARSS '09)*, pp. II769–II772, July 2009.

[22] M. Bachmann, J. Hueso Gonzalez, G. Krieger, M. Schwerdt, J. Walter Antony, and F. De Zan, "Calibration of the bistatic TanDEM-X interferometer," in *Proceedings of the 9th European Synthetic Aperture Radar Conference (EUSAR '12)*, 2012.

Hindawi Publishing Corporation
International Journal of Antennas and Propagation
Volume 2013, Article ID 674878, 6 pages
http://dx.doi.org/10.1155/2013/674878

Research Article

Direction Finding for Bistatic MIMO Radar with Uniform Circular Array

Cao Yunhe, Zhang Zijing, Wang Shenghua, and Dai Fengzhou

National Laboratory of Radar Signal Processing, Xidian University, Xi'an 710071, China

Correspondence should be addressed to Cao Yunhe; cyh_xidian@163.com

Received 11 March 2013; Accepted 23 September 2013

Academic Editor: Ulrich Nickel

A method of direction of arrival (DOA) and direction of departure (DOD) angle estimation based on polynomial rooting for bistatic multiple-input multiple-output (MIMO) radar with uniform circular array (UCA) configuration is proposed in this paper. The steering vector of the UCA is firstly transformed into a steering vector with a Vandermonde structure by using the Jacobi-Anger expansion. Then the null-spectrum function of the MIMO radar can be written as an expression in which the transmit and receive steering vectors are decoupled. Finally, a two-step polynomial rooting is used to estimate DOA and DOD of targets instead of two-dimensional multiple signal classification (MUSIC) search method for bistatic UCA MIMO radar. The angle estimation performance of the proposed method is similar to that of the MUSIC spectral search method, but the computation burden of the proposed polynomial rooting algorithm is much lower than that of the conventional MUSIC method. The simulation results of the proposed algorithm are presented and the performances are investigated and analyzed.

1. Introduction

Research on multiple-input multiple-output (MIMO) radar has been growing as evidenced by an increasing body of literature [1–10]. MIMO radar is characterized by using multiple antennas to simultaneously transmit orthogonal waveforms and multiple antennas to receive the reflected signals. MIMO radar has been shown to provide a number of potential benefits as compared with conventional radar, such as enhancing angle resolution, improving parameter identifiability, and increasing flexibility for transmit beam pattern design. In particular, the problem of multitarget localization in bistatic MIMO radar has received great research interests. Many methods in bistatic MIMO radar are proposed to identify and locate multiple targets [3–9] in which both the transmit array and the receive array are uniform linear arrays (ULAs). In order to avoid angle search, estimation of signal parameters via rotational invariance techniques (ESPRIT) algorithm is applied to bistatic MIMO radar [3–7] by exploiting the invariance property of the transmit and receive arrays. In [8, 9], several algorithms based on polynomial root finding procedure are proposed to estimate DOA and DOD of targets.

Unfortunately, both the ESPRIT and the polynomial rooting method are designed for ULAs. The steering vector of the ULA is dependent on $2\pi d \sin\theta/\lambda$ (where d is the interelement spacing, θ is DOA of the source, and λ is the signal wavelength), and, hence, DOA estimation with ULA becomes ambiguous [10] beyond the range of 180° (from −90° to +90°). The following properties of uniform circular arrays (UCAs) [11–14] make them attractive in the context of DOA estimation. UCAs can provide 360° azimuthal coverage. In addition, direction patterns synthesized with UCAs can be electronically rotated in the plane of the array without significant change of beam shape. ULAs, in contrast, provide only 180° coverage, and beams formed with ULAs broaden as the array is steered away from boresight. Especially, UCAs configuration is very suitable for the MIMO radar, which often transmits orthogonal waveforms in each of the transmit antennas in order to detect the whole 360° in the azimuth angle simultaneously.

In order to come up with computationally efficient high-resolution DOA estimators for UCAs, the so-called beamspace transform [11–13] may be applied. It rebuilds desired Vandermonde structure for the steering vectors. Consequently, methods like root-MUSIC [15–17] and ESPRIT

may be applied to find DOAs. In [11], Tewfik and Hong have shown that it is possible to extend the Root-MUSIC to UCA using the phase mode excitation concept. In [12], Mathews and Zoltowski proposed real beamspace MUSIC to UCA that yields reduced computational complexity and better resolution. The beamspace transform works properly only under certain conditions on the array configuration that may be difficult to satisfy in some applications [13]. These algorithms require a sufficiently large number of antenna elements to avoid spatial aliasing and mapping errors that may cause error floor and excess variance [13]. It also shows that there is a significant difference in the performance of the UCA root-MUSIC technique depending on whether an even or odd number of elements is used [14]. Manifold separation technique [18, 19] shows an alternative method to map the array steering vectors to a Vandermonde structured virtual array with a significantly smaller fitting error than for beamspace transform.

In this paper, direction finding for bistatic MIMO radar with UCA configuration employing polynomial rooting is presented. Transmit and receive steering vectors are firstly decomposed using the Jacobi-Anger expansion [20]. Then two-dimensional direction finding in bistatic MIMO radar is transformed into double one-dimensional direction finding procedure [9]. At last, an algorithm based on polynomial root finding to estimate DOA and DOD of targets in bistatic MIMO radar with UCA configure is proposed. The computational complexity of the proposed method is low without the requirement of costly space searching procedure.

The remainder of this paper is organized as follows. In Section 2, we describe our bistatic UCA MIMO radar scheme and the associated data model. In Section 3, the proposed bistatic UCA MIMO root finding algorithm is described. Moreover, the simulation results of the proposed algorithm are presented and the performances are investigated in Section 4. Finally, Section 5 concludes the paper.

2. Signal Model

Consider a narrowband bistatic MIMO radar system with M_t-element transmit antennas and M_r-element receive antennas, both of which are UCAs with radii R_t and R_r, respectively. At the transmit site, M_t different narrow-band pulse waveforms are emitted simultaneously, which have identical bandwidth and center frequency, but are temporally orthogonal. In each receiver, the echoes are processed for all of the transmitted pulse waveforms. It is assumed that the Doppler frequencies have almost no effect on the orthogonality of the signals. Therefore, the variety of the phase within pulses caused by Doppler frequency can be ignored. There are P uncorrelated targets located at the same range cell. The directions of the pth target with respect to the normal direction of transmit array and receive array denoted by transmit angle θ_p and receive angle φ_p, respectively. The output of the entire matched filters at the receivers can be expressed as [10]

$$\mathbf{X}(n) = \mathbf{A}\mathbf{S}(n) + \mathbf{N}(n), \tag{1}$$

where $\mathbf{A} = [\mathbf{a}(\theta_1, \varphi_1), \ldots, \mathbf{a}(\theta_p, \varphi_p), \ldots, \mathbf{a}(\theta_P, \varphi_P)]$ is a matrix composed of the P steering vectors.

Cosider that

$$\mathbf{a}\left(\theta_p, \varphi_p\right) = \mathbf{a}_t\left(\theta_p\right) \otimes \mathbf{a}_r\left(\varphi_p\right) \tag{2}$$

is the Kronecker product of the transmit and the receive steering vectors for the pth target. $\mathbf{S}(n) = [s_1(n), \ldots, s_p(n), \ldots, s_P(n)]^T$, $s_p(n) = \gamma_p e^{j2\pi f_{dp} n/f_s}$ with γ_p and f_{dp} being the reflection coefficient depending on the target radar cross-section (RCS) and the Doppler frequency of the pth target, respectively. f_s is the pulse repeat frequency, $[\cdot]^T$ denotes the transpose, $\mathbf{N}(n)$ denotes a noise vector assumed to be independent and identically distributed, zero-mean complex Gaussian distribution and spatially white with covariance matrix $\sigma^2\mathbf{I}$, where σ^2 is noise variance and $\mathbf{I}$ is the identity matrix.

The array covariance matrix can be written as

$$\mathbf{R}_x = E\left\{\mathbf{X}(n)\,\mathbf{X}^H(n)\right\}, \tag{3}$$

where $[\cdot]^H$ denotes Hermitian transpose and $E\{\}$ denotes the statistical expectation.

The signals and the noises are assumed to be stationary, uncorrelated random processes; substituting $\mathbf{X}(n)$ from (1) into (3), we have

$$\begin{aligned}\mathbf{R}_x &= \mathbf{A}E\left\{\mathbf{S}(n)\,\mathbf{S}^H(n)\right\}\mathbf{A}^H + E\left\{\mathbf{N}(n)\,\mathbf{N}^H(n)\right\} \\ &= \mathbf{A}\mathbf{R}_s\mathbf{A}^H + \sigma^2\mathbf{I},\end{aligned} \tag{4}$$

where $\mathbf{R}_s = E\{\mathbf{S}(n)\mathbf{S}^H(n)\}$ is the source covariance matrix and σ^2 is the noise power at array sensors.

In practical situations, the exact array covariance matrix $\mathbf{R}_x$ is unavailable and its sample estimate

$$\widehat{\mathbf{R}}_x = \frac{1}{L}\sum_{l=1}^{L}\mathbf{X}(l)\,\mathbf{X}^H(l) \tag{5}$$

is used, where L is the number of snapshots.

The eigenvalue decomposition of $\widehat{\mathbf{R}}_x$ yields [10]

$$\widehat{\mathbf{R}}_x = \sum_{m=1}^{M_tM_r}\lambda_m\mathbf{e}_m\mathbf{e}_m^H, \tag{6}$$

where $\lambda_1 \geq \lambda_2 \geq \cdots \geq \lambda_{P+1} \geq \cdots \geq \lambda_{M_tM_r}$ are the eigenvalues of $\widehat{\mathbf{R}}_x$ and $\mathbf{e}_m$ $(m = 1 \cdots M_tM_r)$ are the corresponding eigenvectors. The matrices

$$\begin{aligned}\mathbf{E}_s &= \left[\mathbf{e}_1, \ldots, \mathbf{e}_P\right], \\ \mathbf{E}_n &= \left[\mathbf{e}_{P+1}, \ldots, \mathbf{e}_{M_tM_r}\right]\end{aligned} \tag{7}$$

are composed of the signal and the noise subspace eigenvectors of the array covariance matrix, respectively.

The MUSIC null-spectrum function is defined as [18]

$$f(\theta, \varphi) = \left\|\mathbf{E}_n^H\mathbf{a}(\theta, \varphi)\right\|^2 = \mathbf{a}^H(\theta, \varphi)\,\mathbf{E}_n\mathbf{E}_n^H\mathbf{a}(\theta, \varphi), \tag{8}$$

where $\|\cdot\|$ denotes the vector 2-norm. The spectral MUSIC technique estimates the signal DOAs from the minima of this function by means of a two-dimensional search over θ and φ.

3. Direction Finding for Bistatic MIMO Radar with UCA Configuration

The transmit and receive steering vectors of the UCAs can be denoted as [11–14]

$$\mathbf{a}_t(\theta) = \left[e^{jkR_t\cos(\theta-\beta_1)}\cdots e^{jkR_t\cos(\theta-\beta_m)}\cdots e^{jkR_t\cos(\theta-\beta_{M_t})}\right]^T, \tag{9a}$$

$$\mathbf{a}_r(\varphi) = \left[e^{jkR_r\cos(\varphi-\alpha_1)}\cdots e^{jkR_r\cos(\varphi-\alpha_m)}\cdots e^{jkR_r\cos(\varphi-\alpha_{M_r})}\right]^T, \tag{9b}$$

where $k = 2\pi/\lambda$, λ is wavelength and $\beta_m = 2m\pi/M_t$ and $\alpha_m = 2m\pi/M_r$ are the azimuth angles of the mth element of transmit and receive arrays, respectively.

By using the Jacobi-Anger expansion, we can mathematically express the mth element of the transmit steering vector as [10, 20]

$$\begin{aligned} e^{jkR_t\cos(\theta-\beta_m)} &= \sum_{n=-\infty}^{+\infty} j^n J_n(kR_t)\, e^{-jn\beta_m} e^{jn\theta} \\ &= \sum_{n=-\infty}^{+\infty} [\mathbf{F}_t]_{m,n} e^{jn\theta}, \end{aligned} \tag{10}$$

where

$$[\mathbf{F}_t]_{m,n} = j^n J_n(kR_t)\, e^{-jn\beta_m} \tag{11}$$

is the (m,n)th element of the sampling matrix $\mathbf{F}_t$ and $J_n(\cdot)$ is the Bessel function of the first kind of order n. Consequently, we can express the transmit steering vector by

$$\mathbf{a}_t(\theta) = \mathbf{F}_t \mathbf{d}_t(\theta). \tag{12}$$

The nth component of $\mathbf{d}_t(\theta)$ is

$$[\mathbf{d}_t(\theta)]_n = e^{jn\theta}. \tag{13}$$

Truncating $\mathbf{F}_t$ and $\mathbf{d}_t(\theta)$ from $-(N_t-1)/2$ to $(N_t-1)/2$ (suppose N_t is odd), the transmit steering vector can be approximated as

$$\mathbf{a}_t(\theta) \approx \widehat{\mathbf{F}}_t \widehat{\mathbf{d}}_t(\theta), \tag{14}$$

where $\widehat{\mathbf{F}}_t$ is an $M_t \times N_t$ matrix and

$$\widehat{\mathbf{d}}_t(\theta) = \left[e^{j(-(N_t-1)/2)\theta}\cdots e^{j((N_t-1)/2)\theta}\right]^T. \tag{15}$$

We can see that $\widehat{\mathbf{d}}_t(\theta)$ is a Vandermonde vector which depends on the steering angle θ and the parameter N_t. The accuracy of the approximation equation (14) increases with increasing the value of N_t.

The receive steering vector can be treated in the same way as the transmit steering vector; therefore, we obtain

$$\mathbf{a}_r(\varphi) \approx \widehat{\mathbf{F}}_r \widehat{\mathbf{d}}_r(\varphi), \tag{16}$$

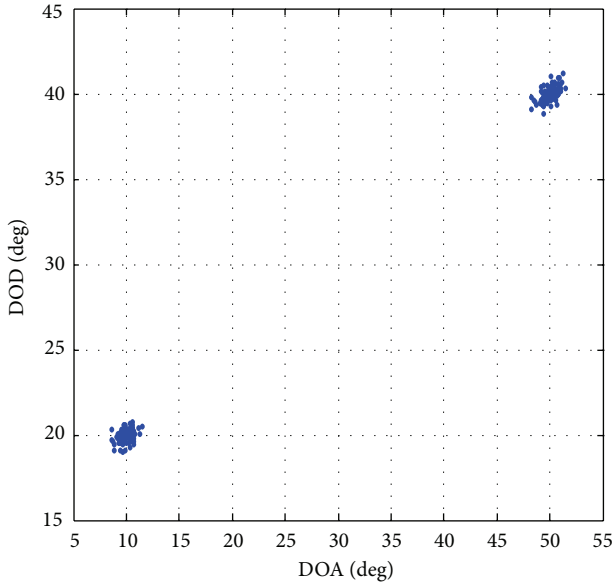

Figure 1: The angle estimation result of two targets.

where $\widehat{\mathbf{F}}_r$ is an $M_r \times N_r$ matrix and

$$\widehat{\mathbf{d}}_r(\varphi) = \left[e^{j(-(N_r-1/2))\varphi}\cdots e^{j((N_r-1)/2)\varphi}\right]^T. \tag{17}$$

We can also see that $\widehat{\mathbf{d}}_r(\varphi)$ is a Vandermonde vector which depends on the steering angle φ and the parameter N_r.

Using the notations $z_\theta = e^{j\theta}$ and $z_\varphi = e^{j\varphi}$, (15) and (17) can be written as

$$\widehat{\mathbf{d}}_t(z_\theta) = \left[z^{-(N_t-1)/2}\cdots z^{(N_t-1)/2}\right]^T, \tag{18a}$$

$$\widehat{\mathbf{d}}_r(z_\varphi) = \left[z^{-(N_r-1)/2}\cdots z^{(N_r-1)/2}\right]^T. \tag{18b}$$

Using (2) and (16), the null-spectrum function equation (8) can be written as

$$\begin{aligned} f(\theta,\varphi) &= [\mathbf{a}_t(\theta)\otimes\mathbf{a}_r(\varphi)]^H \mathbf{E}_n\mathbf{E}_n^H [\mathbf{a}_t(\theta)\otimes\mathbf{a}_r(\varphi)] \\ &= \mathbf{a}_t^H(\theta)\,\mathbf{A}_r^H\mathbf{E}_n\mathbf{E}_n^H\mathbf{A}_r\mathbf{a}_t(\theta) \\ &= \mathbf{a}_t^H(\theta)\left[\boldsymbol{\Omega}\mathbf{D}_r(z_\varphi)\right]^H\mathbf{E}_n\mathbf{E}_n^H\left[\boldsymbol{\Omega}\mathbf{D}_r(z_\varphi)\right]\mathbf{a}_t(\theta) \\ &= \mathbf{a}_t^H(\theta)\,\mathbf{D}_r^H(z_\varphi)\,\boldsymbol{\Omega}^H\mathbf{E}_n\mathbf{E}_n^H\boldsymbol{\Omega}\mathbf{D}_r(z_\varphi)\,\mathbf{a}_t(\theta) \\ &= \mathbf{a}_t^H(\theta)\,\mathbf{G}(z_\varphi)\,\mathbf{a}_t(\theta), \end{aligned} \tag{19}$$

where

$$A_r = \begin{bmatrix} \mathbf{a}_r(\varphi) & \mathbf{0}_{M_r\times 1} & \cdots & \mathbf{0}_{M_r\times 1} \\ \mathbf{0}_{M_r\times 1} & \mathbf{a}_r(\varphi) & \cdots & \mathbf{0}_{M_r\times 1} \\ \vdots & \vdots & \vdots & \vdots \\ \mathbf{0}_{M_r\times 1} & \mathbf{0}_{M_r\times 1} & \cdots & \mathbf{a}_r(\varphi) \end{bmatrix}_{M_rM_t\times M_t},$$

$$\mathbf{G}\left(z_\varphi\right) = \mathbf{D}_r^H\left(z_\varphi\right)\boldsymbol{\Omega}^H\mathbf{E}_n\mathbf{E}_n^H\boldsymbol{\Omega}\mathbf{D}_r\left(z_\varphi\right),$$

$$\boldsymbol{\Omega} = \begin{bmatrix} \widehat{\mathbf{F}}_r & \mathbf{0}_{M_r\times N_r} & \cdots & \mathbf{0}_{M_r\times N_r} \\ \mathbf{0}_{M_r\times N_r} & \widehat{\mathbf{F}}_r & \cdots & \mathbf{0}_{M_r\times N_r} \\ \vdots & \vdots & \vdots & \vdots \\ \mathbf{0}_{M_r\times N_r} & \mathbf{0}_{M_r\times N_r} & \cdots & \widehat{\mathbf{F}}_r \end{bmatrix}_{M_rM_t\times N_rM_t},$$

$$\mathbf{D}_r\left(z_\varphi\right) = \begin{bmatrix} \widehat{\mathbf{d}}_r\left(z_\varphi\right) & \mathbf{0}_{N_r\times 1} & \cdots & \mathbf{0}_{N_r\times 1} \\ \mathbf{0}_{N_r\times 1} & \widehat{\mathbf{d}}_r\left(z_\varphi\right) & \cdots & \mathbf{0}_{N_r\times 1} \\ \vdots & \vdots & \vdots & \vdots \\ \mathbf{0}_{N_r\times 1} & \mathbf{0}_{N_r\times 1} & \cdots & \widehat{\mathbf{d}}_r\left(z_\varphi\right) \end{bmatrix}_{N_rM_t\times M_t}. \tag{20}$$

Therefore, to solve the set in expression (19), we can first find z_φ satisfying [9]

$$\det\left[\mathbf{G}\left(z_\varphi\right)\right] = \det\left[\mathbf{D}_r^H\left(z_\varphi\right)\boldsymbol{\Omega}^H\mathbf{E}_n\mathbf{E}_n^H\boldsymbol{\Omega}\mathbf{D}_r\left(z_\varphi\right)\right] = 0. \tag{21}$$

Suppose $\mathbf{B} = \boldsymbol{\Omega}^H\mathbf{E}_n\mathbf{E}_n^H\boldsymbol{\Omega}$. Obviously matrix B is an $N_rM_t \times N_rM_t$ matrix that can be written as

$$\mathbf{B} = \begin{bmatrix} B_{11} & \cdots & B_{1m} & \cdots & B_{1M_t} \\ \vdots & \vdots & \vdots & \vdots & \vdots \\ B_{m1} & \cdots & B_{mm} & \cdots & B_{mM_t} \\ \vdots & \vdots & \vdots & \vdots & \vdots \\ B_{M_t1} & \cdots & B_{M_tm} & \cdots & B_{M_tM_t} \end{bmatrix}, \tag{22}$$

where B_{ij} is $N_r \times N_r$ matrix. Then we get

$$\mathbf{G}\left(z_\varphi\right) = \begin{bmatrix} \widehat{\mathbf{d}}_r^H\left(z_\varphi\right)B_{11}\widehat{\mathbf{d}}_r\left(z_\varphi\right) & \cdots & \widehat{\mathbf{d}}_r^H\left(z_\varphi\right)B_{1m}\widehat{\mathbf{d}}_r\left(z_\varphi\right) & \cdots & \widehat{\mathbf{d}}_r^H\left(z_\varphi\right)B_{1M_t}\widehat{\mathbf{d}}_r\left(z_\varphi\right) \\ \vdots & \vdots & \vdots & \vdots & \vdots \\ \widehat{\mathbf{d}}_r^H\left(z_\varphi\right)B_{m1}\widehat{\mathbf{d}}_r\left(z_\varphi\right) & \cdots & \widehat{\mathbf{d}}_r^H\left(z_\varphi\right)B_{mm}\widehat{\mathbf{d}}_r\left(z_\varphi\right) & \cdots & \widehat{\mathbf{d}}_r^H\left(z_\varphi\right)B_{mM_t}\widehat{\mathbf{d}}_r\left(z_\varphi\right) \\ \vdots & \vdots & \vdots & \vdots & \vdots \\ \widehat{\mathbf{d}}_r^H\left(z_\varphi\right)B_{M_t1}\widehat{\mathbf{d}}_r\left(z_\varphi\right) & \cdots & \widehat{\mathbf{d}}_r^H\left(z_\varphi\right)B_{M_tm}\widehat{\mathbf{d}}_r\left(z_\varphi\right) & \cdots & \widehat{\mathbf{d}}_r^H\left(z_\varphi\right)B_{M_tM_t}\widehat{\mathbf{d}}_r\left(z_\varphi\right) \end{bmatrix}$$

$$= \begin{bmatrix} \sum_{\forall p-q=i}\left[B_{11}\right]_{pq}z_\varphi^{-i} & \cdots & \sum_{\forall p-q=i}\left[B_{1m}\right]_{pq}z_\varphi^{-i} & \cdots & \sum_{\forall p-q=i}\left[B_{1M_t}\right]_{pq}z_\varphi^{-i} \\ \vdots & \vdots & \vdots & \vdots & \vdots \\ \sum_{\forall p-q=i}\left[B_{m1}\right]_{pq}z_\varphi^{-i} & \cdots & \sum_{\forall p-q=i}\left[B_{mm}\right]_{pq}z_\varphi^{-i} & \cdots & \sum_{\forall p-q=i}\left[B_{mM_t}\right]_{pq}z_\varphi^{-i} \\ \vdots & \vdots & \vdots & \vdots & \vdots \\ \sum_{\forall p-q=i}\left[B_{M_t1}\right]_{pq}z_\varphi^{-i} & \cdots & \sum_{\forall p-q=i}\left[B_{M_tm}\right]_{pq}z_\varphi^{-i} & \cdots & \sum_{\forall p-q=i}\left[B_{M_tM_t}\right]_{pq}z_\varphi^{-i} \end{bmatrix}. \tag{23}$$

The P roots $z_\varphi^{(p)}(p = 1\cdots P)$ inside and closest to the unitary circle of the polynomial $\det[\mathbf{G}(z_\varphi)]$ allow estimating the DOA angles given by $\widehat{\varphi}_p = \text{angle}(z_\varphi^{(p)})$ $(p = 1\cdots P)$. We can see that the computational complexity is burdensome because of the high degree of the polynomial. Here we use a fast root-MUSIC method [17] to reduce the computational complexity. The algorithm, no matter how large the degree of the polynomial is, only needs to calculate P roots (the number of targets).

By substituting the obtained roots $z_\varphi^{(p)}$ $(p = 1\cdots P)$ and using (14) in the expression (19), we constitute the following equation:

$$\begin{aligned} f\left(\theta,\widehat{\varphi}_p\right) &= \widehat{\mathbf{d}}_t^H(\theta)\,\widehat{\mathbf{F}}_t^H\mathbf{G}\left(z_\varphi^{(p)}\right)\widehat{\mathbf{F}}_t\widehat{\mathbf{d}}_t(\theta) \\ &= \widehat{\mathbf{d}}_t^H\left(z_\theta\right)\widehat{\mathbf{F}}_t^H\mathbf{G}\left(z_\varphi^{(p)}\right)\widehat{\mathbf{F}}_t\widehat{\mathbf{d}}_t\left(z_\theta\right) \\ &= \widehat{\mathbf{d}}_t^H\left(z_\theta\right)H\left(z_\varphi^{(p)}\right)\widehat{\mathbf{d}}_t\left(z_\theta\right), \end{aligned} \tag{24}$$

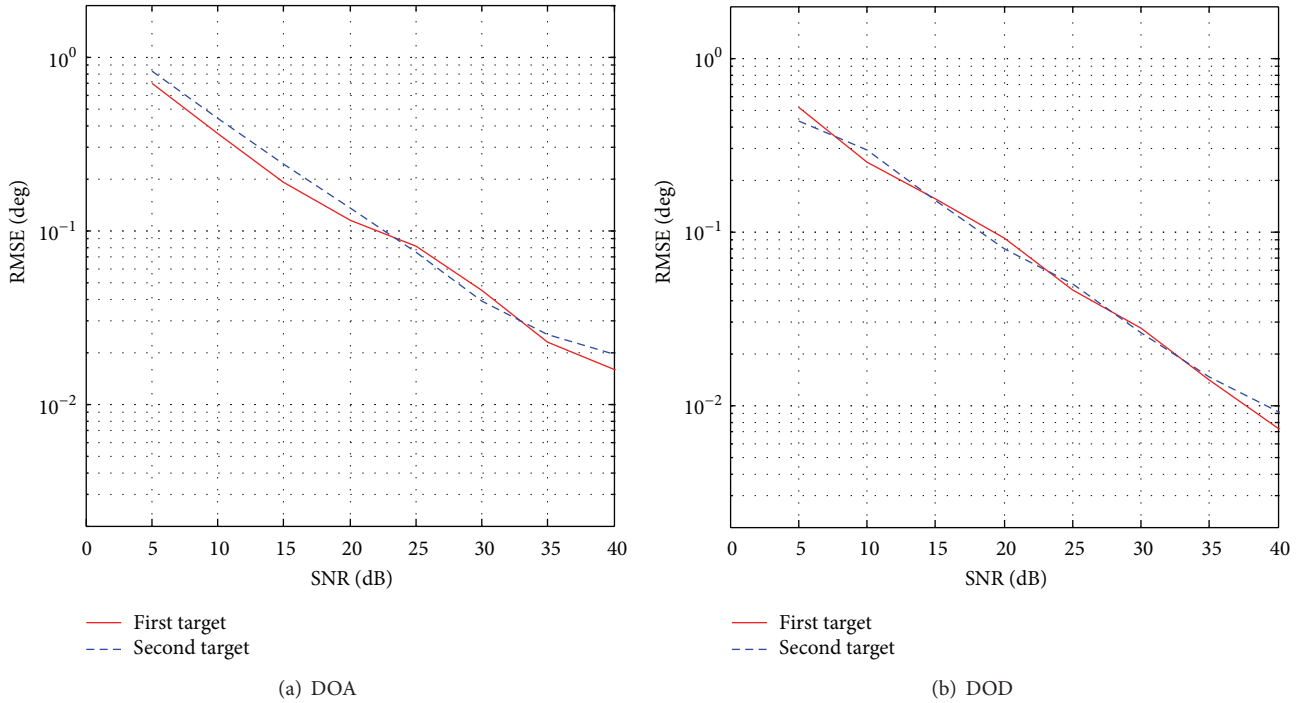

(a) DOA (b) DOD

Figure 2: RMSE in DOA and DOD estimation versus SNR.

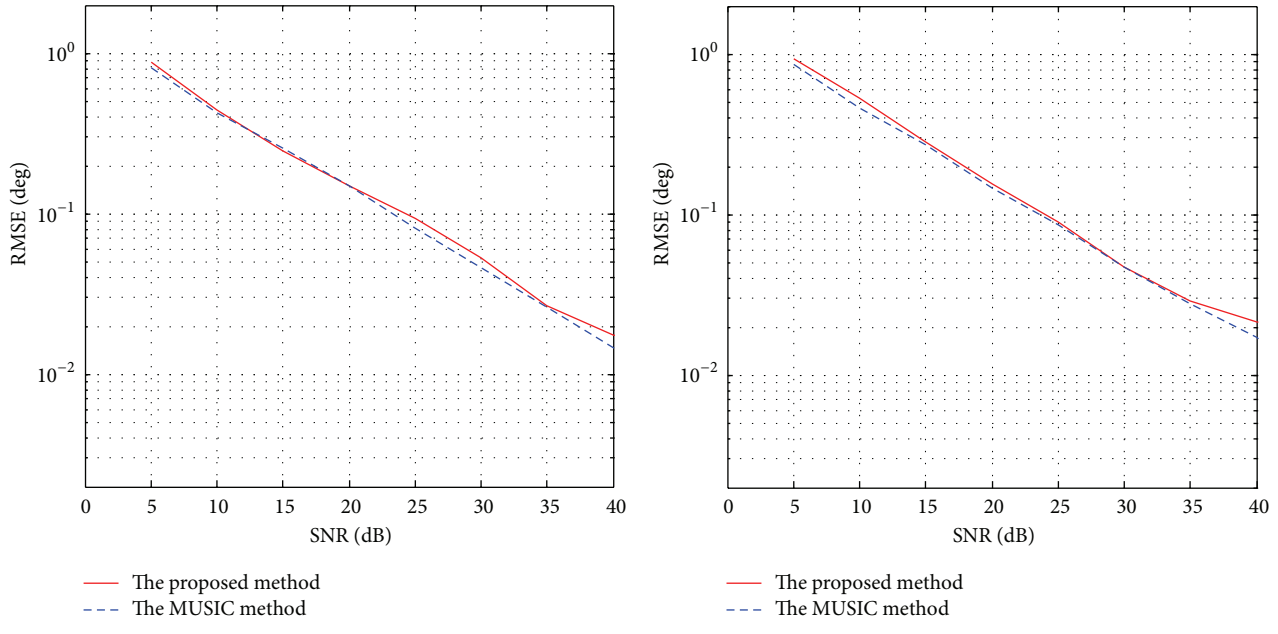

(a) The first target (b) The second target

Figure 3: Angle estimation RMSE versus SNR.

where $\mathbf{H}(z_{\varphi}^{(p)}) = \widehat{\mathbf{F}}_t^H \mathbf{G}(z_{\varphi}^{(p)}) \widehat{\mathbf{F}}_t$. We can again use the polynomial root technique to get the roots $z_{\varphi}^{(p)}$ with the polynomial (24) equal to zero. The correspondent DOD angle can be given by $\widehat{\varphi}_p = \text{angle}(z_{\varphi}^{(p)})$ $(p = 1 \cdots P)$. Note that the pairing is automatically obtained between the DOA and DOD angles, which avoid the traditional bistatic radar problem of synchronization.

4. Simulation Results

Here, we present simulation results showing the statistical performance of the proposed algorithm when using UCA configuration. Consider a narrowband bistatic MIMO radar system with 4 transmit antennas and 3 receive antennas; both are UCAs with radius equal to $\lambda/4$. For the simulations, the following settings have been used: two uncorrelated sources

impinging the arrays with equal powers from the angles $(\theta_1, \varphi_1) = (10^\circ, 20^\circ)$ and $(\theta_2, \varphi_2) = (50^\circ, 40^\circ)$, 256 snapshots, and 100 independent Monte Carlo trials. Figure 1 shows the angle estimation result of two targets for bistatic MIMO radar under the conditions SNR = 10 dB and $N_t = N_r = 11$. We can observe that the target directions are well localized and DOA and DOD are automatically paired.

With the same configuration of the simulation as before, Figure 2 shows the DOA and the DOD estimation versus signal noise ratio (SNR) by using the proposed polynomial root finding algorithm. We observe that the proposed algorithm has almost the same performance, no matter if the direction of the target is near or far away from the boresight. It is the advantage of the UCA configuration.

Finally, we compare angle estimation performance of MUSIC spectrum with the searching step 0.01° and polynomial rooting method with $N_t = N_r = 11$. The root mean squared error (RMSE) of the pth target direction estimation is defined as RMSE $= \sqrt{E(\widehat{\theta}_p - \theta_p)^2 + E(\widehat{\varphi}_p - \varphi_p)^2}$. Figure 3 demonstrates that the proposed polynomial rooting algorithm provides a similar angle estimation performance to the MUSIC spectral search method with the search interval 0.01 degree, but the MUSIC spectral search method is computationally expensive for such a fine grid search over the whole angle range.

5. Conclusion

In this paper, we have proposed a new technique to transform the steering vector of the UCA configuration into a steering vector with a Vandermonde structure in bistatic MIMO radar by using the Jacobi-Anger expansion. The two-step polynomial root finding algorithm has then been used to estimate DOA and DOD of the targets. The simulation results show that the proposed algorithm provides good performances in angle estimation. In addition, the proposed polynomial rooting angle estimation method avoids spectral search and reduces the computational complexity for bistatic MIMO radar with UCA configure.

Acknowledgments

This work was supported in part by the National Natural Science Foundation of China (61372136, 61172137, and 61271290) and in part by the Fundamental Research Funds for the Central Universities (K5051202005, and K5051302089).

References

[1] E. Fishler, A. Haimovich, R. S. Blum, L. J. Cimini Jr., D. Chizhik, and R. A. Valenzuela, "Spatial diversity in radars-models and detection performance," *IEEE Transactions on Signal Processing*, vol. 54, no. 3, pp. 823–838, 2006.

[2] L. Jian, P. Stoica, X. Luzhou et al., "On parameter identifiability of MIMO radar," *IEEE Signal Processing Letters*, vol. 14, no. 12, pp. 968–971, 2007.

[3] C. Duofang, C. Baixiao, and Q. Guodong, "Angle estimation using ESPRIT in MIMO radar," *Electronics Letters*, vol. 44, no. 12, pp. 770–771, 2008.

[4] J. Ming, L. Guisheng, and L. Jun, "Joint DOD and DOA estimation for bistatic MIMO radar," *Signal Processing*, vol. 89, no. 2, pp. 244–251, 2009.

[5] Q. Y. Yin, R. W. Newcomb, and L. H. Zou, "Estimating 2-D angles of arrival via two parallel linear arrays," in *Proceedings of the IEEE International Conference on Acoustics, Speech, and Signal Processing*, pp. 2803–2806, College Park, Md, USA, May 1989.

[6] N. Liu, L. R. Zhang, J. Zhang et al., "Direction finding of MIMO radar through ESPRIT and Kalman filter," *Electronics Letters*, vol. 45, no. 17, pp. 908–910, 2009.

[7] C. Yunhe, "Joint estimation of angle and Doppler frequency for bistatic MIMO radar," *Electronics Letters*, vol. 46, no. 2, pp. 170–172, 2010.

[8] R. Xie, Z. Liu, and Z.-J. Zhang, "DOA estimation for monostatic MIMO radar using polynomial rooting," *Signal Processing*, vol. 90, no. 12, pp. 3284–3288, 2010.

[9] M. L. Bencheikh, Y. Wang, and H. He, "Polynomial root finding technique for joint DOA DOD estimation in bistatic MIMO radar," *Signal Processing*, vol. 90, no. 9, pp. 2723–2730, 2010.

[10] Y. Cao, Z. Zhang, F. Dai et al., "Direction of arrival estimation for monostatic multiple-input multiple-output radar with arbitrary array structures," *IET Radar, Sonar & Navigation*, vol. 6, no. 7, pp. 679–686, 2012.

[11] A. H. Tewfik and W. Hong, "On the application of uniform linear array bearing estimation techniques to uniform circular arrays," *IEEE Transactions on Signal Processing*, vol. 40, no. 4, pp. 1008–1011, 1992.

[12] C. P. Mathews and M. D. Zoltowski, "Eigenstructure techniques for 2-D angle estimation with uniform circular arrays," *IEEE Transactions on Signal Processing*, vol. 42, no. 9, pp. 2395–2407, 1994.

[13] F. Belloni and V. Koivunen, "Beamspace transform for UCA: error analysis and bias reduction," *IEEE Transactions on Signal Processing*, vol. 54, no. 8, pp. 3078–3089, 2006.

[14] R. Goossens, H. Rogier, and S. Werbrouck, "UCA root-MUSIC with sparse uniform circular arrays," *IEEE Transactions on Signal Processing*, vol. 56, no. 8, pp. 4095–4099, 2008.

[15] B. D. Rao and K. V. S. Hari, "Performance analysis of root-MUSIC," *IEEE Transactions on Acoustics, Speech, and Signal Processing*, vol. 37, no. 12, pp. 1939–1949, 1989.

[16] B. Friedlander, "The root-MUSIC algorithm for direction finding with interpolated arrays," *Signal Processing*, vol. 30, no. 1, pp. 15–29, 1993.

[17] J. Zhuang, W. Li, and A. Manikas, "Fast root-MUSIC for arbitrary arrays," *Electronics Letters*, vol. 46, no. 2, pp. 174–176, 2010.

[18] F. Belloni, A. Richter, and V. Koivunen, "DoA estimation via manifold separation for arbitrary array structures," *IEEE Transactions on Signal Processing*, vol. 55, no. 10, pp. 4800–4810, 2007.

[19] M. Rubsamen and A. B. Gershman, "Direction-of-arrival estimation for nonuniform sensor arrays: from manifold separation to Fourier domain MUSIC methods," *IEEE Transactions on Signal Processing*, vol. 57, no. 2, pp. 588–599, 2009.

[20] M. A. Doron and E. Doron, "Wavefield modeling and array processing, part I—spatial sampling," *IEEE Transactions on Signal Processing*, vol. 42, no. 10, pp. 2549–2559, 1994.

Hindawi Publishing Corporation
International Journal of Antennas and Propagation
Volume 2013, Article ID 920639, 16 pages
http://dx.doi.org/10.1155/2013/920639

Research Article

Antenna Array for Passive Radar: Configuration Design and Adaptive Approaches to Disturbance Cancellation

Michelangelo Villano,[1] Fabiola Colone,[2] and Pierfrancesco Lombardo[2]

[1] *German Aerospace Center (DLR), Microwaves and Radar Institute, Oberpfaffenhofen, 82234 Wessling, Germany*
[2] *Department of Information Engineering, Electronics and Telecommunications (DIET), University of Rome "La Sapienza", Via Eudossiana 18, 00184 Rome, Italy*

Correspondence should be addressed to Fabiola Colone; fabiola.colone@diet.uniroma1.it

Received 5 April 2013; Accepted 4 September 2013

Academic Editor: Ulrich Nickel

We consider the selection of an antenna array configuration, composed of a small number of omnidirectional elements, to be exploited for passive radar sensors. Based on properly identified pattern characteristics and design criteria for practical applications, a suitable planar configuration is selected that allows both angular selectivity and direct signal attenuation. The selected configuration is further optimized in terms of sidelobe level by resorting to appropriate amplitude tapering. Moreover, three different approaches are investigated for antenna-based adaptive disturbance cancellation, and a comparative performance analysis is carried out. Simulation results show that an effective clutter suppression is obtained if the direct signal from the transmitter is attenuated by means of spatial adaptive cancellation, and the multipath echoes from stationary obstacles are removed by means of temporal adaptive cancellation. In particular, the approach based on the Sidelobe Canceller is shown to yield good performance while requiring a limited system complexity.

1. Introduction

Passive radar systems are specific variants of bistatic radar that exploit existing transmitters as "illuminators of opportunity". The main advantages of bistatic radar are that the receiver is far less vulnerable to electronic counter measures (ECM) and that bistatic operation has counter stealth properties. Moreover, passive radar systems have much lower cost, as they do not need a dedicated transmitter [1–3].

In spite of all these advantages, which make passive radar attractive for a broad range of applications, they must cope with the use of nonoptimized waveforms and with a strong direct signal from the transmitter of opportunity that typically operates in continuous wave (CW) mode. This strong disturbance must be appropriately cancelled, together with its reflections from stationary obstacles in the scene (clutter/multipath) to improve detection performance. Directive antennas, characterized by a high Front-to-Back Ratio (FBR), are usually employed to attenuate the direct signal. Its residuals are then typically removed by means of temporal adaptive clutter cancellation together with the clutter contribution [4–6]. However, the use of a directive antenna provides only a limited angular coverage for the radar surveillance and does not allow to cover a very wide air space region.

This drawback can be avoided by using an antenna array composed of a set of omnidirectional elements in the plane, in place of a dedicated directive surveillance antenna [7–9]. As long as the elements are properly spaced, a directive pattern may be synthesized by jointly processing the signals received at each element. This also allows the beam to be electronically steered in all directions or, better, a set of directional beams to be generated that globally cover the whole air space of interest. Obviously this would require the availability of multiple coherent receiving channels. However, in this case the same array might be used to collect the transmitted signal by synthesizing a beam pointed toward the transmitter of opportunity. This represents a viable solution if several dislocated illuminators of opportunity should be exploited.

To keep the system cost and its complexity low, proper array configurations should be designed and able to provide good performance using a limited number of elements [10]. In this paper, we describe effective criteria to identify a suitable antenna array configuration for passive radar. According to the proposed strategy, the array is designed so that it yields reasonable characteristics for the resulting antenna pattern (3 dB aperture, sidelobe level) while satisfying a few constraints that allow the 360° operation.

Furthermore, the considered planar array may be provided with spatial adaptivity, so that the clutter/multipath cancellation filter can benefit from space-time adaptivity.

The benefits of antenna-based spatial adaptivity have been shown in the literature with reference to different passive radar applications. A clear demonstration of potentiality of the spatial adaptivity is reported in [11] for a GSM-based passive radar for medium range surveillance, in [12] for an FM radio-based passive radar, and in [13] for a specific passive radar application in the HF frequency bandwidth. In [14], the space-time adaptive beamformer based on constrained least mean squares algorithm has been exploited. Even for the reference signal recovery, adaptive techniques can be used to protect the system against multipath contributions. For example, in [15] the joint exploitation of spatial and temporal degrees of freedom is considered to obtain a multipath-free version of the reference signal.

Therefore, in this paper, we investigate different techniques for antenna-based adaptive disturbance cancellation to be applied before the standard temporal cancellation filter. The comparative analysis allows to identify the main benefits of the different approaches and to select the most suitable space-time processing scheme. Specifically, the simulation results, obtained for an FM radio-based passive radar case, show that the approach based on the Sidelobe Canceller followed by the temporal extensive cancellation algorithm (ECA) [4] yields good performance while requiring a limited system complexity.

The paper is organized as follows. In Section 2, the array design strategy is described, and a suitable antenna array configuration is selected by trading off the achievable performance for the expected system complexity and cost. The selected array configuration is further optimized in Section 3 where a proper amplitude tapering strategy is adopted to control the sidelobe level of the resulting pattern. Section 4 briefly summarizes the considered techniques for antenna-based adaptive disturbance cancellation; moreover, an effective approach is introduced for the synthesis of the reference antenna beam that is exploited to collect the signal from the transmitter. The comparative performance analysis is presented in Section 5 where the results are reported for an FM radio-based passive radar scenario. Finally, our conclusions are drawn in Section 6.

2. Antenna Array Configuration Analysis

The first step of our work consists in identifying an appropriate configuration for the array of antennas that provides good performance using a limited number of elements (to keep the low cost characteristic). Specifically, we refer to 2-dimensional (planar) array configurations. A reasonable criterion to select a planar array configuration may involve the evaluation of some significant pattern parameters, such as the 3 dB aperture and the peak-to-side lobe ratio (PSLR). It is also reasonable to restrict the choice to those configurations, for which the expected (angle estimation) performance does not depend on the Direction of Arrival (DoA) of the signal. In particular, it is possible to refer to the estimation accuracy achievable by the Generalized Likelihood (GL) estimation.

2.1. GL DoA Estimation and Its Accuracy. Let us consider a planar array of N elements and let (x_i, y_i) and $g_i(\theta)$ be the coordinates and the azimuth pattern of the ith element, respectively, being θ the angle formed with the positive y-axis. Then, the target steering vector $\mathbf{s}_{\boldsymbol{\theta}}(\theta)$ can be written as

$$\mathbf{s}_{\boldsymbol{\theta}}(\theta) = \begin{bmatrix} g_1(\theta) \exp\left\{ j\frac{2\pi}{\lambda}\left(x_1 \sin\theta + y_1 \cos\theta\right)\right\} \\ \vdots \\ g_i(\theta) \exp\left\{ j\frac{2\pi}{\lambda}\left(x_i \sin\theta + y_i \cos\theta\right)\right\} \\ \vdots \\ g_N(\theta) \exp\left\{ j\frac{2\pi}{\lambda}\left(x_N \sin\theta + y_N \cos\theta\right)\right\} \end{bmatrix}, \quad (1)$$

where λ is the wavelength of the received signal.

The signals received at a given time by the elements of the array may be collected in an N-element column vector $\mathbf{x}$, called snapshot, and given by

$$\mathbf{x} = a\mathbf{s}_{\boldsymbol{\theta}}(\theta_T) + \mathbf{v}, \qquad \mathbf{v} = \begin{bmatrix} v_1 \\ \vdots \\ v_i \\ \vdots \\ v_N \end{bmatrix}, \quad (2)$$

where θ_T is the signal DoA, a is the complex amplitude of the received signal, which does not include the antenna gain, and $\mathbf{v}$ is the disturbance.

We assume for $\mathbf{x}$ a Gaussian distribution, whose expected value and covariance matrix are given by

$$\begin{aligned} \overline{\mathbf{x}} &= E\{\mathbf{x}\} = \gamma a \mathbf{s}_{\boldsymbol{\theta}}(\theta_T), \\ \gamma &= \begin{cases} 0, & \mathrm{Hp} \cdot \mathrm{H}_0 \,(\text{absence of target}) \\ 1, & \mathrm{Hp} \cdot \mathrm{H}_1 \,(\text{presence of target}), \end{cases} \\ \mathbf{M} &= E\left\{(\mathbf{x} - \overline{\mathbf{x}})(\mathbf{x} - \overline{\mathbf{x}})^H\right\} = \sigma_n^2 \mathbf{I}, \end{aligned} \quad (3)$$

respectively, where σ_n^2 is the noise variance and $\mathbf{v}^H$ denotes the Hermitian transpose of vector $\mathbf{v}$. The DoA θ_T of a monochromatic signal, whose complex amplitude a is unknown, may be estimated by maximizing the Generalized Likelihood, as in

$$\widehat{\theta}_T = \arg\min_{\theta} \left\| \mathbf{x} - \frac{\mathbf{s}_{\boldsymbol{\theta}}^H(\theta)\, \mathbf{x} \mathbf{s}_{\boldsymbol{\theta}}(\theta)}{\mathbf{s}_{\boldsymbol{\theta}}^H(\theta)\, \mathbf{s}_{\boldsymbol{\theta}}(\theta)} \right\|^2, \quad (4)$$

where the operators $\|\mathbf{v}\|$ denote the Euclidean norm of vector $\mathbf{v}$, while the notation $\arg\min_\theta f(\theta)$ denotes the value of θ for which $f(\theta)$ is minimum.

In particular, it can be shown that the resulting estimation accuracy is given by (see, e.g., [16])

$$\sigma_{\theta_T}(\theta_T) = \sqrt{E\left\{\left|\widehat{\theta}_T - \theta_T\right|^2\right\} - \left|E\left\{\widehat{\theta}_T - \theta_T\right\}\right|^2} = \left\{2\frac{|a|^2}{\sigma_n^2}\left[\left\|\dot{\mathbf{s}}_{\boldsymbol{\theta}}(\theta_T)\right\|^2 - \frac{\left|\dot{\mathbf{s}}_{\boldsymbol{\theta}}^H(\theta_T)\,\mathbf{s}_{\boldsymbol{\theta}}(\theta_T)\right|^2}{\left\|\mathbf{s}_{\boldsymbol{\theta}}(\theta_T)\right\|^2}\right]\right\}^{-1/2}, \tag{5}$$

where $\dot{\mathbf{s}}_{\boldsymbol{\theta}}(\theta_T)$ is the first-order derivative of $\mathbf{s}_{\boldsymbol{\theta}}(\theta_T)$ with respect to θ_T.

2.2. Omnidirectional Antennas and Symmetry Conditions. In case all the antennas are omnidirectional, for example,

$$g_i(\theta) = g, \quad i = 1 \cdots N, \tag{6}$$

the target steering vector $\mathbf{s}_{\boldsymbol{\theta}}(\theta)$ and its first-order derivative with respect to θ may be rewritten as

$$\mathbf{s}_{\boldsymbol{\theta}}(\theta) = \begin{bmatrix} g\exp\left\{j\frac{2\pi}{\lambda}(x_1\sin\theta + y_1\cos\theta)\right\} \\ \vdots \\ g\exp\left\{j\frac{2\pi}{\lambda}(x_i\sin\theta + y_i\cos\theta)\right\} \\ \vdots \\ g\exp\left\{j\frac{2\pi}{\lambda}(x_N\sin\theta + y_N\cos\theta)\right\} \end{bmatrix},$$

$$\dot{\mathbf{s}}_{\boldsymbol{\theta}}(\theta) = \begin{bmatrix} jg\frac{2\pi}{\lambda}(x_1\cos\theta - y_1\sin\theta)\exp\left\{j\frac{2\pi}{\lambda}(x_1\sin\theta + y_1\cos\theta)\right\} \\ \vdots \\ jg\frac{2\pi}{\lambda}(x_i\cos\theta - y_i\sin\theta)\exp\left\{j\frac{2\pi}{\lambda}(x_i\sin\theta + y_i\cos\theta)\right\} \\ \vdots \\ jg\frac{2\pi}{\lambda}(x_N\cos\theta - y_N\sin\theta)\exp\left\{j\frac{2\pi}{\lambda}(x_N\sin\theta + y_N\cos\theta)\right\} \end{bmatrix}, \tag{7}$$

respectively, and the quantities $\|\dot{\mathbf{s}}_{\boldsymbol{\theta}}(\theta_T)\|^2$, $|\dot{\mathbf{s}}_{\boldsymbol{\theta}}^H(\theta_T)\,\mathbf{s}_{\boldsymbol{\theta}}(\theta_T)|^2$, and $\|\mathbf{s}_{\boldsymbol{\theta}}(\theta_T)\|^2$ in (5) may be rewritten as follows:

$$\left\|\dot{\mathbf{s}}_{\boldsymbol{\theta}}(\theta_T)\right\|^2 = g^2\frac{4\pi^2}{\lambda^2}\sum_{i=1}^{N}(x_i\cos\theta_T - y_i\sin\theta_T)^2,$$

$$\left|\dot{\mathbf{s}}_{\boldsymbol{\theta}}^H(\theta_T)\,\mathbf{s}_{\boldsymbol{\theta}}(\theta_T)\right|^2 = g^4\frac{4\pi^2}{\lambda^2}\left[\sum_{i=1}^{N}(x_i\cos\theta_T - y_i\sin\theta_T)\right]^2,$$

$$\left\|\mathbf{s}_{\boldsymbol{\theta}}(\theta_T)\right\|^2 = g^2N. \tag{8}$$

Therefore, the estimation accuracy in the case of omnidirectional antennas is given by

$$\sigma_{\theta_T}(\theta_T) = \left[2\frac{|a|^2}{\sigma_n^2}g^2\frac{4\pi^2}{\lambda^2}f(\theta_T)\right]^{-1/2}, \tag{9}$$

where

$$f(\theta_T) = \sum_{i=1}^{N}(x_i\cos\theta_T - y_i\sin\theta_T)^2 - \frac{1}{N}\left[\sum_{i=1}^{N}(x_i\cos\theta_T - y_i\sin\theta_T)\right]^2. \tag{10}$$

If the following sets of symmetry conditions, namely,

$$\sum_{i=1}^{N}x_i = 0, \qquad \sum_{i=1}^{N}y_i = 0, \tag{11}$$

$$\sum_{i=1}^{N}x_i^2 = \sum_{i=1}^{N}y_i^2, \qquad \sum_{i=1}^{N}x_iy_i = 0 \tag{12}$$

hold, the expression of the estimation accuracy in (9) may be further simplified. In particular, the estimation accuracy is no longer dependent on the signal DoA.

Holding (11), in fact, (10) becomes

$$f(\theta_T) = \sum_{i=1}^{N}(x_i\cos\theta_T - y_i\sin\theta_T)^2. \tag{13}$$

Then, $f(\theta_T)$ can be expanded and, holding (12), simplified as follows:

$$\begin{aligned} f(\theta_T) &= \sum_{i=1}^{N} (x_i \cos\theta_T - y_i \sin\theta_T)^2 \\ &= \cos^2\theta_T \sum_{i=1}^{N} x_i^2 + \sin^2\theta_T \sum_{i=1}^{N} y_i^2 \\ &\quad - 2\cos\theta_T \sin\theta_T \sum_{i=1}^{N} x_i y_i \\ &= \left(\cos^2\theta_T + \sin^2\theta_T\right) \sum_{i=1}^{N} x_i^2 \\ &= \sum_{i=1}^{N} x_i^2 = \sum_{i=1}^{N} y_i^2 = \frac{1}{2} \sum_{i=1}^{N} \left(x_i^2 + y_i^2\right) = \frac{1}{2} \sum_{i=1}^{N} R_i^2, \end{aligned} \tag{14}$$

where R_i is the Euclidean distance of the ith element from the origin of the reference system.

2.3. Symmetric Configurations. Those configurations for which the symmetry conditions (11)-(12) hold, are from now on referred to as symmetric configurations. We are indeed interested in these configurations because the considered application does not require specific directions to be preferred.

The next step of our configuration analysis, therefore, consists in identifying some symmetric configurations, characterized by a relatively small number of elements. We first observe that the two-element arrays cannot jointly satisfy (11) and (12). On the other hand, the number N of elements is upper-limited to 10 in order to make the system both compact and low-cost.

Let us denote by R the maximum distance of an element of the array from the origin of the reference system or, equivalently, the radius of the smallest circle containing all the array elements.

It is possible to list different classes of symmetric configurations (in brackets the number of elements required to form such a configuration), namely,

(i) *circular configurations without central element* ($N \geq 3$), where N elements are uniformly arranged on the circumference of a circle of radius R, centered at the origin of the reference system;

(ii) *circular configurations with central element* ($N \geq 4$), where $(N-1)$ elements are uniformly arranged on the circumference of a circle of radius R, and one element is located in the center of such a circle;

(iii) *triangular configurations without central element* ($N = 3k$), where N elements are uniformly arranged on the edges of an equilateral triangle, inscribed in a circle of radius R. The trivial case $k = 1$ is not considered, as it belongs to the class of circular configurations without central element;

(iv) *triangular configurations with central element* ($N = 3k+1$), where $(N-1)$ elements are uniformly arranged on the edges of an equilateral triangle, inscribed in a circle of radius R, and one element is located in the center of such a circle. The trivial case $k = 1$ is not considered, as it belongs to the class of circular configurations with central element;

(v) *squared configurations without central element* ($N = 4k$), where N elements are uniformly arranged on the edges of a square, inscribed in a circle of radius R.The trivial case $k = 1$ is not considered, as it belongs to the class of circular configurations without central element;

(vi) *squared configurations with central element* ($N = 4k+1$), where $(N-1)$ elements are uniformly arranged on the edges of a square, inscribed in a circle of radius R, and one element is located in the center of such a circle. The trivial case $k = 1$ is not considered, as it belongs to the class of circular configurations with central element;

(vii) *Y configurations* ($N = 3k$, $N = 3k+1$), where the elements are uniformly arranged on the radii joining the vertices of an equilateral triangle, inscribed in a circle of radius R, to the center of the circle itself. The trivial case $k = 1$ is not considered, as it belongs to the first two classes of configurations;

(viii) *X configurations* ($N = 4k$, $N = 4k+1$), where the elements are uniformly arranged on the radii joining the vertices of a square, inscribed in a circle of radius R, to the center of the circle itself. The trivial case $k = 1$ is not considered, as it belongs to the first two classes of configurations.

In Table 1, the symmetric configurations belonging to the above mentioned classes are represented for different numbers N of antenna elements. Moreover, for each class, a marker plot is defined that will be used in the following figures (see last row of Table 1).

While our study is focused on planar array configurations, we should mention that alternative solutions could be considered based on combinations of three (or more) linear arrays covering adjacent 120° (or less) sectors to provide the 360° operation. However, such choice would yield a number of drawbacks that should be taken into account for the considered application. In particular,

(i) the resulting system would be a combination of three (or more) separate systems that need to be synchronized and disciplined to manage possible common detections performed in adjacent/overlapped angular sectors;

(ii) the resulting performance would be a function of the target DoA because each linear array has characteristics that change with the pointing angle (e.g., the 3 dB aperture). In this regard, we recall that the symmetric array configurations selected in our study guarantee the estimation accuracy to be independent of the target DoA so that the same performance could be in principle obtained over the 360° coverage;

Table 1: Symmetric configurations belonging to the different classes for $N < 10$.

	Circle without central element	Circle with central element	Triangle without central element	Triangle with central element	Square without central element	Square with central element	Y	X
$N = 3$	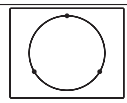							
$N = 4$	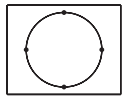	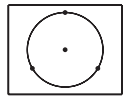						
$N = 5$	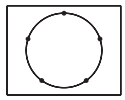	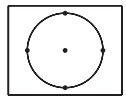						
$N = 6$	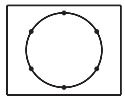	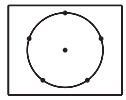	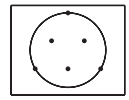				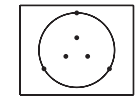	
$N = 7$	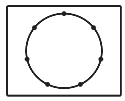	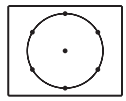		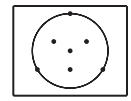			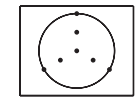	
$N = 8$	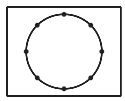	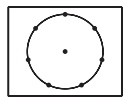			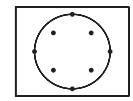			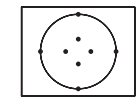
$N = 9$	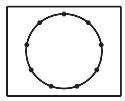	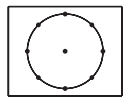	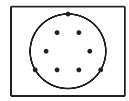			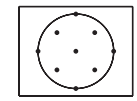	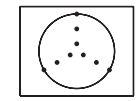	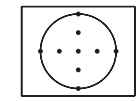

(iii) the problem discussed at point (i) is exacerbated when each array suffers of severe angular ambiguities; to reduce this effect directive antenna elements should be employed to build up each array (e.g., Yagi or Log Periodic antennas could be adopted in the FM radio band). However, this would stress the effect described in (ii). Moreover, using this approach, the overall system would be bulkier and characterized by a much higher cost.

For the above reasons, the symmetric planar array configurations sketched in Table 1 have been preferred and their characteristics are compared in the following subsection with the aim to identify the most suitable solution for the considered application.

2.4. Pattern Characteristics and Array Configuration Selection. The selection of the most appropriate configuration for passive radar applications involves the choice of the number N of antenna elements, the identification of its shape, and the determination of the array radius R.

So far we have established the conditions for which the DoA estimation accuracy is not dependent on the DoA itself and identified some configurations that satisfy these conditions. In the present subsection, we deal with the selection of a suitable configuration among different symmetric ones.

First of all, it is of interest to highlight the relationship between the GL DoA estimation, as defined in (4), and the array pattern of the configuration. Expanding the expression of the estimated DoA in (4) as

$$\begin{aligned}
\widehat{\theta}_T &= \arg\min_{\theta} \left\| \mathbf{x} - \frac{\mathbf{s}_{\boldsymbol{\theta}}^H(\theta)\,\mathbf{x}\mathbf{s}_{\boldsymbol{\theta}}(\theta)}{\mathbf{s}_{\boldsymbol{\theta}}^H(\theta)\,\mathbf{s}_{\boldsymbol{\theta}}(\theta)} \right\|^2 \\
&= \arg\min_{\theta} \left\{ \|\mathbf{x}\|^2 + \frac{\left\|\mathbf{s}_{\boldsymbol{\theta}}^H(\theta)\,\mathbf{x}\mathbf{s}_{\boldsymbol{\theta}}(\theta)\right\|^2}{\left\|\mathbf{s}_{\boldsymbol{\theta}}(\theta)\right\|^4} - \mathbf{x}^H \frac{\mathbf{s}_{\boldsymbol{\theta}}^H(\theta)\,\mathbf{x}\mathbf{s}_{\boldsymbol{\theta}}(\theta)}{\left\|\mathbf{s}_{\boldsymbol{\theta}}(\theta)\right\|^2} \right. \\
&\qquad \left. - \left(\frac{\mathbf{s}_{\boldsymbol{\theta}}^H(\theta)\,\mathbf{x}\mathbf{s}_{\theta}(\theta)}{\left\|\mathbf{s}_{\boldsymbol{\theta}}(\theta)\right\|^2} \right)^H \mathbf{x} \right\} \\
&= \arg\min_{\theta} \left\{ \|\mathbf{x}\|^2 + \frac{\left|\mathbf{s}_{\boldsymbol{\theta}}^H(\theta)\,\mathbf{x}\right|^2}{\left\|\mathbf{s}_{\boldsymbol{\theta}}(\theta)\right\|^2} - \frac{\left|\mathbf{s}_{\boldsymbol{\theta}}^H(\theta)\,\mathbf{x}\right|^2}{\left\|\mathbf{s}_{\boldsymbol{\theta}}(\theta)\right\|^2} - \frac{\left|\mathbf{s}_{\boldsymbol{\theta}}^H(\theta)\,\mathbf{x}\right|^2}{\left\|\mathbf{s}_{\boldsymbol{\theta}}(\theta)\right\|^2} \right\} \\
&= \arg\max_{\theta} \left|\mathbf{s}_{\boldsymbol{\theta}}^H(\theta)\,\mathbf{x}\right|^2,
\end{aligned} \tag{15}$$

it is possible to better understand what GL estimation means in the specific case of symmetric configurations; for each direction θ, the signals received by the N antennas are properly phase-shifted and summed; then the estimated DoA

is that for which the square modulus of such a sum is maximum. In other words, in this specific case, the GL DoA estimation consists in synthesizing infinite beams, pointed to all the directions, being the output of the estimate of the direction, for which the intensity of the signal received by the corresponding synthesized beam is maximum.

The GL estimation accuracy is therefore directly related to the array pattern characteristics, and a suitable configuration may be selected among several ones by evaluating the pattern characteristics themselves. It would not be appropriate to select the configuration for which the estimation accuracy, as defined in (5) or (9), is maximum, because such expression is significant only in the absence of ambiguities, namely, when grating lobes do not occur. A parameter related to the presence/absence of grating lobes, such as the PSLR, has therefore to be considered together with the estimation accuracy. Moreover, since this latter parameter is directly related to the pattern main lobe width, the 3 dB aperture may be considered in place of the accuracy, which leads us to consider two parameters characteristics of the antenna array pattern.

The 3 dB aperture and the PSLR have been plotted in Figure 1 as a function of the ratio R/λ of the array radius R to the wavelength of the received signal λ, so that a visual comparison can be performed. Specifically, Figures 1(a)–1(g) are obtained by progressively increasing the number of array elements from $N = 3$ to $N = 9$ and reporting, for each case, only the applicable configuration classes. The adopted markers are described in Table 1. As both the considered pattern parameters vary with the pointing direction, the worst case is reported, that is, the maximum 3 dB aperture and the minimum PSLR.

A careful observation of the plots in Figure 1 shows that it is not possible to synthesize array patterns characterized by both a narrow beamwidth and a satisfactory PSLR by using less than $N = 8$ elements. At the same time, the introduction of a ninth element does not lead to a significant improvement of the pattern characteristics. We also notice that the choice of $N = 8$ antenna elements allows the exploitation of commercial low-cost components to build up the multichannel radar receiver. Among the 8-element configuration, the circular configuration with central element, represented in Figure 2, is particularly attractive when the radius R of the planar array is selected to be equal to 0.44 λ, as the resulting pattern is characterized by both a narrow beamwidth and a reasonable PSLR, namely, 13 dB.

When the sources of radar transmission are FM radio stations, being the wavelength of the signal comprised between $\lambda_{\min} = 2.78$ m (108 MHz) and $\lambda_{\max} = 3.41$ m (88 MHz), the radius of the array has to be chosen as a compromise value, with special attention to $\lambda_{\min}$.

As a final remark, we notice that the previous analysis of the pattern characteristics has been conducted by assuming that there is no coupling between the array elements. In practice, such coupling effect exists and might significantly modify the resulting antenna pattern. Moreover, it is expected to become more severe as the array radius, and consequently the elements spacing, decreases. Nevertheless, the criteria adopted to identify a suitable antenna array configuration still hold; therefore, the proposed design strategy can still be applied against a more realistic model of the received signal to include the coupling effect as well as its possible compensation according to proper models. Finally, we should mention that, despite the symmetry of the considered array configurations, the coupling effect between different pairs of neighboring elements can be different [7]; however, this is due to nonidealities of array elements, minor errors in array geometry, and nearby obstacles that cannot be taken into account at the design stage but should be measured and compensated for after its assembling.

3. Side Lobe Control by Central Element Tapering

It is well known that it is generally possible to synthesize an array pattern with a higher PSLR by applying appropriate tapering to the single array elements. In the general case, the application of a taper function intrinsically destroys the uniform angular performance. Special considerations apply with reference to the selected configuration, which is made up by eight elements, seven of which are uniformly distributed over a circumference and one of which is located in the center of the same circumference. In fact, in this case, there is a simple way to apply something similar to a taper function by weighting differently the array central element and the circle of seven elements. Specifically, it is of interest to determine whether a higher PSLR may be obtained, by properly tapering only the central element.

By letting the taper of the central element α vary over a large enough interval, being unitary the tapers of all the other elements, the PSLR has been evaluated and plotted in Figure 3 as a function of α. The value of taper which maximizes the PSLR is $\alpha = 1.98$. The PSLR of the synthesized pattern is now greater than 20 dB (see Figure 4), while there is only a slight broadening of the antenna pattern main lobe (the 3 dB beamwidth is about 4° broader than that obtained without tapering). This tapered configuration is especially effective when used for passive radar, since it provides up to 7 dB improvement in the direct signal rejection, when the main beam is not steered 180° away from the transmitter of opportunity.

4. Adaptive Disturbance Cancellation Techniques

As the received power of the direct signal is usually many tens of dBs greater than the power received from a target echo, even using amplitude tapering, the direct signal attenuation might not be sufficient, and an adaptive temporal cancellation is typically used to remove the residual direct signal and the clutter, in order to provide the desired detection performance. The adaptive temporal cancellation is based on the principle that in the passive coherent location (PCL) environment, the disturbance includes the direct signal from the bistatic transmitter and multipath replicas of the direct signal, generated by its reflection from stationary obstacles, which are generally referred to as clutters. In contrast, the useful signal

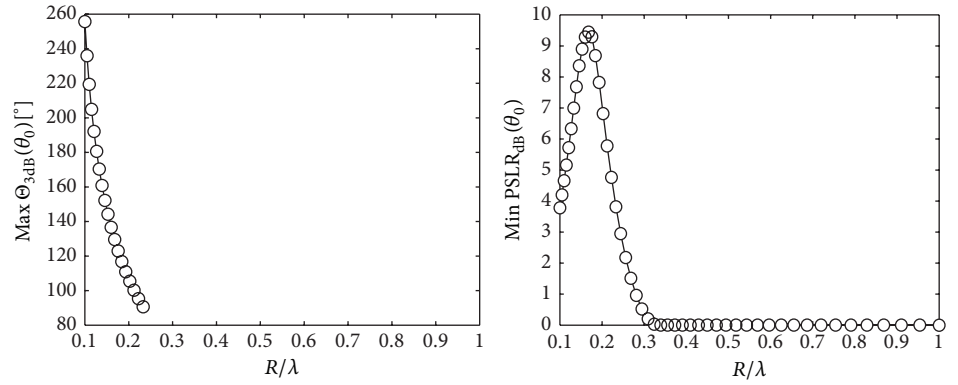

(a)

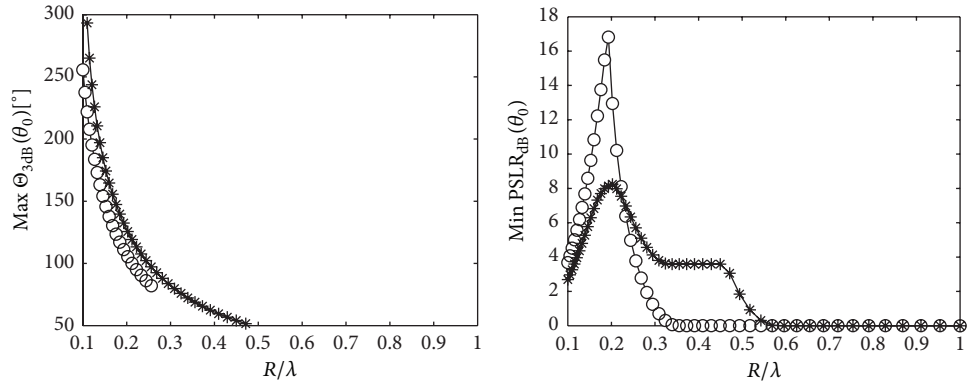

(b)

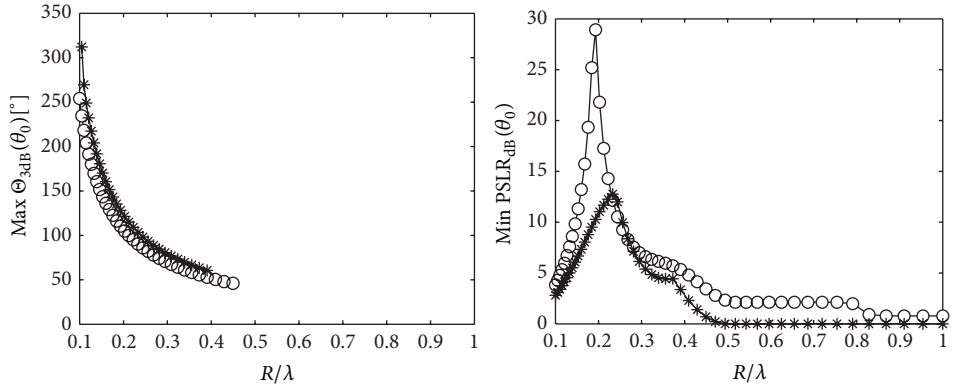

(c)

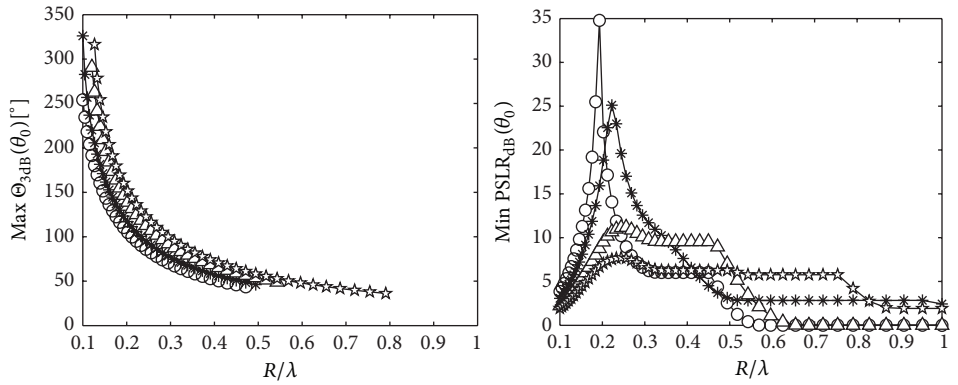

(d)

Figure 1: Continued.

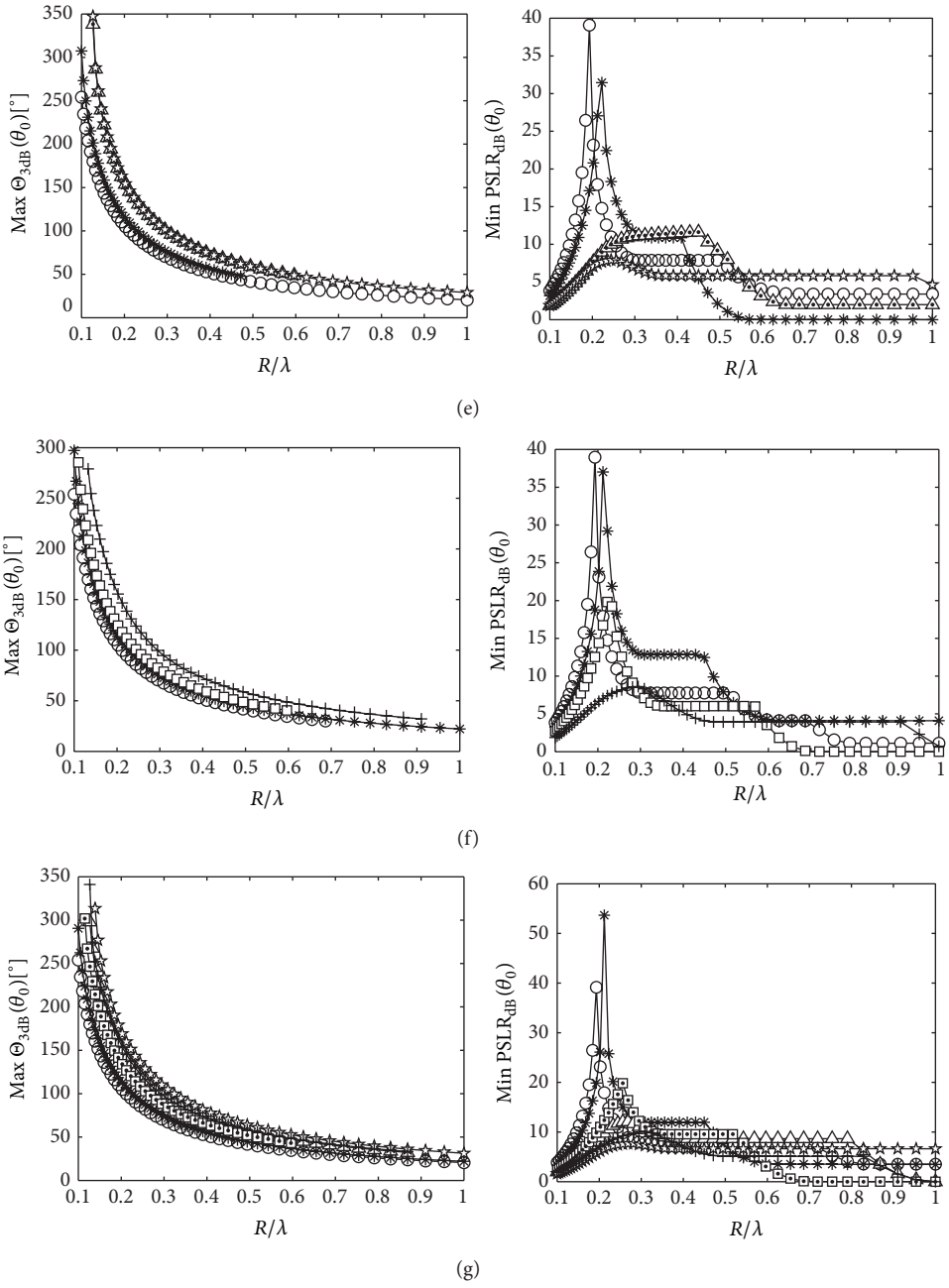

FIGURE 1: 3 dB aperture (left) and PSLR (right) for the configurations of Table 1: (a) 3-element configurations, (b) 4-element configurations, (c) 5-element configuration, (d) 6-element configurations, (e) 7-element configurations, (f) 8-element configurations, and (g) 9-element configurations. The legend is given in the lower row of Table 1.

is a delayed replica of the transmitted signal as well, but it is Doppler-shifted. Therefore, allowing an adaptive temporal filter to cancel only the zero Doppler echoes allows to remove the direct signal and its multipaths, without removing the target echo [4–6].

In the case where the direct signal is especially strong (e.g., when the passive radar receiver is very close to the transmitter of opportunity), the use of the temporal adaptivity following the antenna sidelobe attenuation of the direct signal might still be unsatisfactory. In this case spatially adaptive techniques may be considered to reject the disturbance, leading to an increased detection performance.

Antenna-based adaptive cancellation techniques provide rejection of the disturbance by means of adaptive beamforming. An estimate of the disturbance covariance matrix $\mathbf{M}$ is required to properly weight the received signals. Three approaches to adaptive cancellation are considered and discussed in the following three subsections, while in the last subsection the synthesis of the reference beam for the adaptive temporal filter is dealt with.

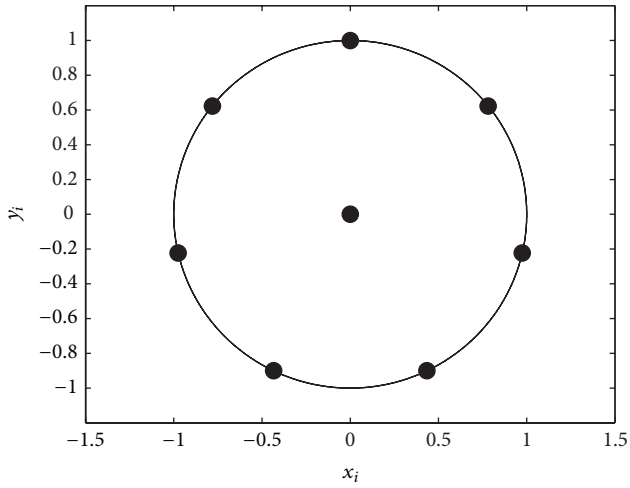

Figure 2: Circular configuration with central element for $N = 8$.

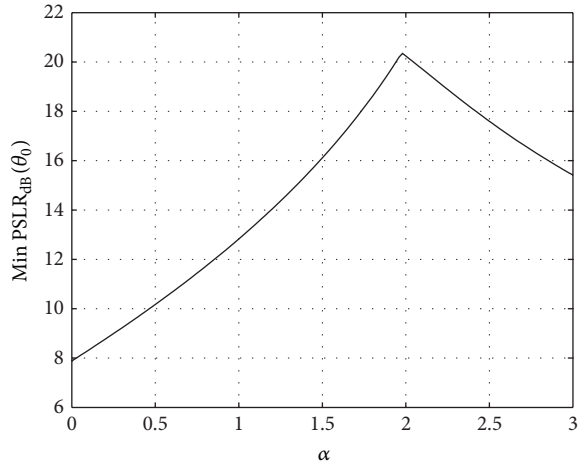

Figure 3: Trend of the PSLR as a function of the taper α for the configuration of Figure 2.

4.1. Optimum Filter. In case the disturbance covariance matrix $\mathbf{M}$ is known, the optimum weights vector, that leads to the maximum detection probability for a given false alarm rate, is given by [17]

$$\mathbf{w}^H(\theta_0) = \mathbf{s}_{\boldsymbol{\theta}}^H(\theta_0)\,\mathbf{M}^{-1}, \tag{16}$$

where θ_0 is the direction towards which the beam is pointed.

As an example, in Figure 5 (solid line), the array pattern obtained by weighting the signals received by the antennas of the selected configuration according to (16), for $\theta_0 = 120^\circ$, is represented, assuming that the disturbance covariance matrix $\mathbf{M}$, but for a multiplicative constant, is given by

$$\mathbf{M} = \mathbf{I} + \text{INR}_1\mathbf{s}_{\boldsymbol{\theta}}(\theta_{I1})\,\mathbf{s}_{\boldsymbol{\theta}}^H(\theta_{I1}) + \text{INR}_2\mathbf{s}_{\boldsymbol{\theta}}(\theta_{I2})\,\mathbf{s}_{\boldsymbol{\theta}}^H(\theta_{I2}), \tag{17}$$

where $\mathbf{I}$ is the identity matrix, θ_{I1} and θ_{I2} are the DoAs of two independent narrow-band interfering signals, and INR_1 and INR_2 represent the signal-to-noise ratios of the interfering signals ($\theta_{I1} = 0^\circ$, $\theta_{I2} = 70^\circ$, $\text{INR}_1 = 30$ dB, and $\text{INR}_2 = 10$ dB). The three components of the modeled disturbance covariance matrix represent the thermal noise, the direct signal, and a multipath replica of it. As it is apparent, the array pattern strongly attenuates the signals coming from the DoAs of both the direct signal and its multipath replica.

In practical applications, the covariance matrix $\mathbf{M}$ is replaced with its estimated version obtained from the received data, which include both the disturbance and the useful signal. This is quite appropriate in the PCL case given

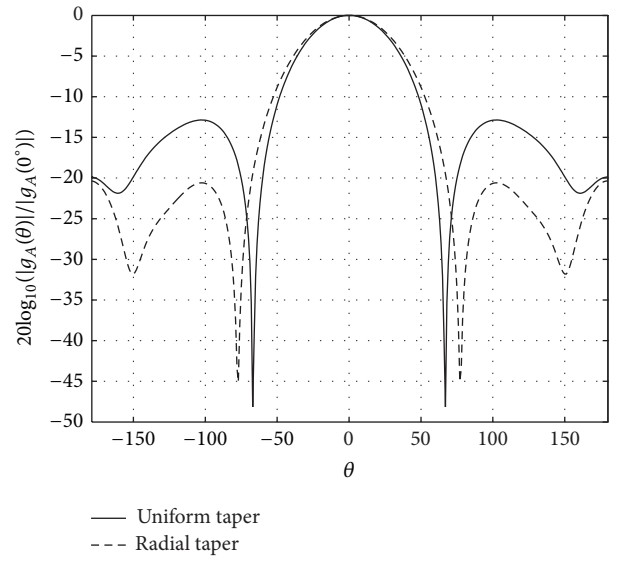

Figure 4: Array pattern with and without central element tapering for the configuration of Figure 2.

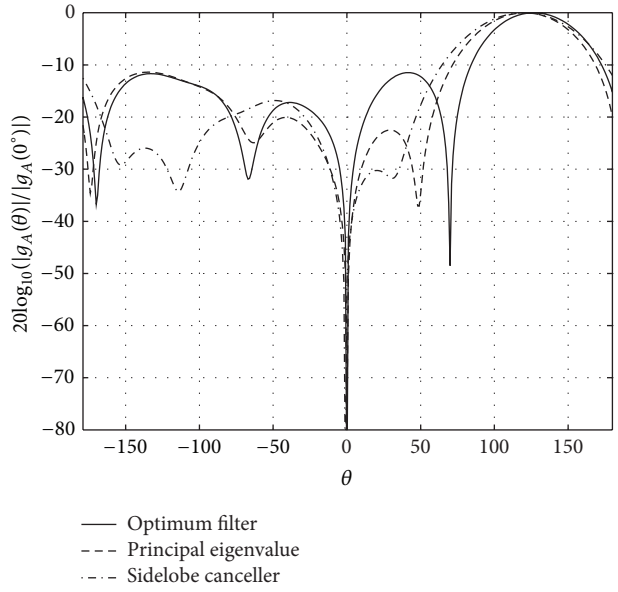

Figure 5: Examples of adaptive array patterns obtained by exploiting the optimum filter, the principal eigenvalue approach, and the Sidelobe Canceller for the case of two independent narrow-band interfering signals.

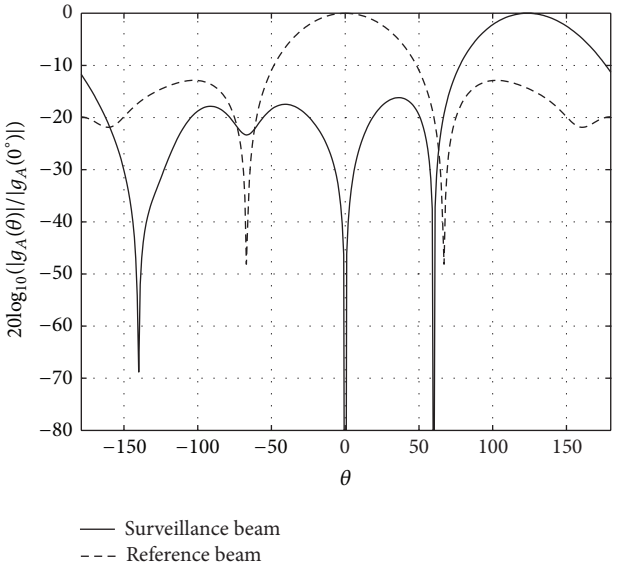

Figure 6: Example of surveillance beam and reference beam orthogonal to the surveillance one.

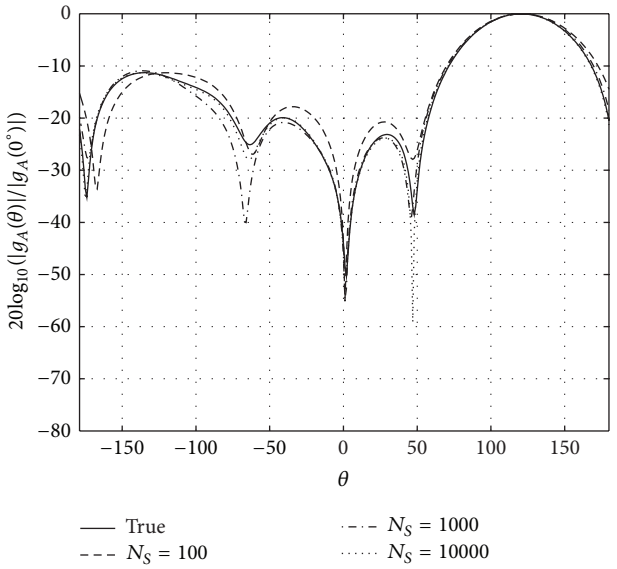

Figure 7: Pattern obtained by using the true and the estimated covariance matrix using $N_S = 100$, $N_S = 1000$, and $N_S = 10000$ for the case of a single narrow-band interfering signal.

that the level of both the direct signal and its multipath reflections is well above that of the useful signal. After combining the received signals according to (16), an adaptive temporal cancellation might be performed only to cancel disturbance residuals not adequately suppressed by the spatial adaptive filter. Then, the standard 2D (range-Doppler) cross-correlation function (2D-CCF) is evaluated, and a proper constant false alarm rate (CFAR) threshold is applied to obtain a detection map.

Notice that, when applying the optimum filter in the presence of a strong multipath reflection from a given direction,

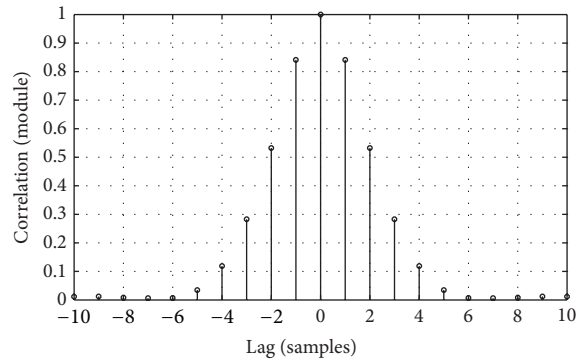

Figure 8: Example of autocorrelation function of an FM signal.

a null is imposed in the synthesized adaptive pattern at this direction. This also cancels all target echoes coming from the same DoA.

4.2. Principal Eigenvalue Approach. A way to circumvent the weakness of the optimum filter for targets at the same DoA of strong multipaths is to reduce the number of degrees of freedom (d.o.f.) available to the spatial adaptivity, so that only a single null can be imposed by the adaptive spatial filter. Since the direct signal is by far the strongest component of the overall disturbance, it is obvious that its effect dominates the spatial covariance matrix and specifically determines its principal eigenvector $\mathbf{q}_{\max}$. Therefore, by estimating only the principal eigenvector of the spatial disturbance covariance matrix, it is possible to strongly attenuate the direct signal, by projecting the target steering vector $\mathbf{s}_{\boldsymbol{\theta}}(\theta)$ on the subspace orthogonal to such eigenvector. The resulting weights vector is given by

$$\mathbf{w}_{\mathrm{PE}}^{H}(\theta_0) = \mathbf{s}_{\boldsymbol{\theta}}^{H}(\theta_0)\left(\mathbf{I} - \mathbf{q}_{\max}\mathbf{q}_{\max}^{H}\right). \tag{18}$$

Figure 5 (dashed line) shows the array pattern obtained by weighting the signals received by the antennas of the selected configuration according to (18), for $\theta_0 = 120^{\circ}$, assuming the same disturbance covariance matrix of the previous example. In this case, the array pattern strongly attenuates only the signals coming from the DoA of the direct signal, so that the clutter contributions have to be cancelled by the adaptive temporal filter. Finally, the 2D-CCF is evaluated, and the CFAR detection map is built.

4.3. Side Lobe Canceller (SLC). In case the disturbance is characterized by a single narrow-band interference, the array pattern obtained by using the optimum filter can be interpreted as the difference of a quiescent beam and a retrodirective beam, pointed in the direction of the disturbance. In particular, both beams are obtained by exploiting all the elements of the array.

A system based on the retrodirective beam, but at the same time characterized by a smaller number of d.o.f., can be obtained by resorting to the sidelobe canceller (SLC) concept [17], which, for the specific array configuration considered, can be exploited by using seven out of the eight elements of

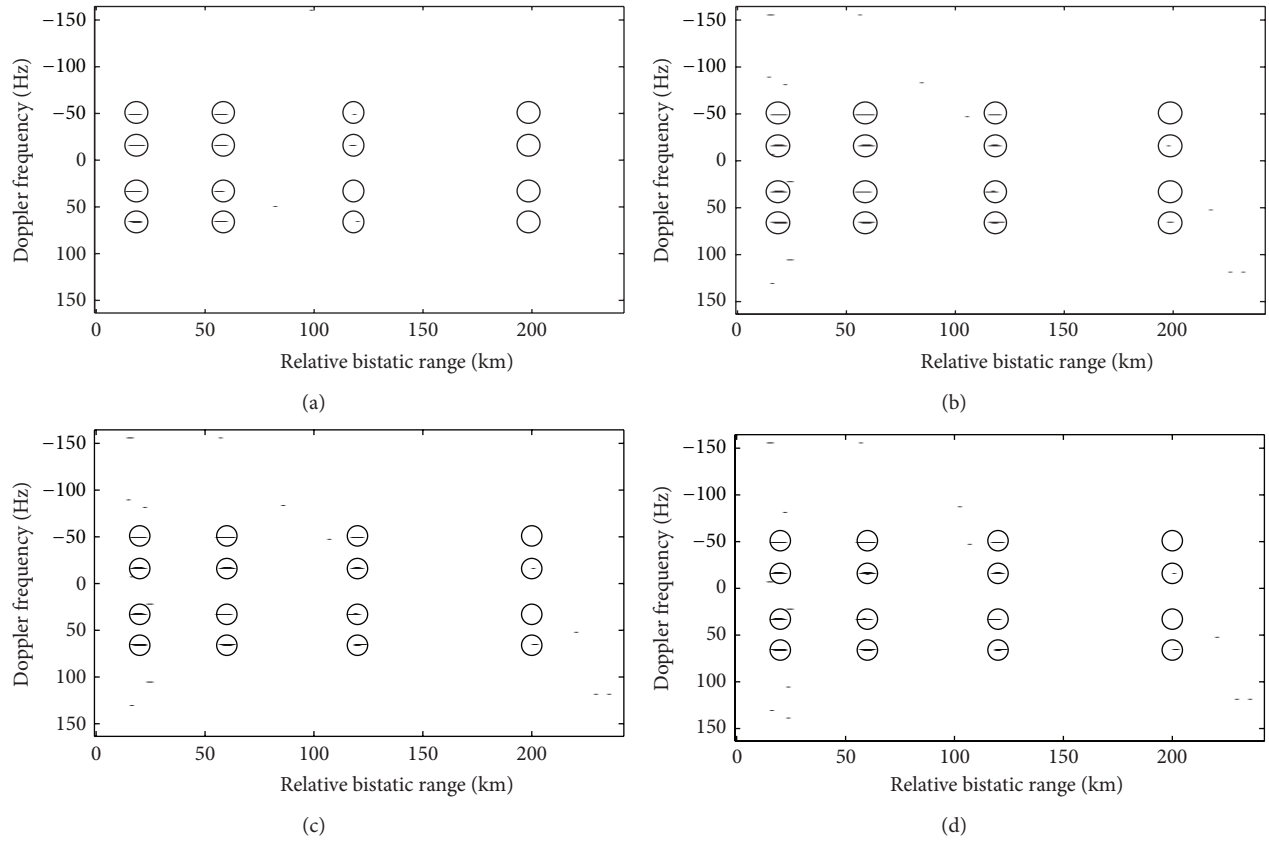

Figure 9: Detection results in the absence of stationary obstacles for (a) side lobe control by central element tapering (nonadaptive), (b) optimum filter, (c) principal eigenvalue approach, and (d) SLC.

the array to form the quiescent beam and the central element as an omnidirectional retrodirective beam.

Having defined the transformation matrix $\mathbf{T}$ as

$$\mathbf{T} = \begin{bmatrix} s^*_{\boldsymbol{\theta}1}(\theta_0) & s^*_{\boldsymbol{\theta}2}(\theta_0) & \cdots & s^*_{\boldsymbol{\theta}7}(\theta_0) & 0 \\ 0 & 0 & \cdots & 0 & s^*_{\boldsymbol{\theta}8}(\theta_0) \end{bmatrix}, \tag{19}$$

where $s_{\theta i}(\theta_0)$ is the ith element of the target steering vector, corresponding $s_{\theta 8}(\theta_0)$ to the central element, the resulting weights vector for the SLC is given by

$$\mathbf{w}^H_{\mathrm{SLC}}(\theta_0) = \mathbf{s}^H_{\boldsymbol{\theta}}(\theta_0)\,\mathbf{T}^H\left(\mathbf{T}\mathbf{M}\mathbf{T}^H\right)^{-1}\mathbf{T}. \tag{20}$$

Notice that in this case a 2×2 matrix in place of an 8×8 matrix has to be inverted.

Figure 5 (dashed-dotted line) shows the array pattern obtained by weighting the signals received by the antennas of the selected configuration according to (20), for $\theta_0 = 120^\circ$, assuming the same disturbance covariance matrix of the previous examples. The resulting antenna pattern is similar to the one obtained by exploiting the principal eigenvalue approach while the main lobe is only slightly broader.

Even in this case, the array pattern strongly attenuates only the signals coming from the DoA of the direct signal; therefore, the multipath reflections have to be cancelled by the adaptive temporal filter; then the 2D-CCF has to be evaluated, and a proper CFAR threshold has to be applied to detect potential targets over the range-Doppler plane.

4.4. Synthesis of the Reference Beam. In order to perform the adaptive temporal clutter cancellation, the direct signal is needed [4–6]. This can be obtained by synthesizing, in addition to the surveillance beam $\mathbf{w}_{\mathrm{SURV}}$, a reference beam $\mathbf{w}_{\mathrm{REF}}$ pointed to the transmitter. In contrast to some passive radar systems based on directive antennas, where different physical antennas are used to collect the reference and the surveillance signals, the considered system uses the same antennas to collect both, by combining the received signals in different ways.

Rather than simply pointing the array beam to the desired direction, we synthesize a reference beam, orthogonal to the surveillance, such that

$$\mathbf{w}^H_{\mathrm{REF}}\mathbf{w}_{\mathrm{SURV}}(\theta_0) = 0. \tag{21}$$

Such an orthogonal reference beam may be obtained by using seven out of the eight elements of the array to point in the desired direction, while using the central element to satisfy

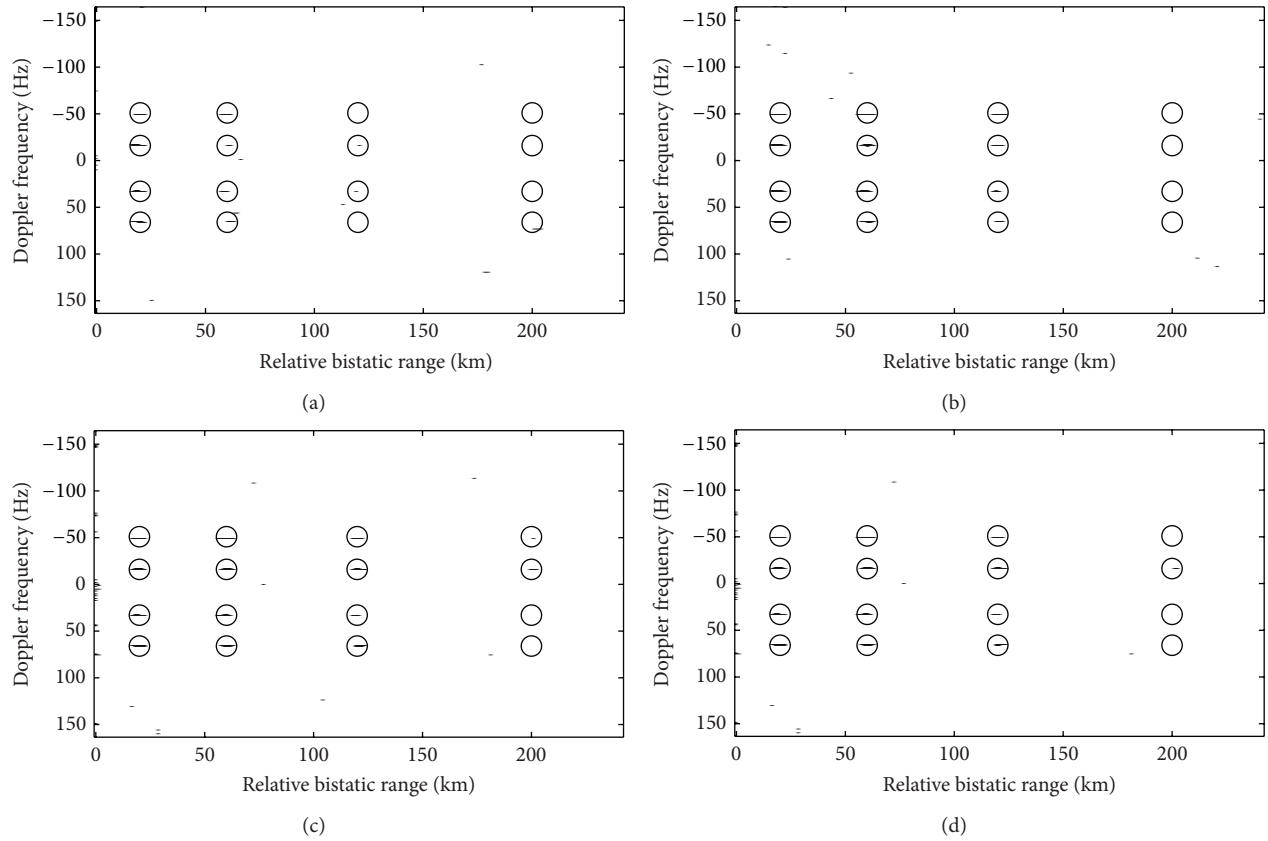

FIGURE 10: Detection results in the presence of a single stationary obstacle (DoA away from targets' DoAs) for (a) side lobe control by central element tapering (nonadaptive), (b) optimum filter (c) principal eigenvalue approach, and (d) SLC.

the condition given in (20). Denoting the surveillance and the reference beams as

$$\mathbf{w}_{\mathrm{SURV}}(\theta_0) = \begin{bmatrix} w_{\mathrm{SURV1}}(\theta_0) \\ w_{\mathrm{SURV2}}(\theta_0) \\ \vdots \\ w_{\mathrm{SURV8}}(\theta_0) \end{bmatrix} = \begin{bmatrix} \mathbf{w}^R_{\mathrm{SURV}}(\theta_0) \\ w_{\mathrm{SURV8}}(\theta_0) \end{bmatrix},$$
$$\mathbf{w}_{\mathrm{REF}} = \begin{bmatrix} s_{\boldsymbol{\theta}1}(\theta_0) \\ s_{\boldsymbol{\theta}2}(\theta_0) \\ \vdots \\ s_{\boldsymbol{\theta}7}(\theta_0) \\ \beta \end{bmatrix} = \begin{bmatrix} \mathbf{s}^R_{\boldsymbol{\theta}}(\theta_0) \\ \beta \end{bmatrix}, \tag{22}$$

respectively, the coefficient β, which leads to an orthogonal reference beam, can be readily expressed as

$$\beta = -\frac{{\mathbf{w}^R_{\mathrm{SURV}}}^H(\theta_0)\,\mathbf{s}^R_{\boldsymbol{\theta}}(\theta_0)}{{w_{\mathrm{SURV8}}}^*(\theta_0)}. \tag{23}$$

An example of reference beam orthogonal to the surveillance one is given in Figure 6.

5. Simulation Results

5.1. Methodology. In this section, a performance comparison is presented between the different approaches, with reference to the antenna array configuration above selected and sketched in Figure 2. To this purpose, a signal software simulator has been developed which is able to generate the signal received by a multichannel passive bistatic radar (PBR) under different conditions and exploiting different waveforms of opportunity. The developed simulator allows to specify the main parameters of both the transmitter and the receivers (the 8 receiving channels are supposed to be identical). Moreover, different bistatic geometries and clutter scenarios can be given as input data. Aiming at assessing the detection performance of the considered techniques, PBR scenarios with a relatively large number of targets have been considered.

In the following, we refer to an FM radio-based PBR, and the corresponding waveforms of opportunity are emulated according to the International Telecommunication Union (ITU) regulations [18].

The signals received by the eight elements of the array are then generated as the sum of several contributions, namely,

(i) the direct signal, which is an attenuated and delayed replica of the FM radio signal;

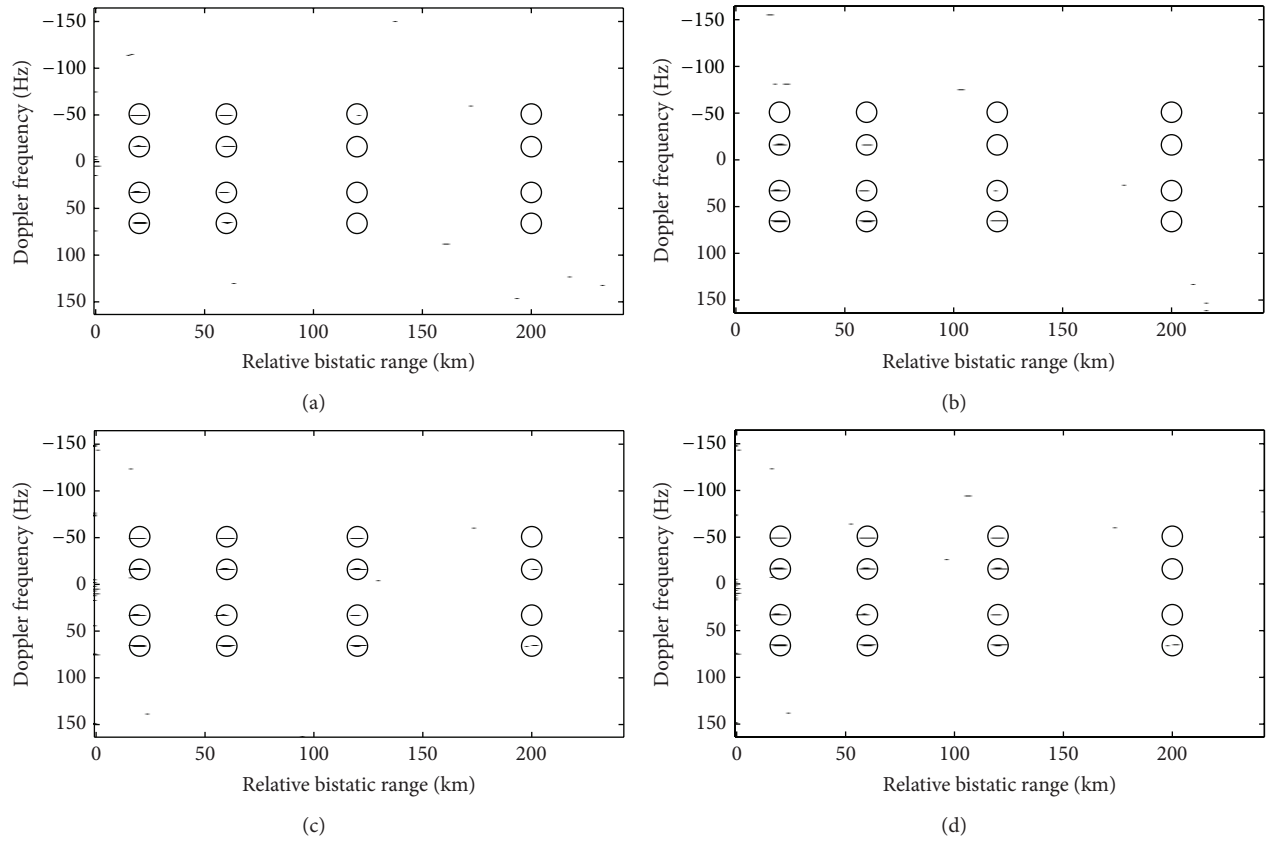

Figure 11: Detection results in the presence of a single stationary obstacle (DoA close to targets' DoAs) for (a) side lobe control by central element tapering (nonadaptive), (b) optimum filter, (c) principal eigenvalue approach, and (d) SLC.

(ii) the contributions of the stationary obstacles (clutter/multipath), which are still attenuated and delayed replicas of the FM radio signal;

(iii) the echoes from targets, which are attenuated, delayed, and Doppler-shifted replicas of the same FM radio signal;

(iv) the thermal noise, which is modeled as Additive White Gaussian Noise (AWGN).

The cascade of a spatial cancellation approach followed by a temporal adaptive cancellation filter is applied against the simulated data set. Specifically, the batch version of the ECA is adopted in the temporal dimension [5], while the spatial approach is selected among those discussed in the previous sections:

(i) side lobe control by central element tapering (nonadaptive);

(ii) optimum filter;

(iii) principal eigenvalue approach;

(iv) SLC.

Finally, the range-Doppler map is computed, and the detection performance is evaluated after the application of a conventional CFAR detection scheme. Several simulations have been run to provide averaged results.

5.2. Estimation of the Disturbance Covariance Matrix. As already mentioned, in case adaptive approaches are exploited, the disturbance covariance matrix has to be estimated from data. As the level of the useful signal is negligible compared to the level of the disturbance, the covariance matrix of the overall signal represents a good approximation of the disturbance covariance matrix.

Denoting $\mathbf{r}_i$ as the row vector containing N_S samples of the signal received by the ith antenna, let us define the $8 \times N_S$ matrix $\mathbf{R}$ as

$$\mathbf{R} = \begin{bmatrix} \mathbf{r}_1 \\ \mathbf{r}_2 \\ \vdots \\ \mathbf{r}_i \\ \vdots \\ \mathbf{r}_8 \end{bmatrix}. \tag{24}$$

An estimate of the covariance matrix is given by

$$\widehat{\mathbf{M}} = \frac{1}{N_S}\mathbf{R}\mathbf{R}^H. \tag{25}$$

As far as the estimation accuracy is concerned, the larger the N_S is, the more accurate the estimation of $\mathbf{M}$ is. In this specific application, $\mathbf{M}$ has to be estimated accurately enough that

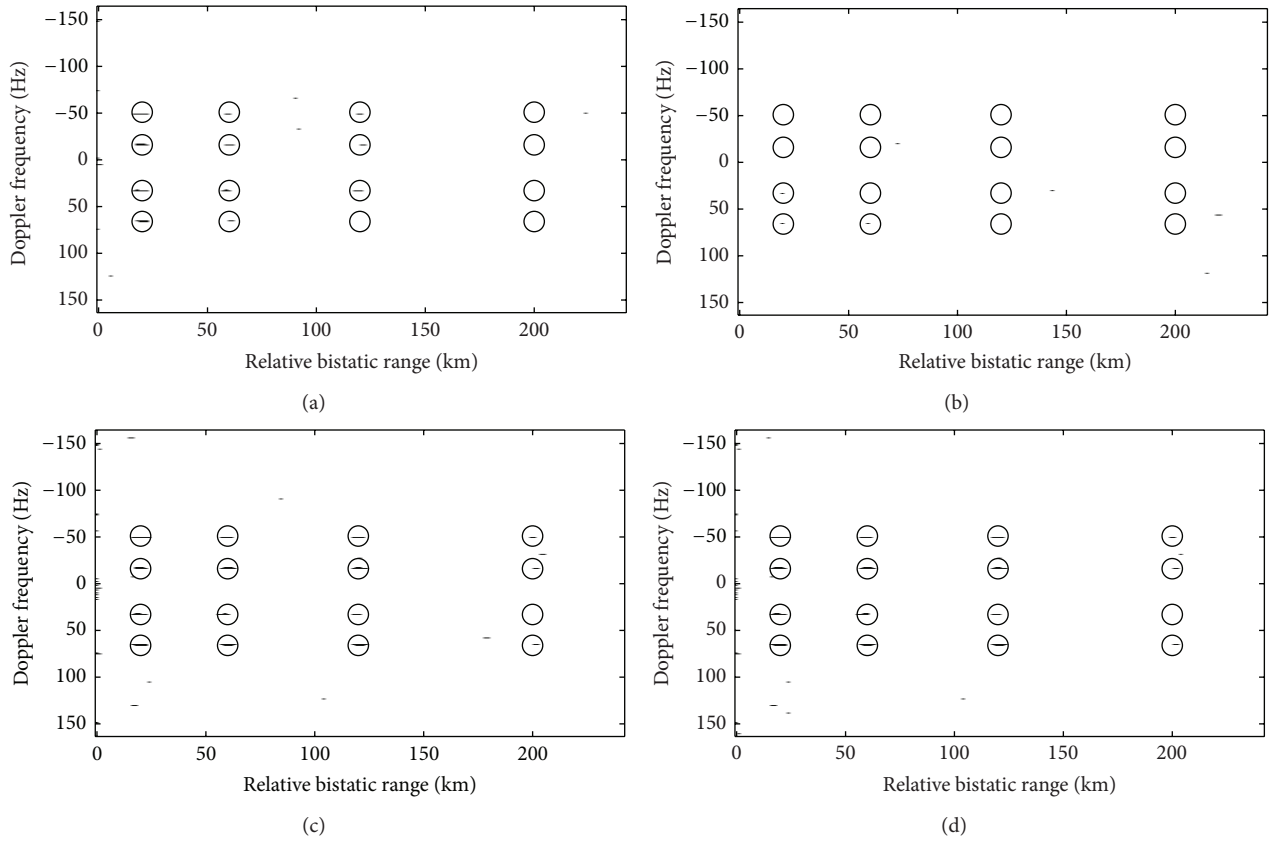

FIGURE 12: Detection results in the presence of several stationary obstacles for (a) side lobe control by central element tapering (nonadaptive), (b) optimum filter, (c) principal eigenvalue approach, and (d) SLC.

the resulting pattern does not differ significantly from the pattern obtained by using the true covariance matrix $\mathbf{M}$. In Figure 7, the pattern obtained for different values of N_S and for the true covariance matrix is shown, in case the disturbance only includes the direct signal and the thermal noise, with power ratio equal to 75 dB. In order to obtain a pattern very similar to the one obtained by using the true covariance matrix, at least $N_S = 1000$ samples have to be used in the estimation. Notice that, for the considered FM radio-based PBR, assuming a sampling frequency equal to 200 kHz, this number of samples would correspond to a signal fragment of 5 ms whose availability is easily guaranteed. Moreover, such duration assures the considered disturbance contribution to be quite stable during the estimation time due to the stationary characteristics in the spatial dimension.

Nevertheless, as consecutive samples are usually correlated (see an example of autocorrelation function of a received FM radio signal in Figure 8), N_S can be reduced, if nonconsecutive samples are used.

5.3. Detection Performance. In the case study reported in this paragraph, sixteen targets have been injected in the simulated data with target-receiver distance ranging from 10 to 100 km, DoAs comprised between 150° and 180°, radial velocities in the range [−150, 200] m/s, and signal-to-noise ratios between −35 and −55 dB. Different clutter scenarios are then considered.

Figures 9(a)–9(d) report the detection results obtained for different processing schemes in the absence of stationary obstacles. As is apparent, the three spatial adaptive approaches (Figures 9(b)–9(d)) yield comparable performance allowing the detection of fourteen out of sixteen targets (circles indicate the injected targets positions over the range-Doppler plane). Only eleven out of sixteen targets are, instead, detected by using the nonadaptive approach (see Figure 9(a)). In the latter case, in fact, the poor detection performance is due to the fact that the direct signal, received with power level 70 dB above thermal noise, is not attenuated enough by the array pattern of the surveillance beam; therefore, the temporal adaptive cancellation of the residual direct signal implies the cancellation of part of the useful signal as well.

Similar performances are observed in case a single stationary obstacle with power level 30 dB above thermal noise, whose DoA is away from the targets' DoAs, is introduced in the scene (see Figure 10).

The detection performances of the three adaptive schemes are no longer similar when the DoA of the stationary scatterer is close to the DoAs of some of the targets (Figure 11). In that case, as is expected, optimum filter experiences some detection losses, specifically failing

in detecting targets with DoAs close to the DOA of the multipath return. In particular, Figure 11(b) shows that the optimum filter does not detect a target characterized by a quite short bistatic range/high bistatic RCS because its DoA is close to that of the obstacle.

Figure 12 reports the detection results obtained for a simulated scenario containing three stationary obstacles with clutter-to-noise ratios ranging between 25 and 30 dB. As it is apparent and as it has been mentioned, the optimum filter yields an effective removal of all the undesired disturbance contributions which, however, implies also many of the injected targets to be lost. In contrast, the exploitation of a reduced number of d.o.f., as required by the principal eigenvalue approach and the SLC, allows the effective cancellation of the sole main disturbance contribution typically represented by the direct signal. However, the clutter/multipath contributions can be effectively cancelled by the temporal adaptive filter. This prevents the undesired target cancellation at the DoA of the strong multipaths thus yielding remarkable detection performance.

As a final remark, we would like to point out that the cascading of an antenna-based adaptive technique and a temporal adaptive cancellation filter makes the system robust also to the presence of strong interferences in the exploited signal frequency band. Notice that the ECA is not effective against such disturbance contributions since, as long as it is concerned, this filter looks for delayed replicas of the exploited signal of opportunity. However, cochannel interferences are typically observed in practical passive radar applications based on broadcast transmissions due to the frequency reuse over neighbouring areas.

6. Conclusions

A suitable array configuration for passive radar application has been identified and optimized by designing a specific tapering solution. The selected antenna array allows both to steer the surveillance beam in order to cover a wide surveillance area and to strongly attenuate the undesired direct signal in the surveillance channel, thus preserving the useful dynamic range of the receiver. Three spatial adaptive approaches have also been investigated and compared, showing their effectiveness in removing the undesired contributions from the surveillance PBR signals. A comparative performance analysis has been carried out among different processing schemes with reference to a simulated case-study. It has been shown that the most effective solution is obtained by resorting to the principal eigenvalue approach or to the SLC for direct signal spatial suppression, and then exploiting a temporal adaptive cancellation filter to remove both direct signal residuals and its multipath reflections in the surveillance channel. In particular, the SLC solution is likely to be preferred due to its limited complexity.

Acknowledgment

At the time the major part of this work was done, M. Villano was developing his master's thesis within the DIET Department, University of Rome "La Sapienza", Italy, which fully funded this work.

References

[1] "Special issue on passive radar systems—IEE proceedings on radar," *Sonar and Navigation*, vol. 152, no. 3, pp. 106–223, 2005.

[2] P. E. Howland, D. Maksimiuk, and G. Reitsma, "FM radio based bistatic radar," *IEE Proceedings on Radar, Sonar and Navigation*, vol. 152, no. 3, pp. 107–115, 2005.

[3] H. D. Griffiths and C. J. Baker, "Passive coherent location radar systems. Part 1: performance prediction," *IEE Proceedings on Radar, Sonar and Navigation*, vol. 152, no. 3, pp. 153–159, 2005.

[4] R. Cardinali, F. Colone, C. Ferretti, and P. Lombardo, "Comparison of clutter and multipath cancellation techniques for passive radar," in *Proceedings of the IEEE Radar Conference*, pp. 469–474, Boston, Mass, USA, April 2007.

[5] F. Colone, D. W. O'Hagan, P. Lombardo, and C. J. Baker, "A multistage processing algorithm for disturbance removal and target detection in passive bistatic radar," *IEEE Transactions on Aerospace and Electronic Systems*, vol. 45, no. 2, pp. 698–722, 2009.

[6] F. Colone, R. Cardinali, and P. Lombardo, "Cancellation of clutter and multipath in passive radar using a sequential approach," in *Proceedings of the IEEE Radar Conference*, pp. 393–399, Verona, NY, USA, April 2006.

[7] M. Malanowski and K. Kulpa, "Digital beamforming for passive coherent location radar," in *Proceedings of the IEEE Radar Conference (RADAR '08)*, Rome, Italy, May 2008.

[8] P. Knott and U. R. O. Nickel, "Design and development of a V-shaped printed dipole antenna array for passive radar," in *Proceedings of the 5th European Conference on Antennas and Propagation (EUCAP '11)*, pp. 961–964, Rome, Italy, April 2011.

[9] F. Belfiori, S. Monni, W. van Rossum, and P. Hoogeboom, "Antenna array characterisation and signal processing for an FM radio-based passive coherent location radar system," *IET Radar, Sonar & Navigation*, vol. 6, no. 8, pp. 687–696, 2012.

[10] M. Villano, F. Colone, and P. Lombardo, "Adaptive clutter suppression in passive phased array radar," in *Proceedings of the International Radar Symposium (IRS '09)*, pp. 343–347, Hamburg, Germany, September 2009.

[11] R. Zemmari, U. Nickel, and W.-D. Wirth, "GSM passive radar for medium range surveillance," in *Proceedings of the European Radar Conference (EuRAD '09)*, pp. 49–52, Rome, Italy, October 2009.

[12] J. Zhu, Y. Hong, and L. Tao, "Adaptive beamforming passive radar based on FM radio transmitter," in *Proceedings of the IET International Conference on Radar Systems*, Edinburgh, UK, October 2007.

[13] G. Fabrizio, F. Colone, P. Lombardo, and A. Farina, "Adaptive beamforming for high-frequency over-the-horizon passive radar," *IET Radar, Sonar and Navigation*, vol. 3, no. 4, pp. 384–405, 2009.

[14] J.-H. Deng, J.-K. Hwang, C.-Y. Lin, and S.-M. Liao, "Adaptive space-time beamforming technique for passive radar system with ultra low signal to interference ratio," in *Proceedings of the IEEE International Conference on Wireless Information Technology and Systems (ICWITS '10)*, September 2010.

[15] F. Colone, R. Cardinali, P. Lombardo et al., "Space-time constant modulus algorithm for multipath removal on the reference signal exploited by passive bistatic radar," *IET Radar, Sonar and Navigation*, vol. 3, no. 3, pp. 253–264, 2009.

[16] A. Farina, P. Lombardo, and L. Ortenzi, "A unified approach to adaptive radar processing with general antenna array configuration," *Signal Processing*, vol. 84, no. 9, pp. 1593–1623, 2004.

[17] A. Farina, *Antenna-Based Signal Processing Techniques for Radar Systems*, Artech House, Norwood, NJ, USA.

[18] A. Lauri, F. Colone, R. Cardinali, C. Bongioanni, and P. Lombardo, "Analysis and emulation of FM radio signals for passive radar," in *Proceedings of the IEEE Aerospace Conference*, pp. 2170–2179, Big Sky, Mont, USA, March 2007.

Hindawi Publishing Corporation
International Journal of Antennas and Propagation
Volume 2013, Article ID 261230, 21 pages
http://dx.doi.org/10.1155/2013/261230

Research Article

Array Processing for Radar: Achievements and Challenges

Ulrich Nickel

Fraunhofer Institute for Communication, Information Processing and Ergonomics (FKIE), Fraunhoferstrasse 20, 53343 Wachtberg, Germany

Correspondence should be addressed to Ulrich Nickel; ulrich.nickel@fkie.fraunhofer.de

Received 26 March 2013; Accepted 26 July 2013

Academic Editor: Hang Hu

Array processing for radar is well established in the literature, but only few of these algorithms have been implemented in real systems. The reason may be that the impact of these algorithms on the overall system must be well understood. For a successful implementation of array processing methods exploiting the full potential, the desired radar task has to be considered and all processing necessary for this task has to be eventually adapted. In this tutorial paper, we point out several viewpoints which are relevant in this context: the restrictions and the potential provided by different array configurations, the predictability of the transmission function of the array, the constraints for adaptive beamforming, the inclusion of monopulse, detection and tracking into the adaptive beamforming concept, and the assessment of superresolution methods with respect to their application in a radar system. The problems and achieved results are illustrated by examples from previous publications.

1. Introduction

Array processing is well established for radar. Publications of this topic have appeared for decades, and one might question what kind of advances we may still expect now. On the other hand, if we look at existing radar systems we will find very few methods implemented from the many ideas discussed in the literature. The reason may be that all processing elements of a radar system are linked, and it is not very useful to simply implement an isolated algorithm. The performance and the property of any algorithm will have an influence on the subsequent processing steps and on the radar operational modes. Predictability of the system performance with the new algorithms is a key issue for the radar designer. Advanced array processing for radar will therefore require to take these interrelationships into account and to adapt the related processing in order to achieve the maximum possible improvement. The standard handbooks on radar [1, 2] do not mention this problem. The book of Wirth [3] is an exception and mentions a number of the array processing techniques described below.

In this tutorial paper, viewpoints are presented which are relevant for the implementation of array processing methods. We do not present any new sophisticated algorithms, but for the established algorithms we give examples of the relations between array processing and preceding and subsequent radar processing. We point out the problems that have to be encountered and the solutions that need to be developed. We start with spatial sampling, that is, the antenna array that has to be designed to fulfill all requirements of the radar system. A modern radar is typically a multitasking system. So, the design of the array antenna has to fulfill multiple purposes in a compromise. In Section 3, we briefly review the approaches for deterministic pattern shaping which is the standard approach of antenna-based interference mitigation. It has the advantage of requiring little knowledge about the interference scenario, but very precise knowledge about the array transfer function ("the array manifold"). Adaptive beamforming (ABF) is presented in Section 4. This approach requires little knowledge about the array manifold but needs to estimate the interference scenario from some training data. Superresolution for best resolution of multiple targets is sometimes also subsumed under adaptive beamforming as it resolves everything, interference and targets. These methods are considered in Section 5. We consider superresolution methods here solely for the purpose of improved parameter estimation. In Section 6, we briefly mention the canonical extension of ABF and superresolution to space-time array processing. Section 7 is the final and most important contribution. Here

we point out how direction estimation must be modified if adaptive beams are used, and how the radar detector, the tracking algorithm, and the track management should be adapted for ABF.

2. Design Factors for Arrays

Array processing starts with the array antenna. This is hardware and is a selected construction that cannot be altered. It must therefore be carefully designed to fulfill all requirements. Digital array processing requires digital array outputs. The number and quality of these receivers (e.g., linearity and number of ADC bits) determine the quality and the cost of the whole system. It may be desirable to design a fully digital array with AD-converters at each antenna element. However, weight and cost will often lead to a system with reduced number of digital receivers. On the other hand, because of the $1/R^4$-decay of the received power, radar needs antennas with high gain and high directional discrimination, which means arrays with many elements. There are different solutions to solve this contradiction.

(i) Thinned arrays: the angular discrimination of an array with a number of elements can be improved by increasing the separation of the elements and thus increasing the aperture of the antenna. Note that the thinned array has the same gain as the corresponding fully filled array.

(ii) Subarrays: element outputs are summed up in an analog manner into subarrays which are then AD-converted and processed digitally. The size and the shape of the subarrays are an important design criterion. The notion of an array with subarrays is very general and includes the case of steerable directional array elements.

2.1. Impact of the Dimensionality of the Array. Antenna elements may be arranged on a line (1-dimensional array), on a plane (a ring or a 2-dimensional planar array), on a curved surface (conformal array), or within a volume (3D-array, also called Crow's Nest antenna, [3, Section 4.6.1]). A 1-dimensional array can only measure one independent angle; 2D and 3D arrays can measure the full polar coordinates in $\mathbb{R}^3$.

Antenna element design and the need for fixing elements mechanically lead to element patterns which are never omnidirectional. The elements have to be designed with patterns that allow a unique identification of the direction. Typically, a planar array can only observe a hemispherical half space. To achieve full spherical coverage, several planar arrays can be combined (multifacetted array), or a conformal or volume array may be used.

2.1.1. Arrays with Equal Patterns. For linear, planar, and volume arrays, elements with nearly equal patterns can be realized. These have the advantage that the knowledge of the element pattern is for many array processing methods not necessary. An equal complex value can be interpreted as a modified target complex amplitude, which is often a nuisance parameter. More important is that, if the element patterns are really absolutely equal, any cross-polar components of the signal are in all channels equal and fulfill the array model in the same way as the copolar components; that is, they produce no error effect.

2.1.2. Arrays with Unequal Array Patterns. This occurs typically by tilting the antenna elements as is done for conformal arrays. For a planar array, this tilt may be used to realize an array with polarization diversity. Single polarized elements are then mounted with orthogonal alignment at different positions. Such an array can provide some degree of dual polarization reception with single channel receivers (contrary to more costly fully polarimetric arrays with receivers for both polarizations for each channel).

Common to arrays with unequal patterns is that we have to know the element patterns for applying array processing methods. The full element pattern function is also called the array manifold. In particular, the cross-polar (or short x-pol) component has a different influence for each element. This means that if this component is not known and if the x-pol component is not sufficiently attenuated, it can be a significant source of error.

2.2. Thinned Arrays. To save the cost of receiving modules, sparse arrays are considered, that is, with fewer elements than the full populated $\lambda/2$ grid. Because such a "thinned array" spans the same aperture, it has the same beamwidth. Hence, the angular accuracy and resolution are the same as the fully filled array. Due to the gaps, ambiguities or at least high sidelobes may arise. In early publications like [1], it was advocated to simply take out elements of the fully filled array. It was early recognized that this kind of thinning does not imply "sufficiently random" positions. Random positions on a $\lambda/16$ grid as used in [3, Chapter 17] can provide quite acceptable patterns. Note that the array gain of a thinned array with N elements is always N, and the average sidelobe level is $1/N$. Today, we know from the theory of compressed sensing that a selection of sufficiently random positions can produce a unique reconstruction of a not too large number of impinging wave fields with high probability [5].

2.3. Arrays with Subarrays. If a high antenna gain with low sidelobes is desired one has to go back to the fully filled array. For large arrays with thousands of elements, the large number of digital channel constitutes a significant cost factor and a challenge for the resulting data rate. Therefore, often subarrays are formed, and all digital (adaptive) beamforming and sophisticated array processing methods are applied to the subarray outputs. Subarraying is a very general concept. At the elements, we may have phase shifters such that all subarrays are steered into a given direction and we may apply some attenuation (tapering) to influence the sidelobe level. The sum of the subarrays then gives the sum beam output. The subarrays can be viewed as a superarray with elements having different patterns steered into the selected direction. The subarrays should have unequal size and shape to avoid grating effects for subsequent array processing, because the subarray centers constitute a sparse array (for details, see [6]).

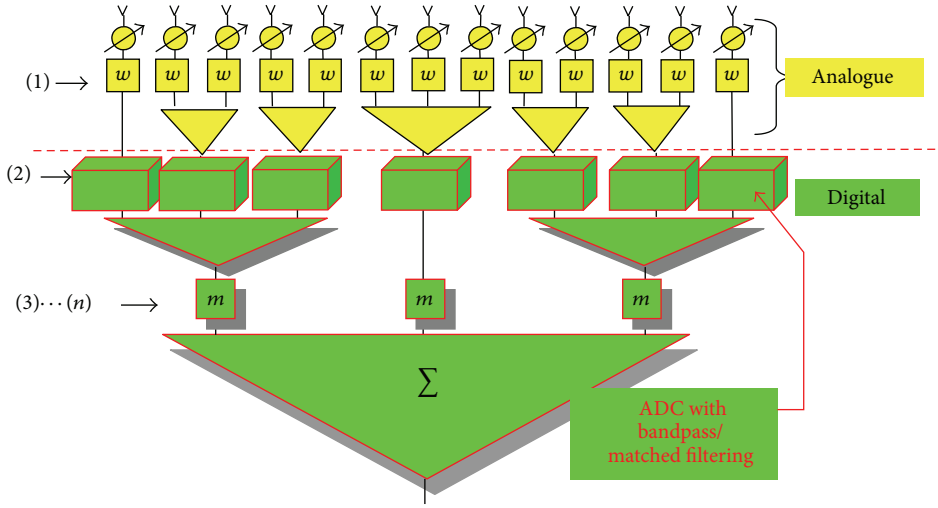

Figure 1: Principle of forming subarrays.

The principle is indicated in Figure 1, and properties and options are described in [6, 7]. In particular, one can also combine new subarrays at the digital level or distribute the desired tapering over the analog level (1) and various digital levels $(2)\cdots(n)$.

Beamforming using subarrays can be mathematically described by a simple matrix operation. Let the complex array element outputs be denoted by $\mathbf{z}$. The subarray forming operation is described by a subarray forming matrix $\mathbf{T}$ by which the element outputs are summed up as $\tilde{\mathbf{z}} = \mathbf{T}^H\mathbf{z}$. For L subarrays and N antenna elements, $\mathbf{T}$ is of size $N \times L$. Vectors and matrices at the subarray outputs are denoted by the tilde. Suppose we steer the array into a look direction $(u_0, v_0) =: \mathbf{u}_0$ by applying phase shifts $a_i(\mathbf{u}_0) = e^{j2\pi f_0(x_i u_0 + y_i v_0)/c}$ and apply additional amplitude weighting g_i at the elements (real vector of length N) for a sum beam with low sidelobes, then we have a complex weighting $g_i a_i(\mathbf{u}_0)$ which can be included in the elements of the matrix $\mathbf{T}$. Here, f_0 denotes the centre frequency, x_i, y_i denote the coordinates of the ith array element, c denotes the velocity of light, and u, v denote the components of the unit direction vector in the planar antenna (x, y)-coordinate system. The beams are formed digitally with the subarray outputs by applying a final weighting $\tilde{m}_i$ $(i = 1, \ldots, L)$ as

$$y = \tilde{\mathbf{m}}^H\tilde{\mathbf{z}}. \tag{1}$$

In the simplest case, $\tilde{\mathbf{m}}$ consists of only ones. The antenna pattern of such a sum beam can then be written as

$$f(\mathbf{u}) = \tilde{\mathbf{m}}^H\mathbf{T}^H\mathbf{a}(\mathbf{u}) = \tilde{\mathbf{m}}^H\tilde{\mathbf{a}}(\mathbf{u}), \tag{2}$$

where $\mathbf{a}(\mathbf{u}) = (a_i(\mathbf{u}))_{i=1\cdots N}$ and $\tilde{\mathbf{a}}(\mathbf{u}) = \mathbf{T}^H\mathbf{a}(\mathbf{u})$ denotes the plane wave response at the subarray outputs. All kinds of beams (sum, azimuth and elevation difference, guard channel, etc.) can be formed from these subarray outputs. We can also scan the beam digitally at subarray level into another direction, [7].

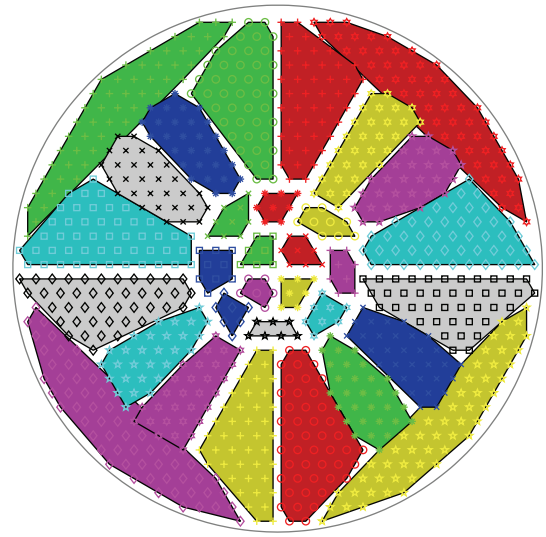

Figure 2: 2D generic array with 902 elements grouped into 32 subarrays.

Figure 2 shows a typical planar array with 902 elements on a triangular grid with 32 subarrays. The shape of the subarrays was optimized by the technique of [6] such that the difference beams have low sidelobes when a −40 dB Taylor weighting is applied at the elements. We will use this array in the sequel for presenting examples.

An important feature of digital beamforming with subarrays is that the weighting for beamforming can be distributed between the element level (the weighting incorporated in the matrix $\mathbf{T}$) and the digital subarray level (the weighting $\tilde{\mathbf{m}}$). This yields some freedom in designing the dynamic range of amplifiers at the elements and the level of the AD-converter input. This freedom also allows to normalize the power of the subarray outputs such that $\mathbf{T}^H\mathbf{T} = \mathbf{I}$. As will be shown in Section 4, this is also a reasonable requirement for adaptive interference suppression to avoid pattern distortions.

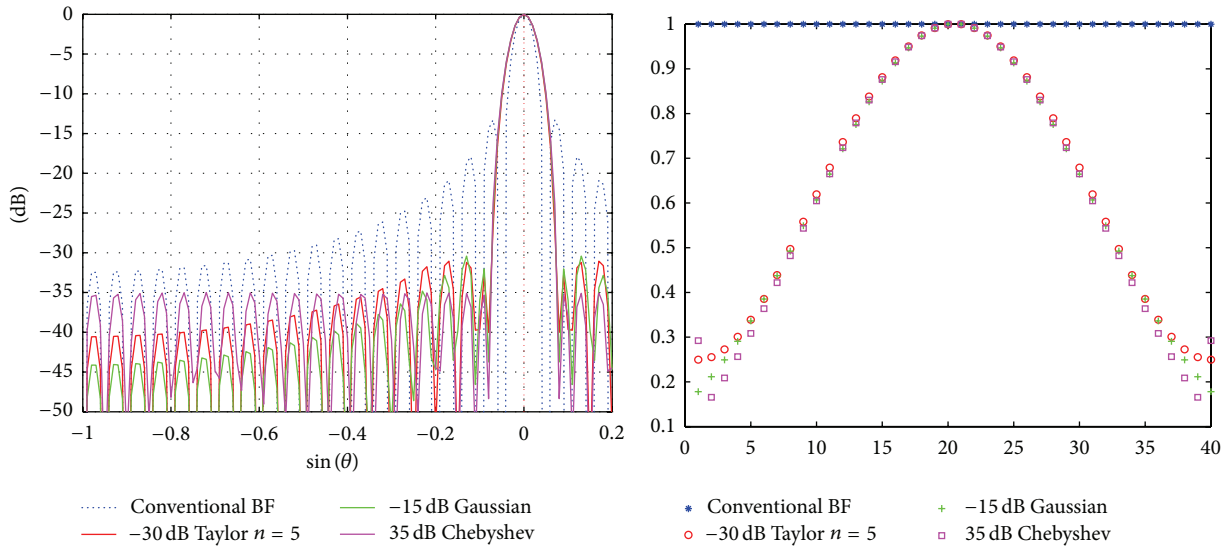

(a) Low sidelobe patterns of equal beamwidth

(b) Taper functions for low sidelobes

FIGURE 3: Low sidelobes by amplitude tapering.

2.4. Space-Time Arrays. Coherent processing of a time series $z_1, \ldots, z_K$ can be written as a beamforming procedure as in (1). For a time series of array snapshots $\mathbf{z}_1, \ldots, \mathbf{z}_K$, we have therefore a double beamforming procedure of the space-time data matrix $\mathbf{Z} = (\mathbf{z}_1, \ldots, \mathbf{z}_K)$ of the form

$$S = \mathbf{m}_s^H \mathbf{Z} \mathbf{m}_t, \tag{3}$$

where $\mathbf{m}_s$, $\mathbf{m}_t$ denote the weight vectors for spatial and temporal beamforming, respectively. Using the rule of Kronecker products, (3) can be written as a single beamforming operation

$$S = \left(\mathbf{m}_t \otimes \mathbf{m}_s\right)^H \operatorname{vec}\{\mathbf{Z}\}, \tag{4}$$

where vec{**Z**} is a vector obtained by stacking all columns of the matrix **Z** on top. This shows that mathematically it does not matter whether the data come from spatial or temporal sampling. Coherent processing is in both cases a beamforming-type operation with the correspondingly modified beamforming vector. Relation (4) is often exploited when spatial and temporal parameters are dependent (e.g., direction and Doppler frequency as in airborne radar; see Section 6).

3. Antenna Pattern Shaping

Conventional beamforming is the same as coherent integration of the spatially sampled data; that is, the phase differences of a plane wave signal at the array elements are compensated, and all elements are coherently summed up. This results in a pronounced main beam when the phase differences match with the direction of the plane wave and result in sidelobes otherwise. The beam shape and the sidelobes can be influenced by additional amplitude weighting.

Let us consider the complex beamforming weights $w_i = g_i e^{j2\pi f \mathbf{r}_i^T \mathbf{u}/c}$, $i = 1 \cdots N$. The simplest way of pattern shaping is to impose some bell-shaped amplitude weighting over the aperture like $g_i = \cos^{\nu}(\pi x_i/A) + \alpha$ (for suitable constants ν, α), or $g_i = e^{-\nu x_i^2}$. The foundation of these weightings is quite heuristical. The Taylor weighting is optimized in the sense that it leaves the conventional (uniformly weighted) pattern undistorted except for a reduction of the first n sidelobes below a prescribed level. The Dolph-Chebyshev weighting creates a pattern with all sidelobes equal to a prescribed level. Figure 3 shows examples of such patterns for a uniform linear array with 40 elements. The taper functions for low sidelobes were selected such that the 3 dB beamwidth of all patterns is equal. The conventional pattern is plotted for reference showing how tapering increases the beamwidth. Which of these taperings may be preferred depends on the emphasis on close in and far off sidelobes. Another point of interest is the dynamic range of the weights and the SNR loss, because at the array elements only attenuations can be applied. One can see that the Taylor tapering has the smallest dynamic range. For planar arrays the efficiency of the taperings is slightly different.

The rationale for low sidelobes is that we want to minimize some unknown interference power coming over the sidelobes. This can be achieved by solving the following optimization problem, [8]:

$$\begin{aligned} &\min_{\mathbf{w}} \quad \int_{\Omega} \left|\mathbf{w}^H \mathbf{a}(\mathbf{u})\right|^2 p(\mathbf{u})\, d\mathbf{u} \\ &\text{subject to} \quad \mathbf{w}^H \mathbf{a}_0 = 1, \text{ or equivalently} \\ &\min_{\mathbf{w}} \quad \mathbf{w}\mathbf{C}\mathbf{w} \\ &\text{s.t.} \quad \mathbf{w}^H \mathbf{a}_0 = \mathbf{1}, \\ &\text{with } \mathbf{C} = \int_{\Omega} \mathbf{a}(\mathbf{u})\, \mathbf{a}(\mathbf{u})^H p(\mathbf{u})\, d\mathbf{u}. \end{aligned} \tag{5}$$

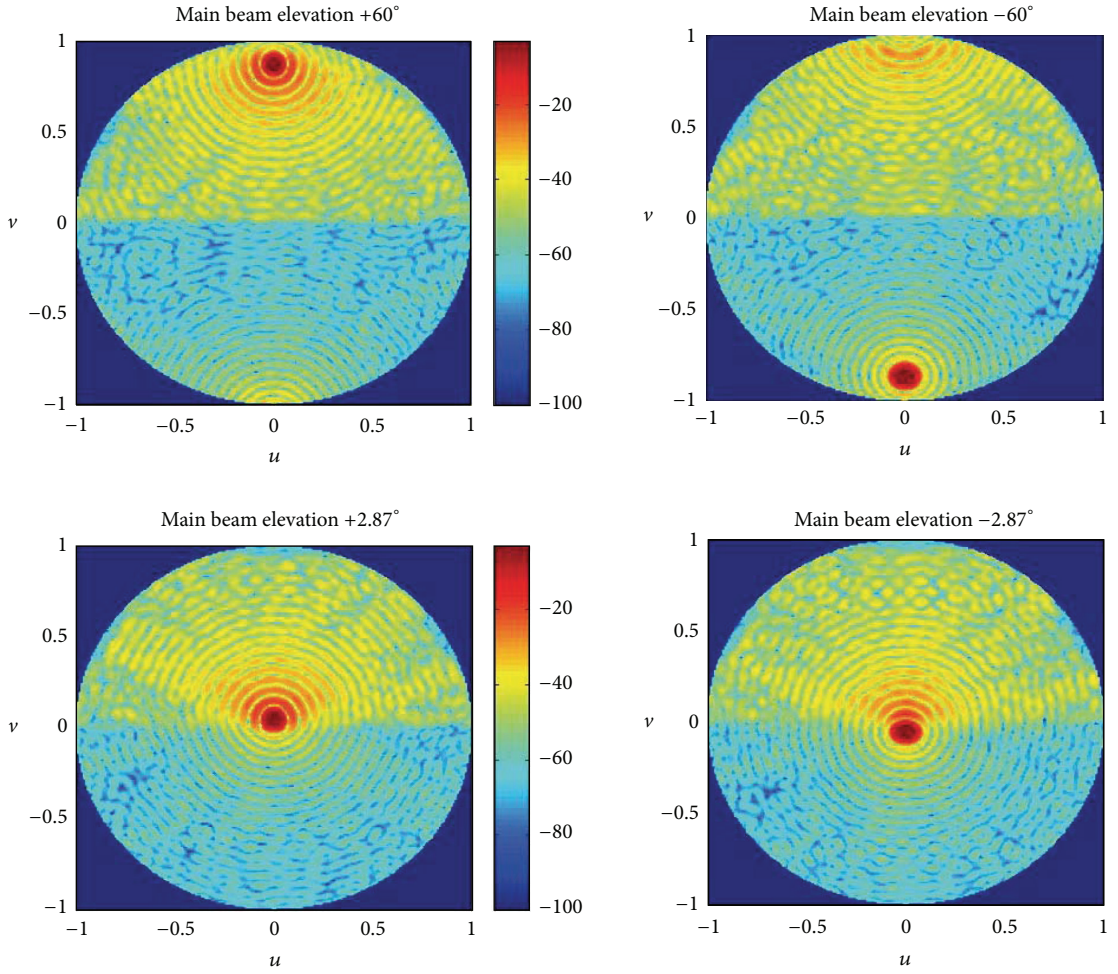

Figure 4: Antenna patterns of planar array with reduced sidelobes at lower elevations for different beam pointing directions (by courtesy of W. Bürger of Fraunhofer (FHR)).

Ω denotes the angular sector where we want to influence the pattern, for example, the whole visible region $u^2 + v^2 < 1$, and p is a weighting function which allows to put different emphasis on the criterion in different angular regions. The solution of this optimization is

$$\mathbf{w} = \frac{\mathbf{C}^{-1}\mathbf{a}_0}{\mathbf{a}_0^H \mathbf{C}^{-1}\mathbf{a}_0}. \tag{6}$$

For the choice of the function p, we remark that for a global reduction of the sidelobes when $\Omega = \{\mathbf{u} \in \mathbb{R}^2 \mid u^2 + v^2 \leq 1\}$, one should exclude the main beam from the minimization by setting $p = 0$ on this set of directions (in fact, a slightly larger region is recommended, e.g., the null-to-null width) to allow a certain mainbeam broadening. One may also form discrete nulls in directions $\mathbf{u}_1, \ldots, \mathbf{u}_M$ by setting $p(\mathbf{u}) = \sum_{k=1}^{M} \delta(\mathbf{u} - \mathbf{u}_k)$. The solution of (5) then can be shown to be

$$\mathbf{w} = \frac{\mathbf{P}\mathbf{a}_0}{\mathbf{a}_0^H \mathbf{P}\mathbf{a}_0} \quad \text{with } \mathbf{P} = \mathbf{I} - \mathbf{A}\left(\mathbf{A}^H\mathbf{A}\right)^{-1}\mathbf{A}^H, \qquad \mathbf{A} = \left(\mathbf{a}\left(\mathbf{u}_1\right), \ldots, \mathbf{a}\left(\mathbf{u}_M\right)\right). \tag{7}$$

This is just the weight for deterministic nulling. To avoid insufficient suppression due to channel inaccuracies, one may also create small extended nulls using the matrix $\mathbf{C}$. The form of these weights shows the close relationship to the adaptive beamforming weights in (11) and (17).

An example for reducing the sidelobes in selected areas where interference is expected is shown in Figure 4. This is an application from an airborne radar where the sidelobes in the negative elevation space have been lowered to reduce ground clutter.

4. Adaptive Interference Suppression

Deterministic pattern shaping is applied if we have rough knowledge about the interference angular distribution. In the sidelobe region, this method can be inefficient because the antenna response to a plane wave (the vector $\mathbf{a}(\mathbf{u})$) must be exactly known which is in reality seldom the case. Typically, much more suppression is applied than necessary with the price paid by the related beam broadening and SNR loss. Adaptive interference suppression needs no knowledge of the directional behavior and suppresses the interference only as

much as necessary. The proposition for this approach is that we are able to measure or learn in some way the adaptive beamforming (ABF) weights.

In the sequel, we formulate the ABF algorithms for subarray outputs as described in (1). This includes element space ABF for subarrays containing only one element.

4.1. Adaptive Beamforming Algorithms. Let us first suppose that we know the interference situation; that is, we know the interference covariance matrix $\mathbf{Q}$. What is the optimum beamforming vector $\mathbf{w}$? From the Likelihood Ratio test criterion, we know that the probability of detection is maximized if we choose the weight vector that maximizes the signal-to-noise-plus-interference ratio (SNIR) for a given (expected) signal $\mathbf{a}_0$,

$$\max_{\mathbf{w}} \frac{\left|\mathbf{w}^H\mathbf{a}_0\right|^2}{E\left\{\left|\mathbf{w}^H\mathbf{n}\right|^2\right\}} = \max_{\mathbf{w}} \frac{\left|\mathbf{w}^H\mathbf{a}_0\right|^2}{\mathbf{w}^H\mathbf{Q}\mathbf{w}}. \tag{8}$$

The solution of this optimization is

$$\mathbf{w} = \mu\mathbf{Q}^{-1}\mathbf{a}_0 \quad \text{with } \mathbf{Q} = E\left\{\mathbf{n}\mathbf{n}^H\right\}. \tag{9}$$

μ is a free normalization constant and $\mathbf{n}$ denotes interference and receiver noise. This weighting has a very intuitive interpretation. If we decompose $\mathbf{Q}^{-1} = \mathbf{L}\mathbf{L}^H$ and apply this weight to the data, we have $\mathbf{w}^H\mathbf{z} = \mathbf{a}_0^H\mathbf{Q}^{-1}\mathbf{z} = \mathbf{a}_0^H\mathbf{L}^H\mathbf{L}\mathbf{z} = (\mathbf{L}\mathbf{a}_0)^H(\mathbf{L}\mathbf{z})$. This reveals that ABF does nothing else but a pre-whiten and match operation: if $\mathbf{z}$ contains only interference, that is, $E\{\mathbf{z}\mathbf{z}^H\} = \mathbf{Q}$, then $E\{(\mathbf{L}\mathbf{z})(\mathbf{L}\mathbf{z})^H\} = \mathbf{I}$, the prewhitening operation; the operation of $\mathbf{L}$ on the (matched) signal vector $\mathbf{a}_0$ restores just the matching necessary with the distortion from the prewhitening operation.

This formulation for weight vectors applied at the array elements can be easily extended to subarrays with digital outputs. As mentioned in Section 2.3, a subarrayed array can be viewed as a superarray with directive elements positioned at the centers of the subarrays. This means that we have only to replace the quantities $\mathbf{a}$, $\mathbf{n}$ by $\tilde{\mathbf{a}} = \mathbf{T}^H\mathbf{a}$, $\tilde{\mathbf{n}} = \mathbf{T}^H\mathbf{n}$. However, there is a difference with respect to receiver noise. If the noise at the elements is white with covariance matrix $\sigma^2\mathbf{I}$ it will be at subarray outputs with covariance matrix $\widetilde{\mathbf{Q}} = \sigma^2\mathbf{T}^H\mathbf{T}$. Adaptive processing will turn this into white noise. Furthermore, if we apply at the elements some weighting for low sidelobes, which are contained in the matrix $\mathbf{T}$, ABF will reverse this operation by the pre-whiten and match principle and will distort the low sidelobe pattern. This can be avoided by normalizing the matrix $\mathbf{T}$ such that $\mathbf{T}\mathbf{T}^H = \mathbf{I}$. This can be achieved by normalizing the element weight as mentioned in Section 2.3 (for nonoverlapping subarrays).

Sometimes interference suppression is realized by minimizing only the jamming power subject to additional constraints, for example, $\mathbf{w}^H\mathbf{c}_i = k_i$, for suitable vectors $\mathbf{c}_i$ and numbers k_i, $i = 1\cdots r$. Although this is an intuitively reasonable criterion, it does not necessarily give the maximum SNIR. For certain constraints however both solutions are equivalent. The constrained optimization problem can be written in general terms as

$$\begin{aligned} &\min_{\mathbf{w}} \quad \mathbf{w}^H\mathbf{Q}\,\mathbf{w} \\ &\text{s.t.} \quad \mathbf{w}^H\mathbf{C} = \mathbf{k} \quad \left(\text{or } \mathbf{w}^H\mathbf{c}_i = k_i,\ i = 1\cdots r\right), \end{aligned} \tag{10}$$

and it has the solution

$$\mathbf{w} = \sum_{i=1}^{r} \lambda_i\mathbf{Q}^{-1}\mathbf{c}_i = \mathbf{Q}^{-1}\mathbf{C}\left(\mathbf{C}^H\mathbf{Q}^{-1}\mathbf{C}\right)^{-1}\mathbf{k}. \tag{11}$$

Examples of special cases are as follows:

(i) Single unit gain directional constraint: $\mathbf{w}^H\mathbf{a}_0 = 1 \Rightarrow \mathbf{w} = (\mathbf{a}_0^H\mathbf{Q}^{-1}\mathbf{a}_0)^{-1}\mathbf{Q}^{-1}\mathbf{a}_0$. This is obviously equivalent to the SNIR-optimum solution (9) with a specific normalization.

(ii) Gain and derivative constraint: $\mathbf{w}^H\mathbf{a}_0 = 1$, $\mathbf{w}^H\mathbf{a}_0' = 0 \Rightarrow \mathbf{w} = \mu\mathbf{Q}^{-1}\mathbf{a}_0 + \kappa\mathbf{Q}^{-1}\mathbf{a}_0'$ with suitable values of the Lagrange parameters μ, λ. A derivative constraint is added to make the weight less sensitive against mismatch of the steering direction.

(iii) Gain and norm constraint: $\mathbf{w}^H\mathbf{a}_0 = 1$, $\mathbf{w}^H\mathbf{w} = c \Rightarrow \mathbf{w} = \mu(\mathbf{Q} + \delta\mathbf{I})^{-1}\mathbf{a}_0$. The norm constraint is added to make the weight numerically stable. This is equivalent to the famous diagonal loading technique which we will consider later.

(iv) Norm constraint only: $\mathbf{w}^H\mathbf{w} = 1 \Rightarrow \mathbf{w} = \min EV(\mathbf{Q})$. Without a directional constraint the weight vector produces a nearly omnidirectional pattern, but with nulls in the interference directions. This is also called the power inversion weight, because the pattern displays the inverted interference power.

As we mentioned before, fulfilling the constraints may imply a loss in SNIR. Therefore, several techniques have been proposed to mitigate the loss. The first idea is to allow a compromise between power minimization and constraints by introducing coupling factors b_i and solve a soft constraint optimization

$$\begin{aligned} &\min_{\mathbf{w}} \quad \mathbf{w}^H\mathbf{Q}\mathbf{w} + \sum_{i=1}^{r} b_i\left|\mathbf{w}^H\mathbf{c}_i - k_i\right|^2 \text{ or} \\ &\min_{\mathbf{w}} \quad \mathbf{w}^H\mathbf{Q}\mathbf{w} + \left(\mathbf{w}^H\mathbf{C} - \mathbf{k}\right)^H\mathbf{B}\left(\mathbf{w}^H\mathbf{C} - \mathbf{k}\right) \end{aligned} \tag{12}$$

with $\mathbf{B} = \text{diag}\{b_1, \ldots, b_r\}$. The solution of the soft-constraint optimization is

$$\mathbf{w} = \left(\mathbf{Q} + \mathbf{C}\mathbf{B}\mathbf{C}^H\right)^{-1}\mathbf{C}\mathbf{B}\mathbf{k}. \tag{13}$$

One may extend the constrained optimization by adding inequality constraints. This leads to additional and improved robustness properties. A number of methods of this kind have been proposed, for example, in [9–12]. As we are only presenting the principles here we do not go into further details.

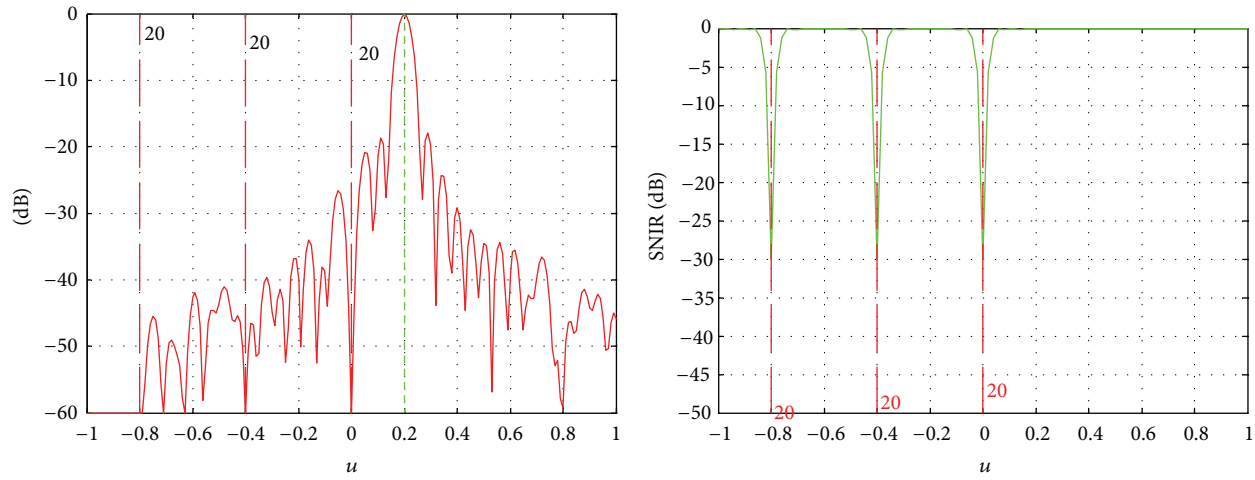

(a) Adapted antenna pattern

(b) SNIR

FIGURE 5: Antenna and normalized SNIR patterns for a three jammer configuration and generic array.

The performance of ABF is often displayed by the adapted antenna pattern. A typical adapted antenna pattern with 3 jammers of 20 dB SNR is shown in Figure 5(a) for generic array of Figure 2. This pattern does not show how the actual jamming power and the null depth play together.

Plots of the SNIR are better suited for displaying this effect. The SNIR is typically plotted for varying target direction while the interference scenario is held fixed, as seen in Figure 5(b). The SNIR is normalized to the SNR in the clear absence of any jamming and without ABF. In other words, this pattern shows the insertion loss arising from the jamming scenario with applied ABF.

The effect of target and steering direction mismatch is not accounted for in the SNIR plot. This effect is displayed by the scan pattern, that is, the pattern that arises if the adapted beam scans over a fixed target and interference scenario. Such a plot is rarely shown because of the many parameters to be varied. In this context, we note that for the case that the training data contains the interference and noise alone the main beam of the adapted pattern is fairly broad similar to the unadapted sum beam and is therefore fairly insensitive to pointing mismatch. How to obtain an interference-alone covariance matrix is a matter of proper selection of the training data as mentioned in the following section.

Figure 5 shows the case of an untapered planar antenna. The first sidelobes of the unadapted antenna pattern are at −17 dB and are nearly unaffected by the adaptation process. If we have an antenna with low sidelobes, the peak sidelobe level is much more affected; see Figure 6. Due to the tapering we have a loss in SNIR of 1.7 dB compared to the reference antenna (untapered without ABF and jamming).

4.2. Estimation of Adaptive Weights. In reality, the interference covariance matrix is not known and must be estimated from some training data $\mathbf{Z} = (\mathbf{z}_1, \ldots, \mathbf{z}_K)$. To avoid signal cancellation, the training data should only contain the interference alone. If we have a continuously emitting interference source (noise jammer) one may sample immediately after or before the transmit pulse (leading or rear dead zone). On the other hand, if we sample the training data before pulse compression the desired signal is typically much below the interference level, and signal cancellation is negligible. Other techniques are described in [13]. The maximum likelihood estimate of the covariance matrix is then

$$\widehat{\mathbf{Q}}_{\mathrm{SMI}} = \frac{1}{K}\sum_{k=1}^{K}\mathbf{z}_k\mathbf{z}_k^H. \tag{14}$$

This is called the Sample Matrix Inversion algorithm (SMI). The SMI method is only asymptotically a good estimate. For small sample size, it is known to be not very stable. For matrix invertibility, we need at least $K = N$ samples. According to Brennan's Rule, for example, [1], one needs $2K$ samples to obtain an average loss in SNIR below 3 dB. For smaller sample size, the performance can be considerably worse. However, by simply adding a multiple of the identity matrix to the SMI estimate, a close to optimum performance can be achieved. This is called the loaded sample matrix estimate (LSMI)

$$\widehat{\mathbf{Q}}_{\mathrm{LSMI}} = \frac{1}{K}\sum_{k=1}^{K}\mathbf{z}_k\mathbf{z}_k^H + \delta\cdot\mathbf{I}. \tag{15}$$

The drastic difference between SMI and LSMI is shown in Figure 7 for the planar array of Figure 2 for three jammers of 20 dB input JNR with 32 subarrays and only 32 data snapshots. For a "reasonable" choice of the loading factor (a rule of thumb is $\delta = 2\sigma^2 \cdots 4\sigma^2$ for an untapered antenna) we need only $2M$ snapshots to obtain a 3 dB SNIR loss, if M denotes the number of jammers (dominant eigenvalues) present, [13]. So the sample size can be considerably lower than the dimension of the matrix. The effect of the loading factor is that the dynamic range of the small eigenvalues is compressed. The small eigenvalues possess the largest statistical fluctuation but have the greatest influence on the weight fluctuation due to the matrix inversion.

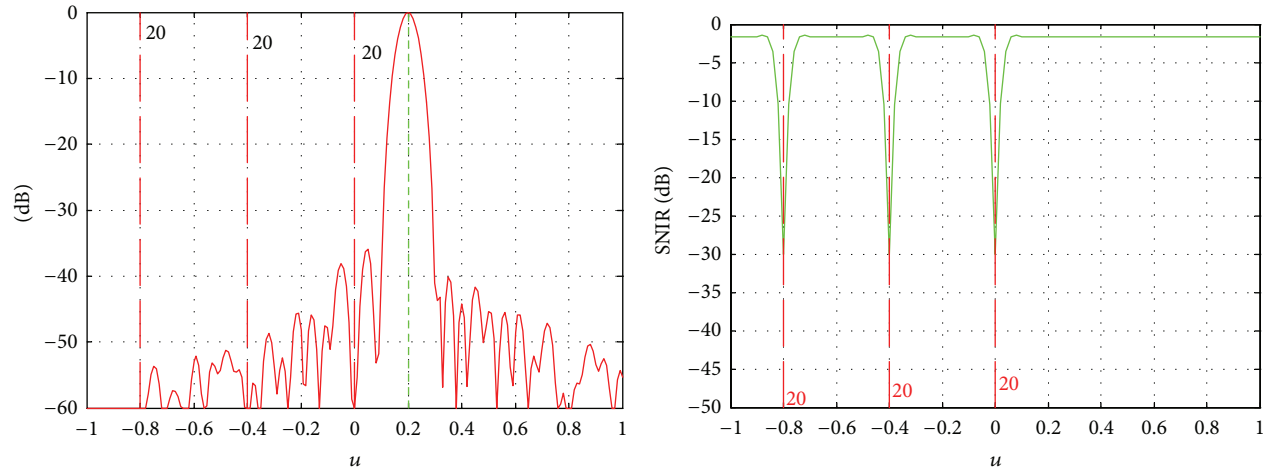

(a) Adapted antenna pattern (b) SNIR

FIGURE 6: Antenna and normalized SNIR patterns for a three jammer configuration for antenna with low sidelobes (−40 dB Taylor weighting).

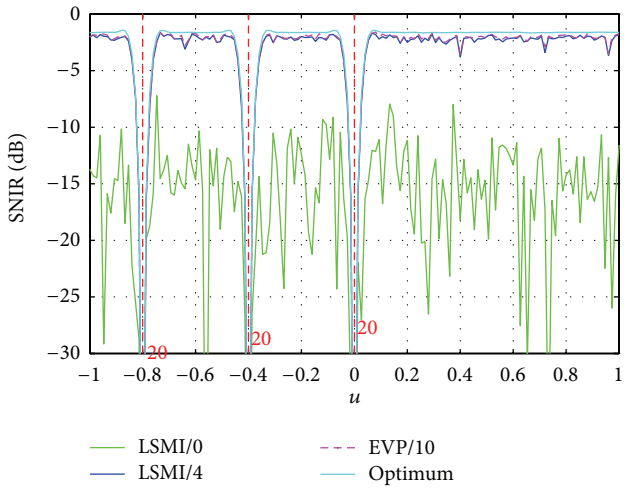

FIGURE 7: SNIR for SMI, LSMI ($\delta = 4\sigma^2$), and eigenvector projection with dim (JSS) = 3.

One may go even further and ignore the small eigenvalue estimates completely; that is, one tries to find an estimate of the inverse covariance matrix based on the dominant eigenvectors and eigenvalues. For high SNR, we can replace the inverse covariance matrix by a projection matrix. Suppose we have M jammers with amplitudes $b_1(t), \ldots, b_M(t)$ in directions $\mathbf{u}_1, \ldots, \mathbf{u}_M$. If the received data has the form $\mathbf{z}(t_k) = \sum_{m=1}^{M} \mathbf{a}(\mathbf{u}_m) b_m(t_k) + \mathbf{n}(t_k)$, or short $\mathbf{z}_k = \mathbf{A}\mathbf{b}_k + \mathbf{n}_k$, then

$$E\left\{\mathbf{z}\mathbf{z}^H\right\} = \mathbf{Q} = \mathbf{A}\mathbf{B}\mathbf{A}^H + \mathbf{I}. \tag{16}$$

Here, we have normalized the noise power to 1 and $\mathbf{B} = E\{\mathbf{b}\mathbf{b}^H\}$. Using the matrix inversion lemma, we have

$$\begin{aligned} \mathbf{Q}^{-1} &= \mathbf{I} - \mathbf{A}\left(\mathbf{B}^{-1} + \mathbf{A}^H\mathbf{A}\right)^{-1}\mathbf{A}^H \\ &\underset{\mathbf{B}\to\infty}{\longrightarrow} \mathbf{I} - \mathbf{A}\left(\mathbf{A}^H\mathbf{A}\right)^{-1}\mathbf{A}^H = \mathbf{P}_{\mathbf{A}}^{\perp}. \end{aligned} \tag{17}$$

$\mathbf{P}_{\mathbf{A}}^{\perp}$ is a projection on the space orthogonal to the columns of $\mathbf{A}$. For strong jammers, the space spanned by the columns of $\mathbf{A}$ will be the same as the space spanned by the dominant eigenvectors. We may therefore replace the estimated inverse covariance matrix by a projection on the complement of the dominant eigenvectors. This is called the EVP method. As the eigenvectors $\mathbf{X}$ are orthonormalized, the projection can be written as $\mathbf{P}_X^{\perp} = \mathbf{I} - \mathbf{X}\mathbf{X}^H$.

Figure 7 shows the performance of the EVP method in comparison with SMI, LSMI. Note the little difference between LSMI and EVP. The results with the three methods are based on the same realization of the covariance estimate.

For EVP, we have to know the dimension of the jammer subspace (dimJSS). In complicated scenarios and with channel errors present, this value can be difficult to determine. If dimJSS is grossly overestimated, a loss in SNIR occurs. If dimJSS is underestimated the jammers are not fully suppressed. One is therefore interested in subspace methods with low sensitivity against the choice of the subspace dimension. This property is achieved by a "weighted projection," that is, by replacing the projection by

$$\mathbf{P}_{\text{LMI}} = \mathbf{I} - \mathbf{X}\mathbf{D}\mathbf{X}^H, \tag{18}$$

where $\mathbf{D}$ is a diagonal weighting matrix and $\mathbf{X}$ is a set orthonormal vectors spanning the interference subspace. $\mathbf{P}_{\text{LMI}}$ does not have the mathematical properties of a projection. Methods of this type of are called lean matrix inversion (LMI). A number of methods have been proposed that can be interpreted as an LMI method with different weighting matrices $\mathbf{D}$. The LMI matrix can also be economically calculated by an eigenvector-free QR-decomposition method, [14].

One of the most efficient methods for pattern stabilization while maintaining a low desired sidelobe level is the constrained adaptive pattern synthesis (CAPS) algorithm, [15], which is also a subspace method. Let $\mathbf{m}$ be the vector for

beamforming with low sidelobes in a certain direction. In full generality, the CAPS weight can be written as

$$\mathbf{w}_{\mathrm{CAPS}} = \frac{1}{\mathbf{m}^H \widehat{\mathbf{R}}^{-1}\mathbf{m}} \widehat{\mathbf{Q}}_{\mathrm{SMI}}^{-1}\mathbf{m} - \mathbf{X}_\perp \left(\mathbf{X}_\perp^H \mathbf{C}\mathbf{X}_\perp\right)^{-1} \times \mathbf{X}_\perp^H \mathbf{C}\left(\frac{1}{\mathbf{m}^H \widehat{\mathbf{R}}^{-1}\mathbf{m}} \widehat{\mathbf{Q}}_{\mathrm{SMI}}^{-1}\mathbf{m} - \mathbf{m}\right), \tag{19}$$

where the columns of the matrix $\mathbf{X}_\perp$ span the space orthogonal to $[\mathbf{X}, \mathbf{m}]$ and $\mathbf{X}$ is again a unitary $L \times M$ matrix with columns spanning the interference subspace which is assumed to be of dimension M. $\mathbf{C}$ is a directional weighting matrix, $\mathbf{C} = \int_\Omega \mathbf{a}(\mathbf{u})\mathbf{a}(\mathbf{u})^H p(\mathbf{u}) d\mathbf{u}$, Ω denotes the set of directions of interest, and $p(\mathbf{u})$ is a directional weighting function. If we use no directional weighting, $\mathbf{C} \approx \mathbf{I}$, the CAPS weight vector simplifies to

$$\mathbf{w}_{\mathrm{CAPS}} = \mathbf{m} + \mathbf{P}_{[\mathbf{X},\mathbf{m}]}\left(\frac{1}{\mathbf{m}^H \widehat{\mathbf{R}}^{-1}\mathbf{m}} \widehat{\mathbf{Q}}_{\mathrm{SMI}}^{-1}\mathbf{m} - \mathbf{m}\right), \tag{20}$$

where $\mathbf{P}_{[\mathbf{X},\mathbf{m}]}$ denotes the projection onto the space spanned by the columns of $\mathbf{X}$ and $\mathbf{m}$.

4.3. Determination of the Dimension of Jammer Subspace (dimJSS). Subspace methods require an estimate of the dimension of the interference subspace. Usually this is derived from the sample eigenvalues. For complicated scenarios and small sample size, a clear decision of what constitutes a dominant eigenvalue may be difficult. There are two principle approaches to determine the number of dominant eigenvalues, information theoretic criteria and noise power tests.

The information theoretic criteria are often based on the sphericity test criterion; see, for example, [16],

$$T(m) = \frac{(1/(N-m))\sum_{i=m+1}^{N} \lambda_i}{\left(\prod_{i=m+1}^{N} \lambda_i\right)^{1/(N-m)}}, \tag{21}$$

where λ_i denote the eigenvalues of the estimated covariance matrix ordered in decreasing magnitude. The ratio of the arithmetic to geometric mean of the eigenvalues is a measure of the equality of the eigenvalues. The information theoretic criteria minimize this ratio with a penalty function added; for example, the Akaike Information Criterion (AIC) and Minimum Description Length (MDL) choose dimJSS $\widehat{M}$ as the minimum of the following functions:

$$\begin{aligned} \mathrm{AIC}(m) &= K(N-m)\log[T(m)] + m(2N-m) \\ \mathrm{MDL}(m) &= K(N-m)\log[T(m)] + \left(\frac{m}{2}\right)(2N-m)\log K. \end{aligned} \tag{22}$$

The noise power threshold tests (WNT) assume that the noise power σ^2 is known and just check the estimated noise power against this value, [16]. This leads to the statistic

$$L(m) = \frac{2K}{\sigma^2}\sum_{i=m+1}^{N} \lambda_i, \tag{23}$$

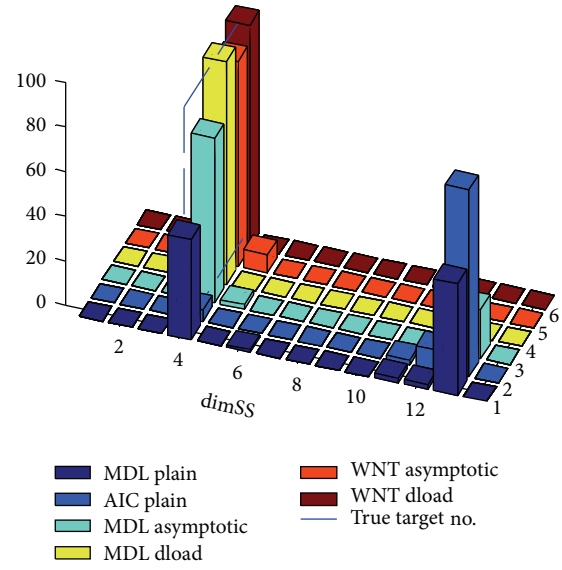

Figure 8: Comparison of tests for linear array with $N = 14$ elements, $K = 14$ snapshots, with and without asymptotic correction or diagonal loading (dload) of $1\sigma^2$.

and the decision is found if the test statistic is for the first time below the threshold:

$$\begin{aligned} &\text{for } i = 1 \cdots N \text{ do} \\ &\quad \text{if } L(m) \le \chi^2_{2K(N-m);\alpha} : \widehat{M} = m;\ \text{STOP}; \\ &\text{end.} \end{aligned} \tag{24}$$

The symbol $\chi^2_{r;\alpha}$ denotes the α-percentage point of the χ^2-distribution with r degrees of freedom. The probability to overestimate dimJSS is then asymptotically bounded by α. More modern versions of this test have been derived, for example, [17].

For small sample size, AIC and MDL are known for grossly overestimating the number of sources. In addition, bandwidth and array channels errors lead to a leakage of the dominant eigenvalues into the small eigenvalues, [18]. Improved eigenvalue estimates for small sample size can mitigate this effect. The simplest way could be to use the asymptotic approximation using the well-known linkage factors, [19],

$$\widehat{\widehat{\lambda}}_i = \widehat{\lambda}_i - \frac{1}{K}\widehat{\lambda}_i \sum_{\substack{j=1 \\ j \ne i}}^{N} \frac{\widehat{\lambda}_i}{\widehat{\lambda}_i - \widehat{\lambda}_j}. \tag{25}$$

More refined methods are also possible; see [16]. However, as explained in [16], simple diagonal loading can improve AIC and MDL for small sample size and make these criteria robust against errors. For the WNT this loading is contained in the setting of the assumed noise level σ^2. Figure 8 shows an example of a comparison of MDL and AIC without any corrections, MDL and WNT with asymptotic correction (25), and MDL and WNT with diagonal loading of $\mu = 1\sigma^2$. The

threshold for WNT was set for a probability to overestimate the target number of $\alpha = 10\%$. The scenario consists of four sources at $u = -0.7, -0.55, -0.31, -0.24$ with SNR of 18, 6, 20, 20.4 dB and a uniform linear antenna with 14 elements and 10% relative bandwidth leading to some eigenvalue leakage. Empirical probabilities were determined from 100 Monte Carlo trials. Note that the asymptotic correction seems to work better for WNT than for MDL. With diagonal loading, all decisions with both MDL and WNT were correct (equal to 4).

A more thorough study of the small sample size dimJSS estimation problem considering the "effective number of identifiable signals" has been performed in [20], and a new modified information theoretic criterion has been derived.

5. Parameter Estimation and Superresolution

The objective of radar processing is not to maximize the SNR but to detect targets and determine their parameters. For detection, the SNR is a sufficient statistic (for the likelihood ratio test); that is, if we maximize the SNR we maximize also the probability of detection. Only for these detected targets we have then a subsequent procedure to estimate the target parameters: direction, range, and possibly Doppler. Standard radar processing can be traced back to maximum likelihood estimation of a single target which leads to the matched filter, [21]. The properties of the matched filter can be judged by the beam shape (for angle estimation) and by the ambiguity function (for range and Doppler estimation). If the ambiguity function has a narrow beam and sufficiently low sidelobes, the model of a single target is a good approximation as other targets are attenuated by the sidelobes. However, if we have closely spaced targets or high sidelobes, multiple target models have to be used for parameter estimation. A variety of such estimation methods have been introduced which we term here "superresolution methods." Historically, these methods have often been introduced to improve the limited resolution of the matched filter.

5.1. Superresolution. The resolution limit for classical beamforming is the 3 dB beamwidth. An antenna array provides spatial samples of the impinging wavefronts, and one may define a multitarget model for this case. This opens the possibility for enhanced resolution. These methods have been discussed since decades, and textbooks on this topic are available, for example, [22]. We formulate here the angle parameter estimation problem (spatial domain), but corresponding versions can be applied in the time domain as well. In the spatial domain, we are faced with the typical problems of irregular sampling and subarray processing.

From the many proposed methods, we mention here only some classical methods to show the connections and relationships. We have spectral methods which generate a spiky estimate of the angular spectral density like.

Capon's method:

$$S_{\mathrm{C}}(\mathbf{u}) = \left(\mathbf{a}(\mathbf{u})^H \widehat{\mathbf{R}}_{\mathrm{ML}}^{-1} \mathbf{a}(\mathbf{u})\right)^{-1} \quad \text{with } \widehat{\mathbf{R}}_{\mathrm{ML}} = \frac{1}{K}\sum_{k=1}^{K} \mathbf{z}_k \mathbf{z}_k^H, \tag{26}$$

and MUSIC method (Multiple Signal Classification):

$$S_{\mathrm{MUSIC}}(\mathbf{u}) = \left(\mathbf{a}(\mathbf{u})^H \mathbf{P}^{\perp} \mathbf{a}(\mathbf{u})\right)^{-1}, \tag{27}$$

with $\mathbf{P}^{\perp} = \mathbf{I} - \mathbf{X}\mathbf{X}^H$, and $\mathbf{X}$ spanning the dominant subspace. An LMI-version instead of MUSIC would also be possible. The target directions are then found by the M highest maxima of these spectra (M 1- or 2-dimensional maximizations).

An alternative group of methods are parametric methods, which deliver only a set of "optimal" parameter estimates which explain in a sense the data for the inserted model by M or $2M$ dimensional optimization [21].

Deterministic ML method (complex amplitudes are assumed deterministic):

$$F_{\mathrm{det}}(\boldsymbol{\theta}) = \mathrm{tr}\left(\mathbf{P}_{\mathbf{A}}^{\perp} \widehat{\mathbf{R}}_{\mathrm{ML}}\right), \quad \text{with } \mathbf{P}_{\mathbf{A}}^{\perp} = \mathbf{I} - \mathbf{A}\left(\mathbf{A}^H\mathbf{A}\right)^{-1}\mathbf{A}^H, \quad \mathbf{A} = \left(\mathbf{a}(\mathbf{u}_1), \ldots, \mathbf{a}(\mathbf{u}_M)\right). \tag{28}$$

Stochastic ML method (complex amplitudes are complex Gaussian):

$$F_{\mathrm{sto}}(\boldsymbol{\theta}) = \mathrm{logdet}(\mathbf{R}(\boldsymbol{\theta})) + \mathrm{tr}\left(\mathbf{R}(\boldsymbol{\theta})^{-1} \widehat{\mathbf{R}}_{\mathrm{ML}}\right), \tag{29}$$

where $\mathbf{R}(\boldsymbol{\theta})$ denotes the completely parameterized covariance matrix. A formulation with the unknown directions as the only parameters can be given as

$$F_{\mathrm{sto}}(\boldsymbol{\theta}) = \det\left\{\mathbf{A}(\boldsymbol{\theta})\,\mathbf{B}(\boldsymbol{\theta})\,\mathbf{A}^H(\boldsymbol{\theta}) + \sigma^2(\boldsymbol{\theta})\,\mathbf{I}\right\} \text{ with } \sigma^2(\boldsymbol{\theta}) = \frac{1}{N-M}\,\mathrm{tr}\left\{\mathbf{P}_{\mathbf{A}}^{\perp}\widehat{\mathbf{R}}_{\mathrm{ML}}\right\}, \quad \mathbf{B}(\boldsymbol{\theta}) = \left(\mathbf{A}^H\mathbf{A}\right)^{-1}\mathbf{A}^H\left(\widehat{\mathbf{R}}_{\mathrm{ML}} - \sigma^2(\boldsymbol{\theta})\,\mathbf{I}\right)\mathbf{A}\left(\mathbf{A}^H\mathbf{A}\right)^{-1} \text{ for } \mathbf{A} = \mathbf{A}(\boldsymbol{\theta}). \tag{30}$$

The deterministic ML method has some intuitive interpretations:

(1) $F_{\mathrm{det}}(\boldsymbol{\theta}) = (1/K)\sum_{k=1}^{K} \mathbf{z}_k^H \mathbf{P}_{\mathbf{A}}^{\perp} \mathbf{z}_k = (1/K)\sum_{k=1}^{K} \|\mathbf{P}_{\mathbf{A}}^{\perp}\mathbf{z}_k\|^2 = (1/K)\sum_{k=1}^{K} \|\mathbf{z}_k - \underbrace{\mathbf{A}(\mathbf{A}^H\mathbf{A})^{-1}\mathbf{A}^H\mathbf{z}_k}_{=\hat{\mathbf{b}}}\|^2$, which means that the mean squared residual error after signal extraction is minimized.

(2) $F_{\mathrm{det}}(\boldsymbol{\theta}) = C - \sum_{k=1}^{K} \mathbf{z}_k^H \mathbf{A}(\mathbf{A}^H\mathbf{A})^{-1}\mathbf{A}^H\mathbf{z}_k$, which can be interpreted as maximizing a set of decoupled sum beams $(\mathbf{a}^H(\mathbf{u}_1)\mathbf{z}_{\mathbf{k}}, \ldots, \mathbf{a}^H(\mathbf{u}_M)\mathbf{z}_{\mathbf{k}})$.

(3) $F_{\mathrm{det}}(\boldsymbol{\theta}) = C - \mathbf{a}_{\mathrm{null}}^H \widehat{\mathbf{R}} \mathbf{a}_{\mathrm{null}} / \mathbf{a}_{\mathrm{null}}^H \mathbf{a}_{\mathrm{null}}$ with $\mathbf{a}_{\mathrm{null}} = \mathbf{P}_{\breve{\mathbf{A}}}^{\perp}\mathbf{a}(\mathbf{u})$, where we have partitioned the matrix of steering vectors into $\mathbf{A} = (\mathbf{a}, \breve{\mathbf{A}})$. This property is valid due to the projection decomposition lemma which says that for any partitioning $\mathbf{A} = (\mathbf{F}, \mathbf{G})$ we can write $\mathbf{P}_{\mathbf{A}}^{\perp} = \mathbf{P}_{\mathbf{G}}^{\perp} - \mathbf{P}_{\mathbf{G}}^{\perp}\mathbf{F}(\mathbf{F}^H\mathbf{P}_{\mathbf{G}}^{\perp}\mathbf{F})^{-1}\mathbf{F}^H\mathbf{P}_{\mathbf{G}}^{\perp}$. If we keep the directions in $\breve{\mathbf{A}}$ fixed, this relation says that we have to maximize the scan pattern over $\mathbf{u}$ while the sources in the directions of $\breve{\mathbf{A}}$ are deterministically nulled (see (7)). One can

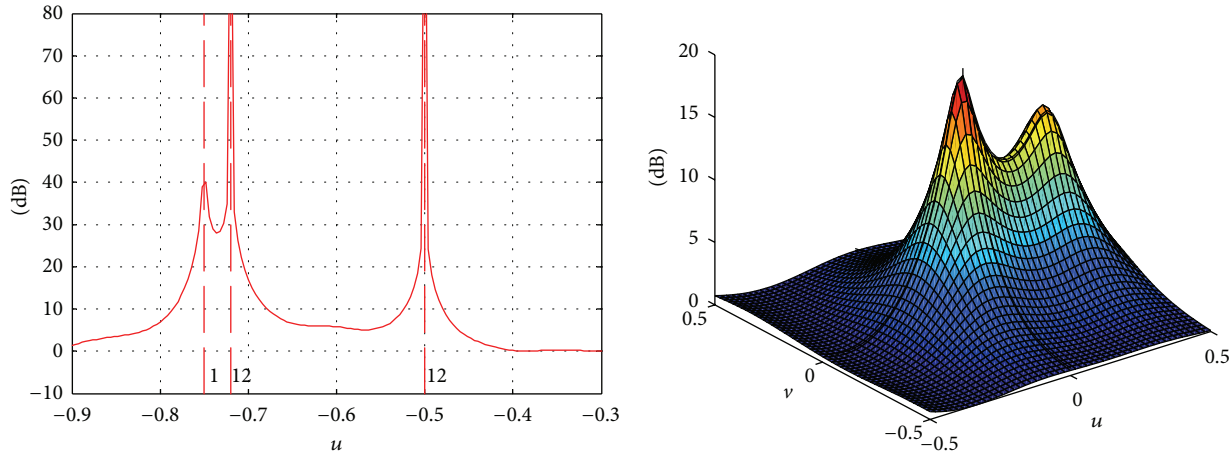

(a) Simulated data

(b) Measured real data

FIGURE 9: MUSIC spectra with a planar array of 7 elements.

now perform the multidimensional maximization by alternating 1-dimensional maximizations and keeping the remaining directions fixed. This is the basis of the alternating projection (AP) method or IMP (Incremental MultiParameter) method, [22, page 105].

A typical feature of the MUSIC method is illustrated in Figure 9. This figure shows the excellent resolution in simulation while for real data the pattern looks almost the same as with Capon's method.

A result with real data with the deterministic ML method is shown in Figure 10. Minimization was performed here with a stochastic approximation method. This example shows in particular that the deterministic ML-method is able to resolve highly correlated targets which arise due to the reflection on the sea surface for low angle tracking. The behavior of the monopulse estimates reflect the variation of the phase differences of direct and reflected path between 0° and 180°. For 0° phase difference the monopulse points into the centre, for 180° it points outside the 2-target configuration.

The problems of superresolution methods are described in [21, 23]. A main problem is the numerical effort of finding the M maxima (one M-dimensional optimization or M 1-dimensional optimizations for a linear antenna). To mitigate this problem a stochastic approximation algorithm or the IMP method has been proposed for the deterministic ML method. The IMP method is an iteration of maximizations of an adaptively formed beam pattern. Therefore, the generalized monopulse method can be used for this purpose, see Section 7.1 and [24].

Another problem is the exact knowledge of the signal model for all possible directions (the vector function $\mathbf{a}(\mathbf{u})$). The codomain of this function is sometimes called the array manifold. This is mainly a problem of antenna accuracy or calibration. While the transmission of a plane wave in the main beam direction can be quite accurately modeled (using calibration) this can be difficult in the sidelobe region.

For an array with digital subarrays, superresolution has to be performed only with these subarray outputs. The array manifold has then to be taken at the subarray outputs as in (2). This manifold (the subarray patterns) is well modeled in the main beam region but often too imprecise in the sidelobe region to obtain a resolution better than the conventional. In that case it is advantageous to use a simplified array manifold model based only on the subarray gains and centers, called the Direct Uniform Manifold model (DUM). This simplified model has been successfully applied to MUSIC (called Spotlight MUSIC, [25]) and to the deterministic ML method. Using the DUM model requires little calibration effort and gives improved performance, [25].

More refined parametric methods with higher asymptotic resolution property have been suggested (e.g., COMET, Covariance Matching Estimation Technique, [26]). However, application of such methods to real data often revealed no improvement (as is the case with MUSIC in Figure 9). The reason is that these methods are much more sensitive to the signal model than the accuracy of the system provides. A sensitivity with an very sharp ideal minimum of the objective function may lead to a measured data objective function where the minimum has completely disappeared.

5.2. Target Number Determination. Superresolution is a combined target number and target parameter estimation problem. As a starting point all the methods of Section 4.3 can be used. If we use the detML method we can exploit that the objective function can be interpreted as the residual error between model (interpretation 2) and data. The WNT test statistic (23) is just an estimate of this quantity. The detML residual can therefore be used for this test instead of the sum of the eigenvalues.

These methods may lead to a possibly overestimated target number. To determine the power allocated to each target a refined ML power estimate using the estimated directions $\mathbf{A}(\boldsymbol{\theta})$ can be used $\mathbf{B}(\boldsymbol{\theta}) = (\mathbf{A}^H\mathbf{A})^{-1}\mathbf{A}^H(\widehat{\mathbf{R}}_{\mathrm{ML}} - \sigma^2(\boldsymbol{\theta})\mathbf{I})\mathbf{A}(\mathbf{A}^H\mathbf{A})^{-1}$ with $\sigma^2(\boldsymbol{\theta}) = (1/(N-M))\,\mathrm{tr}\{\mathbf{P}_{\mathbf{A}}^{\perp}\widehat{\mathbf{R}}_{\mathrm{ML}}\}$ as in (30). This estimate can even reveal correlations between the targets. This has been successfully demonstrated with

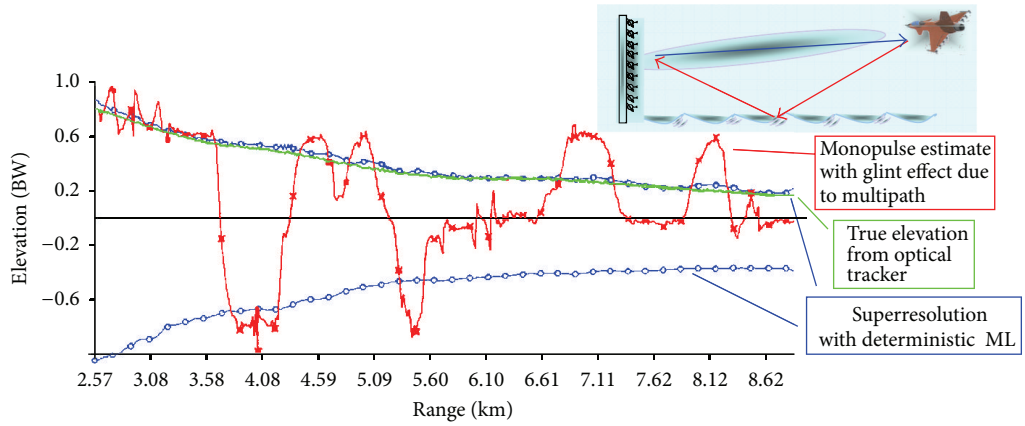

FIGURE 10: Superresolution of multipath propagation over sea with deterministic ML method (real data from vertical linear array with 32 elements, scenario illustrated above).

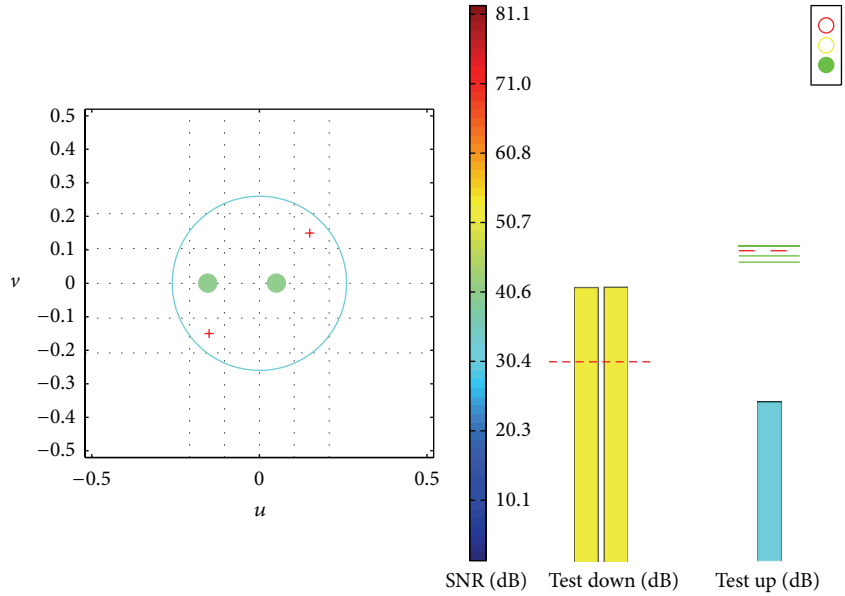

FIGURE 11: Combined target number and direction estimation for 2 targets with 7-element planar array.

the low angle tracking data of Figure 10. In case that some target power is too low, the target number can be reduced and the angle estimates can be updated. This is an iterative procedure of target number estimation and confirmation or reduction. This way, all target modeling can be accurately matched to the data.

The deterministic ML method (28) together with the white noise test (24) is particularly suited for this kind of iterative model fitting. It has been implemented in an experimental system with a 7-element planar array at Fraunhofer FHR and was first reported in [21, page 81]. An example of the resulting output plot is shown in Figure 11. The estimated directions in the u, v-plane are shown by small dishes having a color according to the estimated target SNR corresponding to the color bar. The circle indicates the 3 dB contour of the sum beam. One can see that the two targets are at about 0.5 beamwidth separation. The directions were estimated by the stochastic approximation algorithm used in Figure 10. The test statistic for increasing the target number is shown by the right most bar. The thresholds for increasing the number are indicated by lines. The dashed line is the actually valid threshold (shown is the threshold for 2 targets). The target number can be reduced if the power falls below a threshold shown in two yellow bars in the middle. The whole estimation and testing procedure can also be performed adaptively with changing target situations. We applied it to two blinking targets alternating between the states "target 1 on", "both targets on", "target 2 on", "both targets on", and so forth. Clearly, these test works only if the estimation procedure has converged. This is indicated by the traffic light in the right up corner. We used a fixed empirically determined iteration number to switch the test procedure on (=green traffic light).

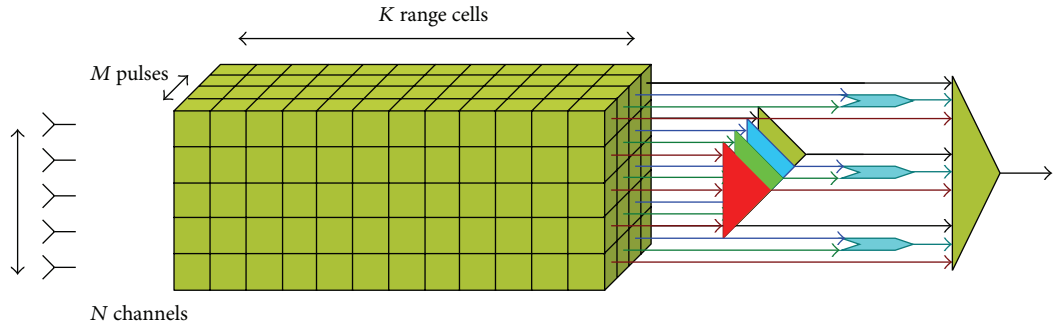

Figure 12: Symmetric auxiliary sensor/echo processor of Klemm [4], as an example for forming space-time subarrays.

All thresholds and iteration numbers have to be selected carefully. Otherwise, situations may arise where this adaptive procedure switches between two target models, for example, between 2 and 3 targets.

The problem of resolution of two closely spaced targets becomes a particular problem in the so called threshold region, which denotes configurations where the SNR or the separation of the targets lead to an angular variance departing significantly from the Cramer-Rao bound (CRB). The design of the tests and this threshold region must be compatible to give consistent joint estimation-detection resolution result. These problems have been studied in [27, 28]. One way to achieve consistency and improving resolution proposed in [27] is to detect and remove outliers in the data, which are basically responsible for the threshold effect. A general discussion about the achievable resolution and the best realistic representation of a target cluster can be found in [28].

6. Extension to Space-Time Arrays

As mentioned in Section 2.4, there is mathematically no difference between spatial and temporal samples as long as the distributional assumptions are the same. The adaptive methods and superresolution methods presented in the previous sections can therefore be applied analogously in the time or space-time domain.

In particular, subarraying in time domain is an important tool to reduce the numerical complexity for space-time adaptive processing (STAP) which is the general approach for adaptive clutter suppression for airborne radar, [4]. With the formalism of transforming space-time 2D-beamforming of a data matrix into a usual beamforming operation of vectors introduced in (4), the presented adaptive beamforming and superresolution methods can be easily transformed into corresponding subarrayed space-time methods.

Figure 12 shows an example of an efficient space-time subarraying scheme used for STAP clutter cancellation for airborne radar.

7. Embedding of Array Processing into Full Radar Data Processing

A key problem that has to be recognized is that the task of a radar is not to maximize the SNR, but to give the best relevant information about the targets after all processing. This means that for implementing refined methods of interference suppression or superresolution we have also to consider the effect on the subsequent processing. To get optimum performance all subsequent processing should exploit the properties of the refined array signal processing methods applied before. In particular it has been shown that for the tasks of detection, angle estimation and tracking significant improvements can be achieved by considering special features.

7.1. Adaptive Monopulse. Monopulse is an established technique for rapid and precise angle estimation with array antennas. It is based on two beams formed in parallel, a sum beam and a difference beam. The difference beam is zero at the position of the maximum of the sum beam. The ratio of both beams gives an error value that indicates the offset of a target from the sum beam pointing direction. In fact, it can be shown that this monopulse estimator is an approximation of the Maximum-Likelihood angle estimator, [24]. The monopulse estimator has been generalized in [24] to arrays with arbitrary subarrays and arbitrary sum and difference beams.

When adaptive beams are used the shape of the sum beam will be distorted due to the interference that is to be suppressed. The difference beam must adaptively suppress the interference as well, which leads to another distortion. Then the ratio of both beams will no more indicate the target direction. The generalized monopulse procedure of [24] provides correction values to compensate these distortions.

The generalized monopulse formula for estimating angles $(\widehat{u}, \widehat{v})^T$ with a planar array and sum and difference beams formed into direction $(u_0, v_0)^T$ is

$$\begin{pmatrix} \widehat{u} \\ \widehat{v} \end{pmatrix} = \begin{pmatrix} u_0 \\ v_0 \end{pmatrix} - \begin{pmatrix} c_{xx} & c_{xy} \\ c_{yx} & c_{yy} \end{pmatrix} \begin{pmatrix} R_x - \mu_x \\ R_y - \mu_y \end{pmatrix}, \tag{31}$$

where $\mathbf{C} = \begin{pmatrix} c_{xx} & c_{xy} \\ c_{yx} & c_{yy} \end{pmatrix}$ is a slope correction matrix and $\boldsymbol{\mu} = \begin{pmatrix} \mu_x \\ \mu_y \end{pmatrix}$ is a bias correction. $R_x = \mathrm{Re}\{\mathbf{d}_x^H \mathbf{z} / \mathbf{w}^H \mathbf{z}\}$ is the monopulse ratio formed with the measured difference and sum beam outputs $D_x = \mathbf{d}_x^H \mathbf{z}$ and $S = \mathbf{w}^H \mathbf{z}$, respectively, with difference and sum beam weight vectors $\mathbf{d}_x$, $\mathbf{w}$ (analogous for elevation estimation with $\mathbf{d}_y$). The monopulse ratio is a function of the unknown target directions (u, v). Let the vector of monopulse ratios be denoted by $\mathbf{R}(u, v) = (R_x(u, v), R_y(u, v))^T$. The correction quantities are determined such that the expectation

of the error is unbiased and a linear function with slope 1 is approximated. More precisely, for the following function of the unknown target direction:

$$\mathbf{M}(u,v) = \mathbf{C}\cdot\left(E\left\{\mathbf{R}(u,v)\right\} - \boldsymbol{\mu}\right), \tag{32}$$

we require

$$\mathbf{M}(u_0,v_0) = \mathbf{0},$$
$$\frac{\partial \mathbf{M}}{\partial u}(u_0,v_0) = \begin{pmatrix}1\\0\end{pmatrix}, \qquad \frac{\partial \mathbf{M}}{\partial v}(u_0,v_0) = \begin{pmatrix}0\\1\end{pmatrix} \text{ or} \tag{33}$$
$$\mathbf{C}\left(\frac{\partial \mathbf{R}}{\partial u} \quad \frac{\partial \mathbf{R}}{\partial v}\right)(u_0,v_0) = \mathbf{I}.$$

These conditions can only approximately be fulfilled for sufficiently high SNR. Then, one obtains for the bias correction for a pointing direction $\mathbf{a}_0 = \mathbf{a}(u_0,v_0)$, [24]

$$\mu_\alpha = \operatorname{Re}\left\{\frac{\mathbf{d}_\alpha^H \mathbf{a}_0}{\mathbf{w}^H \mathbf{a}_0}\right\} \quad \text{for } \alpha = x, y. \tag{34}$$

For the elements of the inverse slope correction matrix $(c^{\alpha,h})_{\substack{a=x,y\\h=u,v}} = \mathbf{C}^{-1}$, one obtains

$$c^{\alpha,h} = \frac{\operatorname{Re}\left\{\mathbf{d}_\alpha^H \mathbf{a}_{h,0}\mathbf{a}_0^H\mathbf{w} + \mathbf{d}_\alpha^H \mathbf{a}_0\mathbf{a}_{h,0}^H\mathbf{w}\right\}}{\left|\mathbf{w}^H\mathbf{a}_0\right|^2} - \mu_a 2\operatorname{Re}\left\{\frac{\mathbf{w}^H\mathbf{a}_{h,0}}{\mathbf{w}^H\mathbf{a}_0}\right\} \tag{35}$$

with $\alpha = x$ or y and $h = u$ or v, and $\mathbf{a}_{h,0}$ denotes the derivative $(\partial\mathbf{a}/\partial h)|_{(u_0,v_0)}$. In general, these are fixed antenna determined quantities. For example, for omnidirectional antenna elements, and phase steering at the elements we have $\mathbf{a}_0 = G_e(1,\ldots,1)^T$, where G_e is the antenna element gain, and $\mathbf{a}_{u,0}^T = G_e(j2\pi f/c)(x_1,\ldots,x_N)$.

It is important to note that this formula is independent of any scaling of the difference and sum weights. Constant factors in the difference and sum weight will be cancelled by the corresponding slope correction. Figure 13 shows theoretically calculated bias and variances for this corrected generalized monopulse using the formulas of [24] for the array of Figure 2. The biases are shown by arrows for different possible single target positions with the standard deviation ellipses at the tip. A jammer is located in the asterisk symbol direction with JNR = 27 dB. The hypothetical target has a SNR of 6 dB. The 3 dB contour of the unadapted sum beam is shown by a dashed circle. The 3 dB contour of the adapted beam will be of course different. One can see that in the beam pointing direction (0, 0) the bias is zero and the variance is small. The errors increase for target directions on the skirt of the main beam and close to the jammer.

The large bias may not be satisfying. However, one may repeat the monopulse procedure by repeating the monopulse estimate with a look direction steered at subarray level into the new estimated direction. This is an all-offline procedure with the given subarray data. No new transmit pulse is needed. We have called this the multistep monopulse procedure [24]. Multistep monopulse reduces the bias considerably

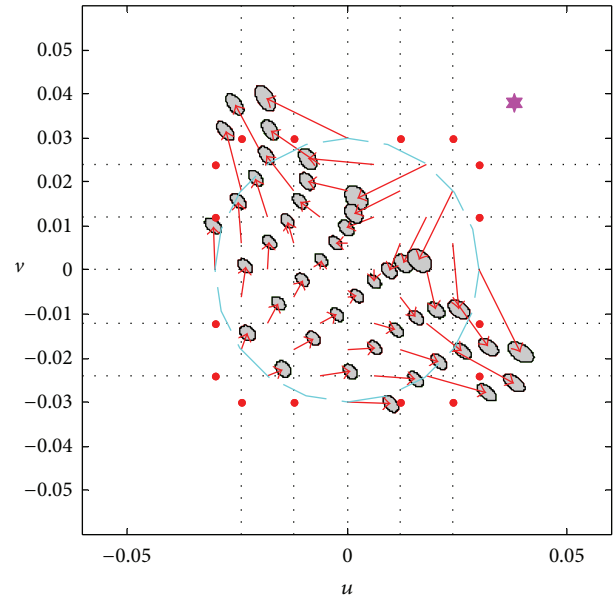

Figure 13: Bias and standard deviation ellipses for different target positions.

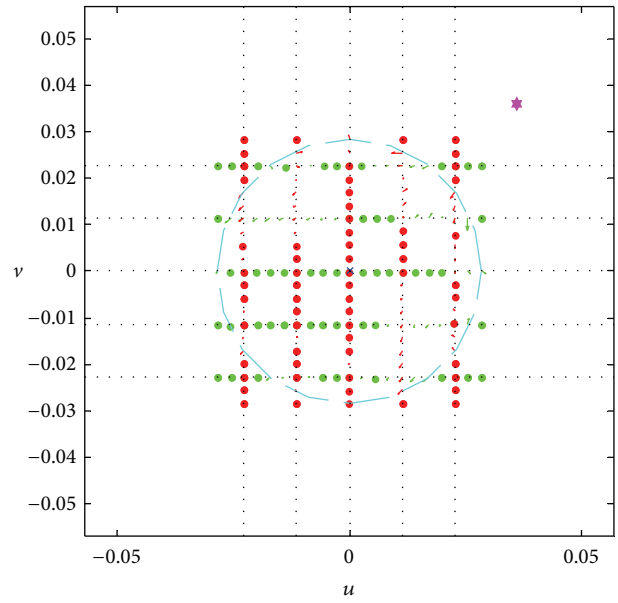

Figure 14: Bias for 2-step monopulse for different target positions and jammer scenario of Figure 13.

with only one additional iteration as shown in Figure 14. The variances appearing in Figure 13 are virtually not changed with the multistep monopulse procedure and are omitted for better visibility.

7.2. Adaptive Detection. For detection with adaptive beams, the normal test procedure is not adequate because we have a test statistic depending on two different kinds of random data: the training data for the adaptive weight and the data under test. Various kinds of tests have been developed accounting

for this fact. The first and basic test statistics were the GLRT, [29], the AMF detector, [30], and the ACE detector, [31]. These have the form

$$T_{\mathrm{GLRT}}(\widetilde{\mathbf{z}}) = \frac{\left|\widetilde{\mathbf{a}}_0^H \widehat{\mathbf{Q}}_{\mathrm{SMI}}^{-1} \widetilde{\mathbf{z}}\right|^2}{\widetilde{\mathbf{a}}_0^H \widehat{\mathbf{Q}}_{\mathrm{SMI}}^{-1} \widetilde{\mathbf{a}}_0 \left(1 + (1/K)\, \widetilde{\mathbf{z}}^H \widehat{\mathbf{Q}}_{\mathrm{SMI}}^{-1} \widetilde{\mathbf{z}}\right)}, \tag{36}$$

$$T_{\mathrm{AMF}}(\widetilde{\mathbf{z}}) = \frac{\left|\widetilde{\mathbf{a}}_0^H \widehat{\mathbf{Q}}_{\mathrm{SMI}}^{-1} \widetilde{\mathbf{z}}\right|^2}{\widetilde{\mathbf{a}}_0^H \widehat{\mathbf{Q}}_{\mathrm{SMI}}^{-1} \widetilde{\mathbf{a}}_0}, \tag{37}$$

$$T_{\mathrm{ACE}}(\widetilde{\mathbf{z}}) = \frac{\left|\widetilde{\mathbf{a}}_0^H \widehat{\mathbf{Q}}_{\mathrm{SMI}}^{-1} \widetilde{\mathbf{z}}\right|^2}{\widetilde{\mathbf{a}}_0^H \widehat{\mathbf{Q}}_{\mathrm{SMI}}^{-1} \widetilde{\mathbf{a}}_0 \cdot \widetilde{\mathbf{z}}^H \widehat{\mathbf{Q}}_{\mathrm{SMI}}^{-1} \widetilde{\mathbf{z}}}. \tag{38}$$

The quantities $\widetilde{\mathbf{z}}$, $\widetilde{\mathbf{a}}_0$, $\widehat{\mathbf{Q}}$ are here all generated at the subarray outputs, $\widetilde{\mathbf{a}}_0$ denotes the plane wave model for a direction $\mathbf{u}_0$.

Basic properties of these tests are

$$\text{(i)} \quad T_{\mathrm{GLRT}} = \frac{T_{\mathrm{AMF}}}{1 + (1/K)\, \widetilde{\mathbf{z}}^H \widehat{\mathbf{Q}}_{\mathrm{SMI}}^{-1} \widetilde{\mathbf{z}}}, \qquad T_{\mathrm{ACE}} = \frac{T_{\mathrm{AMF}}}{\widetilde{\mathbf{z}}^H \widehat{\mathbf{Q}}_{\mathrm{SMI}}^{-1} \widetilde{\mathbf{z}}}. \tag{39}$$

(ii) The AMF detector represents an estimate of the signal-to-noise ratio because it can be written as

$$T_{\mathrm{AMF}} = \frac{\left|\widetilde{\mathbf{w}}^H \widetilde{\mathbf{z}}\right|^2}{\widetilde{\mathbf{w}}^H \widehat{\mathbf{Q}}_{\mathrm{SMI}} \widetilde{\mathbf{w}}} \quad \text{with } \widetilde{\mathbf{w}} = \widehat{\mathbf{Q}}_{\mathrm{SMI}}^{-1} \widetilde{\mathbf{a}}_0. \tag{40}$$

This provides a meaningful physical interpretation. A complete statistical description of these tests has been given in very compact form in [32, 33]. These results are valid as well for planar arrays with irregular subarrays and also mismatched weighting vector.

Actually, all these detectors use the adaptive weight of the SMI algorithm which has unsatisfactory performance as mentioned in Section 4.2. The unsatisfactory finite sample performance is just the motivation for introducing weight estimators like LSMI, LMI, or CAPS. Clutter, insufficient adaptive suppression and surprise interference are the motivation for requiring low sidelobes. Recently several more complicated adaptive detectors have been introduced with the aim of achieving additional robustness properties, [34–38]. However, another and quite simple way would be to generalize the tests of (36), (37), (38) to arbitrary weight vectors with the aim of inserting well known robust weights as derived in Section 4.1. This has been done in [39]. First, we observe that the formulation of (40) can be used for any weight vector. Second, one can observe that the ACE and GLRT have the form of a sidelobe blanking device. In particular it has already been shown in [35] that diagonal loading provides significant better detection performance.

A guard channel is implemented in radar systems to eliminate impulsive interference (hostile or from other neighboring radars) using the sidelobe blanking (SLB) device. The guard channel receives data from an omnidirectional antenna element which is amplified such that its power level is above the sidelobe level of the highly directional radar antenna, but below the power of the radar main beam, [1, page 9.9]. If the received signal power in the guard channel is above the power of the main channel, this must be a signal coming via the sidelobes. Such signals will be blanked. If the guard channel power is below the main channel power it is considered as a detection.

With phased arrays it is not necessary to provide an external omnidirectional guard channel. Such a channel can be generated from the antenna itself; all the required information is in the antenna. We may use the noncoherent sum of the subarrays as guard channel. This is the same as the average omnidirectional power. Some shaping of the guard pattern can be achieved by using a weighting for the noncoherent sum:

$$G = \sum_{i=1}^{L} \widetilde{g}_i |\widetilde{z}_i|^2. \tag{41}$$

If all subarrays are equal, a uniform weighting $\widetilde{\mathbf{g}} = (1, \ldots, 1)^T$ may be suitable; for unequal irregular subarrays as in Figure 2 the different contributions of the subarrays can be weighted. The directivity pattern of such guard channel is given by $S_G(\mathbf{u}) = \sum_{i=1}^{L} \widetilde{g}_i |\widetilde{a}_i(\mathbf{u})|^2$. More generally, we may use a combination of noncoherent and coherent sums of the subarrays with weights contained in the matrices $\mathbf{D}$, $\mathbf{K}$, respectively,

$$G = \widetilde{\mathbf{z}}^H \mathbf{K}\mathbf{D}\mathbf{K}^H \widetilde{\mathbf{z}}, \qquad S_G(\mathbf{u}) = \widetilde{\mathbf{a}}^H(\mathbf{u})\, \mathbf{K}\mathbf{D}\mathbf{K}^H \widetilde{\mathbf{a}}(\mathbf{u}). \tag{42}$$

Examples of such kind of guard channels are shown in Figure 15 for the generic array of Figure 2 with −35 dB Taylor weighing for low sidelobes. The nice feature of these guard channels is (i) that they automatically scan together with the antenna look direction, and (ii) that they can easily be made adaptive. This is required if we want to use the SLB device in the presence of CW plus impulsive interference. A CW jammer would make the SLB blank all range cells, that is, would just switch off the radar. To generate an adaptive guard channel we only have to replace in (42) the data vector of the cell under test (CUT) by the pre-whitened data $\widetilde{\mathbf{z}}_{\text{pre-}w} = \widehat{\mathbf{R}}^{-1/2} \widetilde{\mathbf{z}}$. Then, the test statistic can be written as $T = T_{\mathrm{AMF}}(\widetilde{\mathbf{z}})/G_{\mathrm{adapt}}(\widetilde{\mathbf{z}})$, where $G_{\mathrm{adapt}}(\widetilde{\mathbf{z}}) = \widetilde{\mathbf{z}}^H \widehat{\mathbf{R}}^{-1} \widetilde{\mathbf{z}}$ for ACE and $G_{\mathrm{adapt}}(\widetilde{\mathbf{z}}) = 1 + (1/K) \widetilde{\mathbf{z}}^H \widehat{\mathbf{R}}^{-1} \widetilde{\mathbf{z}}$ for GLRT. Hence G_{adapt} is just the incoherent sum of the pre-whitened subarray outputs; in other words, T_{ACE} can be interpreted as an AMF detector with an adaptive guard channel and T_{GLRT} the same with guard channel on a pedestal. Figure 16 shows examples of some adapted guard channels generated with the generic array of Figure 2 and −35 dB Taylor weighting. The unadapted patterns are shown by dashed lines.

This is the adaptive generalization of the usual sidelobe blanking device (SLB) and the AMF, ACE and GLRT tests can be used as extension of the SLB detector to the adaptive case, [32], called the 2D adaptive sidelobe blanking (ASB) detector. The AMF is then the test for the presence of a potential target and the generalized ACE or GRLT are used confirming this target or adaptive sidelobe blanking.

A problem with these modified tests is to define a suitable threshold for detection. For arbitrary weight vector it is nearly impossible to determine this analytically. In [39] the detection

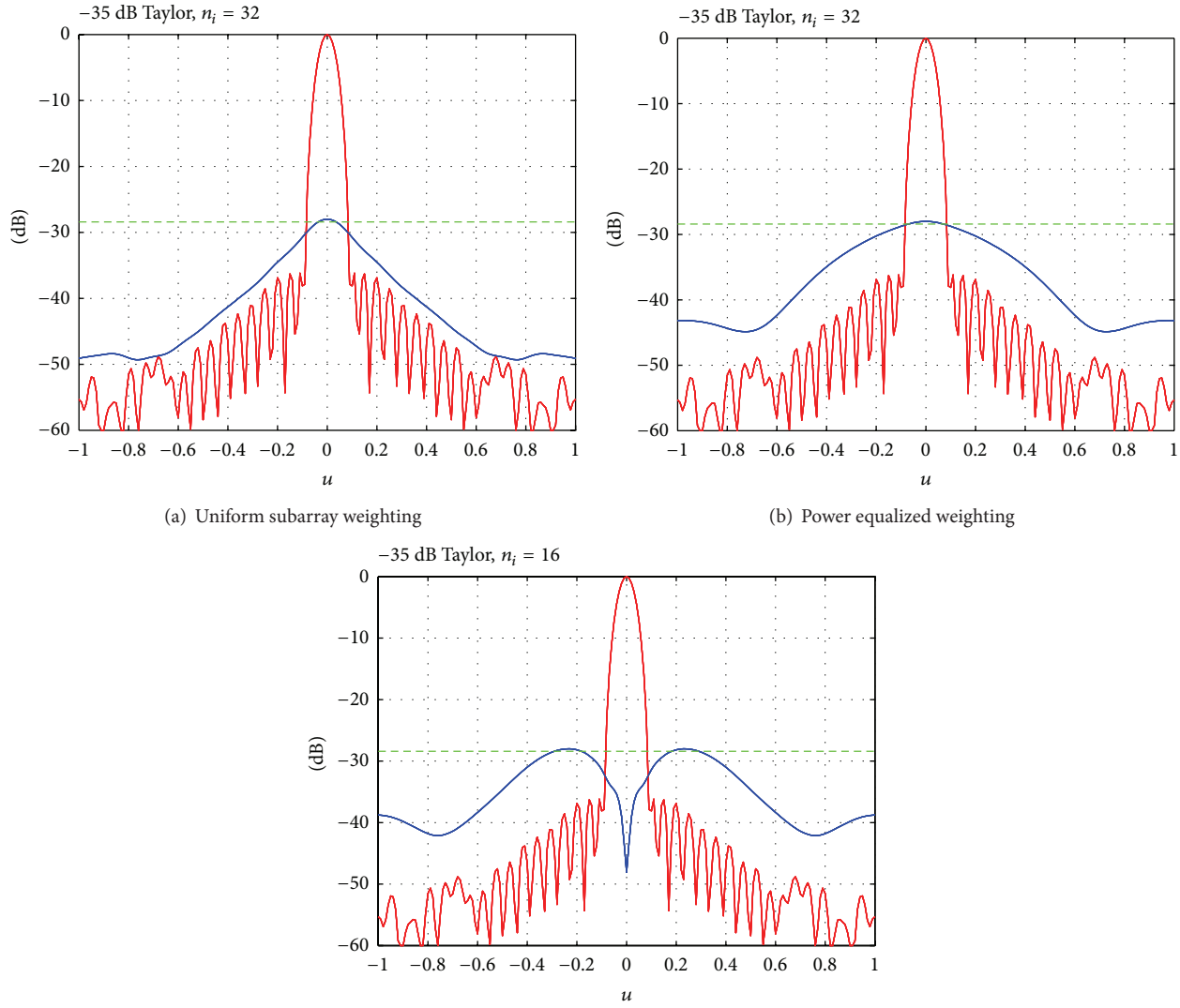

(a) Uniform subarray weighting

(b) Power equalized weighting

(c) Power equalized + difference weighting

FIGURE 15: Guard channel and sum beam patterns for generic array of Figure 2.

margin has been introduced as an empirical tool for judging a good balance between the AMF and ASB threshold for given jammer scenarios. The detection margin is defined as the difference between the expectation of the AMF statistic and the guard channel, where the expectation is taken only over the interference complex amplitudes for a known interference scenario. In addition one can also calculate the standard deviation of these patterns. The performance against jammers close to the main lobe is the critical feature. The detection margin provides the mean levels together with standard deviations of the patterns. An example of the detection margin is shown in Figure 17 (same antenna and weighting as in Figures 15 and 16).

Comparing the variances of the ACE and GLRT guard channels in [39] revealed that the GLRT guard performs significantly better in terms of fluctuations. The GLRT guard channel may therefore be preferred for its better sidelobe performance and higher statistical stability.

7.3. Adaptive Tracking. A key feature of ABF is that overall performance is dramatically influenced by the proximity of the main beam to an interference source. The task of target tracking in the proximity of a jammer is of high operational relevance. In fact, the information on the jammer direction can be made available by a jammer mapping mode, which determines the direction of the interferences by a background procedure using already available data. Jammers are typically strong emitters and thus easy to detect. In particular, the Spotlight MUSIC method [25] working with subarray outputs is suited for jammer mapping with a multifunction radar.

Let us assume here for simplicity that the jammer direction is known. This is highly important information for the tracking algorithm of a multifunction radar where the tracker determines the pointing direction of the beam. We will use for angle estimation the adaptive monopulse procedure of Section 7.1. ABF will form beams with a notch in the jammer direction. Therefore one cannot expect target echoes from

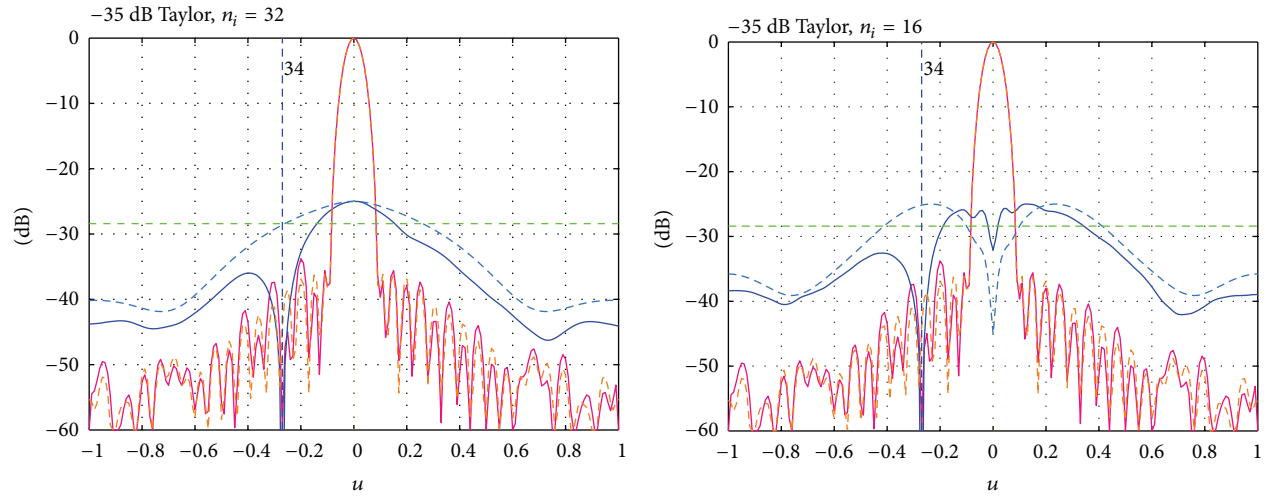

(a) Weighting for equal subarray power

(b) Difference type guard with weighting for equal subarray power

FIGURE 16: Adapted guard patterns for jammer at $u = -0.27$ (-15.7°) with JNR of 34 dB for generic array.

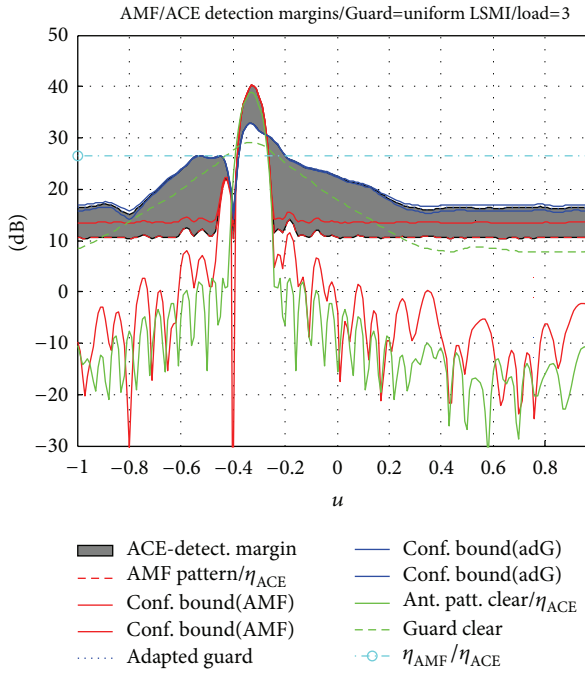

FIGURE 17: Detection margin (gray shading) between AMF and nonweighted adapted guard pattern with confidence bounds for ACE with LSMI (64 snapshots and $3\sigma^2$ diagonal loading). Two CW interferences of 40 dB INR are present at $u = -0.8, -0.4$.

directions close to the jammer and therefore it does not make sense to steer the beam into the jammer notch. Furthermore, in the case of a missing measurement of a tracked target inside the jammer notch, the lack of a successful detection supports the conclusion that this negative contact is a direct result of jammer nulling by ABF. This is so-called negative information [40]. In this situation we can use the direction of the jammer as a pseudomeasurement to update and maintain the track file. The width of the jammer notch defines the uncertainty of this pseudo measurement. Moreover, if one knows the jammer direction one can use the theoretically calculated variances for the adaptive monopulse estimate of [24] as a priori information in the tracking filter. The adaptive monopulse can have very eccentric uncertainty ellipses as shown in Figure 13 which is highly relevant for the tracker. The large bias appearing in Figure 13, which is not known by the tracker, can be reduced by applying the multistep monopulse procedure, [24].

All these techniques have been implemented in a tracking algorithm and refined by a number of stabilization measures in [41]. The following special measures for ABF tracking have been implemented and are graphically visualized in Figure 18.

(i) Look direction stabilization: the monopulse estimate may deliver measurements outside of the 3 dB contour of the sum beam. Such estimates are also heavily biased, especially for look directions close to the jammer, despite the use of the multistep monopulse procedure. Estimates of that kind are therefore corrected by projecting them onto the boundary circle of sum beam contour.

(ii) Detection threshold: only those measurements are considered in the update step of the tracking algorithm whose sum beam power is above a certain detection threshold (typically 13 dB). This guarantees useful and valuable monopulse estimates. It is well known that the variance of the monopulse estimate decreases monotonically with this threshold increasing.

(iii) Adjustment of antenna look direction: look directions in the jammer notch should generally be avoided due to the expected lack of good measurements. In case that the proposed look direction lies in the jammer notch, we select an adjusted direction on the skirt of the jammer notch.

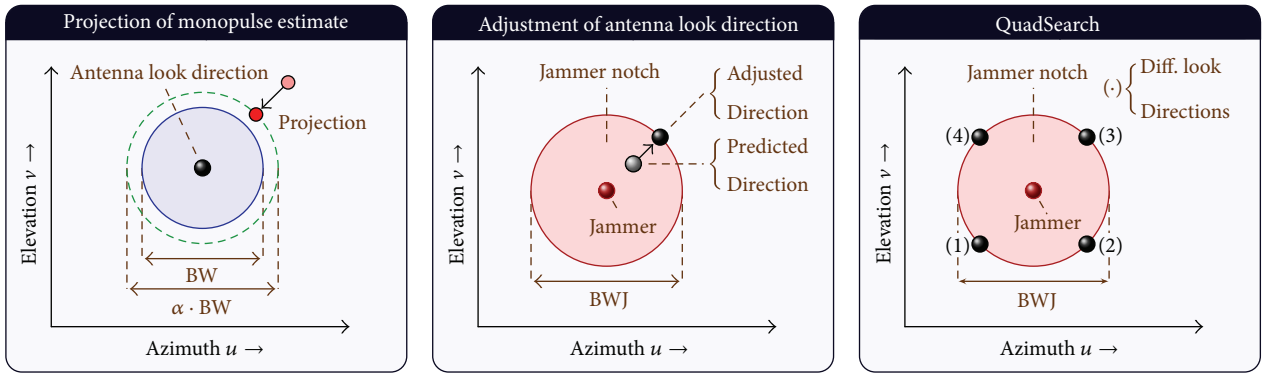

FIGURE 18: Illustration of different stabilization measures to improve track stability and track continuity.

(iv) Variable measurement covariance: a variable covariance matrix of the adaptive monopulse estimation according to [24] is considered only for a mainlobe jammer situation. For jammers in the sidelobes, there is little effect on the angle estimates, and we can use the fixed covariance matrix of the nonjammed case.

(v) QuadSearch and Pseudomeasurements: if the predicted target direction lies inside the jammer notch and if, despite all adjustments of the antenna look direction, the target is not detected, a specific search pattern is initiated (named QuadSearch) which uses look directions on the skirt of the jammer notch to obtain acceptable monopulse estimates. If this procedure does not lead to a detection, we know that the target is hidden in the jammer notch and we cannot see it. We use then the direction of the jammer as a pseudobearing measurement to maintain the track file. The pseudomeasurement noise is determined by the width of the jammer notch.

(vi) LocSearch: in case of a permanent lack of detections (e.g., for three consecutive scans) while the track position lies outside the jammer notch, a specific search pattern is initiated (named LocSearch) that is similar to the QuadSearch. The new look directions lie on the circle of certain radius around the predicted target direction.

(vii) Modeling of target dynamics: the selection of a suitable dynamics model plays a major role for the quality of tracking results. In this context, the so-called interacting multiple model (IMM) is a well-known method to reliably track even those objects whose dynamic behavior remains constant only during certain periods.

(viii) Gating: in the vicinity of the jammer, the predicted target direction (as an approximation of the true value) is used to compute the variable angle measurement covariance. Strictly speaking, this is only valid exactly in the particular look direction. Moreover, the tracking algorithm regards all incoming sensor data as unbiased measurements. To avoid track instabilities, an acceptance region is defined for each measurement depending on the predicted target state and the assumed measurement accuracy. Sensor reports lying outside this gate are considered as invalid.

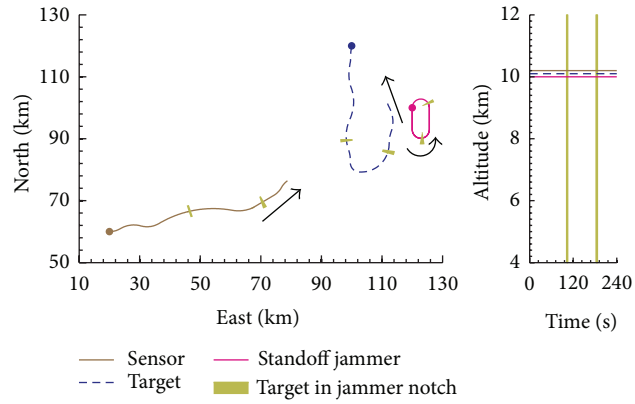

FIGURE 19: Target tracking scenario with standoff jammer: geographic plot of platform trajectories.

In order to evaluate our stabilization measures we considered a realistic air-to-air target tracking scenario [41]. Figure 19 provides an overview of the different platform trajectories. In this scenario, the sensor (on a forward looking radar platform flying with a constant speed of 265 m/s) employs the antenna array of Figure 2 (sum beamwidth BW = 3.4°, field of view 120°, scan interval 1 s) and approaches the target (at velocity 300 m/s), which thereupon veers away after a short time. During this time, the target is hidden twice in the jammer notch of the standoff jammer (SOJ)—first for 3 s and then again for 4 s. The SOJ is on patrol (at 235 m/s) and follows a predefined race track at constant altitude. Figure 20 shows exemplary the evaluation of the azimuth measurements and estimates over time in a window where the target first passes through the jammer notch. The different error bars of a single measurement illustrate the approximation error of the variable measurement covariance: $\sigma_{u_k}^{\mathrm{SIM}}$

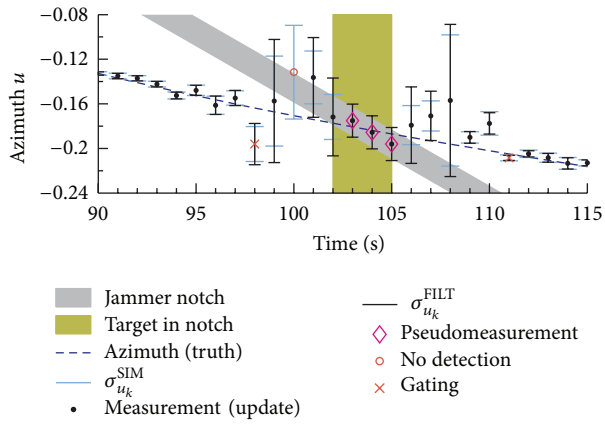

FIGURE 20: Exemplary azimuth measurements and models for a specific time window for tracking scenario of Figure 19.

denotes the true azimuth standard deviation (std) which is generated in the antenna simulation; $\sigma_{u_k}^{FILT}$ corresponds to the std which is used in the tracking algorithm. More precisely, the tracking program computes the adaptive angle measurement covariance only in the vicinity of the jammer with a diameter of this zone of 8.5°. Outside of this region, the tracking algorithm uses a constant std of 0.004 for both components of the angle measurement. The constant std for the other parameters are 75 m and 7.5 m/s for range and range-rate measurements. The signal-to-noise and jammer-to-noise ratios were set to 26 dB and 27 dB at a reference range of 70 km. From Figure 20 the benefits of using pseudobearing measurements become apparent.

From these investigations, it turned out that tracking only with adaptive beamforming and adaptive monopulse nearly always leads to track loss in the vicinity of the jammer. With additional stabilization measures that did not require the knowledge of the jammer direction (projection of monopulse estimate, detection threshold, LocSearch, gating) still track instabilities occurred culminating finally in track loss. An advanced tracking version which used pseudomeasurements mitigated this problem to some degree. Finally, the additional consideration of the variable measurement covariance with a better estimate of the highly variable shape of the angle uncertainty ellipse resulted in significantly fewer measurements that were excluded due to gating. In this case all the stabilization measures could not only improve track continuity, but also track accuracy and thus track stability, [41]. This tells us that it is absolutely necessary to use all information of the adaptive process for the tracker to achieve the goal of detection and tracking in the vicinity of the interference.

8. Conclusions and Final Remarks

In this paper, we have pointed out the links between array signal processing and antenna design, hardware constraints and target detection, and parameter estimation and tracking. More specifically, we have discussed the following features.

(i) Interference suppression by deterministic and adaptive pattern shaping: both approaches can be reasonably combined. Applying ABF after deterministic sidelobe reduction allows reducing the requirements on the low sidelobe level. Special techniques are available to make ABF preserve the low sidelobe level.

(ii) General principles and relationships between ABF algorithms and superresolution methods have been discussed, like dependency on the sample number, robustness, the benefits of subspace methods, problems of determining the signal/interference subspace, and interference suppression/resolution limit.

(iii) Array signal processing methods like adaptive beamforming and superresolution methods can be applied to subarrays generated from a large fully filled array. This means applying these methods to the sparse superarray formed by the subarray centers. We have pointed out problems and solutions for this special array problem.

(iv) ABF can be combined with superresolution in a canonical way by applying the pre-whiten and match principle to the data and the signal model vector.

(v) All array signal processing methods can be extended to space-time processing (arrays) by defining a corresponding space-time plane wave model.

(vi) Superresolution is a joint detection-estimation problem. One has to determine a multitarget model which contains the number, directions and powers of the targets. These parameters are strongly coupled. A practical joint estimation and detection procedure has been presented.

(vii) The problems for implementation in real system have been discussed, in particular the effects of limited knowledge of the array manifold, effect of channel errors, eigenvalue leakage, unequal noise power in array channels, and dynamic range of AD-converters.

(viii) For achieving best performance an adaptation of the processing subsequent to ABF is necessary. Direction estimation can be accommodated by using ABF-monopulse; the detector can be accommodated by adaptive detection with ASLB, and the tracking algorithms can be extended to adaptive tracking and track management with jammer mapping.

With a single array signal processing method alone no significant improvement will be obtained. The methods have to be reasonably embedded in the whole system, and all functionalities have to be mutually tuned and balanced. This is a task for future research. The presented approaches constitute only a first ad hoc step, and more thorough studies are required. Note that in most cases tuning the functionalities is mainly a software problem. So, there is the possibility to upgrade existing systems softly and step-wise.

Disclosure

The main part of this work was performed while the author was with the Fraunhofer Institute for High Frequency Physics and Radar Techniques (FHR) in Wachtberg, Germany.

References

[1] M. I. Skolnik, *Radar Handbook*, McGraw Hill, 2nd edition, 1990.

[2] M. A. Richards, J. A. Scheer, and W. A. Holden, *Principles of Modern Radar*, SciTech Publishing, 2010.

[3] W. D. Wirth, *Radar Techniques Using Array Antennas*, IEE Publishers, 2001.

[4] R. Klemm, *Principles of Space-Time Adaptive Processing*, IET Publishers, London, UK, 3rd edition, 2006.

[5] J. H. G. Ender, "On compressive sensing applied to radar," *Signal Processing*, vol. 90, no. 5, pp. 1402–1414, 2010.

[6] U. Nickel, "Subarray configurations for digital beamforming with low sidelobes and adaptive interference suppression," in *Proceedings of the IEEE International Radar Conference*, pp. 714–719, Alexandria, Egypt, May 1995.

[7] U. Nickel, "Properties of digital beamforming with subarrays," in *Proceedings of the International Conference on Radar (CIE '06)*, pp. 6–19, Shanghai, China, October 2006.

[8] W. Bürger, "Sidelobe forming for ground clutter and jammer suppression for airborne active array radar," in *Proceedings of the IEEE International Symposium on Phased Array Systems and Technology*, Boston, Mass, USA, 2003.

[9] J. Liu, A. B. Gershman, Z.-Q. Luo, and K. M. Wong, "Adaptive beamforming with sidelobe control: a second-order cone programming approach," *IEEE Signal Processing Letters*, vol. 10, no. 11, pp. 331–334, 2003.

[10] S. A. Vorobyov, A. B. Gershman, Z.-Q. Luo, and N. Ma, "Adaptive beamforming with joint robustness against mismatched signal steering vector and interference nonstationarity," *IEEE Signal Processing Letters*, vol. 11, no. 2, pp. 108–111, 2004.

[11] G. A. Fabrizio, A. B. Gershman, and M. D. Turley, "Robust adaptive beamforming for HF surface wave over-the-horizon radar," *IEEE Transactions on Aerospace and Electronic Systems*, vol. 40, no. 2, pp. 510–525, 2004.

[12] Y. Hua, A. B. Gershman, and Q. Cheng, *High Resolution and Robust Signal Processing*, Marcel Dekker, 2004.

[13] U. Nickel, "Adaptive Beamforming for Phased Array Radars," in *Proceedings of the IEEE International Radar Symposium (IRS '98)*, pp. 897–906, DGON and VDE/ITG, September 1998.

[14] C. H. Gierull, "Fast and effective method for low-rank interference suppression in presence of channel errors," *Electronics Letters*, vol. 34, no. 6, pp. 518–520, 1998.

[15] G. M. Herbert, "New projection based algorithm for low sidelobe pattern synthesis in adaptive arrays," in *Proceedings of the Radar Edinburgh International Conference*, pp. 396–400, October 1997.

[16] U. Nickel, "Determination of the dimension of the signal subspace for small sample size," in *Proceedings of the IASTED international conference on Signal Processing and Communication Systems*, pp. 119–122, IASTED/Acta Press, 1998.

[17] S. Kritchman and B. Nadler, "Non-parametric detection of the number of signals: hypothesis testing and random matrix theory," *IEEE Transactions on Signal Processing*, vol. 57, no. 10, pp. 3930–3941, 2009.

[18] U. Nickel, "On the influence of channel errors on array signal processing methods," *International Journal of Electronics and Communications*, vol. 47, no. 4, pp. 209–219, 1993.

[19] R. J. Muirhead, *Aspects of Multivariate Analysis Theory*, John Wiley & Sons, New York, NY, USA, 1982.

[20] R. R. Nadakuditi and A. Edelman, "Sample eigenvalue based detection of high-dimensional signals in white noise using relatively few samples," *IEEE Transactions on Signal Processing*, vol. 56, no. 7, pp. 2625–2638, 2008.

[21] U. Nickel, "Radar target parameter estimation with antenna arrays," in *Radar Array Processing*, S. Haykin, J. Litva, and T. J. Shepherd, Eds., pp. 47–98, Springer, 1993.

[22] S. Haykin, *Advances in Spectrum Analysis and Array Processing. Vol. II*, Prentice Hall, 1991.

[23] U. Nickel, "Aspects of implementing super-resolution methods into phased array radar," *International Journal of Electronics and Communications*, vol. 53, no. 6, pp. 315–323, 1999.

[24] U. Nickel, "Overview of generalized monopulse estimation," *IEEE Aerospace and Electronic Systems Magazine*, vol. 21, no. 6, pp. 27–55, 2006.

[25] U. Nickel, "Spotlight MUSIC: super-resolution with subarrays with low calibration effort," *IEE Proceedings*, vol. 149, no. 4, pp. 166–173, 2002.

[26] B. Ottersten, P. Stoica, and R. Roy, "Covariance matching estimation techniques for array signal processing applications," *Digital Signal Processing*, vol. 8, no. 3, pp. 185–210, 1998.

[27] Y. I. Abramovich, N. K. Spencer, and A. Y. Gorokhov, "GLRT-based threshold detection-estimation performance improvement and application to uniform circular antenna arrays," *IEEE Transactions on Signal Processing*, vol. 55, no. 1, pp. 20–31, 2007.

[28] Y. I. Abramovich and B. A. Johnson, "Detection-estimation of very close emitters: performance breakdown, ambiguity, and general statistical analysis of maximum-likelihood estimation," *IEEE Transactions on Signal Processing*, vol. 58, no. 7, pp. 3647–3660, 2010.

[29] E. J. Kelly, "Performance of an adaptive detection algorithm; rejection of unwanted signals," *IEEE Transactions on Aerospace and Electronic Systems*, vol. 25, no. 2, pp. 122–133, 1992.

[30] F. C. Robey, D. R. Fuhrmann, E. J. Kelly, and R. Nitzberg, "A CFAR adaptive matched filter detector," *IEEE Transactions on Aerospace and Electronic Systems*, vol. 28, no. 1, pp. 208–216, 1992.

[31] S. Kraut and L. L. Scharf, "Adaptive subspace detectors," *IEEE Transactions on Signal Processing*, vol. 49, no. 1, pp. 1–16, 2001.

[32] C. D. Richmond, "Performance of the adaptive sidelobe blanker detection algorithm in homogeneous environments," *IEEE Transactions on Signal Processing*, vol. 48, no. 5, pp. 1235–1247, 2000.

[33] C. D. Richmond, "Performance of a class of adaptive detection algorithms in nonhomogeneous environments," *IEEE Transactions on Signal Processing*, vol. 48, no. 5, pp. 1248–1262, 2000.

[34] T. F. Ayoub and A. M. Haimovich, "Modified GLRT signal detection algorithm," *IEEE Transactions on Aerospace and Electronic Systems*, vol. 36, no. 3, pp. 810–818, 2000.

[35] Y. I. Abramovich, N. K. Spencer, and A. Y. Gorokhov, "Modified GLRT and AMF framework for adaptive detectors," *IEEE Transactions on Aerospace and Electronic Systems*, vol. 43, no. 3, pp. 1017–1051, 2007.

[36] O. Besson, J.-Y. Tourneret, and S. Bidon, "Knowledge-aided Bayesian detection in heterogeneous environments," *IEEE Signal Processing Letters*, vol. 14, no. 5, pp. 355–358, 2007.

[37] A. De Maio, S. De Nicola, A. Farina, and S. Iommelli, "Adaptive detection of a signal with angle uncertainty," *IET Radar, Sonar and Navigation*, vol. 4, no. 4, pp. 537–547, 2010.

[38] A. De Maio and E. Conte, "Adaptive detection in gaussian interference with unknown covariance after reduction by invariance," *IEEE Transactions on Signal Processing*, vol. 58, no. 6, pp. 2925–2934, 2010.

[39] U. Nickel, "Design of generalised 2D adaptive sidelobe blanking detectors using the detection margin," *Signal Processing*, vol. 90, no. 5, pp. 1357–1372, 2010.

[40] W. R. Blanding, W. Koch, and U. Nickel, "Adaptive phased-array tracking in ECM using negative information," *IEEE Transactions on Aerospace and Electronic Systems*, vol. 45, no. 1, pp. 152–166, 2009.

[41] M. Feldmann and U. Nickel, "Target parameter estimation and tracking with adaptive beamforming," in *Proceedings of the International Radar Symposium (IRS '11)*, pp. 585–590, Leipzig, Germany, September 2011.

Hindawi Publishing Corporation
International Journal of Antennas and Propagation
Volume 2013, Article ID 382516, 11 pages
http://dx.doi.org/10.1155/2013/382516

Research Article

Weak Target Detection within the Nonhomogeneous Ionospheric Clutter Background of HFSWR Based on STAP

Xin Zhang, Qiang Yang, and Weibo Deng

School of Electronics Information Engineering, Harbin Institute of Technology, Harbin 150001, China

Correspondence should be addressed to Weibo Deng; dengweibo@hit.edu.cn

Received 1 April 2013; Revised 28 July 2013; Accepted 7 August 2013

Academic Editor: Ulrich Nickel

High Frequency Surface Wave Radar (HFSWR) can perform the functions of ocean environment monitoring, target detection, and target tracking over the horizon. However, its system's performance is always limited by the severe ionospheric clutter environment, especially by the nonhomogeneous component. The nonhomogeneous ionospheric clutter generally can cover a few Doppler shift units and a few angle units. Consequently, weak targets masked by the nonhomogeneous ionospheric clutter are difficult to be detected. In this paper, a novel algorithm based on angle-Doppler joint eigenvector which considers the angle-Doppler map of radar echoes is adopted to analyze the characteristics of the nonhomogeneous ionospheric clutter. Given the measured data set, we first investigate the correlation between the signal of interest (SOI) and the nonhomogeneous ionospheric clutter and then the correlation between the nonhomogeneous ionospheric clutters in different two ranges. Finally, a new strategy of training data selection is proposed to improve the joint domain localised (JDL) algorithm. Simulation results show that the improved-JDL algorithm is effective and the performance of weak target detection within nonhomogeneous ionospheric clutter is improved.

1. Introduction

HFSWR exploits the surface wave mode of vertical polarization electromagnetic wave propagating over the sea water to detect ships and aircrafts at distances beyond the line of sight. It has drawn much attention in recent years for its notable features of large scale, long distance, and all-day adaptability. In general, the factors which affect the performance of HFSWR are the sea clutter, ionospheric clutter, radio interference, and noise, among which, the key factor that determines targets detection performance is the ionospheric clutter [1]. The situation herein is very complex, since the motion states of the ionosphere are distinct at different temporal and spatial locations. Until now, a widely accepted model for the ionospheric clutter in HFSWR is still not found. It follows that how to suppress the ionospheric clutter and how to improve the weak target detection performance in HFSWR systems are hot topics worth further investigation.

In HFSWR systems, long coherent integration time is necessary for better detection performance and higher Doppler resolution. During this process, the state of the ionosphere is changing rapidly and irregularly, which leads to an obvious problem that the ionospheric clutter can cover a few Doppler shift units after the coherent integration. Therefore, it is difficult for the frequency domain adaptive matched filtering algorithm to detect the weak targets buried in the ionospheric clutter. On the other hand, both the beam-broadening effect resulting from the smaller array aperture compared to the wavelength, and the regional characteristic of ionosphere can lead to the fact that ionospheric clutter always covers a broad angular region. Consequently, the ionospheric clutter is difficult to be suppressed either in the Doppler domain or in the angle domain.

Space-time adaptive processing (STAP) is proposed by Brennan and Reed in the 1970s and has become one of the major research directions around the world [2]. It has been mainly exploited to suppress homogeneous and nonhomogeneous clutters in airborne radar systems in the Doppler-angle domain [3–6]. It also has been applied in many other specific applications, both in military and civil fields, such as spaceborne radar, communication, sonar, navigation, and microphone array [7, 8]. In HFSWR systems, STAP has been adopted to counter the sea clutter in shipborne radar systems

[9] and suppress the ionospheric clutter in shore-based radar systems.

Groups led by Fabrizio and Adve have begun to investigate the problem of ionospheric clutter suppression based on STAP and obtained a bulk of measured data [10–13]. In [13], Ravan et al. developed a new model to predict the radio wave propagation in ionosphere plasma density irregularities, and it turns out that their model fits the data gathered in Canada well. Ravan and Saleh et al. also analyzed a group of STAP algorithms such as joint domain localized, direct data domain, hybrid, PAMF, and further a new proposed fast algorithm FFA [13, 14]. Joint domain localized (JDL) is a classical statistical STAP algorithm broadly used in airborne radar [15]. It features preferable low computational cost and high performance in homogeneous clutter suppression. Especially for the clutter with independent and identical distribution, JDL is highly effective. But in HFSWR, the ionospheric clutter is nonhomogeneous. It is always difficult to obtain enough training data for JDL. Direct data domain (D3), hybrid, and PAMF are classical STAP algorithms for nonhomogeneous clutter in airborne radar systems. These algorithms suffer from high computational cost and poor real-time performance in HFSWR due to the long coherent integration time (CIT) and large space-time dimension. FFA is also a low computational cost algorithm, but how to divide the space-time region is still under investigation.

In this paper, we first analyze the correlation between the SOI and the nonhomogeneous ionospheric clutter; and then, the correlation between the nonhomogeneous ionospheric clutters at two different ranges has been analyzed. On this basis, we propose a new strategy to select the training data set. By means of the reasonable training data selection, the nonhomogeneous ionospheric clutter can be suppressed more effectively. Meanwhile, weak targets in the direction of ionospheric can also be detected.

In Section 2, we first analyze the correlation including the correlation between the SOI and the nonhomogeneous ionospheric clutter and the one between the nonhomogeneous ionospheric clutters at two different ranges. In Section 3, we proposed an improved-JDL algorithm according to the analysis results given in Section 2. Finally, the superiority of the improved-JDL algorithm is demonstrated via simulation based on practically measured data.

2. Characteristic Analysis of Nonhomogeneous Ionospheric Clutter

In HFSWR, the electromagnetic waves travel not only mainly over the sea surface but also partly into the sky due to nonidealities of the receiver antenna array. Under certain conditions, the electromagnetic waves emitted into the sky can be reflected by the ionosphere and then received by the nonideal receiver antenna array. This is how the ionospheric clutter emerges. The ionospheric clutter is very intricate as a result of the nonhomogeneous layered structure and the rapidly changing state of the ionosphere. For these reasons, ionospheric clutter suppression is a critical difficulty in HFSWR. The study of ionospheric clutter suppression depends heavily on the understanding of the characteristics of ionospheric clutter.

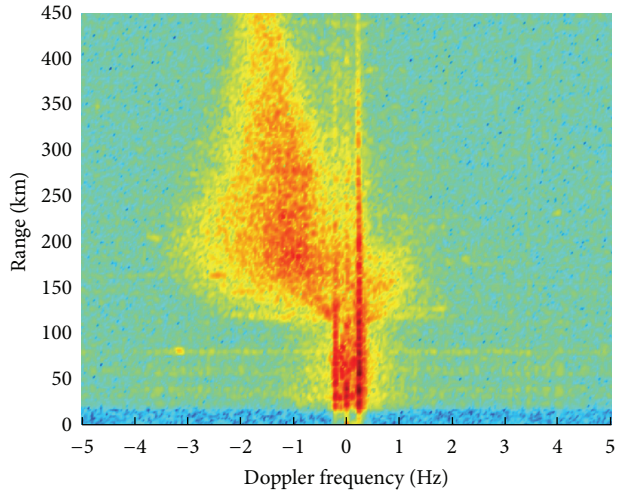

Figure 1: Range-Doppler Map.

Firstly, we analyze the characteristics of the ionospheric clutter. The measured data is obtained through the HFSWR system in Weihai, China on May 12, 2012, and then processed by matched filters in range, Doppler, and digital beamforming in turn. A range-Doppler map in one beam is shown in Figure 1, and an angle-Doppler map in one range bin is shown in Figure 2.

In STAP, the data is processed on the basis of the angle-Doppler map. In this case, characteristics of the nonhomogeneous ionospheric clutter should be analyzed based on the angle-Doppler map.

In Figure 2, the nonhomogeneous ionospheric clutter covers a large region of the angle-Doppler map. It does not make any sense to analyze such a broad region. So we divide the whole angle-Doppler region into small scales, and the characteristic analysis of the nonhomogeneous ionospheric clutter should also be in the light of the small local angle-Doppler region. We call this small local region the Angle-Doppler Local Region (ADLR). The analysis in Section 2 is solely concentrated on the concept of ADLR.

In Section 2.1, we have to decide what the appropriate size of ADLR is in order to make sure that the clutter in the ADLR is simple.

We suppose $\mathbf{X}_l$ is an ADLR sequence for $l = 0, 1, 2, \ldots$ of independent range samples as discussed in the literature [2]. But the sample in one range bin may relate with some samples in other independent range bins.

In Section 2.2, we propose the correlation analyzing method based on the angle-doppler joint eigenvector (ADJE) of ADLR.

Based on the correlation analyzing method in Section 2.2 and the size of ADLR decided in Section 2.1, we analyze the SOI correlation in the noise environment (in Section 2.3) and in the ionospheric clutter environment (in Section 2.4).

In the last Section 2.5, we analyze the ionospheric clutter correlation between ADLRs in different range bins.

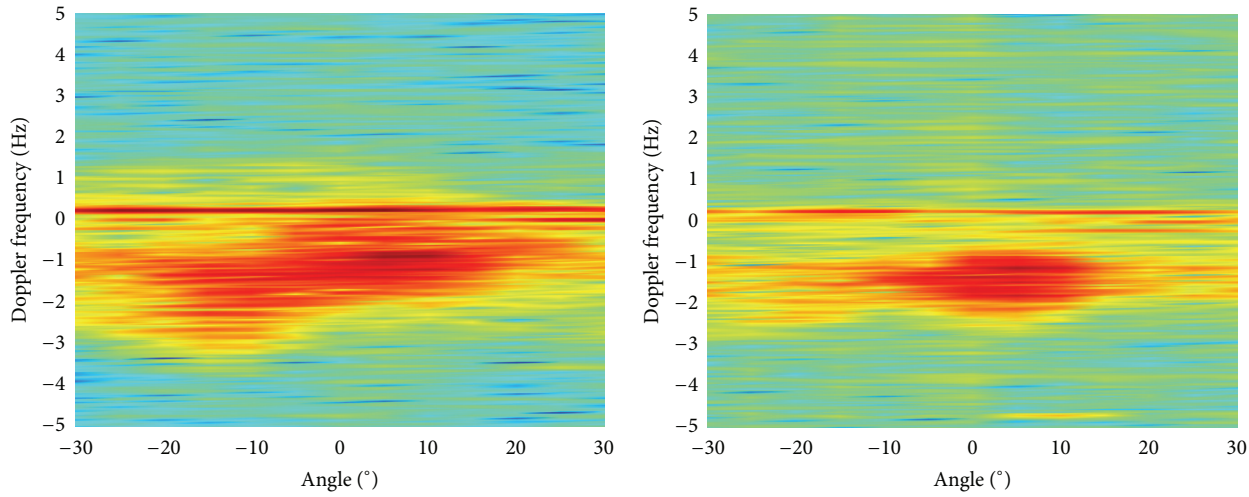

(a) 200 km (b) 350 km

Figure 2: Angle-Doppler Map.

2.1. Size of the ADLR. In this part, we try to make an appropriate decision of the size of ADLR in order to make sure that the clutter in this ADLR is as simple as possible. If the data in the ADLR are with high correlation both in beam-domain and frequency-domain, we can consider the clutter in the ADLR simple.

The correlation coefficient of the data with two different beams can be calculated by (1); The correlation coefficient of the data with two different Doppler shifts can be calculated by (2):

$$\rho_{k,j} = \frac{(1/N_r)\sum_r X_k(r, f_{d0})\, X_j^*(r, f_{d0})}{\sqrt{(1/N_r)\sum_r |X_k(r, f_{d0})|^2\, (1/N_r)\sum_r |X_j^*(r, f_{d0})|^2}}, \tag{1}$$

$$\rho_{f_{d1},f_{d2}} = \frac{(1/N_r)\sum_r X_{f_{d1}}(r, \varphi_0)\, X_{f_{d2}}^*(r, \varphi_0)}{\sqrt{(1/N_r)\sum_r |X_{f_{d1}}(r, \varphi_0)|^2\, (1/N_r)\sum_r |X_{f_{d2}}^*(r, \varphi_0)|^2}}, \tag{2}$$

where r indicates the index of range bins, N_r is the number of range bins which are used to calculate the correlation coefficient, X_k and X_j are the training data with direction k and j with Doppler shift f_{d0}, $(\cdot)^*$ is the complex conjugate operator, and $X_{f_{d1}}$ and $X_{f_{d2}}$ are the training data with Doppler shift f_{d1} and f_{d2} with direction φ_0.

We analyze the angle correlation with different angle intervals as given by (1). The results are shown in Figure 3.

Figure 3(a). The ionospheric clutter exists within the Doppler shifts between −2 Hz and 0.12 Hz. The correlation coefficient at beam interval 5° is greater than the ones when the beam intervals are 10° and 15°.

Figure 3(b). The correlation coefficient decreases as the beam interval increases. We can deduce from these two figures that the ionospheric clutters have similar characteristics when the beam interval is narrower than 5°.

We also analyze the Doppler frequency correlation with different Doppler shift intervals as given by (2). The results are shown in Figure 4.

Figure 4(a). The ionospheric clutter exists within all the angles ranging from −30° to 30°. The correlation coefficient achieves its maximum when the Doppler shift interval is 34 mHz. The ones when the Doppler shift intervals are 68 mHz and 102 mHz are almost the same and both less than the one with 34 mHz.

Figure 4(b). The correlation coefficient decreases as the Doppler shift interval increases. From these two figures, we can also deduce that the ionospheric clutters have similar characteristics when the Doppler shift interval is less than 34 mHz.

In order to maintain the characteristics of ADLR, correlation coefficients within the ADLR data must be high enough. It follows that the size of ADLR cannot be too large. Synthetically, it is preferable to choose the ±5°, ±34 mHz interval around the cell under test. This is in agreement with the radar theory that correlation coefficient increases as the beam interval and Doppler shift interval decrease.

2.2. Correlation Analysis Method Based on ADJE. In the case of HFSWR, the data in an ADLR cannot be absolutely simple. An ADLR often consists of multiple echo components such as noise, clutter, interference, and targets. The characteristics of ADLRs with different echo components are different. In this part, we mainly analyze the correlation between ADLRs with different echo components.

We first calculate the self-correlation matrix of the data in one ADLR and then obtain the ADJEs through the decomposition of the covariance matrix. In this case, the characteristic of the ADLR is represented by the vector sum of the ADJEs. The following correlation analysis is based on the ADJEs representation.

Firstly, we choose the ADLR which covers ±5° (3 beams) and ±34 mHz (3 Doppler shifts) in one range bin and

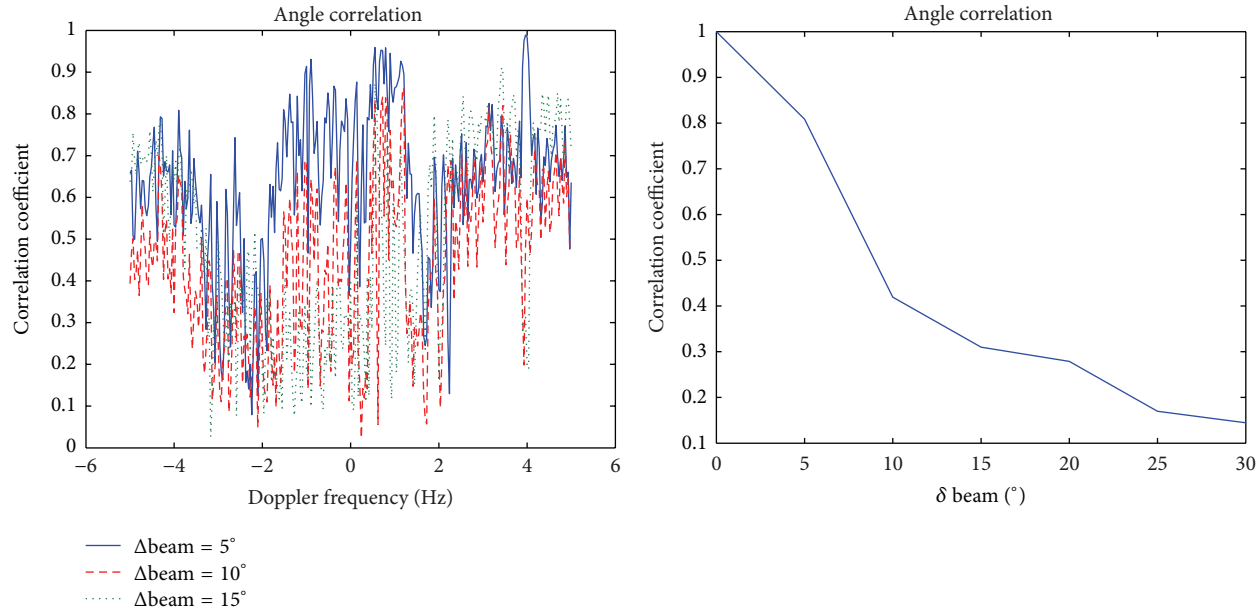

(a) Range = 200 km

(b) Range = 200 km, $f_{d0} = -1.2$ Hz

Figure 3: Correlation coefficients with different beam intervals.

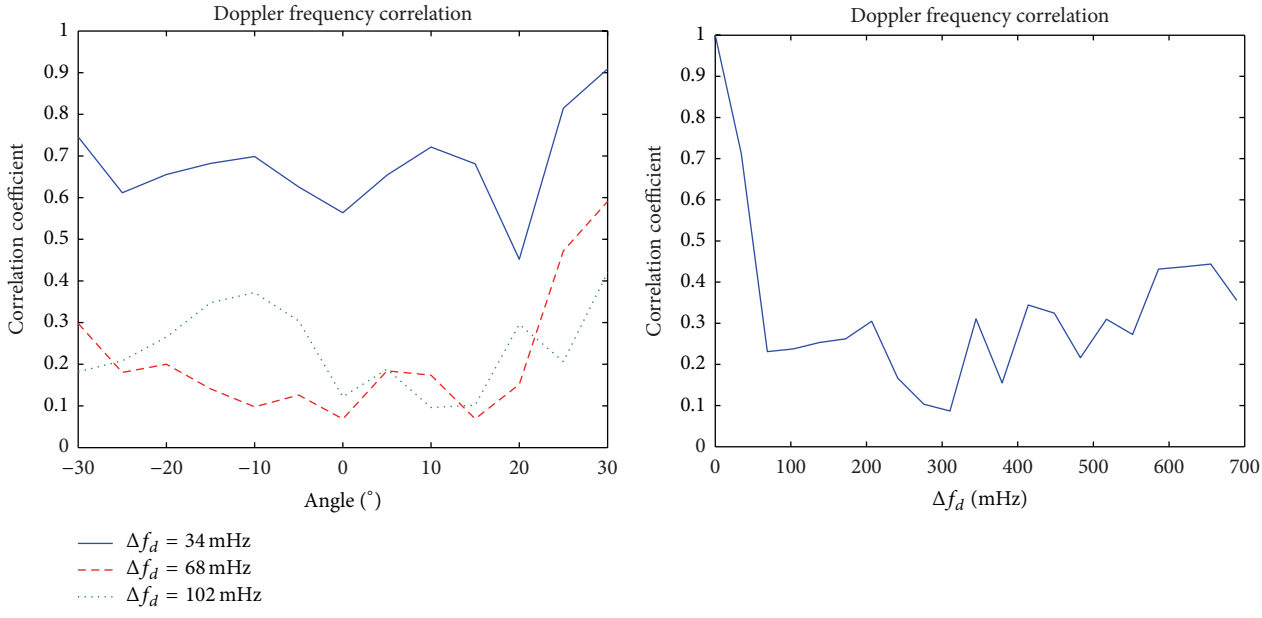

(a) Range = 200 km

(b) Range = 200 km, $\varphi_0 = -10^\circ$

Figure 4: Correlation coefficients with different Doppler shift intervals.

a 9×1 vector $\mathbf{X}_r$ can be written by Kronecker product. So the self-correlation matrix is 9×9, and we can get 9 ADJEs by eigen decompostion. A certain number of ADJEs which make greater contribution to represent the characteristics of the ADLR are selected to calculate the correlation coefficient.

The correlation analysis method based on ADJE is as follows.

(i) Calculate the self-correlation matrix $\mathbf{R}_x$ of the data $\mathbf{X}_r$ in the ADLR with rth range bin by $\mathbf{R}_x = \mathbf{X}_r^H \mathbf{X}_r$.

(ii) Eigen-decompose $\mathbf{R}_x$ to obtain 9 eigenvalues $\lambda_1, \lambda_2, \ldots, \lambda_9$ and 9 ADJEs $\boldsymbol{\xi}_1, \boldsymbol{\xi}_2, \ldots, \boldsymbol{\xi}_9$, then the normalized ADJEs by $\bar{\boldsymbol{\xi}}_i = \boldsymbol{\xi}_i / |\boldsymbol{\xi}_i|$, $i = 1, \ldots, 9$.

(iii) Determine the contribution of the normalized ADJEs $\lambda_i(\bar{\boldsymbol{\xi}}_i, \mathbf{X}_r), i = 1, 2, \ldots, 9$;

(iv) Choose the normalized ADJE $\boldsymbol{\varsigma}$ which makes the greatest contribution for $\mathbf{X}_r$. And $\boldsymbol{\varsigma}$ can represent the characteristic of $\mathbf{X}_r$. In the case of HFSWR, especially

for the Es layer ionospheric clutter, there may be more than one kind of clutter component that exists in an ADLR. Hence, for uncorrelated clutters, there may be two or more dominant normalized ADJEs, and the vector sum of the ADJEs is introduced to represent the characteristics of this ADLR.

(v) Repeat the above procedure; we can obtain K normalized ADJEs $\boldsymbol{\varsigma}_i$, $i = 1, 2, \ldots, K$ in K different range bins.

(vi) Calculate the correlation coefficients utilizing the K normalized ADJEs $\boldsymbol{\varsigma}_i$, $i = 1, 2, \ldots, K$ from step (v) by

$$\rho_{ij} = \boldsymbol{\varsigma}_i^H \boldsymbol{\varsigma}_j, \quad i, j = 1, 2, \ldots, K. \tag{3}$$

2.3. SOI Correlation in the Noise Environment. The following analysis is based on the assumption that the noise in HFSWR is Gaussian. We consider two ADLRs: one is with SOI only, and in the other one there exist both SOI and noise, and the signal-to-noise ratio (SNR) is changing.

Gracheva and Cerutti-Maori have analyzed the channel correlation of sea data and have mentioned the relationship between channel correlation and the clutter to noise ratio (CNR) [16]. CNR is defined as

$$\mathrm{CNR} = \frac{(1/N_r)\sum_r \left\|X_c(r_c)\right\|_2}{\sigma_n^2}. \tag{4}$$

We consider the ADLR in a single range bin ($N_r = 1$). The CNR in this ADLR can be defined as

$$\mathrm{CNR}_{\mathrm{ADLR}} = \frac{\left\|X_c(r_c)\right\|_2}{\sigma_n^2}. \tag{5}$$

The SNR is defined as

$$\mathrm{SNR} = \frac{\left\|X_t(r_t)\right\|_2}{\sigma_n^2}. \tag{6}$$

We can replace the $\mathrm{CNR}_{\mathrm{ADLR}}$ in the literature [16] with the SNR as

$$\rho = \frac{1}{1 + 1/\mathrm{SNR}}. \tag{7}$$

We analyze the correlation between two ADLRs (ADLR_1 and ADLR_2) by utilizing the algorithm introduced in Section 2.2. The relationship between correlation coefficient and the SNR is obtained via 10000 Monte-Carlo trials.

Under the condition that there are only SOI in ADLR_1 and only Gaussian noise in ADLR_2, the correlation between ADLR_1 and ADLR_2 is shown as the red dotted line in Figure 5. The correlation coefficient is kept at a low level. This result is consistent with the radar theory that the SOI is uncorrelated with the noise.

In this case, there are both SOI and noise in ADLR_2, and the SNR is variant. The simulation result by (7) is shown as the green dotted line with marker "$*$" in Figure 5. The correlation coefficient is very close to 1 when the SNR is greater than 20 dB and very close to zero when the SNR is less than −20 dB. When SNR $\in$ [−20, 20] dB, the correlation coefficient increases as the SNR increases.

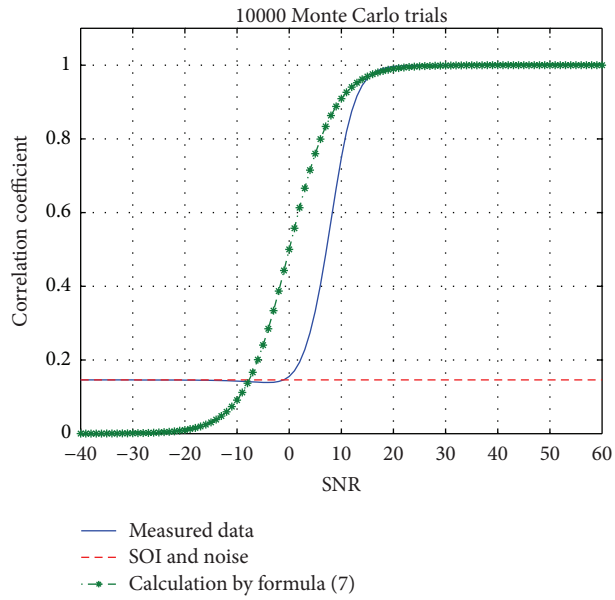

Figure 5: The relationship between correlation and SNR.

We make a similar analysis with the measured data in ADLR_2. The result is shown as a blue solid line in Figure 5. Compared to the simulation results, the correlation coefficient decreases faster as the SNR decreases and the correlation coefficient is greater than zero when the SNR is less than 0 dB. The reason for this error is that the characteristics of SOI and noise could be both reflected in ADLR_2 when the SNR is small.

In light of the error present in the above analysis, we modify the equation as follows.

We mark the ADLR_1 which only contains SOI_1 as SD_1 and the Doppler-angle data as $\mathbf{Z}_t$; we also mark the ADLR_2 which contains SOI_2 and Gaussian noise as SD_2 and the Doppler-angle data as $\mathbf{Z}_{sn}$, and the power of the noise is σ^2. We calculate the normalized ADJEs of ADLR_1 and ADLR_2 utilizing $\mathbf{Z}_t$ and $\mathbf{Z}_{sn}$ for $\boldsymbol{\xi}_t$ and $\boldsymbol{\xi}_{sn}$, respectively. So $\boldsymbol{\xi}_{sn}$ can be written as

$$\boldsymbol{\xi}_{sn} \approx \frac{\lambda_t \boldsymbol{\xi}_t' + \sigma^2 \boldsymbol{\xi}_n}{\sqrt{\lambda_t^2 + \sigma^4}}, \tag{8}$$

where λ_t is the eigenvalue of SOI_2, $\boldsymbol{\xi}_t'$ is the eigenvector of SOI_2, and $\boldsymbol{\xi}_n$ is the eigenvector of noise.

So the correlation coefficient can be written as

$$\begin{aligned} \rho &= \boldsymbol{\xi}_t^H \boldsymbol{\xi}_{sn} \\ &\approx \boldsymbol{\xi}_t^H \cdot \frac{\lambda_t \boldsymbol{\xi}_t' + \sigma^2 \boldsymbol{\xi}_n}{\sqrt{\lambda_t^2 + \sigma^4}} \\ &= \frac{\lambda_t}{\sqrt{\lambda_t^2 + \sigma^4}} \cdot \frac{1}{1 + 1/\mathrm{SNR}} + \frac{\sigma^2}{\sqrt{\lambda_t^2 + \sigma^4}} \cdot \rho_{sn}, \end{aligned} \tag{9}$$

where $\boldsymbol{\xi}_t^H \boldsymbol{\xi}_t' = 1/(1 + 1/\mathrm{SNR})$, ρ_{sn} is a statistical value related to the SOI and distribution of the noise, $\rho_{sn} = \boldsymbol{\xi}_t^H \boldsymbol{\xi}_n$.

When SOI_2 is dominant in SD_2, $\boldsymbol{\xi}_{sn} \approx \boldsymbol{\xi}_t'$, the correlation coefficient is $\rho = \boldsymbol{\xi}_t^H \boldsymbol{\xi}_t' = 1/(1 + 1/\mathrm{SNR})$.

When noise is dominant in SD_2, $\boldsymbol{\xi}_{sn} \approx \boldsymbol{\xi}_n$, correlation coefficient is $\rho = \boldsymbol{\xi}_t^H \boldsymbol{\xi}_n = \rho_{sn}$.

The simulation result based on (9) are shown as a black dot-dash line in Figure 6 fits the measured data much better than the simulation result given by (7) does.

2.4. SOI Correlation in the Ionospheric Clutter Environment. We mark the ADLR_1 which only contains SOI_1 as SD_1 and the Doppler-angle data as $\mathbf{Z}_t(r_t)$; we also mark the ADLR_3 which contains SOI_2 and the ionospheric clutter as SD_3 and the Doppler-angle data as $\mathbf{Z}_c(r_c)$, and r_t and r_c are the range bins of SD_1 and SD_3. The SCR of SOI_2 and the ionospheric clutter are written as

$$\mathrm{SCR} = \frac{\left\|\mathbf{Z}_t(r_t)\right\|_2}{(1/N_r)\sum_r \left\|\mathbf{Z}_c(r_c)\right\|_2}. \tag{10}$$

We analyze the SOI correlation in the ionospheric clutter background as in Section 2.3. We can get the following:

$$\rho = \begin{cases} \dfrac{1}{1 + 1/\mathrm{SCR}}, & \text{for SCR} > H_{\mathrm{SCR}}, \\ \rho_{sc}, & \text{for SCR} < L_{\mathrm{SCR}}, \\ \dfrac{\lambda_t}{\sqrt{\lambda_t^2 + \lambda_c^2}} \cdot \dfrac{1}{1 + 1/\mathrm{SCR}} & \\ \quad + \dfrac{\lambda_c}{\sqrt{\lambda_t^2 + \lambda_c^2}} \cdot \rho_{sc}, & \text{others}, \end{cases} \tag{11}$$

where ρ_{sc} is the correlation coefficient between SOI and the ionospheric clutter, λ_t and λ_c are the eigenvalues of SOI_2 and the ionospheric clutter in ADLR_3, and L_{SCR} and H_{SCR} are the upper limit and lower limit of SCR, respectively, and they are related to the characteristics of the ionospheric clutter.

The correlation of SOI in the ionospheric clutter environment utilizing the measured data at the range of 180 km and 185 km is shown in Figure 7.

If there is only ionospheric clutter in ADLR_3, the correlation coefficients between ADLR_1 and ADLR_2 are shown as a red-dotted line. It is related to the characteristic of ionospheric clutter and has different values at different ranges. The result of correlation analysis utilizing measured data is shown as a blue solid line. And the result calculated by (11) fits the measured data well.

It can be seen from (11) and Figure 7 that the relationship between correlation and SCR can be divided into three parts:

(a) the correlation coefficient keeps a low value when the SCR is small, and it mainly depends on the characteristics of the ionospheric clutter;

(b) when the SCR is large enough, the correlation coefficient is close to 1;

(c) when the SCR is an intermediate value, the correlation coefficient is related not only to the SCR but also to the characteristics of SOI and ionospheric clutter.

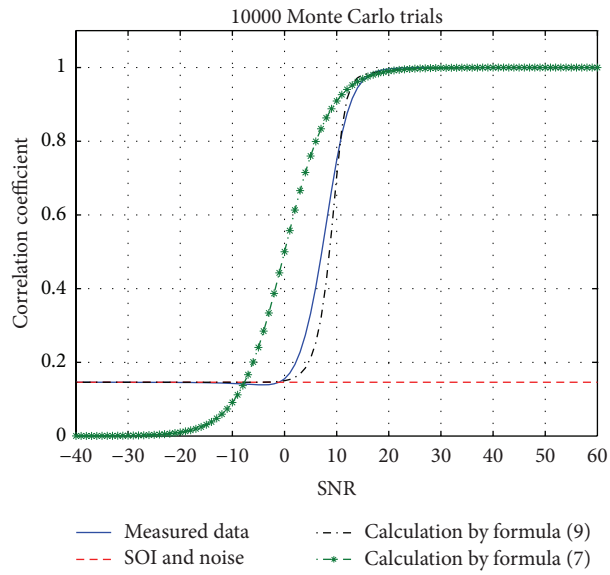

FIGURE 6: The relationship between correlation and SNR.

2.5. Range Correlation of Nonhomogeneous Ionospheric Clutter. The motion of ionosphere is complex with the major factor of nonuniform plasma. Due to this complex motion, the ionospheric clutter in HFSWR is nonhomogeneous.

We calculate the correlation coefficients of ADLRs in different ranges within 150 km to 430 km referred to 225 km at the Doppler shift −1.2 Hz utilizing the algorithm mentioned in Section 2.2. The result is shown in Figure 8. The correlation of nonhomogeneous ionospheric clutter decreased as the range interval increased. But there may be a few high correlated range data due to the nonhomogeneous characteristics of the ionospheric clutter.

3. Strategy of Choosing the Training Data Based on Correlation

The full STAP algorithm is ideal and requires the training data to meet two conditions. One is that the clutter must be independent, and identically distributed. The other is that the number of the training data must be twice greater than the degrees of freedom of the clutter [17].

In HFSWR, the first condition is difficult to meet due to the complex echoes. The long coherent integrated time (CIT) leads to the large degrees of freedom. So it requires considerable training data which are difficult to be attained in the practical system. Compared with the fully STAP, the partial STAP algorithm has the advantage of less computation. So the partial STAP has become the researchers priority.

The JDL algorithm is one of the partial STAP algorithms. It can reduce the degrees of freedom by using a transformation matrix $\mathbf{T}$. Therefore, it can solve the problem of the limited training data and it also can reduce the computation.

The result of Section 2.5 showed that the range of correlation of the nonhomogeneous ionospheric clutter rise, and fall irregularly. In order to suppress the nonhomogeneous ionospheric clutter effectively utilizing the JDL, we should

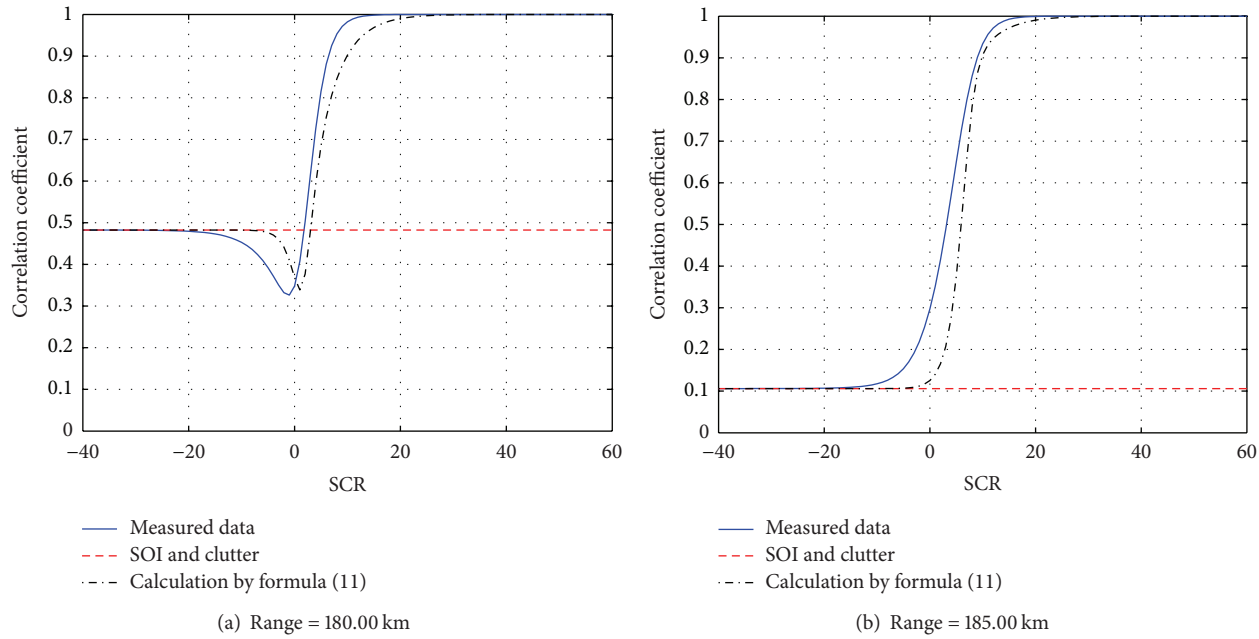

FIGURE 7: The relationship between correlation and SCR.

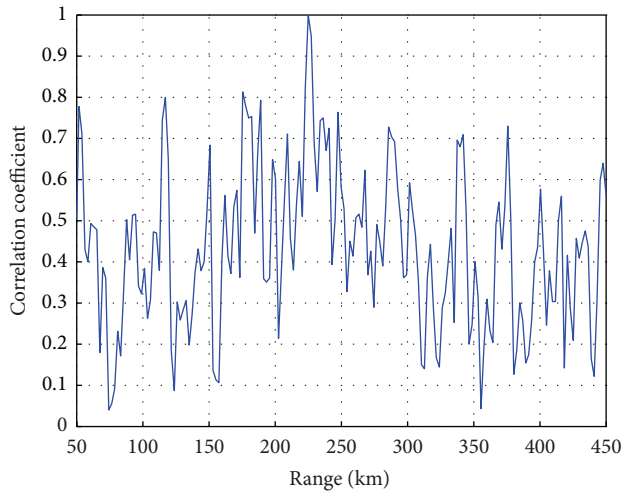

FIGURE 8: Range correlation of ionospheric clutter at −1.2 Hz.

ensure that the training data are highly related with the clutter cell under test.

3.1. Strategy Based on the Correlation. In this part, we choose the appropriate samples as the training data to obtain the covariance matrix more accurately based on the correlation analysis above.

The receiver antenna array of HFSWR is described as the N elements uniform linear array (ULA). d is the interelement spacing, a coherent integrated time contains M pulses, T is the pulse repetition time, and f_s is the system sampling rate. For a given range bin, the data sampled by the N elements form an N-dimensional vector, and the data received by one element in a CIT form an M-dimensional vector. So that an $NM \times 1$ dimensional vector of the space-time snapshots in lth range bin is formed as defined by

$$\mathbf{X}_l = \left[\mathbf{x}_1 \;\; \mathbf{x}_2 \;\; \cdots \;\; \mathbf{x}_M\right]^T, \tag{12}$$

where $\mathbf{x}_i = \left[x_{i,1} \;\; x_{i,2} \;\; \cdots \;\; x_{i,N}\right]^T$, $i = 1, 2, \ldots, M$.

We define the space-time steering vector as

$$\mathbf{v}\left(\phi_t, f_t\right) = \mathbf{b}\left(f_t\right) \otimes \mathbf{a}\left(\phi_t\right), \tag{13}$$

where $\mathbf{a}(\phi_t)$ is a space steering vector as defined by (14) and $\mathbf{b}(f_t)$ is a time steering vector as defined by (15):

$$\mathbf{a}\left(\phi_t\right) = \left[1 \;\; Z_s \;\; Z_s^2 \;\; \cdots \;\; Z_s^{N-1}\right]^T, \tag{14}$$

$$\mathbf{b}\left(f_t\right) = \left[1 \;\; Z_t \;\; Z_t^2 \;\; \cdots \;\; Z_t^{M-1}\right]^T, \tag{15}$$

where $Z_s = e^{j2\pi(d/\lambda)\sin\phi_t}$ and $Z_t = e^{j2\pi(f_t/f_R)}$.

JDL algorithm can transform the independent range samples to the LPR by using the transformation matrix $\mathbf{T}$ to reduce the degrees of freedom. Thus, $\mathbf{T}$ is the key of the JDL algorithm. Wang has discussed how to choose the LPR in the literature [18]: the clutter can be suppressed more effectively as the LPR larger, at the same time the heavily computational cost is a big problem. With all things considered in the case of HFSWR, the LPR we are concerned about contains three angle units and three Doppler shift units ($\eta_a = 3, \eta_d = 3$), which is the same size as the ADLR we mentioned in Section 2. So that the transformation matrix $\mathbf{T}$ can be written as

$$\mathbf{T} = \left[\mathbf{b}\left(f_{-1}\right) \;\; \mathbf{b}\left(f_0\right) \;\; \mathbf{b}\left(f_1\right)\right] \otimes \left[\mathbf{a}\left(\phi_{-1}\right) \;\; \mathbf{a}\left(\phi_0\right) \;\; \mathbf{a}\left(\phi_1\right)\right]. \tag{16}$$

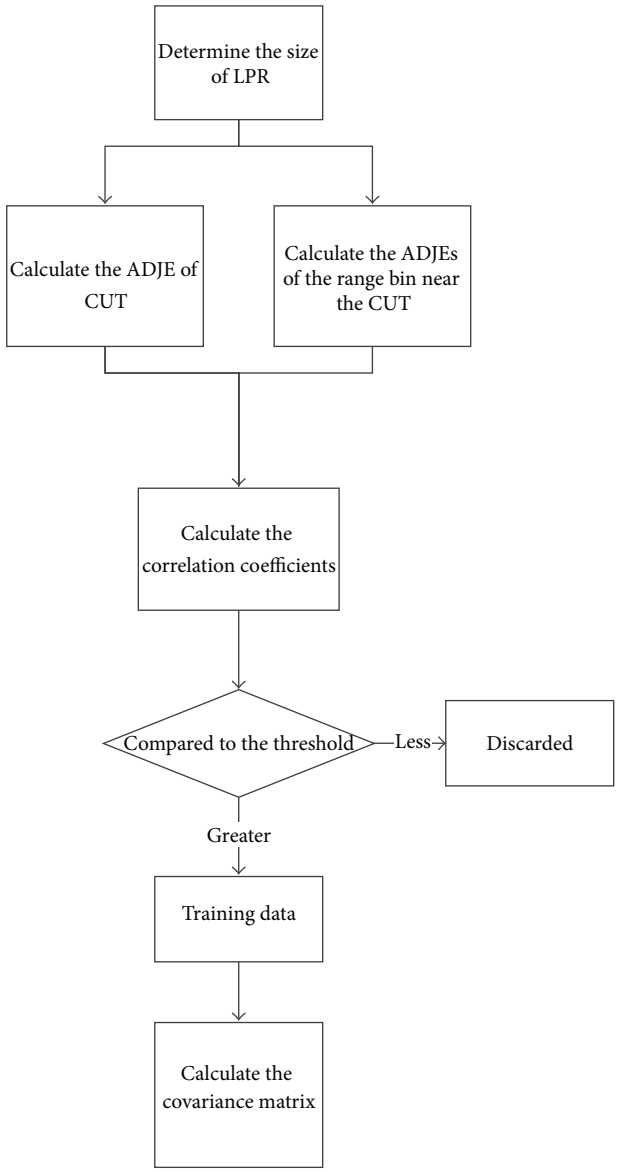

Figure 9: Implementation of improved-JDL.

Thus the new range samples and the new space-time steering vector in JDL can be written as

$$\widetilde{\mathbf{X}}_l = \mathbf{T}^H \cdot \mathbf{X}_l, \qquad \widetilde{\mathbf{v}} = \mathbf{T}^H \cdot \mathbf{v}. \tag{17}$$

Then, we analyze the correlation of the range samples utilizing algorithm in Section 2. We choose the K training data which is highly correlated with the cell under test (CUT) by setting a threshold. Finally, we calculate the covariance matrix $\widehat{\mathbf{R}}$ utilizing the K chosen training data as defined by

$$\widehat{\mathbf{R}} = \frac{1}{K} \sum_{0}^{K-1} \mathbf{Z}_k \mathbf{Z}_k^H. \tag{18}$$

We assume that CUT is the tth range bin. $\mathbf{X}_t$ is the sample in CUT. Therefore, training data $\mathbf{Z}_k$ should be highly correlated with the sample $\mathbf{X}_t$. And $\mathbf{Z}_k$ are chosen from $\mathbf{X}_l$, $l = 1, 2, \ldots, t-p, t+p, \ldots$ where p is the number of protected range bins which are used to keep the training data to be independent of $\mathbf{X}_t$. That is because the target in HFSWR often spreads a few range bins, and the range samples in these range bins are nonindependent.

When we get the covariance matrix $\widehat{\mathbf{R}}$, the optimal weights can be expressed as

$$\mathbf{W}_{\text{opt}} = \widehat{\mathbf{R}}^{-1} \widetilde{\mathbf{v}}. \tag{19}$$

The implementation of the improved-JDL can be shown as in the following steps and Figure 9.

(i) Determine the size of LPR and the transformation matrix $\mathbf{T}$ as shown in (16).

(ii) Calculate the ADJEs of CUT and the range samples near the CUT as mentioned in steps (i)~(v) in Section 2.2.

(iii) Calculate the correlation coefficients between the CUT and the nearby range samples as (3).

(iv) Compare the correlation coefficients with the threshold c_0. If it is greater than c_0, these range samples can be treated as training data; otherwise it will be discarded.

(v) Calculate the covariance matrix of the ionospheric clutter utilizing the chosen training data as (18).

3.2. Threshold Chosen. The key point of the improved-JDL is the threshold c_0. Due to different c_0, the chosen training data can be absolutely different. This can result in different covariance matrix and space-time weights. Curve of the improvement factor (IF) and the threshold is shown in Figure 10. The IF is no longer improved as the threshold raised when the threshold is greater than 0.4. Thus, we can choose the threshold that is greater than 0.4 for single target situation.

In the case of HFSWR, the targets often travel with batch. In this condition, the interference between targets must be concerned. Figure 11 shows the correlation between the range sample 1 with only strong target and the range sample 2 with weak target and the ionospheric clutter. The SCR in Figure 11 is the weak target to ionospheric clutter ratio in range sample 2.

When the SCR $<$ 0 dB, the correlation coefficients between the strong target and the weak target are mostly less than 0.8. When the SCR $<$ -10 dB, the correlation coefficients are mostly less than 0.7. As the threshold increased, the number of chosen training data may decrease and the covariance matrix may be calculated inexactly because there are not enough training data.

With both of the correlation and the number of training data considered, the threshold should be little greater than 0.7. Thus it cannot only keep the training meeting highly correlated but also avoid the interferences of the strong targets.

4. Results of Measured Data

We inject one target in the measured data represented in Figure 1 for the single target situation and two targets for

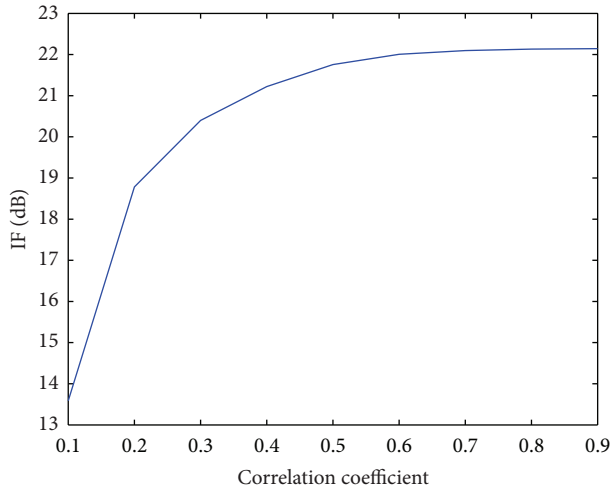

Figure 10: The relationship between the IF and correlation coefficient threshold.

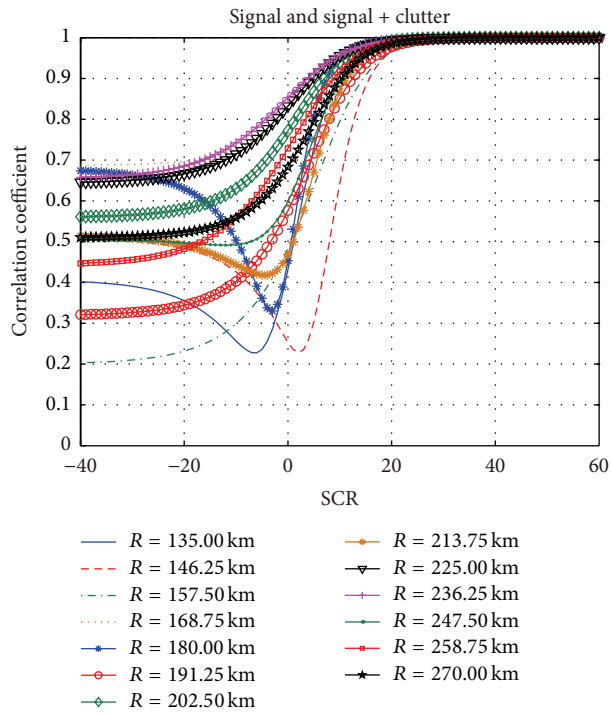

Figure 11: Correlation between the strong target and the weak target within ionospheric clutter.

Table 1: Single target situation.

Range (km)	Doppler shift (Hz)	Angle (°)	SCR (dB)
200.25	−1.2	0	5

the multitargets situation. The parameters of the targets are shown in Tables 1 and 2.

For the single target situation, the injected target can be detected when the threshold is over 0.6 as shown in Figure 12. Compared with the results of the three thresholds, the IF is almost the same. That is in agreement with the conclusion in Section 3.2. However, there are four fake targets at 159.75 km, 231.75 km, 265.5 km, and 319.5 km when the threshold is 0.8. And two fake targets exist when the threshold is 0.7. When the threshold decreases to 0.6, there is no fake target any more. That is because when we process the data in these ranges with threshold 0.7 or 0.8, the training data we have obtained is too few to suppress the ionospheric clutter when the threshold is higher. In this case, the energy of the ionospheric clutter stays at a high level and it is easy to be treated as a "fake target." But the number of the training data increased as the threshold decreased. Thus, there is no fake target when the threshold is lower.

Table 2: Mutitargets situation.

Range (km)	Doppler shift (Hz)	Angle (°)	SCR (dB)
200.25	−1.2	0	0
211.25	−1.2	0	10

Table 3: Range-spread targets situation.

Range (km)	Doppler shift (Hz)	Angle (°)	SCR (dB)
186.75–191.25	−1.2	0	0
227.25–231.75	−1.2	0	10

So for the single target situation, the threshold is set mainly considering the fake targets.

For the multitargets' situation, the results are shown in Figure 13. Focusing on the two-injected targets at range of 200.25 km and 211.25 km, they can both be detected when the threshold is 0.7 or 0.8. And the IF of target 1 is almost the same. But when the threshold is 0.6, the energy of target 1 is weakened. That is because is when the threshold down to 0.6, target 2 is treated as training data. Thus, the covariance matrix of the ionospheric clutter contains the characteristics of target, and so target 1 is weakened.

Similar to the single target situation, there may be fake targets when the thresholds are high and the number of fake targets decreased as the threshold increased. In the actual situation, the multitargets situation is common. So the analysis of this part can make great sense.

Considering both the IF and fake targets problem, the threshold should be set within 0.6 and 0.7 when the improved-JDL algorithm is utilized in HFSWR.

We also consider the range-spread targets in HFSWR as shown in Table 3; we can suppress the ionospheric clutter and detect the two targets as shown in Figure 14 utilizing the improved-JDL method with correlation threshold $c_0 = 0.6$ and the number of protected range bins $p = 2$.

5. Conclusion

To counter the nonhomogeneous ionospheric clutter background of HFSWR, this paper proposes a feature analytical algorithm based on the Angle-Doppler Joint Eigenvector to analyze the range correlation of the nonhomogeneous ionospheric clutter. It turns out that the range correlation coefficient is irregular in its variation. In light of this prior

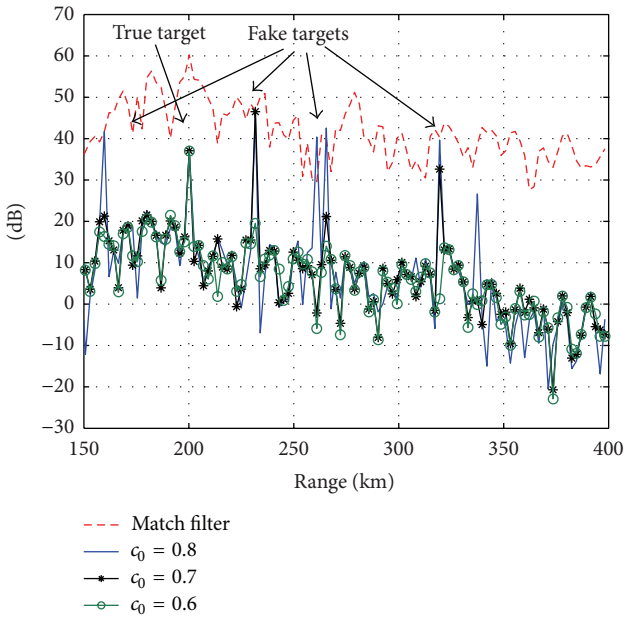

Figure 12: The results by using the improved-JDL for single target situation.

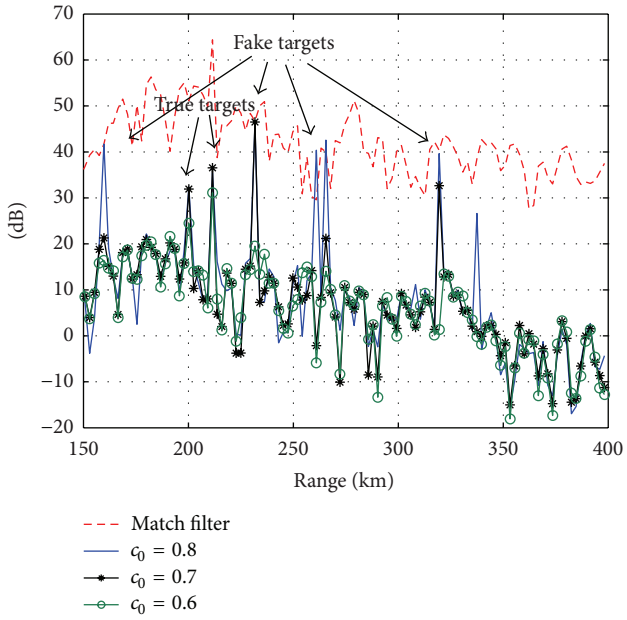

Figure 13: The results by using the improved-JDL for multitarget situation.

knowledge, a further step is taken to deal with the weak target detection problem in HFSWR by analyzing the correlation between targets' signals and the ionospheric clutter and the negative effect imposed by strong targets on weak targets detection. To sum up, this paper proposes a correlation based training data chosen strategy for the JDL algorithm, and discusses the corresponding decision threshold selection in detail. Consequently, decision thresholds should be set up according to the practical situation of the nonhomogeneous

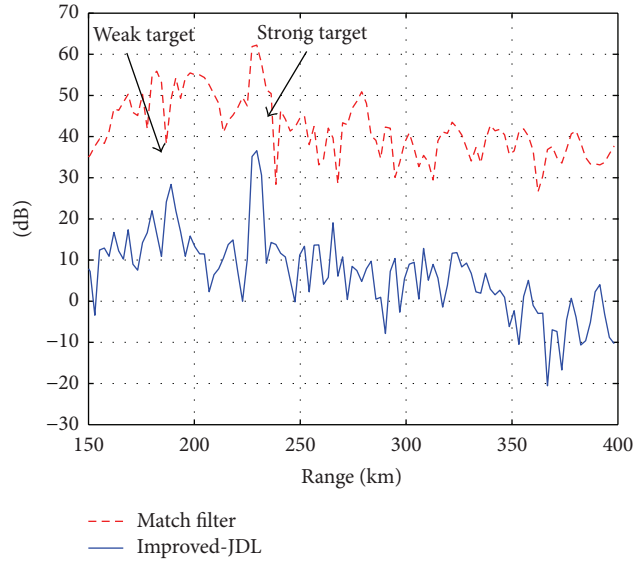

Figure 14: The results by using the improved-JDL for multitarget situation (range-spread targets).

ionospheric clutter and values between 0.6 and 0.7 are preferable. This improved-JDL algorithm is validated by measured data which shows that the weak target detection performance can be notably improved in the background of nonhomogeneous ionospheric clutter.

Acknowledgment

The authors express gratitude to the Institute of Electronic and Information Technology, which provided the HFSWR data, and to those who helped during the writing of this paper. This work was supported in part by the National Science Fund Committee (NSFC) under Grant 61032011.

References

[1] T. Mao, W. Xia, C. Qu, and J. Luo, "A study on characteristics and applications of HF ground wave OTH radar," *Modern Radar*, no. 3, pp. 7–10, 2009.

[2] L. E. Brennan and L. S. Reed, "Theory of adaptive radar," *IEEE Transactions on Aerospace and Electronic Systems*, vol. 9, no. 2, pp. 237–252, 1973.

[3] S. Bidon, O. Besson, and J.-Y. Tourneret, "Knowledge-aided STAP in heterogeneous clutter using a hierarchical bayesian algorithm," *IEEE Transactions on Aerospace and Electronic Systems*, vol. 47, no. 3, pp. 1863–1879, 2011.

[4] X. Zhu, J. Li, and P. Stoica, "Knowledge-aided space-time adaptive processing," *IEEE Transactions on Aerospace and Electronic Systems*, vol. 47, no. 2, pp. 1325–1336, 2011.

[5] J. Wu, T. Wang, X. Meng, and Z. Bao, "Clutter suppression for airborne non-sidelooking radar using ERCB-STAP algorithm," *IET Radar, Sonar and Navigation*, vol. 4, no. 4, pp. 497–506, 2010.

[6] Y. R. Zheng, T. Shao, and E. Blasch, "A fast-converging space-time adaptive processing algorithm for non-Gaussian clutter suppression," *Digital Signal Processing*, vol. 22, no. 1, pp. 74–86, 2012.

[7] W. L. Melvin, "A STAP overview," *IEEE Aerospace and Electronic Systems Magazine*, vol. 19, no. 1, pp. 19–35, 2004.

[8] F. Letestu, "Space-time adaptive processing for navigation," in *Proceedings of the International Radar Symposium (IRS '11)*, pp. 769–773, September 2011.

[9] J. Xie, Y. Yuan, and Y. Liu, "Suppression of sea clutter with orthogonal weighting for target detection in shipborne HFSWR," *IEE Proceedings: Radar, Sonar and Navigation*, vol. 149, no. 1, pp. 39–44, 2002.

[10] G. Fabrizio, D. Holdsworth, and A. Farina, "Experimental HF radar trial of real-time STAP," in *Proceedings of the International Conference on Waveform Diversity and Design (WDD '07)*, pp. 316–320, June 2007.

[11] R. S. Adve, T. B. Hale, and M. C. Wicks, "Practical joint domain localised adaptive processing in homogeneous and nonhomogeneous environments—part 1: homogeneous environments," *IEE Proceedings: Radar, Sonar and Navigation*, vol. 147, pp. 57–65, 2000.

[12] R. S. Adve, T. B. Hale, and M. C. Wicks, "Practical joint domain localised adaptive processing in homogeneous and nonhomogeneous environments—part 2: nonhomogeneous environments," *IEE Proceedings: Radar, Sonar and Navigation*, vol. 147, pp. 66–74, 2000.

[13] M. Ravan, O. Saleh, and R. S. Adve, "KB-STAP Implementation for HFSWR," Final Reprot, University of Toronto, 2008.

[14] O. Saleh, R. S. Adve, and R. J. Riddolls, "Fast fully adaptive processing: a multistage STAP approach," in *Proceedings of the IEEE Radar Conference (RADAR '09)*, pp. 1–6, May 2009.

[15] H. Wang and L. Cai, "On adaptive spatial-temporal processing for airborne surveillance radar systems," *IEEE Transactions on Aerospace and Electronic Systems*, vol. 30, no. 3, pp. 660–670, 1994.

[16] V. Gracheva and D. Cerutti-Maori, "Multi-channel analysis of sea clutter for STAP applications," in *Proceedings of the 9th European Conference on Synthetic Aperture Radar (EUSAR '12)*, pp. 195–198, 2012.

[17] I. S. Reed, J. D. Mallett, and L. E. Brennan, "Rapid convergence rate in adaptive arrays," *IEEE Transactions on Aerospace and Electronic Systems*, vol. 10, no. 6, pp. 853–863, 1974.

[18] Z. Wang, *Research on STAP-based ionospheric clutter suppressing method in high frequency surface wave radar [M.S. thesis]*, Harbin Institute of Technology, Harbin, China, 2010.

Hindawi Publishing Corporation
International Journal of Antennas and Propagation
Volume 2013, Article ID 276310, 5 pages
http://dx.doi.org/10.1155/2013/276310

Research Article

Cross Beam STAP for Nonstationary Clutter Suppression in Airborne Radar

Yongliang Wang, Keqing Duan, and Wenchong Xie

Key Research Laboratory, Wuhan Early Warning Academy, Wuhan 430019, China

Correspondence should be addressed to Keqing Duan; duankeqing@yahoo.cn

Received 4 April 2013; Accepted 30 August 2013

Academic Editor: Hang Hu

A novel space-time adaptive processing (STAP) method for nonstationary clutter suppression is proposed. The developed method forms a multibeam along the cross line to participate in adaptive processing, which sufficiently utilizes the spatial information both in azimuth and elevation and guarantees the least system degrees of freedom (DOFs). The characteristics of this structure help to suppress the short-range clutter which is the primary component of nonstationary clutter. Therefore, this method provides favorable clutter suppression performance when clutter range dependence exists. Approach analysis and simulation results are given to demonstrate the effectiveness of the method.

1. Introduction

Space-time adaptive processing (STAP) can achieve perfect clutter suppression performance in stationary clutter circumstance [1]. However, for non-side looking airborne radar (non-SLAR) (i.e., the radar with inclined side looking array and forward looking array), the clutter is range dependent or nonstationary, especially at short range [2]. In other words, the clutter is mostly nonstationary in practice because of detecting in all directions. Nonstationary clutter can result in the degraded performance of the adaptive processor compared to theoretical predictions.

So far, much effort has been put into this problem. The multiple-PRFs STAP scheme can relieve the blind regions induced by non-side looking and range ambiguity [3]. The main contribution of this attempt is just for solving the range ambiguity problem and not resolving the short-range clutter problem in essence. Compensation methods [4–6] work well when range ambiguity does not exist. Once the radar works at the medium or high pulse repletion frequency (PRF), it cannot identically compensate the ambiguity clutter. In fact, the short-range clutter, induced from the array elevation sidelobe, is the dominant reason for the clutter nonstationarity. The 3D STAP [7] with elevation elements or subarrays can cancel the short-range clutter effectively in theory. Unfortunately, it is hard to get enough independent identically distributed (IID) sample data and requires more computation load because of its large system DOFs. Subarray synthesis algorithm with prefiltering in elevation [8] can effectively suppress the short-range clutter when the element errors do not exist. However, the array antenna errors are inevitable in practice, thereby significantly degrading the performance. In this paper, a STAP method based on cross beam forming is presented in which the auxiliary beams are reasonably chosen in elevation and azimuth to cancel the clutter induced by elevation and azimuth sidelobes.

This paper is organized as follows. In Section 2, the principle of the cross beam STAP method is introduced. Section 3 shows the approach analysis. Simulation results are shown in Section 4, and Section 5 gives the conclusions.

2. Clutter Characteristics for Non-SLAR

In this section, the clutter math model is described and the clutter characteristics for non-SLAR are analyzed. Note that range ambiguity is considered in this model. As shown in Figure 1, the airplane flies along X-axis with velocity V, the θ_p is the angle between the array axes and flying direction, θ_a

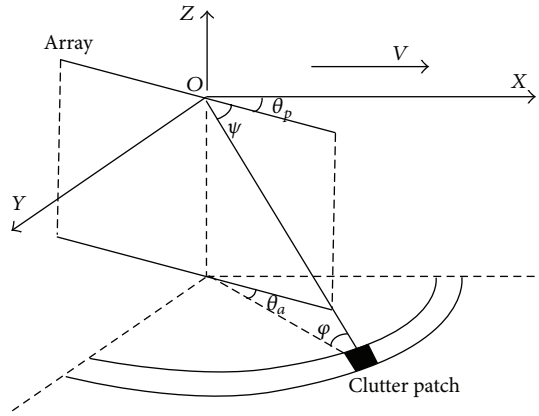

Figure 1: Geometry of non-SLAR.

and φ are the azimuth angle and elevation angle of the clutter patch, respectively, and Ψ denotes the cone angle.

The normalized Doppler frequency of the clutter patch can be described as follows:

$$\begin{aligned}\overline{f}_d &= \frac{2f_d}{f_r} = \frac{4V}{\lambda f_r}\cos\left(\theta_a + \theta_p\right)\cos\left(\varphi\right) \\ &= \frac{4V}{\lambda f_r}\left(\cos\psi\cos\theta_p - \sin\theta_p\sqrt{\cos^2\varphi - \cos^2\psi}\right),\end{aligned} \tag{1}$$

where λ is the wavelength, f_d and f_r denote the Doppler frequency and the PRF, respectively. From (1) we see that the Doppler frequency of the clutter patch varies with the cone cosine when θ_p is nonzero (i.e., the situation of non-SLAR). In other words, the distribution of clutter spectrum varies with range.

The clutter spectrum characteristic of a forward-looking planar array in azimuth-Doppler plane and range-Doppler plane is shown in Figures 2 and 3, respectively. The scenario parameters are given in Section 5. In Figure 2, we see that the clutter is comprised of three parts which are named X_1, X_2, and X_3. According to the conventional planar array pattern, we can conclude that X_1, X_2, and X_3 are, respectively, induced from elevation sidelobe, azimuth main lobe, and azimuth sidelobe. From Figure 3, we can see that the Doppler frequency of short-range clutter X_1 severely varies with range.

3. Principle of the Cross Beam STAP

A schematic of the proposed STAP architecture is shown in Figure 4. An M row by N column vertical rectangular array is considered. The first stage is beam forming involving MN digitized spatial elements or subarray channels. This results in a total of $P + Q - 1$ beams which include main beam, $Q - 1$ auxiliary beams along elevation with the azimuth main lobe, and $P - 1$ auxiliary beams along azimuth with the elevation main lobe. One thing to be noted is that P or Q is always an odd number. After Digital Fourier Transform (DFT) for the data received from each beam, adaptive processing is applied for clutter suppression.

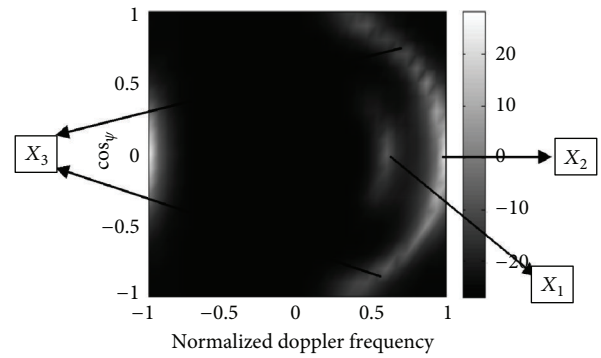

Figure 2: Clutter spectrum distribution of forward-looking planar array in azimuth-Doppler plane.

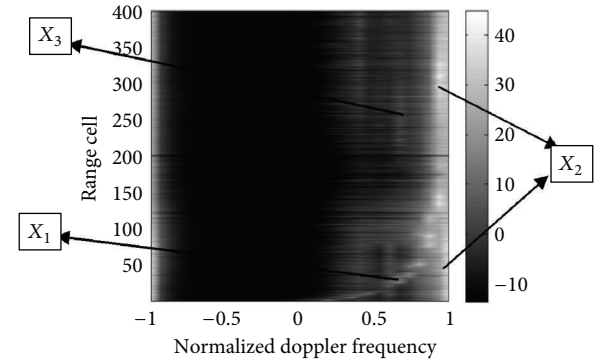

Figure 3: Clutter spectrum distribution of forward-looking planar array in range-Doppler plane.

The received data can be reshaped into an $MN \times K$ data cube $\mathbf{X}$. Let $\mathbf{X}_{MN} \in C^{1\times K}$ denote the echo signals received by the mth element or subarray channel in elevation and the nth element or subarray channel in azimuth, and let K be the pulse number in one coherent pulse interval. The multiple beams can be obtained by

$$\mathbf{A} = \mathbf{T}_a^H\mathbf{X}, \qquad \mathbf{E} = \mathbf{T}_e^H\mathbf{X}, \tag{2}$$

where $(\cdot)^H$ denotes the conjugate transpose, $\mathbf{T}_a \in C^{MN\times P}$ and $\mathbf{T}_e \in C^{MN\times Q}$ are the azimuth and elevation beam transformation matrix, respectively. The pth column of $\mathbf{T}_a$ and the qth column of $\mathbf{T}_e$ have the following forms:

$$\begin{aligned}\mathbf{T}_{ap} &= \Big[\mathbf{S}_{se0}, \mathbf{S}_{se0}e^{j\pi\cos\theta_p\cos\varphi_0}, \ldots, \\ &\qquad \mathbf{S}_{se0}e^{j\pi(N-1)\cos\theta_p\cos\varphi_0}\Big]^T, \quad p = 1, 2, \ldots, P, \\ \mathbf{T}_{eq} &= \Big[\mathbf{S}_{seq}, \mathbf{S}_{seq}e^{j\pi\cos\theta_0\cos\varphi_q}, \ldots, \\ &\qquad \mathbf{S}_{seq}e^{j\pi(N-1)\cos\theta_0\cos\varphi_q}\Big]^T, \quad q = 1, 2, \ldots, Q,\end{aligned} \tag{3}$$

where $(\cdot)^T$ denotes the transpose, θ_p $(p = 1, 2, \ldots, P)$ and φ_q $(q = 1, 2, \ldots, Q)$ are the angle of beams in azimuth and the angle of beams in elevation, respectively, and $\theta_0 = \theta_{(p+1)/2}$

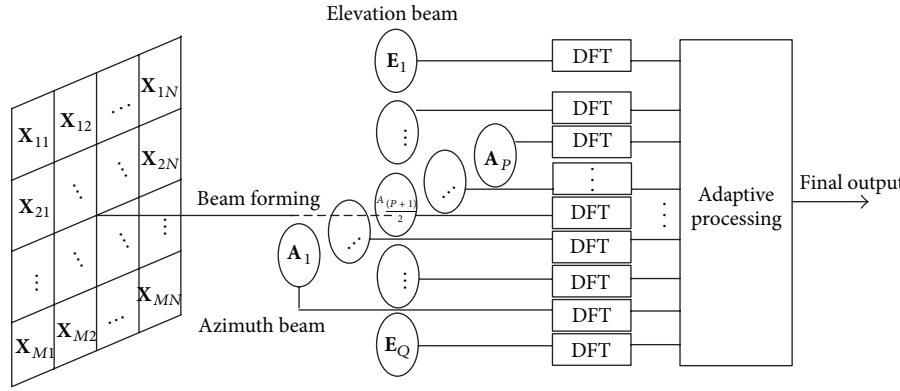

Figure 4: Schematic of the cross beam STAP method.

and $\varphi_0 = \varphi_{(q+1)/2}$ are the azimuth angle and elevation angle of the main lobe. $\mathbf{S}_{se0}$ and $\mathbf{S}_{seq}$ are defined as follows:

$$\mathbf{S}_{se0} = \left[1, e^{j\pi \sin\varphi_0}, \ldots, e^{j\pi(M-1)\sin\varphi_0}\right],$$
$$\mathbf{S}_{seq} = \left[1, e^{j\pi \sin\varphi_q}, \ldots, e^{j\pi(M-1)\sin\varphi_q}\right]. \quad (4)$$

Then the transformation matrix for cross beams can be written as

$$\mathbf{T}_s = \left[\mathbf{T}_a, \mathbf{T}_e\left(1, 2, \ldots, \frac{Q-1}{2}, \frac{Q+3}{2}, \ldots, Q\right)\right]. \quad (5)$$

Let $\mathbf{T} \in C^{MNK\times(P+Q-1)L}$ be the transformation matrix in space and time domain. Then it has the following form:

$$\mathbf{T} = \mathbf{T}_t \otimes \mathbf{T}_s, \quad (6)$$

where L is the dimension after dimension reducing in time domain, $\otimes$ denotes the Kronecker product, and $\mathbf{T}_t \in C^{K\times L}$ is the dimension-reduced matrix in time domain and often transforms the pulse data to several adjacent Doppler bins in most conventional STAP algorithms.

After transforming the received data $\mathbf{X}$ to beam-Doppler domain, we can get the optimum weight by solve the following optimization problem:

$$\begin{aligned} \min \quad & \mathbf{W}^H\left(\mathbf{T}^H\mathbf{R}\mathbf{T}\right)\mathbf{W}, \\ \text{s.t.} \quad & \mathbf{W}^H\left[\mathbf{T}^H\left(\mathbf{S}_t \otimes \mathbf{S}_s\right)\right] = 1, \end{aligned} \quad (7)$$

where $\mathbf{R} = E[\mathrm{Vec}(\mathbf{X})\,\mathrm{Vec}(\mathbf{X})^H]$, $\mathrm{Vec}(\cdot)$ denotes the matrices operation that stacks the matrix under each other to form a column vector, and $\mathbf{S}_t$ and $\mathbf{S}_s$ are the time domain and space domain steering vectors which can be represented by

$$\mathbf{S}_t = \left[1, e^{j2\pi f_d/f_r}, \ldots, e^{j2\pi(K-1)f_d/f_r}\right]^T,$$
$$\mathbf{S}_s = \left[\mathbf{S}_{se0}, \mathbf{S}_{se0}e^{j\pi\cos\theta_0\cos\varphi_0}, \ldots, \mathbf{S}_{se0}e^{j\pi(N-1)\cos\theta_0\cos\varphi_0}\right]^T. \quad (8)$$

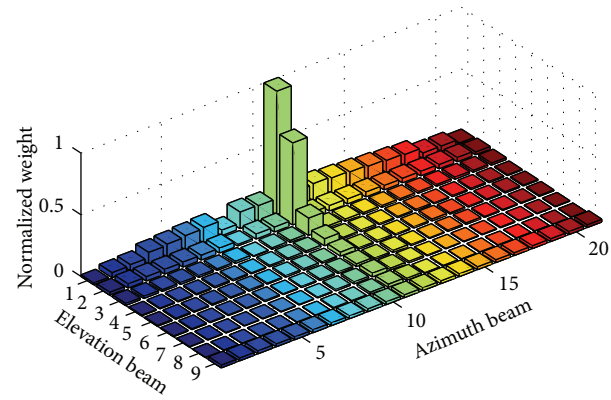

Figure 5: Adaptive weight normalized amplitude of the multibeams at the 28th Doppler bin.

4. Approach Analysis

For STAP in non-SLAR, the more system degrees of freedom (DOFs) in elevation, the better the nonstationary clutter suppression performance can be achieved [7, 8]. However, the added elements or subarrays in elevation lead to the huge requirements for IID samples and computation load. The 3D STAP [7] is a typical example for that. Fortunately, it can be more flexible and effective to utilize the information in elevation if the data are transformed into beam domain. Figure 5 shows the normalized amplitude of the adaptive weight in space domain at the 28th Doppler bin when all the received data are transformed to multibeams. The clutter at the 28th Doppler bin is comprised of short-range clutter and azimuth sidelobe clutter. It can be seen from Figure 5 that the adaptive weight amplitude is large in the cross lines aiming at the elevation and azimuth main beam region, and small in the other position. It further demonstrates that the selection strategy of the cross beams is reasonable for nonstationary clutter suppression.

Figure 6 shows the eigenspectrum of the clutter at the 28th Doppler bin. The scenario parameters are described in the next part. From Figure 6 we can see that the eigenvalue number of cross beams is the least and the eigenvalue number

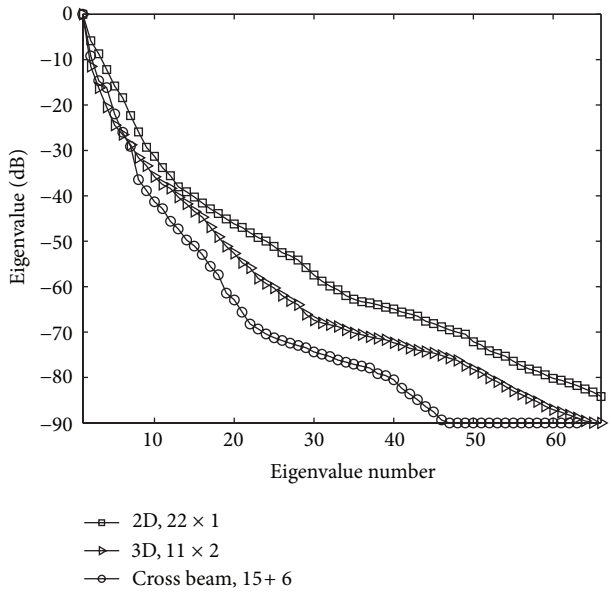

Figure 6: Eigenspectrum of clutter at the 28th Doppler bin.

of synthesized channels is the most. This result indicates that there are more redundant system DOFs to suppress clutter [9] for the new method compared with conventional 2D and 3D STAP method.

5. Simulation Results

A 220-element forward-looking planar array steered to 0° in azimuth and 3° in elevation is used, in which 22 elements are in azimuth and 10 elements are in elevation. Three correlative STAP methods are considered in this simulation for comparison. The typical 2D STAP with synthesized 22 spatial channels in azimuth is firstly considered. The second is the 3D STAP method with synthesized 11 × 2 spatial channels in azimuth and elevation. The recent STAP method based on elevation spatial prefiltering is also investigated in ideal and error conditions, respectively. The platform height is 8000 m. The platform velocity is chosen so that there are no Doppler ambiguities. The pulse number and Doppler bins are both 32 and the short-range clutter distributed at the 24th to 30th Doppler bins. The number of Doppler bins for STAP is selected as 3. The range cell under test is chosen as 50. The numbers of formed beams are 21 and 9 in azimuth and elevation, and P and Q are, respectively, chosen as 15 and 7.

Figure 7 shows the signal-to-clutter-plus-noise ratio (SCNR) loss (i.e., loss relative to the clutter-free case) against Doppler frequency for a target located at the look direction when there are no errors in array. From Figure 7 we can see that the short-range clutter suppression performance of 3D STAP is better than that of the 2D STAP and worse than elevation prefiltering and cross beam STAP method when array errors are ignored. In this condition, the performance of cross beam STAP is close to the elevation prefiltering STAP method.

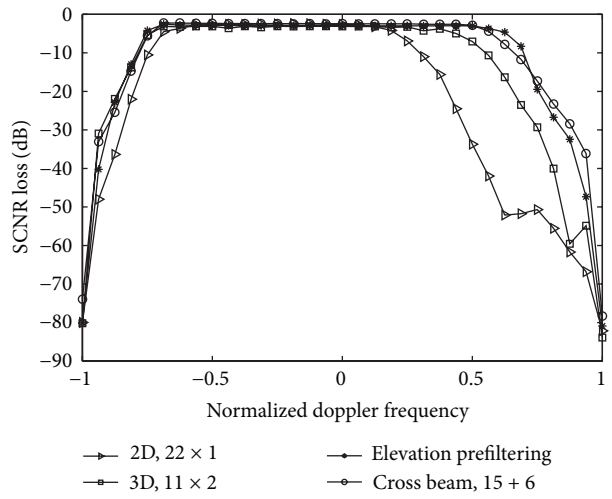

Figure 7: SCNR loss comparison of 2D STAP, 3D STAP, elevation prefiltering STAP, and cross beam STAP (no errors).

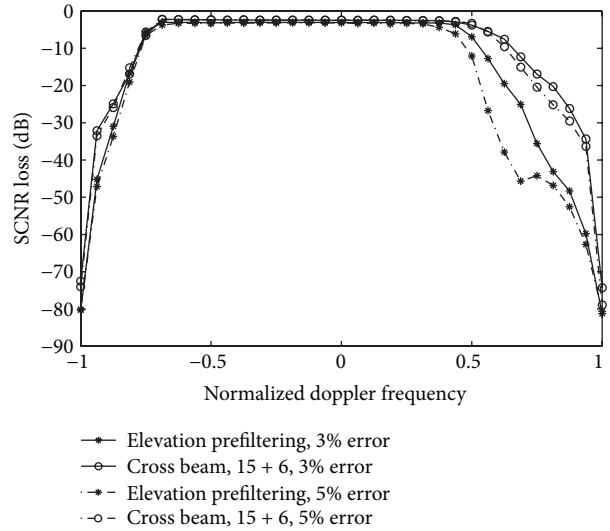

Figure 8: SCNR loss comparison of elevation prefiltering STAP and cross beam STAP with different errors.

Figure 8 shows the SCNR loss of the elevation prefiltering STAP method and cross beam STAP method when element errors exist. From Figure 8 we can see that the clutter suppression performance in short-range region of elevation prefiltering STAP method evidently degrades than the no error situation. However, the proposed cross beam STAP method's performance only slightly degrades and is significantly superior to the elevation prefiltering STAP method. Therefore, the cross beam STAP method has better robustness than the elevation prefiltering STAP method.

6. Conclusions

A new postbeam STAP method for nonstationary clutter suppression in airborne radar has been presented. Simulation

results show that the short-range clutter suppression performance of cross beam STAP is superior to the existing 2D STAP, 3D STAP, and elevation prefiltering STAP methods. The computation load of the new method is close to the 2D and 3D STAP when the system DOF is chosen to be the same, and is larger than the elevation prefiltering STAP.

Acknowledgment

This work was supported in part by the National Nature Science Foundation of China under contract 60925005 and 61102169.

References

[1] R. Klemm, *Principles of Space-Time Adaptive Processing*, IEE, London, UK, 2002.

[2] Y. L. Wang and Y. N. Peng, "Space-time adaptive processing for airborne radar with various array orientations," *IEE Proceedings*, vol. 144, no. 6, pp. 330–340, 1997.

[3] Y. Wang, Z. Bao, and Y. Peng, "STAP with medium PRF mode for non-side-looking airborne radar," *IEEE Transactions on Aerospace and Electronic Systems*, vol. 36, no. 2, pp. 609–620, 2004.

[4] O. Kreyenkamp and R. Klemm, "Doppler compensation in forward-looking STAP radar," *IEE Proceedings*, vol. 148, no. 5, pp. 253–258, 2001.

[5] B. Himed and A. Hajjari, "STAP with angle-doppler compensation for bistatic airborne radars," in *Proceedings of the 2002 IEEE Radar Conference*, pp. 22–25, Long Beach, Calif, USA, April 2002.

[6] W. L. Melvin and M. E. Davis, "Adaptive cancellation method for geometry-induced nonstationary bistatic clutter environments," *IEEE Transactions on Aerospace and Electronic Systems*, vol. 43, no. 2, pp. 651–672, 2007.

[7] P. M. Corbell and T. B. Hale, "3-dimensional STAP performance analysis using the cross-spectral metric," in *Proceedings of the IEEE Radar Conference*, pp. 610–615, Long Beach, Calif, USA, April 2004.

[8] X. Meng, T. Wang, J. Wu, and Z. Bao, "Short-range clutter suppression for airborne radar by utilizing prefiltering in elevation," *IEEE Geoscience and Remote Sensing Letters*, vol. 6, no. 2, pp. 268–272, 2009.

[9] Z. H. Zhang, W. C. Xie, and W. D. Hu, "Local degrees of freedom of airborne array radar clutter for STAP," *IEEE Geoscience and Remote Sensing Letters*, vol. 6, no. 1, pp. 97–101, 2009.

Hindawi Publishing Corporation
International Journal of Antennas and Propagation
Volume 2013, Article ID 862029, 8 pages
http://dx.doi.org/10.1155/2013/862029

Research Article

A Frequency Selection Method Based on the Pole Characteristics

Songyan Yang,[1] Weibo Deng,[1] Qiang Yang,[1] Guangxin Wu,[2] and Ying Suo[1]

[1] *Harbin Institute of Technology, Harbin 150001, China*
[2] *Nanjing Research Institution of Electronic Technology, Nanjing 210000, China*

Correspondence should be addressed to Songyan Yang; verayang88@126.com

Received 4 April 2013; Revised 18 June 2013; Accepted 18 June 2013

Academic Editor: Krzysztof Kulpa

Due to the heavy jamming band of high frequency, frequency selecting strategies are serious issues for the system designed to achieve its best performance. Pole is independent of the direction and polarization of the incident wave, but the residue corresponding to the pole is related to the direction and polarization of the incident wave. And the value of residue is proportional to the value of the pole. This paper chooses the frequency which can maximize the residue in the high-frequency band as the optimal frequency for accurate extraction. The simulation result of a large number of ship targets shows remarkable rise in average recognition rate by using this method, compared with the average recognition rate of randomly selected frequency.

1. Introduction

With the extensive application of high-frequency radar, radar frequency selection has become an important research topic [1–5]. The propagation characteristics of the high-frequency electromagnetic waves are not only a function of the distance but also a function of frequency [4]. In the case of the same distance, the higher the frequency, the faster the attenuation of electromagnetic waves. The frequency selection will seriously affect the performance of the high-frequency surface wave radar on target detection. It is necessary to optimize the selection of operating frequency of the high-frequency radar in order to get excellent detection performance of high-frequency radar. This paper uses pole characteristic to select frequency, explore criteria for frequency selection optimization, and get the selected frequency optimization method. Finally, the result of simulation for a variety of ship target detection verified the correctness and validity of the method.

2. Frequency Optimization Criterion

To get an optimal operating frequency, the first thing to consider is the frequency optimization criterion. A high-frequency radar operating frequency can be obtained through scientific quantitative calculation in accordance with this criterion so that the high-frequency radar can achieve optimal detection performance. Radar is able to find the goal, that is to say, the average correct recognition rate to meet certain requirements. Paper [6] puts forward that radar working frequency optimization selection is investigated for an optimization selection method based on the minimum classification error rule in order to improve airplane target identification performance and that MER can change to the principle of average correct recognition rate maximum. Optimal operating frequency is the one which makes the average correct identification rate maximum. This also can be called as the principle of average correct recognition rate maximum. The average correct recognition rate can be got from dividing the number of correctly identified test by the total number of randomized trials.

Pole is independent of the direction and polarization of the incident wave, but the residue corresponding to the pole is related to the direction of polarization of the incident wave. And the value of residue is proportional to the value of the pole. Considering the above two factors, select the frequency which corresponds to the maximum value of residue as the optimal frequency.

3. Calculation of Residue

Matrix Pencil Method [7] is proposed on the basis of Pencil of Function [8] and has a higher computational efficiency. It only needs two Hankel matrices constructed by time-domain data sequence of the target. Then seeking the generalized eigenvalue of these two Hankel matrix we can calculate the poles of target. Because Matrix Pencil Method needs not to calculate the root of the characteristic equation as Prony method, Matrix Pencil Method has high antinoise performance. To improve the anti-noise performance of Matrix Pencil Method, Sarkar first applied Matrix Pencil Method in matrix singular value decomposition [9] and gave a method to decide the number of poles, through the matrix low rank approximation which could well inhibit the effects of noise, and the efficiency of the algorithm is improved greatly. But Matrix Pencil Method depends on the selection of relevant parameters; Sarkar studies the beam parameters selection [10] and the method for determining the number of target poles [9]. Matrix Pencil Method has high computational efficiency in certain SNR and good operation steadiness, which is very suitable for the extraction of the target pole.

From previous research we can see that the properties of Matrix Pencil Method are superior than others among a large number of pole extraction methods [6]. But there are some disadvantages, such as the unknown number of poles that will to a large extent affect the matrix method of pole extraction results. We use the improved the overall minimum square Matrix Pencil Method to extract the pole of complex targets [5, 9].

3.1. Principles of Matrix Beam Method. In 1971, after a lot of electromagnetic pulses tests, Baum found that, when objects are excited by electromagnetic pulse, their late response is a series of superposition of attenuation sinusoidal oscillation, and that attenuation factor and oscillation frequency composed the complex natural resonant frequency, which is the pole of target. Baum puts forward the theory of singularity expansion method on the basis of the above phenomena [11, 12].

The late transient response in time domain of target can be represented by a finite sum of damped sinusoids:

$$y(t) = \sum_{i=1}^{M} R_i e^{s_i t}, \tag{1}$$

where $R_i = \alpha_i + j\beta_i$, $S_i = \sigma_i + j\omega_i$; R_i are complex residue; S_i is pole; σ_i, ω_i is, respectively, attenuation factor and resonance pulsation. The discrete form after sampling is

$$y(n) = \sum_{i=1}^{M} R_i z_i^n, \tag{2}$$

where $n = 1, 2, \ldots, N$; N are sampling points. To define the matrix disaggregatedly

$$\mathbf{Y} = [\mathbf{y}_L, \ldots, \mathbf{y}_1, \mathbf{y}_0], \tag{3}$$

$$\mathbf{Y}_1 = [\mathbf{y}_L, \ldots, \mathbf{y}_2, \mathbf{y}_1], \tag{4}$$

$$\mathbf{Y}_2 = [\mathbf{y}_{L-1}, \ldots, \mathbf{y}_1, \mathbf{y}_0], \tag{5}$$

where $\mathbf{y}_l = [y(l), y(l+1), \ldots, y(l+N-L-1)]^T$ $l = 1, 2, \ldots, L$; L is called beam parameters.

Equations (4) and (5), can be written as

$$\mathbf{Y}_1 = \mathbf{Z}_L \mathbf{R} \mathbf{Z}_0 \mathbf{Z}_R, \tag{6}$$

$$\mathbf{Y}_2 = \mathbf{Z}_L \mathbf{R} \mathbf{Z}_R, \tag{7}$$

where,

$$\begin{aligned}
\mathbf{Z}_L &= \begin{bmatrix} 1 & 1 & \cdots & 1 \\ z_1 & z_2 & & z_M \\ \vdots & & \ddots & \vdots \\ z_1^{N-L-1} & z_2^{N-L-1} & \cdots & z_M^{N-L-1} \end{bmatrix}, \\
\mathbf{Z}_R &= \begin{bmatrix} z_1^{L-1} & z_1^{L-2} & \cdots & 1 \\ z_2^{L-1} & z_2^{L-2} & & 1 \\ \vdots & & \ddots & \vdots \\ z_M^{L-1} & z_M^{L-2} & \cdots & 1 \end{bmatrix}, \\
\mathbf{R} &= \operatorname{diag}\{R_1, R_2, \ldots, R_M\}, \\
\mathbf{Z}_0 &= \operatorname{diag}\{z_1, z_2, \ldots, z_M\}.
\end{aligned} \tag{8}$$

Define the matrix pencil

$$\mathbf{Y}_1 - \lambda \mathbf{Y}_2 = \mathbf{Z}_L \mathbf{R} (\mathbf{Z}_0 - \lambda \mathbf{I}) \mathbf{Z}_R, \tag{9}$$

If beam parameters L satisfie $M \le L \le N - M$, then the rank of matrix pencil is M. If $\lambda = z_i$, then the rank of matrix pencil decreased to $M - 1$. In other words, $\{z_i\}$ is generalized eigenvalue of matrix $\{Y_1, Y_2\}$.

$$\mathbf{Y}_1 r_i = z_i \mathbf{Y}_2 r_i, \tag{10}$$

r_i are eigenvectors corresponding to eigenvalue z_i. Equation (10) can also be written as

$$\left(\mathbf{Y}_2^{\dagger} \mathbf{Y}_1 - z_i \mathbf{I}\right) r_i = 0, \tag{11}$$

where superscript "†" represents the generalized inverse of the matrix. It can be seen from (11) that it is possible to obtain the required target pole when eigenvalue of $\mathbf{Y}_1^{\dagger} \mathbf{Y}_2$ is a known value.

And then, target complex residue can be obtained through the least squares method:

$$\mathbf{x} = \left(\mathbf{A}^T \mathbf{A}\right)^{-1} \mathbf{A}^T \mathbf{b}, \tag{12}$$

where

$$\begin{aligned}
\mathbf{A} &= \begin{bmatrix} 1 & 1 & \cdots & 1 \\ z_1 & z_2 & & z_M \\ \vdots & & \ddots & \vdots \\ z_1^{N-1} & z_2^{N-1} & \cdots & z_M^{N-1} \end{bmatrix}, \\
\mathbf{x} &= [R_1, R_2, \ldots, R_M]^T, \\
\mathbf{b} &= [y_0, y_1, \ldots, y_{N-1}]^T.
\end{aligned} \tag{13}$$

3.2. The Choice of Pole Number. Advanced transient response of fully conducting targets can expand into an infinite number of decaying sinusoidal vibrations and forms. And formula (1) constrained the complex attenuation frequency on the M. It is One of the important questions about extracting pole of complex targets is how to select the appropriate M [13]. If the M value is selected too small, it will miss the target's true pole, and the pole will have a large deviation; if the M value is selected too large, it will not only produce false pole but also will lead to true pole position moved.

Pole number of simple targets within a certain frequency band can be easy to get; but for the aircraft and ship target, the pole number M contains in the signal is unknown. For this issue, this paper uses the selection method based on time-domain signal reconstruction error minimized to decide the number of poles [5, 14].

In order to get better results of pole extraction, we can apply the singular value decomposition technique to pole extraction problem with matrix beam methods. Let us suppose formula (1) is accurate; if we ignore deviation and noise which come from modeling and calculations, matrix $\mathbf{Y}$ will become a full rank matrix.

By singular value of formula (3), we can get this:

$$\begin{aligned}
\mathbf{Y} &= \begin{bmatrix}\mathbf{U} & \mathbf{U}'\end{bmatrix}\begin{bmatrix}\Sigma & 0\\ 0 & \Sigma'\end{bmatrix}\begin{bmatrix}\mathbf{V}^{H}\\ \mathbf{V}'^{H}\end{bmatrix},\\
\Sigma &= \operatorname{diag}\left\{\sigma_1, \sigma_2, \ldots, \sigma_M\right\},\\
\Sigma' &= \begin{bmatrix}\sigma_{M+1} & 0 & \cdots & 0\\ 0 & \sigma_{M+2} & & 0\\ \vdots & & \ddots & \vdots\\ 0 & 0 & \cdots & 0\end{bmatrix}_{(N-L-M)\times(L+1-M)}.
\end{aligned} \tag{14}$$

$\sigma_1, \sigma_2, \ldots, \sigma_M$ is the biggest M singular values of $\mathbf{Y}$. If there is no noise, $\sigma_{M+1}, \sigma_{M+2}, \ldots$ will be zero. Take low rank of $\mathbf{Y}$ to approximation of matrix $\widehat{\mathbf{Y}}$:

$$\widehat{\mathbf{Y}} = \mathbf{U}\Sigma\mathbf{V}^{\mathbf{H}}. \tag{15}$$

And we can remove the last column of $\widehat{\mathbf{Y}}$, then we will get matrix $\widehat{\mathbf{Y}}_1$, and if we remove the first column, we will get matrix $\widehat{\mathbf{Y}}_2$ like this

$$\widehat{\mathbf{Y}} = \begin{bmatrix}\widehat{\mathbf{Y}}_1 & \mathbf{y_0}\end{bmatrix} = \begin{bmatrix}\mathbf{y_L} & \widehat{\mathbf{Y}}_2\end{bmatrix}. \tag{16}$$

$\widehat{\mathbf{Y}}_1$, $\widehat{\mathbf{Y}}_2$ singular values can be decomposed as

$$\begin{aligned}
\widehat{\mathbf{Y}}_1 &= \mathbf{U}\Sigma\mathbf{V}_{\mathbf{1}}^{\mathbf{H}},\\
\widehat{\mathbf{Y}}_2 &= \mathbf{U}\Sigma\mathbf{V}_{\mathbf{2}}^{\mathbf{H}}.
\end{aligned} \tag{17}$$

removes the last column of matrix $\mathbf{V}^{\mathbf{H}}$ will get $\mathbf{V}_{\mathbf{1}}^{\mathbf{H}}$, and if remove the first column, we'll get $\mathbf{V}_{\mathbf{2}}^{\mathbf{H}}$.

Theorem [15] If matrix $\mathbf{Y}$'s rank greater than or equal M, then there exists the only matrix of the same dimensions $\widehat{\mathbf{Y}}$, and the rank is equal to M, which makes the norm of $\|\mathbf{Y} - \widehat{\mathbf{Y}}\|_F$ Frobenius minimum. The extent of best approximation is described by $\|\mathbf{Y} - \widehat{\mathbf{Y}}\|_F = \sum_{i=M+1}^{N-L} \sigma_i$, where $\|\cdot\|_F$ indicates Frobenius norm.

Theorem explains that the use of $\widehat{\mathbf{Y}}$ is the optimal approximation to $\mathbf{Y}$ under F-norm in theory. We will get $\widehat{\mathbf{Y}}_1$ and $\widehat{\mathbf{Y}}_2$ through $\widehat{\mathbf{Y}}$; then the eigenvalue of $\widehat{\mathbf{Y}}_1^{\dagger}\widehat{\mathbf{Y}}_2$ will be got. This method can effectively inhibit the effects of noise on pole extraction. This singular value decomposition technique applied to a method of matrix beam method is called total least square matrix beam method [5].

Theorem in the assumption of formula (1) is accurate and on the condition of M is known. In the actual pole extraction, M is unknown, and it cannot be determined only through the distribution of singular values $\sigma_1, \sigma_2, \ldots, \sigma_M, \sigma_{M+1}, \sigma_{M+2}, \ldots$. Because of the distribution of singular value, neither M is rendered when you select a value, then the singular value is far smaller than the preceding singular value, nor M appears when you select a value, followed by singular value of size are essentially the same. Therefore you need to focus on pole number M of selection method.

It can judged by pole extraction results to decide the parameters selection is good or not. We will use the deviations between theoretical and extraction as criteria to constrain parameters selection and to get the best parameters M. But the most target theoretical pole is unknown, so it needs to give a reasonable and actionable criterion.

If the target number of pole M is known, pole z_i can be achieved by matrix beam method, and the complex residue of target R_i can be got by arithmetic expression (4). It also can reconstruct the time domain signal $y_{\mathrm{rec}}(k)$ of target, then we will use the error between the reconstructed domain signal $y_{\mathrm{rec}}(k)$ and domain signal $y_{\mathrm{cal}}(k)$

$$S(M) = \sum_{k=1}^{N}\left(y_{\mathrm{rec}}(k) - y_{\mathrm{cal}}(k)\right)^2. \tag{18}$$

As a criterion

$$\min_{M}\sum_{k=1}^{N}\left(y_{\mathrm{rec}}(k) - y_{\mathrm{cal}}(k)\right)^2 \tag{19}$$

Choosing the appropriate parameter M_{opt}.

Cause M can meet

$$M \in \mathbf{N}, \quad 1 \le M \le \min\{L, N - L\} \tag{20}$$

And usually target scattering data length N is not too long; the value of L is generally around $N/3$. So the value of M is an integer from 1 to $N/3$. We can directly choose all parameters M within the interval range to calculate $S(M)$ select minimal parameter $S(M)$ which is corresponding to M as the most appropriate parameters M_{opt}. Figure 1 shows that the ship target error $S(M)$ and pole number determine the results of process variation of $S(M)$ with parameter M. It can be seen that as M is increasing, errors it first shows shock reducing, then minimum is reached, and at last it will be larger again.

We can see from Figure 1 that in this paper, the best number of pole is $M = 46$. This approach can reduce the impact because models are inaccurate, and there are deviations in the data and the noise, extracting the precise targets pole.

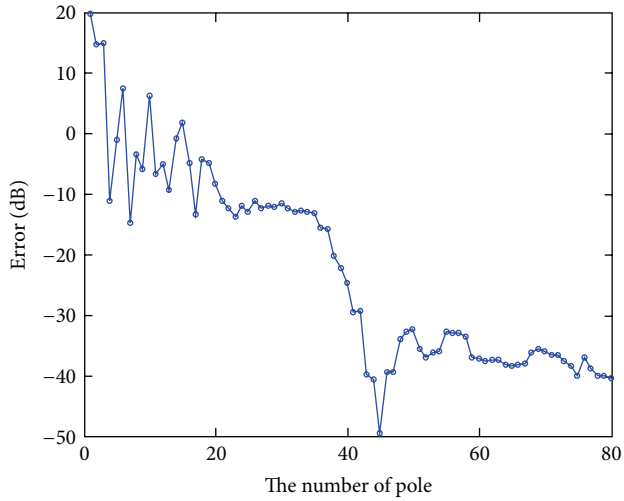

Figure 1: The error is changing with the value of M in different.

4. Simulation

4.1. The Rationality of the Residue Selected Frequency. To prove the rationality of the residue selected frequency, we need to verify that the residue is a main contribution to RCS. Because the residue is obtained from the late response, we need to compare the contribution of the early and late response to the RCS for the first step.

4.1.1. How to Recover RCS by Using Late Response Only. Target time-domain transient response and frequency response are the Fourier transform for each other. If we can recover the time-domain transient response, the frequency domain response of the target can be obtained naturally. Target time-domain transient response is composed of early and late responses, which can be written as

$$y_{\text{all}}(t) = y_{\text{ear}}(t) + y_{\text{lat}}(t), \tag{21}$$

where $y_{\text{ear}}(t)$, $y_{\text{lat}}(t)$ represent the early and late responses. And $y_{\text{lat}}(t)$ is the $y(t)$ in formula $y(t) = \sum_{i=1}^{M} R_i e^{s_i t}$; we can rewrite formula $y(t) = \sum_{i=1}^{M} R_i e^{s_i t}$ as

$$y_{\text{lat}}(t) = \sum_{i=1}^{M} R_i e^{s_i t}. \tag{22}$$

In theory, no matter what form of target transient response $y_{\text{all}}(t)$ is in formula $y_{\text{all}}(t) = y_{\text{ear}}(t) + y_{\text{lat}}(t)$, it can be expanded into an infinite sum number of complex exponential

$$y_{\text{all}}(t) = \sum_{i=1}^{\infty} \widetilde{R}_i e^{\widetilde{s}_i t}, \tag{23}$$

where $\widetilde{R}_i$ is the coefficient of expansion corresponding to exponential term $e^{\widetilde{s}_i t}$. Basis function set $\{\widetilde{s}_1, \widetilde{s}_2, \ldots\}$ definitely contains the target pole set $\{s_1, s_2, \ldots, s_M\}$. Although using only the pole set $\{s_1, s_2, \ldots, s_M\}$ to expand the transient response $y_{\text{all}}(t)$ may exist certain error, but that error is admissible.

$$y_{\text{all}}(t) \approx \sum_{i=1}^{M} \widehat{R}_i e^{s_i t}, \tag{24}$$

where $\widehat{R}_i$ can be called the new residue corresponding S_i to different from R_i.

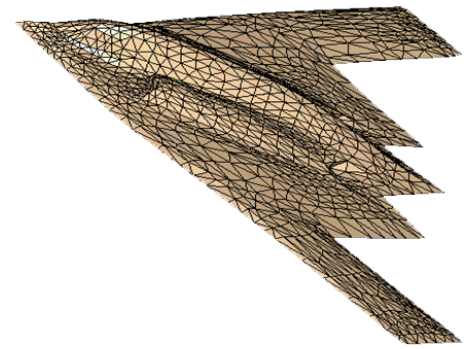

Figure 2: Airplane model using FEMAP ($L \times W \times H$ (m): 49.05 × 56.39 × 12.40).

4.1.2. The Comparison Simulation. Here we get the original RCS by using software FEMAP to model the ship target and FEKO to calculate the RCS. The target we choose 49.05 meters long, 12.40 meters high, and 56.39 meters wingspan airplane, the model of airplane, is shown in Figure 2. The comparison result is shown in Figures 3 and 4, red line represents recovered RCS only by late time response and blue line shows the original RCS, which proves that the late response is a very important contribution to RCS. The above conclusion implies that the residue calculated from late response is also very important to RCS. Next, we will test and verify the above conclusion by estimating the contribution of residue to RCS.

To make the simulation contain common complex goal, this time I use software FEMAP and FEKO to model one ship and calculate its RCS, the model is shown in Figure 5. Then calculating the residue according to the method I described in the paper, incident angle ranges from 0° to 180° at a 10° interval. The frequency selection is from 0.2 MHz to 20 MHz at a 0.2 MHz interval. The number of the pole is 46. The result is shown in Figure 6, We can see that the residue changes with frequency and angle. It shows peak appeared when angle is 90° and frequency is 9.6 MHz.

We can set that maximum residue as zero and then recover the RCS. Comparing the variation of RCS before and after. Figure 7 shows that when maximum residue was replaced by 0, RCS declined to 8 dB–10 dB; the above simulation proves the influence of residue on the value of RCS. The simulation results provide a theoretical basis for using residue to select frequency.

4.2. Compare the Average Correct Recognition Rate

4.2.1. Nearest Neighbor Rule Classification. Modeling E types different target by software FEMAP, discrete the

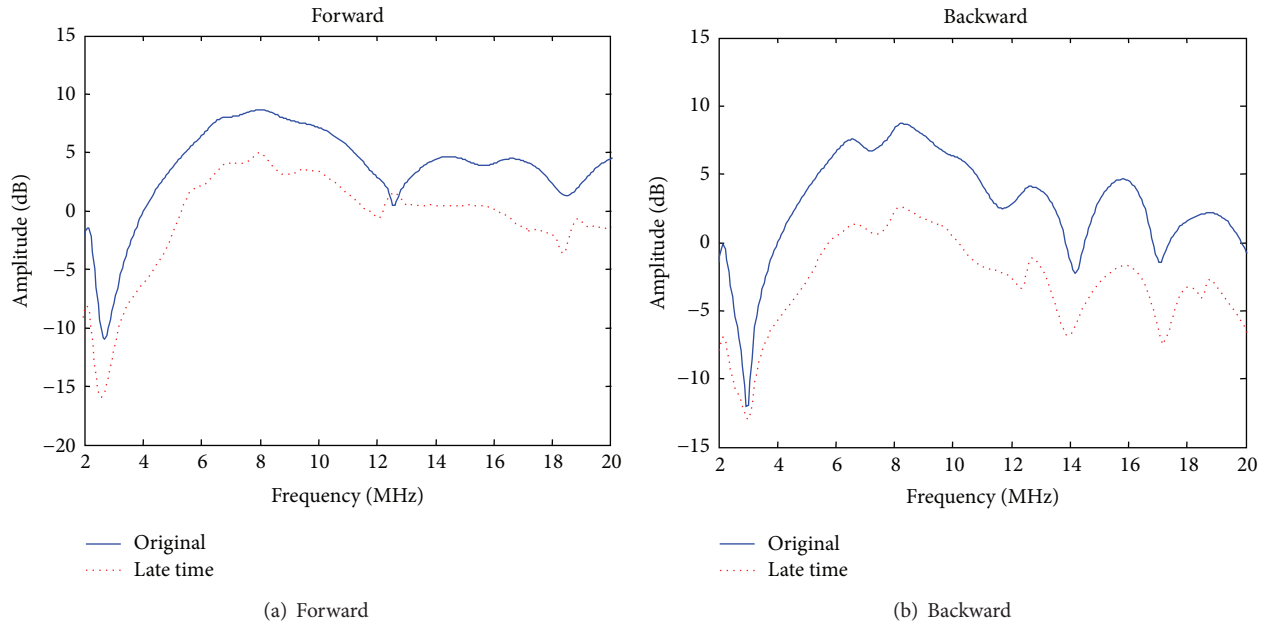

(a) Forward (b) Backward

FIGURE 3: The comparison between original RCS and the RCS recovered only by late time response in frequency domain. (a) The angle between the incident and the bow is 0°. (b) The angle between the incident and the bow is 180°.

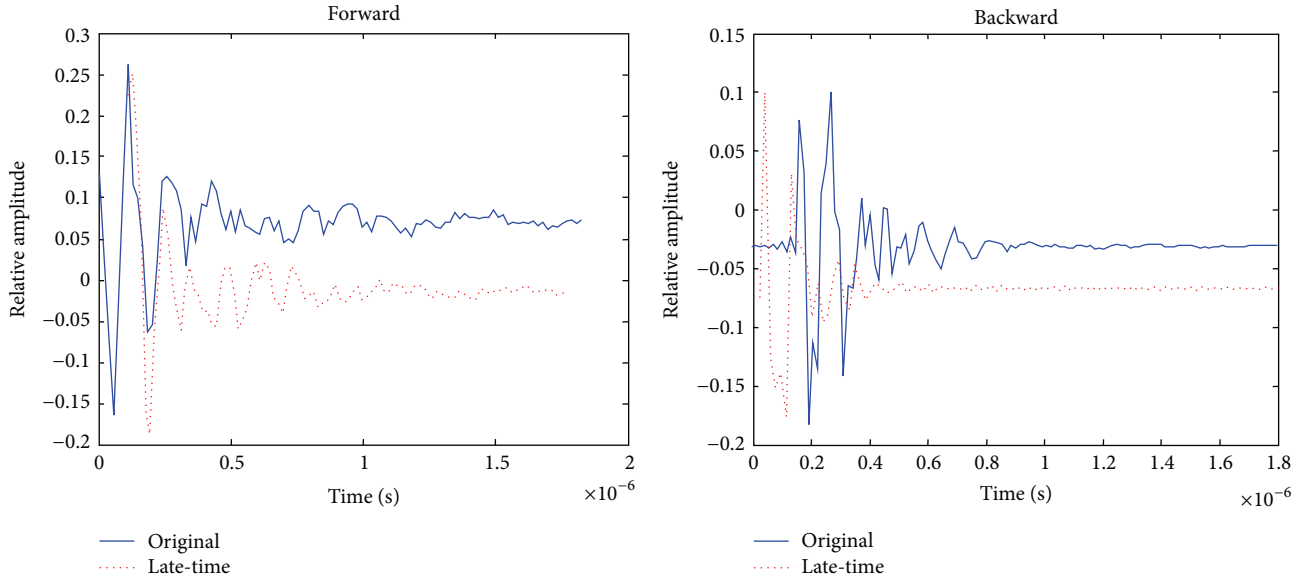

(a) Forward (b) Backward

FIGURE 4: The comparison between original RCS and the RCS recovered only by late time response in time domain. (a) The angle between the incident and the bow is 0°. (b) The angle between the incident and the bow is 180°.

high-frequency band into K frequency points with a fixed interval, obtain the RCS by FEKO calculating in all angle, we can get a target database in high-frequency band:

$$\mathbf{D} = \begin{bmatrix} \mathbf{D}_1 & \mathbf{D}_2 & \cdots & \mathbf{D}_E \end{bmatrix} = \begin{bmatrix} D_{11} & D_{12} & \cdots & D_{1K} \\ D_{21} & D_{22} & \cdots & D_{2K} \\ \vdots & \vdots & \ddots & \vdots \\ D_{E1} & D_{E2} & \cdots & D_{EK} \end{bmatrix}. \quad (25)$$

Extracted k frequency points from K frequency points, are equivalent to extracted k column vectors from K column vectors in above matrix, to constitute a submatrix:

$$\overline{\mathbf{D}} = \begin{bmatrix} \overline{\mathbf{D}}_1 & \overline{\mathbf{D}}_2 & \cdots & \overline{\mathbf{D}}_E \end{bmatrix}^T = \begin{bmatrix} D_{11} & D_{12} & \cdots & D_{1k} \\ D_{21} & D_{22} & \cdots & D_{2k} \\ \vdots & \vdots & \ddots & \vdots \\ D_{E1} & D_{E2} & \cdots & D_{Ek} \end{bmatrix}. \quad (26)$$

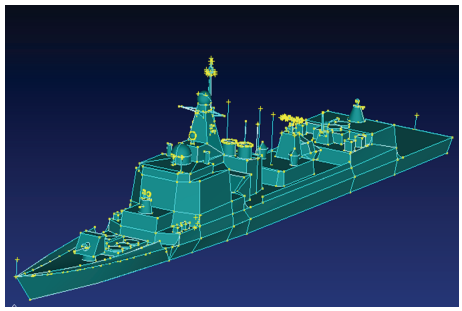

Figure 5: Ship model using FEMAP Destroyer ($L \times W \times H$ (m): $154.0 \times 17.0 \times 6.0$).

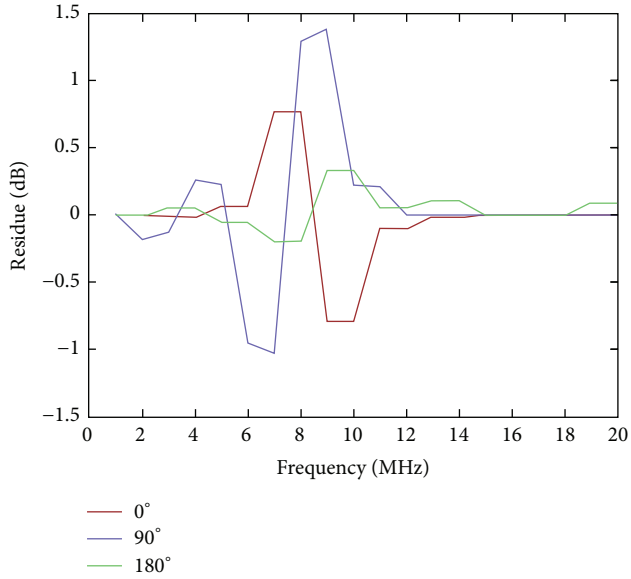

Figure 6: The ship target residue varies with frequency and angle where the x-axis is frequency and y-axis is residue. The red line represents the residue changing trend with frequency when angle is 0°, blue line represents 90°, and green line is 180°.

$\overline{\mathbf{D}}_i$ is a radar target feature vector; name $\overline{\mathbf{D}}$ as radar target feature space composite of E types target feature vector.

Obtain the RCS on k frequency points by actual measurement, write it as

$$\widehat{\mathbf{D}} = \left[\widehat{D}_1, \widehat{D}_2, \ldots \widehat{D}_k\right], \tag{27}$$

name it radar target measurements eigenvectors.

According to the existing research Ksienski and Lin show that the nearest neighbor classification method for the class of complex radar target aircraft has better recognition results [11]. The Euclidean distance between measuring characteristic feature and the E types target in target feature space is

$$d_m = \left\|\widehat{\mathbf{D}} - \overline{\mathbf{D}}_m\right\| = \left[\sum_{j=1}^{k} (\widehat{D}_j - D_{mj})^2\right]^{1/2}. \tag{28}$$

According to nearest neighbor classification, if

$$d_m < d_n, \quad m, n = 1, 2, \ldots E; \; n \neq m \tag{29}$$

target is E type.

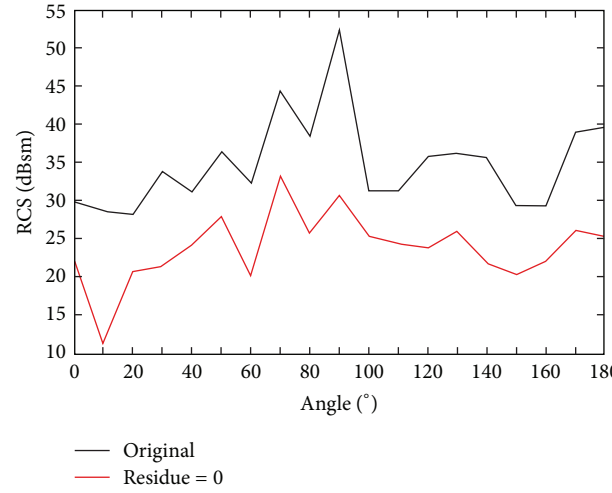

Figure 7: Comparison of RCS between original and residue = 0.

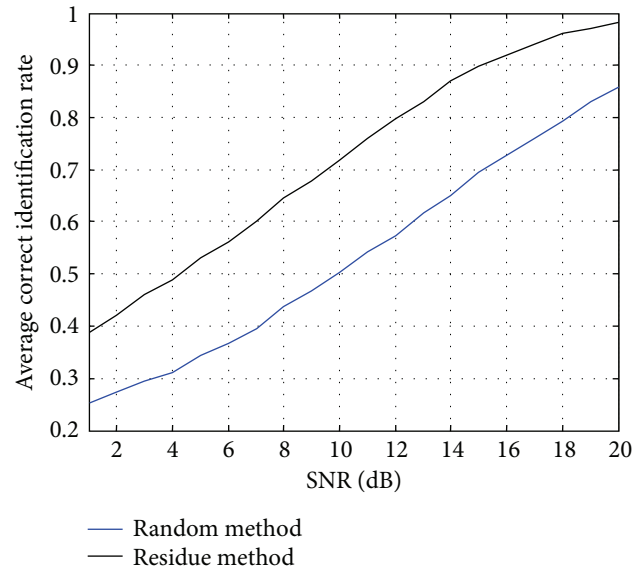

Figure 8: Average correct recognition rate changes with the signal-to-noise ratio by different frequency selection methods for 6 classes of target.

4.2.2. Simulation. In order to study the effect of the maximum number residue frequency-selective method of ship target also verifies that the maximum residue frequency selection method can effectively improve the recognition effect. I do a large number of random tests to verify the correctness of the theory and the effectiveness of the method.

The simulation selected 6 typical classes of ship target as a target to be classified from the library of high-band ship target characteristics; the type of ship targets and basic dimensions are shown in Table 1, Including aircraft carriers, cruisers, destroyers, frigates, hunting submarines, missile boats, and different types of ships. Here added noise to calculated target RCS to simulate the measured data, cause many of them are secret we cannot get the measured data. Here we can name this RCS calculated RCS with noise to different from below.

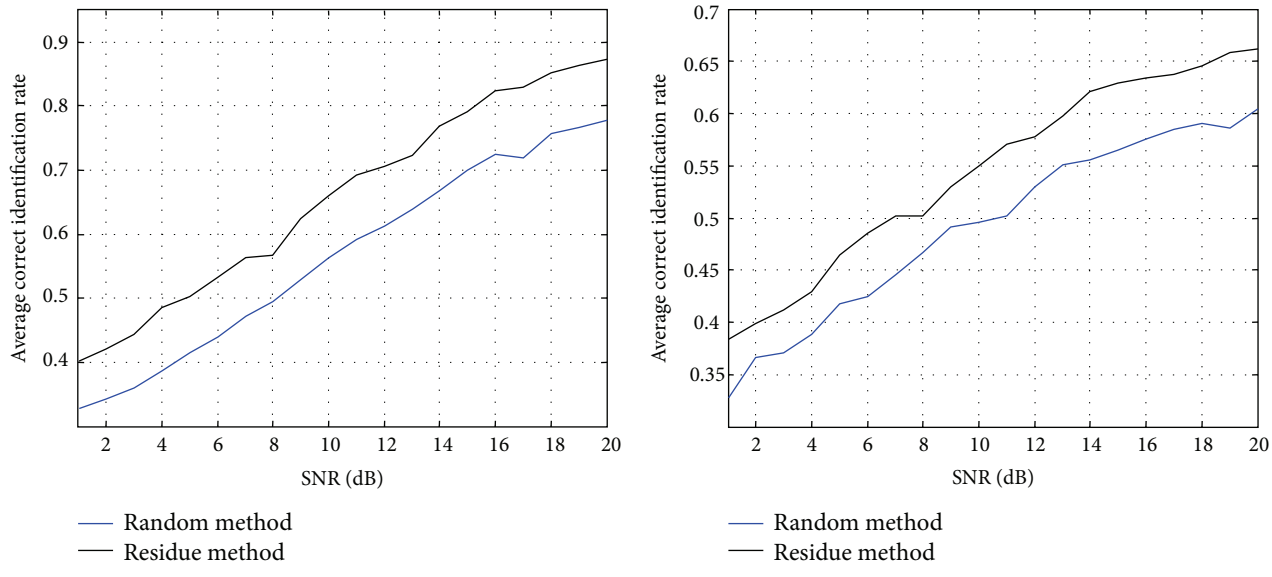

(a) The measuring deviation is ±1 dB

(b) The measuring deviation is ±2 dB

Figure 9: The average correct identification rate changes trend of 6 targets with different SNR when deviations exist. (a) The measuring deviation is ±1 dB. (b) The measuring deviation is ±2 dB.

Table 1: Ship targets size.

Serial	Target type	$L \times W \times$ draft (m)
1	Aircraft carrier	$323.6 \times 39.6 \times 11.4$
2	Cruisers	$172.8 \times 16.8 \times 9.5$
3	Destroyers	$154.0 \times 17.0 \times 6.0$
4	Frigate	$138.7 \times 13.5 \times 4.7$
5	Submarine chasers	$58.8 \times 7.2 \times 2.2$
6	Missile boat	$60.0 \times 8.8 \times 2.3$

Assume that select the m target, add Gaussian white noise with zero mean; mean square deviation is σ, and signal-to-noise ratio is calculated using

$$\mathrm{SNR} = \frac{1}{k}\sum_{j=1}^{k}\frac{D_{mj}}{\sigma^2}. \tag{30}$$

Here does not consider the situation that the target is not included in the target class to be classified.

1000 randomized tests are conducted to study the changes of the correct identification rate in different signal-to-noise ratios with the different frequency selection method. Figure 8 shows average correct recognition rate comparison between maximum residue frequency selection method and random frequency selection method of 6 goals. Apparently, the average correct recognition rate of maximum residue selection frequency method is better than random frequency selection method. The former method is about six percent higher than the latter. The average correct recognition rate of maximum residue selection frequency method can be as high as 0.8.

To make the simulation much more closer to real conditions, we need to consider that there may be deviations between the measurement RCS and calculated RCS from simulation. That deviations may come from the bug of software or the noise that affects the measurement of RCS. In this simulation, a larger amount of uniformly distributed random value is added to calculated RCS as that deviation. Taking into account that the RCS deviation may occur in the reality as x dB, to m target's j frequency, we add uniformly distributed random value in the range of $[-\Delta D_{mj}, \Delta D_{mj}]$, satisfying $x = 10 \cdot \log(\Delta D_{mj}/D_{mj})$. At the same time, Gaussian white noise we discuss in Figure 6 is still added (calculated RCS with noise). Figure 9 shows the recognition results of 6 ship targets at two operating frequencies 13.4 MHz and 15 MHz when taking consideration of the deviations between the measure RCS and calculated RCS.

From Figure 8, Compare the average correct recognition rate of the above method and the random frequency selection method when angle is 90°; average correct identification rate of my method is 82.76% when SNR is 13 dB, while the average correct identification rate of the random frequency selection mode is 61.33% when SNR is 13 dB, which verifies the effectiveness of the method.

In Figure 9, we can see that the average correct recognition rate declined quickly when measuring deviation becomes larger. When measuring deviation is ±1 dB, the average correct recognition rate can reach 0.87. When measuring deviation is ±2 dB, the average correct recognition rate can reach 0.68. Comparing Figure 9 with Figure 8 we can that the measuring deviation does have an influence on the average correct recognition rate. But it can be overcome by adding more frequency. The simulation of 4 frequencies 13.4 MHz, 15 MHz, 16.6 MHz, and 20 MHz is shown in Figure 10, from which we can see that the average correct recognition rate can reach 0.85.

From above comparison we can get the conclusion that the measuring deviation has a great influence on recognition

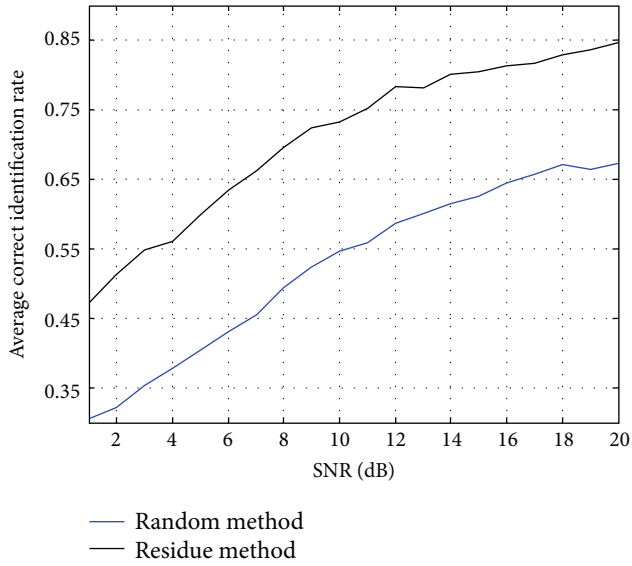

Figure 10: The measuring deviation is ±2 dB, and the frequencies are 4: 13.4 MHz, 15 MHz, 16.6 MHz, and 20 MHz.

rate. But this problem can be overcome by adding more frequency even when the measuring deviation exists, and the average recognition rate of the method adopted in this paper is significantly larger than random selected frequency method, which indicated that the robustness of the method is absolutely better than random selected frequency method. And the method is feasible.

5. Conclusion

This paper studies the frequency selection method in high-frequency band radar target recognition. Based on the average correct recognition rate maximization principle, considering the residues corresponding to pole is related to the incident wave direction and polarization; the value of residue is proportional to the value of the pole, a maximum residue frequency selection method was proposed, and satisfactory recognition result is obtained with the simulation experiment on multiclass ship targets. Considering the difference between real measured RCS, and software calculated RCS, we add measurement deviation in software calculated RCS, and the ship target recognition effect under the conditions of different measurement deviations is analyzed. This verifies the correctness and validity of the frequency optimization method.

Acknowledgments

This work was supported in part by the Harbin Institute of Technology (HIT) and in part by the National Natural Science Foundation of China (NSFC) under the Project no. 61171182.

References

[1] A. Taflove and K. R. Umashankar, "Review of FD-TD numerical modeling of electromagnetic wave scattering and Radar Cross Section," *Proceedings of the IEEE*, vol. 77, no. 5, pp. 682–699, 1989.

[2] D. J. Emery, "The choice of operating frequency in HF surface wave radar design," in *Proceedings of the 9th International Conference on HF Radio Systems and Techniques*, pp. 278–281, AMS Radar Systems, June 2003.

[3] H.-T. Su, Z. Bao, and S.-H. Zhang, "Adaptive operating frequency selection for SKW-OTHR," *Journal of Electronics and Information Technology*, vol. 27, no. 2, pp. 274–277, 2005.

[4] J.-S. Tian and X.-B. Wu, "Optimized HF radar work frequency on-line real-time," *Modern Radar*, vol. 27, no. 2, pp. 8–10, 2005.

[5] G.-X. Wu, *Radar Target Features Extraction and Target Indentification in Resonance Region*, Harbin Institute of Technology, Heilongjiang, China, 2008.

[6] G.-X. Wu and W.-B. Deng, "HF radar target identification based on optimized multi-frequency features," in *Proceedings of CIE International Conference on Radar (ICR '06)*, pp. 1–4, Shanghai, China, October 2006.

[7] Y. Hua and T. K. Sarkar, "Generalized pencil-of-function method for extracting poles of an EM system from its transient response," *IEEE Transactions on Antennas and Propagation*, vol. 37, no. 2, pp. 229–234, 1989.

[8] V. K. Jain, "Filter analysis by use of pencil of functions," *IEEE Transactions on Circuits and Systems*, vol. 21, no. 5, pp. 574–579, 1974.

[9] T. K. Sarkar and O. Pereira, "Using the matrix pencil method to estimate the parameters of a sum of complex exponentials," *IEEE Antennas and Propagation Magazine*, vol. 37, no. 1, pp. 48–55, 1995.

[10] Y. Hua and T. K. Sarkar, "Matrix pencil and system poles," *Signal Processing*, vol. 21, no. 2, pp. 195–198, 1990.

[11] C. E. Baum, "The singularity expansion method for the solution of electromagnetic interaction problems," Interaction Note 88, Air Force Weapons Lab, December 1971.

[12] C. E. Baum, "Emerging technology for transient and broadband analysis and synthesis of antenna and scatterers," *Proceedings of the IEEE*, vol. 64, no. 11, pp. 1598–1616, 1976.

[13] A. A. Ksienski, Y.-T. Lin, and L. J. White, "Low-frequency approach to target identification," *Proceedings of the IEEE*, vol. 63, no. 12, pp. 1651–1660, 1975.

[14] W. C. Chen and N. Shuley, "Utilizing the energy of each of the extracted poles to identify the dominant complex natural resonances of the radar target," in *Proceedings of IEEE Antennas and Propagation Society International Symposium*, vol. 1-12, pp. 69–72, June 2007.

[15] X. Zhang, *Modern Signal Processing*, Tsinghua University Press, Beijing, China, 1995.

Hindawi Publishing Corporation
International Journal of Antennas and Propagation
Volume 2013, Article ID 635069, 7 pages
http://dx.doi.org/10.1155/2013/635069

Application Article

First TerraSAR-X TOPS Mode Antenna Pattern Measurements Using Ground Receivers

Gabriel Castellanos Alfonzo,[1] Marco Schwerdt,[1] Steffen Wollstadt,[1] Markus Bachmann,[1] Björn Döring,[1] and Dirk Geudtner[2]

[1] *German Aerospace Center (DLR), Oberpfaffenhofen, 82234 Wessling, Germany*
[2] *European Space Agency (ESA-ESTEC), Keplerlaan 1, 2200 AG Noordwijk, The Netherlands*

Correspondence should be addressed to Gabriel Castellanos Alfonzo; gabriel.castellanosalfonzo@dlr.de

Received 5 April 2013; Accepted 18 June 2013

Academic Editor: Krzysztof Kulpa

The antenna model used for correcting the influence of the antenna pattern on synthetic aperture radar (SAR) images requires on-ground validation and in-flight verification. A methodology for the in-flight verification that is based upon the measurement of azimuth antenna patterns using ground receivers has been successfully demonstrated for the operational SAR modes of the TerraSAR-X (TSX) and TanDEM-X (TDX) missions. Recently, the novel (terrain observation by progressive scans) TOPS mode was for the first time implemented as an experimental mode on TerraSAR-X to demonstrate its feasibility in support of its implementation on ESA's Sentinel-1 mission. In this mode, besides scanning in elevation, the antenna beam is steered in flight direction from aft to the front at a constant rate to achieve an enhanced radiometric image performance. This paper discusses the methodology and presents results of the first in-flight antenna characterization of a SAR instrument operating in TOPS mode, in this case TerraSAR-X, using ground receivers. The results demonstrate that the TOPS one-way azimuth antenna pattern can be accurately modeled by the TSX antenna model indicating the general suitability of this approach for the in-flight antenna model verification during TOPS mode operations.

1. Introduction

The correct modeling of the phased-array antenna in a synthetic aperture radar (SAR) system is of main importance for precise SAR image processing. Accurate knowledge of the antenna characteristics is required in order to remove the influence of the antenna pattern from the image during SAR processing. The large number of SAR beams used by modern SAR satellite missions along with the requirement for having a short duration of the commissioning campaigns requires a SAR calibration concept that is mainly based on the use of a precise antenna model [1]. Other elements of such a calibration concept include the internal calibration and in-orbit health check of the SAR antenna system based on the pseudonoise gating method [2]. Thus, only a limited number of SAR imaging beams would need to be actually measured during the commissioning phase. Following a previous on-ground validation, the antenna model needs to be verified in orbit: in elevation by analyzing the two-way elevation pattern using acquisitions across homogeneous distributed scatterers, that is, Amazon rainforest, and in azimuth by measuring the one-way azimuth pattern using ground receivers (GRs).

In the case of TerraSAR-X (TSX) as well as TanDEM-X (TDX), the accuracy of the antenna model was verified to be ±0.2 dB for the two-way elevation pattern and ±0.1 dB for the one-way azimuth pattern [3]. Furthermore, the peak to peak gain offset between different beams in elevation was verified by evaluating ScanSAR data and proved to be less than ±0.2 dB (peak to peak) [4]. These results demonstrated that the patterns of thousands of possible beam combinations could be accurately calculated from the available antenna model. Even as the TSX mission reaches its nominal end of life, the long-term monitoring of the SAR system has shown that the antenna gain and consequently the antenna model still achieve these accuracies [5].

Novel SAR modes such as the (terrain observation by progressive scans) TOPS mode impose new challenges on the SAR system calibration. In this mode, just like in ScanSAR, several subswaths are acquired by subswath switching in elevation from burst to burst. In addition to the elevation beam steering, the antenna azimuth beam is steered from aft to the fore within each burst at a constant rate [6]. As a result and in contrary to ScanSAR, all targets on ground are observed by the complete azimuth antenna pattern eliminating almost entirely the scalloping effect and achieving constant azimuth ambiguities and signal-to-noise ratio (SNR) along azimuth. However, the fast azimuth beam steering reduces the target dwell time and as such causes the virtual shrinking of the antenna footprint and thus a reduction of the spatial resolution in azimuth. Besides, TOPS acquisitions may still be affected by a residual scalloping caused by the shape of the subarray antenna element pattern [7, 8], albeit inferior to the scalloping observed in normal ScanSAR.

The novel TOPS mode was first implemented as an experimental mode on TSX to demonstrate its feasibility in support of its implementation on ESA's Sentinel-1 mission where it will be used as an operational imaging mode, that is, the interferometric-wide swath (IW) and the extrawide swath (EW) modes [9].

The motivation of this paper is to demonstrate that ground receiver measurements can be used for the in-flight characterization of TOPS one-way azimuth antenna pattern and as such for the verification of the antenna model. In particular, the methodology for preprocessing and analyzing TSX TOPS one-way azimuth antenna pattern acquired by GRs is discussed. This considers the beam switching not only between subswaths in elevation but especially in azimuth and consequently the beam-to-beam gain variation in elevation and in azimuth.

First, the characteristics of the implementation of the TOPS mode on TerraSAR-X and the impact on the TOPS antenna footprint are discussed. Second, the approach based on GR measurements and the reconstruction of the azimuth antenna pattern using the antenna model is explained along with the experimental setup. Finally, the TSX GR measurement results are presented and discussed.

2. TOPS Mode Characteristics

2.1. TSX TOPS Mode Implementation. The operation flexibility of the TSX mission [10] enabled the experimental implementation of the TOPS mode and the acquisition of TOPS data, which was demonstrated for the first time in 2007 [11]. However, the commanding of a TSX TOPS data take is challenging because the TSX SAR instrument was not designed for operating the TOPS imaging mode. Thus, acquisition parameters must be optimized taking into account the instrument constraints. Such constraints were explained by Meta et al. in [12]: first, only a limited number of azimuth beams can be stored on board; therefore the instrument cannot be continuously steered from pulse to pulse, causing a coarse steering angle step size; second, there is a limited number of azimuth beams that can be commanded on a single acquisition; third, because of the limited number of azimuth beams that can be steered, the azimuth steering step size has a direct impact on the steering rate which determines the achievable azimuth resolution. As a consequence of the coarse azimuth steering step size (the minimum step for TSX is 0.013 deg), an amplitude modulation in the azimuth antenna pattern is introduced [7, 12].

2.2. TOPS Antenna Pattern. The TOPS antenna pattern, as seen by a point target and defined in a flat-earth coordinate frame, was approximated by [6] using

$$G_T\left(\vartheta\left(\tau\right)\right) \simeq G_0 \mathrm{sinc}^2\left(\frac{L}{\lambda}\frac{v_s\tau}{R_0}\left(1+\frac{R_0\left|k_\psi\right|}{v_s}\right)\right), \quad (1)$$

where G_0 is the antenna power gain, $\vartheta(\tau)$ is the azimuth angle as a function of time τ, v_s is the velocity of the satellite, λ is the radar wavelength, R_0 is the slant range to the closest approach point, L is the azimuth antenna length, and k_ψ is the antenna steering rate. The expression in (1) is equal to the ground footprint of a fixed antenna, that is, strip map, but shrunken by a factor [6]

$$\alpha = 1 + \frac{R_0\left|k_\psi\right|}{v_s}. \quad (2)$$

The antenna pattern, as seen by a point target on the ground, can be simulated for the TSX case using the parameters shown in Table 1 and inserting them in (1). The resulting one-way azimuth pattern is shown as a full line in Figure 1. The plot shows that the TOPS azimuth pattern is compressed as compared to the pattern of a fixed antenna. It should be noted that the steering in elevation, that is, different subswaths, is not simulated.

The effects of the steering angle quantization described in the previous subsection are observed in the staircase shape of the pattern in Figure 1. However it should be noted that (1) is only an approximation, since it assumes a sinc^2-like shape (bell) of the pattern. A more accurate representation of the TOPS antenna pattern is achieved by using a precise antenna model, which provides the exact steered azimuth beam patterns by means of changing the excitation coefficients of the active antenna array at a given rate.

3. Methods and Measurement Setup

3.1. Methodology. For measuring the TOPS antenna pattern during a satellite overpass, the deployed ground receivers (GRs) need to be aligned in direction to the line of sight of the SAR antenna in zero-Doppler position [13]. The used DLR ground receivers detect the received power with a logarithmic detector. The detector amplitude is digitized with an analog-to-digital converter. The digital values are stored within the GR and are read out in the laboratory after each overpass. The first step for data analysis is to transform the recorded digital samples to power expressed in dBm over a time axis. The time axis is derived from a GPS pulse-per-second signal, which was recorded by the ground receiver in parallel to the received power.

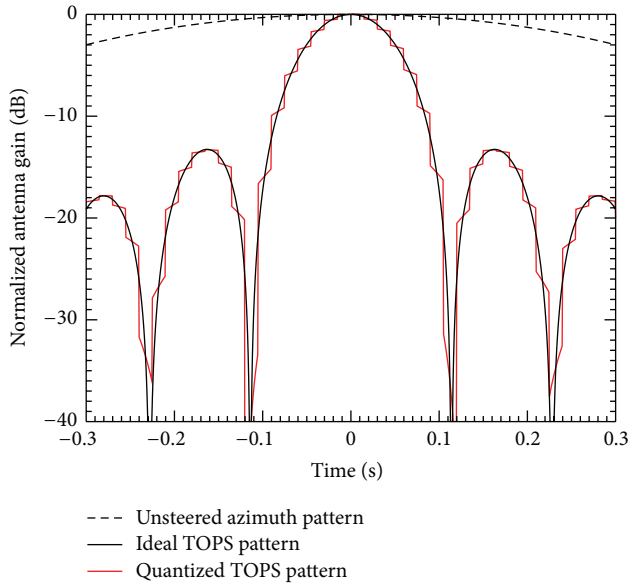

Figure 1: One-way azimuth antenna pattern gain in TSX TOPS mode as seen by a point target.

Due to the movement of the platform, the signal recorded by the GR represents a cut through the spherical antenna pattern. Naturally, the GRs can only measure the transmit pattern of the SAR antenna. This one-way azimuth antenna pattern is then obtained by considering the position of the target and the platform and transforming time units into equivalent azimuth angles. A correct time synchronization between the SAR instrument in orbit and the GR is required, because each received radar pulse must be mapped to the nominal excitation coefficients in elevation and azimuth.

Once this measurement is correctly time-labeled, the main focus is to obtain a reference pattern to which the measured azimuth antenna pattern can be compared. Therefore, a novel method was developed which enables the reconstruction of the actual TOPS azimuth antenna pattern using the following information:

(i) the timed sequence of antenna excitation coefficients (in azimuth and in elevation) that are used to steer the antenna during the acquisition,

(ii) the antenna model providing the reference patterns for each switched beam (pair of azimuth/elevation pattern),

(iii) the exact knowledge of the imaging geometry, that is, the line of sight vector between the platform and the GR.

3.2. Measurement Setup and Configuration. For this experiment, four TSX descending passes in TOPS mode were commanded and acquired during the spring of 2012. The equipment used for measuring the azimuth pattern is a set of GRs in X-band. In particular, three GRs were deployed at each of the two test sites (D28 and D30) within the DLR calibration field located in Southern Germany, as shown in Figure 2.

Table 1: Parameters of TSX TOPS data take over DLR calibration field.

Parameter	Value, [subswath 1/2/3/4]
Ground swath width	≈[30/27/27/27] Km
Pulse repetition frequency	[3233/3728/3465/3752] Hz
Azimuth resolution	≈19 m
Incidence angle/midslant range	≈52°/790 km
Burst width	≈10.4 km
Number of bursts per subswath	[13/13/13/13]
Maximum azimuth steering angle	[0.47/0.47/0.46/0.46]°
Minimum azimuth steering angle	[−0.47/−0.47/−0.46/−0.46]°
Number of azimuth beams per burst	[25/25/36/36]
Angle steering quantization step	[0.039/0.039/0.026/0.026] deg
Pulses per azimuth beam	[45/52/34/37]

The test sites were located in an overlap region between two subswaths (here strip_018 and strip_019) and two bursts. The different bursts of interest (regions filled by green color) are labeled with a number (from 0 to 5) which will be used from now on in the following analysis. Due to the relatively small size of the burst overlap area on ground, not only the GRs had to be accurately deployed and configured but also at instrument level the TOPS acquisition had to be precisely and reliably commanded.

The acquisition parameters used for these four TSX passes are presented on Table 1. These parameters have been optimized taking into account the instrument-related constraints explained in Section 2.1.

4. Measurement Results

The conformity of azimuth antenna pattern derived from the antenna model with the actual GR measurements is shown in Figure 3. As previously outlined, the azimuth angles of the horizontal axis correspond to time, which was converted to azimuth angle using the exact knowledge of the imaging geometry between the satellite and the GR. It can be seen that the measurements match the reconstructed theoretical pattern match very closely including in the lower sidelobes. This demonstrates that the TSX antenna model can accurately predict the beam-to-beam gain offsets not only between elevation beams but also for the steered azimuth beams.

In Figure 3, four peaks can be observed, which correspond to the four neighboring bursts in the vicinity of the test site D28, when the SAR antenna was steered while imaging the GR. The peaks correspond from right to left to bursts 0-1-2-3. In each burst, the antenna is steered in the azimuth direction following a sequence of beams. As this sequence is not continuous, the antenna beam configuration remains in a determinate beam (as expected from the values in Table 1) during 45 PRIs for the first subswath and 52 PRIs for the second subswath, originating the staircase shape of the pattern (see Figure 1). Sharp changes in the staircase sequence correspond to not only burst but also subswath changes

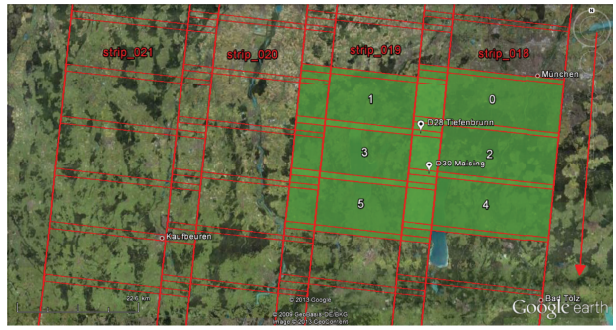

Figure 2: TSX TOPS acquisition coverage with subswaths and bursts indicated. The target position and burst labeling are also shown. The arrow indicates the flight direction (Google Earth).

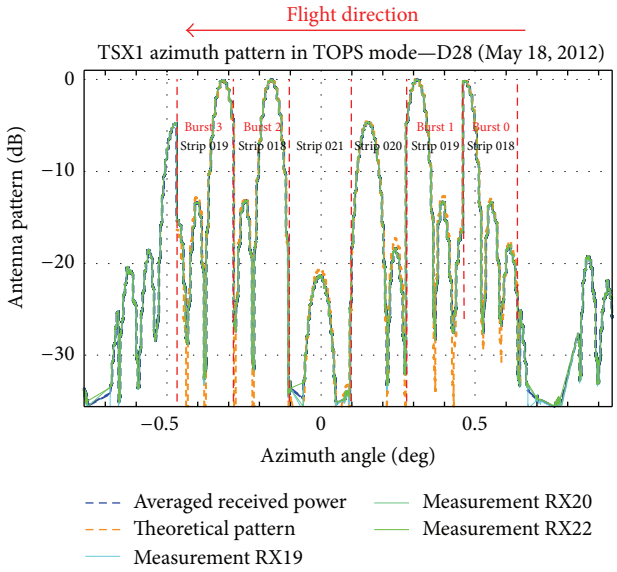

Figure 3: Comparison of the normalized TOPS azimuth pattern measured by GRs during one overpass and the reconstructed pattern derived from the antenna model. Only the relevant azimuth angles corresponding to bursts 0-1-2-3 are shown.

(e.g., transition from burst 0 to 1 at approximately +0.45°). Other peaks with lower amplitude correspond to other subswaths (strip_020 and strip_021). Furthermore, it should be mentioned that, just as expected, the 3 dB beamwidth is narrower than in the fixed-antenna case, because the TOPS azimuth antenna pattern is compressed due to the steering, as predicted by (1).

Looking closer at a single burst, the staircase shape of the pattern becomes obvious, as shown in Figure 4. Here only burst 2 is shown, since it is one of the bursts covering the overlap region for test sites D28 and D30. Due to the different imaging geometries, a different segment of the pattern is seen by the GRs at each test site. At a given time, the backward looking beams are observable by the GRs at D28, while the forward looking beams are observable by the GRs at D30; that is, while D28 is illuminated directly with the main lobe of these backward beams (main lobe in Figure 4(a)), D30 is irradiated with the sidelobe of the backward beams (sidelobes in Figure 4(b)), and when D30 is illuminated with the main lobe of the forward beams (main lobe in Figure 4(a)), then D28 is irradiated by the sidelobe of these forward beams (sidelobes in Figure 4(b)).

The interesting area for the analysis is the 3 dB region of the pattern, which represents the main lobe of the SAR antenna that illuminates the target. As previously discussed, the main lobe is composed of many azimuth beams. For this region, the difference between the measurement and the theoretical pattern derived from the antenna model has been calculated and is likewise shown in Figures 4(a) and 4(b). Since each GR has slightly different characteristics, the measurements of 3 GRs deployed at a single test site are combined to obtain an averaged measurement pattern. The graphs show that the deviation is kept between ±0.1 dB along the 3 dB region of the azimuth patterns for different beams as well as for different azimuth look angles (corresponding to the different bursts and sites).

These results are remarkable since they demonstrate that the antenna model can accurately predict the antenna pattern gain with extreme precision also in the case of TOPS. Hence, the accuracy of the TSX antenna model of ±0.1 dB for one-way azimuth antenna patterns is also achieved for measurements in the experimental TOPS mode, after 5 years of mission time.

In Figure 5(a) the difference between the measurement and the theoretical antenna pattern is shown for the 3 dB region of the pattern (for each of the analyzed six bursts). The measurements are again averaged over the three deployed GRs per test site and pass. The statistics are presented by the vertical bars on the left of the graphs. The upper and lower ends of each bar represent the minimum and the maximum, the star is the mean deviation, and the triangles are the standard deviation. For this specific pass, the deviation exceeds ±0.1 dB. However, the deviation decreases when the pattern derived from the antenna model is shifted slightly by about 0.005 degrees, as shown in Figure 5(b). As this shift can be observed for both test sites (each test site has a different color: D28 is blue, D30 is yellow), which means that for different lines of sight between the satellite and the test site, the same residual "mispointing" has been measured. This residual mispointing is in the order of a few millidegrees which represents the order of accuracy of the TSX attitude

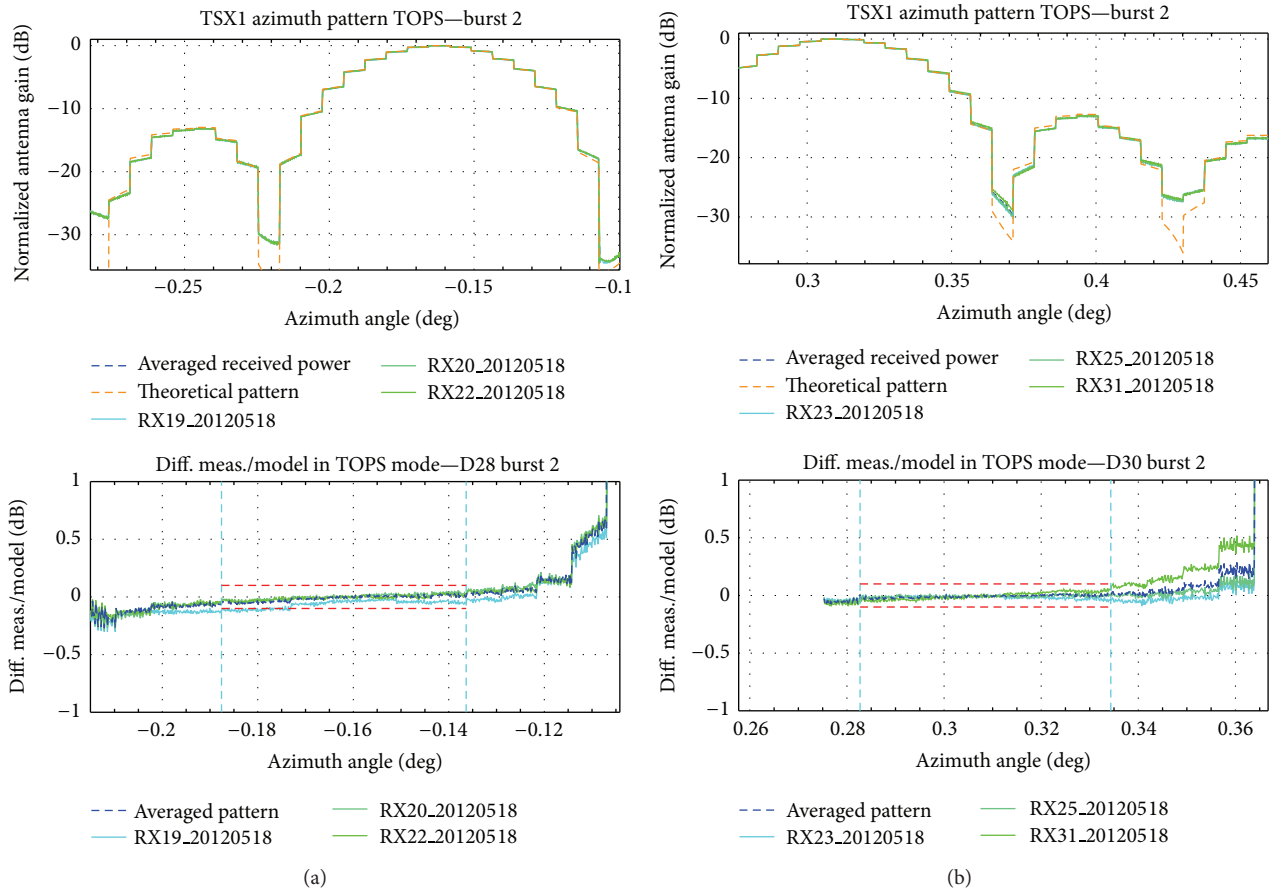

FIGURE 4: TOPS measurements of burst 2 acquired on May 18, 2012, (a) at test site D28 and (b) at test site D30.

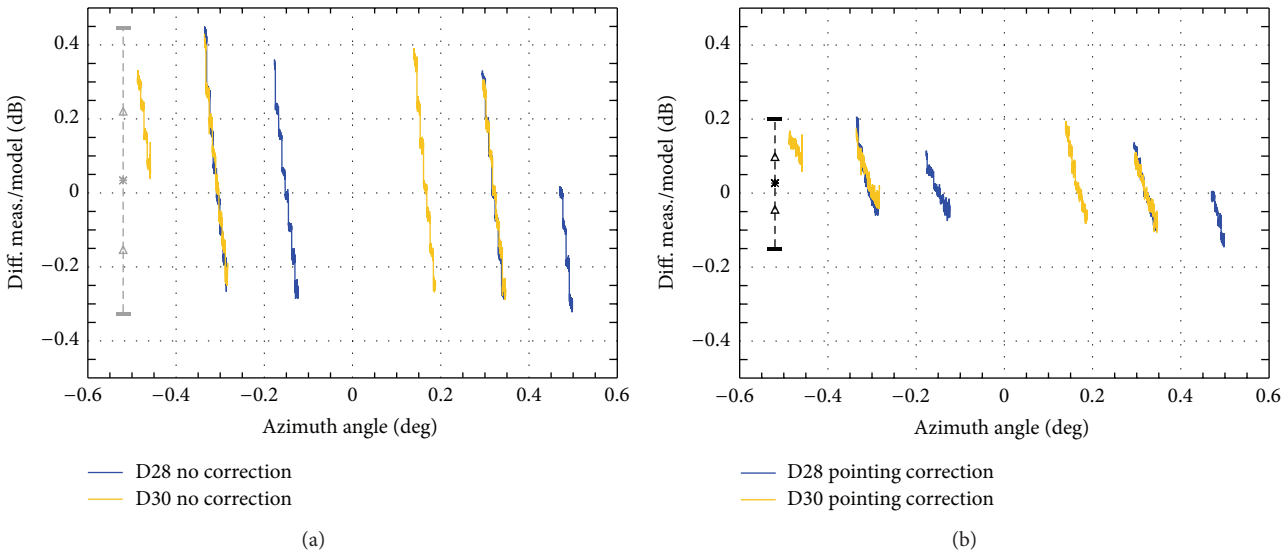

FIGURE 5: Difference between measurement on March 24, 2012, and model for the 3 db region of the TOPS azimuth patterns, statistical values: grey/black. (a) Without pointing correction, (b) with pointing correction.

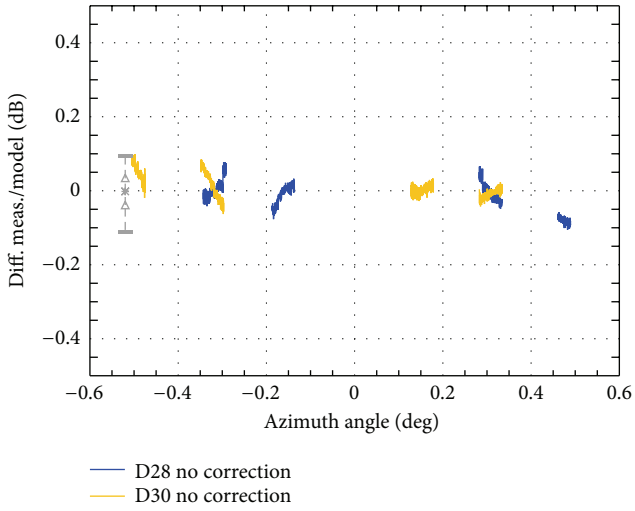

Figure 6: Difference between measurement on May 18, 2012, and model for the 3 db region of the TOPS azimuth patterns, statistical values: grey/black. No pointing correction was needed for this data set.

knowledge. This was verified at the beginning of the TSX mission [3, 14] (i.e., having a pointing accuracy of 0.002 degrees). The antenna mispointing changes from pass to pass due to the total zero-Doppler attitude steering of the satellite, but it stays rather constant during one pass. For example, the measurement on 2012/05/18 presents a very low deviation value even for the uncorrected case, as it is shown in Figure 6.

Finally, when applying the pointing correction, the difference between measurement and model, including the minima and the maxima, is less than ±0.2 dB. Thus, the characterization of the TOPS mode azimuth antenna pattern using GRs is also well suited for deriving the actual SAR antenna pointing in the azimuth direction.

5. Conclusions

The method for azimuth antenna pattern verification based on ground receiver measurements was applied to the TerraSAR-X instrument operating in TOPS mode during four passes/four acquisitions at two different test sites with 3 GRs per test site. The results show that for reconstructing the azimuth pattern by means of the antenna model, taking into account the accurate knowledge of the imaging geometry (i.e., between the satellite and the GR position on the Earth's surface) as well as the antenna excitation coefficients, the deviation between the measured azimuth patterns and the theoretical patterns is in the order of two tenths of a dB.

Compensating for a slight antenna mispointing caused by a finite knowledge of the attitude of the satellite, an accuracy of the antenna model of better than ±0.15 dB has been achieved for the experimental TSX TOPS mode. The accuracy includes both the shape within the main lobe and the gain offset between subswaths in elevation, as well as between backward and forward steered azimuth beams. This accuracy is similar to that demonstrated for all operational TSX modes, considering that the satellite is now reaching its nominal end-of-life phase.

The current analysis was performed for each transmitted radar pulse. In other words, for the method described in Section 3.1, the number of azimuth beams that were steered during the acquisition is of no relevance. Instead, precise knowledge of the right sequence of steered azimuth beams and scanned elevation beams, together with the correct synchronization of the data, is required. Therefore this calibration method is suitable for other satellite missions such as Sentinel-1 that will use TOPS as an operational mode. However, the complexity of analyzing ground receiver measurements may increase with a higher amount of steered azimuth beams.

Finally, the method based on GRs and proposed for measuring the azimuth pattern of a SAR system in the complex TOPS mode is well suitable for the verification of the antenna model using TOPS acquisitions and deriving a residual mispointing.

Acknowledgments

The authors would like to thank the entire calibration team of the Microwaves and Radar Institute at DLR for their support during the measurement campaigns. The work in this paper has been funded by the ESA Contract no. 4000106082/12/NL/MP.

References

[1] M. Bachmann, M. Schwerdt, and B. Bräutigam, "TerraSAR-X antenna calibration and monitoring based on a precise antenna model," *IEEE Transactions on Geoscience and Remote Sensing*, vol. 48, no. 2, pp. 690–701, 2010.

[2] D. Hounam, M. Schwerdt, and M. Zink, "Active antenna module characterisation by pseudo-noise gating," in *Proceedings of the 25th ESA Antenna Workshop on Satellite Antenna Technology*, Noordwijk, The Netherlands, 2002.

[3] M. Schwerdt, B. Bräutigam, M. Bachmann, B. Döring, D. Schrank, and J. H. Gonzalez, "Final TerraSAR-X calibration results based on novel efficient methods," *IEEE Transactions on Geoscience and Remote Sensing*, vol. 48, no. 2, pp. 677–689, 2010.

[4] M. Bachmann, M. Schwerdt, and B. Bräutigam, "Accurate antenna pattern modeling for phased array antennas in SAR applications—demonstration on TerraSAR-X," *International Journal of Antennas and Propagation*, vol. 2009, Article ID 492505, 9 pages, 2009.

[5] N. T. Ramon, D. Schrank, M. Bachmann et al., "Long term system monitoring status of the TerraSAR-X/TanDEM-X satellites," in *European Conference on Synthetic Aperture Radar (EUSAR '12)*, pp. 163–166, April 2012.

[6] F. De Zan and A. M. Guarnieri, "TOPSAR: terrain observation by progressive scans," *IEEE Transactions on Geoscience and Remote Sensing*, vol. 44, no. 9, pp. 2352–2360, 2006.

[7] A. Meta, J. Mittermayer, P. Prats, R. Scheiber, and U. Steinbrecher, "TOPS imaging with TerraSAR-X: mode design and performance analysis," *IEEE Transactions on Geoscience and Remote Sensing*, vol. 48, no. 2, pp. 759–769, 2010.

[8] S. Wollstadt, P. Prats, M. Bachmann, J. Mittermayer, and R. Scheiber, "Scalloping Correction in TOPS Imaging Mode SAR

Data," *IEEE Geoscience and Remote Sensing Letters*, vol. 9, no. 4, pp. 614–618, 2012.

[9] D. Geudtner, P. Potin, R. Torres, P. Snoeij, and D. Bibby, "Overview of the GMES Sentinel-1 mission," in *Proceedings of the 9th European Conference on Synthetic Aperture Radar (EUSAR '12)*, pp. 159–161, 2012.

[10] U. Steinbrecher, D. Schulze, J. Böer, and J. Mittermayer, "TerraSAR-X instrument operations rooted in the system engineering and calibration project," *IEEE Transactions on Geoscience and Remote Sensing*, vol. 48, no. 2, pp. 633–641, 2010.

[11] A. Meta, P. Prats, U. Steinbrecher, J. Mittermayer, and R. Scheiber, "First topsar image and interferometry results with TerraSAR-X," in *Proceedings of Workshop on Advances in SAR Interferometry from Envisat and ERS Missions (Fringe '07)*, November 2007.

[12] A. Meta, J. Mittermayer, U. Steinbrecher, and P. Prats, "Investigations on the TOPSAR acquisition mode with TerraSAR-X," in *Proceedings of IEEE International Geoscience and Remote Sensing Symposium (IGARSS '07)*, pp. 152–155, June 2007.

[13] B. D. Döring, M. Schwerdt, and R. Bauer, "TerraSAR-X calibration ground equipment," in *Wave Propagation in Communication, Microwaves Systems and Navigation (WFMN '07)*, June 2007.

[14] H. Fiedler, T. Fritz, and R. Kahle, "Verification of the total zero doppler steering," in *Proceedings of International Conference on Radar (Radar '08)*, pp. 340–342, September 2008.

Hindawi Publishing Corporation
International Journal of Antennas and Propagation
Volume 2013, Article ID 384756, 14 pages
http://dx.doi.org/10.1155/2013/384756

Research Article

Intelligent Motion Compensation for Improving the Tracking Performance of Shipborne Phased Array Radar

J. Mar,[1,2] K. C. Tsai,[2] Y. T. Wang,[2] and M. B. Basnet[2]

[1] *Communication Research Center, Yuan-Ze University, 135 Yuan-Tung Road, Jungli, Taoyuan 320, Taiwan*
[2] *Department of Communications Engineering, Yuan-Ze University, 135 Yuan-Tung Road, Jungli, Taoyuan 320, Taiwan*

Correspondence should be addressed to J. Mar; eejmar@saturn.yzu.edu.tw

Received 26 March 2013; Accepted 22 May 2013

Academic Editor: Ulrich Nickel

The shipborne phased array radar must be able to compensate the ship's motion and track the maneuvering targets automatically. In this paper, the real-time beam pointing error compensation mechanism of a planar array antenna for ship's motion is designed to combine with the Kalman filtering. The effect of beam pointing error on the tracking performance of shipborne phased array radar is examined. A compensation mechanism, which can automatically correct the beam pointing error of the planar antenna array, is proposed for shipborne phased array radar in order to achieve the required tracking accuracy over the long dwell time. The automatic beam pointing error compensation mechanism employs the parallel fuzzy basis function network (FBFN) architecture to estimate the beam pointing error caused by roll and pitch of the ship. In the simulation, the models of roll and pitch are used to evaluate the performance of beam pointing error estimation mechanism based on the proposed parallel FBFN architecture. In addition, the effect of automatic beam pointing error compensation mechanism on the tracking performance of adaptive extended Kalman filter (AEKF) implemented in ship borne phased array radar is also investigated. Simulations find out that the proposed algorithms are stable and accurate.

1. Introduction

Beam pointing error caused by ship motion over the ocean affects the tracking performance of the shipborne phased array radar. The antenna stabilization to achieve the beam pointing accuracy over the long dwell time is an important issue for shipborne phased array radar [1]. There are two ship motion compensations: compensation for rotational motion (i.e., pitch, roll, and heading angle) and compensation for translational motion (i.e., radial speed relative to the earth). Figure 1 shows the shipborne phased array radar system [2, 3], which consists of the gyro sensor, beam steering controller (BSC), array antenna, radar control computer (RCC), digital signal processor (DSP), transmitter and receiver (XMTR/RCVR), and display. Gyro sensor provides pitch, roll, heading angles of the ship, speed, course, vertical velocity of antenna installed on the ship at a data rate of 100 Hz. To compensate the translational motion, the speed, course, and vertical velocity acquired from the Gyro sensor are averaged for the duration of radar-dwell time. Then the Doppler shift introduced by the translational motion is calculated to compensate the radial velocity estimated in the digital signal processor (DSP). The radar control computer (RCC) provides the target locations relative to earth, scheduled beam directions, and predicted beam pointing error to the beam steering controller (BSC), which compensate the beam pointing error and controls the phased array antenna to point the beam at the target direction relative to the ship coordinates.

The idea of the extended Kalman filter (EKF) was originally proposed by Stanley Schmidt so that the Kalman filter could be applied to nonlinear spacecraft navigation problems [4]. The well-known conventional EKFs give the optimal solution but require synchronous measurements, an accurate system model, and exact stochastic noise characteristics. Thus, the performance of EKF with incomplete information and asynchronous sensors measurements may be degraded or even diverged. In order to reduce the effect of noise variance uncertainty, adaptive extended Kalman filter (AEKF) is proposed to overcome this drawback.

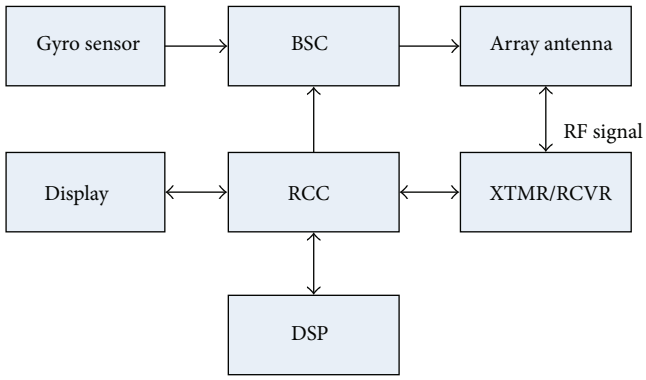

Figure 1: High level structure of shipborne phased array radar.

In this paper, we focus on the design of an automatic beam pointing error correction mechanism based on the proposed parallel fuzzy basis function network (FBFN) architecture, which predicts the beam pointing error caused by roll and pitch in real time. The AEKF algorithm is used to track the air target in three-dimensional space, and the covariance matrix values of process noise and measurement noise are adaptively estimated to ensure the AEKF convergence.

The rest of this paper is organized as follows: the model of ship rotational motion, coordinates transform and planar array antenna of shipborne phased array radar are described in detail in Section 2. The architecture of parallel FBFN beam pointing error estimator is presented in Section 3. The AEKF algorithm is described in Section 4. In Section 5, the tracking performance of shipborne phased array radar using the proposed beam pointing error compensation method is simulated for six different cases. Finally, we conclude the paper in Section 6.

2. Ship Rotational Motion Compensation

The shipborne phased array radar must be able to compensate the ship's motion and track the maneuvering targets automatically. The algorithm of real-time compensating for ship's motion is designed to combine with the Kalman filtering. The block diagram of rotational motion compensation system for shipborne phased array radar is shown in Figure 2 [3], which consists of beam pointing error prediction, ship coordinates/earth coordinates conversion, earth coordinates/ship coordinates conversion, and adaptive extended Kalman filter (AEKF). Assume that the beam steering angle is (θ_0, ϕ_0), the antenna point angle offset caused by the ship motion (roll, pitch) is (θ_e, ϕ_e), and then the current antenna pointing angle is (θ_E, ϕ_E) as

$$\begin{aligned} \theta_E &= \theta_0 + \theta_e, \\ \phi_E &= \phi_0 + \phi_e. \end{aligned} \tag{1}$$

If the beam pointing error is predicted as $(\Delta\theta_E, \Delta\phi_E)$, then the beam pointing angle is corrected as

$$\begin{aligned} \theta_{EC} &= \theta_0 + \theta_e - \Delta\theta_E, \\ \phi_{EC} &= \phi_0 + \phi_e - \Delta\phi_E. \end{aligned} \tag{2}$$

The (θ_{EC}, ϕ_{EC}) is approximated to (θ_0, ϕ_0).

Table 1: Sea state parameters.

Sea state	Roll		Pitch	
	A_R (°)	T_R (sec)	A_P (°)	T_P (sec)
4	2	8	0.4	5
5	10	10	2	7
6	18	13	4	8

2.1. Ship Rotational Motion Model. Ship is affected by the waves in the ocean, resulting in six degrees of freedom of movement. In this paper, assuming zero yaw angle, the simplified roll and pitch model [1, 5] are adopted to describe the ship rotational motion in the earth coordinates. Ship's rotational motion is modeled with sinusoidal signal. The roll angle is

$$\phi_R(t) = A_R \sin(\omega_R t) + n_R. \tag{3}$$

The pitch angle is

$$\theta_P(t) = A_P \sin(\omega_P t) + n_P, \tag{4}$$

where A_R and A_P are the amplitude of ship's roll and pitch angles, n_r and n_P are assumed to be zero mean Gaussian noise, T_R and T_P are the roll and pitch periods, and $\omega_R = 2\pi/T_R$ and $\omega_P = 2\pi/T_P$ are the roll and pitch angular frequencies. The beam pointing errors caused by other unknown factors, including ship's traveling direction changing and whether changing, in the actual ship navigation environment will be considered in the standard deviation of the noise terms. The amplitude and period parameters of sea states 4, 5, and 6 are listed in Table 1 [1].

2.2. Coordinates Transform. Since the phased array antenna is installed on the ship, the beam steering control employs the ship body coordinates. But the target tracking of Kalman filter employs the Earth coordinates. The Euler coordinates transform formula is used to convert antenna beam pointing angle relative to the earth (θ_E, ϕ_E) into antenna beam pointing angle relative to the ship body (θ_A, ϕ_A) [5] as

$$\begin{bmatrix} \sin\theta_A \cos\phi_A \\ \sin\theta_A \sin\phi_A \\ \cos\theta_A \end{bmatrix} = T(\phi)\, T(\theta)\, T(\psi) \begin{bmatrix} \sin\theta_E \cos\phi_E \\ -\sin\theta_E \sin\phi_E \\ \cos\theta_E \end{bmatrix}, \tag{5}$$

where the coordinates transform matrices are defined as

$$\begin{aligned} T(\phi) &= \begin{bmatrix} 1 & 0 & 0 \\ 0 & \cos\phi & \sin\phi \\ 0 & -\sin\phi & \cos\phi \end{bmatrix} \\ T(\theta) &= \begin{bmatrix} \cos\theta & 0 & \sin\theta \\ 0 & 1 & 0 \\ -\sin\theta & 0 & \cos\theta \end{bmatrix} \\ T(\psi) &= \begin{bmatrix} \cos\psi & -\sin\psi & 0 \\ \sin\psi & \cos\psi & 0 \\ 0 & 0 & 1 \end{bmatrix}, \end{aligned} \tag{6}$$

where ϕ is the ship roll angle, θ is the ship pitch angle, and ψ is the ship yaw angle.

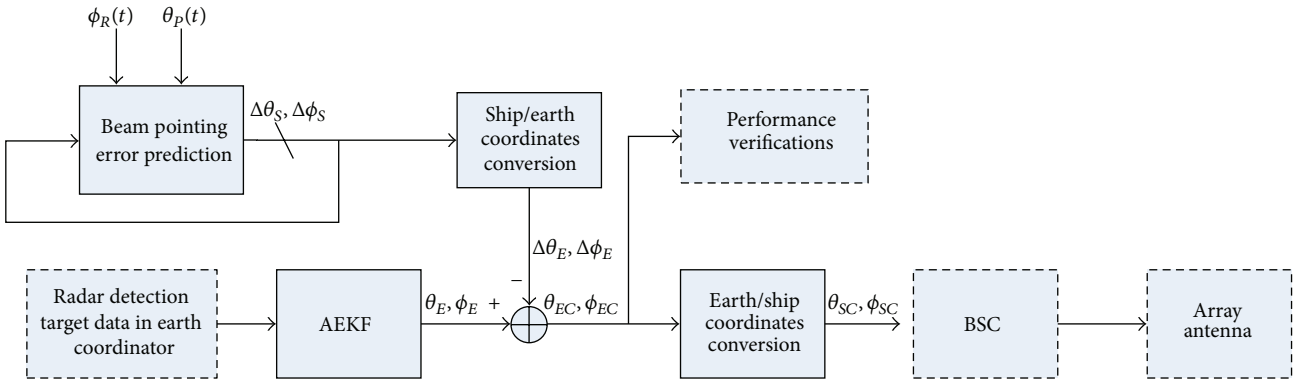

Figure 2: System diagram of rotational motion compensation for AEKF of shipborne phased array radar.

2.3. Planar Array Antenna. An $M \times N$ element planar array, as shown in Figure 3, is designed for the shipborne phased array radar system, which includes the beamforming (BF) mode and direction of arrival (DOA) mode. The planar array can produce multibeams in the azimuth and elevation by using the beamformer network (BFN), which consists of a set of power dividers and phase shifters. The planar array using amplitude comparison method [6] generates the difference signal patterns for the DOA estimation. The difference signals obtained from two neighboring beams can measure the DOA of the subscriber signal of the shipborne phased array radar system. The beam pattern is expressed as [6, 7]

$$\begin{aligned} AF(\theta,\phi) &= \sum_{n=1}^{N} I_{1n} \left[\sum_{m=1}^{M} I_{m1} e^{j(m-1)(kd_x \sin\theta\cos\phi+\beta_x)} \right] \\ &\quad \times e^{j(n-1)(kd_y \sin\theta\sin\phi+\beta_y)} \\ &= S_{xm} S_{yn}, \end{aligned} \tag{7}$$

where

$$\begin{aligned} S_{xm} &= \sum_{m=1}^{M} I_{m1} e^{j(m-1)(kd_x \sin\theta\cos\phi+\beta_x)}, \\ S_{ym} &= \sum_{n=1}^{N} I_{1n} e^{j(n-1)(kd_y \sin\theta\sin\phi+\beta_y)}, \\ \beta_x &= -kd_x \sin\theta_t \cos\phi_t, \\ \beta_y &= -kd_y \sin\theta_t \sin\phi_t, \end{aligned} \tag{8}$$

where $I_{m1} = I_{1n}$ = Chebyshev weighting [5], M = the number of array elements in the x-axis, N = the number of array elements in the y-axis, ϕ_t = the azimuth steering angle of the main beam, θ_t = the elevation steering angle of the main beam, d_x = the interelement spacing in the x-axis, and d_y = the interelement spacing in the y-axis.

The phase of the RF signal at each array element is adjusted to steer the beam to the coordinates (θ_t, ϕ_t). For $M = N = 6$ and $dx = dy = \lambda/2$, the computed antenna radiation pattern of a beam steered to $(\theta, \phi) = (0^\circ, 0^\circ)$ is shown in Figure 4. The side-lobe suppression is −30 dB by using the Chebyshev weighting = [0.54 0.78 1 1 0.78 0.54]. The 6×6 planar array antenna is chosen to simulate the beam pointing error compensation and the tracking accuracy of maneuvering target position (θ_t, ϕ_t).

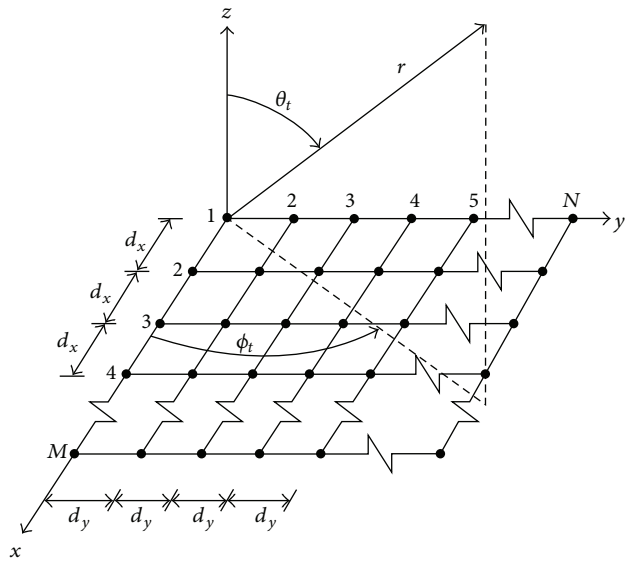

Figure 3: $M \times N$ planar array antenna.

3. Parallel FBFN Architecture

The beam pointing error of the shipborne phased array radar over the ocean is always changing from time to time, so it is necessary to intelligently predict and compensate the beam pointing error through the collected ship's roll and pitch angles data. For reducing the computation load and meeting the real-time requirement of the automatic beam pointing error correction system, a simplified parallel FBFN architecture, which makes use of the roll angle and pitch angle measurements mapped onto the beam pointing error model to nonlinearly estimate the angle error of the planar antenna array, is proposed. The parallel FBFN architecture is shown in Figure 5, which is implemented with four-layer feed forward network. The input vectors $\mathbf{A}_n$ including K beam-pointing

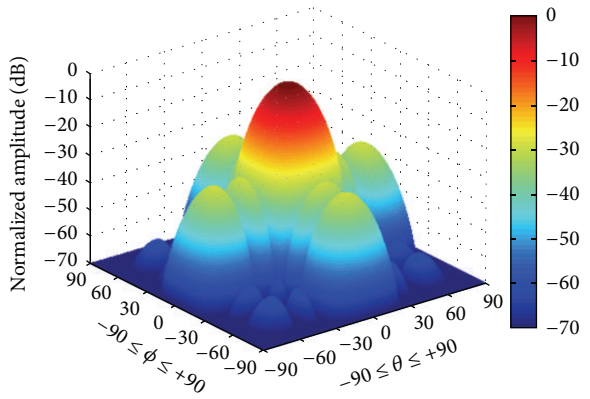

Figure 4: Three-dimensional antenna radiation pattern for 6 × 6 planar array antenna.

angles at the time $n, n-1, \ldots, n-K$ are input to membership functions to determine its membership grade.

The RLS algorithm and the FBFN algorithm with the properly normalized Gaussian membership function are employed to automatically correct the beam pointing error caused by the ship's roll angle and pitch angle. The beam pointing error correction mechanism using the RLS algorithm is realized with a Kth order adaptive prediction filter. The RLS algorithm is summarized as follows [8].

Initialize $\mathbf{P}(0) = \delta_R^{-1}\mathbf{I}$, $\widehat{\mathbf{w}}(0) = \mathbf{0}$.

At each instant of time, $n = 1, 2, \ldots$, compute $M \times M$ inverse correlation matrix as

$$\mathbf{P}(n) = \xi^{-1}\mathbf{P}(n-1) - \xi^{-1}\mathbf{k}(n)\,\theta^H(n)\,\mathbf{P}(n-1). \quad (9)$$

The $M \times 1$ gain vector is

$$\mathbf{k}(n) = \frac{\xi^{-1}\mathbf{P}(n-1)\,\theta(n)}{1 + \xi^{-1}\theta^H(n)\,\mathbf{P}(n-1)\,\theta(n)}. \quad (10)$$

The predicted correction angle is obtained by

$$Y(n) = \theta^H(n)\,\widehat{\mathbf{w}}(n-1). \quad (11)$$

The estimation error is

$$f_M(n) = \theta(n+1) - Y(n), \quad (12)$$

where $\theta_P(n+1)$ is the beam point error at $n+1$ time instant. The update weightings of the prediction filter are

$$\widehat{\mathbf{w}}(n) = \widehat{\mathbf{w}}(n-1) + \mathbf{k}(n)\,f_M(n). \quad (13)$$

The RLS algorithm is convergent if the following condition is satisfied:

$$\delta_r < 0.01\sigma_\theta^2, \quad (14)$$

where σ_θ^2 is the variance of the Gaussian distribution of beam pointing error for pitch angle. The forgetting factor ξ is a constant in (0, 1). Here we assume that $\delta_r = 0.0008$, $\xi = 1$, and $M = K$.

The FBFN-based beam pointing error correction mechanism of the LMDS system is shown in Figure 7. The FBFN is a 4-layer feed forward network. The input vectors $\vec{A}$ include K beam-pointing angles at $n, n-1, \ldots, n-K$. In the first layer, the rule base $\mu_i(\vec{x})$ contains Takagi and Sugeno's type fuzzy if-then rules [9, 10]. The normalized Gaussian-shaped membership functions are

$$\mu_i(\vec{x}) = \exp\left\{-\frac{\left\|\vec{x} - \vec{c}_i\right\|^2}{\sigma_i^2}\right\}, \quad i = 1, 2, \ldots, m, \quad (15)$$

where the input vector $\vec{x}$ could be pitch $\vec{\theta}_p$ or roll $\vec{\theta}_r$; "|| ||" represents Euclidean form. $\vec{c}_i$, $i = 1, 2, \ldots, m$ are the mean vectors of the Gaussian membership functions for ship's roll or pitch, which are generated by different sea states as

$$\vec{c}_i = A\sin(\omega n_i), \quad i = 1, 2, 3, \ldots, m, \quad (16)$$

where the discrete sampling time is $n_i = i\Delta T = i/f_s$ and f_s is the sampling frequency. Each mean vector consists of K samples of the normalized Gaussian function with corresponding mean to the sampled sinusoidal signal value. The standard deviation σ_i determines the range of Gaussian membership functions for ship's roll or pitch.

The input pitch vector is given by

$$\vec{x} = \vec{\theta}_{p,n} = \left[\theta_p(n), \theta_p(n-1), \ldots, \theta_p(n-K)\right]^T, \quad (17)$$

where "T" means transpose. The ratio of the ith rule's firing strength to the sum of all rule's firing strengths is calculated in the ith node as

$$\overline{\mu}_i = \frac{\mu_i}{\sum_i \mu_i}, \quad i = 1, \ldots, m. \quad (18)$$

For convenience, the outputs of this layer are called "normalized firing strength." The output of the third layer is

$$O_{i,n}^3 = \vec{\mu}_{i,n} \times f_{i,n}. \quad (19)$$

The consequent parameters are

$$f_i = \sum_{k=0}^{K} \alpha_{i,k}\theta_p(n-k) + \alpha_{i,K+1}, \quad i = 1, 2, \ldots, m, \quad (20)$$

where $\alpha_{i,k}$ is the coefficients of the consequent parameters. The consequent parameter vector is

$$\vec{\alpha} = \left[\alpha_{i,k} \,\middle|\, i = 1, 2, \ldots, m;\ k = 0, 1, \ldots, K\right]^T_{(m(K+2))\times 1}. \quad (21)$$

The output of the fourth layer is obtained as

$$Y(n) = \frac{\sum_{i=1}^m \vec{\mu}_{i,n} f_{i,n}}{\sum_{i=1}^m \vec{\mu}_{i,n}}. \quad (22)$$

The matrix form of FBFN beam pointing error estimator can be expressed as

$$\mathbf{W}\vec{\alpha} = \vec{Y}, \quad (23)$$

where

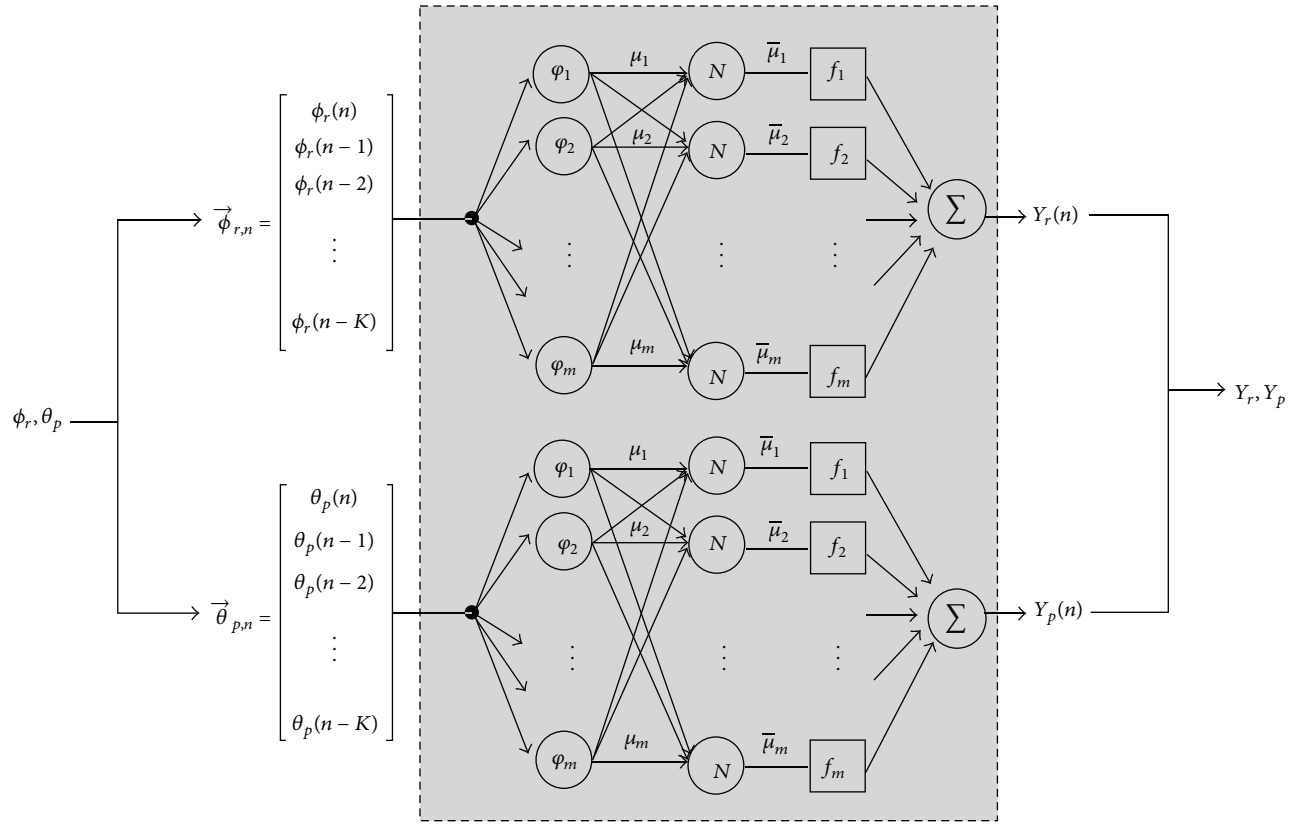

Figure 5: Parallel FBFN beam pointing error estimator.

$$\mathbf{W} = \begin{bmatrix} \vec{\mu}_{1,n}A(n) & \vec{\mu}_{1,n}A(n-1) & \cdots & \vec{\mu}_{1,n}A(n-K) & \vec{\mu}_{2,n} & \vec{\mu}_{2,n}A(n) & \cdots & \vec{\mu}_{m,n} \\ \vec{\mu}_{1,n+1}A(n+1) & \vec{\mu}_{1,n+1}A(n) & \cdots & \vec{\mu}_{1,n+1}A(n-K+1) & \vec{\mu}_{2,n+1} & \vec{\mu}_{2,n+1}A(n+1) & \cdots & \vec{\mu}_{m,n+1} \\ \vdots & \vdots & \vdots & \vdots & \vdots & \vdots & \vdots & \vdots \\ \vec{\mu}_{1,n+q-1}A(n+q-1) & \vec{\mu}_{1,n+q-1}A(n+q-2) & \cdots & \vec{\mu}_{1,n+q-1}A(n+q-K-1) & \vec{\mu}_{2,n+q-1} & \vec{\mu}_{2,n+q-1}A(n+q-1) & \cdots & \vec{\mu}_{m,n+q-1} \end{bmatrix}_{q\times(m(K+2))} \tag{24}$$

Each input training vector correspond to one row in the matrix, which contains $m*(K+2)$ data elements. Therefore, q must be greater than or equal to $m*(K+2)$ in order to solve the consequent parameters. The vector of the desired output in fuzzy inference rules is defined as

$$\vec{Y} = \left[y(n), y(n+1), y(n+2), \ldots, y(n+q-1)\right]^T. \tag{25}$$

A reinforcement learning scheme termed the least-square estimator (LSE) is used to optimally adjust f_i in layer three for approximating the desired output of FBFN beam pointing error estimator. The consequent parameter vector is trained as

$$\hat{\vec{\alpha}} = \left(\mathbf{W}^T\mathbf{W}\right)^{-1}\mathbf{W}\vec{Y}. \tag{26}$$

4. Adaptive Extended Kalman Filter [4]

The AEKF-based target tracking algorithm [11, 12] is used by shipborne phased array radar to recursively update the linear and nonlinear target trajectories and it further improves its tracking accuracy. The distance between the flying target and radar at a time point t_j is represented as

$$r\left(x_j, y_j, z_j\right) = \sqrt{\left(x_j - x_r\right)^2 + \left(y_j - y_r\right)^2 + \left(z_j - z_r\right)^2}, \tag{27}$$

where (x_r, y_r, z_r) and (x_j, y_j, z_j) are the coordinates of radar and air target, respectively. As shown in Figure 3, in polar coordinates, the horizontal angle is expressed as

$$\phi = \tan^{-1}\left(\frac{y_j - y_r}{x_j - x_r}\right). \tag{28}$$

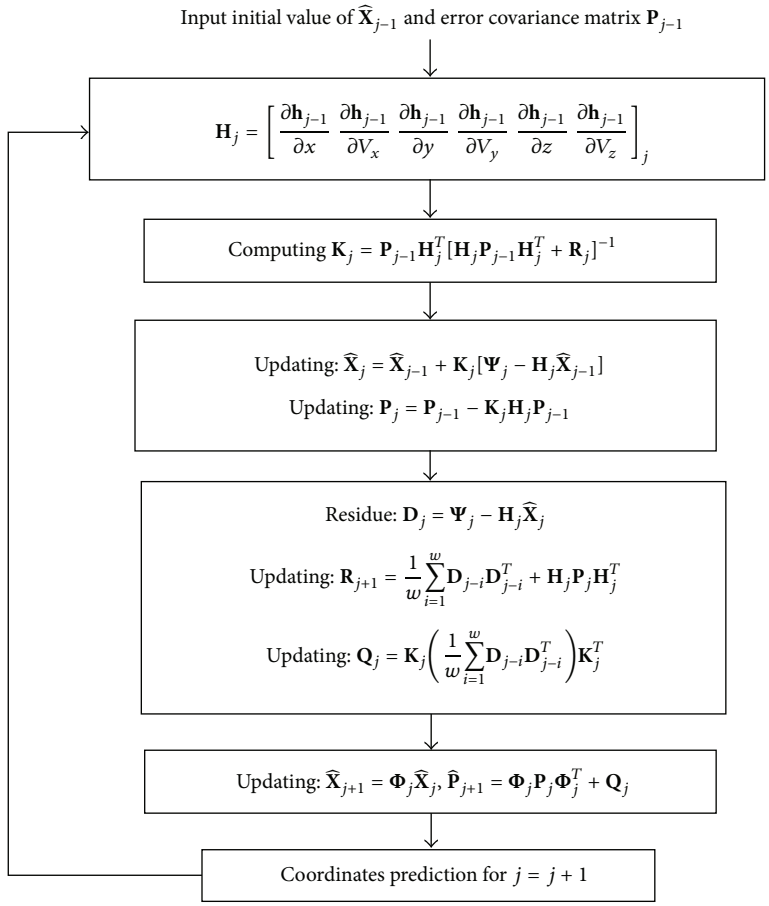

Figure 6: The flow chart of AEKF algorithm.

The vertical angle is expressed as

$$\theta = 90^\circ - \tan^{-1}\left(\frac{z_j - z_r}{\sqrt{\left(x_j - x_r\right)^2 + \left(y_j - y_r\right)^2}}\right). \quad (29)$$

The system state equation in matrix form is

$$\mathbf{X}_{j+1} = \Phi_j\mathbf{X}_j + \mathbf{w}_j, \quad (30)$$

where $\mathbf{X}_j = \begin{bmatrix} x & V_x & y & V_y & z & V_z \end{bmatrix}_j^T$ is the target state vector, where x_j, y_j, $V_{x,j}$, $V_{y,j}$ are the relative position of the target in the x- and y-axes and relative velocity in the x- and y-axes, respectively. The relative acceleration in the x- and y-axes is defined as modeling error $\mathbf{w}_j$, which is assumed to be random with white Gaussian noise (WGN). $\Delta t = t_j - t_{j-1}$ is the detection cycle time. The transition matrix is

$$\Phi_j = \begin{bmatrix} 1 & \Delta t & 0 & 0 & 0 & 0 \\ 0 & 1 & 0 & 0 & 0 & 0 \\ 0 & 0 & 1 & \Delta t & 0 & 0 \\ 0 & 0 & 0 & 1 & 0 & 0 \\ 0 & 0 & 0 & 0 & 1 & \Delta t \\ 0 & 0 & 0 & 0 & 0 & 1 \end{bmatrix}. \quad (31)$$

The measurement equation in matrix form only considers the position measurements in r, θ, and ϕ, which are not linear equation as

$$\mathbf{z}_j = \mathbf{h}_j\mathbf{X}_j + \mathbf{v}_j, \quad (32)$$

$$\mathbf{h}_j\mathbf{X}_j = \begin{bmatrix} r & \phi & \theta \end{bmatrix}_j^T, \quad (33)$$

where $\mathbf{v}_j$ is assumed to be zero mean WGN. The nonlinear equation (32) is linearized by using the first-order Taylor approximation as

$$\mathbf{z}_j \approx \mathbf{z}_{j-1} + \mathbf{H}_j\mathbf{X}_j - \mathbf{H}_j\mathbf{X}_{j-1} + \mathbf{v}_j, \quad (34)$$

where the measurement matrix is

$$\mathbf{H}_j = \begin{bmatrix} \frac{\partial r}{\partial x} & \frac{\partial r}{\partial Vx} & \frac{\partial r}{\partial y} & \frac{\partial r}{\partial Vy} & \frac{\partial r}{\partial z} & \frac{\partial r}{\partial Vz} \\ \frac{\partial \phi}{\partial x} & \frac{\partial \phi}{\partial Vx} & \frac{\partial \phi}{\partial y} & \frac{\partial \phi}{\partial Vy} & \frac{\partial \phi}{\partial z} & \frac{\partial \phi}{\partial Vz} \\ \frac{\partial \theta}{\partial x} & \frac{\partial \theta}{\partial Vx} & \frac{\partial \theta}{\partial y} & \frac{\partial \theta}{\partial Vy} & \frac{\partial \theta}{\partial z} & \frac{\partial \theta}{\partial Vz} \end{bmatrix}. \quad (35)$$

From (34), the linear measurement equation is redefined as

$$\mathbf{\Psi}_j \approx \mathbf{H}_j\mathbf{X}_j + \mathbf{v}_j, \quad (36)$$

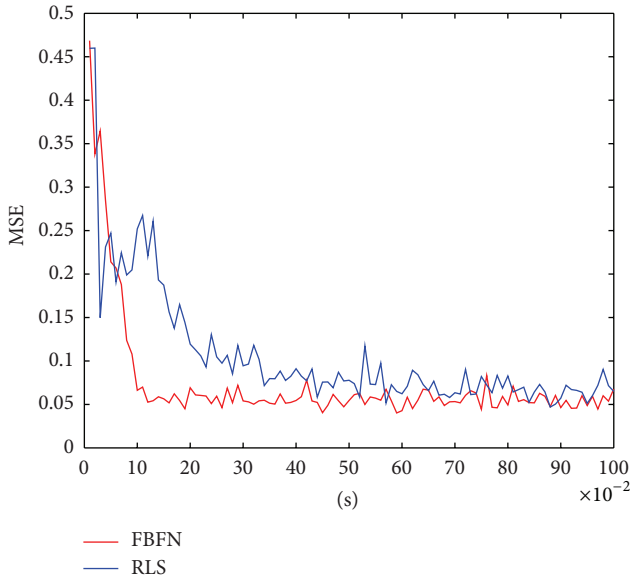

Figure 7: Beam pointing error correction for roll angle.

where

$$\frac{\partial r}{\partial x} = \left(x_{j-1} - x_r\right) \times \left(\sqrt{\left(x_{j-1} - x_r\right)^2 + \left(y_{j-1} - y_r\right)^2 + \left(z_{j-1} - z_r\right)^2}\right)^{-1},$$

$$\frac{\partial \phi}{\partial x} = \frac{-\left(y_{j-1} - y_r\right)}{\left(x_{j-1} - x_r\right)^2 + \left(y_{j-1} - y_r\right)^2},$$

$$\frac{\partial \theta}{\partial x} = -\left(x_{j-1} - x_r\right)\left(z_{j-1} - z_r\right) \times \left(\left[\left(x_{j-1} - x_r\right)^2 + \left(y_{j-1} - y_r\right)^2 + \left(z_{j-1} - z_r\right)^2\right] \times \sqrt{\left(x_{j-1} - x_r\right)^2 + \left(y_{j-1} - y_r\right)^2}\right)^{-1},$$

$$\frac{\partial r}{\partial y} = \frac{\left(y_{j-1} - y_r\right)}{\sqrt{\left(x_{j-1} - x_r\right)^2 + \left(y_{j-1} - y_r\right)^2 + \left(z_{j-1} - z_r\right)^2}},$$

$$\frac{\partial \phi}{\partial y} = \frac{\left(x_{j-1} - x_r\right)}{\left(x_{j-1} - x_r\right)^2 + \left(y_{j-1} - y_r\right)^2},$$

$$\frac{\partial \theta}{\partial y} = -\left(y_{j-1} - y_r\right)\left(z_{j-1} - z_r\right) \times \left(\left[\left(x_{j-1} - x_r\right)^2 + \left(y_{j-1} - y_r\right)^2 + \left(z_{j-1} - z_r\right)^2\right] \times \sqrt{\left(x_{j-1} - x_r\right)^2 + \left(y_{j-1} - y_r\right)^2}\right)^{-1},$$

$$\frac{\partial r}{\partial z} = \frac{\left(z_{j-1} - z_r\right)}{\sqrt{\left(x_{j-1} - x_r\right)^2 + \left(y_{j-1} - y_r\right)^2 + \left(z_{j-1} - z_r\right)^2}},$$

$$\frac{\partial \theta}{\partial z} = \frac{\sqrt{\left(x_{j-1} - x_r\right)^2 + \left(y_{j-1} - y_r\right)^2}}{\left[\left(x_{j-1} - x_r\right)^2 + \left(y_{j-1} - y_r\right)^2 + \left(z_{j-1} - z_r\right)^2\right]},$$

$$\frac{\partial r}{\partial Vx} = \frac{\partial r}{\partial Vy} = \frac{\partial r}{\partial Vz} = \frac{\partial \theta}{\partial Vx} = \frac{\partial \theta}{\partial Vy} = \frac{\partial \theta}{\partial Vz} = \frac{\partial \phi}{\partial Vx} = \frac{\partial \phi}{\partial Vy} = \frac{\partial \phi}{\partial Vz} = \frac{\partial \phi}{\partial z} = 0. \tag{37}$$

The covariance matrix of process noise is defined as

$$\mathbf{Q}_j = E\left\{\mathbf{w}_j \mathbf{w}_j^T\right\}. \tag{38}$$

The covariance matrix of measurement noise is defined as

$$\mathbf{R}_j = E\left\{\mathbf{v}_j \mathbf{v}_j^T\right\}. \tag{39}$$

Due to the impact of ship movement and environmental noise, process noise and measurement noise will dynamically change, so that the covariance matrix values of process noise and measurement noise are adaptively estimated to ensure the extended Kalman filter convergence. The covariance matrix of measurement noise is obtained with

$$\mathbf{R}_{j+1} = \widehat{\mathbf{C}}_v + \mathbf{H}_j \mathbf{P}_j \mathbf{H}_j^T, \tag{40}$$

where

$$\widehat{\mathbf{C}}_v = \frac{1}{w}\sum_{i=1}^{w}\left(\mathbf{\Psi}_{j-i} - \mathbf{H}_{j-i}\widehat{\mathbf{X}}_{j-i}\right)\left(\mathbf{\Psi}_{j-i} - \mathbf{H}_{j-i}\widehat{\mathbf{X}}_{j-i}\right)^T = \frac{1}{w}\sum_{i=1}^{w}\mathbf{D}_{j-i}\mathbf{D}_{j-i}{}^T, \tag{41}$$

where the residual value $\mathbf{D}_j$ is the difference between measurement and estimation, and w is the moving window size. The covariance matrix of process noise is obtained with

$$\mathbf{Q}_j = \mathbf{K}_j \widehat{\mathbf{C}}_v \mathbf{K}_j^T. \tag{42}$$

The flow chart of AEKF algorithm is shown in Figure 6.

5. Computer Simulations

Six scenarios are used to simulate the tracking performance of shipborne phased array radar using the proposed beam pointing error compensation mechanism.

Case 1 (beam pointing error compensation for stationary ship and target). The ship's roll and pitch signals are simulated according to (3) and (4) with roll and pitch angle parameters of sea state 5 listed in Table 1 and standard deviation of 0.05.

The beam of 6 × 6 planar array antenna is steered to $(\theta, \phi) = (45^\circ, 60^\circ)$. The sampling frequency is set as 100 Hz. Therefore, the ship's roll and pitch signals are sampled 1000 points within 10 seconds, which is used as the center value of 1000 membership functions for parallel beam pointing error estimator. The simulated ship's roll and pitch signals are applied for the FBFN architecture and the RLS adaptive prediction filter to simulate the performance of pointing error estimation. Each of the ship's roll and pitch signals is sampled 13 points for each of simulations. The simulation replicates 1000 times. The input samples are updated by one new sample for the next iteration. Figures 7 and 8 compare the ensemble-averaged square error performance of the FBFN architecture and RLS adaptive prediction filter for roll and pitch angles, respectively, per 0.01 sec iteration time. Table 2 compares the convergent values of ensemble-averaged square beam pointing error for FBFN architecture and RLS adaptive prediction filter under different sea states and standard deviation of 0.05. The ensemble-averaged square error is defined as

$$\mathrm{MSE}(n) = \frac{1}{1000}\sum_{m=1}^{1000}\left[\theta_m(n+1) - Y_m(n)\right]^2, \quad (43)$$

where m represents the mth Monte-Carlo simulation; $n = 1, \ldots, 100$ represents the number of the iterations.

Based on the simulation results, we may make the following observations. The FBFN architecture converges much faster than the RLS adaptive prediction filter and it has lower ensemble-averaged square error than RLS adaptive prediction filter. The steady state values of the ensemble-averaged square error for both the FBFN architecture and RLS adaptive prediction filter approximate to the standard deviation of the Gaussian noise. In summary, the convergent time and accuracy of the automatic beam error correction system using the FBFN architecture is superior to the RLS adaptive prediction filter. The shortest convergent time is 0.1 sec when FBFN beam pointing error estimator is used (see Table 3).

Case 2 (beam pointing error estimation and compensation for linear moving ship and target). Figures 9(a) and 9(b) shows the simulation scenario of beam pointing error compensation for linear moving air target and ship with linear motion. Assuming the ship is along the Y-axis of XY plane in the earth coordinates, the ship speed is 10 m/sec and the flying target speed is 300 m/sec. The flying target is parallel to the XY plane, 9.84 km above the ground, and the angle between the flight direction and the Y-axis is 30°. The largest reconnaissance distance of shipborne radar is 150 km. while the air target is flying within the radar detection range, the beam pointing error estimation and compensation of shipborne phased array radar are simulated.

The linear ship path equation is

$$ws_t(x_t, y_t, z_t) = ws_0 + v_{ws}t, \quad (44)$$

where $t = 1, 2, 3, \ldots, 1010, 1011$ sec, v_{ws} is ship velocity, and ws_0 is initial ship position. The linear target trajectory equation is

$$ms_t(x_t, y_t, z_t) = ms_0 + v_{ms}t, \quad (45)$$

Table 2: Comparison of the convergent values for different sea states.

Algorithm	Sea state					
	Sea 4		Sea 5		Sea 6	
	Angle					
	Roll	Pitch	Roll	Pitch	Roll	Pitch
No correction	2.53	0.21	43.90	3.01	90.49	9.96
RLS	0.062	0.059	0.067	0.061	0.071	0.064
FBFN	0.055	0.081	0.056	0.056	0.057	0.059

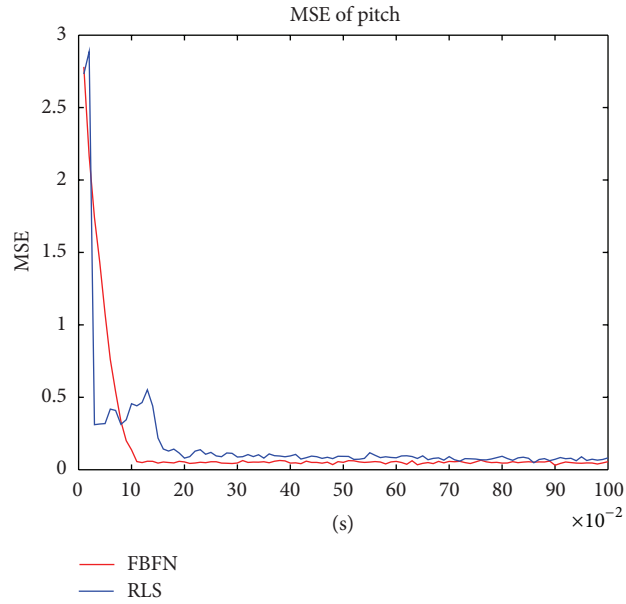

Figure 8: Beam pointing error correction for pitch angle.

where v_{ms} is the target velocity, and ms_0 is the initial target position.

Figures 10(a) and 10(b) compare the beam pointing error compensation performance of the FBFN architecture, RLS adaptive prediction filter for roll and pitch angles, respectively, under the sea state 5 condition. The green curve represents the real beam steering angle of the shipborne phased array radar. The initial beam angle is steered to $(\theta, \phi) = (70^\circ, 150^\circ)$, and the following beam angles are calculated by (20) and (21). The FBFN architecture converges faster than the RLS adaptive prediction filter. The peak response of the RLS adaptive prediction filter will result in the performance degradation of the shipborne phased array radar.

Case 3 (beam pointing error estimation and compensation for linear moving ship and circular trajectory target). Figures 11(a) and 11(b) show the simulation scenario of beam pointing error compensation for circular maneuvering air target and linear moving ship. The ship has the same linear moving speed and path equation. The flying target is parallel to the XY plane, 9.84 km above the ground, and the angle between the initial position and the Y-axis is 30°. The trajectory of the equal speed flight vehicle is a circle with a radius of 10 km, and

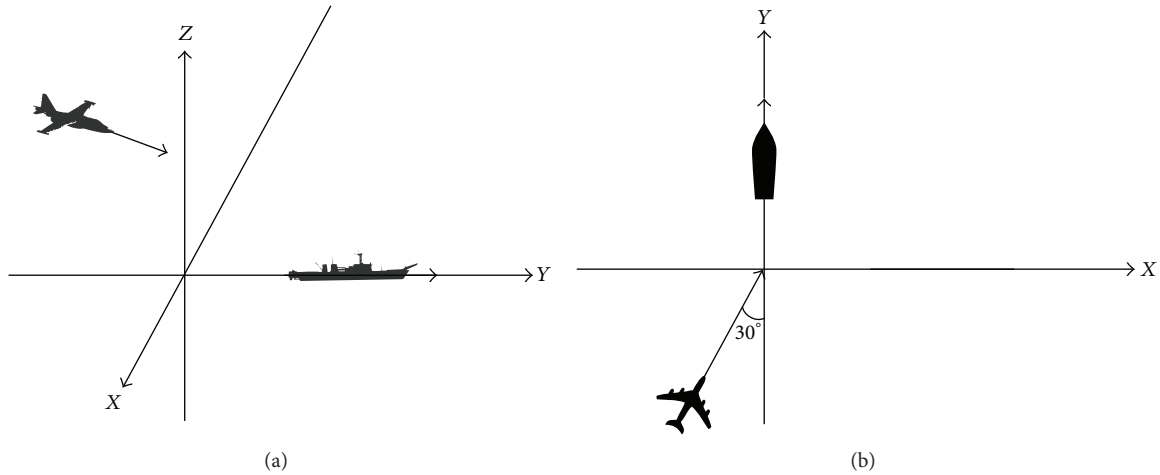

Figure 9: Simulation scenarios of Case 2 for (a) 3D and (b) top view diagrams.

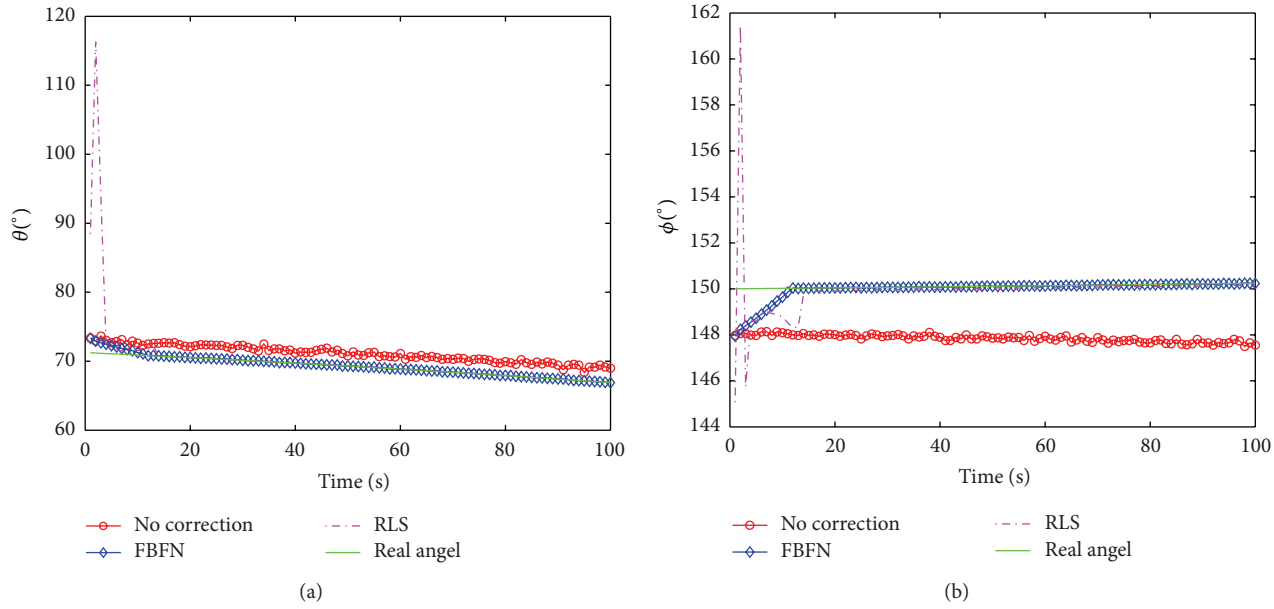

Figure 10: (a) Elevation and (b) horizontal beam pointing error compensation for linear moving target.

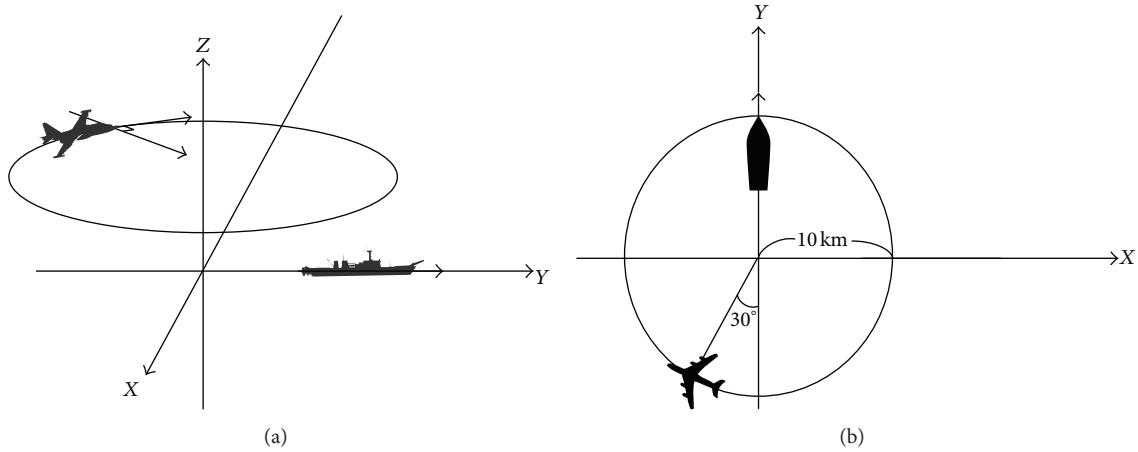

Figure 11: Simulation scenarios of Case 3 for (a) 3D and (b) top view diagrams.

Table 3: Comparison of the convergent values for different standard deviations.

Algorithm	Standard deviation 0.01		0.05		0.1		0.5		1	
	Angle									
	Roll	Pitch	Roll	Pitch	Roll	Pitch	Roll	Pitch	Roll	Pitch
No correction	43.831	2.9585	43.903	3.0071	43.956	3.0428	44.404	3.4406	44.971	3.9836
RLS	0.0145	0.0127	0.0674	0.0608	0.1292	0.1291	0.6479	0.6357	1.3071	1.2154
FBFN	0.0113	0.0105	0.0556	0.0555	0.1122	0.1072	0.5607	0.5239	1.1057	1.4081

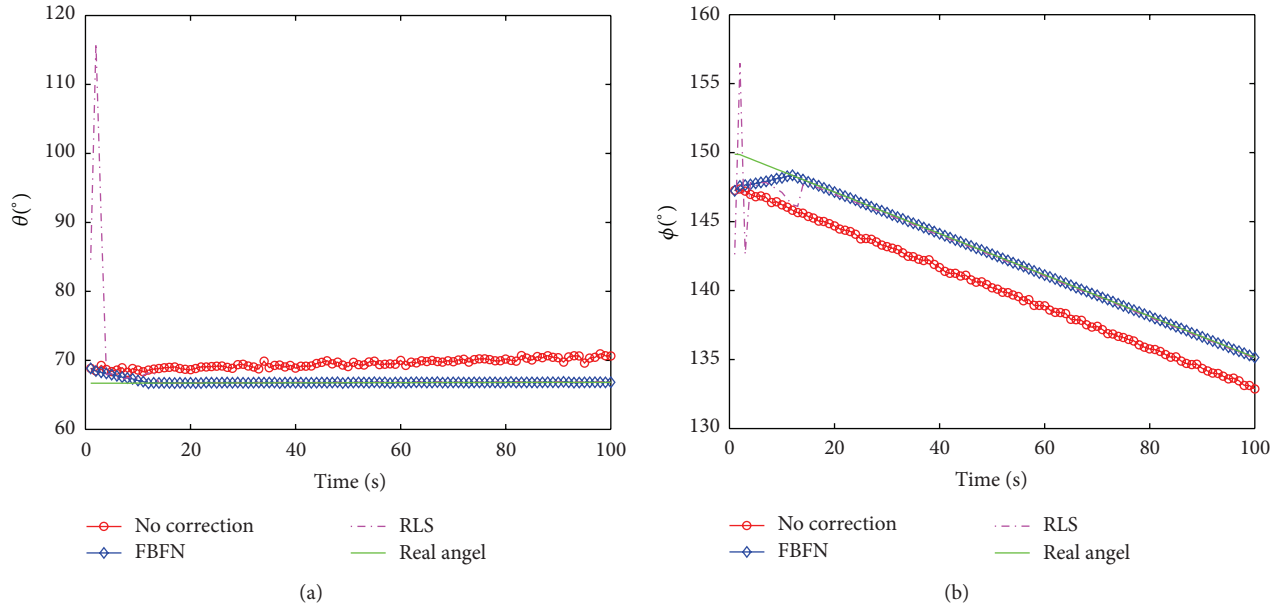

Figure 12: (a) Elevation and (b) horizontal beam pointing error compensation for circular maneuvering target.

the Y-axis is the center. The rotational cycle time of the flight target is 209 seconds.

The circular trajectory equation is

$$ms_t(x_t, y_t, z_t) = (r\cos(\theta_0 - \omega t), r\sin(\theta_0 - \omega t), 9.84), \quad (46)$$

where $t = 1, 2, 3, \ldots, 418, 419$ sec, r is the circular flight radius, θ_0 is the initial angle between the flight vehicle and the X-axis, and ω is the angular speed of flight vehicle.

When the vehicle flies in circles with constant speed, the simulation results for roll and pitch angles are shown in Figures 12(a) and 12(b), respectively. The FBFN architecture converges faster than the RLS adaptive prediction filter and compensates the beam pointing error effectively.

Case 4 (AEKF with no beam pointing error for linear trajectory target). Assuming the ship is not affected by the sea waves (antenna beam pointing error is zero), the tracking performance of AEKF for a straight flight target trajectory is simulated. As shown in Figure 13, the initial position of radar is (0, 0, 0). The ship moves with a speed of 10 m/sec in the Y axial direction. The radar position is updated every second. The initial position of flying targets is −74840, −129620, and 9100 meters, about 150 km from the radar. The flight speed of target is 300 m/sec (X axial velocity of 150 m/sec and Y axial velocity of 260 m/sec). The target location is updated every second. The tracking accuracy of AEKF for a straight flight target is shown in Figure 14, where the trajectory estimation error is calculated by

$$E_j = \sqrt{(x_j - \hat{x}_j)^2 + (y_j - \hat{y}_j)^2 + (z_j - \hat{z}_j)^2}. \quad (47)$$

It shows that the AEKF converges to less than about 20 m after 550 iterations.

Case 5 (AEKF with no beam pointing error for circular trajectory target). Assuming the ship is not affected by the sea waves (antenna beam pointing error is zero), the tracking performance of AEKF for a circular trajectory target is simulated. As shown in Figure 15, the initial position of radar is (0, 0, 0). The ship moves with a speed of 10 m/sec in the Y axial direction. The radar position is updated every second. The initial position of flying targets is −5000, −8660, and 9100 meters about 13.5 km from the radar. The flying target is parallel to the XY plane, 9.84 km above the ground, and the angle between the initial position and the Y-axis is 30°. The flying object has uniform velocity and circular trajectory of radius of 10 km, and the Y-axis is the center. The rotational

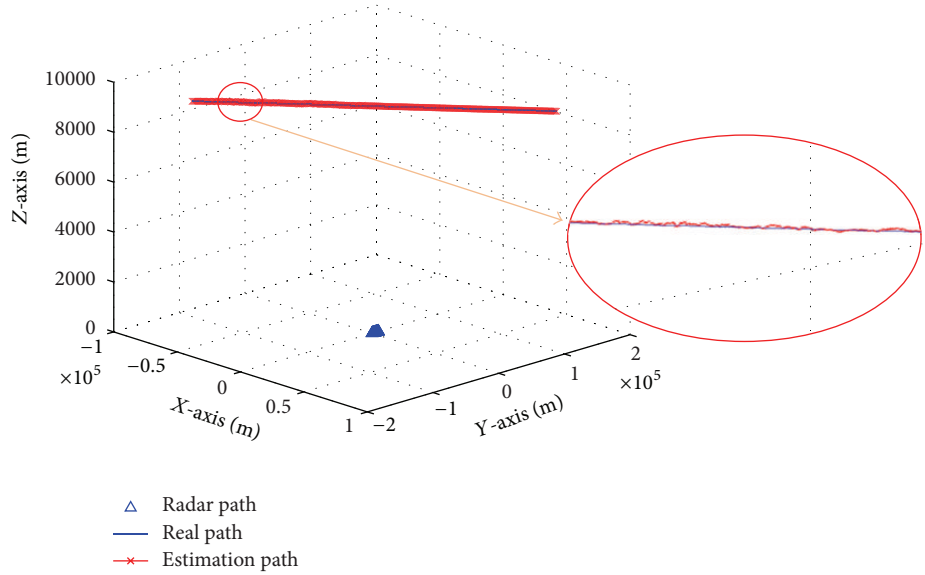

Figure 13: 3D scenario diagram of Case 4.

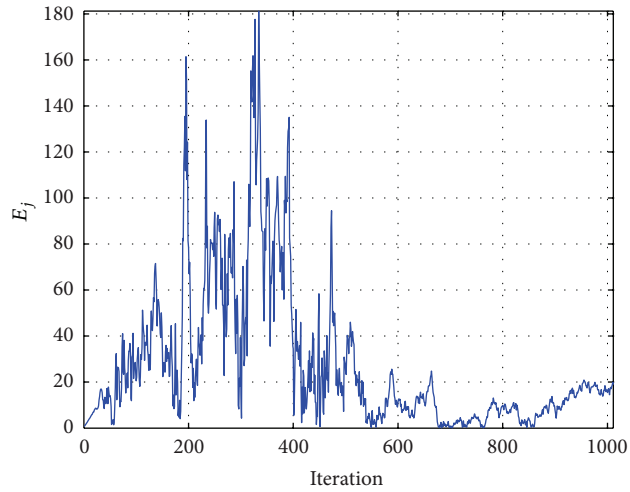

Figure 14: Tracking accuracy of AEKF for straight flight target.

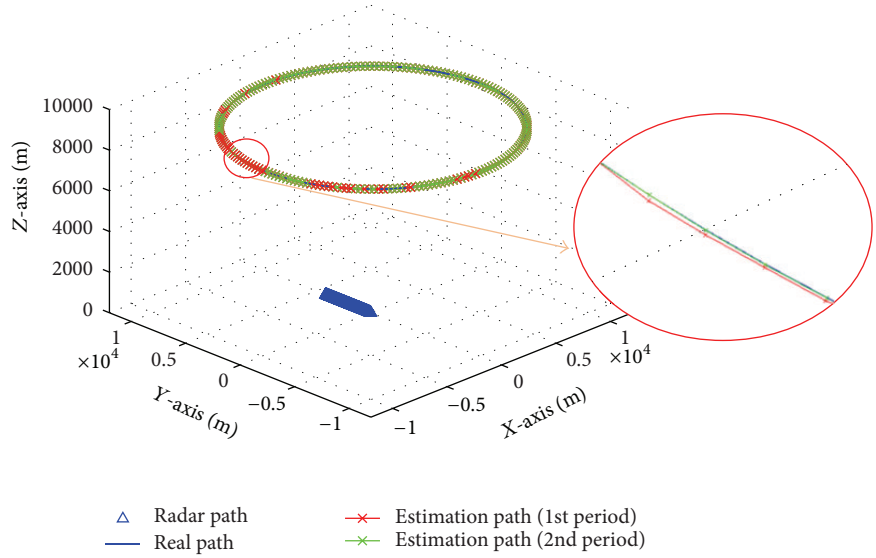

Figure 15: 3D scenario diagram of Case 5.

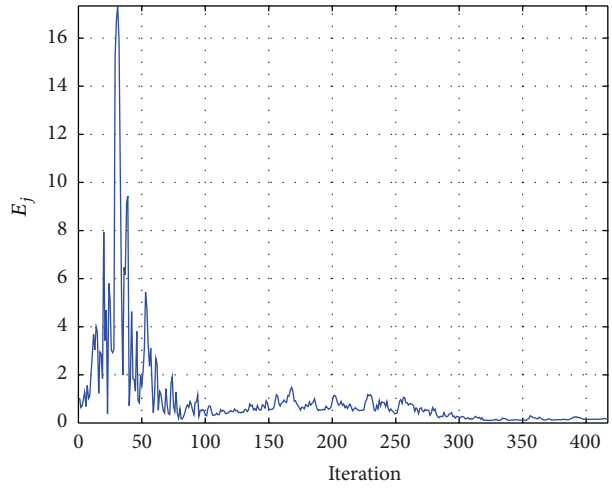

Figure 16: Tracking accuracy of AEKF for straight flight target.

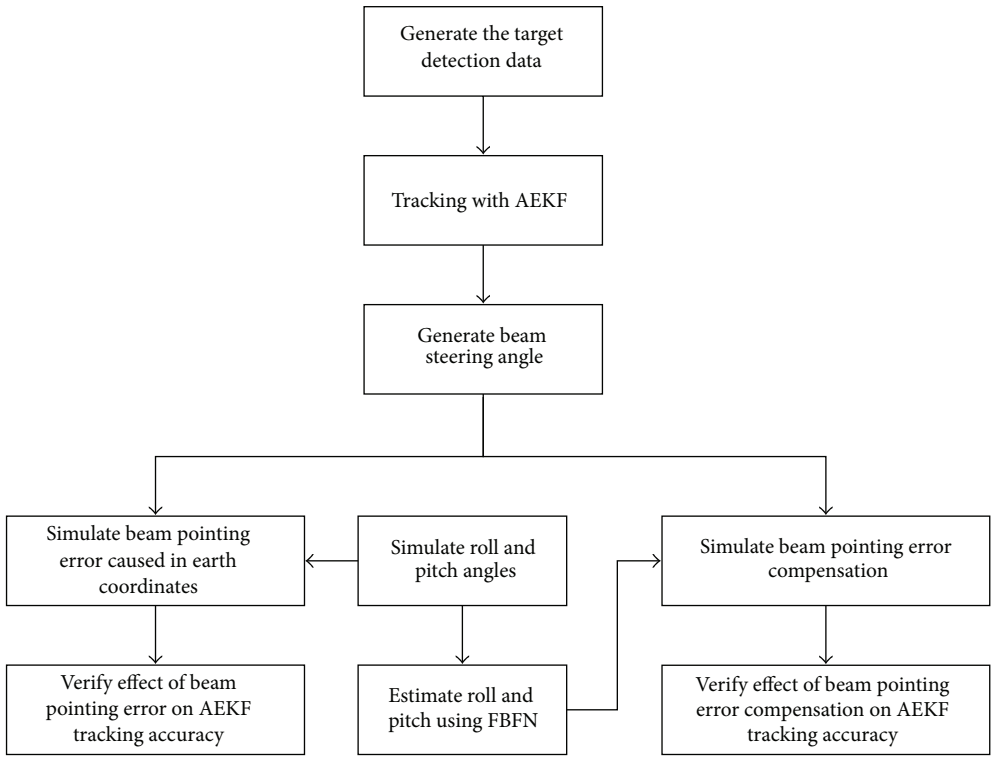

Figure 17: Flow chart of simulation used to verify the effect of beam pointing error compensation on AEKF tracking accuracy.

cycle time of the flying target is 209 seconds. The target flies two cycles in the simulation. The tracking accuracy of AEKF for a circular trajectory flight target is shown in Figure 16. The AEKF converges to less than 1 m after 100 iterations, because the distance between radar and flight target in Case 3 is less than Case 5.

Case 6 (combining AEKF with beam pointing error compensation for linear trajectory target). Figure 17 is a simulation flow chart used to verify the effect of beam pointing error compensation on AEKF tracking accuracy. The shipbone radar and flight target have the same experimental scenario as Case 4, but beam pointing error generated by roll and pitch angle parameters of sea state 5 is considered. The linear trajectory target is shown in Figure 13.

When the beam pointing of shipborne phased array antenna is affected by the roll and pitch angles, the target tracking error of AEKF is shown in Figure 18. It shows that the AEKF converges to less than about 20 m at 550 iterations but the estimation error increases to 100 m at 1000 iterations. We conclude that the tracking accuracy is affected by the beam pointing error and the increasing distance between

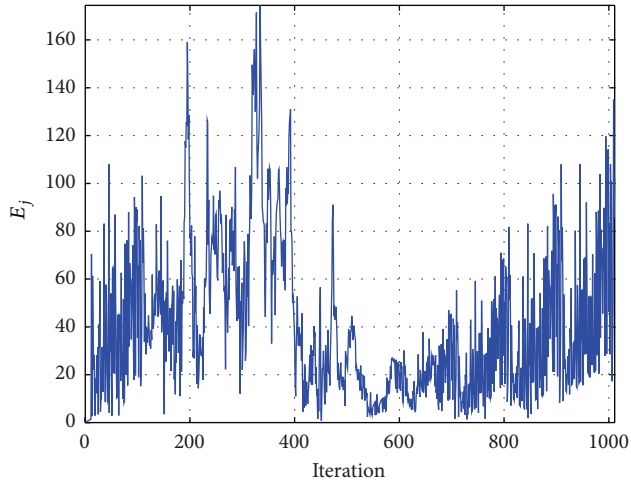

Figure 18: Estimation error of AEKF without beam pointing error compensation.

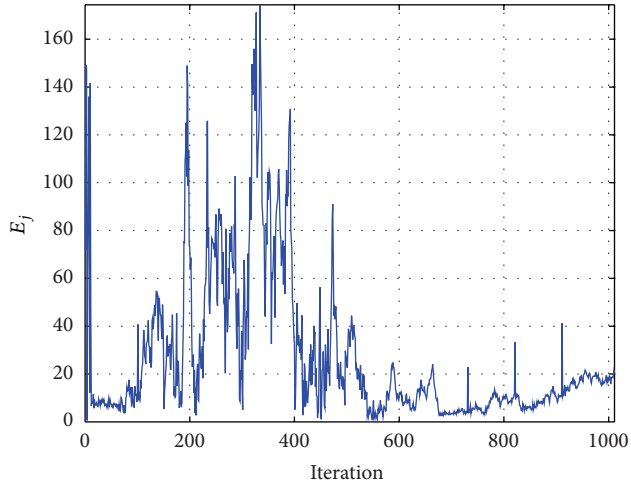

Figure 19: Estimation error of AEKF with FBFN based beam pointing error compensation.

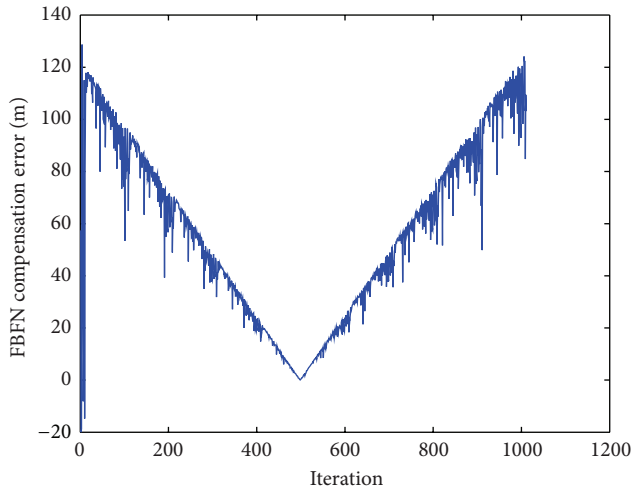

Figure 20: Error compensation value of FBFN controller.

the radar and flight target obviously when the simulation result of Figure 18 is compared with Figure 14. When the beam pointing error of shipborne phased array antenna is compensated with FBFN controller, the target tracking error of AEKF is shown in Figure 19. It shows that the tracking error of AEKF converges to less than about 20 m at 550 iterations and the estimation error will remain within the range of about 20 m when beam pointing error is compensated by FBFN controller. The error compensation values of FBFN controller are shown in Figure 20, which is calculated by subtracting the trajectory estimation error of Figure 18 from Figure 19. The error compensation values of FBFN controller present a V-shaped curve. The tracking performance of AEKF is proportional to the distance between moving target and the ship. In the simulation of the starting point and end point, moving targets far from the shipborne radar, the FBFN controller generates the largest estimation error. When the moving target closes the radar just above the ship, the FBFN controller generates the smallest estimation error.

6. Conclusions

This paper proposed an intelligent beam pointing error compensation mechanism for shipborne two-dimensional phase array antenna radar. The FBFN controller estimates the roll and pitch angle of the ship driving in the sea and thus compensates for the antenna beam pointing error in order to enhance the accuracy of phased array radar system tracking a moving target. Six cases of simulations are used to verify the performance of shipborne phased array radar using the proposed beam pointing error compensation mechanism for six different scenarios. Cases 1, 2, and 3 simulate the accuracy of beam pointing error compensation mechanism and Cases 4, 5, and 6 simulate the effect of beam pointing error compensation mechanism on the tracking accuracy of AEKF.

The simulation results show that the convergent time and accuracy of the automatic beam pointing error compensation mechanism using the FBFN architecture are superior to the RLS adaptive prediction filter. The tracking accuracy is affected by the beam pointing error and the distance between the radar and moving target. In summary, the use of the proposed FBFN beam pointing error compensation mechanism with the AEKF can reduce the amount of estimation error significantly.

Acknowledgment

This work is supported in part by research grants from the National Science Council, Taiwan (NSC 102-2218-E-155-001).

References

[1] Z. Fang and Q. Rundong, "Ship-borne phased array radar motion compensation," in *System Engineering and Electronic Technologies*, pp. 4–8, 1998.

[2] S. L. Chen, *Modeling, dynamics and control of large amplitude motion of vessel in beam seas [Ph.D. thesis]*, Department of Mechanical Engineering, Michigan State University, 1996.

[3] L.-X. Wang, "Stable adaptive fuzzy control of nonlinear systems," *IEEE Transactions on Fuzzy Systems*, vol. 1, no. 2, pp. 146–155, 1993.

[4] V. Fathabadi, M. Shahbazian, K. Salahshour, and L. Jargani, "Comparison of adaptive Kalman filter methods in state estimation of a nonlinear system using asynchronous measurements," in *Proceedings of the World Congress on Engineering and Computer Science (WCECS '09)*, vol. 2, pp. 20–22, San Francisco, Calif, USA, October 2009.

[5] D. C. Law, S. A. McLaughlin, M. J. Post et al., "An electronically stabilized phased array system for shipborne atmospheric wind profiling," *Journal of Atmospheric and Oceanic Technology*, vol. 19, no. 6, pp. 924–933, 2002.

[6] C. A. Balanis, *Antenna Theory: Analysis and Design*, John Wiley & Sons, 3rd edition, 2005.

[7] J. Mar and Y.-R. Lin, "Implementation of SDR digital beamformer for microsatellite SAR," *IEEE Geoscience and Remote Sensing Letters*, vol. 6, no. 1, pp. 92–96, 2009.

[8] S. Haykin, *Adaptive Filter Theory*, Prentice Hall, 3rd edition, 1996.

[9] E. Mosca, *Optimal, Predictive, and Adaptive Control*, Prentice Hall, 1995.

[10] Y. Li and Y.-T. Jang, "Complex adaptive fuzzy inference systems," in *Proceedings of the Asian Fuzzy Systems Symposium*, pp. 551–556, December 1996.

[11] A. Almagbile, J. L. Wang, and W. Ding, "Evaluating the performance of adaptive Kalman filter methods in GPS/INS integration," *Journal of Global Positioning System*, vol. 9, no. 1, pp. 33–40, 2010.

[12] K. H. Kim, J. G. Lee, and C. G. Park, "Adaptive two-stage extended kalman filter for a fault-tolerant INS-GPS loosely coupled system," *IEEE Transactions on Aerospace and Electronic Systems*, vol. 45, no. 1, pp. 125–137, 2009.

Hindawi Publishing Corporation
International Journal of Antennas and Propagation
Volume 2013, Article ID 320645, 18 pages
http://dx.doi.org/10.1155/2013/320645

Research Article

An Ionospheric Es Layer Clutter Model and Suppression in HF Surfacewave Radar

Yajun Li, Yinsheng Wei, Rongqing Xu, Zhuoqun Wang, and Tianqi Chu

Research Institute of Electronic Engineering Technology, Harbin Institute of Technology, No. 807, Harbin 150001, China

Correspondence should be addressed to Yinsheng Wei; weiys@hit.edu.cn

Received 31 March 2013; Revised 28 May 2013; Accepted 29 May 2013

Academic Editor: Krzysztof Kulpa

This paper based on a fast implemented multiphase screen method using DFT puts forward an ionospheric Es layer clutter model and uses the newly developed dimensionality reduction space-time adaptive processing- (STAP-) JDL algorithm to suppress Es layer clutter, which proves the validity of the proposed model. Firstly, the multiphase screen method was analyzed, and a fast algorithm using DFT was proposed. Then, based on the multiphase screen method and thorough simulation, we reached a conclusion of the high-frequency radio wave propagation's fluctuation characteristics in the ionosphere. According to the results of the analysis, a new Es layer ionospheric clutter model was established and was compared with the measured data and verification was made. Finally, based on the built clutter model, JDL algorithm was applied to the high-frequency surface wave radar ionospheric clutter suppression, using the measured data to verify the validity of the model and algorithm. The simulation results showed that the built model can show the characteristics of the ionospheric Es layer clutter and that the JDL algorithm can suppress ionospheric Es layer clutter quite effectively.

1. Introduction

HF surface wave radar has been gradually applied as an efficient tool to detect the ocean dynamics elements and to maneuver targets with low speed, especially to monitor exclusive economic zone (EEZ) globally. When HF surface wave radar emits electromagnetic waves to the surface of the sea horizontally, some energy is emitted to the sky and reflected by the ionosphere owing to the nonideality of the antenna in the zenith direction, which forms the ionospheric clutter finally. Ionospheric clutter mainly locates at the height of 100 km~120 km in the sporadic-E layer (Es layer) and above 210 km in the F layer, and due to the nonstationary property of the ionosphere, the sea echo is often completely submerged in the ionospheric clutter, which causes the radar's detection performance to decrease dramatically. Ionospheric clutter has become the bottleneck that limits the development of remote HF ground wave radar currently, and especially the Es layer clutter in it that has the ionosphere irregularities structure, which makes the suppression of the clutter more difficult [1].

At present, according to the relevant literature and the tests results, most adaptive methods that suppress ionospheric clutter are often more suitable for processing the steady or slowly varying disturbances. Because of the complex features of the ionospheric medium itself, the methods in the literature always fail. The main reason is that the problem is difficult to break through in the perspective of signal processing. Therefore, it is necessary to study the characteristics of radio wave propagation in the ionosphere and establish a reasonable ionospheric clutter model to suppress the clutter essentially.

Es layer of the ionosphere can be seen as a random medium. Some primary methods to deal with the problems of the wave propagation in the random medium include geometrical optics approximation, the Born approximation method, the Rytov approximation method, and multiphase screen method [2–6]. Geometrical optics approximation can be only applied to the situation that the wavelength of the radio waves is small enough to be neglected comparing with the characteristic dimension of the medium. The Born approximation is the single scattering solution of the scattering problem and it approximates the ionosphere propagation in the condition of weak fluctuation. However, multiphase screen method equals the ionosphere into several phase screens, taking the hierarchical characteristic of the

ionosphere into consideration; so, we could simulate the propagation of the radio waves with high qualities simply selecting a sufficient number of phase screen in the ionosphere. Furthermore, it is suitable for the case of the weak and strong fluctuation, but its calculation speed is very slow.

Based on what is presented previously, the paper proposed an ionospheric Es layer clutter model using multiphase screen method with DFT fast implementation, and then, we applied STAP method to suppress the Es layer clutter under this model. At the beginning, we analyzed the basic principle of the multiphase screen method in the disturbed layered ionosphere and proposed a fast algorithm implemented by DFT. Then, we obtained the fluctuating characteristics of the high-frequency radio wave propagation in the ionosphere according to the experiment simulation at both weak and strong scintillation. Using the statistical analysis results of the multiphase screen method together with the height variation of the reflection points in the ionospheric Es layer, we established a new reflecting model in the ionospheric Es layer. We also compared and analyzed the model with the measured data to verify the reasonableness and correctness. Finally, based on the proposed ionospheric clutter model, we used the newly developed descending dimensional STAP-JDL algorithm to suppress the Es layer clutter, and the simulation with measured data verified the ability of this algorithm to suppress the ionospheric clutter. The simulation results showed that the established model can present the characteristics of the ionospheric Es layer clutter basically, and the JDL algorithm can suppress ionospheric Es layer clutter quite effectively. The method proposed in this paper provided a theoretical basis for the ionospheric clutter suppression techniques and the use of STAP in anti-ionospheric clutter.

2. The Analysis of Radio Wave's Propagation Characteristics in the Ionospheric Es Layer Based on the Multiphase Screen Method

2.1. The Basic Theory of the Multiscreen Method. Multiphase screen technology equals the irregularities' path of the high-frequency radio wave signals in the ionosphere to a plurality of thin screens that only change the phase of the signal, and each thin screen corresponds to the impact of the ionospheric on radio wave signal over path, while we assumed that it was vacuum between each of the thin screens, that is, using the principle of equivalent. The propagation of high-frequency waves on the screen causes the signal phase to fluctuate, and the diffraction effect between the thin screens leads to the fluctuation of the amplitude and phase.

Assume that the electric field of the incident wave is field $E_0(z)$ with no irregularities, and after passing through the ionosphere its form $E(\vec{r})$ is as follows:

$$E(\vec{r}) = u(\vec{r})\, E_0(z), \tag{1}$$

where

$$u(\vec{r}) = \exp\left[-j\Phi(\vec{r})\right]. \tag{2}$$

To illustrate fluctuation of the amplitude and phase, respectively, set $u(\vec{r})$ as the following form [2, 3]:

$$u(\vec{r}) = \exp\left[\chi(\vec{r}) - jS_1(\vec{r})\right] = \exp\left[-\phi(\vec{r})\right], \tag{3}$$

where $\chi(\vec{r})$ is the amplitude part of $u(\vec{r})$ and $S_1(\vec{r})$ is the phase part of $u(\vec{r})$. We can use Kirchhoff diffraction formula to solve the problem that radio waves propagate from one screen to another. Besides in the forward scattering assumption, the Kirchhoff diffraction can produce the results as follows:

$$u(\vec{p}, z) = \frac{jkA_0}{2\pi z} \iint e^{-j[\phi(\vec{p}') + (k/2\pi)|\vec{p}-\vec{p}'|^2]} d^2\vec{p}'. \tag{4}$$

In the condition of shallow screen, we can get the relationship from the previous formulas:

$$\begin{aligned} \chi(\vec{p}, z) &= \frac{k}{2\pi z} \iint \phi(\vec{p}') \cos\left[\frac{k\left|\vec{p}-\vec{p}'\right|^2}{2z}\right] d^2\vec{p}', \\ S_1(\vec{p}, z) &= \frac{k}{2\pi z} \iint \phi(\vec{p}') \sin\left[\frac{k\left|\vec{p}-\vec{p}'\right|^2}{2z}\right] d^2\vec{p}'. \end{aligned} \tag{5}$$

The statistical characteristics of the waves through each phase screen can be obtained by calculating the moments of formula (5). Among the moments, the mean value of the amplitude and phase fluctuation is 0, and the correlation function of the amplitude and phase fluctuations are

$$\begin{aligned} B_\chi(\vec{p}) &= \iint \Phi_\phi(\vec{k}_\perp) \sin^2\left(\frac{k_\perp^2 z}{2k}\right) \cos\vec{k}_\perp \cdot \vec{p}\, d^2k_\perp, \\ B_{S_1}(\vec{p}) &= \iint \Phi_\phi(\vec{k}_\perp) \cos^2\left(\frac{k_\perp^2 z}{2k}\right) \cos\vec{k}_\perp \cdot \vec{p}\, d^2k_\perp, \end{aligned} \tag{6}$$

where $\Phi_{\phi_{n-1,n}}$ is power spectrum of the phase screen at $z = (z_{n-1} + z_n)/2$. Taking the previous formulas (6) for Fourier transform, we can have the power spectrum of the amplitude and phase fluctuations. Consider the following:

$$\begin{aligned} \Phi_{\chi_{n-1,n}}(\vec{k}_\perp) &= \sin^2\left(\frac{k_\perp^2 z}{2k}\right) \Phi_{\phi_{n-1,n}}(\vec{k}_\perp), \\ \Phi_{S_{n-1,n}}(\vec{k}_\perp) &= \cos^2\left(\frac{k_\perp^2 z}{2k}\right) \Phi_{\phi_{n-1,n}}(\vec{k}_\perp). \end{aligned} \tag{7}$$

In order to simplify the discussion and calculation of the problem, we only consider the two-dimensional case which assumes that the irregularities are independent of y direction; thus, the relationships in the previous formulas become

$$\Phi_{\chi_{n-1,n}}(k_x) = \sin^2\left(\frac{k_x z}{2k}\right) \Phi_{\phi_{n-1,n}}(k_x), \tag{8a}$$

$$\Phi_{S_{n-1,n}}(k_x) = \cos^2\left(\frac{k_x z}{2k}\right) \Phi_{\phi_{n-1,n}}(k_x). \tag{8b}$$

Ionosphere can be characterized by the relative dielectric constant $\varepsilon(\vec{r})$, which is composed of regular portion

$\langle \varepsilon(z) \rangle$ ($z > 0$) and the random part $\varepsilon_1(\vec{r})$. In the disturbed stratified ionosphere, the relative dielectric constant can be expressed as

$$\begin{aligned} \varepsilon(x,z) &= \langle \varepsilon(z) \rangle + \varepsilon_1(x,z), \\ \langle \varepsilon(z) \rangle &= 1 - \frac{e^2}{m\varepsilon_0\omega^2} \langle N(z) \rangle = 1 - \frac{z}{z_\Gamma}, \end{aligned} \tag{9}$$

$$\varepsilon_1(x,z) = \frac{-e^2}{m\varepsilon_0\omega^2} \Delta N(x,z) = -\left(\frac{z}{z_\Gamma}\right) N_f(x,z), \tag{10}$$

where e and m are the charge and mass of the electron; $\langle N(z) \rangle$ is the electron concentration of the background, and it is a linear function of z; $\Delta\langle N(x,z) \rangle$ is its fluctuations portion. $N_f(x,z)$ is the relative fluctuation of the electron concentration:

$$N_f(x,z) = \frac{\Delta N(x,z)}{\langle N(z) \rangle}. \tag{11}$$

The power spectrum of the ionospheric electron concentration fluctuation of the two-dimensional irregularities can be characterized using the available Shkarofsky spectrum:

$$\begin{aligned} \Phi_{N_f}(k_x,k_z) = {} & \frac{\sigma^2{}_{N_f} (k_0 r_0)^{(p-3)/2} r_0^3 K_{p/2}\left(r_0\sqrt{k_x^2+k_z^2+k_0^2}\right)}{(2\pi)^{3/2} K_{(p-3)/2}(k_0 r_0)} \\ & \cdot \left(r_0\sqrt{k_x^2+k_z^2+k_0^2}\right)^{-p/2}, \end{aligned} \tag{12}$$

where r_0 and $L_0 = 2\pi/k_0$ are the internal and external dimensions of the irregularities, K_v is the modified Bessel function of the second kind with the order v. By solving the Helmholtz equation of radio wave propagation, we can yield

$$u(x,z_n) = u(x,z_{n-1})\, e^{j\phi_{n-1,n}(x)}, \tag{13}$$

where

$$\phi_{n-1,n}(x) = -\frac{k}{2} \int_{z_{n-1}}^{z_n} \frac{\varepsilon_1(x,z)}{\sqrt{1 - z/z_\Gamma}} dz. \tag{14}$$

Substitute formula (10) into (14) and calculate the correlation function of the phase deviation. The result is shown as follows:

$$\begin{aligned} B_{\phi_{n-1,n}}(x) = {} & \frac{k^2}{4}\left[z_\Gamma \ln\left(\frac{z_\Gamma - z_{n-1}}{z_\Gamma - z_n}\right) - \frac{z_n^2 - z_{n-1}^2}{2z_\Gamma} - \Delta z\right] \\ & \cdot \int_{-\infty}^{+\infty} B_{N_f}(x,\xi)\, d\xi. \end{aligned} \tag{15}$$

Taking formula (15) for FFT, we can get the power spectrum of the phase deviation:

$$\begin{aligned} \Phi_{\phi_{n-1,n}}(k_x) = {} & \frac{\pi k_x^2}{2}\left[z_\Gamma \ln\left(\frac{z_\Gamma - z_{n-1}}{z_\Gamma - z_n}\right) - \frac{z_n^2 - z_{n-1}^2}{2z_\Gamma} - \Delta z\right] \\ & \cdot \Phi_{N_f}(k_x,k_z)\Big|_{k_z=0} \\ = {} & \frac{\pi k_x^2}{2}\left[z_\Gamma \ln\left(\frac{z_\Gamma - z_{n-1}}{z_\Gamma - z_n}\right) - \frac{z_n^2 - z_{n-1}^2}{2z_\Gamma} - \Delta z\right] \\ & \cdot \Phi_{N_f}(k_x,0). \end{aligned} \tag{16}$$

Formula (16) links up the power spectrum of the phase deviation and the power spectrum of the undulating electron concentration.

According to the previously obtained power spectra of the phase deviation in the phase screen, we substitute it into formula (8a) and (8b) to obtain the corresponding power spectrum of the amplitude and the phase fluctuations. As long as the power spectrum of the amplitude and phase fluctuations are obtained, the amplitude and phase deviation of the simulation phase screen in the $z = (z_{n-1} + z_n)/2$ can be obtained via the numerical procedure using FFT. Assume that the horizontal size of each phase screen is L_h and that it is divided into N equal parts, the fluctuations of the random amplitude and phase at the point $x = m \cdot \Delta x$ can be described as

$$\begin{aligned} \chi_{n-1,n}(m\cdot\Delta x) &= \sum_{s=0}^{N-1} \sqrt{\Phi_{\chi_{n-1,n}}(s\cdot\Delta k)\cdot\Delta k}\cdot\cos\left(\frac{2\pi sm}{N} + \varphi_s\right), \\ S_{n-1,n}(m\cdot\Delta x) &= \sum_{s=0}^{N-1} \sqrt{\Phi_{S_{n-1,n}}(s\cdot\Delta k)\cdot\Delta k}\cdot\cos\left(\frac{2\pi sm}{N} + \varphi_s\right), \end{aligned} \tag{17}$$

where $m = 0, 1, 2, \ldots, N-1$; $\Delta x = L_h/N$; $\Delta k = 2\pi/L_h$; here, we also introduce a random phase angle φ_s, which is subjected to the uniform distribution in the interval 0~2π and meets the following qualifications: $\varphi_s = -\varphi_{-s}$.

2.2. A New DFT-Based Fast Algorithms. Through the multiphase screen method previously mentioned, we obtained the expression of the signal amplitude and phase fluctuation that occur in the ionosphere. The formula is shown by summing, which will be very slow and inefficient when calculating directly. We make appropriate transform after which the calculation can be implemented by FFT algorithm. By the transformation formula of the trigonometric function, we can obtain

$$\begin{aligned} \cos\left(\frac{2\pi sm}{N} + \varphi_s\right) = {} & \cos\left(\frac{2\pi sm}{N}\right)\cos(\varphi_s) \\ & - \sin\left(\frac{2\pi sm}{N}\right)\sin(\varphi_s). \end{aligned} \tag{18}$$

To be convenient, we can set

$$\begin{aligned} x_{n-1,n}(s) &= \sqrt{\Phi_{\chi_{n-1,n}}(s\cdot\Delta k)\cdot\Delta k}, \\ x1_{n-1,n}(s) &= x_{n-1,n}(s)\cos(\varphi_s), \\ x2_{n-1,n}(s) &= x_{n-1,n}(s)\sin(\varphi_s), \\ y_{n-1,n}(s) &= \sqrt{\Phi_{S_{n-1,n}}(s\cdot\Delta k)\cdot\Delta k}, \\ y1_{n-1,n}(s) &= y_{n-1,n}(s)\cos(\varphi_s), \\ y2_{n-1,n}(s) &= y_{n-1,n}(s)\sin(\varphi_s). \end{aligned} \tag{19}$$

Then, the first item of formula (17) can be rewritten as follows:

$$\begin{aligned} &\chi_{n-1,n}(m\cdot\Delta x) \\ &= \sum_{s=0}^{N-1}\sqrt{\Phi_{\chi_{n-1,n}}(s\cdot\Delta k)\cdot\Delta k}\cdot\cos\left(\frac{2\pi sm}{N}+\varphi_s\right) \\ &= \sum_{s=0}^{N-1}x_{n-1,n}(s)\cdot\left(\cos\left(\frac{2\pi sm}{N}\right)\cos(\varphi_s)\right. \\ &\qquad\left.-\sin\left(\frac{2\pi sm}{N}\right)\sin(\varphi_s)\right) \\ &= \sum_{s=0}^{N-1}x1_{n-1,n}(s)\cos\left(\frac{2\pi sm}{N}\right) \\ &\quad - x2_{n-1,n}(s)\sin\left(\frac{2\pi sm}{N}\right) \\ &= \frac{1}{2}\sum_{s=0}^{N-1}\left\{x1_{n-1,n}(s)\left(\exp\left(\frac{j2\pi sm}{N}\right)+\exp\left(-\frac{j2\pi sm}{N}\right)\right)\right. \\ &\qquad + jx2_{n-1,n}(s)\left(\exp\left(\frac{j2\pi sm}{N}\right)\right. \\ &\qquad\left.\left.-\exp\left(-\frac{j2\pi sm}{N}\right)\right)\right\}. \end{aligned} \tag{20}$$

If we set $W_N = \exp(-j2\pi/N)$, then the previous formula can sequentially be simplified to the following form:

$$\begin{aligned} \chi_{n-1,n}(m\cdot\Delta x) &= \frac{1}{2}\sum_{s=0}^{N-1}\left\{x1_{n-1,n}(s)\left(W_N^{-sm}+W_N^{sm}\right)\right. \\ &\qquad\left.+jx2_{n-1,n}(s)\left(W_N^{-sm}-W_N^{sm}\right)\right\} \\ &= \frac{1}{2}\left\{\mathrm{DFT}\left(x1_{n-1,n}\right)+N\cdot\mathrm{IDFT}\left(x1_{n-1,n}\right)\right\} \\ &\quad+\frac{j}{2}\left\{N\cdot\mathrm{IDFT}\left(x2_{n-1,n}\right)-\mathrm{DFT}\left(x2_{n-1,n}\right)\right\}. \end{aligned} \tag{21}$$

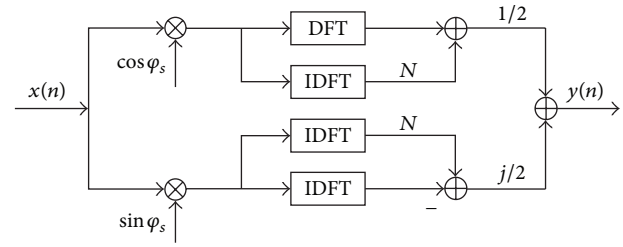

Figure 1: The realization of the phase screen method using DFT.

The fast algorithm for phase fluctuation can be obtained through the same method:

$$\begin{aligned} S_{n-1,n}(m\cdot\Delta x) &= \frac{1}{2}\left\{\mathrm{DFT}\left(y1_{n-1,n}\right)+N\cdot\mathrm{IDFT}\left(y1_{n-1,n}\right)\right\} \\ &\quad+\frac{j}{2}\left\{N\cdot\mathrm{IDFT}\left(y2_{n-1,n}\right)-\mathrm{DFT}\left(y2_{n-1,n}\right)\right\}. \end{aligned} \tag{22}$$

We simplify the random amplitude and phase fluctuations formulas, expressing them using DFT and IDFT algorithm, respectively, which significantly improve the computational efficiency.

The multiphase screen simulation algorithm is shown as following steps.

Step 1. Substitute the corresponding parameters in the upper section into formula (12) to obtain the power spectrum of the electron concentration fluctuations.

Step 2. The obtained value of the electron concentration fluctuations would be substituted into formula (16) to get the power spectrum of the complex phase deviation.

Step 3. According to the formula (8a) and (8b), we can obtain the power spectrum of amplitude and phase fluctuations.

Step 4. Use the relation of (17) to obtain the amplitude and phase fluctuation which we can regard as a complex phase $\varphi_{n-1,n}$.

Step 5. Use formula (13) to associate the phase deviations between different phase screens with each other.

The diagram of the fast algorithm in the fourth step using DFT to implement its function is shown in Figure 1.

In Figure 1, when the input is the power spectrum of the amplitude fluctuation in the phase screen, the corresponding output is the fluctuation of the amplitude; when the input is the power spectrum of the phase fluctuation in the phase screen, the corresponding output is the fluctuation of the phase.

2.3. Simulations and Experimental Results of Multiphase Screen Method. When we use the multiphase screen method to simulate the ionospheric wave propagation problem, some values of certain parameters in the simulation process are set to be known, and the simulation results of the phase

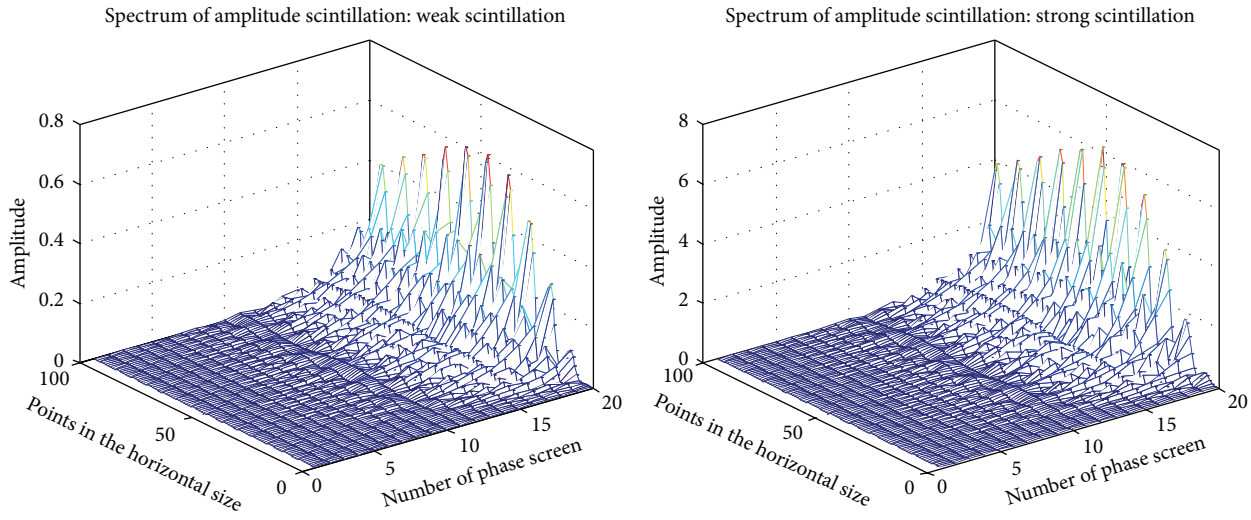

Figure 2: The power spectrum of amplitude scintillation.

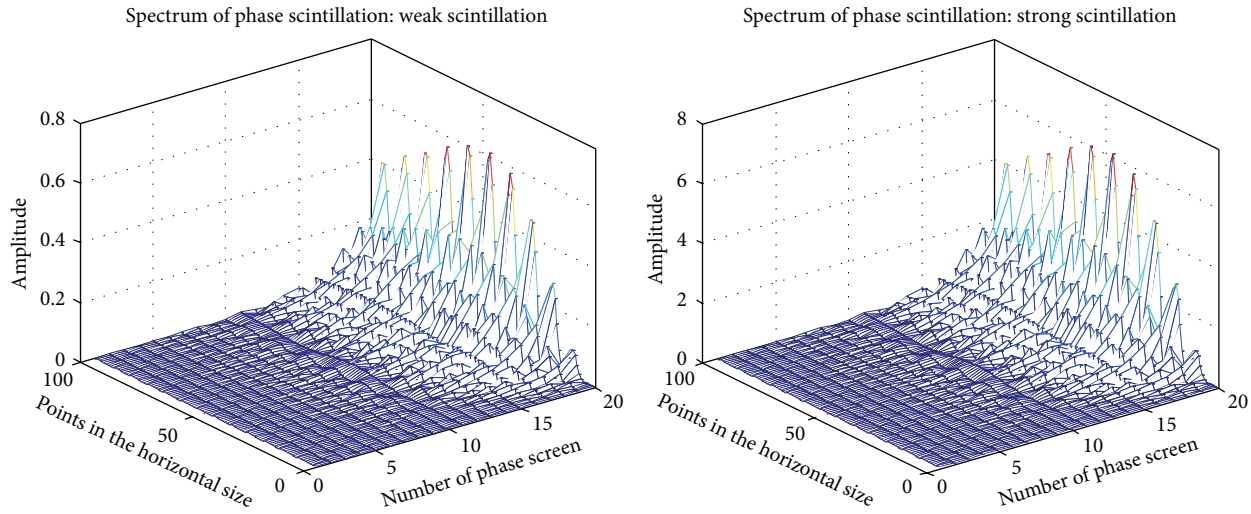

Figure 3: The power spectrum of phase scintillation.

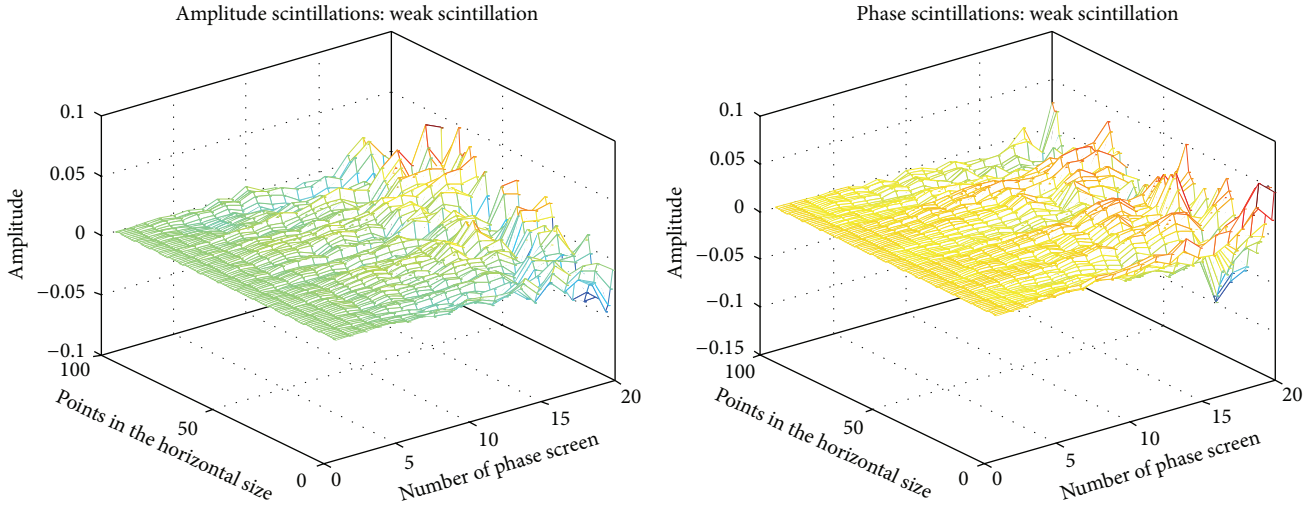

Figure 4: Amplitude and phase changes in phase screens in weak scintillation.

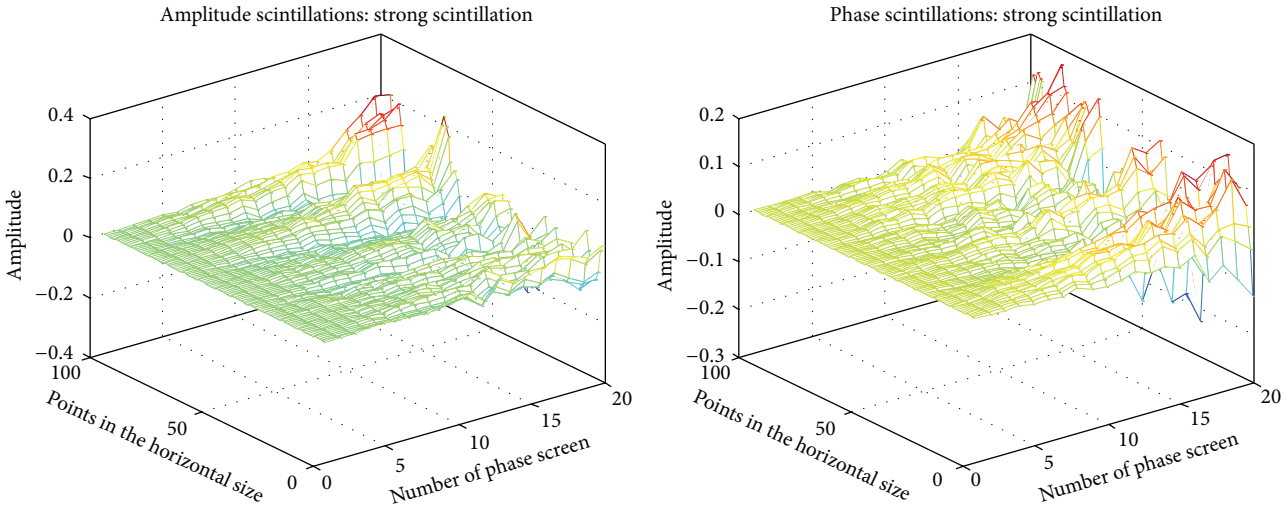

FIGURE 5: Amplitude and phase changes in phase screens in strong scintillation.

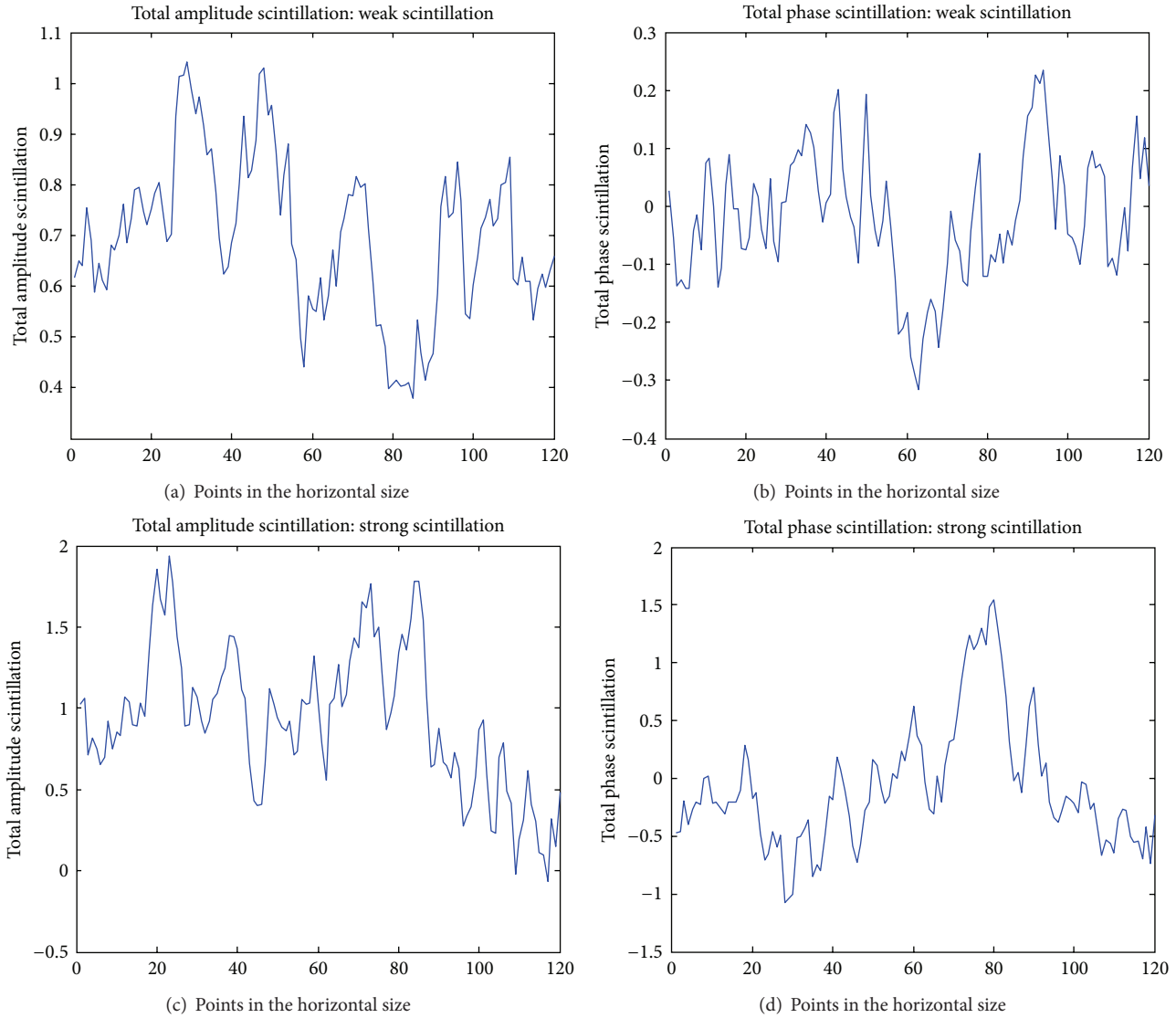

(a) Points in the horizontal size

(b) Points in the horizontal size

(c) Points in the horizontal size

(d) Points in the horizontal size

FIGURE 6: The overall amplitude and phase scintillation.

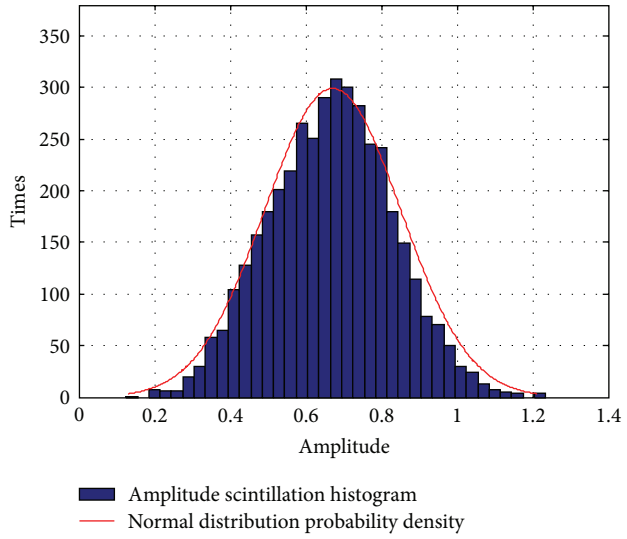

FIGURE 7: The histogram of amplitude scintillation and fitting results of normal distribution.

screen method can be derived by using such values as initial condition. These parameters include the radar operating frequency $f = 4$ MHz; analog of the background medium: $Z_\Gamma = 20$ km (corresponding to the ionization layer region thickness when $f = 4$ MHz), $Z_L = 90$ km is the distance from the ground to the bottom of the ionosphere. To ensure the sampling rate and numerical calculations convenient under the simulated conditions of phase screen [2, 3], take a typical case. We place 20 phase screens in the ionsphere, that is, $M = 20$, and thus, the relative thickness of the screen $\Delta z = Z_\Gamma/M$; in the ionospheric 2D random field, electron concentration's relative fluctuation $N_f(r)$ was characterized by the Shkarofsky spectrum, in which the internal dimensions of the irregularities take typical value $r_0 = 15$ m, and the external dimensions take $L_0 = 2.5$ km. The spectral index of the ionospheric irregularities (i.e., the exponent) p takes the value 4 or 5 and 4 herein; the horizontal dimension of each phase screen is $L_h = 122880$ m and is divided into $N = 4096$ copies; the fluctuation of the electron concentration take $\sigma_{Nf} = 10^{-3}$ in the strong situation and $\sigma_{Nf} = 10^{-4}$ in the weak one. σ_{Nf} is standard deviation, indicating the strength of the turbulence of ionosphere.

2.3.1. The Power Spectrum of the Amplitude and Phase Scintillation. The power spectrum of the amplitude and phase fluctuations by complex phase screen's power spectrum using (8a) and (8b) are shown in Figures 2 and 3 in the conditions of weak and strong fluctuation.

2.3.2. The Scintillations of Amplitude and Phase. According to the derivation of the foregoing formula (21) and (22), we can obtain the amplitude and phase fluctuation value in each phase screen using the FFT algorithm, and the values are shown in Figures 4 and 5.

From Figures 4 and 5, we can see that the fluctuation of amplitude and phase is gradually increasing from the 1st to 20th phase screens because the electron concentration increases with the rising of height and the corresponding fluctuation also increases. The fluctuation of amplitude and phase at some point reaches the maximum within the same phase screen, which embodies the randomness of the ionospheric undulation in the same height. Meanwhile, in the condition of intensity fluctuation, the fluctuation of the signal amplitude and phase increases more significantly than that in the case of weak scintillation.

2.3.3. The Total Scintillation of the Amplitude and Phase. The scintillation of the amplitude and phase within each phase screen at a corresponding point is superimposed to get the overall scintillation caused by the signal going through the ionospheric region, as shown in Figure 6.

Figures 6(a) and 6(b) show the total amplitude and phase scintillation value generated by the signal going through the ionosphere in the conditions of weak scintillation, in which the fluctuation of the signal amplitude ranges from about 0.4 to 1.1 and basically concentrates on the 0.7 or 0.8, and the fluctuation of the phase basically centre on 0 and maximizes to 0.4 radians. Figures 6(c) and 6(d) show the total amplitude and phase fluctuation values produced by the signal going through the ionosphere in the conditions of intensity fluctuation, in which the fluctuation is significant. The amplitude's fluctuation sets 0.4 as the center basically, while the maximum fluctuation value can reach about 1.8. The fluctuations of phase increased more than that in the case of weak fluctuation and the maximal fluctuation, can reach up to more than 1 rad.

2.4. The Statistical Properties of the Magnitude and Phase Scintillation

2.4.1. The Probability Distribution of the Amplitude Scintillation. Figure 7 shows the histogram of the amplitude value frequency after the signal going through ionosphere in the weak scintillation conditions using multiphase screen method, and the probability density function curve of Gaussian distribution with the parameters (0.7, 0.17). As we can see from Figure 7, the amplitude of the signal in the case of weak scintillation approximates the Gaussian distribution. Figure 8(a) with the q-q figure is to test whether experimental data and the given parameters' normal distribution come from the same kind of distribution. If the data in the q-q figure approximately has a linear relationship, we can hold the opinion that the data is subjected to the Gaussian distribution. Conversely, if the data point bends seriously, they are not the same kind of distribution. From Figure 8(a), we can know that in the weak scintillation case, the fluctuation of the signal amplitude approximately obeys $\mu = 0.7$, $\sigma_2 = 0.17$ Gaussian distribution. Figure 8(b) is the normal probability picture (NPP) to test normal distribution. Each value in the data corresponds to a "+" sign, whose location is decided jointly by the point value and the empirical probability, and solid lines connect the 25% and 75% percentile and represent the robustness of the linear fit. The ratio of y axis in the normal probability plot is uneven, and it indicates the probability

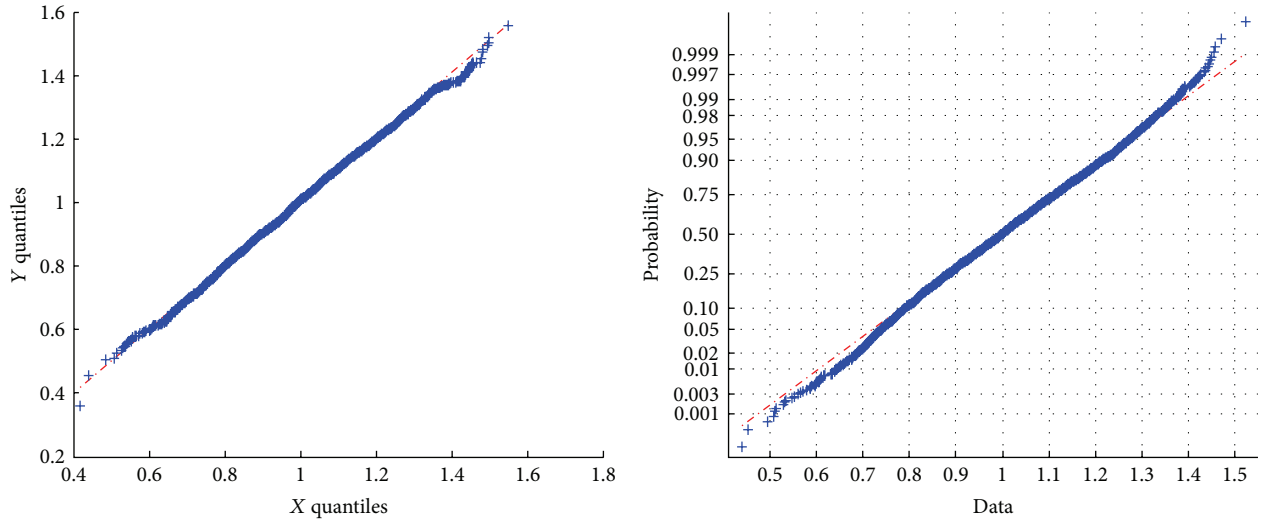

(a) Inspection in the q-q figure

(b) Inspection in the NNP

Figure 8: The inspection of amplitude distribution.

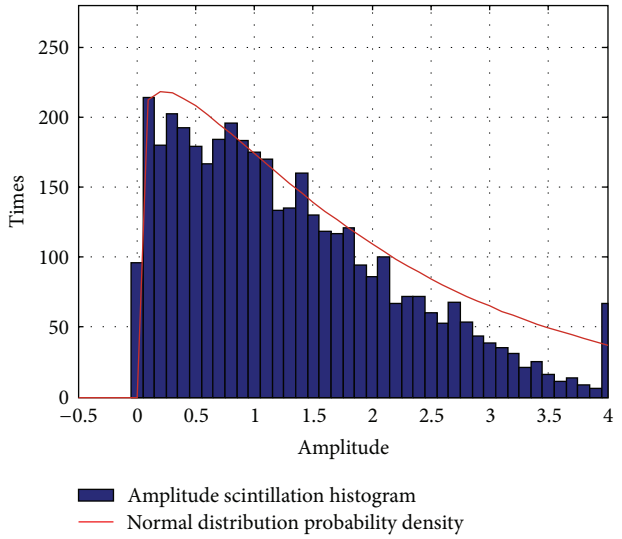

Figure 9: The histogram of amplitude scintillation and the fitting results of the Weibull distribution.

value between 0~1. If all the data points fall near the line, we can regard that the data follows a normal distribution. The curve of Figure 8(b) is approximately linear because it can be considered that the fluctuation of the signal amplitude in the weak undulation conditions approximately obeys Gaussian distribution. At a significance level of 0.05, with the Kolmogorov-Smirnov test method [7], we validate further that in the case of weak ionospheric scintillation, phase screen method simulation shows that amplitude fluctuations obey Gaussian distribution.

Figure 9 shows that in a strong scintillation condition frequency histogram of the amplitude. The curve obeys the Weibull distribution with parameters $a = b = 1.5$. As it can be seen in Figure 9, the signal amplitude can be fitted quite well in the Weibull distribution. In Figure 10, we test fitting degree of signal amplitude fluctuation distribution with Weibull distribution of given parameters in the q-q figure as well with normal probability distribution in the intense fluctuation conditions. As is shown in Figure 10(a), the signal amplitude fluctuation approximately obeys the Weibull distribution. While in Figure 10(b), each amplitude point seriously deviates from the straight line. Therefore, the signal amplitude fluctuation is no longer a Gaussian distribution when it is under an intense condition. At a significance level of 0.05, with the Kolmogorov-Smirnov test method, we validate further that in the case of strong ionospheric scintillation, phase screen method simulation shows that amplitude fluctuations obey the Weibull distribution.

To sum up, the distribution of the signal amplitude's fading is closely linked to the intensity of the fluctuation of the ionosphere. With the intensifying of the ionospheric fluctuation, the fading of the signal amplitude has undergone a transition from a Gaussian distribution to the Weibull distribution.

2.4.2. Phase Scintillation's Probability Distribution. In the case of weak scintillation, the frequency histogram of the signal phase distribution and normal distribution curve with parameters $\mu = 0$, $\sigma^2 = 0.2$ is shown in Figure 11. From the figure, we can see that under the conditions of weak scintillation, the signal's maximum of the phase deviation is about 0.6 radians, and the signal is also in good agreement with normal distribution. We get the conclusion that in weak scintillation case, the random phase deviation of the signal obeys normal distribution with parameters $\mu = 0$, $\sigma^2 = 0.2$. At a significance level of 0.05, with the Kolmogorov-Smirnov test method, we validate further that in the case of weak ionospheric scintillation, phase screen method simulation shows that phase fluctuations obey Gaussian distribution.

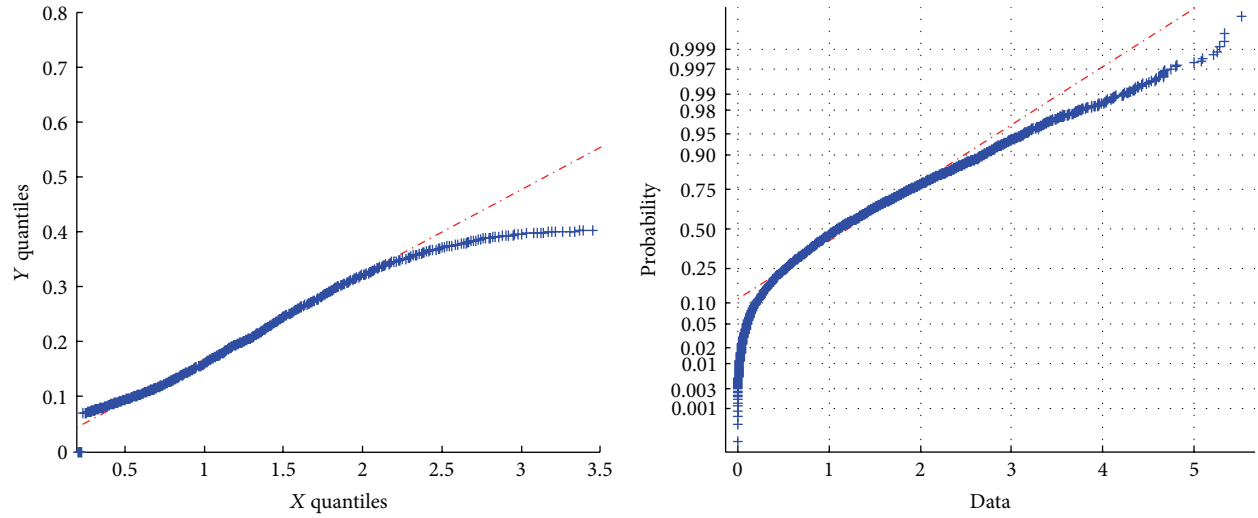

(a) Inspection of the q-q figure

(b) Inspection in the NNP

FIGURE 10: The inspection of amplitude distribution.

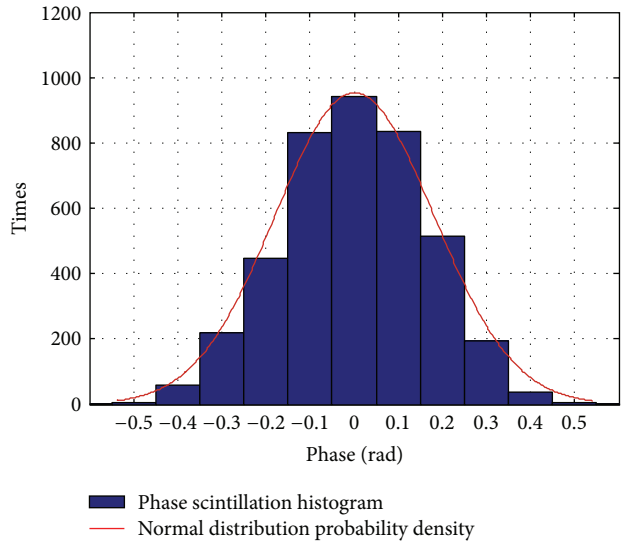

FIGURE 11: The histogram of phase scintillation and the fitting results of normal distribution.

Figure 12(a) is to verify the fitting degree of Gaussian distribution of corresponding parameters with the phase distribution of the signal using the q-q figure. In q-q figure, the phase approximately shows linearly, and therefore, we consider that the phase scintillation belongs to the Gaussian distribution.

Figure 13 is the frequency histogram of the signal phase distribution, in the case of the strong scintillation, and the normal distribution curve with parameters $\mu = 0$, $\sigma^2 = 0.7$. The inspection of phase scintillation is shown in Figure 14. We can see from Figure 13 that the maximum phase deviation of the signal reaches about 2 radians, but the histogram of signal phase deviation gets good fit of the normal distribution curve with the corresponding parameters (0, 0.7). Figure 14(a) is to examine fitness of the phase distribution of the signal and the corresponding parameters of the Gaussian distribution with the q-q figure. It can be seen that the curve in the q-q figure is approximately linear, and therefore, we can consider that the phase undulation obeys Gaussian distribution. Figure 14(b) is to examine fitness of the phase distribution of the signal and the Gaussian distribution with corresponding parameters with normal probability plot. Seen from the figure, the curve in the normal probability pot is approximately linear, and therefore we can consider signal phase undulation obeys Gaussian distribution in case of strong scintillation. At a significance level of 0.05, with the Kolmogorov-Smirnov test method, we validate further that in the case of strong ionospheric scintillation, phase screen method simulation shows that phase fluctuations also obey Gaussian distribution.

The conclusion can be drawn by the phase screen method that in weak scintillation case, the signal amplitude and phase scintillation are relatively small, while its amplitude and phase fit the Gaussian distribution. In the case of strong scintillation, the Weibull distribution is a much better choice to characterize the scintillation of the signal amplitude. Phase scintillation still approximates the Gaussian distribution, while the deviation has increased than that of the weak case.

2.4.3. The Comparison with Measured Data. The amplitude and phase distribution characteristics can be calculated by statistics analysis based on the measured data of ionospheric Es layer clutter echo, which can be used as the basis to test whether the simulation results of the phase screen method can reflect real ionospheric characteristics.

The frequency distribution histogram of an amplitude of 6 batches of real ionospheric echo is shown in Figure 15. The abscissa is the normalized amplitude of the ionospheric echo, and the ordinate is the occurrence frequency of the corresponding amplitude. Red curve is a Weibull distributions with certain parameters, from which we can see

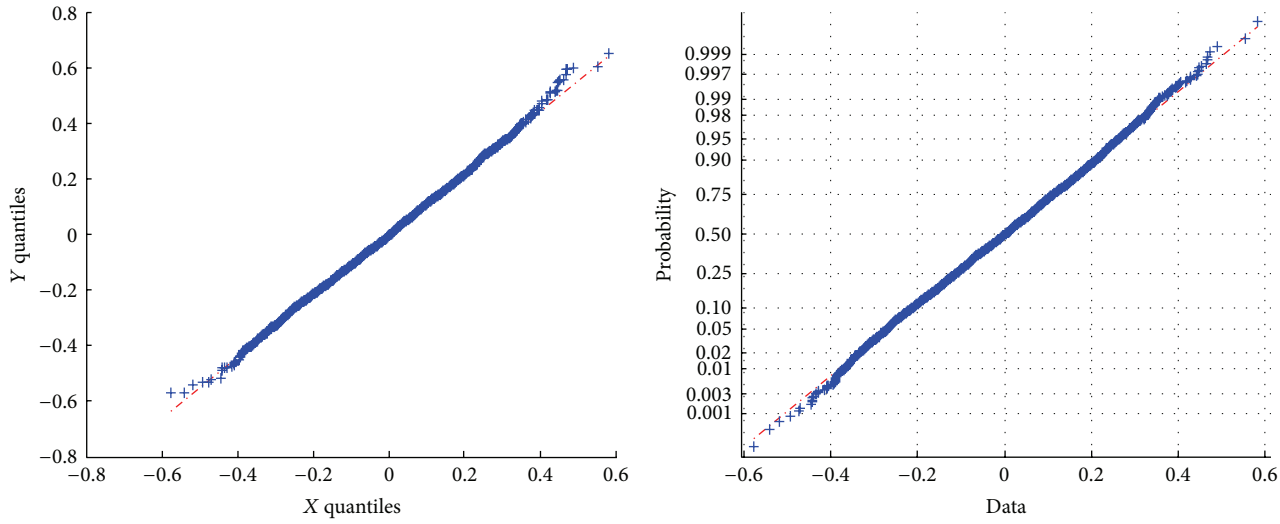

(a) Inspection of the q-q figure

(b) Inspection in the NNP

Figure 12: The inspection of phase distribution.

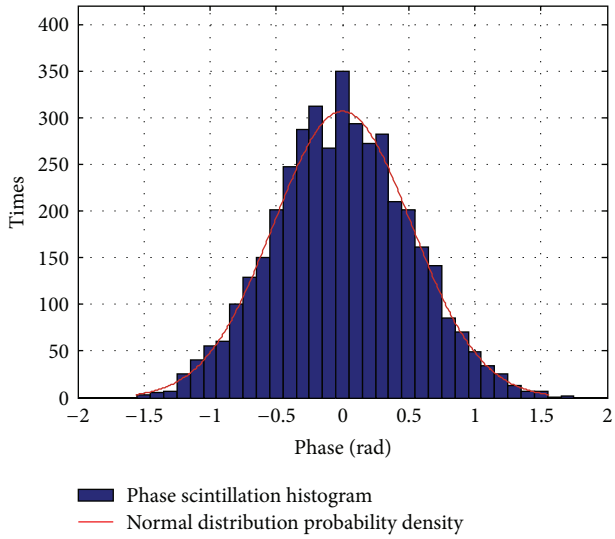

Figure 13: The histogram of phase scintillation and the fitting results of normal distribution.

that the amplitude scintillation approximately obeys the Weibull distribution and that amplitude distribution of the signal derived from our simulation in the strong scintillation basically coincides with the previous one. At a significance level of 0.05, we further verify the validity of the conclusion that the amplitude fluctuations of measured data obey the Weibull distribution by using the Kolmogorov-Smirnov test method.

We simulate ionospheric echo by phase screen method, obtain the phase of the simulated echo signal, and then process statistical analysis to finally get the phase distribution of the ionosphere echo signal. Then, we do the same statistical analysis to the corresponding measured ionospheric echo signal to obtain its phase fluctuation frequency distribution histogram. The phase distribution histogram of the simulated echo signal is shown in Figure 16. We can get the phase distribution of the actual ionospheric echo after we analyze the measured data, which is shown in Figure 17.

As can be seen from Figure 16, due to the ionosphere, the phase of the echo signal approximately subjects to uniform distribution. Figure 17 shows the histogram statistical analysis of a phase of 6 batches of measured data. As can be seen from Figure 17, ionospheric echo signal's phase also approximately obeys uniform distribution, which is consistent with the conclusions of theoretical simulation. In order to confirm that the phase screen simulation results and the actual data come from the same distribution, we test six sets of data available with the q-q figure. Figure 18 shows the results of a set of data with the q-q figure.

As can be seen from Figure 18, ionospheric echoes' phase distribution derived from phase screen method is able to fit the actual ionospheric echo data, that is, the models created by the phase screen method can preferably simulate the echoes' phase. At a significance level of 0.05, we further verify the validity of the conclusion that the echo's phases of measured data obey uniform distribution by using the Kolmogorov-Smirnov test method. To sum up, in strong scintillation condition, the scintillation of amplitude and phase by simulation is close to the statistical results of actual data and basically characterize the impact ionospheric irregularities on high-frequency radio waves.

3. Ionospheric Es Layer Clutter Model Based on Multiphase Screen Method

3.1. The Proposition of Ionospheric Es Layer Clutter Model. Es layer is an ionization cloud with a variety of different shapes that appear in the height of the E layer, and its electronic peak concentrations are often many times higher than the concentration of the E layer around. Es layer appears in

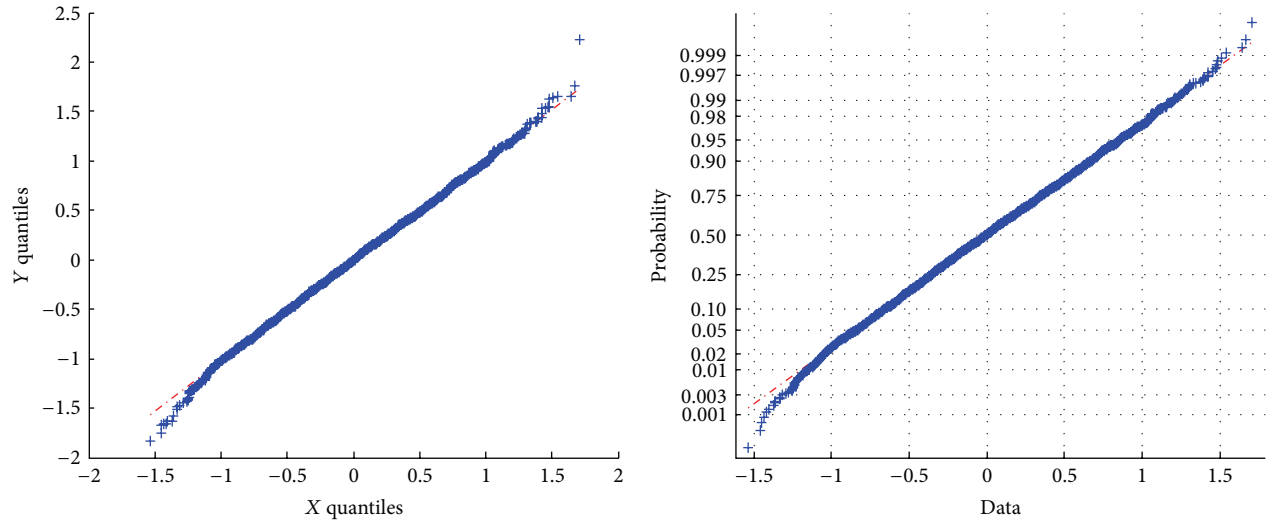

(a) Inspection of the q-q figure

(b) Inspection in the NNP

Figure 14: The inspection of phase distribution.

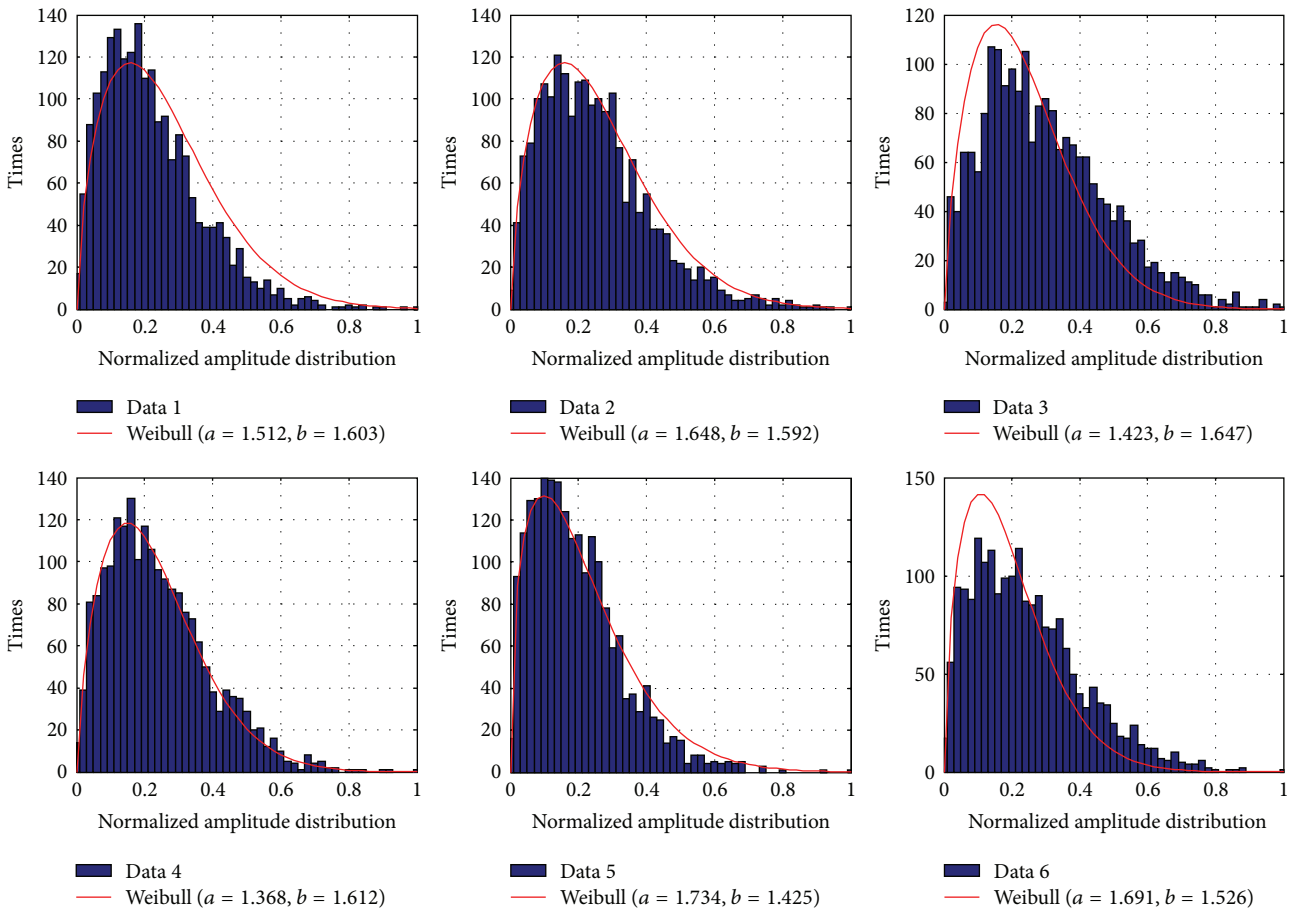

Figure 15: Actual measured ionospheric echo amplitude histogram.

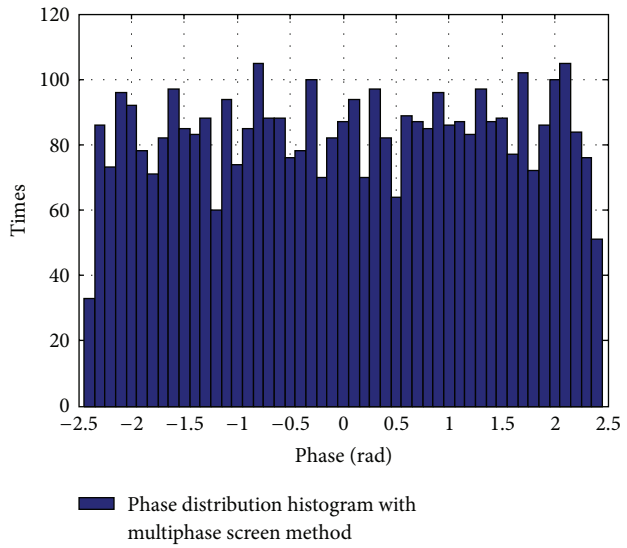

Figure 16: The phase distribution of ionospheric echo by phase screen method simulation.

the corresponding state of strong scintillation of ionosphere. According to the previous study of the propagation characteristics in the ionospheric Es layer, under strong scintillation conditions, we can conclude the signal amplitude scintillation probability distribution of radio signals that through the ionosphere can use the Weibull distribution to overfit, and phase scintillation probability distribution approximates to a Gaussian distribution. Using the results obtained by the multiphase screen method, taking into account of the variation in the height of the ionospheric reflection wave reflection points, we give a new reflected wave model of the ionosphere Es layer.

For HF surface wave radar, the difference frequency signal of uniform motion target's echo after passing mixer is

$$s(t) = A \cdot \sum_{n=0}^{N-1} e^{j\cdot 2\tau\cdot(f_0\tau-(a\tau^2/2)+a\tau(t-nT_s))}, \tag{23}$$

where A represents echo amplitude, $\tau = 2(R_0 + \nu t)/c$ represents the echo delay, R_0 is the initial distance of the target distance to radar, ν shows radial velocity of the target relative to the radar, a is the chirp rate, and T_s is the sweep cycle.

In contrast, the ionospheric Es layer clutter echo is more complex. Three main aspects need to be considered: there is a random amplitude fluctuation in clutter echoes' difference frequency signal of ionospheric Es layer; there is a random phase fluctuation in clutter echoes' difference frequency signal of ionospheric Es layer; the echoes' height of reflection point in ionospheric Es layer clutter may randomly change. When waves vertically incident to the ionosphere, refractive index in each height under the reflecting surface will generate a Doppler frequency shift as time changes, and the movement of the reflecting surface will also produce Doppler shift.

According to previous theoretical analysis, simulation data analysis, and the conclusion of the actual data analysis, we establish a new echo model as follows.

Step 1. In the difference frequency signal of the standard uniform motion target, we superimpose on a random fluctuation amplitude. The distribution of the random fluctuations obeys the Weibull distribution.

Step 2. In the difference frequency signal of the standard uniform motion target, we superimpose on a random fluctuation phase. The distribution of the random fluctuations obeys Gaussian distribution.

Step 3. The height of ionospheric echo reflection point is a random variable. We can handle this change by dividing the whole coherent cycle sweep cycle M into N portions. In each section, the target velocity corresponding to a single sweep cycle of ionospheric echoes (i.e., the height of the ionospheric reflection point) is fixed, and the target moving speed is different in the different sweep cycle of ionospheric echoes. All of the M/N targets' speed corresponding to theionospheric echoes within the M/N sweep cycles obey Gaussian random distribution which takes a fixed speed as the mean value. The corresponding N fixed speed uniformly distributes in $(-\nu, \nu)$, typically $\nu = 10$ m/s.

According to the ionospheric echo model established previously, the difference frequency signal of the Es layer ionospheric clutter echoes after mixing is given by the following formula:

$$s(t) = \text{Amplitude}(t) \cdot A \cdot \sum_{n=0}^{N-1} e^{j\cdot(2\pi\cdot(f_0\tau-(a\tau^2/2)+a\tau(t-nT_s))+\text{Phase}(t))}, \tag{24}$$

where Amplitude(t) represents the amplitude of the Weibull random fluctuations, Phase(t) represents the Gaussian random fluctuations in the phase, ν presents ionospheric echoes variation in the height of the reflection point, and R_0 corresponds to Es layer height in delay characterization $\tau = 2(R_0 + \nu t)/c$.

3.2. The Comparison of Simulating Ionospheric Es Layer Clutter and the Actual Ionospheric Es Layer Clutter. The range of ionospheric Es layer clutter of high-frequency ground wave radar is generally from 100 km to 200 km, and to reduce sea clutter's impact on the accuracy of statistical characteristics analysis of the ionosphere clutter, we use a method based on eigenvalue decomposition to suppress the sea clutter composition in the time domain signal [8] and then do the statistical analysis of remaining ionospheric Es layer clutter. According to the model of ionosphere Es layer built in the last section, the simulation can produce the ionospheres' Es layer clutter after selecting the height value corresponds to the Es layer. At this time, the stochastic amplitudes obey the Weibull distribution with the parameters of (7, 2.8), and the phase of stochastic volatility obey Gaussian distribution with the parameters of (0, 0.4), wherein the unit of phase distribution's parameter 0.4 is radians. Figure 19(a) shows the spectrum of simulating ionospheric Es layer clutter corresponding to the range gate at the reflection height of Es layer. For

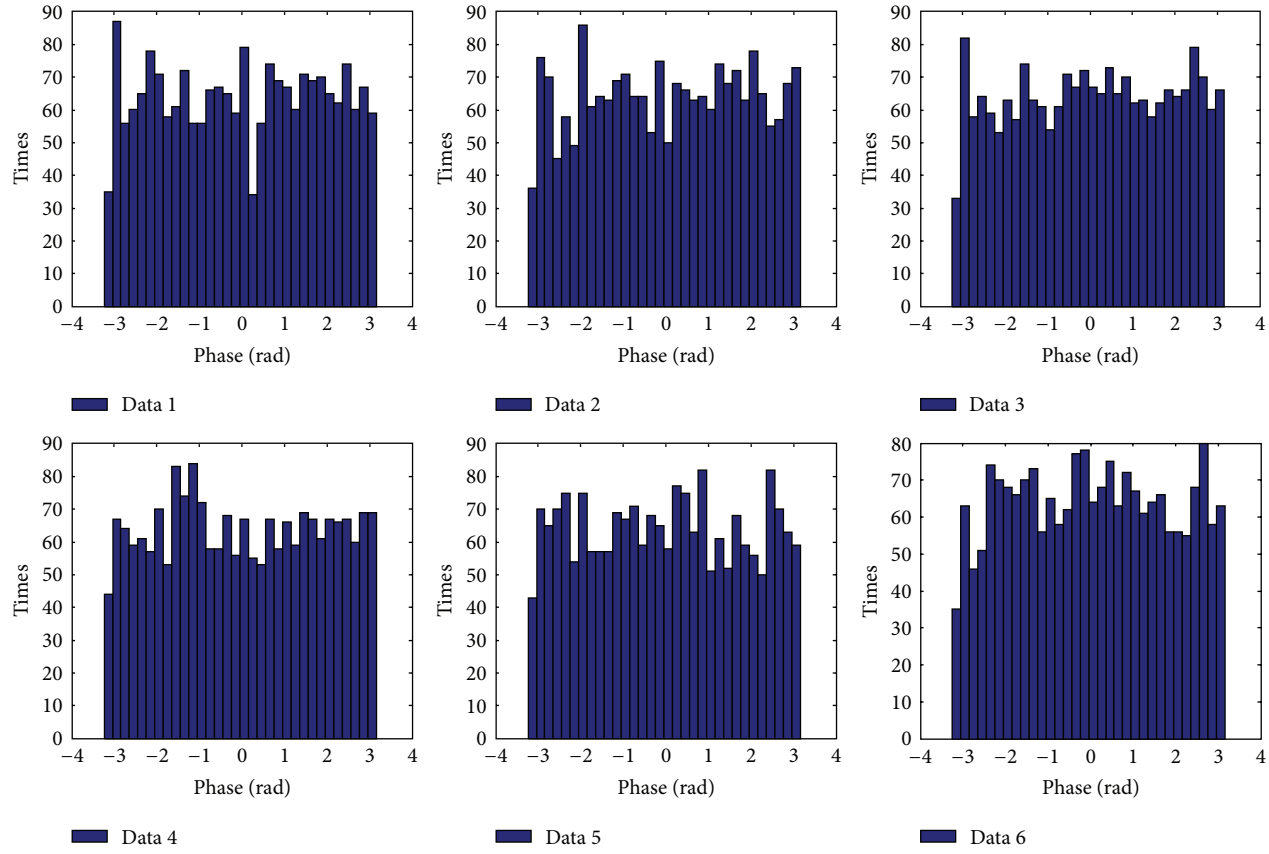

Figure 17: The phase distribution of the actual ionospheric echo.

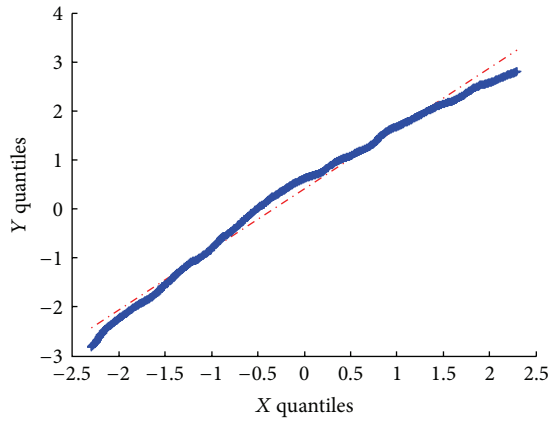

Figure 18: The examination of the echo phase distribution.

the comparison, Figure 19(b) shows the spectrum of actual ionospheric Es layer clutter corresponding to the range gate at the height of Es layer.

From the comparison of Figures 19(a) and 19(b), we can intuitively see that the spectrums of simulating and actual Es layer ionospheric clutter are very similar. The centered section of the spectrum of the simulating Es layer ionospheric clutter is obviously raised, which is in accordance with the actual one. From Figure 19(a), the centered raised section covers the range of −0.25 Hz~0.25 Hz, which is exactly the range corresponding to the ship targets detected by HF surface wave radar. The amplitudes of the centered raised section are nearly 30 dB higher than the amplitudes of neighbouring sections which do not include Es layer clutter. From Figure 19(b), we can see the same phenomenon; the target and Bragg crest are both submerged by the ionospheric Es layer clutter.

From the comparison and analysis of simulating and actual clutter echoes, we can see that the proposed model can represent the actual Es layer ionospheric clutter well.

4. The Ionospheric Es Layer Clutter Suppression Based the JDL Algorithm

Space-time adaptive processing (STAP) is a kind of low complexity and effective way for using training samples to suppress clutter, having become an important direction of research scholars from various countries and has been used in airborne radar [9–15]. Similar to ground clutter, there are certain orientation-Doppler frequency characteristics in high-frequency surface wave radar ionospheric clutter; so, using STAP to suppress ionospheric clutter becomes possible. The traditional fully space-time adaptive algorithm has a large number of degrees of freedom. It is impossible for high-frequency surface wave radar to have enough secondary data samples to estimate the covariance matrix, and

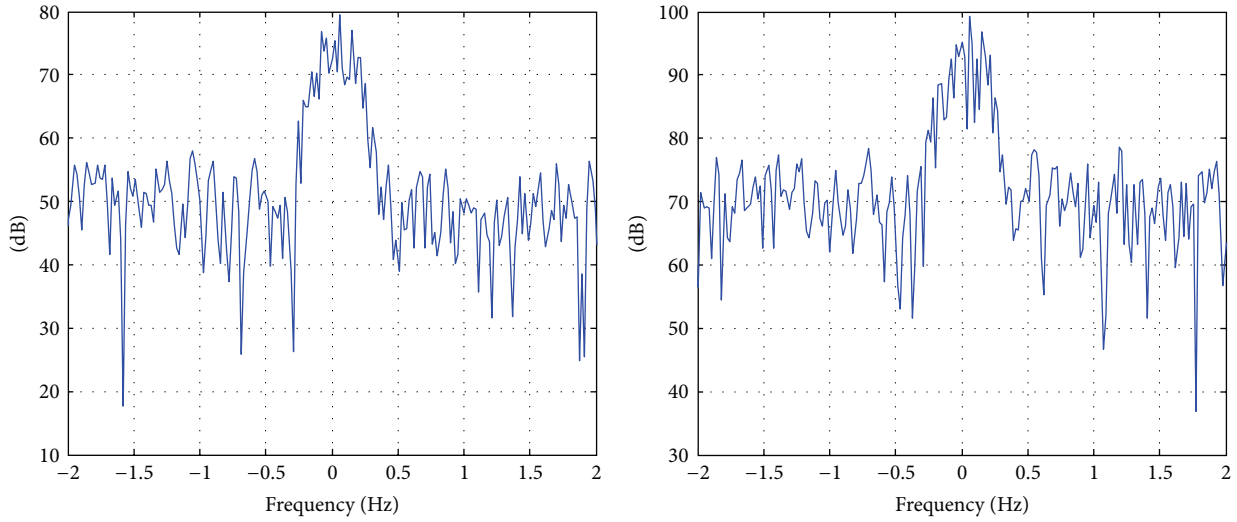

(a) Clutter spectrum of simulating

(b) Clutter spectrum of actual

Figure 19: Spectrums of simulating and actual Es layer clutter.

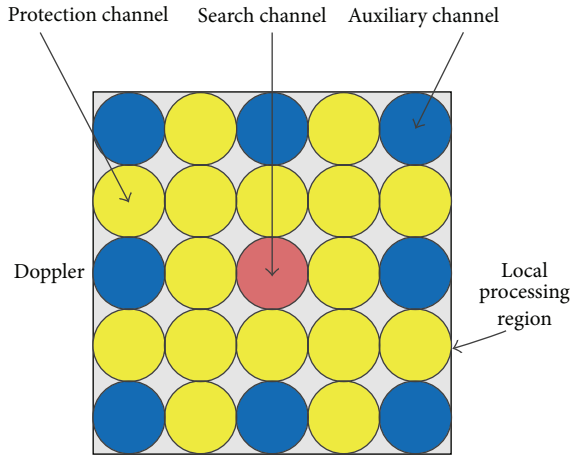

Figure 20: JDL schematic diagram.

the computation load is too large. Therefore, in this section we inject an ideal point target to the simulated ionospheric clutter data and measured ionospheric clutter data, majoring in a kind of dimension reduced STAP algorithm and JDL's ability to suppress the ionospheric clutter and find the target.

4.1. Joint Domain Localized (JDL) Algorithm Principle. Space-time adaptive processing is using the training samples close to the range bin to be detected to estimate clutter and noise covariance matrix R, and according to linearly constrained minimum variance criteria (LCMV) to estimate adaptive weights w, and then to weigh the received data to maximize SNR. Covariance matrix is given by

$$R = \frac{1}{K}\sum_{i=1}^{K} X_i \cdot X_i^H, \tag{25}$$

where X_i is a training sample data.

Weight vector can be given by

$$w = \mu R^{-1} v = \mu \left(R^{-1/2}\right)\left(R^{-1/2} v\right), \tag{26}$$

where μ is a complex normalized constant.

The JDL algorithm's mainly take advantage of the transformation vector T to transform the space-time data to the angle-Doppler domain and select a small local area for adaptive processing. It is a kind of dimension reduced algorithm of the STAP processing, solving the lack of training samples and excessive computation load.

S_s and S_t, respectively, are space steering vector and time steering vector. Elements of theirs are the discrete Fourier transform coefficients. Therefore, the inner product of the spatial and temporal steering vector is equivalent to 2-D DFT, and then, the process of transforming the received data from space-time domain to the ith angle bin w_{si}, the jth Doppler bin, we concern can be expressed as

$$\widetilde{X} = \left(S_s\left(w_{si}\right)\right) \otimes \left(S_t\left(w_{tj}\right)\right)^H X. \tag{27}$$

The JDL algorithm transforming matrix can be represented as

$$T = \begin{pmatrix} \left[S_s\left(w_{si}\right) \otimes S_t\left(w_{tj}\right)\right]^T \\ \left[S_s\left(w_{si}\right) \otimes S_t\left(w_{tj+w_k}\right)\right]^T \\ \vdots \\ \left[S_s\left(w_{si}\right) \otimes S_t\left(w_{tj+(q-1)\,w_k}\right)\right]^T \\ \vdots \\ \left[S_s\left(w_{si+(p-1)\,w_n}\right) \otimes S_t\left(w_{tj+(q-1)\,w_k}\right)\right]^T \end{pmatrix}^T, \tag{28}$$

where w_n and w_k, respectively, represent angle and Doppler interval, p represents the number of adjacent angle bins, and

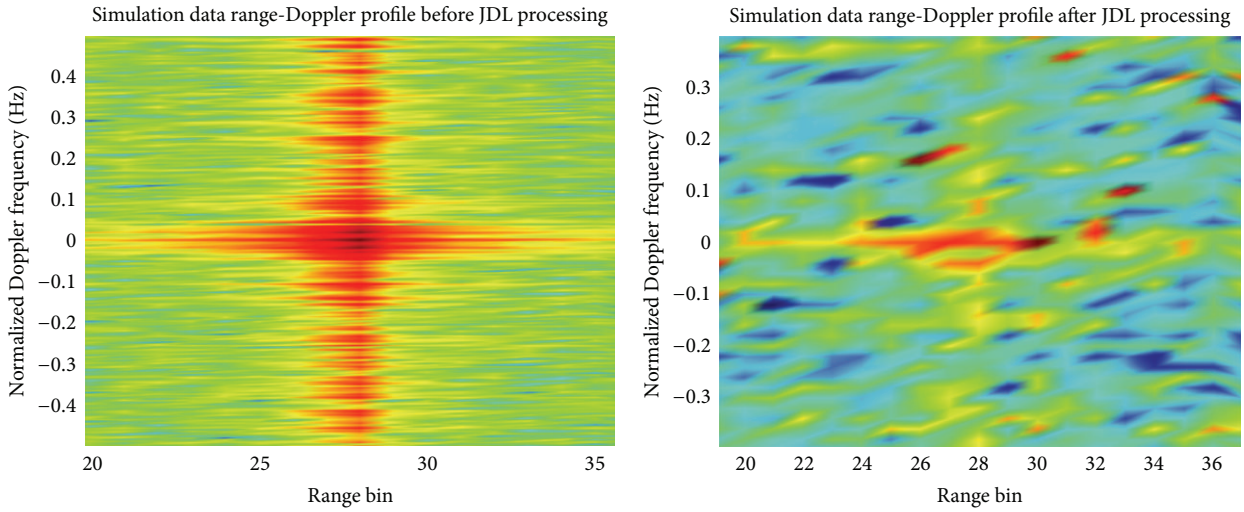

(a) Range-Doppler profile before the JDL algorithm

(b) Range-Doppler profile after the JDL algorithm

Figure 21: Angle-Doppler profile before and after the JDL algorithm.

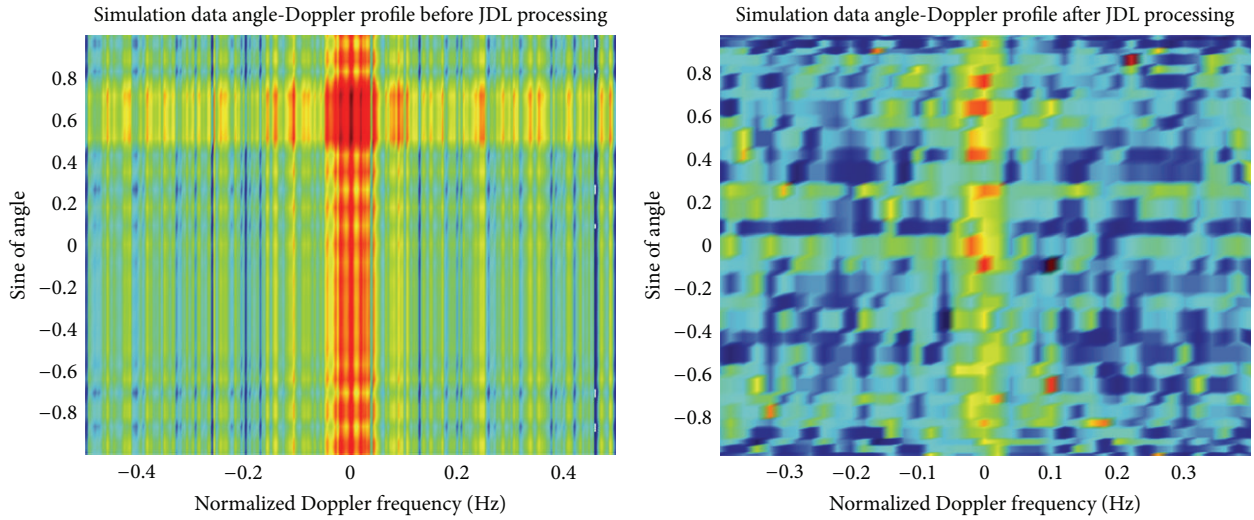

(a) Angle-Doppler profile before the JDL algorithm

(b) Angle-Doppler profile after the JDL algorithm

Figure 22: Angle-Doppler profile before and after the JDL algorithm.

q represents the number of adjacent Doppler bins. Schematic diagram 20 is as follows.

In Figure 20, the red channel is the search channel, the blue channel is the auxiliary channel, and the yellow channel is the protection channel. The selection of a protection channel in angle-Doppler domain may be effective in preventing the spread of the target signal to clutter covariance matrix, affecting the actual detection performance.

When selecting the 3×3 local shown in Figure 20, space -time transformation matrix can be expressed as

$$T = \left[S_t\left(w_{t,j-2}\right); S_t\left(w_{t,j}\right); S_t\left(w_{t,j+2}\right)\right] \otimes \left[S_s\left(w_{s,i-2}\right); S_s\left(w_{s,i}\right); S_s\left(w_{s,i+2}\right)\right]. \quad (29)$$

The transformed space-time steering vector is

$$\widetilde{v} = T^H \cdot v. \quad (30)$$

The receiving data vector is

$$\widetilde{X} = T^H \cdot X. \quad (31)$$

The corresponding adaptive weight vector is

$$\widetilde{w} = \mu \widetilde{R}^{-1} \widetilde{v}. \quad (32)$$

4.2. The JDL Algorithm Performance Analysis Based on Es Layer Cutter Simulation Model. Parameter setting of the simulation data: the carrier frequency $f_c = 4.05$ MHz, the sampling frequency $f_s = 10$ kHz, the bandwidth $B = 20$ kHz,

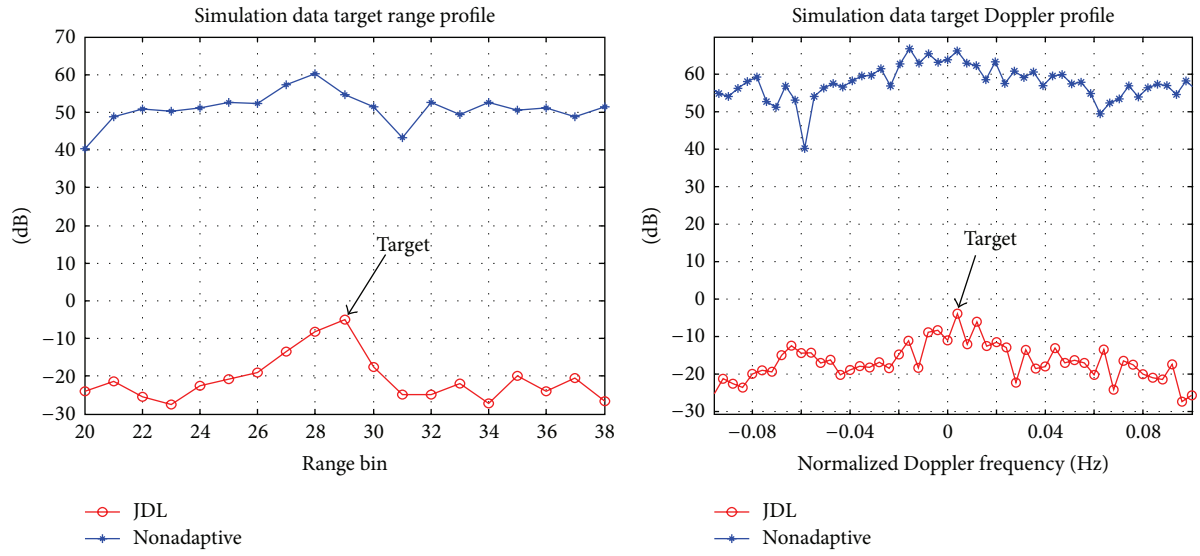

(a) Target range profile before and after the JDL algorithm

(b) Target Doppler profile before and after the JDL algorithm

Figure 23: Target range profile and Doppler profile before and after the JDL algorithm after injecting a target.

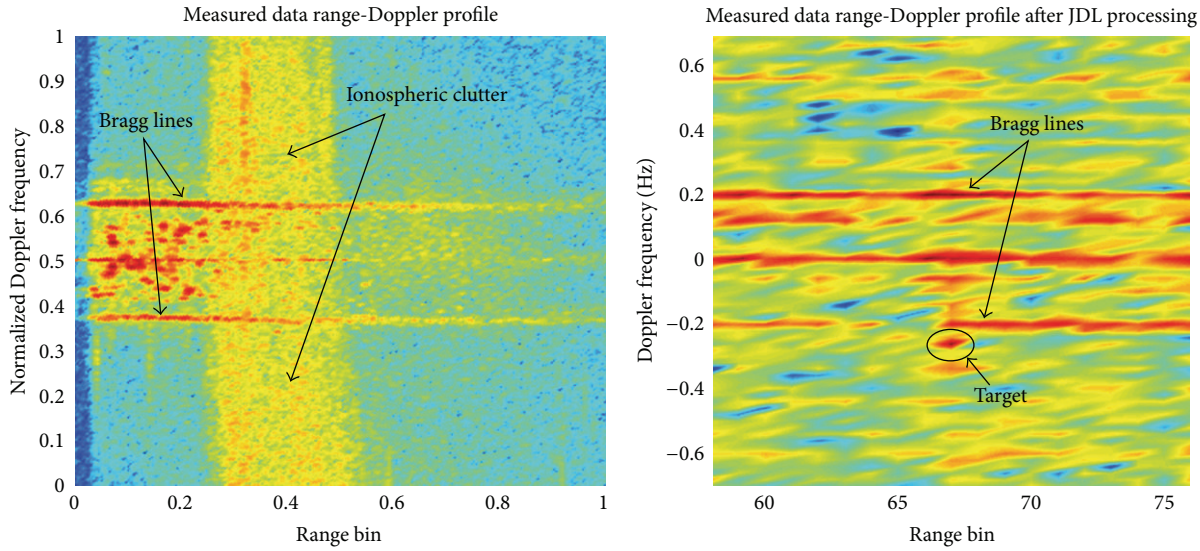

(a) The distance-Doppler profile without JDL algorithm

(b) The range-Doppler profile after JDL algorithm

Figure 24: Range-Doppler profile before and after JDL.

the pulse period is 20ms, the number of array elements $N = 32$, the accumulated pulse numbers $M = 4096$, the angle between the target incident direction and the array normal is 30°, the target normalized Doppler frequency $f_{\_\text{Doppler}} = 0.004$ Hz, target range bin is 29, Es layer height $h = 200$ km, and signal to clutter ratio (SCR) is −10 dB. Based on the established ionospheric Es layer clutter model, when the target is not injected, comparing the range-Doppler profile before and after the JDL algorithm processing, as Figures 21(a) and 21(b) show.

Figures 22(a) and 22(b) compared the angle-Doppler output before and after the JDL algorithm processing when the target is not injected.

From Figures 21 and 22, we can see that the simulated ionospheric clutter exists obvious broadening in range, angle and Doppler profile after conventional processing, while after JDL processing, the clutter is significantly reduced. So, JDL algorithm can achieve good suppression performance for simulated ionospheric clutter. Figures 23(a) and 23(b) show the target range profile and the target Doppler profile before

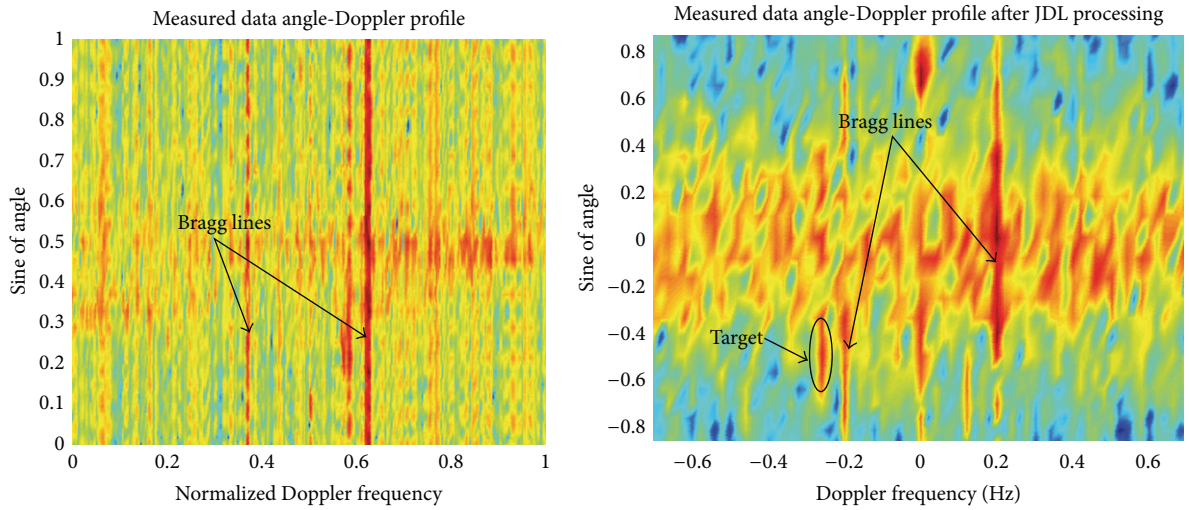

(a) Angle-Doppler profile before JDL algorithm

(b) Angle-Doppler profile after JDL algorithm

Figure 25: Angle-Doppler profile before and after JDL algorithm.

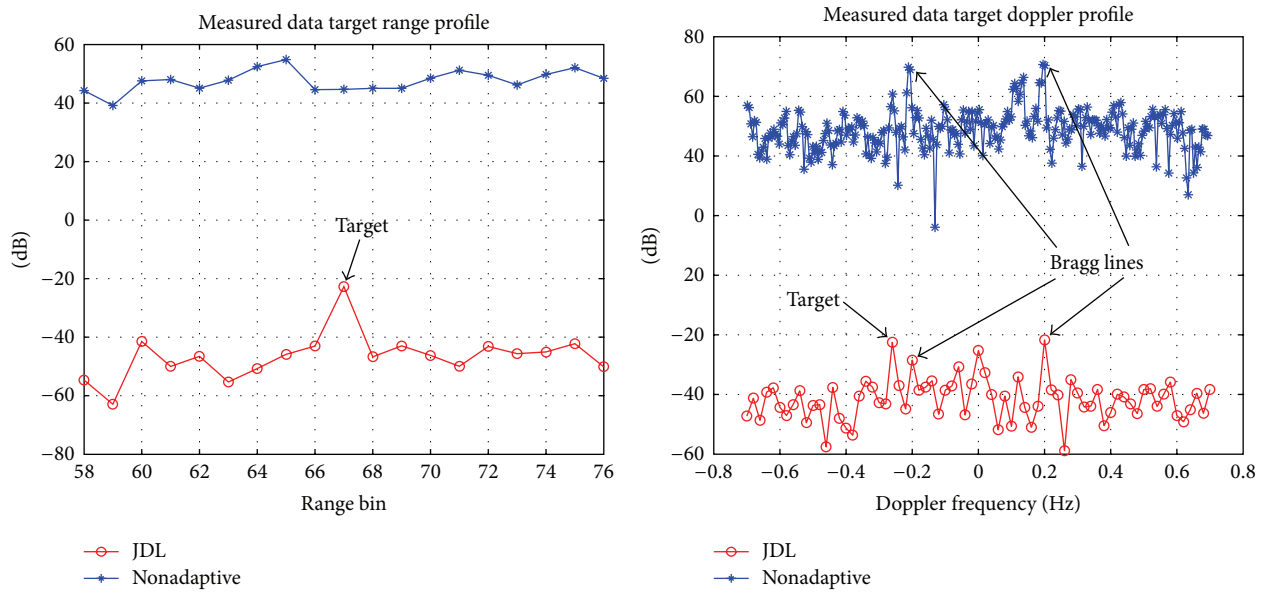

(a) Target range profile before and after JDL algorithm

(b) Target doppler profile before and after JDL algorithm

Figure 26: Target range profile and doppler profile before and after the JDL algorithm after injecting a target.

and after the JDL algorithm processing after injecting an ideal target for simulated ionospheric clutter.

We can see from the simulation results in Figure 23 that SCR is −10dB before JDL processing, and SCR in the range and Doppler dimension is greatly improved after JDL processing. This further illustrates that the JDL algorithm can effectively suppress the ionosphere clutter and detect target submerged by ionospheric clutter.

4.3. Analysis of the JDL Algorithm Performance Based on Measured Data. Parameter settings for the measured data: carrier frequency $f_c = 4.05$ MHz, coherent integration time $T = 184.32$ s, the angle between the target incident direction and the array normal is -30°, target normalized Doppler frequency $f_{\_\text{Doppler}} = -0.26$ Hz, target range bin is 69, and SCR $= -10$ dB. Figure 24(a) shows the range-Doppler profile of a batch of HF ground wave radar data in actual measurement after regular processing. Figure 24(b) is the range-Doppler profile after JDL processing, and the range bin of the injected target is 69.

Figure 25(a) shows the angle-Doppler profile of measured data after regular processing; Figure 25(b) is the angle-Doppler profile after JDL processing. Figures 26(a) and 26(b) show the target range profile and the target Doppler profile

before and after the JDL algorithm processing after injecting an ideal target for measured ionospheric clutter.

We can see, from the JDL processing results of the previously measured data, that the SCR in range and Doppler dimension are greatly improved, further illustrating the effectiveness of the JDL algorithm in suppressing the ionosphere clutter and verifying the reasonableness of the built clutter model.

5. Conclusions

An ionospheric Es layer clutter model based on multiphase screen method with DFT fast implementation was proposed, and then, the Es layer clutter was suppressed by STAP method in this paper. First, the basic principle of the multiphase screen method in the disturbed layered ionosphere was analyzed, and the DFT-based fast algorithm was proposed. Then, we utilized the multiphase screen method to obtain statistical analysis results as well as took into account the height of the reflection points' variation in the ionospheric Es layer to create a new reflecting model in the ionospheric Es layer. We also compared it with the measured data and analysis to verify the reasonableness and correctness of the established clutter model. Finally, based on the ionospheric clutter model, the newly developed descending dimensional JDL algorithm was used to suppress the Es layer clutter and simulated with measured data to provide the validity of this algorithm to suppress the ionospheric clutter. The simulation results showed that the established model can show the characteristics of the ionospheric Es layer clutter basically, and the JDL algorithm can suppress ionospheric Es layer clutter well. This method provided a theoretical basis for the ionospheric clutter suppression technology and the use of STAP in anti-ionospheric clutter.

Acknowledgments

At the point of finishing this paper, one of the authors would like to express his/her sincere thanks to the National Natural Science Foundation Key Project (no. 61032011) and members of the School of Electronics and Information Engineering, Research Center, Harbin Institute of Technology for technical support.

References

[1] H. C. Chan, "Characterization of ionospheric clutter in HF surface wave radar," Tech. Rep. 2003-114, Defence R&D Canada, Ottawa, Canada, 2003.

[2] D. L. Knepp, "Multiple phase-screen calculation of the temporal behavior of stochastic waves," *Proceedings of the IEEE*, vol. 71, no. 6, pp. 722–737, 1983.

[3] Y. W. Kiang and C. H. Liu, "Multiple phase-screen simulation of HF wave propagation in the turbulent stratified ionosphere," *Radio Science*, vol. 20, no. 3, pp. 652–668, 1985.

[4] J. F. Wagen and K. C. Yeh, "A numerical study of waves reflected from a turbulent ionosphere," *Radio Science*, vol. 21, no. 4, pp. 538–604, 1986.

[5] D. L. Knepp and L. J. Nickisch, "Multiple phase screen calculation of wide bandwidth propagation," *Radio Science*, vol. 44, p. 1, 2009.

[6] M. Ravan, R. J. Riddolls, and R. S. Adve, "Ionospheric and auroral clutter models for HF surface wave and over-the-horizon radar systems," *Radio Science*, vol. 47, no. 3, 2012.

[7] F. J. Massey, "The Kolmogorov-Smirnov test for goodness of fit," *Journal of the American Statistical Association*, vol. 46, no. 253, pp. 68–78, 1951.

[8] M. W. Y. Poon, R. H. Khan, and S. Le-Ngoc, "Singular value decomposition (SVD) based method for suppressing ocean clutter in high frequency radar," *IEEE Transactions on Signal Processing*, vol. 41, no. 3, pp. 1421–1425, 1993.

[9] M. Ravan, O. Saleh, and R. Adve, "KB-STAP implementaion for HFSWR: final report," Tech. Rep. W7713-060999/001/SV, 2008.

[10] O. Saleh, *Adaptive processing in HF surface wave radar [M.S. thesis]*, University of Toronto, 2008.

[11] O. Saleh, R. S. Adve, R. J. Riddolls, M. Ravan, and K. Plataniotis, "Adaptive processing in high frequency surface wave radar," in *Proceedings of the IEEE Radar Conference, RADAR 2008*, pp. 1–6, Rome, Italy, May 2008.

[12] G. A. Fabrizio and A. Farina, "GLRT-based adaptive doppler processing for HF radar systems," in *Proceedings of the IEEE International Conference on Acoustics, Speech and Signal Processing (ICASSP '07)*, pp. II949–II952, Honolulu, Hawaii, USA, April 2007.

[13] E. J. Yang, J. Chun, R. Adve, and J. Chun, "A hybrid D3-sigma delta STAP algorithm in non-homogeneous clutter," in *Proceedings of the IET International Conference on Radar Systems (RADAR '07)*, p. 76, Edinburgh, UK, October 2007.

[14] E. Aboutanios and B. Mulgrew, "Hybrid detection approach for STAP in heterogeneous clutter," *IEEE Transactions on Aerospace and Electronic Systems*, vol. 46, no. 3, pp. 1021–1033, 2010.

[15] J. Goldstein, I. Reed, and P. Zulch, "Multistage partially adaptive STAP CFAR detection algorithm," *IEEE Transactions on Aerospace and Electronic Systems*, vol. 35, no. 2, pp. 645–651, 1999.

Hindawi Publishing Corporation
International Journal of Antennas and Propagation
Volume 2013, Article ID 853746, 8 pages
http://dx.doi.org/10.1155/2013/853746

Research Article

Spectrum Sensing under Correlated Antenna Array Using Generalized Detector in Cognitive Radio Systems

Modar Safir Shbat and Vyacheslav Tuzlukov

School of Electronics Engineering, College of IT Engineering, Kyungpook National University, 1370 Sankyuk-dong, Buk-gu, Daegu 702-701, Republic of Korea

Correspondence should be addressed to Vyacheslav Tuzlukov; tuzlukov@ee.knu.ac.kr

Received 5 April 2013; Accepted 29 May 2013

Academic Editor: Krzysztof Kulpa

We derive the probability of false alarm and detection threshold under employment of the generalized detector (GD) in cognitive radio (CR) systems for two scenarios: firstly, the independent antenna array elements; the secondly, the correlated antenna array elements. The energy detector (ED) and GD spectrum sensing performances are compared under the same initial conditions. The simulation results show that implementation of the GD improves the spectrum sensing performance in CR systems both for independent and correlated antenna array elements.

1. Introduction

Simple random access protocols such as the carrier sense multiple access (CSMA) are widely used in many network applications. Using these protocols, the users and nodes have to define an availability of the radio channel or possibility to use a definite spectrum in order to start the transmission process after an arbitrary delay. The cognitive radio (CR) concept depends on the spectrum sharing and opportunistic spectrum access when there is a secondary network additionally to the primary network that has priority in access to spectral resources. The CR is an effective approach to improve spectrum utilization or radio resources by introducing an opportunistic use of frequency bands unused by the primary or licensed users. The CR systems have ability to measure, sense, learn, and define the radio channel parameters, the spectrum availability, and the radio operating conditions.

Two types of users are considered in the CR systems, namely, the primary user and the secondary user. The primary users (the licensed users) have a priority to use the available designated spectrum. The secondary users are allowed to temporally use idle spectrum unused by the primary users. The secondary user should take down the radio resources if the primary user needs to use the same radio resources. Thus, the secondary user should try to find another idle radio resources or frequency bands.

In general, most of the existed spectrum sensing approaches are based on the energy detector [1, 2], matched filter, [3, 4], and cyclostationary detector [5, 6]. The matched filter requires a complete knowledge about the signal received from the primary user and signaling features. The cyclostationary detector exploits features of signal received from the primary user caused by periodicity. Advantage of the energy detector (ED) is an absence of any required information about the signal sent by the primary user. The ED is considered to be optimal in the case of independent antenna array elements [1], but it is not true in the opposite case, that is, the correlated antenna array elements. In general, the ED is sensitive to noise when variations in the noise power can cause a serious decline in the detection performance.

The employment of ED with dynamic threshold in CR systems is investigated in [7] when the detection performance is defined under the fast fluctuated average noise power. The ED dynamic threshold is proposed to solve the problem of degradation in detection performance and sensitivity under the fast fluctuated average noise power, especially, at low values of the signal-to-noise ratio (SNR). The spectrum sensing performance under implementation of ED in CR systems is investigated in [8] using the dynamic threshold.

Several spectrum sensing approaches based on the generalized likelihood ratio test (GLRT) are investigated in [8] with

the purpose to be implemented by CR systems. The techniques proposed in [9] use the eigenvalues of the sample covariance matrix of the received signal vector by treating unknown parameters of the probability density function (pdf) of observed data independently of the presence of the signal from the primary user. Another signal detection scheme based on the eigenvalues of the covariance matrix of the signal vector received from the primary user is proposed in [10]. This scheme generates a decision statistics for the detection of signal sent by the primary user based on the ratio between the largest and the smallest eigenvalues of the covariance matrix of the received signal vector. In this case, the probability of miss is defined as a function of the number of cooperative receivers, number of samples, and SNR [11].

Detection performance improving can be achieved by cooperative spectrum sensing using the two-step threshold ED [12]. The two-step thresholds are used for local detection allowing us to make a reliable local decision at each sensing node. The final decision is defined by combining the results of local decisions using the data fusion center. Under the spectrum sensing based on known signal pattern (waveform) of the primary user [13], the preamble (a known data sequence transmitted before each data burst) and the midamble (a known data sequence transmitted in the middle of the data burst) are used. Thus, if the signal pattern is known, the sensing process is performed by correlating the received signal with a known copy of itself (the coherent sensing). Some parameters extracted from the received signal, for example, the signal energy, and power spectral density are employed by radio identification sensing approach [14, 15]. More information about other spectrum sensing techniques such as the multitaper spectral estimation, wavelet transform estimation, and time-frequency analysis can be found in [13].

There are many problems under spectrum sensing in CR systems, namely, the detection of the signal received from the primary user under correlation of the antenna array elements, interference cancellation, hidden primary user, and sensing efficiency when the data transmission is not allowed for the CR users during the observation period. The last problem decreases the transmission opportunities [16].

Because of the low computation costs and implementation complexity, the ED is widely used in the spectrum sensing. Additionally, it does not need any knowledge about the signal sent by the primary user. The ED detects the signal by comparing the decision statistics with the detection threshold depended on the noise power (variance) [17]. The ED has some problems related to spectrum sensing including the threshold selection, interference cancellation, noise differentiation, noise power estimation, and detection performance degradation under the correlated antenna array elements and at the low SNR. The noise variance estimation problem is solved by distinguishing the noise and signal subspaces using the multiple signal classification (MUSIC) algorithm [18].

The idea to employ the generalized detector (GD) for spectrum sensing in CR is proposed with the purpose to improve the sensing performance under the correlated antenna array elements because the GD has the same advantage as the ED; that is, no knowledge about parameters of the signal sent by the primary user is required. The GD is a combination of the Neyman-Pearson (NP) detector and ED based on the generalized approach to signal processing in noise [19]. As well known, the NP detector is optimal for the detection of signals with known parameters and the ED is optimal for the detection of signals with unknown parameters. The GD allows us to formulate a decision-making rule about the presence or absence of the signal based on definition of the jointly sufficient statistics of the mean and variance of likelihood function [20]. The GD implementation in wireless communication systems and GD detection performance are discussed in [21]. How we can improve the detection performance employing GD in radar sensor systems is investigated in [22, 23].

In this paper, the spectrum sensing in CR systems based on employment of the GD is evaluated. We define the detection threshold and the probability of false alarm under GD employment in CR systems. The sensing performance of the ED and GD is compared under the same conditions for two scenarios: firstly, the independent antenna array elements; secondly, the correlated antenna array elements. The simulation results demonstrate the better sensing performance of the GD in comparison with the ED one both for independent and correlated antenna array elements.

The remainder of this paper is organized as follows. The system model is presented in Section 2. The GD main structure and the decision statistics are introduced in Section 3. Section 4 describes a definition of the GD threshold and a derivation of the probability of false alarm. The threshold and the probability of false alarm for ED are discussed in Section 5. The simulation results are presented in Section 6. The conclusion remarks are made in Section 7.

2. Spectrum Sensing in Correlated Antenna Array Elements

Assume that the spectrum sensing is carried out by the secondary user and/or secondary sensing node with the number of antennas equal to M (M antenna array elements). At the specific kth time instant and for the ith antenna array element, the binary hypothesis test for the spectrum sensing can be presented in the following form:

$$x_i[k] = \begin{cases} w_i[k], \\ \quad i = 1, \ldots, M; k = 0, \ldots, N-1 \Longrightarrow \mathcal{H}_0; \\ h_i[k]\, a[k] + w_i[k], \\ \quad i = 1, \ldots, M; k = 0, \ldots, N-1 \Longrightarrow \mathcal{H}_1, \end{cases} \tag{1}$$

where $x_i[k]$ is the discrete-time received signal at the input of secondary user or secondary sensing node; $a[k]$ is the discrete-time shift phase keying (PSK) modulated transmitted signal with the equal likely probability of transmission for all symbols; $h_i[k]$ is the discrete-time channel coefficient; and $w_i[k]$ is the discrete-time additive white Gaussian noise (AWGN) with zero mean and variance equal to σ_n^2, that is, $w_i[k] \sim \mathcal{CN}(0, \sigma_n^2)$, where $\mathcal{C}$ denotes that $w_i[k]$ is the complex random variable. The PSK modulated signal $a[k]$ is transmitted over a Rayleigh fading channel with coefficients obeying the complex Gaussian distribution with zero mean

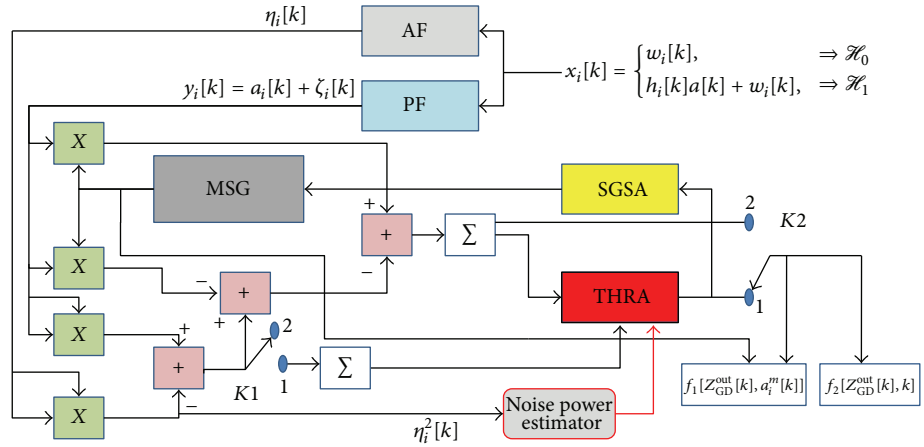

Figure 1: GD structure.

and variance equal to σ_h^2, that is, $h_i[k] \sim \mathcal{CN}(0, \sigma_h^2)$. The channel coefficients $h_i[k]$ corresponding to the ith antenna array element, $i = 1, \ldots, M$, are correlated between each other and independent of the time. The PSK modulated signal $a[k]$, the channel coefficients $h_i[k]$, and the AWGN $w_i[k]$ are independent between each other.

The exponential correlation model of antenna array elements is widely used owing to its simplicity and complete description of the spatial correlation [24]. The components of the $M \times M$ correlation matrix **Cor** are presented in the following form:

$$Cor_{ij} = \begin{cases} \rho^{i-j}, & i \le j, \\ Cor_{ji}^*, & i > j, \end{cases} \quad i, j = 1, \ldots, M, \tag{2}$$

where ρ is the coefficient of correlation between two adjacent antenna array elements, $0 \le \rho \le 1$ (real values), and $*$ denotes the complex conjugate. Using the approximated cross-correlation function defined in [25], the correlation coefficient ρ can be given as

$$\rho = \exp\left(-23\Lambda^2\left(\frac{d}{\lambda_c}\right)^2\right), \tag{3}$$

where Λ is the angular spread, λ_c is the wavelength, and d is the distance between adjacent antenna array elements (antenna spacing). Thus, under these conditions, the correlation matrix **Cor** is the symmetric Toeplitz matrix [26].

The signals are received by M antenna array elements. If the sample size of received signals is N, the $MN \times 1$ received signal vector can be defined in the following form

$$\mathbf{X} = \left[x_1(0), \ldots, x_M(0), \ldots, x_1(N-1), \ldots, x_M(N-1)\right]^T, \tag{4}$$

where T denotes a transpose. The covariance matrices of the received signal vector $\mathbf{X}$ under the hypotheses $\mathcal{H}_0$ and $\mathcal{H}_1$ can be written in the following form:

$$\begin{aligned} \mathcal{H}_0 &\Longrightarrow \mathbf{Cov}_0 = E\left[\mathbf{X}\mathbf{X}^H \mid \mathcal{H}_0\right] = \sigma_n^2\mathbf{I}, \\ \mathcal{H}_1 &\Longrightarrow \mathbf{Cov}_1 = E\left[\mathbf{X}\mathbf{X}^H \mid \mathcal{H}_1\right] = E_a\sigma_h^2\mathbf{A} + \sigma_n^2\mathbf{I}, \end{aligned} \tag{5}$$

where H denotes the Hermitian conjugate (conjugate transpose), $\mathbf{I}$ is the $MN \times MN$ identity matrix, E_a is the received signal energy at the input of the secondary user or sensing node, and $\mathbf{A}$ is the $MN \times MN$ matrix defined based on the correlation matrix **Cor** [26]

$$\mathbf{A} = \begin{bmatrix} \mathbf{Cor} & \mathbf{0}_M & \cdots & \mathbf{0}_M \\ \mathbf{0}_M & \ddots & \ddots & \vdots \\ \vdots & \ddots & \ddots & \mathbf{0}_M \\ \mathbf{0}_M & \cdots & \mathbf{0}_M & \mathbf{Cor} \end{bmatrix}_{MN \times MN}, \tag{6}$$

where $\mathbf{0}_M$ is an $M \times M$ zero matrix.

3. GD Structure and Decision Statistics

The GD structure is presented in Figure 1. Here MSG is the model signal generator (local oscillator), AF is the additional filter, and PF is the preliminary filter. The threshold apparatus (THRA) device defines the GD threshold and the signal model generator switching apparatus (SGSA) is used to switch on the MSG with the purpose to define the unknown parameters of the detected signal. The noise power estimator evaluates σ_n^2 that is the variance of the noise at the GD input.

PF and AF are two linear systems at the GD front end that can be presented, for example, as the band-pass filters with the impulse responses $h_{PF}(\tau)$ and $h_{AF}(\tau)$. For simplicity of analysis, we think that these filters have the same amplitude-frequency responses and bandwidths. Moreover, a resonant or centered frequency of the AF is detuned relative to a resonant frequency of the PF on such a value that the information signal cannot pass through the AF. Thus, the information signal and noise can appear at the PF output and only the noise appear at the AF output. If a value of detuning between the AF and PF resonant frequencies is more than $4 \div 5\Delta f_a$, where Δf_a is the information signal bandwidth, the processes forming at the AF and PF outputs can be considered as independent and uncorrelated processes. In practice, under this condition the coefficient of correlation is not more than 0.05 [20, Chapter 3]. When the Gaussian noise $w(t)$ comes in at

the AF and PF inputs (the GD linear system front end), the noise forming at the AF and PF outputs is Gaussian, too, because the AF and PF are the linear systems. We may think that the AF and PF do not change the statistical parameters of input process since they are the linear GD front end systems. For this reason, the AF can be considered as a generator of reference sample with a priori information a "no" signal. A detailed discussion of the AF and PF can be found in [27, Chapter 5].

The signal at the PF output can be defined as $y_i[k] = a_i[k] + \zeta_i[k]$, where $\zeta_i[k]$ is the observed noise at the PF output and $a_i[k] = h_i[k]a[k]$. Under the hypothesis $\mathscr{H}_0$ and for all ith and kth, $y_i[k]$ is subjected to the complex Gaussian distribution with zero mean and variance σ_n^2 and is considered as the independent and identically distributed (i.i.d) process. The AF output signal is the reference noise $\eta_i[k]$. The model signal is defined as

$$a_i^m[k] = \beta a_i[k], \tag{7}$$

where $a_i^m[k]$ is the generated model signal and β is the coefficient of the proportionality. The main functioning condition of GD is an equality over the whole range of parameters between the model signal forming at the GD MSG output and the detected signal forming at the GD input linear system (the PF) output [19]. How we can do it in practice is discussed in [20, Chapter 7].

The decision statistics at the GD output can be presented in the following form [20, Chapter 3]:

$$T_{\mathrm{GD}}(\mathbf{X}) = \sum_{k=0}^{N-1}\sum_{i=1}^{M} 2y_i[k]\, a_i^m[k] - \sum_{k=0}^{N-1}\sum_{i=1}^{M} y_i^2[k] + \sum_{k=0}^{N-1}\sum_{i=1}^{M} \eta_i^2[k] \underset{\mathscr{H}_0}{\overset{\mathscr{H}_1}{\gtrless}} \mathrm{THR}_{\mathrm{GD}}, \tag{8}$$

where $\mathrm{THR}_{\mathrm{GD}}$ is the GD threshold. The first term in (8) corresponds to the NP detector with twice the gain and is considered as the sufficient statistics of the likelihood function mean. The second term in (8) corresponds to the ED and is considered as the sufficient statistics of the likelihood function variance. The third term in (8) presents the reference noise power generated according to the main functioning principles of the GD [19, Chapter 3]. Under the hypothesis $\mathscr{H}_1$ corresponding to $y_i[k] = a_i[k] + \zeta_i[k]$ and the condition $a_i^m[k] = a_i[k]$, the GD decision statistics takes the form

$$T_{\mathrm{GD}}(\mathbf{X}) = \sum_{k=0}^{N-1}\sum_{i=1}^{M} a_i^2[k] - \sum_{k=0}^{N-1}\sum_{i=1}^{M} \eta_i^2[k] - \sum_{k=0}^{N-1}\sum_{i=1}^{M} \zeta_i^2[k], \tag{9}$$

where the second and third terms in (9) present the background noise at the GD output. The background noise is a difference between the noise power forming at the PF and AF outputs. In the opposite case (the hypothesis $\mathscr{H}_0$) corresponding to $y_i[k] = \zeta_i[k]$, the right side of (9), is the background noise only.

4. Spectrum Sensing Performance of GD

4.1. Correlated Antenna Array Elements. According to the GD decision statistics at the hypothesis $\mathscr{H}_1$ given by (9) if the energy of signal received by each of M antenna elements is combined with equal gain and the condition $a_i[k] = a_i^m[k]$ is satisfied, the GD defines the total received signal energy within the limits of the observation interval and compares this energy with the GD threshold $\mathrm{THR}_{\mathrm{GD}}$ to make a decision of a "yes" or a "no" signal sent by the primary user. The probability of false alarm $P_{\mathrm{FA}}^{\mathrm{GD}}$ and the probability of miss $P_{\mathrm{miss}}^{\mathrm{GD}}$ are defined using the following forms [20, Chapter 6]:

$$\begin{aligned} P_{\mathrm{FA}}^{\mathrm{GD}} &= P\left(T_{\mathrm{GD}}(\mathbf{X}) \geq \mathrm{THR}_{\mathrm{GD}} \mid \mathscr{H}_0\right) \\ &= 1 - \Phi\left(\frac{\mathrm{THR}_{\mathrm{GD}} - m_{\mathscr{H}_0}^{\mathrm{GD}}}{\sqrt{\mathrm{Var}_{\mathscr{H}_0}^{\mathrm{GD}}}}\right), \\ P_{\mathrm{miss}}^{\mathrm{GD}} &= P\left(T_{\mathrm{GD}}(\mathbf{X}) < \mathrm{THR}_{\mathrm{GD}} \mid \mathscr{H}_1\right) \\ &= \Phi\left(\frac{\mathrm{THR}_{\mathrm{GD}} - m_{\mathscr{H}_1}^{\mathrm{GD}}}{\sqrt{\mathrm{Var}_{\mathscr{H}_1}^{\mathrm{GD}}}}\right), \end{aligned} \tag{10}$$

where

$$\Phi(x) = \frac{1}{2} + \frac{1}{2}\,\mathrm{erf}\left(\frac{x}{\sqrt{2}}\right) \tag{11}$$

is the integral of probability,

$$\mathrm{erf}(x) = \int_0^x \exp\left(-t^2\right) dt \tag{12}$$

is the error function which is identical to $\Phi(x)$, $m_{\mathscr{H}_0}^{\mathrm{GD}}$ is the mean of the decision statistics $T_{\mathrm{GD}}(\mathbf{X})$ under the hypothesis $\mathscr{H}_0$, $\mathrm{Var}_{\mathscr{H}_0}^{\mathrm{GD}}$ is the variance of the decision statistics $T_{\mathrm{GD}}(\mathbf{X})$ under the hypothesis $\mathscr{H}_0$, and $m_{\mathscr{H}_1}^{\mathrm{GD}}$ and $\mathrm{Var}_{\mathscr{H}_1}^{\mathrm{GD}}$ are the mean and variance of the decision statistics under the hypothesis $\mathscr{H}_1$, respectively. The decision statistics $T_{\mathrm{GD}}(\mathbf{X})$ is a sum of $M \times N$ i.i.d. random variables. Using a relationship between the probability of detection P_D^{GD} and the probability of miss $P_{\mathrm{miss}}^{\mathrm{GD}}$

$$P_D^{\mathrm{GD}} = 1 - P_{\mathrm{miss}}^{\mathrm{GD}} \tag{13}$$

and taking into consideration a definition of the Gaussian Q-function

$$Q(x) = \frac{1}{2} - \frac{1}{2}\,\mathrm{erf}\left(\frac{x}{\sqrt{2}}\right), \tag{14}$$

based on (10) the probability of false alarm $P_{\mathrm{FA}}^{\mathrm{GD}}$ and the probability of detection P_D^{GD} can be defined in the following forms:

$$\begin{aligned} P_{\mathrm{FA}}^{\mathrm{GD}} &= P\left(T_{\mathrm{GD}}(\mathbf{X}) \geq \mathrm{THR}_{\mathrm{GD}} \mid \mathscr{H}_0\right) \\ &= Q\left(\frac{\mathrm{THR}_{\mathrm{GD}} - m_{\mathscr{H}_0}^{\mathrm{GD}}}{\sqrt{\mathrm{Var}_{\mathscr{H}_0}^{\mathrm{GD}}}}\right), \end{aligned} \tag{15}$$

$$P_D^{\mathrm{GD}} = P\left(T_{\mathrm{GD}}(\mathbf{X}) > \mathrm{THR}_{\mathrm{GD}} \mid \mathscr{H}_1\right) = Q\left(\frac{\mathrm{THR}_{\mathrm{GD}} - m_{\mathscr{H}_1}^{\mathrm{GD}}}{\sqrt{\mathrm{Var}_{\mathscr{H}_1}^{\mathrm{GD}}}}\right), \tag{16}$$

where the Gaussian Q-function can be presented in another form:

$$Q(x) = \frac{1}{\sqrt{2\pi}} \int_x^{\infty} \exp\left(-\frac{t^2}{2}\right) dt. \tag{17}$$

The moment generating function (MGF) of the partial decision statistics given by

$$T_{\mathrm{GD}}(\mathbf{X}_k) = \sum_{i=1}^{M} a_i^2[k] + \sum_{i=1}^{M} \eta_i^2[k] - \sum_{i=1}^{M} \zeta_i^2[k], \tag{18}$$

where $\sum_{i=1}^{M} a_i^2[k]$ is the sum of correlated random variables, can be delivered using the procedure discussed in [28]. As follows from (18), the MGF is defined as

$$\mathscr{M}_{T_{\mathrm{GD}}(\mathbf{X}_k)}(s) = \prod_{i=1}^{M}\left(1 - s\left(E_a\sigma_h^2\lambda_i\right)\right)^{-1} \times \prod_{i=1}^{M}\left(1 - s\left(\sqrt{2}\sigma_n^2\right)\right)^{-1}\prod_{i=1}^{M}\left(1 + s\left(\sqrt{2}\sigma_n^2\right)\right)^{-1}, \tag{19}$$

where λ_i is the eigenvalue of the ith spatial channel of the correlation matrix **Cor**. The mean and the variance of the partial decision statistics under the hypothesis $\mathscr{H}_1$ can be presented in the following form:

$$m_{\mathscr{H}_1}^{\mathrm{GD}} = E\left[T_{\mathrm{GD}}(\mathbf{X}_k) \mid \mathscr{H}_1\right] = M\left(E_a\sigma_h^2\right),$$
$$\mathrm{Var}_{\mathscr{H}_1}^{\mathrm{GD}} = \mathrm{Var}\left[T_{\mathrm{GD}}(\mathbf{X}_k) \mid \mathscr{H}_1\right] = \sum_{i=1}^{M}\left(E_a\sigma_h^2\lambda_i\right)^2 + 4M\sigma_n^4. \tag{20}$$

Similarly, the variance of the partial decision statistics $T_{\mathrm{GD}}(\mathbf{X}_k)$ under the hypothesis $\mathscr{H}_0$ takes the form

$$\mathrm{Var}_{\mathscr{H}_0}^{\mathrm{GD}} = \mathrm{Var}\left[T_{\mathrm{GD}}(\mathbf{X}_k) \mid \mathscr{H}_0\right] = 4M\sigma_n^4. \tag{21}$$

Under the hypothesis $\mathscr{H}_0$, the mean of the partial decision statistics $T_{\mathrm{GD}}(\mathbf{X}_k)$ is equal to zero, $m_{\mathscr{H}_0}^{\mathrm{GD}} = 0$ [20, Chapter 3]. For large values of N, the central limit theorem can be applied to obtain the pdf of the GD decision statistics.

With the purpose of avoiding the interference for the primary user in the CR systems, we define a lower bound of the probability of detection P_D. Thus, the sensing performance is evaluated by the probability of false alarm P_{FA} while the probability of detection P_D is maintained in accordance with the determined lower bound. In this case, there is a need to define the GD threshold $\mathrm{THR}_{\mathrm{GD}}$ as a function of the probability of detection P_D applying the required lower bound. In practice, in the case of GD, a knowledge of the GD input noise variance is sufficient to define the detection threshold. In other words, the noise variance at the GD input can be estimated.

We assume that the probability of detection is lower bounded, that is, $P_D^{\mathrm{GD}} \geq \alpha$, where α is the constraint. Based on (16), the GD threshold $\mathrm{THR}_{\mathrm{GD}}$ can be presented in the following form:

$$\mathrm{THR}_{\mathrm{GD}} = m_{\mathscr{H}_1}^{\mathrm{GD}} + \sqrt{\mathrm{Var}_{\mathscr{H}_1}^{\mathrm{GD}}}\,Q^{-1}(\alpha). \tag{22}$$

As follows from (20), the GD threshold $\mathrm{THR}_{\mathrm{GD}}$ can be rewritten in the following form:

$$\mathrm{THR}_{\mathrm{GD}} = NME_a\sigma_h^2 + Q^{-1}(\alpha)\sqrt{N\left\{\sum_{i=1}^{M}\left(E_a\sigma_h^2\lambda_i\right)^2 + 4M\sigma_n^4\right\}}. \tag{23}$$

The SNR at the secondary sensing node input is defined as

$$\gamma = \frac{E_a\sigma_h^2}{\sigma_n^2}. \tag{24}$$

Taking into account (24), the $\mathrm{THR}_{\mathrm{GD}}$ can be presented in the following form:

$$\mathrm{THR}_{\mathrm{GD}} = NM\gamma\sigma_n^2 + Q^{-1}(\alpha)\sqrt{N\left\{\sum_{i=1}^{M}\left(\gamma\sigma_n^2\lambda_i\right)^2 + 4M\sigma_n^4\right\}}. \tag{25}$$

Based on (15), (21), and (23), the probability of false alarm $P_{\mathrm{FA}}^{\mathrm{GD}}$ under correlated antenna array elements is defined in the following form:

$$P_{\mathrm{FA}}^{\mathrm{GD}_{\mathrm{cor}}} = Q\left(\frac{NME_a\sigma_h^2 + Q^{-1}(\alpha)\sqrt{N\left\{\sum_{i=1}^{M}\left(E_a\sigma_h^2\lambda_i\right)^2 + 4M\sigma_n^4\right\}}}{\sqrt{4NM\sigma_n^4}}\right). \tag{26}$$

After some elementary mathematical transformations and using (24), we can rewrite the $P_{\mathrm{FA}}^{\mathrm{GD}_{\mathbf{cor}}}$ as follows:

$$P_{\mathrm{FA}}^{\mathrm{GD}_{\mathrm{cor}}} = Q\left(\frac{\gamma\sqrt{NM} + Q^{-1}(\alpha)\sqrt{(1/M)\left(\sum_{i=1}^{M}\left(\gamma\lambda_i\right)^2 + 4M\right)}}{2}\right). \tag{27}$$

4.2. Independent Antenna Array Elements. Under conditions that the value of d/λ_c is high and the angular spread Λ value is close to π, there is no correlation between the adjacent antenna array elements in the GD; that is, the correlation coefficient is equal to zero ($\rho = 0$). Then, taking into consideration that the correlation matrix becomes $M \times M$ identity matrix, the probability of false alarm P_{FA} can be presented as a limiting case [26]:

$$P_{\mathrm{FA}}^{\mathrm{uncor}} = \lim_{\rho \to 0} P_{\mathrm{FA}}^{\mathrm{cor}}. \tag{28}$$

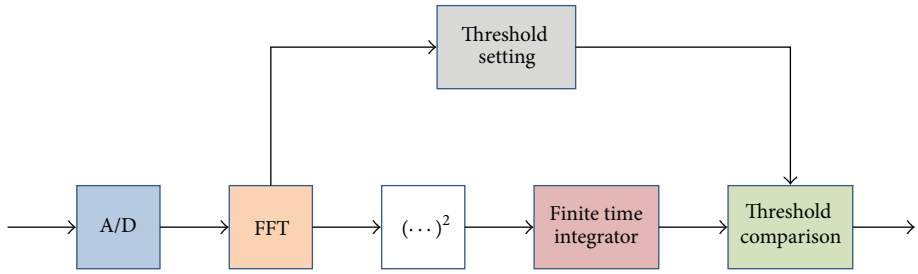

Figure 2: ED structure.

Thus, based on (27), the probability of false alarm $P_{\mathrm{FA}}^{\mathrm{GD}}$ under uncorrelated antenna array elements can be presented in the following form:

$$P_{\mathrm{FA}}^{\mathrm{GD_{uncor}}} = \lim_{\rho \to 0} P_{\mathrm{FA}}^{\mathrm{GD_{cor}}} = Q\left(\frac{Q^{-1}(\alpha)\sqrt{(\gamma^2+4)}+\gamma\sqrt{NM}}{2} \right). \tag{29}$$

Equation (29) presents the lower bound of the probability of false alarm $P_{\mathrm{FA}}^{\mathrm{GD}}$.

5. ED Spectrum Sensing Performance

The ED flowchart is presented in Figure 2 where we use the following notations: A/D is the analog-to-digital converter, FFT is the fast Fourier transform, and $(\cdots)^2$ denotes the square law function. The spectrum sensing performance of ED was discussed in [26] for two cases: there is correlation between the antenna array elements and there is no correlation between the antenna array elements. Under the initial conditions discussed in Section 2, the decision statistics at the ED output can be defined as

$$T_{\mathrm{ED}}(\mathbf{X}) = \sum_{k=0}^{N-1} \sum_{i=1}^{M} x_i^2[k]. \tag{30}$$

The ED decision statistics under the hypotheses $\mathscr{H}_0$ and $\mathscr{H}_1$ obeys the following distributions [26]:

$$\mathscr{H}_0 \Longrightarrow T_{\mathrm{ED}}(\mathbf{X}) \sim \mathscr{N}\left(NM\sigma_n^2, NM\sigma_n^4\right),$$

$$\mathscr{H}_1 \Longrightarrow T_{\mathrm{ED}}(\mathbf{X}) \sim \mathscr{N}\left(NM\left(E_a\sigma_h^2+\sigma_n^2\right), N\sum_{i=1}^{M}\left(E_a\sigma_h^2\lambda_i+\sigma_n^2\right)^2 \right). \tag{31}$$

In the case of correlated antenna array elements, the probability of false alarm $P_{\mathrm{FA}}^{\mathrm{ED}}$ can be derived also based on the detection threshold and the lower bounded probability of detection P_D^{ED}, that is, $P_D^{\mathrm{ED}} \geq \alpha$. According to [26], the probability of false alarm $P_{\mathrm{FA}}^{\mathrm{ED}}$ can be written as

$$P_{\mathrm{FA}}^{\mathrm{ED_{cor}}} = Q\left[Q^{-1}(\alpha)\sqrt{\frac{1}{M}\sum_{i=1}^{M}(\gamma\lambda_i+1)^2} + \gamma\sqrt{NM} \right]. \tag{32}$$

In the case when the antenna array elements are uncorrelated, the probability of false alarm $P_{\mathrm{FA}}^{\mathrm{ED}}$ takes the following form [26]:

$$P_{\mathrm{FA}}^{\mathrm{ED_{uncor}}} = \lim_{\rho \to 0} P_{\mathrm{FA}}^{\mathrm{ED_{cor}}} = Q\left[Q^{-1}(\alpha)(\gamma+1) + \gamma\sqrt{NM} \right]. \tag{33}$$

6. Simulation Results

The ED and GD sensing performances in CR systems are compared under the same initial conditions for two cases, namely, the independent antenna array elements and the correlated antenna array elements. We verify the spectrum sensing performance analysis for both detectors using MATLAB where the simulation conditions and parameters are established according to IEEE 802.22 [29]. The main simulation parameters are presented in Table 1.

In Figure 3, the probability of false alarm P_{FA} of ED and GD is presented as a function of SNR when the antenna array elements are independent, and when the antenna array elements are correlated with the coefficient of correlation $\rho = 1$, the number of antenna array elements is $M = 6$. The GD demonstrates better performance in comparison with the ED for all cases. For example, in the case of independent antenna array elements, at the probability of false alarm P_{FA} equal to 0.5 the SNR gain in favor of GD is approximately 4 dB in comparison with the ED. Under the correlated antenna array elements and at the same probability of false alarm $P_{\mathrm{FA}} = 0.5$, the SNR gain is about 2 dB in favor of GD comparing with the ED. In general, as shown in Figure 3, the probability of false alarm P_{FA} for the correlated antenna array elements both for the ED and GD is higher in comparison with the case when the correlation between antenna array elements is absent.

Figure 4 presents the receiver operation characteristic (ROC) curves for the GD and ED when the antenna array elements are independent; the number of antenna array elements is $M = 6$ and SNR= −5 dB and −10 dB. The GD demonstrates superiority in sensing performance. For example, at the probability of false alarm P_{FA} being equal to 0.1 and SNR = −10 dB, the probability of detection P_D in the case of ED is equal approximately to 0.45, while the GD achieves the probability of detection P_D equal to 0.8 under the same conditions. At the SNR = −5 dB and if the probability of false alarm P_{FA} is equal to 0.1, both ED and GD achieve a probability of detection P_D of more than 0.9.

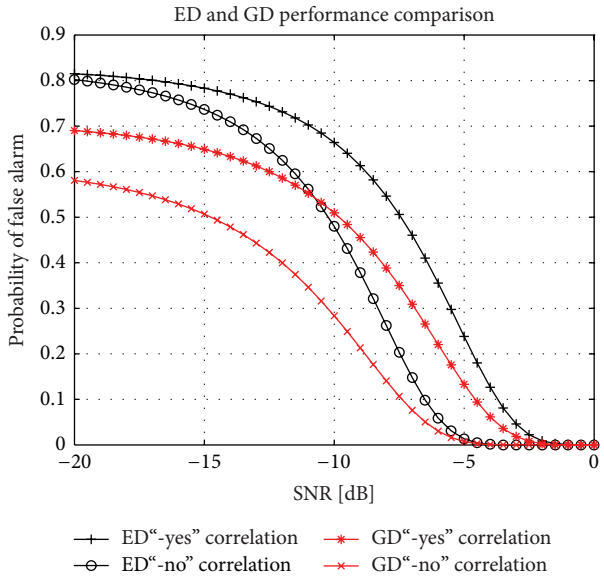

Figure 3: Comparison between the ED and GD sensing performance.

Table 1: Simulation parameters.

Parameter	Value
The angular spread (Λ), the correlated antenna array elements	0.5°
The angular spread (Λ), the uncorrelated antenna array elements	180°
Distance between antenna elements (d), the correlated antenna array elements	$d = \lambda_c/8$
Distance between antenna elements (d), the uncorrelated antenna array elements	$d = \lambda_c/2$
Number of antenna array elements (M)	$2 \div 10$
SNR	$-20 \div 0$ (dB)
P_D constraint (α)	0.99
Coefficient of correlation (ρ)	0; 0.1; 0.25; 0.5; 0.75; 1
Channel parameter (σ_h^2)	1
N	20

In Figure 5, we illustrate the GD performance in terms of the probability of false alarm $P_{\mathrm{FA}}^{\mathrm{GD}}$; when the number of antenna array elements is variable $2 \leq M \leq 10$, the coefficient of correlation ρ is changed as a parameter within the limits of $0.1 \leq \rho \leq 1$, and the SNR = −5 dB. As we can see from Figure 5, the probability of false alarm $P_{\mathrm{FA}}^{\mathrm{GD}}$ increases monotonically with the increasing in the coefficient of correlation ρ between antenna array elements. The use of large number of antenna array elements M allows us to reduce the negative action of the coefficient of correlation ρ on the probability of false alarm $P_{\mathrm{FA}}^{\mathrm{GD}}$.

7. Conclusions

Comparison of the spectrum sensing performance between the ED and GD is performed under the independent and correlated antenna array elements in CR systems at the low

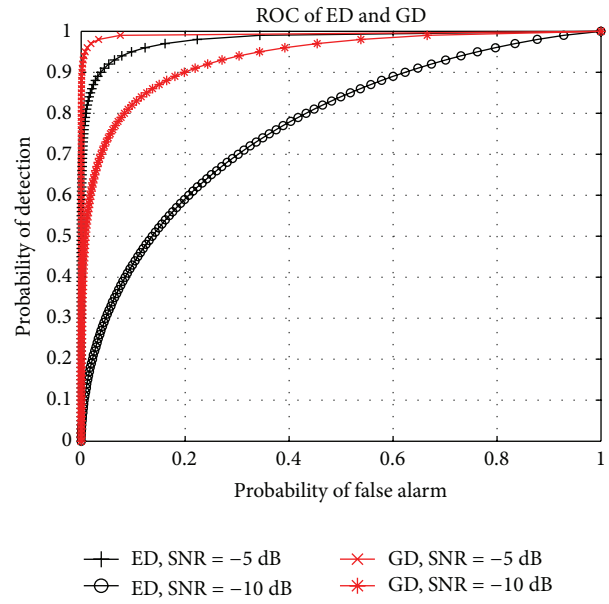

Figure 4: ROC of ED and GD.

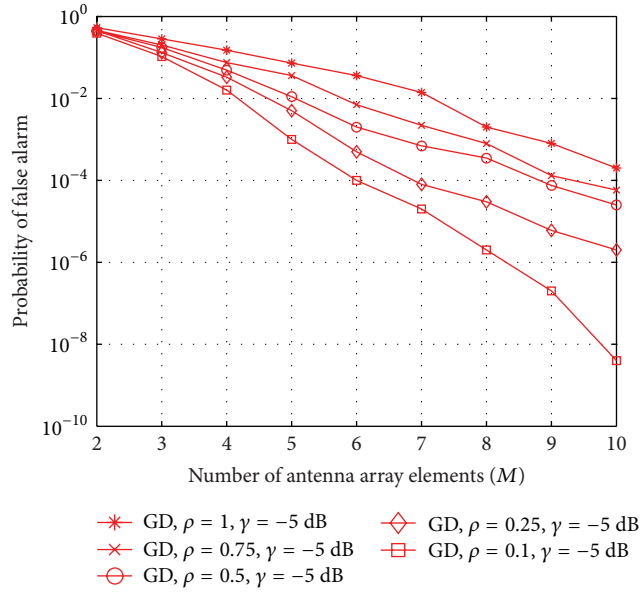

Figure 5: The probability of false alarm for GD versus the number of antenna array elements at various values of the coefficient of correlation.

SNR. The GD overcomes the ED in the sensing performance when the antenna array elements are either independent or correlated. The simulation results show a validity to use the GD for spectrum sensing in CR systems and confirm a superiority of GD implementation in comparison with ED. GD and ED performance analysis allows us to conclude that the probability of false alarm is lower bounded when the antenna array elements are independent. The GD sensing performance is a function of the coefficient of correlation between the antenna array elements. It follows from the fact that the probability of false alarm increases with the increasing in the coefficient of correlation between the antenna array elements. The use of large number of antenna array elements allows us to reduce

a negative influence of correlation between the antenna array elements and, consequently, a degradation of the GD sensing performance.

Acknowledgment

This research was supported by the Kyungpook National University research grant 2012.

References

[1] A. Sonnenschein and P. M. Fishman, "Radiometric detection of spread-spectrum signals in noise of uncertain power," *IEEE Transactions on Aerospace and Electronic Systems*, vol. 28, no. 3, pp. 654–660, 1992.

[2] S. M. Kay, *Fundamentals of Statistical Signal Processing: Detection Theory*, vol. 2, Prentice Hall, Upper Saddle River, NJ, USA, 1998.

[3] H.-S. Chen, W. Gao, and D. G. Daut, "Signature based spectrum sensing algorithms for IEEE 802.22 WRAN," in *Proceedings of the IEEE International Conference on Communications (ICC '07)*, pp. 6487–6492, Glasgow, Scotland, June 2007.

[4] D. Cabric, A. Tkachenko, and R. W. Brodersen, "Spectrum sensing measurements of pilot, energy, and collaborative detection," in *Proceedings of the Military Communications Conference (MILCOM '06)*, pp. 1–7, Washington, DC, USA, October 2006.

[5] W. A. Gardner, "Exploitation of spectral redundancy in cyclostationary signals," *IEEE Signal Processing Magazine*, vol. 8, no. 2, pp. 14–36, 1991.

[6] N. Han, S. H. Shon, J. O. Joo, and J. M. Kim, "Spectral correlation based signal detection method for spectrum sensing in IEEE 802.22 WRAN systems," in *Proceedings of the 8th International Conference Advanced Communication Technology (ICACT '06)*, pp. 1765–1770, Gangwon-Do, South Korea, February 2006.

[7] G. Yu, C. Long, M. Xiang, and X. I. Wei, "A Novel energy detection scheme based on dynamic threshold in cognitive radio systems," *Journal of Computational Information Systems*, vol. 8, no. 6, pp. 2245–2252, 2012.

[8] C. Korumilli, C. Gadde, and I. Hemalatha, "Performance analysis of energy detection algorithm in cognitive radio," *International Journal of Engineering Research and Applications*, vol. 2, no. 4, pp. 1004–1009, 2012.

[9] T. J. Lim, R. Zhang, Y. C. Liang, and Y. Zeng, "GLRT-based spectrum sensing for cognitive radio," in *Proceedings of the IEEE Global Telecommunications Conference (GLOBECOM '08)*, pp. 4391–4395, New Orleans, La, USA, December 2008.

[10] Y. Zeng and Y.-C. Liang, "Maximum-minimum eigenvalue detection for cognitive radio," in *Proceedings of the 18th Annual IEEE International Symposium on Personal, Indoor and Mobile Radio Communications (PIMRC '07)*, pp. 1–5, Athens, Greece, September 2007.

[11] F. Penna, R. Garello, and M. A. Spirito, "Probability of missed detection in eigenvalue ratio spectrum sensing," in *Proceedings of the 5th IEEE International Conference on Wireless and Mobile Computing Networking and Communication (WiMob '09)*, pp. 117–122, Marrakech, Morocco, October 2009.

[12] H. Chen and J. Liu, "Cooperative spectrum sensing based on double threshold detection and Dempster-Shafer theory," in *Proceedings of the IEEE 12th International Conference on Communication Technology (ICCT '2010)*, pp. 1212–1215, Nanjing, China, November 2010.

[13] T. Yücek and H. Arslan, "A survey of spectrum sensing algorithms for cognitive radio applications," *IEEE Communications Surveys and Tutorials*, vol. 11, no. 1, pp. 116–130, 2009.

[14] M. Mehta, N. Drew, G. Vardoulias, N. Greco, and C. Niedermeier, "Reconfigurable terminals: an overview of architectural solutions," *IEEE Communications Magazine*, vol. 39, no. 8, pp. 82–89, 2001.

[15] J. Palicot and C. Roland, "A new concept for wireless reconfigurable receivers," *IEEE Communications Magazine*, vol. 41, no. 7, pp. 124–132, 2003.

[16] W.-Y. Lee and I. F. Akyildiz, "Optimal spectrum sensing framework for cognitive radio networks," *IEEE Transactions on Wireless Communications*, vol. 7, no. 10, pp. 3845–3857, 2008.

[17] F. F. Digham, M.-S. Alouini, and M. K. Simon, "On the energy detection of unknown signals over fading channels," in *Proceedings of the International Conference on Communications (ICC '03)*, pp. 3575–3579, Seattle, Wash, USA, May 2003.

[18] M. P. Olivieri, G. Barnett, A. Lackpour, A. Davis, and P. Ngo, "A scalable dynamic spectrum allocation system with interference mitigation for teams of spectrally agile software defined radios," in *Proceedings of the 1st IEEE International Symposium on New Frontiers in Dynamic Spectrum Access Networks (DySPAN '05)*, pp. 170–179, Baltimore, Md, USA, November 2005.

[19] V. P. Tuzlukov, "A new approach to signal detection theory," *Digital Signal Processing: A Review Journal*, vol. 8, no. 3, pp. 166–184, 1998.

[20] V. Tuzlukov, *Signal Detection Theory*, Springer, Boston, Mass, USA, 2001.

[21] V. Tuzlukov, "Generalized approach to signal processing in wireless communications: the main aspects and some examples," in *Wireless Communications and Networks- Recent Advances*, Ch 11, pp. 305–338, InTech, Rijeka, Croatia, 2012.

[22] M. S. Shbat and V. Tuzlukov, "Generalized approach to signal processing in noise for closing vehicle detection application using FMCW radar sensor system," in *Proceedings of the International Radar Symposium (IRS '11)*, pp. 459–464, Warsaw, Poland, September 2011.

[23] M. S. Shbat and V. Tuzlukov, "Noise power estimation under generalized detector employment in automotive detection and tracking systems," in *Proceedings of 9th IET Data Fusion and Target Tracking Conference (DF & TT '12)*, London, UK, 2012.

[24] S. L. Loyka, "Channel capacity of MIMO architecture using the exponential correlation matrix," *IEEE Communications Letters*, vol. 5, no. 9, pp. 369–371, 2001.

[25] G. D. Durgin and T. S. Rappaport, "Effects of multipath angular spread on the spatial cross-correlation of received voltage envelopes," in *Proceedings of the IEEE VTS 49th Vehicular Technology Conference (VTC '99)*, pp. 996–1000, Houston, Tex, USA, September 1999.

[26] S. Kim, J. Lee, H. Wang, and D. Hong, "Sensing performance of energy detector with correlated multiple antennas," *IEEE Signal Processing Letters*, vol. 16, no. 8, pp. 671–674, 2009.

[27] V. Tuzlukov, *Signal Processing Noise*, CRC Press, Taylor & Francis Group, Washington, DC, USA, 2002.

[28] M.-S. Alouini, A. Abdi, and M. Kaveh, "Sum of gamma variates and performance of wireless communication systems over Nakagami-fading channels," *IEEE Transactions on Vehicular Technology*, vol. 50, no. 6, pp. 1471–1480, 2001.

[29] IEEE 802.22 working group on wireless regional area networks (WRAN), http://grouper.ieee.org/groups/802/22/.

Hindawi Publishing Corporation
International Journal of Antennas and Propagation
Volume 2013, Article ID 657653, 7 pages
http://dx.doi.org/10.1155/2013/657653

Research Article

Passive Localization of 3D Near-Field Cyclostationary Sources Using Parallel Factor Analysis

Jian Chen, Guohong Liu, and Xiaoying Sun

College of Communication and Engineering, Jilin University, Changchun 130022, China

Correspondence should be addressed to Jian Chen; chenjian@jlu.edu.cn

Received 6 February 2013; Accepted 2 June 2013

Academic Editor: Krzysztof Kulpa

By exploiting favorable characteristics of a uniform cross-array, a passive localization algorithm of narrowband cyclostationary sources in the spherical coordinates (azimuth, elevation, and range) is proposed. Firstly, we construct a parallel factor (PARAFAC) analysis model by computing the third-order cyclic moment matrices of the properly chosen sensor outputs. Then, we analyze the uniqueness of the constructed model and obtain three-dimensional (3D) near-field parameters via trilinear alternating least squares regression (TALS). The investigated algorithm is well suitable for the localization of the near-field cyclostationary sources. In addition, it avoids the multidimensional search and pairing parameters. Results of computer simulations are carried out to confirm the satisfactory performance of the proposed method.

1. Introduction

There has been considerable interest in bearing estimation for radar, sonar, communication, and electronic surveillance [1]. Various high-resolution algorithms, such as MUSIC [2] and ESPRIT [3], have been proposed to obtain the direction-of-arrival estimation of the far-field sources. In addition, when the sources are localized at the Fresnel region [4] of the array aperture, both the azimuth and range should be estimated. Recently, a significant amount attention has been paid to this issue and several near-field sources localization algorithms [5–7] are also available. However, all these methods as mentioned above only address the 2D problem of estimating azimuth and range and rely on the assumption of the stationary sources.

In recent years, several 3D near-field sources localization methods have been developed to obtain azimuth, elevation, and range. Meraim and Hua [8] proposed a second-order based method to cope with this issue. By translating the 1D uniform linear array of near field into a virtual rectangular array of virtual far field, Challa and Shamsunder [9] developed a fourth-order cumulants based Unitary-ESPRIT method. Moreover, [10, 11] also introduced efficient localization methods for 3-D near-field non-Gaussian stationary sources. It is obviously seen that all these methods still require that the incoming signals should be stationary ones; in addition, a multidimensional search or pairing parameters is also failed to avoid.

Cyclostationarity, which is a statistical property processed by most man-made communication signals, is related to the underlying periodicity arising from cyclic frequency of based rates. Besson et al. [12] introduced an original far-field approximation [13] based method to deal with the bearings estimation of near-field cyclostationary sources. Due to the fact that the effect caused by the mismatch between the actual spherical wavefront phase vector and assumed planar wavefront vector was alleviated, the proposed technique showed a satisfactory performance for the near-field sources far away from the sensor array. The estimations for elevation and range, however, have not been well considered.

In this paper, we consider the problem of jointly estimating elevation, azimuth, and range of the near-field cyclostationary sources; what is more, a two-stage passive localization method has been proposed. In the first stage, several third-order cyclic moment matrices of a cross-array observations data are computed, and a parallel factor analysis model in the cyclic statistic domain is constructed. In the second stage, the uniqueness of the constructed model is proved;

in addition, the 3-D localizing parameters for the near-field sources have also been obtained through TALS. The algorithm developed in this paper would be well suitable for near-field cyclostationary sources, and it does not require multidimensional search or pairing parameters; in addition, it also can effectively alleviates the array aperture loss.

The rest of this paper is organized as follows. Section 2 introduces the signal model of near-field localization based on cross-array. Section 3 develops a joint estimation algorithm of three parameters in near-field. Section 4 shows simulation results. Section 5 presents the conclusion of the whole paper.

2. Near-Field Signal Model Based Cross-Array

2.1. Near-Field Signal Model. We consider a near-field scenario of M uncorrelated narrowband signals impinging on a cross-array signed with the x and y axes (Figure 1), which consists of $L = 2N + 3$ sensors with element spacing d.

Let the array center be the phase reference point, and the signals received by the $(l, 0)$th and the $(l, 0)$th can be, respectively, expressed as

$$\begin{aligned} x_{l,0}(t) &= \sum_{m=1}^{M} s_m(t) \exp\left(j\left(\gamma_{xm} l + \varphi_{xm} l^2\right)\right) + n_{l,0}(t), \\ x_{0,l}(t) &= \sum_{m=1}^{M} s_m(t) \exp\left(j\left(\gamma_{jm} l + \varphi_{jm} l^2\right)\right) + n_{0,l}(t), \end{aligned} \tag{1}$$

where $n(t)$ donates the sensor additive noise, and

$$\begin{aligned} \gamma_{xm} &= -2\pi \frac{d}{\lambda} \sin\alpha_m \cos\theta_m, \\ \varphi_{xm} &= \pi \frac{d^2}{\lambda r_m}\left(1 - \sin^2\alpha_m \cos^2\theta_m\right), \\ \gamma_{ym} &= -2\pi \frac{d}{\lambda} \sin\alpha_m \sin\theta_m, \\ \varphi_{ym} &= \pi \frac{d^2}{\lambda r_m}\left(1 - \sin^2\alpha_m \sin^2\theta_m\right), \end{aligned} \tag{2}$$

where α_m, θ_m, and r_m indicate elevation, azimuth, and range of mth signal, respectively, and λ is wavelength of source signal.

The mth source signal with amplitude $z_m(t)$ can be modeled as

$$s_m(t) = z_m(t) \exp(j\omega t) \quad m = 1, 2, \ldots, M, \tag{3}$$

where $\tilde{\omega}$ is the center frequency.

2.2. Assumption of Signal Model. The main problem addressed in this paper is to jointly estimate the sets of parameters (α_m, θ_m, and r_m), and then the following assumptions are assumed to hold:

(1) the envelope $z_m(t)$ is non-Gaussian stationary random process with zero mean and nonzero skewness;

(2) the sensor noise is the additive stationary one and independent from the source signals;

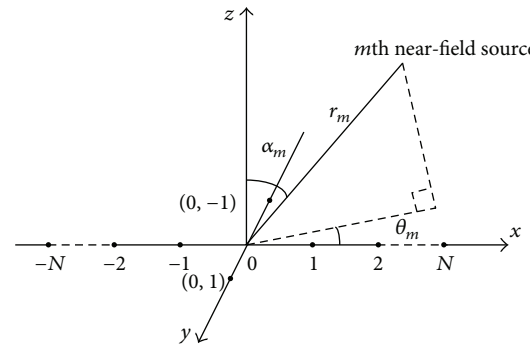

Figure 1: Sensor-source configuration for the near-field problem.

(3) the sensor array is a uniform linear array with element spacing $d \le \lambda/4$; in addition, the source number M is not more than sensor number N.

2.3. Parallel Factor Analysis. We need to introduce the following notation that will be used in the sequel.

Definition 1 (see [14]). Let $x_{k,n,p}$ stand for the (k, n, p) element of a three-dimensional tensor $\mathbf{X}$, if

$$x_{k,n,p} = \sum_{m=1}^{M} a_{k,m} b_{n,m} c_{p,m}, \tag{4}$$

where $a_{k,m}$ denotes the (k, m) element of matrix $\mathbf{A}$ and similarly for the others. Equation (4) indicates $x_{k,n.p}$ as a sum of triple products, which is variably known as the trilinear model, trilinear decomposition, triple product decomposition, canonical decomposition, or parallel factor (PARAFAC) analysis.

Definition 2 (see [14]). For a matrix $\mathbf{B} \in C^{I \times J}$, if all $I < J$ columns of $\mathbf{B}$ are linearly independent, but there exists a collection of $I + 1$ linearly dependent columns of $\mathbf{B}$, then it has Kruskal-rank (k-rank) $k_{\mathbf{B}} = I$.

Theorem 3 (see [15]). *Consider a three dimensional tensor* $\mathbf{X}$ *as defined in* (4)*, and* M *represents the common dimension, if*

$$k_{\mathbf{A}} + k_{\mathbf{B}} + k_{\mathbf{C}^T} \ge 2M + 2, \tag{5}$$

then $\mathbf{A}$*,* $\mathbf{B}$*, and* $\mathbf{C}$ *are unique up to permutation and (complex) scaling of columns.*

3. PARAFAC Based 3D Near-Field Sources Localization

3.1. Compute the Third-Order Cyclic Moments Matrices. Let $M^a_{3,x}(0, -l-1, -l)$ denote the third-order cyclic moment with cyclic frequency α defined as

$$\begin{aligned} &M^a_{3,x}(0, -l-1, -l) \\ &= \lim_{T\to\infty} \frac{1}{T} \sum_{t=1}^{T} E\left\{x_{0,0}(t)\, x_{-l-1,0}(t)\, x^*_{-l,0}(t)\right\} \exp\left(-j\alpha t\right), \end{aligned} \tag{6}$$

where the superscript "$*$" denotes the complex conjugate operation; in addition, $E\{x_{0,0}(t)x_{-l-1,0}(t)x^*_{-l,0}(t)\}$ can be given by

$$\begin{aligned}
&E\left\{x_{0,0}(t)\,x_{-l-1,0}(t)\,x^*_{-l,0}(t)\right\}\\
&\quad=\sum_{m=1}^{M} m_{3,z_m}\exp\left(j\left(-\gamma_{xm}+\phi_{xm}\right)\right)\exp\left(j2\phi_{xm}l\right)\exp\left(j\omega t\right)\\
&\qquad+m_{1,n}\sum_{m=1}^{M} m_{2,z_m}\exp\left(j\left[\gamma_{xm}(-l-1)+\phi_{xm}(-l-1)^2\right]\right)\\
&\qquad\qquad\times\exp\left(j2\omega t\right)\\
&\qquad+m_{1,n}\sum_{m=1}^{M} m_{2,z_m}\exp\left(-j\left[\gamma_{xm}(-l)+\phi_{xm}(-l)^2\right]\right)\\
&\qquad+m_{2,n}\sum_{m=1}^{M} m_{1,z_m}\exp\left(j\omega t\right)\\
&\qquad+m_{1,n}\sum_{m=1}^{M} m_{2,z_m}\exp\left(j\left(-\gamma_{xm}+\phi_{xm}\right)\right)\exp\left(j2\phi_{xm}l\right)\\
&\qquad+m_{2,n}\sum_{m=1}^{M} m_{1,z_m}\exp\left(j\left[\gamma_{xm}(-l-1)+\phi_{xm}(-l-1)^2\right]\right)\\
&\qquad\qquad\times\exp\left(j\omega t\right)\\
&\qquad+m_{2,n}\sum_{m=1}^{M} m_{1,z_m}\exp\left(-j\left[\gamma_{xm}(-l)+\phi_{xm}(-l)^2\right]\right)\\
&\qquad\qquad\times\exp\left(j\omega t\right)+m_{3,n},
\end{aligned}\tag{7}$$

where m_{1,z_m}, m_{2,z_m}, and m_{3,z_m} denote mean, variance, and the third-order moment of $z_m(t)$; in addition, $m_{1,n}$, $m_{2,n}$, and $m_{3,n}$ represent mean, variance, and the third-order cyclic moment of $n(t)$, respectively.

With assumption being considered, we further obtain

$$\begin{aligned}
&M^a_{3,x}(0,-l-1,-l)\\
&\quad=\sum_{m=1}^{M} m_{3,z_m}\exp\left(j\left(-\gamma_{xm}+\phi_{xm}\right)\right)\exp\left(j2\phi_{xm}l\right)\delta(\omega-\alpha)\\
&\qquad+m_{1,n}\sum_{m=1}^{M} m_{2,z_m}\exp\left(j\left[\gamma_{xm}(-l-1)+\phi_{xm}(-l-1)^2\right]\right)\\
&\qquad\qquad\times\delta(2\omega-\alpha)\\
&\qquad+m_{1,n}\sum_{m=1}^{M} m_{2,z_m}\exp\left(-j\left[\gamma_{xm}(-l)+\phi_{xm}(-l)^2\right]\right)\delta(\alpha)\\
&\qquad+m_{1,n}\sum_{m=1}^{M} m_{2,z_m}\exp\left(j\left(-\gamma_{xm}+\phi_{xm}\right)\right)\exp\left(j2\phi_{xm}l\right)\delta(\alpha)\\
&\qquad\qquad+m_{3,n}\delta(\alpha),
\end{aligned}\tag{8}$$

where δ is impulse function. Letting $a=\widetilde{\omega}$ and substituting (8) into (6) yield

$$\begin{aligned}
&M^a_{3,x}(0,-l-1,-l)\\
&\quad=\sum_{m=1}^{M} m_{3,z_m}\exp\left(j\left(-\gamma_{xm}+\varphi_{xm}\right)\right)\exp\left(j2l\varphi_{xm}\right).
\end{aligned}\tag{9}$$

Based on (9), we reconstruct the spatial third-order cyclic moment matrix $\mathbf{M}^a_1$, in which the (k,q)th element can be expressed as follows:

$$\begin{aligned}
\mathbf{M}^a_1(k,q)&=M^a_{3,x}(0,q-k-1,q-k)\\
&=\sum_{m=1}^{M} m_{3,z_m}\exp\left(j\left(-\gamma_{xm}+\varphi_{xm}\right)\right)\\
&\qquad\times\exp\left(j2\left(k-q\right)\varphi_{xm}\right).
\end{aligned}\tag{10}$$

In a matrix form, (10) can be written as

$$\mathbf{M}^a_1=\mathbf{A}\mathbf{M}^a_z\mathbf{\Omega}^*_1\mathbf{\Phi}_1\mathbf{A}^H,\tag{11}$$

where the superscript "H" represents conjugate transpose operation, $\mathbf{M}^a_z$ denotes the third-order moment matrix of source signals, and

$$\begin{aligned}
\mathbf{A}&=\left[\mathbf{a}_1,\mathbf{a}_2,\ldots,\mathbf{a}_M\right],\\
\mathbf{a}_m&=\left[1,\exp\left(j2\varphi_{xm}\right),\ldots,\exp\left(j2\left(N-1\right)\varphi_{xm}\right)\right],\\
\mathbf{\Omega}_1&=\operatorname{diag}\left(\exp\left(j\gamma_{x1}\right),\exp\left(j\gamma_{x2}\right),\ldots,\exp\left(j\gamma_{xM}\right)\right),\\
\mathbf{\Phi}_1&=\operatorname{diag}\left(\exp\left(j\varphi_{x1}\right),\exp\left(j\varphi_{x2}\right),\ldots,\exp\left(j\varphi_{xM}\right)\right).
\end{aligned}\tag{12}$$

On the other hand, following the same process described above, we can easily obtain

$$\begin{aligned}
&M^a_{3,x}(0,l+1,l)\\
&\quad=m_{3,u}\sum_{m=1}^{M} m_{3,z_m}\exp\left(j\left(\gamma_{xm}+\varphi_{xm}\right)\right)\exp\left(j2l\varphi_{xm}\right),\\
&M^a_{3,x}(1,-l-1,-l)\\
&\quad=m_{3,u}\sum_{m=1}^{M} m_{3,z_m}\exp\left(j\left(-\gamma_{xm}+\varphi_{xm}\right)\right)\\
&\qquad\times\exp\left(j\left(\gamma_{ym}+\varphi_{ym}\right)\right)\exp\left(j2l\varphi_{xm}\right),\\
&M^a_{3,x}(-1,-l-1,-l)\\
&\quad=m_{3,u}\sum_{m=1}^{M} m_{3,z_m}\exp\left(j\left(-\gamma_{xm}+\varphi_{xm}\right)\right)\\
&\qquad\times\exp\left(j\left(-\gamma_{ym}+\varphi_{ym}\right)\right)\exp\left(j2l\varphi_{xm}\right).
\end{aligned}\tag{13}$$

And the elements of the other three matrices can be expressed as

$$\begin{aligned}
\mathbf{M}_2^a(k,q) &= M_{3,x}^a(0,k-q+1,k-q)\\
&= \sum_{m=1}^{M} m_{3,z_m} \exp\left(j(\gamma_{xm}+\varphi_{xm})\right)\exp\left(j2(k-q)\varphi_{xm}\right),\\
\mathbf{M}_3^a(k,q) &= M_{3,x}^a(1,q-k-1,q-k)\\
&= \sum_{m=1}^{M} m_{3,z_m} \exp\left(j(-\gamma_{xm}+\varphi_{xm})\right)\\
&\quad\times \exp\left(j\left(\gamma_{ym}+\varphi_{ym}\right)\right)\exp\left(j2(k-q)\varphi_{xm}\right),\\
\mathbf{M}_4^a(k,q) &= M_{3,x}^a(-1,q-k-1,q-k)\\
&= \sum_{m=1}^{M} m_{3,z_m} \exp\left(j(-\gamma_{xm}+\varphi_{xm})\right)\\
&\quad\times \exp\left(j\left(-\gamma_{ym}+\varphi_{ym}\right)\right)\exp\left(j2(k-q)\varphi_{xm}\right).
\end{aligned} \tag{14}$$

Finally, we have

$$\begin{aligned}
\mathbf{M}_2^a &= \mathbf{A}\mathbf{M}_z^a\boldsymbol{\Omega}_1\boldsymbol{\Phi}_1\mathbf{A}^H,\\
\mathbf{M}_3^a &= \mathbf{A}\mathbf{M}_z^a\boldsymbol{\Omega}_1^*\boldsymbol{\Phi}_1\boldsymbol{\Omega}_2\boldsymbol{\Phi}_2\mathbf{A}^H,\\
\mathbf{M}_4^a &= \mathbf{A}\mathbf{M}_z^a\boldsymbol{\Omega}_1^*\boldsymbol{\Phi}_1\boldsymbol{\Omega}_2\boldsymbol{\Phi}_2\mathbf{A}^H
\end{aligned} \tag{15}$$

with

$$\begin{aligned}
\boldsymbol{\Omega}_2 &= \operatorname{diag}\left(\exp\left(j\gamma_{y1}\right),\exp\left(j\gamma_{y2}\right),\ldots,\exp\left(j\gamma_{yM}\right)\right),\\
\boldsymbol{\Phi}_2 &= \operatorname{diag}\left(\exp\left(j\varphi_{y1}\right),\exp\left(j\varphi_{y2}\right),\ldots,\exp\left(j\varphi_{yM}\right)\right).
\end{aligned} \tag{16}$$

3.2. Build the Parallel Factor Analysis Model. Considering the situation of limited samples, we build a parallel factor analysis model that uses the third-order cyclic moments as

$$\widetilde{\mathbf{M}}^a = \begin{bmatrix}\widetilde{\mathbf{M}}^a(:,:,1)\\ \widetilde{\mathbf{M}}^a(:,:,2)\\ \widetilde{\mathbf{M}}^a(:,:,3)\\ \widetilde{\mathbf{M}}^a(:,:,4)\end{bmatrix} = \begin{bmatrix}\widetilde{\mathbf{M}}_1^a\\ \widetilde{\mathbf{M}}_2^a\\ \widetilde{\mathbf{M}}_3^a\\ \widetilde{\mathbf{M}}_4^a\end{bmatrix} = \begin{bmatrix}\mathbf{A}\mathbf{M}_z^a\boldsymbol{\Omega}_1^*\boldsymbol{\Phi}_1\mathbf{A}^H\\ \mathbf{A}\mathbf{M}_z^a\boldsymbol{\Omega}_1\boldsymbol{\Phi}_1\mathbf{A}^H\\ \mathbf{A}\mathbf{M}_z^a\boldsymbol{\Omega}_1^*\boldsymbol{\Phi}_1\boldsymbol{\Omega}_2\boldsymbol{\Phi}_2\mathbf{A}^H\\ \mathbf{A}\mathbf{M}_z^a\boldsymbol{\Omega}_1^*\boldsymbol{\Phi}_1\boldsymbol{\Omega}_2^*\boldsymbol{\Phi}_2\mathbf{A}^H\end{bmatrix} + \nu_1 \tag{17}$$

with $\mathbf{C} = \mathbf{A}^*$, and the Khatri-Rao product [15] for (17) shows

$$\widetilde{\mathbf{M}}^a = (\mathbf{D}\otimes\mathbf{A})\,\mathbf{C}^T + \nu_1, \tag{18}$$

where

$$\mathbf{D} = \begin{bmatrix} g^{-1}\left(\mathbf{M}_z^a\boldsymbol{\Omega}_1^*\boldsymbol{\Phi}_1\right)\\ g^{-1}\left(\mathbf{M}_z^a\boldsymbol{\Omega}_1\boldsymbol{\Phi}_1\right)\\ g^{-1}\left(\mathbf{M}_z^a\boldsymbol{\Omega}_1^*\boldsymbol{\Phi}_1\boldsymbol{\Omega}_2\boldsymbol{\Phi}_2\right)\\ g^{-1}\left(\mathbf{M}_z^a\boldsymbol{\Omega}_1^*\boldsymbol{\Phi}_1\boldsymbol{\Omega}_2^*\boldsymbol{\Phi}_2\right)\end{bmatrix}, \tag{19}$$

with $g^{-1}(\mathbf{M}_z^a\boldsymbol{\Omega}_1^*\boldsymbol{\Phi}_1)$ denoting a row vector consisting of diagonal matrix $\mathbf{M}_z^a\boldsymbol{\Omega}_1^*\boldsymbol{\Phi}_1$.

Similarly, (18) also yields

$$\begin{aligned}
\widetilde{\mathbf{X}} &= (\mathbf{A}\otimes\mathbf{C})\,\mathbf{D}^T + \nu_2,\\
\widetilde{\mathbf{Y}} &= (\mathbf{C}\otimes\mathbf{D})\,\mathbf{A}^T + \nu_3.
\end{aligned} \tag{20}$$

3.3. Solve the Parallel Factor Analysis Model, and Estimate 3-D Parameters. As it stands, **A** and **C** are both Vandermonde matrices, and then they have Kruskal-rank (k-rank) $k_{\mathbf{A}} = k_{\mathbf{C}^T} = M$. On the other hand, the k-rank of **D** will be $k_{\mathbf{D}} = \min(4, M)$. When the condition that the number of signals being $M \geq 2$ holds, then **A**, **C**, and **D** are unique up to permutation and scaling of columns. With trilinear alternating least squares regression, we obtain that

$$\begin{aligned}
\widetilde{\mathbf{C}}^T &= \arg\min_{\mathbf{C}^T}\left\|\widetilde{M}^{\alpha} - (\mathbf{D}\otimes\mathbf{A})\,\mathbf{C}^T\right\|_F^2,\\
\widetilde{\mathbf{D}}^T &= \arg\min_{\mathbf{D}^T}\left\|\widetilde{\mathbf{X}} - (\mathbf{A}\otimes\mathbf{C})\,\mathbf{D}^T\right\|_F^2,\\
\widetilde{\mathbf{A}}^T &= \arg\min_{\mathbf{A}^T}\left\|\widetilde{\mathbf{Y}} - (\mathbf{C}\otimes\mathbf{D})\,\mathbf{A}^T\right\|_F^2.
\end{aligned} \tag{21}$$

Then using these estimates, we can associate with each pair (γ_{xm}, γ_{ym}, and φ_{ym}) as follows:

$$\begin{aligned}
\widetilde{\gamma}_{xm} &= \frac{1}{2}\arg\left(\frac{\widetilde{\mathbf{D}}(2,m)}{\widetilde{\mathbf{D}}(1,m)}\right),\\
\widetilde{\gamma}_{ym} &= \frac{1}{2}\left\{\arg\left(\frac{\widetilde{\mathbf{D}}(3,m)}{\widetilde{\mathbf{D}}(1,m)}\right) - \arg\left(\frac{\widetilde{\mathbf{D}}(4,m)}{\widetilde{\mathbf{D}}(1,m)}\right)\right\},\\
\widetilde{\varphi}_{ym} &= \frac{1}{2}\left\{\arg\left(\frac{\widetilde{\mathbf{D}}(3,m)}{\widetilde{\mathbf{D}}(1,m)}\right) + \arg\left(\frac{\widetilde{\mathbf{D}}(4,m)}{\widetilde{\mathbf{D}}(1,m)}\right)\right\}.
\end{aligned} \tag{22}$$

Finally, the sources parameters can be estimated as

$$\widetilde{\alpha}_m = \operatorname{asin}\left(\frac{\lambda}{2\pi d}\left(\widetilde{\gamma}_{xm}^2 + \widetilde{\gamma}_{ym}^2\right)^{1/2}\right), \tag{23}$$

$$\widetilde{\theta}_m = \operatorname{atan}\left(\frac{\widetilde{\gamma}_{ym}}{\widetilde{\gamma}_{xm}}\right), \tag{24}$$

$$\widetilde{r}_m = \frac{\pi d^2\left(1-\sin^2\widetilde{\alpha}_m\sin^2\widetilde{\theta}_m\right)}{\lambda\widetilde{\varphi}_{ym}}. \tag{25}$$

4. Computer Simulation Results

In this section, we explicit some simulation results to evaluate the performance of proposed method. For all examples, a uniform linear array with number of 15 sensors and element spacing 0.25λ is displayed, where λ is the wavelength of the narrowband source signals. Two near-field or far-field equal power cyclostationary signals are impinging on the array with center frequency 0.25π, and their envelopes can be modeled as exponentially distributed. To be compared, we simultaneously execute the method of [12], which is suitable for the

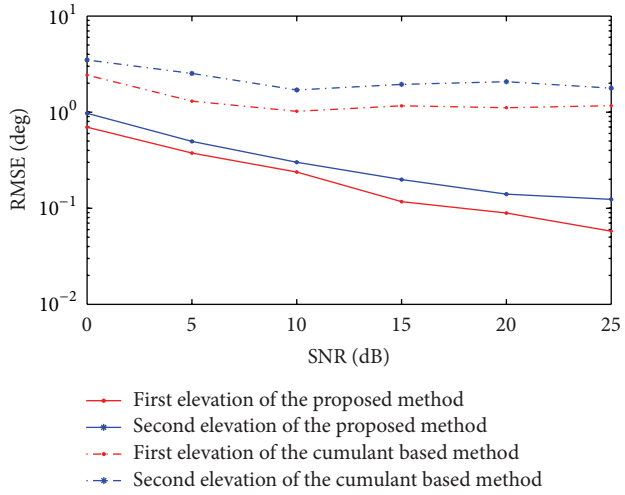

Figure 2: The RMSE of elevation estimations for two near-field sources using the proposed method and the cumulant based method versus SNR.

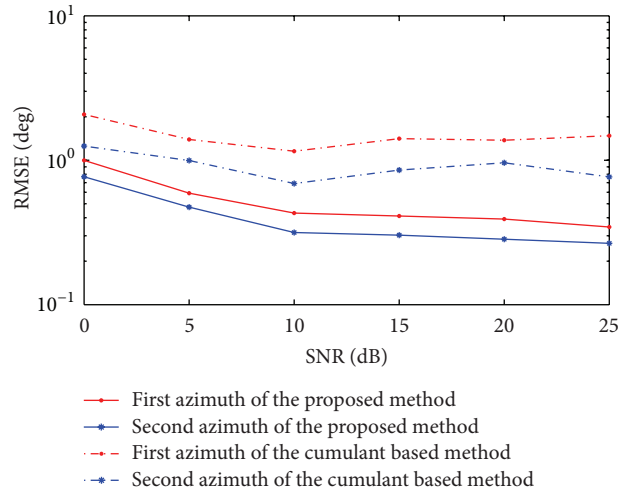

Figure 3: RMSE of azimuth estimations for two near-field sources using the proposed method and the cumulant based method versus SNR.

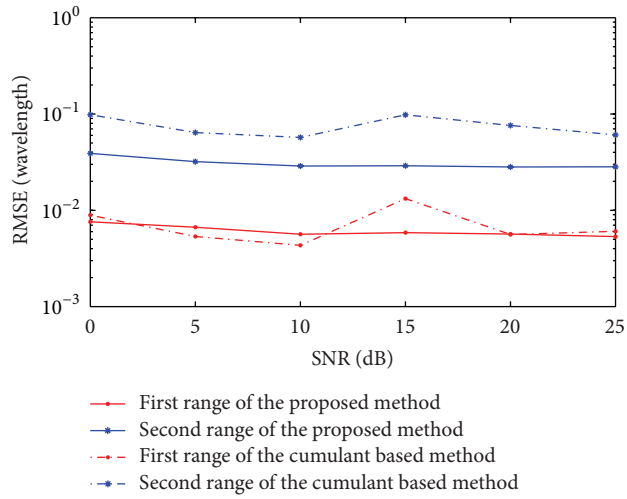

Figure 4: The RMSE of range estimations for two near-field sources using the proposed method and the cumulant based method versus SNR.

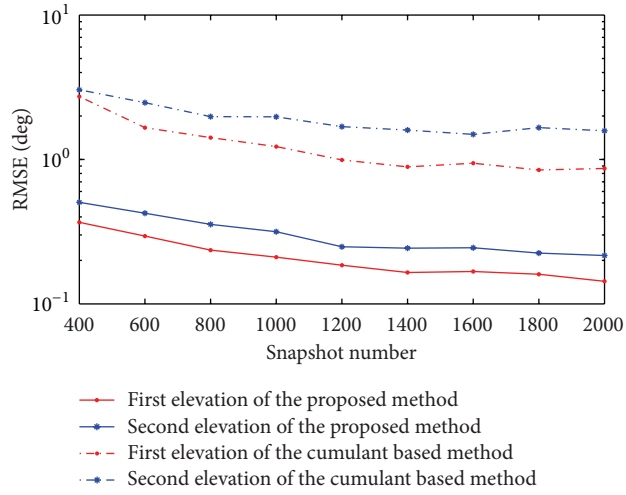

Figure 5: The RMSE of elevation estimations for two near-field sources using the proposed method and the cumulant based method versus snapshot number.

3-D near-field non-Gaussian stationary sources localization. The presented results are evaluated by the estimated root mean square error (RMSE) from the averaged results of 200 independent Monte-Carlo simulations.

In the first example, Two near-field sources are located at $(35^\circ, 46^\circ, \text{and } 1/6\lambda)$ and $(20^\circ, 60^\circ, \text{and } 2/5\lambda)$, respectively. The additive noise is time and spatially white Gaussian with zero mean and unit variance. In addition, the snapshot number is set equal to 1024. When SNR varies from 0 dB to 25 dB, the RMSE of the elevation, azimuth, and range estimations for two near-field cyclostationary sources can be shown in Figures 2, 3, and 4. For the comparison, the performance in the same situation for the fourth-order cumulants based method has also been displayed. From these three figures, it is obvious that the proposed method performs better in elevation, azimuth, and range estimation than the FFA based algorithm for all SNRs. What is more, the RMSE of range estimations for the first source that is closer to the array is less than the second one. This phenomenon is well agreement with the theoretical analysis that the sources closer to sensor array would hold a smaller standard deviation than the one far from the array [7].

In the second example, the simulation condition is similar to the first example, except that the SNR is set at 10 dB, and the snapshot number is varied from 400 to 2000. The RMSE of elevation, azimuth, and range estimations of two near-field cyclostationary sources obtained from the proposed method as well as the cumulant based method can be displayed in Figures 5, 6, and 7. From these three figures, we can see that the proposed method still shows a more satisfactory accuracy than the cumulant based method in all available snapshots. In addition, the range estimations for the first sources are

Table 1: RMSE of 3D parameters for near-field localization in the third example.

Example	Source	True	Mean	Variance	Source	True	Mean	Variance
White noise	α_1	35°	34.95°	0.1923	α_2	20°	20.03°	0.1647
	θ_1	40°	39.99°	0.0419	θ_2	60°	59.99°	0.1000
	r_1	$\lambda/6$	0.1669λ	3.5744×10^{-5}	r_2	$2\lambda/5$	0.3984λ	8.2107×10^{-4}
Colored noise	α_1	35°	35.02°	0.2146	α_2	20°	19.98°	0.0618
	θ_1	40°	40.03°	0.0795	θ_2	60°	60.02°	0.1165
	r_1	$\lambda/6$	0.1662λ	2.8455×10^{-5}	r_2	$2\lambda/5$	0.4036λ	8.4173×10^{-4}

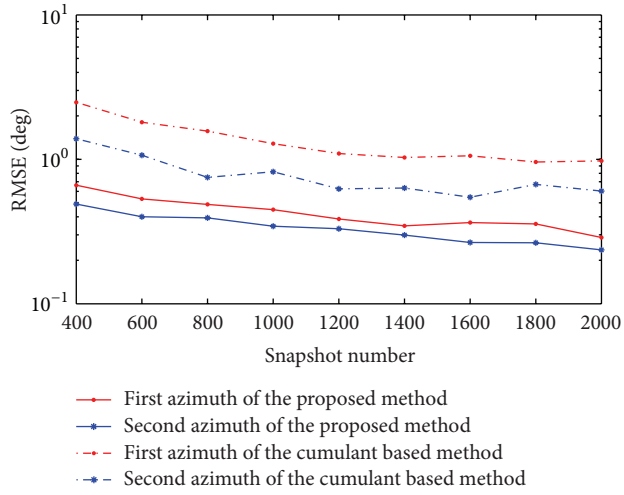

Figure 6: The RMSE of azimuth estimations for two near-field sources using the proposed method and the cumulant based method versus snapshot number.

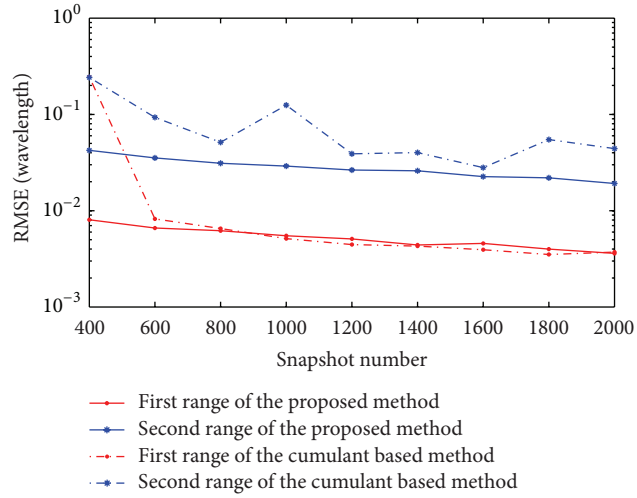

Figure 7: The RMSE of range estimations for two near-field sources using the proposed method and the cumulant based method versus snapshot number.

much better than the second one, while the elevation and azimuth estimations for both near-field sources are similar for the proposed method.

In the third example, the additive noise is time and spatially white Gaussian random process and the colored noise from a second-order AR model with parameter (−1.8,0.9), respectively. In addition, the other simulation condition is similar to the first example, except that the SNR is set at 10 dB, and snapshot number is equal to 1024. The mean and variance of the elevation, azimuth, and range estimations for two near-field cyclostationary sources can be shown in Table 1. From this table, we can easily see that the effectiveness of the proposed method is not little affected by the difference of the sensor noise.

5. Conclusion

This paper considers the problem of the passive localization of 3-D near-field cyclostationary sources and proposes an efficient third-order cyclic moment based algorithm. The construction of the parallel factor analysis model in the cyclic domain avoids the multidimensional search and pairing parameters. Moreover, the utilization of trilinear alternating least squares regression deals with the joint estimation of elevation, azimuth, and range. From the simulation results mentioned above, the proposed method outperforms the cumulant based method in locating near-field cyclostationary sources; in addition, the stationary noise has a little influence on the estimated accuracy of the proposed method.

Acknowledgments

This work is supported by the National Natural Science Foundation of China (61171137) and Specialized Research Fund for the Doctoral Program of Higher Education (20090061120042).

References

[1] J. Liang, X. Zeng, B. Ji, J. Zhang, and F. Zhao, "A computationally efficient algorithm for joint range-DOA-frequency estimation of near-field sources," *Digital Signal Processing*, vol. 19, no. 4, pp. 596–611, 2009.

[2] H. Krim and M. Viberg, "Two decades of array signal processing research: the parametric approach," *IEEE Signal Processing Magazine*, vol. 13, no. 4, pp. 67–94, 1996.

[3] A. J. Weiss and B. Friedlander, "Range and bearing estimation using polynomial rooting," *IEEE Journal of Oceanic Engineering*, vol. 18, no. 2, pp. 130–137, 1993.

[4] W. Zhi and M. Y.-W. Chia, "Near-field source localization via symmetric subarrays," in *Proceedings of the IEEE International*

Conference on Acoustics, Speech and Signal Processing (ICASSP '07), pp. II1121–II1124, Honolulu, Hawaii, USA, April 2007.

[5] D. Starer and A. Nehorai, "Path-following algorithm for passive localization of near-field sources," in *Proceedings of the 5th ASSP Workshop on Spectrum Estimation and Modeling*, pp. 322–326, 1990.

[6] D. Starer and A. Nehorai, "Passive localization on near-field sources by path following," *IEEE Transactions on Signal Processing*, vol. 42, no. 3, pp. 677–680, 1994.

[7] R. A. Harshman, "Foundation of the PARAFAC procedure: model and conditions for an explanatory mutil-mode factor analysis," *UCLA Working Papers in Phonetics*, vol. 22, no. 7, pp. 111–117, 1972.

[8] K. Aberd Meraim and Y. Hua, "3-D near field source localization using second order statistics," in *Proceedings of 31st Alisomar Conference on Signals, Systems and Computers*, vol. 2, pp. 1307–1310, 1997.

[9] R. N. Challa and S. Shamsunder, "Passive near-field localization of multiple non-Gaussian sources in 3-D using cumulants," *Signal Processing*, vol. 65, no. 1, pp. 39–53, 1998.

[10] K. Deng and Q. Yin, "Closed form parameters estimation for 3-D near field sources," in *Proceedings of the IEEE International Conference on Acoustics, Speech and Signal Processing (ICASSP '06)*, pp. IV1133–IV1136, Toulouse, France, May 2006.

[11] C. M. Lee, K. S. Yoo, and K. K. Lee, "Efficient algorithm for localizing 3-D narrowband multiple sources," *IEE Proceedings of Radar, Sonar and Navigation*, vol. 38, no. 1, pp. 23–26, 2001.

[12] O. Besson, P. Stoica, and A. B. Gershman, "Simple and accurate direction of arrival estimator in the case of imperfect spatial coherence," *IEEE Transactions on Signal Processing*, vol. 49, no. 4, pp. 730–737, 2001.

[13] A. L. Swindlehurst and T. Kailath, "A performance analysis of subspace-based methods in the presence of model errors—I: the MUSIC algorithm," *IEEE Transactions on Signal Processing*, vol. 40, no. 7, pp. 1758–1774, 1992.

[14] N. D. Sidiropoulos, R. Bro, and G. B. Giannakis, "Parallel factor analysis in sensor array processing," *IEEE Transactions on Signal Processing*, vol. 48, no. 8, pp. 2377–2388, 2000.

[15] J.-L. Liang, B.-J. Ji, F. Zhao, and J.-Y. Zhang, "Near-field source localization algorithm using parallel factor analysis," *Acta Electronica Sinica*, vol. 35, no. 10, pp. 1909–1915, 2007.

Hindawi Publishing Corporation
International Journal of Antennas and Propagation
Volume 2013, Article ID 934509, 9 pages
http://dx.doi.org/10.1155/2013/934509

Research Article

Design and Analysis of Ultra-Wideband Split Transmit Virtual Aperture Array for Through-the-Wall Imaging

Biying Lu, Yang Zhao, Xin Sun, and Zhimin Zhou

School of Electronic Science and Engineering, National University of Defense Technology, Changsha 410073, China

Correspondence should be addressed to Biying Lu; joelu76@aliyun.com

Received 15 February 2013; Accepted 29 May 2013

Academic Editor: Krzysztof Kulpa

The concept of virtual aperture and the point spread function for designing and characterizing ultra-wideband near-field multiple-input multiple-output active imaging array are investigated. Combining the approach of virtual aperture desynthesis with the monostatic-to-bistatic equivalence theorem, a kind of linear UWB MIMO array, the split transmit virtual aperture (STVA) array, was designed for through-the-wall imaging. Given the virtual aperture, the STVA array is the shortest in physical aperture length. The imaging performance of the designed STVA array in the near field is fully analyzed through both numerical and measured data. The designed STVA array has been successfully applied to imaging moving targets inside buildings.

1. Introduction

Through-the-wall imaging (TWI) is an emerging technology that has a variety of potential applications including earthquake rescue, covert target detection, surveillance, and reconnaissance. Ultra-wideband (UWB) microwave imaging has been identified as a viable approach for TWI. Typically, a synthetic aperture approach is employed for imaging purposes while fixed aperture (i.e., antenna array) rather than synthetic aperture imaging systems preferred in such hostile or time-sensitive applications [1–9].

To simplify the array imaging system, two kinds of arrays, the switched antenna array [1–5] and the multiple input multiple output (MIMO) array [6–9], have mostly been used. The switched array concept is based on one transmit array and one receive array. The transmit array switches between antenna elements one at a time. The receive array also switches between antenna elements one at a time. In this way, the number of required transmit and receive antennas is significantly saved. Moreover, using the high speed electronic switch, the time to acquire a data set across the aperture is greatly reduced compared to that of a synthetic aperture imaging system [1]. MIMO array imaging is characterized by using multiple transmit antennas to transmit orthogonal waveforms simultaneously and by using multiple receive antennas to receive the scattered waveforms from the target simultaneously. Two types of MIMO array, array with widely separated antenna elements and array with collocated transmit and receive antennas, have been proposed [10, 11]. For array imaging, the latter is preferred, and the use of orthogonal waveform is to increase the update rate rather than using diversity to improve the detection performance.

For active microwave imaging, both the switched antenna array and the MIMO array exhibit similar advantages of fast data acquisition and require less antenna elements. Further, the properties of both arrays are usually analyzed using the equivalent one-way co-array [6–9, 12–14] or two-way virtual aperture array [1–5, 15]. Considering we are concentrating on two-way active microwave imaging, the more versatile term of MIMO array and the concept of virtual aperture are used in the following section.

The configuration of MIMO array has great effects on radar imaging, such as resolution and peak side lobe level. The theory of virtual aperture (co-array) together with its beam pattern provides a unified and convenient method for analyzing and designing MIMO arrays under narrow band far-field condition [1–7, 12, 16].

The concept of virtual aperture (co-array) was extended to ultra wide band (UWB) imaging MIMO array in [8, 9, 12–14], with a modified definition of the beam pattern, which is a function of both the azimuth direction and the additional dimension of time or range [17–20]. UWB MIMO array design methods based on the concept of virtual aperture have been presented in [8, 9, 14].

Unfortunately, the same virtual aperture may be synthesized from MIMO arrays with different configurations. Further, high cross-range resolution of the UWB MIMO array imaging system requires large accumulation angle of the array to the imaging location, which conflicts with the far-field condition assumption of the virtual array approach. And the radar cross section (RCS) of a point scatterer is dependent on the imaging geometry of the MIMO array. Taking all these factors into account, a UWB MIMO array with the minimal physical aperture among those synthesizing the same virtual aperture, the split transmit virtual aperture array (STVA), for through the wall imaging application is presented. The performance of the designed array is fully analyzed using the point spread function (PSF), and the MIMO array has been successfully applied to image targets inside buildings.

This paper is organized as follows. In Section 2, the concept of co-array and virtual aperture together with the radiation pattern for wideband MIMO array is explained. The PSF of UWB array applicable for both far-and near-field conditions is presented in Section 3. The equivalence of PSF and beam pattern under far-field narrow band condition is also demonstrated. In Section 4, the linear UWB MIMO array design method is described, and a specific array configuration, the STVA, for TWI is proposed. The performance of the designed array is analyzed using the PSF. The experimental imaging results of the UWB MIMO imaging system are presented in Section 5. Conclusions are summarized in the final section.

2. Co-Array and Virtual Aperture

2.1. Co-Array. For each two-way array, an equivalent array can be synthesized whose one-way beam pattern is identical to a two-way pattern of the initial array. The aperture function of the synthesized array is referred to as effective aperture. The most famous effective array for MIMO array is the co-array.

Consider a linear two-way MIMO array composed of M transmit and N receive *omni*directional elements located along the x-axis as shown in Figure 1. The location of the mth transmit element is $\mathbf{r}_{t,m} = (x_{t,m}, 0)$, $m = 0, 1, 2, \ldots, M-1$, and the location of the nth receive element is $\mathbf{r}_{r,n} = (x_{r,n}, 0)$, $n = 0, 1, 2, \ldots, N-1$. For active imaging, the equivalent co-array consists of MN one-way element and the location of the ith synthesized element (virtual element) of the co-array is defined as [16]

$$\mathbf{r}_{c,i} = (x_{c,i}, 0) = \mathbf{r}_{t,m} + \mathbf{r}_{r,n} = (x_{t,m} + x_{r,n}, 0), \quad (1)$$

where $i = (m+1)(n+1) - 1$ for $m = 0, 1, 2, \ldots, M-1$ and $n = 0, 1, 2, \ldots, N-1$.

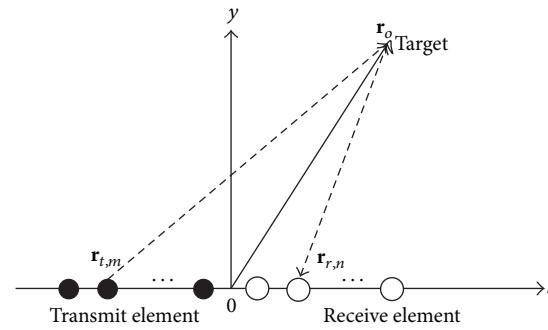

Figure 1: Linear transmit and receive arrays.

The weighting coefficient of the ith virtual element of the co-array is

$$w_{c,i} = w_{t,m} w_{r,n}, \quad (2)$$

where $w_{t,m}$ and $w_{r,n}$ are the weighting coefficients of the mth transmit and nth receive elements of the MIMO array, respectively.

It should be noted that (1) and (2) are defined under the condition that no redundancy exists within the co-array. If different transmit/receive pairs within the MIMO array result in the same virtual element position, the corresponding weights at the same virtual element shall be summed.

Under narrow band far-field condition, assuming that the steering is fixed and pointed broadside, the performance of a one-way array may be fully described with the well-known beam pattern or radiation pattern, given by the Fourier transform of the array aperture weighting function (or in its discrete form). The radiation pattern of the two-way MIMO array is the beam pattern of the equivalent co-array, given as

$$P_{\mathrm{MIMO}}(\theta) = P_c(\theta) = \sum_{i=0}^{MN-1} w_{c,i} e^{-jkx_{c,i}\sin\theta}, \quad (3)$$

where θ is the incidence angle from the normal of the aperture and $k = 2\pi/\lambda$ is the wave number with λ as the wavelength of the signal. Substitute (1) and (2) into (3), $P_{\mathrm{MIMO}}(\theta)$ can be expressed as

$$P_{\mathrm{MIMO}}(\theta) = \sum_{m=0}^{M-1} w_{t,m} e^{-jkx_{t,m}\sin\theta} \sum_{n=0}^{N-1} w_{r,n} e^{-jkx_{r,n}\sin\theta}. \quad (4)$$

The first sum of (4) is the beam pattern of the transmit array $P_t(\theta)$, and the second sum is the beam pattern of the receive array $P_r(\theta)$. Thus, the radiation pattern of the two-way MIMO array is the multiplication of the transmit and receive patterns.

The concept of co-array was extended to wideband imaging MIMO array in [8, 9, 12–14, 17]. It should be noted that the equivalent concept of effective array other than co-array was used in [8, 9, 17]. For narrow band far-field imaging, the co-array together with its radiation pattern can fully describe the overall performance over the azimuth direction θ of the MIMO array. However, for wideband far-field imaging,

the radiated waveforms vary throughout time and angle, even in the far fields of the array. Therefore, the radiation pattern is a function of both the azimuth direction θ and the additional dimension of time or range. The wideband radiation pattern of the co-array is expressed as [14, 15]

$$P_c(\theta, t) = \sum_{i=0}^{MN-1} w_{c,i} A\left(t - \frac{x_{c,i}\sin\theta}{c}\right) e^{-jkx_{c,i}\sin\theta}, \quad (5)$$

where k is the wavenumber of the central carrier frequency, c is the speed of light, and $A(t)$ is the envelope of the transmitted wideband pulse, possibly after pulse compression. In the ideal monochromatic case, $A(t)$ is a constant equal to unity.

To compare with narrowband beam pattern, the time dimension of the wideband beam pattern must be reduced. There are many ways to reduce the time dimension of the wideband beam pattern. The commonly used method is to take the maximum time response at each angular location [17, 18]

$$P_c(\theta) = \max_t \left|P_c(\theta, t)\right|. \quad (6)$$

It should be noted that the method loses the information concerning the temporal shape of the radiation pattern.

2.2. Virtual Aperture. In the field of radar imaging, the concept of two-way virtual aperture rather than the co-array is usually adopted to analyze the MIMO array. The equivalent monostatic illumination angle is approximated by the bisector of the bistatic angle of the measurement using the physical-optic model for bistatic scattering of point scatterers at small bistatic angles [19]. Based on this theorem, an equivalent monostatic transmit/receive element (virtual element) located midway between the transmit and the receive elements was introduced under the far-field condition in [4]. Therefore, the location of the ith virtual element of the virtual aperture for the MIMO array mentioned above is given as

$$\mathbf{r}_{v,i} = (x_{v,i}, 0) = \left(\frac{x_{t,m} + x_{r,n}}{2}, 0\right), \quad (7)$$

where $i = (m+1)(n+1) - 1$ for $m = 0, 1, 2, \ldots M-1$ and $n = 0, 1, 2, \ldots, N-1$. The weighting coefficients of the virtual elements are the same as those of co-array elements, that is, $w_{v,i} = w_{c,i}$ for $i = 0, 1, 2, \ldots, MN-1$.

Within the assumption that the wave field propagates with half of the actual speed, the monostatic transmit/receive element can be treated as one-way element at the same location. Thus, the radiation pattern of the virtual array for wideband far-field imaging is

$$P_v(\theta) = \sum_{i=0}^{MN-1} w_{v,i} A\left(t - \frac{2x_{v,i}\sin\theta}{c}\right) e^{-j2kx_{v,i}\sin\theta}. \quad (8)$$

Note that $w_{v,i} = w_{c,i}$ and $x_{v,i} = x_{c,i}/2$ for $i = 0, 1, 2, \ldots, MN-1$, we get

$$P_v(\theta) = P_c(\theta). \quad (9)$$

Equation (9) indicates the equivalence of the concept of the one-way co-array and the concept of the two-way virtual aperture. In this paper, we are mainly concerned about active imaging. The concept of the two-way virtual aperture is adopted.

3. Point Spread Function

Beam pattern mentioned above can fully describe the overall performance of the array in the far field. Unfortunately, it does not work in the near field. Actually, an imaging system can be fully characterized by the point spread function (PSF) defined as the response of the imaging system to an ideal point source, despite the variations of the transmitted waveform, angle, and distance of focus. The main lobe width of the PSF is a measurement of achievable resolution the grating lobes location and levels of the PSF determine the ambiguity region and their intensities, and the side lobe level of the PSF indicates the capabilities of distinguishing weaker scatterers in the proximity of the strong ones.

For narrow band far-field imaging, the equivalence between the virtual aperture and the original MIMO array has been demonstrated. Unfortunately, there are increasing approximate errors with shorter focus distance and wider band of transmitted signal. The approximation error for the wide band imaging MIMO array can be estimated and analyzed based on the analysis of the PSF of the virtual aperture and the PSF of the original MIMO array.

The imaging geometry of the MIMO array with an ideal point scatterer located at $\mathbf{r}_o = (x_o, y_o)$ is shown in Figure 1. Suppose $S(\omega)$ is the spectrum of the transmitted wideband signal $s(t)$, then $s(t)$ is the inverse Fourier transform of $S(\omega)$, given by

$$s(t) = \frac{1}{2\pi}\int_{-\infty}^{\infty} S(\omega) e^{j\omega t} d\omega. \quad (10)$$

Ideally, if the signal $s(t)$ is time limited, the spectrum $S(\omega)$ spreads all over the frequency and vice versa. Practically, the transmitted waveform is specially designed such that it is approximately both time limited and bandwidth limited. Further, the spectrum $S(\omega)$ is approximated by its uniformly sampled discrete values, resulting in the well-known stepped frequency (SF) waveform. Suppose the frequency bandwidth of the spectrum is $[f_0, f_{P-1}]$, a stepped frequency approximation to (10) is given as

$$s(t) = \sum_{p=0}^{P-1} S\left(f_p\right) e^{j2\pi f_p t}, \quad (11a)$$

$$f_p = \left(f_0 + p\Delta f\right), \quad p = 0, 1, \ldots, P-1, \quad (11b)$$

where $S(f_p)$ can be considered as the frequency weighting function of the SF waveform. For simplicity, we use unity weighting function with $S(f_p) = 1$ in the following text. It should be noted that the P frequency samples are usually transmitted in the form of gated narrowband pulse, step by step. Further description of the SF waveform can be found in [5, 13].

Under the assumption of free space propagation and for the pth frequency, the two-way Green's function of the mth transmit and nth receive pair to the point scatterer is given by

$$\begin{aligned} &G\left(\mathbf{r}_{t,m}, \mathbf{r}_{r,n}, \mathbf{r}_o, f_p\right) \\ &= \frac{1}{4\pi\left|\mathbf{r}_{t,m}-\mathbf{r}_o\right|} e^{-jk_p\left|\mathbf{r}_{t,m}-\mathbf{r}_o\right|} \cdot \left(\frac{1}{4\pi\left|\mathbf{r}_{r,n}-\mathbf{r}_o\right|} e^{-jk_p\left|\mathbf{r}_{r,n}-\mathbf{r}_o\right|}\right) \\ &= \frac{1}{16\pi^2\left|\mathbf{r}_{t,m}-\mathbf{r}_o\right|\left|\mathbf{r}_{r,n}-\mathbf{r}_o\right|} e^{-jk_p\left(\left|\mathbf{r}_{t,m}-\mathbf{r}_o\right|+\left|\mathbf{r}_{r,n}-\mathbf{r}_o\right|\right)}, \end{aligned} \tag{12}$$

where $k_p = 2\pi/\lambda_p$ is the wavenumber and $\lambda_p = c/f_p$ is the wavelength of the pth frequency step.

PSF of the MIMO array imaging system is the output image of the ideal point source for scanning position $\mathbf{r} = (x, y)$, formulated by

$$\begin{aligned} &\mathrm{PSF}_M\left(\mathbf{r}, \mathbf{r}_o\right) \\ &= \sum_{m=0}^{M-1}\sum_{n=0}^{N-1}\sum_{p=0}^{P-1}\left(G\left(\mathbf{r}_{t,m}, \mathbf{r}_{r,n}, \mathbf{r}_o, f_p\right) G^{-1}\left(\mathbf{r}_{t,m}, \mathbf{r}_{r,n}, \mathbf{r}, f_p\right)\right) \\ &= \sum_{m=0}^{M-1}\sum_{n=0}^{N-1}\sum_{p=0}^{P-1}\frac{\left|\mathbf{r}_{t,m}-\mathbf{r}\right|\left|\mathbf{r}_{r,n}-\mathbf{r}\right|}{\left|\mathbf{r}_{t,m}-\mathbf{r}_o\right|\left|\mathbf{r}_{r,n}-\mathbf{r}_o\right|} \\ &\qquad \times e^{-jk_p\left(\left|\mathbf{r}_{t,m}-\mathbf{r}_o\right|+\left|\mathbf{r}_{r,n}-\mathbf{r}_o\right|-\left|\mathbf{r}_{t,m}-\mathbf{r}\right|-\left|\mathbf{r}_{r,n}-\mathbf{r}\right|\right)}. \end{aligned} \tag{13}$$

Equation (13) indicates that the PSF of the active imaging MIMO array is a spatial variant function of the target location $\mathbf{r}_o$, scanning position $\mathbf{r}$, and the frequency of the transmitted signal.

Similarly, we can get the approximate PSF from the equivalent virtual array, expressed as

$$\begin{aligned} &\mathrm{PSF}_V\left(\mathbf{r}, \mathbf{r}_o\right) \\ &= \sum_{i=0}^{MN-1}\sum_{p=0}^{P-1}\frac{\left|\mathbf{r}_{v,i}-\mathbf{r}\right|^2}{\left|\mathbf{r}_{v,i}-\mathbf{r}_o\right|^2} e^{-j2k_p\left(\left|\mathbf{r}_{v,i}-\mathbf{r}_o\right|-\left|\mathbf{r}_{v,i}-\mathbf{r}\right|\right)}. \end{aligned} \tag{14}$$

Actually, the concepts of PSF and beam pattern are identical under far-field narrow band condition. Let the carrier frequency of the narrow band signal is f_0, then $s(t) = e^{j2\pi f_0 t}$. Under far-field condition, the following approximations hold for $m = 0, 1, 2, \ldots, M-1$ and $n = 0, 1, 2, \ldots, N-1$:

$$\left|\mathbf{r}-\mathbf{r}_{t,m}\right| = |\mathbf{r}| - x_{t,m}\sin\theta, \tag{15a}$$

$$\left|\mathbf{r}_o-\mathbf{r}_{t,m}\right| = \left|\mathbf{r}_o\right| - x_{t,m}\sin\theta_0, \tag{15b}$$

$$\left|\mathbf{r}-\mathbf{r}_{r,n}\right| = |\mathbf{r}| - x_{r,n}\sin\theta, \tag{15c}$$

$$\left|\mathbf{r}_o-\mathbf{r}_{r,n}\right| = \left|\mathbf{r}_o\right| - x_{r,n}\sin\theta_0, \tag{15d}$$

$$\left|\mathbf{r}_{t,m}-\mathbf{r}\right| \approx \left|\mathbf{r}_{t,m}-\mathbf{r}_o\right|, \tag{15e}$$

$$\left|\mathbf{r}_{r,n}-\mathbf{r}\right| \approx \left|\mathbf{r}_{r,n}-\mathbf{r}_o\right|, \tag{15f}$$

where θ and θ_0 are the incidence angles of plane wave from $\mathbf{r}$ and $\mathbf{r}_o$, respectively.

Substitute (15a), (15b), (15c), (15d), (15e), and (15f) and $p = 0$ into (13), the $\mathrm{PSF}_M(\mathbf{r}, \mathbf{r}_o)$ can be further expressed as the function of θ, θ_0, and k_0

$$\begin{aligned} &\mathrm{PSF}_M\left(\theta, \theta_0\right) \\ &= \sum_{m=0}^{M-1}\sum_{n=0}^{N-1} e^{jk_0 2\left(|\mathbf{r}|-|\mathbf{r}_o|\right)} e^{jk_0\left(x_{t,m}+x_{r,n}\right)\sin\theta_0} e^{-jk_0\left(x_{t,m}+x_{r,n}\right)\sin\theta}. \end{aligned} \tag{16}$$

If we are only interested in the performance of the PSF over the azimuth direction θ, the fixed coefficient $e^{j2k_0(|\mathbf{r}|-|\mathbf{r}_o|)}$ can be ignored. Using a change of variables

$$w_{t,m} = e^{jk_p x_{t,m}\sin\theta_0}, \tag{17a}$$

$$w_{r,m} = e^{jk_p x_{r,n}\sin\theta_0}. \tag{17b}$$

Expression (16) would take the form

$$\mathrm{PSF}_M\left(\theta, \theta_0\right) = \sum_{m=0}^{M-1} w_{t,m} e^{-jk_p x_{t,m}\sin\theta} \sum_{n=0}^{N-1} w_{r,n} e^{-jk_p x_{r,n}\sin\theta} \tag{18}$$

which is the same expression as the radiation pattern of the MIMO array as shown in (4).

4. UWB STVA Array

4.1. UWB MIMO Array Design. Proper array design is helpful for simplifying the system structure and improving the imaging quality. The virtual aperture concept offers a basic framework for selecting transmit and receive aperture functions [8, 14]. A virtual aperture desynthesis approach is applied to design the UWB MIMO array with uniform weighting according to the desired main lobe width and side lobe level in [8, 14]. The essential step of the approach is the deconvolution process of (7). Unfortunately, given the two-way virtual aperture and the number of transmit and receive elements, the result of the de-convolution is not unique. Consider a linear virtual aperture with 32 virtual elements located uniformly within an aperture of 3.1 m; five MIMO arrays with different topology are desynthesized each is composed of 2 transmit elements and 16 receive elements, as shown in Figure 2. Additional metric must be involved to evaluate the performance of the five different MIMO arrays. Further, in UWB MIMO array imaging application, the performance of a UWB MIMO array is related not only to the topology of the array and the number of the array elements, but also to the spectrum of the transmitted signal.

The spectrum of the transmitted signal may be approximated by its uniformly sampled discrete values, which is the form of stepped frequency waveform. In TWI application, stepped frequency continuous wave (SFCW) is one of the mostly used UWB waveforms [5, 20].

For UWB SFCW signal, the design process of an imaging MIMO array starts from the required resolution and the peak

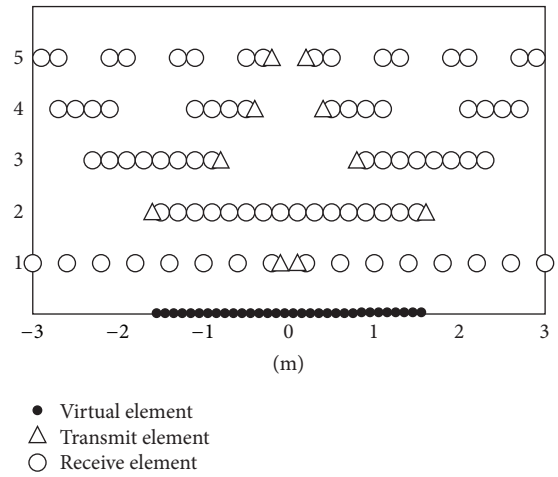

Figure 2: Linear MIMO arrays with the same virtual aperture array.

side lobe of the image, which determines the minimal aperture length and the number of virtual elements of the two-way virtual aperture from (14). In the far-field narrowband condition, the 3 dB width of the PSF main lobe in the azimuth direction steering to Θ from the boresight is approximately as [21]

$$\Delta\theta \approx \frac{0.886\lambda}{2L\cos(\Theta)}, \tag{19}$$

where L is the two-way aperture length and λ is the wavelength of the transmitted waveform.

Then the number of transmit and receive elements can be chosen under the relation

$$N_v = N_t \cdot N_r, \tag{20}$$

where N_t, N_r, and N_v are the numbers of transmit, receive, and the virtual elements, respectively.

In the next step, the transmit and receive array topology can be derived through deconvolution of (7), which is similar to the process in [5, 20]. The de-convolution procedure is not unique and allows for multiple solutions. To select the optimal one among them, the monostatic-to-bistatic equivalence condition in radar signal processing should be considered. Remarking that the radar cross section (RCS) of a point scatterer (the object is modeled as a set of discrete scattering centers) is dependent on the incidence and reflection angle, the equivalence is valid only at a small range of angle. Thus, we hope to decrease the overall length of the physical aperture including all the transmit and receive elements, and we also hope that the transmit aperture and the receive aperture have similar illumination geometry to all the point scatterers. For the case listed in Figure 2, option 2 with the two transmit elements located at either end of the linear uniform receive array is the optimal selection. We called the linear MIMO with similar topology as the split transmitter virtual aperture (STVA) array.

After that, the configuration of the STVA array is adjusted considering the mutual coupling and the UWB antenna

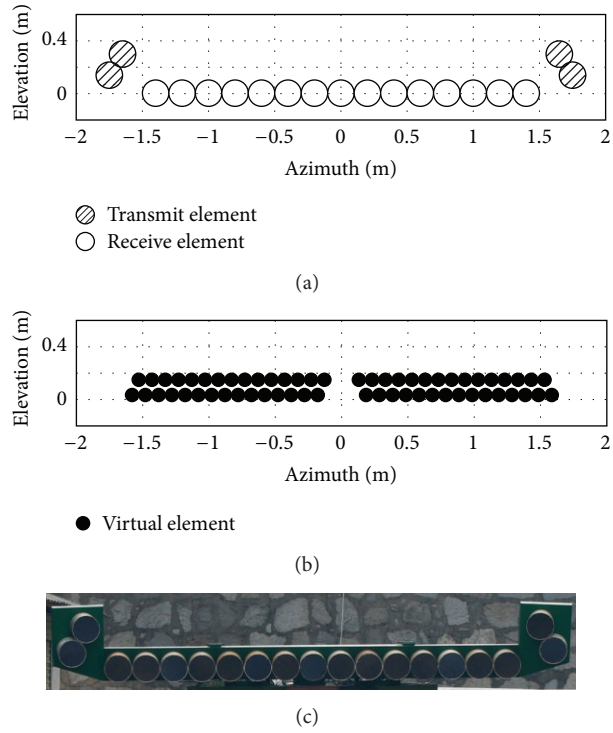

Figure 3: Designed split transmitter virtual aperture array. (a) Topology; (b) equivalent two-way virtual aperture; (c) front view of the of the STVA array.

element size. For array transmitting continuous waveform, the direct coupling from the transmit to the receive elements decreases the receiver sensitivity, saturates the receiver, and even damages the receiver. The transmit and receive elements should be placed at a proper distance to improve the T/R isolation, assuring that the receiver is not jammed. The transmit elements may move a little distance away at both azimuth and elevation levels. It should be noted that theoretically the displacement in elevation of the transmit elements does not influence the array performance in the azimuth direction.

Finally, during the array design, the center carrier frequency is used to calculate the main lobe width and side lobe level. In TWI application, the transmitted UWB signal extends across multiple octaves in the frequency domain. The spacing of the designed array elements may cause grating lobes at the higher operational frequency. If this does occur, the number of transmit elements should be increased.

4.2. UWB STVA Array Analysis. Using the array design approach described above, an example of STVA array has been designed for TWI application. The topology of the STVA array is shown in Figure 3(a). The STVA array consists of 4 transmit and 15 receive elements. The receive array consists of 15 elements with interelement spacing of 0.2 m. The four transmit elements are located at (−1.75 m, 0.1268 m), (−1.65 m, 0.3 m), (1.65 m, 0.3 m), and (1.75 m, 0.1268 m), respectively, two at either end of the receive array. The physical aperture length of the array is 3.5 m (the largest distance between two elements of the array measured from

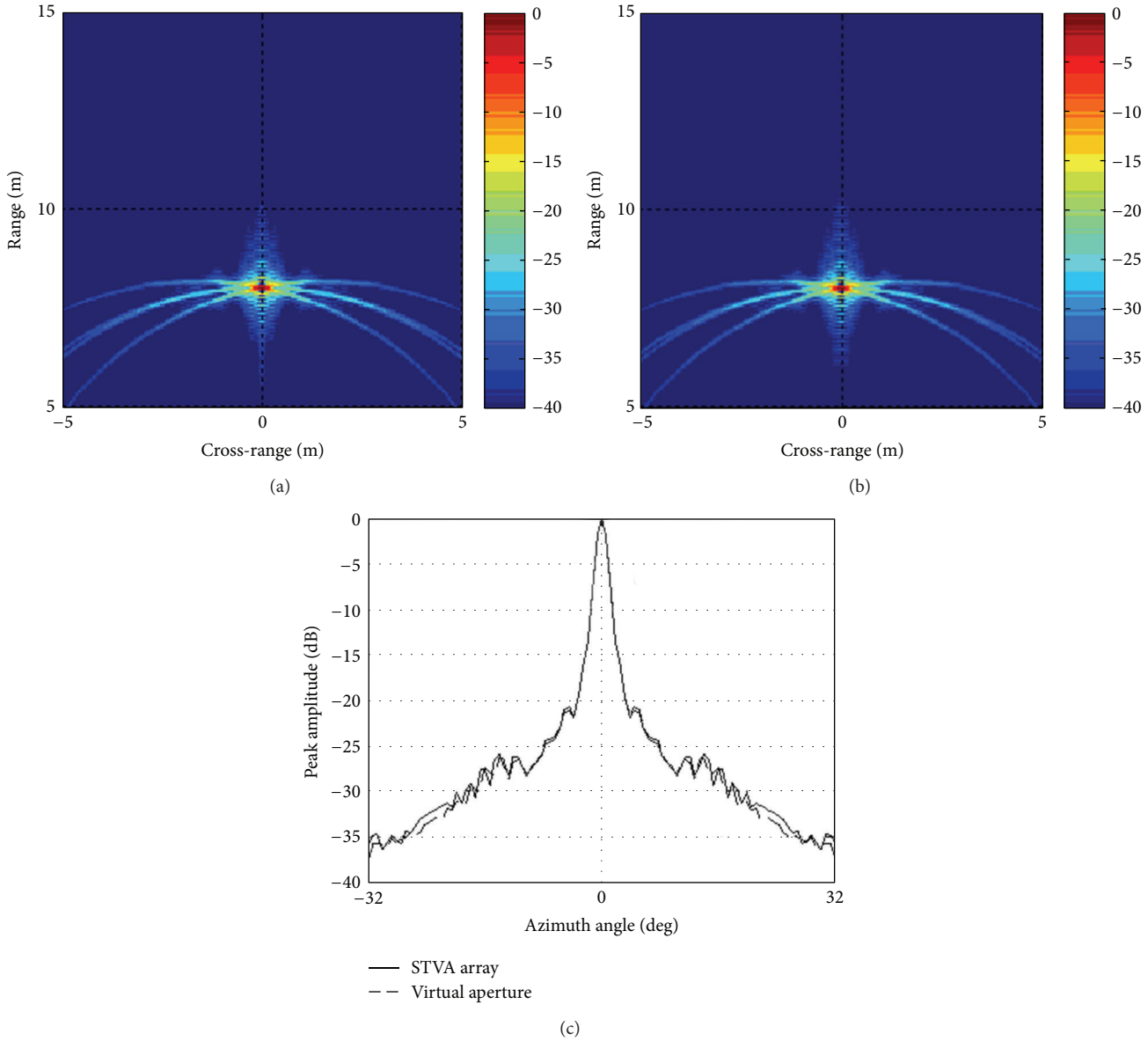

FIGURE 4: Comparison of the PSFs between the STVA array and its virtual array with focal point at 8 m. (a) STVA array. (b) Virtual array. (c) Peak amplitude pattern in azimuth angle.

phase center to phase center). The transmit elements are located at least 0.37 m away from the nearest receive element (from phase center to phase center) to reduce the direct coupling from the transmit elements to the receive elements to an acceptable level. Using the concept of virtual phase center, a virtual aperture with 60 virtual transmit/receive (T/R) elements is synthesized, as shown in Figure 3(b). The interelement spacing of the synthesized virtual aperture is 0.05 m except a gap of 0.25 m at the midpoint, synthesizing a total aperture length of 3.15 m. The gap at the midpoint is due to the separation of the transmit elements. And it will result in a slight acceptable increase of the side lobe level, which will be shown in the following. Both the transmit and receive antennas are UWB Archimedean spirals with a diameter of 0.2 m, working at the frequency band of 0.5 G Hz ~ 2.0 GHz. The array is mounted on the top of a van with the front view of the STVA array shown in Figure 3(c).

It has been demonstrated that under the narrowband far-field condition, the equivalence of the PSF between the MIMO array and its virtual aperture is exact, and the virtual aperture fully describes the overall performance of the original MIMO array, while under wideband conditions, the equivalence becomes approximate. Therefore, it is necessary to compare the PSF between the original MIMO array and its virtual aperture to verify the feasibility of the design approach.

For narrow band array, the boundary of the far-field region is $R_f > L^2/\lambda$, where L is the largest distance

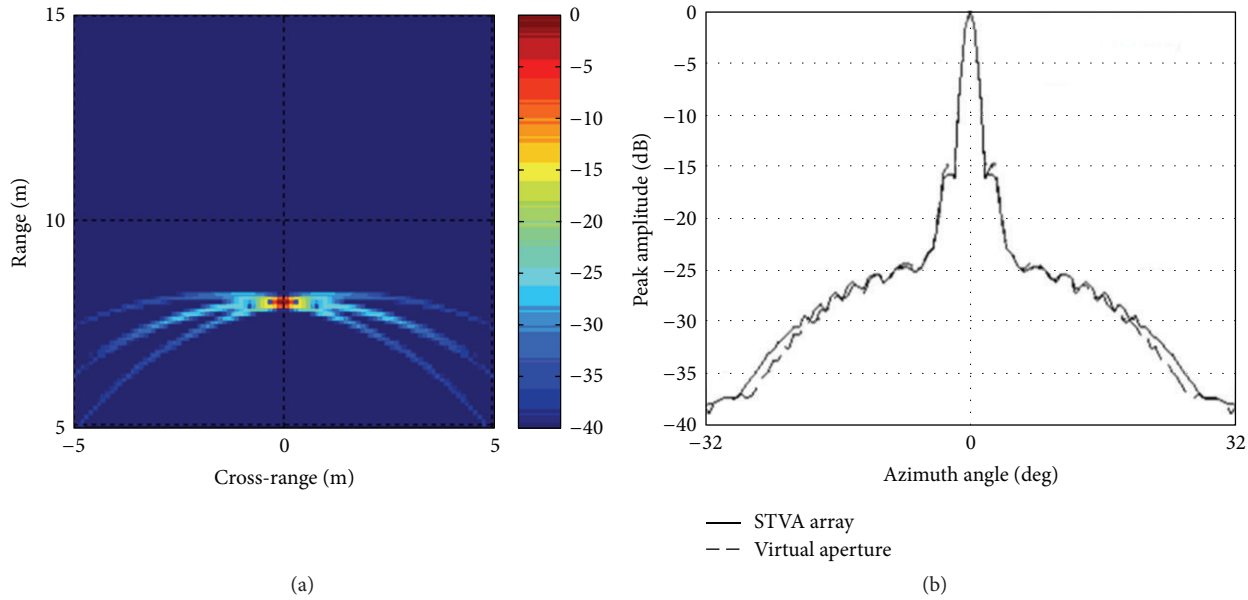

Figure 5: Imaging results of the STVA array with Hamming function in frequency. (a) Imaging result. (b) Peak amplitude pattern in azimuth angle.

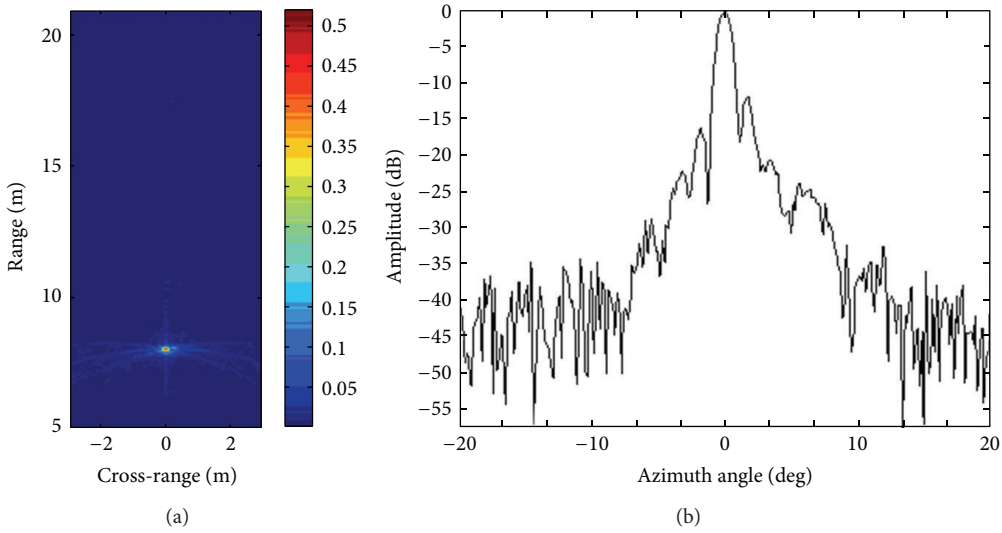

Figure 6: Image of metal trihedral corner reflector. (a) Imaging result. (b) Peak amplitude pattern in azimuth angle.

Figure 7: Experimental imaging scene.

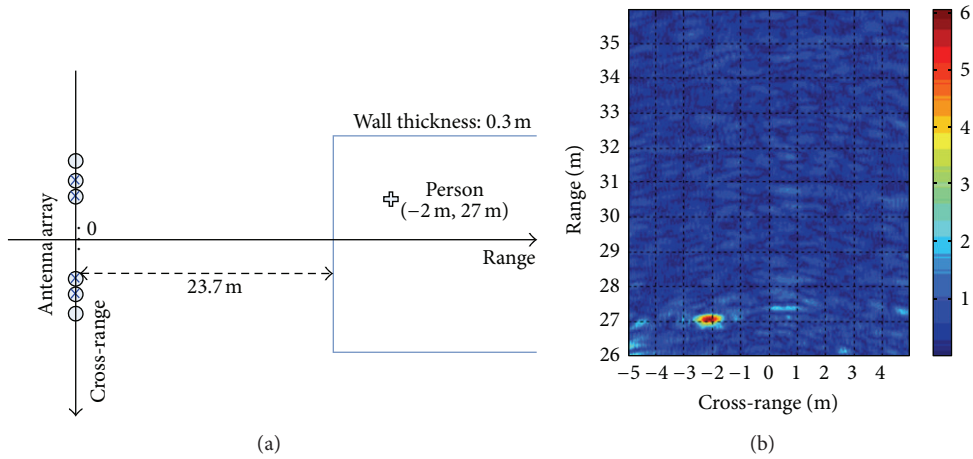

Figure 8: Image of a person inside the building. (a) Geometry of imaging. (b) Imaging result.

between two elements of the array. Using this equation, for the designed UWB STVA array, we get the far-field boundary of 16.5 m at the lowest operational frequency and 66 m at the highest operational frequency. For a vehicle-borne TWI system, the detection range is usually between 5 m and 50 m, which spans the near-and far-field boundary region. Thus, the influence of target distance on the performance of the MIMO array should also be investigated.

The PSF of the original STVA array and the PSF of its virtual aperture with focal point at the location (0, 8 m) are illustrated in Figures 4(a) and 4(b), respectively. The peak amplitude patterns in the azimuth angle of both the PSFs are shown in Figure 4(c) for more direct comparison, which demonstrated that both patterns are almost equivalent. The farther the focal distance, the smaller the approximation error.

The cross-range resolution of the point target at 8 m is about 0.246 m. For the large relative bandwidth of the transmitting UWB waveform (120%), the first side lobe is about 22 dB lower than the peak of the main lobe. In theory, the wider the bandwidth, the lower the side lobe. In the ideal narrow band case, the first side lobe level is about −13 dB.

During the calculation of PSFs, frequency weight coefficients are set to unity, which will result in the high level range side lobe of about −13 dB. In practical imaging processing, different types of frequency weighting function are used to reduce the range side lobe level. Unfortunately, frequency weighting function also affects the performance of the azimuth of the UWB array. The image results of the same ideal point target with hamming weighting function in frequency are shown in Figure 5. The range side lobe level is reduced to about −40 dB, while the azimuth side lobe level is increased to −15 dB.

The simulation results are verified with measured data. A 0.1 m metal trihedral corner reflector was placed 8 m in front of the STVA array on a plane ground. The resulting image is shown in Figure 6. The cross-range resolution and the location distribution of the side lobe are much the same as the simulation, but the level of the first right side lobe is a little higher than the simulation, which is likely due to the nonideality of the measurement setup.

5. Experimental Results

The designed STVA array has been successfully applied in TWI application. One of the active imaging scenes is shown in Figure 7. The imaging array is placed at the left side of the cinderblock garage, and the array is parallel to the side wall, at a distance of 23.7 m. The thickness of the cinderblock wall is about 30 cm. The garage is 10 m wide and 16 m deep. During the acquisition of data, a man with the height of 172 cm walks between the front wall and the back wall along the range direction in the room.

A standard differential back projection (BP) imaging algorithm [5] is adopted to process the acquired data. The time interval of differential processing is 300 ms. The static background clutter is eliminated and the moving person is imaged. A series of differential images is acquired, and walking history of the person is clearly shown combining all the frames of images. One of the images with the person located at (−2 m, 27 m) is shown in Figure 8.

6. Conclusion

The virtual aperture concept offers a basic framework for selecting transmit and receive aperture functions of MIMO array under narrow band far-field condition. In this paper, the MIMO array design approach is extended for the near-field wide band case. Combining the approach of virtual aperture decomposition with the monostatic-to-bistatic equivalence theorem, a kind of linear UWB MIMO array with the shortest physical aperture length among these synthesizing the same virtual aperture, the STVA array, was designed for through the wall imaging. The PSF of the original STVA array and the PSF of its virtual aperture are compared, demonstrating that the approximation error is negligible even at the nearest focal range.

The imaging performance of the designed STVA array in the near field is fully analyzed through both numerical and measured data. The designed STVA array has been successfully applied to imaging moving targets inside buildings.

References

[1] G. L. Charvat, L. C. Kempel, E. J. Rothwell, C. M. Coleman, and E. L. Mokole, "An ultrawideband (UWB) switched-antenna-array radar imaging system," in *Proceedings of the 4th IEEE International Symposium on Phased Array Systems and Technology (Array '10)*, pp. 543–550, October 2010.

[2] A. G. Yarovoy, T. G. Savelyev, P. J. Aubry, P. E. Lys, and L. P. Ligthart, "UWB array-based sensor for near-field imaging," *IEEE Transactions on Microwave Theory and Techniques*, vol. 55, no. 6, pp. 1288–1295, 2007.

[3] A. Nelander, "Switched array concepts for 3-D radar imaging," in *Proceedings of the IEEE International Radar Conference (RADAR '10)*, pp. 1019–1024, Washington, DC, USA, May 2010.

[4] K. E. Browne, R. J. Burkholder, and J. L. Volakis, "Through-wall opportunistic sensing system utilizing a low-cost flat-panel array," *IEEE Transactions on Antennas and Propagation*, vol. 59, no. 3, pp. 859–868, 2011.

[5] B. Lu, Q. Song, Z. Zhou, and X. Zhang, "Detection of human beings in motion behind the wall using SAR interferogram," *IEEE Geoscience and Remote Sensing Letters*, vol. 9, no. 5, pp. 968–971, 2012.

[6] F. Ahmad, M. G. Amin, and S. A. Kassam, "Synthetic aperture beamformer for imaging through a dielectric wall," *IEEE Transactions on Aerospace and Electronic Systems*, vol. 41, no. 1, pp. 271–283, 2005.

[7] F. Ahmad, Y. Zhang, and M. G. Amin, "Three-dimensional wideband beamforming for imaging through a single wall," *IEEE Geoscience and Remote Sensing Letters*, vol. 5, no. 2, pp. 176–179, 2008.

[8] X. Zhuge and A. Yarovoy, "Near-field ultra-wideband imaging with two-dimensional sparse MIMO array," in *Proceedings of the 4th European Conference on Antennas and Propagation (EuCAP '10)*, pp. 1–4, Barcelona, Spain, April 2010.

[9] X. Zhuge and A. G. Yarovoy, "A sparse aperture MIMO-SAR-based UWB imaging system for concealed weapon detection," *IEEE Transactions on Geoscience and Remote Sensing*, vol. 49, no. 1, pp. 509–518, 2011.

[10] D. W. Bliss and K. W. Forsythe, "Multiple-input multiple-output (MIMO) radar and imaging: degrees of freedom and resolution," *IEEE Transactions on Ultrasonics, Ferroelectrics and Frequency Control*, vol. 43, no. 1, pp. 7–14, 1996.

[11] J. Li and P. Stoica, "MIMO radar with colocated antennas," *IEEE Signal Processing Magazine*, vol. 24, no. 5, pp. 106–114, 2007.

[12] F. Ahmad and S. A. Kassam, "Coarray analysis of the wide-band point spread function for active array imaging," *Signal Processing*, vol. 81, no. 1, pp. 99–115, 2001.

[13] F. Ahmad, G. J. Frazer, S. A. Kassam, and M. G. Amin, "Design and implementation of near-field, wideband synthetic aperture beamformers," *IEEE Transactions on Aerospace and Electronic Systems*, vol. 40, no. 1, pp. 206–220, 2004.

[14] Z. Li, T. Jin, B. Chen, and Z. Zhou, "A coarray based MIMO array design method for UWB imaging," in *Proceedings of the IET International Conference on Radar Systems*, pp. 1–4, Glasgow, UK, October 2012.

[15] W.-Q. Wang, "Virtual antenna array analysis for MIMO synthetic aperture radars," *International Journal of Antennas and Propagation*, vol. 2012, Article ID 587276, 10 pages, 2012.

[16] R. T. Hoctor and S. A. Kassam, "The unifying role of the coarray in aperture synthesis for coherent and incoherent imaging," *Proceedings of the IEEE*, vol. 78, no. 4, pp. 735–752, 1990.

[17] J. L. Schwartz and B. D. Steinberg, "Ultrasparse, ultrawideband arrays," *IEEE Transactions on Ultrasonics, Ferroelectrics, and Frequency Control*, vol. 45, no. 2, pp. 376–393, 1998.

[18] V. Murino, A. Trucco, and A. Tesei, "Beam pattern formulation and analysis for wide-band beamforming systems using sparse arrays," *Signal Processing*, vol. 56, no. 2, pp. 177–183, 1997.

[19] C. J. Bradley, P. J. Collins, D. G. Falconer, J. Fortuny-Guasch, and A. J. Terzuoli Jr., "Evaluation of a near-field monostatic-to-bistatic equivalence theorem," *IEEE Transactions on Geoscience and Remote Sensing*, vol. 46, no. 2, pp. 449–456, 2008.

[20] M. G. Amin, *Through-the-Wall Radar Imaging*, CRC Press, New York, NY, USA, 2011.

[21] G. Franceschetti and R. Lanari, *Synthetic Aperture Radar Processing*, CRC Press, Boca Raton, Fla, USA, 1999.

Hindawi Publishing Corporation
International Journal of Antennas and Propagation
Volume 2013, Article ID 837639, 7 pages
http://dx.doi.org/10.1155/2013/837639

Research Article

A Modified STAP Estimator for Superresolution of Multiple Signals

Zhongbao Wang, Junhao Xie, Zilong Ma, and Taifan Quan

Department of Electronic Engineering, Harbin Institute of Technology, Harbin 150001, China

Correspondence should be addressed to Zhongbao Wang; wzb969@163.com

Received 22 January 2013; Accepted 8 April 2013

Academic Editor: Ulrich Nickel

A modified space-time adaptive processing (STAP) estimator is described in this paper. The estimator combines the incremental multiparameter (IMP) algorithm and the existing beam-space preprocessing techniques yielding a computationally cheap algorithm for the superresolution of multiple signals. It is a potential technique for the remote sensing of the ocean currents from the broadened first-order Bragg sea echo spectrum of shipborne high-frequency surface wave radar (HFSWR). Some simulation results and real-data analysis are shown to validate the proposed algorithm.

1. Introduction

The measurement of the near-surface currents is a very difficult task by using conventional methods, especially under some harsh sea conditions. Many advanced marine measurement instruments, such as drifting buoys [1] and acoustic current meters [2], have been used to collect sea state information. However, it would be very expensive to collect and interpret data from these devices for the sparse spatial sampling provided. Therefore, it is virtually impossible to form the current maps over a widespread ocean surface timely and accurately with these conventional meters.

In recent years, HFSWR has already become a powerful remote-sensing tool which receives increasing attention from oceanographers and research groups for its good ability to determine the large-scale sea state under all weather conditions [3, 4]. The measurement principle of HFSWR mainly depends on the Bragg resonant scattering theory and Doppler frequency effect theory in the sea echo spectrum of HFSWR. In the absence of ocean currents, the first-order Bragg lines would appear symmetrically above and below the zero Doppler frequency, which are caused by the ocean waves with precisely one-half wavelength of the radar moving towards and away from the radar. In practical application, some displacements will happen in the first-order Bragg lines since the near-surface currents always exist on the ocean [5].

As an extension of shore-based HFSWR, shipborne HFSWR not only inherits all the advantages of shore-based HFSWR but also shows some outstanding features, such as flexibility and mobility. However, some new problems emerge as the radar on board is a moving ship. One of the worst problems is that the first-order Bragg lines have been broadened into two pass bands (when the speed of ship is slow) or one low pass band (when the ship is sailing at a high speed) in the first-order Bragg sea echo spectrum of shipborne HFSWR [6]. For these cases, it will be hard to determine the ocean currents from the broadened sea echo spectrum. Furthermore, the moving ship yields different Doppler shifts to the different azimuth sea echoes. Thus, there exists a certain space-time coupling relation in the received sea echo spectrum of shipborne HFSWR.

The novel space-time IMP algorithm was proposed by Clarke and Spence [7] which was based on one-dimensional IMP algorithm and modified to detect and estimate multiple signals from the conventional beamwidth and (or) Doppler resolution bin. Although space-time IMP estimator effectively improves the robustness of the detection and estimation of multiple signals, the computational load of two-dimensional search process is too heavy for real-time application. Lately, Chadwick [8] used the eigendecomposition method instead of the full-search process to reduce the heavy

computational burden in his proposed polarisation-sensitive IMP algorithm. However, for surface wave radar, this method becomes invalid since the returns of HFSWR are mostly vertical polarization sensitive components.

Many researchers, such as Shaw and Wilkins [9], used beam-space preprocessing technique to reduce the computational load and improve robust performance of high-resolution DOA (direction-of-arrival) estimation algorithms. Recently, Hassanien et al. [10, 11], proposed a new concept about beam-space preprocessing algorithm which was able to suppress the out-of-sector interferences accompanied with the updated array data. This technique was proven to be more robust than the aforementioned beam-space methods.

In this paper, we combine the space-time IMP algorithm and the adaptive beam-space preprocessing technique yielding a computationally cheap space-time adaptive estimator for detection, estimation and super-resolution of multiple signals. The proposed algorithm is validated by simulation results as well as experimental examples.

This paper is organized as follows. First we introduce the signal model. In the following section, the proposed algorithm and some simulation results are presented. The measurement of the near-surface currents of the ocean by shipborne HFSWR and some real-data analysis are presented in Section 4. The final part is the study conclusion.

2. Signal Model

Consider a uniform linear array (ULA) with M omnidirectional antennas and the antenna spacing d. If there are N sources that have been received from a far field with different relative delays and attenuations. The received data $\mathbf{X}$ is then given by [7] as follows:

$$\mathbf{X} = \mathbf{A}\Lambda\mathbf{B}^H + \mathbf{N}, \tag{1}$$

where

$$\begin{aligned} \mathbf{X} &= \left[x_1 \;\; x_2 \;\; \cdots \;\; x_M\right]^T, \\ x_i &= \left[x_i(1) \;\; x_i(2) \;\; \cdots \;\; x_i(L)\right], \end{aligned} \tag{2}$$

$x_i(l)$, $i = 1, 2, \ldots, M$, $l = 1, 2, \ldots, L$ denotes the data received from the ith sensor at lth sampling time, $[\cdot]^T$ denotes the transpose operation, $\mathbf{A} = [\mathbf{a}(\varphi_1) \;\; \mathbf{a}(\varphi_2) \;\; \cdots \;\; \mathbf{a}(\varphi_N)]^T$ is the array manifold matrix,

$$\mathbf{a}(\varphi_i) = \left[1 \;\; \cdots \;\; e^{-j2\pi d(M-1)\sin\varphi_i/\lambda}\right]^T \tag{3}$$

is the steering vector points to the direction φ_i, $i = 1, 2, \ldots, N$, λ denotes wavelength of the radar, Λ is a $(N \times N)$ diagonal matrix containing the signal magnitudes, $\mathbf{B} = [\mathbf{b}(f_1) \;\; \mathbf{b}(f_2) \;\; \cdots \;\; \mathbf{b}(f_N)]$ is a $(L \times N)$ matrix comprising the normalized source waveforms, $\mathbf{b}(f_i) = [1 \;\; e^{-j2\pi f_i} \;\; \cdots \;\; e^{-j2\pi f_i(L-1)}]^T$ is the normalized source waveform, f_i, $i = 1, 2, \ldots, N$ is the frequency of jth source, $[\cdot]^H$ denotes the Hermitian transpose operation, and $\mathbf{N}$ is the $(M \times L)$ matrix comprising the zero mean and σ^2 variance Gaussian noise.

The $(M \times M)$ covariance matrix of the received data is given by

$$\mathbf{R} = E\left\{\mathbf{X}\mathbf{X}^H\right\} = \mathbf{A}\mathbf{S}\mathbf{A}^H + \sigma^2\mathbf{I}, \tag{4}$$

where $E\{\cdot\}$ is the statistical expectation operator, $\mathbf{S} = E\{\Lambda\mathbf{B}^H\mathbf{B}\Lambda^H\}$ is the $(L \times L)$ source covariance matrix, and $\mathbf{I}$ is the identity matrix.

3. Modified STAP Estimator

3.1. Space-Time IMP. Space-time IMP is a two-dimensional maximum likelihood method which uses a set of space-time calibration response vectors to match with the received data. Thus, the primary objective of space-time IMP is to maximize the "signal plus noise" to "expected noise" power ratio (SNR). If the maximum output power is over the threshold, then a target is detected and the corresponding space-time calibration response vector is recorded. In order to reduce the sidelobe leakage of the detected targets and improve the detection and estimation of the potential signals in the residual data, the detected targets are removed from the original data through an orthogonal subspace projection matrix before each iterative stage.

According to the definition of SNR in space-time IMP, we have the following [7]:

$$F(\theta, f) = \frac{\mathbf{W}^H(\theta, f)\,\mathbf{Q}\,\mathrm{vec}(\mathbf{X})\,\mathrm{vec}(\mathbf{X})^H\mathbf{Q}\mathbf{W}(\theta, f)}{\mathbf{W}^H(\theta, f)\,\mathbf{Q}\mathbf{W}(\theta, f)}, \tag{5}$$

where

$$\mathbf{W}(\theta, f) = \mathrm{vec}\left\{\left(\frac{\mathbf{a}(\theta)}{\mathbf{a}^H(\theta)\,\mathbf{a}(\theta)}\right)\left(\frac{\mathbf{b}(f)}{\mathbf{b}^H(f)\mathbf{b}(f)}\right)^H\right\} \tag{6}$$

is the $(ML \times 1)$ space-time calibration response matrix, $\mathrm{vec}\{\cdot\}$ is the vectorization operation, and $\mathbf{Q}$ is an $(ML \times ML)$ orthogonal projection matrix, which is given by

$$\mathbf{Q} = \mathbf{I} - \mathbf{M}\left[\mathbf{M}^H\mathbf{M}\right]^{-1}\mathbf{M}^H, \tag{7}$$

where $\mathbf{M}$ denotes a sum of space-time calibration response vectors corresponding to the detected signals; that is, $\mathbf{Q}$ projects the received data into a subspace orthogonal to the detected signals.

3.2. Adaptive Beam-Space Preprocessing. The adaptive beam-space preprocessing technique was first mentioned in [10] which used the updated data for adaptive suppression of out-of-sector interferences. This technique had been shown to be more robust than the aforementioned beam-space methods.

The primary objective of the data-adaptive beam-space preprocessing is to solve the optimal beam-space matrix

design problem through minimizing the output power of the transformed data, which can be expressed as follows [12]:

$$\begin{aligned} \min_{\mathbf{C}} \quad & \operatorname{tr}\left(\mathbf{C}^H\mathbf{R}\mathbf{C}\right) \\ \text{subject to} \quad & \mathbf{C}^H\mathbf{C} = \mathbf{I} \\ & \mathbf{C}^H\mathbf{a}\left(\theta_b\right) = 1 \quad b = 1, 2, \ldots, B \\ & \left\|\mathbf{C}^H\mathbf{a}\left(\overline{\theta}_k\right)\right\| \le \gamma \quad \overline{\theta}_k \in \overline{\Theta},\ k = 1, \ldots, K, \end{aligned} \tag{8}$$

where $\operatorname{tr}\{\cdot\}$ is the trace of a matrix, $\mathbf{C}$ is the $(M \times B)$ beam-space matrix, B $(B \le M)$ is the beam-space dimension, $\|\cdot\|$ is the vector 2-norm, $\overline{\Theta}$ denotes all out-of-sector directions which are divided into K angular grids, $\{\theta_b\}_{b=1}^{B}$ and $\{\overline{\theta}_k\}_{k=1}^{K}$ are the angles corresponding to the in-of-sector and out-of-sector directions, and γ is the stopband attenuation parameter which should meet the requirement [12]

$$\begin{aligned} \min_{\mathbf{C}} \quad & \gamma \\ \text{subject to} \quad & \mathbf{C}^H\mathbf{C} = \mathbf{I} \\ & \mathbf{C}^H\mathbf{a}\left(\theta_b\right) = 1 \quad b = 1, 2, \ldots, B \\ & \left\|\mathbf{C}^H\mathbf{a}\left(\overline{\theta}_k\right)\right\| \le \gamma \quad \overline{\theta}_k \in \overline{\Theta},\ k = 1, \ldots, K. \end{aligned} \tag{9}$$

After the beam-space transformation, the array steering vector matrix $\mathbf{a}$ and manifold matrix $\mathbf{A}$ have already transformed into

$$\begin{aligned} \widetilde{\mathbf{a}} &= \mathbf{C}^H\mathbf{a}, \\ \widetilde{\mathbf{A}} &= \mathbf{C}^H\mathbf{A}. \end{aligned} \tag{10}$$

Then, the $(B \times B)$ covariance matrix $\widetilde{\mathbf{R}}$ in beam-space should be rewritten as

$$\widetilde{\mathbf{R}} = \widetilde{\mathbf{A}}\mathbf{S}\widetilde{\mathbf{A}}^H + \sigma^2\mathbf{I}. \tag{11}$$

Obviously, the dimension of the matrix $\widetilde{\mathbf{R}}$ is lower than that of $\mathbf{R}$. This fact is exploited in all beam-space-based methods to reduce computational load compared with the element-space algorithms [10].

3.3. Space-Time Adaptive Beam-Space IMP. In this section, we show how the conventional space-time estimator combines with the adaptive beam-space preprocessing technique to present a computationally cheap space-time adaptive beam-space IMP estimator.

Following the discussion above, the two-dimensional discriminants shown in (5) should be modified as

$$\widetilde{F}\left(\theta, f\right) = \frac{\widetilde{\mathbf{W}}^H\left(\theta, f\right)\widetilde{\mathbf{Q}}\operatorname{vec}\left(\mathbf{C}^H\mathbf{X}\right)\operatorname{vec}\left(\mathbf{C}^H\mathbf{X}\right)^H\widetilde{\mathbf{Q}}\widetilde{\mathbf{W}}\left(\theta, f\right)}{\widetilde{\mathbf{W}}^H\left(\theta, f\right)\widetilde{\mathbf{Q}}\widetilde{\mathbf{W}}\left(\theta, f\right)}, \tag{12}$$

where

$$\mathbf{W}'\left(\theta, f\right) = \operatorname{vec}\left\{\left(\frac{\mathbf{C}^H\mathbf{a}\left(\theta\right)}{\mathbf{a}^H\left(\theta\right)\mathbf{C}\mathbf{C}^H\mathbf{a}\left(\theta\right)}\right)\left(\frac{\mathbf{b}\left(f\right)}{\mathbf{b}^H\left(f\right)\mathbf{b}\left(f\right)}\right)^H\right\}, \tag{13}$$

and $\widetilde{\mathbf{Q}}$ has been reduced to a $BL \times BL$ matrix in beam-space domain, which is given by

$$\widetilde{\mathbf{Q}} = \mathbf{I} - \widetilde{\mathbf{M}}\left[\widetilde{\mathbf{M}}^H\widetilde{\mathbf{M}}\right]^{-1}\widetilde{\mathbf{M}}^H, \tag{14}$$

where $\widetilde{\mathbf{M}}$ denotes a sum of space-time calibration response vectors corresponding to the detected signals in beam-space domain.

3.4. Threshold Setting. How to select an appropriate threshold to terminate the iterative process in IMP algorithm is very important. Theoretically, when all "significant peaks" have been detected and cleared out from the received data, there is only a completely flat plane in the residual scan [13]. However, it is impossible to accurately estimate the noise statistics from the limited received data. Furthermore, the definition of "significant peak" in IMP algorithm has not been clearly reported.

In the paper, we use a double-threshold setting method to ensure that the iterative process is halted timely. First, we check two successive scans before the next iteration. If the difference between the two scans is comparable to that of the "expected noise" level, that is, no "significant peak" appears during the last scan, then the iterative process should be halted. Besides, if the difference between two successive estimations has reached the preset threshold, which suggests that the iterations are estimating the same target, then the iterative process should be halted as well.

3.5. Simulation Results. Several simulation results are shown in this section to test the performance of the modified algorithm through comparing it with several conventional algorithms.

During the simulations, we assume that the radar works at $f = 6\,\text{MHz}$, which contains an ULA with $M = 8$ omnidirectional sensors and the elements are spaced one-half wavelength apart. The half power beamwidth is approximately 13°. The number of snapshots $L = 32$ and the beam-space dimension $B = 2$ are chosen for our simulations. The adaptive beam-space matrix has been solved using the cvx optimization MATLAB toolbox. Since the minimum value in (9) is $\gamma_{\min} = 0.0676$, we take the parameter $\gamma = 0.07$ for (8). Furthermore, the two simulation targets (0.2 Hz, 86°) and (0.3 Hz, 90°) are also selected in the simulations.

To define a successful experiment, we use the criterion mentioned in [14] if

$$\sum_{i=1}^{2}\left|\widehat{\theta}_i - \theta_i\right| < \left|\theta_1 - \theta_2\right|, \tag{15}$$

where $\widehat{\theta}_i$ and θ_i $(i = 1, 2)$ are, respectively, the estimated and truth values, then the two signals are successfully resolved.

Figures 1 and 2 illustrate the probability of source resolution and their root mean square error (RMSE) versus SNR in Doppler domain, respectively. The conventional space-time IMP, space-time beam-space IMP which combines space-time IMP with discrete fourier transform (DFT) matrix beam-space processing technique [15], and 64 points and 256

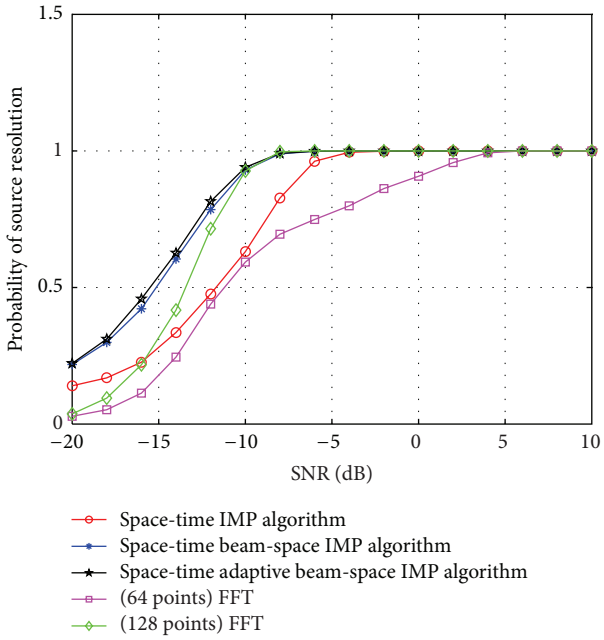

Figure 1: Probability of source resolution versus SNR in Doppler domain.

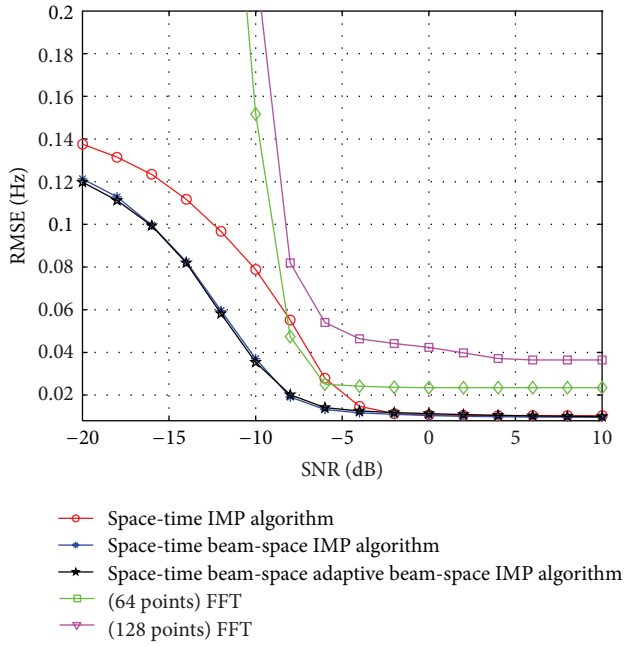

Figure 2: Doppler estimated RMSE versus SNR.

points FFT results are used for the comparison in the figures. We find that the beam-space-based algorithms show better resolution and smaller RMSE than the other algorithms in resolving the two simulation targets. Thus, it is reasonable to conclude that the beam-space-based methods require less observation time but maintain high Doppler accuracy compared with the conventional algorithms. By the way, all the simulation results shown in this section have averaged over 1000 independent Monte Carlo experiments.

Figures 3 and 4 are the probability of source resolution and their RMSE versus SNR in azimuth domain, respectively. According to these figures, the beam-space-based algorithms show better performance than the other algorithms. Comparing these methods, the space-time adaptive beam-space IMP algorithm shows the highest robust and lowest RMSE in resolving the two simulation targets. Thus, it is reasonable to conclude that the proposed algorithm requires smaller antenna array and lower SNR threshold for detection and estimation of multiple signals when compared with the conventional DOA algorithms.

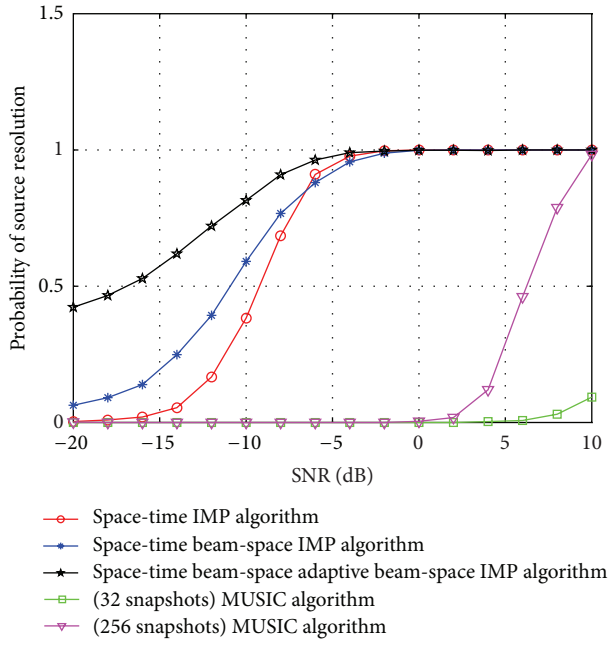

Figure 3: Probability of source resolution versus SNR in azimuth domain.

4. Shipborne HFSWR

4.1. Space-Time Coupling Relation. In [6], Xie et al. had proven that the first-order Bragg spectrums were broadened along the azimuthal directions from the real-data analysis. The authors concluded that there was a space-time coupling relation existed in the first-order Bragg sea echo spectrum of shipborne HFSWR.

Assuming that both the transmitting and the receiving antennas of HFSWR are mounted on a ship which is moving in the positive direction of the x-axis at a constant speed v_s (m/s), as shown in Figure 5.

In the absence of ocean current, the space-time coupling relation in the first-order Bragg sea echo spectrum of shipborne HFSWR can be expressed as follows [16]:

$$f_d = \frac{2v_s}{\lambda}\cos\phi + f_B, \tag{16}$$

where $\phi \in [0, \pi]$ is the azimuth direction, $f_B = \pm\sqrt{g/\pi\lambda}$ are the first-order Bragg frequencies, the positive and negative

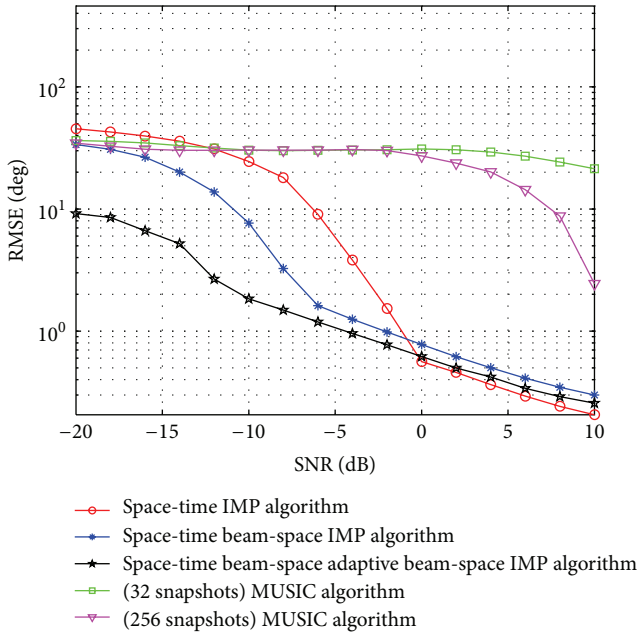

Figure 4: Azimuth estimated RMSE versus SNR.

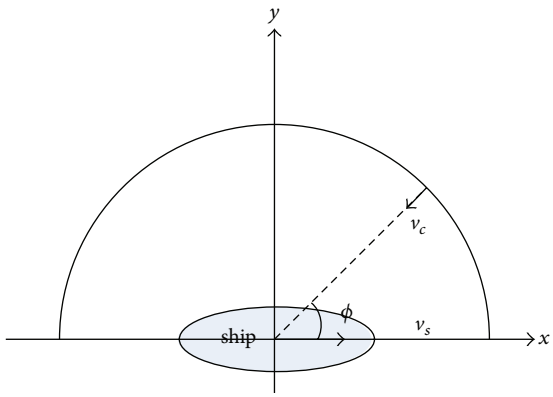

Figure 5: Schematic of shipborne HFSWR and current vector.

signs are, respectively, the Bragg waves moving towards and away from the radar.

4.2. Current Measurement. In the presence of ocean currents, the first-order Bragg lines in (16) are shifted from the theoretical positions. The displacements are proportional to the radial current velocities. Thus, (16) should be rewritten as [17]

$$f_d = \frac{2v_s}{\lambda}\cos\phi + f_B + \frac{2v_c(\phi)}{\lambda}. \quad (17)$$

As shown in (17), the first-order Bragg lines are related to the azimuth directions as well as the speed of ship and currents. Therefore, the first-order Bragg peaks are not only displaced, but also broadened into two pass bands (for slow ship speed case) in the first-order Bragg sea echo spectrum of shipborne HFSWR.

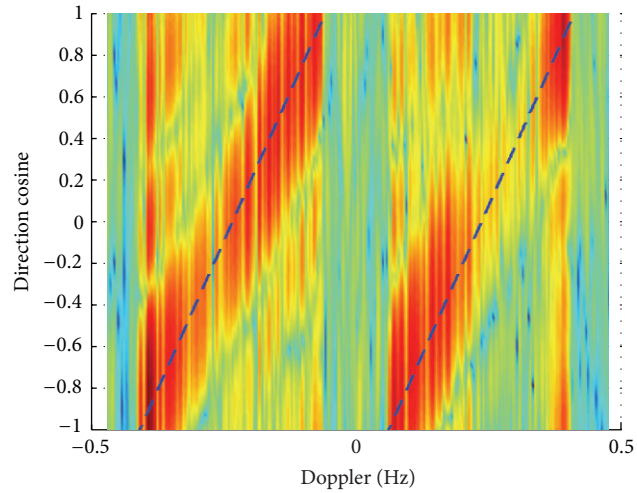

Figure 6: Space-time spectrum of real data processed by DFT and DBF cascaded processing. – – denotes the theoretical value (f_0 = 5.283 MHz, T_p = 0.262 s, d = 14 m).

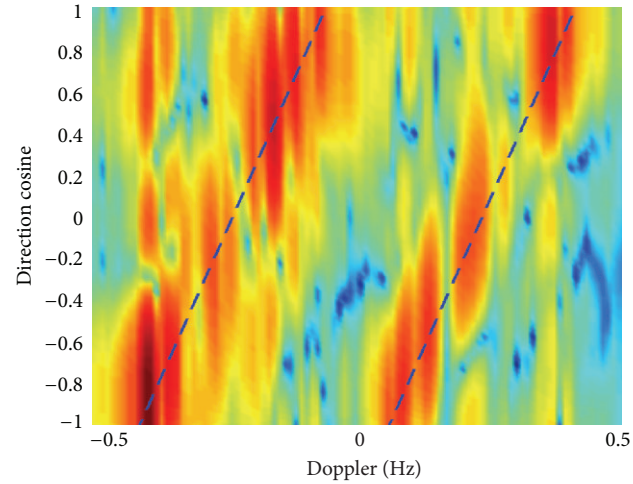

Figure 7: Space-time spectrum of real data processed by IMP.

4.3. Real-Data Analysis. The real data used in this paper was received from the shipborne HFSWR experiments conducted on the Yellow Sea of China on September 8, 1998 [6]. Figures 6 and 7 show the space-time coupling relation in the sixth range bin of the real-data file 1128 (containing 7 channels × 256 samples × 32 range bins and the ship speed was about 4.8 m/s), which is processed through the DFT plus DBF (Digital Beamforming) cascade processing and the proposed algorithm. As shown in the figures, the first-order Bragg lines are broadened along the azimuth directions, which tally well with the theoretical lines in (16). The displacements may be caused by ocean currents or interferences.

Table 1 is an example of the DOA and Doppler estimations. The modified STAP estimator is used to process the above-mentioned real data within the section between the azimuth 40° and 90°. Since there was no information about the sea state recorded during the experiment, we

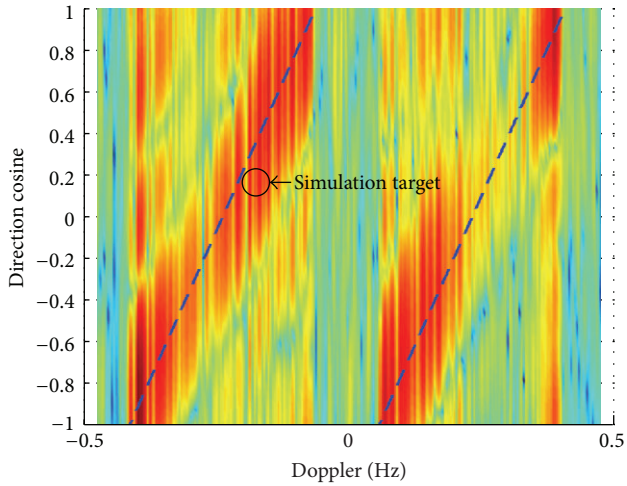

Figure 8: Space-time spectrum of real data adds simulation target.

Table 1: DOA and Doppler estimations.

Target	1	2	3	4	5
DOA (Deg)	62.72	50.12	64.06	52.56	63.35
Doppler (Hz)	−0.1582	−0.1154	−0.1596	−0.1292	−0.1589
Theoretical (Hz)	−0.1541	−0.1220	−0.1577	−0.1278	−0.1558
Velocity (m/s)	0.1166	−0.1869	0.0519	0.0398	0.0885

Table 2: DOA and Doppler estimations.

Target	1	2	3	4	5
DOA (Deg)	82.97	67.33	64.19	81.97	52.56
Doppler (Hz)	−0.1833	−0.1627	−0.1567	−0.1825	−0.1176
Theoretical (Hz)	−0.2130	−0.1668	−0.1581	−0.2100	−0.1238

here assume that the detected targets near the theoretical first-order Bragg lines are considered as ocean currents and their displacements are proportional to their radial velocities. Based on this assumption, five currents have been detected and estimated. All of them are very close to the theoretical first-order Bragg frequencies and their corresponding radial velocities are calculated in the table.

Table 2 is another example for better understanding the robustness of the proposed algorithm, where we add a simulation target (−0.18 Hz, 80°) to the real data used previously, as shown in Figure 8. The added simulation target is detected correctly and the estimations of DOA and Doppler frequency are within 2° and 0.0025 Hz of the true signal position.

5. Conclusion

In this paper, we have introduced a modified space-time adaptive processing estimator that can be used for the detection, estimation, and superresolution of multiple signals. The method combines the conventional IMP method and the existing adaptive beam-space preprocessing techniques yielding a computationally cheap algorithm for estimating the near-surface currents of the ocean from the broadening of the first-order Bragg sea echo spectrum of shipborne HFSWR. The proposed algorithm is validated by simulation results as well as experimental examples.

Acknowledgment

This work is supported by the State Key Program of National Natural Science of China (Grant no. 61132005).

References

[1] S. Tyrberg, O. Svensson, V. Kurupath, J. Engström, E. Strömstedt, and M. Leijon, "Wave buoy and translator motions-on-site measurements and simulations," *IEEE Journal of Oceanic Engineering*, vol. 36, no. 3, pp. 377–385, 2011.

[2] F. J. Bugnon and I. A. Whitehouse, "Acoustic doppler current meter," *IEEE Journal of Oceanic Engineering*, vol. 16, no. 3, pp. 420–426, 1991.

[3] L. Wyatt, "Wave mapping with HF radar," in *Proceedings of the 10th IEEE/OES Working Conference on Current, Waves and Turbulence Measurement (CWTM '11)*, pp. 25–30, Monterey, Calif, USA, March 2011.

[4] J. S. Bathgate, M. L. Heron, and A. Prytz, "A method of swell-wave parameter extraction from HF ocean surface radar spectra," *IEEE Journal of Oceanic Engineering*, vol. 31, no. 4, pp. 812–818, 2006.

[5] B. J. Lipa and D. E. Barrick, "Least-squares methods for the extraction of surface currents from CODAR crossed-loop data: application at ARSLOE," *IEEE Journal of Oceanic Engineering*, vol. 8, no. 4, pp. 226–253, 1983.

[6] J. Xie, Y. Yuan, and Y. Liu, "Experimental analysis of sea clutter in shipborne HFSWR," *IEE Proceedings: Radar, Sonar and Navigation*, vol. 148, no. 2, pp. 67–71, 2001.

[7] I. J. Clarke and G. Spence, "A space-time estimator for the detection and estimation of multiple sinusoidal signals," in *Proceedings of the IEE Colloquium High Resolution Radar and Sonar (Ref. No. 1999/051)*, pp. 9/1–9/6, London, UK, 1999.

[8] A. Chadwick, "Superresolution for high-frequency radar," *IET Radar, Sonar and Navigation*, vol. 1, no. 6, pp. 431–436, 2007.

[9] A. Shaw and N. Wilkins, "Frequency invariant electro-magnetic source location using true time delay beam space processing," in *Proceedings of the 4th IEEE International Symposium on Phased Array Systems and Technology (Array '10)*, pp. 998–1003, Boston, Mass, USA, October 2010.

[10] A. Hassanien, S. A. Elkader, A. B. Gershman, and K. M. Wong, "Convex optimization based beam-space preprocessing with improved robustness against out-of-sector sources," *IEEE Transactions on Signal Processing*, vol. 54, no. 5, pp. 1587–1595, 2006.

[11] A. Hassanien and S. A. Vorobyov, "A robust adaptive dimension reduction technique with application to array processing," *IEEE Signal Processing Letters*, vol. 16, no. 1, pp. 22–25, 2009.

[12] A. Hassanien and S. A. Vorobyov, "New results on robust adaptive beamspace preprocessing," in *Proceedings of the 5th IEEE Sensor Array and Multichannel Signal Processing Workshop (SAM '08)*, pp. 315–319, July 2008.

[13] J. Mather, "The incremental multi-parameter algorithm," in *Proceedings of the 24th Asilomar Conference on Signals, Systems & Computers*, vol. 1, pp. 368–372, 1990.

[14] A. B. Gershman, "Direction finding using beamspace root estimator banks," *IEEE Transactions on Signal Processing*, vol. 46, no. 11, pp. 3131–3135, 1998.

[15] M. D. Zoltowski, G. M. Kautz, and S. D. Silverstein, "Beamspace root-MUSIC," *IEEE Transactions on Signal Processing*, vol. 41, no. 1, pp. 344–364, 1993.

[16] L. R. Wyatt, "Progress in the interpretation of HF sea echo: HF radar as a remote sensing tool," *IEE Proceedings F*, vol. 137, no. 2, pp. 139–147, 1990.

[17] K. W. Gurgel and H. H. Essen, "On the performance of a shipborne current mapping HF radar," *IEEE Journal of Oceanic Engineering*, vol. 25, no. 1, pp. 183–191, 2000.